# INDUCED PLURIPOTENT STEM CELL-BASED DISEASE MODELING AND DRUG DISCOVERY: CAN WE RECAPITULATE CARDIOVASCULAR DISEASE ON A CULTURE DISH?

EDITED BY: Jong-Kook Lee, Shinsuke Yuasa and Masayuki Yazawa
PUBLISHED IN: Frontiers in Cell and Developmental Biology and
Frontiers in Cardiovascular Medicine

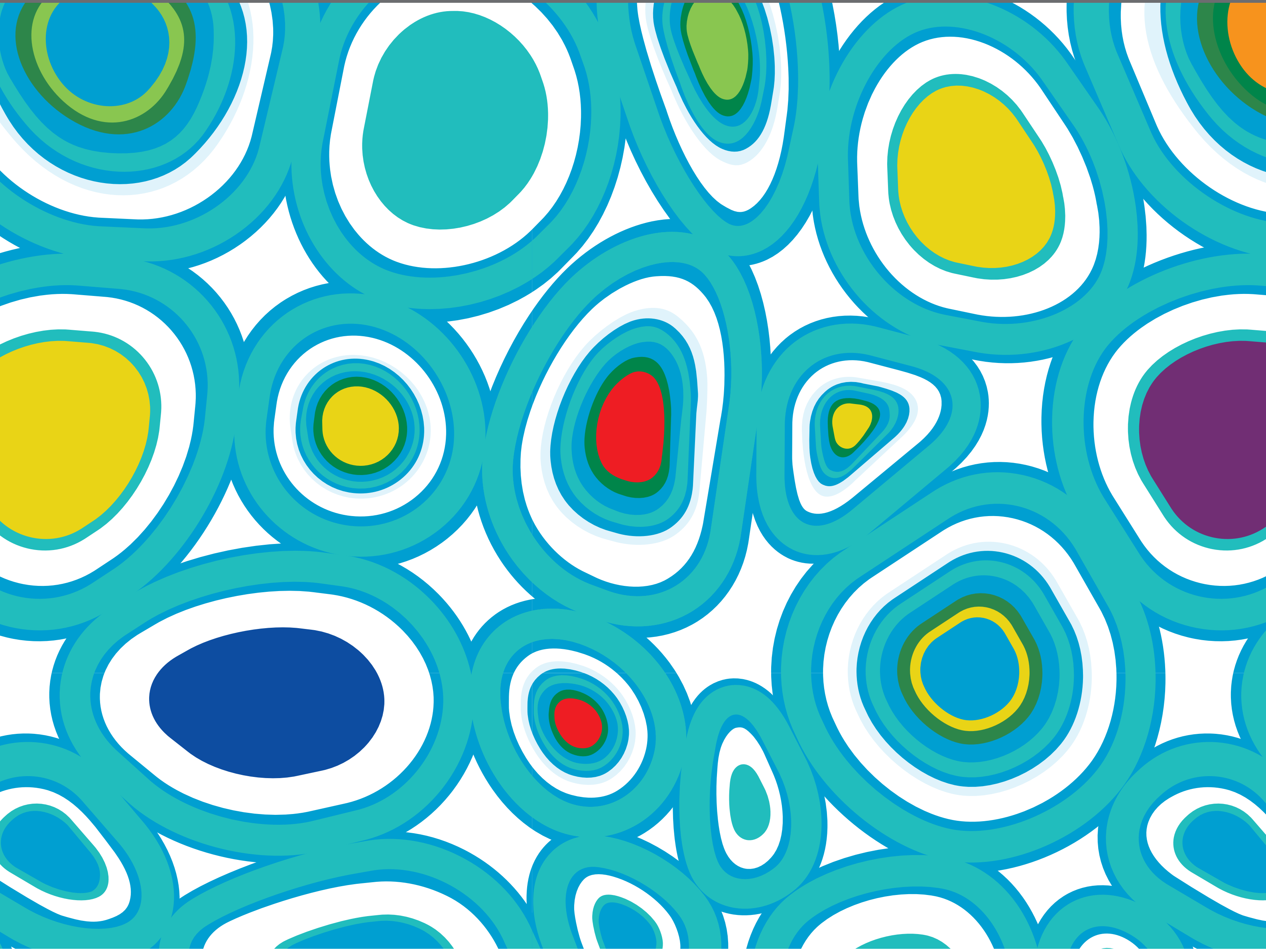

frontiers Research Topics

ISSN 1664-8714
ISBN 978-2-88974-505-0
DOI 10.3389/978-2-88974-505-0

## About Frontiers

Frontiers is more than just an open-access publisher of scholarly articles: it is a pioneering approach to the world of academia, radically improving the way scholarly research is managed. The grand vision of Frontiers is a world where all people have an equal opportunity to seek, share and generate knowledge. Frontiers provides immediate and permanent online open access to all its publications, but this alone is not enough to realize our grand goals.

## Frontiers Journal Series

The Frontiers Journal Series is a multi-tier and interdisciplinary set of open-access, online journals, promising a paradigm shift from the current review, selection and dissemination processes in academic publishing. All Frontiers journals are driven by researchers for researchers; therefore, they constitute a service to the scholarly community. At the same time, the Frontiers Journal Series operates on a revolutionary invention, the tiered publishing system, initially addressing specific communities of scholars, and gradually climbing up to broader public understanding, thus serving the interests of the lay society, too.

## Dedication to Quality

Each Frontiers article is a landmark of the highest quality, thanks to genuinely collaborative interactions between authors and review editors, who include some of the world's best academicians. Research must be certified by peers before entering a stream of knowledge that may eventually reach the public - and shape society; therefore, Frontiers only applies the most rigorous and unbiased reviews.
Frontiers revolutionizes research publishing by freely delivering the most outstanding research, evaluated with no bias from both the academic and social point of view. By applying the most advanced information technologies, Frontiers is catapulting scholarly publishing into a new generation.

## What are Frontiers Research Topics?

Frontiers Research Topics are very popular trademarks of the Frontiers Journals Series: they are collections of at least ten articles, all centered on a particular subject. With their unique mix of varied contributions from Original Research to Review Articles, Frontiers Research Topics unify the most influential researchers, the latest key findings and historical advances in a hot research area! Find out more on how to host your own Frontiers Research Topic or contribute to one as an author by contacting the Frontiers Editorial Office: frontiersin.org/about/contact

# INDUCED PLURIPOTENT STEM CELL-BASED DISEASE MODELING AND DRUG DISCOVERY: CAN WE RECAPITULATE CARDIOVASCULAR DISEASE ON A CULTURE DISH?

Topic Editors:
**Jong-Kook Lee,** Osaka University, Japan
**Shinsuke Yuasa,** Keio University, Japan
**Masayuki Yazawa,** Columbia University, United States

**Citation:** Lee, J.-K., Yuasa, S., Yazawa, M., eds. (2022). Induced Pluripotent Stem Cell-Based Disease Modeling and Drug Discovery: Can We Recapitulate Cardiovascular Disease on a Culture Dish? Lausanne: Frontiers Media SA.
doi: 10.3389/978-2-88974-505-0

# Table of Contents

frontiers
in Cell and Developmental Biology

EDITORIAL
published: 31 January 2022
doi: 10.3389/fcell.2021.831304

# Editorial: Induced Pluripotent Stem Cell-Based Disease Modeling and Drug Discovery: Can We Recapitulate Cardiovascular Disease on a Culture Dish?

*Shinsuke Yuasa*[1]*, *Masayuki Yazawa*[2,3,4] *and Jong-Kook Lee*[5]*

[1]*Department of Cardiology, Keio University School of Medicine, Tokyo, Japan,* [2]*Department of Rehabilitation and Regenerative Medicine, Vagelos College of Physicians and Surgeons, Columbia University, New York City, NY, United States,* [3]*Department of Molecular Pharmacology and Therapeutics, Vagelos College of Physicians and Surgeons, Columbia University, New York City, NY, United States,* [4]*Columbia Stem Cell Initiative, Vagelos College of Physicians and Surgeons, Columbia University, New York City, NY, United States,* [5]*Department of Cardiovascular Regenerative Medicine, Osaka University Graduate School of Medicine, Suita, Japan*

**Keywords: iPS cell, cardiomyocyte, endothelial cell, disease modeling, drug discovery**

**Editorial on the Research Topic**

**Induced Pluripotent Stem Cell-Based Disease Modeling and Drug Discovery: Can We Recapitulate Cardiovascular Disease on a Culture Dish?**

***Edited and reviewed by:***
*Valerie Kouskoff,*
*The University of Manchester,*
*United Kingdom*

***Correspondence:**
*Shinsuke Yuasa*
*yuasa@keio.jp*
*Jong-Kook Lee*
*jlee@cardiology.med.osaka-u.ac.jp*

***Specialty section:***
*This article was submitted to*
*Stem Cell Research,*
*a section of the journal*
*Frontiers in Cell and Developmental*
*Biology*

***Received:*** *08 December 2021*
***Accepted:*** *20 December 2021*
***Published:*** *31 January 2022*

***Citation:***
*Yuasa S, Yazawa M and*
*Lee J-K (2022) Editorial: Induced*
*Pluripotent Stem Cell-Based Disease*
*Modeling and Drug Discovery: Can We*
*Recapitulate Cardiovascular Disease*
*on a Culture Dish?*
*Front. Cell Dev. Biol. 9:831304.*
*doi: 10.3389/fcell.2021.831304*

Since induced pluripotent stem (iPS) cells were first generated in 2006 (Takahashi and Yamanaka, 2006), human iPS cell culture and differentiation into various cell types have been widely established as research platforms for elucidating disease mechanisms and for drug discovery research, and promising cell sources for regenerative medicine (Tanaka et al., 2015). Human iPS cells can be generated from patient's somatic cells, such as skin fibroblasts or blood cells, and the approach using iPS cells offers an ethical advantage over embryonic stem cells (Seki et al., 2010; Seki et al., 2012). There have been a variety of established methods to differentiate many cell types from human iPS cells. In terms of cardiovascular disease, recent accumulating progress has enabled human iPS cells to be efficiently differentiated and purified into subtypes of cardiomyocytes, such as ventricular-, atrial- and nodal-like myocytes, as well as smooth muscle cells and endothelial cells. Based on these advances, disease-specific iPS cells can be generated from patients with intractable cardiovascular diseases, such as inherited cardiomyopathies and arrhythmic disorders. There are substantial reports to elucidate the molecular and cellular mechanisms underlying disease onset and/or the pathophysiological process through various disease-specific iPS cell studies (Yazawa et al., 2011; Egashira et al., 2012; Tanaka et al., 2014; Yasutake et al., 2021). It is also conceivable that iPS cell-derived cardiomyocytes can be utilized for drug screening. For robust applications using human iPS cells for research and clinics, there remains several barriers to be overcome, such as immaturity of iPS cell-derived cardiomyocytes, lack of cell-cell interaction, and absence of organ structure. Many studies still struggle against these issues, which should be solved step by step.

Although iPS cells are supposedly differentiated into any types of cells, most of the differentiated cells that are currently available show immature/fetal feature. To model adult-onset diseases, it is required to mature the differentiated cells. In terms of regeneration therapy, immature cardiomyocyte transplantation may induce arrhythmic event and reduce the efficacy of functional recovery. To mature cardiomyocytes, it is important to understand the difference between embryonic and adult cardiomyocytes. Anzai et al. identified gene sets to monitor the developmental stage in murine and human cardiomyocytes. Comparative transcriptome data analysis of mouse and human hearts in several developmental stages revealed the difference and similarity of two species. While some reports previously showed maturation markers, the proposed markers were either mouse specific or human specific. Importantly, identified gene sets can be markers for both mouse and human cardiomyocyte maturation. Li et al. reported their cardiomyocyte maturation method in human iPS cell-derived cardiomyocytes. Aligned fiber substrate culture induced mature-like properties including rod shape morphology, shortened action potential duration, accelerated conduction velocity, and elevated adult-type gene expression. Contractility of the heart increases as its beating rate is elevated, which is observed in human matured heart, but not in mouse heart and immature iPS cell-derived cardiomyocytes. Izumi-Nakaseko et al. reported that motion directional regulation by electrical pacing could induce positive force-frequency relationship in monolayers of human iPS cell-derived cardiomyocytes. These findings facilitate us to establish sophisticated methods to mature cardiomyocytes and analysis method to understand the molecular and cellular pathophysiological mechanisms underlying heart diseases.

To model human cardiovascular disease and establish regeneration therapy using iPS cell-derived cells, it is essential for us to develop new methods to differentiate iPS cells into cardiovascular cells and understand the properties of iPS cell-derived cells. Although endothelial progenitor cells (EPCs) have been used for vascular regeneration therapy, it is inefficient to obtain EPCs from adult donors. Farkas et al. reported the efficient protocol to differentiate EPCs from human iPS cells. As for EPCs, immature phenotype is not disadvantageous because mature endothelial cells lack angiogenic and vasculogenic potential. However, to use iPS cell-derived immature cardiomyocytes, it is critically important to understand the difference from adult cardiomyocytes. Muscular dystrophies are caused by the mutation in genes encoding the protein involved in the dystrophin-associated protein complex (DAPC). Cardiomyopathies are crucial phenotypes and could be a lethal cause. To model this disease, it is important to examine the expression and function of DAPC in iPS cell-derived cardiomyocytes. Gilbert et al. showed the robust expression of DYSTROPHIN, but the absence of several other DAPC proteins, suggesting that it is still difficult to model the disease using current immature cardiomyocytes. The type 2 ryanodine receptor (RYR2) is an essential $Ca^{2+}$ release channel of sarcoplasmic reticulum (SR) in adult cardiomyocyte. Luo et al., generated *RYR2*−/− iPS cell line and investigated the role of RYR2 in iPS cell-derived cardiomyocytes. RYR2 is not required for cardiomyocyte differentiation but plays a role in survival and contractile function. Without RyR2, another calcium release channel, IP3R mediates $Ca^{2+}$ release as a compensatory mechanism for $Ca^{2+}$ handling in iPS cell-derived cardiomyocyte.

Atrial fibrillation (AF) is the most common cardiac arrhythmic disease. Loss of function and gain of function mutations in *KCNA5*, encoding the Kv1.5α-subunit of the ion channel carrying the atrial-specific ultrarapid delayed rectifier $K^+$ current ($I_{kur}$) are reported in approximately 10% of the patients with AF. Hilderink et al. examined the effects of virtual $I_{Kur}$ injection in iPS cell-derived atrial-like cardiomyocyte because native $I_{Kur}$ density is too small to be examined. Virtual modulation study revealed that a decrease in $I_{Kur}$, mimicking loss-of-function mutations, significantly prolonged action potential duration, but an increase in $I_{Kur}$, mimicking gain-of-function mutations, mildly shortened that in iPS cell-derived atrial-like cardiomyocyte. Long QT (LQT) syndrome is an inherited life-threatening arrhythmogenic disease. Although recent report showed the efficacy of β-blockers on the LQT type3 (LQT3) (Wilde et al., 2016), the pharmacological mechanism remains unclear. Hirose et al. modeled the LQT3 and confirmed the efficacy of β-blocker in the model. Interestingly, β-blocker reduced the disease-causing late sodium current in the presence of guanosine diphosphate βs (GDPβs), an inhibitor of G proteins, suggesting that the effect of β-blocker may be independent of β-adrenergic receptor. Hypoplastic left heart syndrome (HLHS) is a severe form of congenital heart disease. While genetic variants in *MYH6* are reported, the disease mechanism remains unknown. Kim et al. model HLHS by iPS cell-derived cardiomyocytes and showed multiple impairment in cardiomyocyte differentiation, sarcomere organization, slower contraction, and decreased velocity phenotypes. HLHS patients sample showed sarcomere disorganization in atrial but not ventricular tissues. These results suggest that reduced contractility in atrium of HLHS patients may negatively affect hemodynamics and result in the development of a left ventricle.

Cardiovascular diseases are highly prevalent globally as a main cause of death. Several therapeutic strategies have been developed, such as medical therapy, catheter intervention, cardiac assist device, and heart transplantation. However, the therapeutics remain insufficient, and we still require innovative approaches to improve the therapeutics. To develop the therapeutics further, it is important to understand the disease pathogenesis and develop the drug discovery and optimization platforms. Various innovative analysis methods have been proposed, developed, and contributed to the cardiovascular research (Kusumoto et al., 2018; Kusumoto and Yuasa, 2019; Kusumoto et al., 2021). Therefore, the research using human iPS cells with genetic variants is still highly valuable. Continuous iPS cell study will allow us to understand the diseases and develop the innovative therapy to improve human health.

## AUTHOR CONTRIBUTIONS

All authors listed have made a substantial, direct, and intellectual contribution to the work and approved it for publication.

## FUNDING

This work was supported by JSPS KAKENHI (grant numbers 20H03678, 20K08193, 20K08461, 19H03622), Keio University Academic Development Funds for Individual Research, and SENSHIN Medical Research Foundation (SY). The study was partially supported by the Agency for Medical Research and Development, AMED (JP17bm0804008h0001 to J-KL), JSPS KAKENHI (Grant Number JP18H03517), and Co-Create Knowledge for Pharma Innovation with Takeda (COCKPI-T®) Funding (J-KL). This study received funding from Alchemedicine, Inc. (SY), Screen Holdings Co. Ltd (J-KL) and Alpha MED Scientific, Inc. (J-KL). The funders were not involved in the study design, collection, analysis, interpretation of data, the writing of this article or the decision to submit it for publication.

## REFERENCES

Egashira, T., Yuasa, S., Suzuki, T., Aizawa, Y., Yamakawa, H., Matsuhashi, T., et al. (2012). Disease Characterization Using LQTS-specific Induced Pluripotent Stem Cells. *Cardiovasc. Research.95* 95, 419–429. doi:10.1093/cvr/cvs206

Kusumoto, D., Lachmann, M., Kunihiro, T., Yuasa, S., Kishino, Y., Kimura, M., et al. (2018). Automated Deep Learning-Based System to Identify Endothelial Cells Derived from Induced Pluripotent Stem Cells. *Stem Cel Rep.* 10 (10), 1687–1695. doi:10.1016/j.stemcr.2018.04.007

Kusumoto, D., Seki, T., Sawada, H., Kunitomi, A., Katsuki, T., Kimura, M., et al. (2021). Anti-senescent Drug Screening by Deep Learning-Based Morphology Senescence Scoring. Nat Commun. *Jan* 11 (12), 257. doi:10.1038/s41467-020-20213-0

Kusumoto, D., and Yuasa, S. (2019). The Application of Convolutional Neural Network to Stem Cell Biology. *Inflamm. Regen.* 39 (39), 14. doi:10.1186/s41232-019-0103-3

Seki, T., Yuasa, S., and Fukuda, K. (2012). Generation of Induced Pluripotent Stem Cells from a Small Amount of Human Peripheral Blood Using a Combination of Activated T Cells and Sendai Virus. *Nat. Protoc.* 7 (7), 718–728. doi:10.1038/nprot.2012.015

Seki, T., Yuasa, S., Oda, M., Egashira, T., Yae, K., Kusumoto, D., et al. (2010). Generation of Induced Pluripotent Stem Cells from Human Terminally Differentiated Circulating T Cells. *Cell Stem Cell.* 7 (7), 11–14. doi:10.1016/j.stem.2010.06.003

Takahashi, K., and Yamanaka, S. (2006). Induction of Pluripotent Stem Cells from Mouse Embryonic and Adult Fibroblast Cultures by Defined Factors. *Cell.* 126 (126), 663–676. doi:10.1016/j.cell.2006.07.024

Tanaka, A., Yuasa, S., Mearini, G., Egashira, T., Seki, T., Kodaira, M., et al. (2014). Endothelin-1 Induces Myofibrillar Disarray and Contractile Vector Variability in Hypertrophic Cardiomyopathy–Induced Pluripotent Stem Cell–Derived Cardiomyocytes. *J. Am. Heart Assoc.* 3, e001263. doi:10.1161/JAHA.114.001263

Tanaka, A., Yuasa, S., Node, K., and Fukuda, K. (2015). Cardiovascular Disease Modeling Using Patient-specific Induced Pluripotent Stem Cells. *Int. J. Mol. Sci.* 16, 18894–18922. doi:10.3390/ijms160818894

Wilde, A. A. M., Moss, A. J., Kaufman, E. S., Shimizu, W., Peterson, D. R., Benhorin, J., et al. (2016). Clinical Aspects of Type 3 Long-QT Syndrome. *Circulation* 134, 872–882. doi:10.1161/circulationaha.116.021823

Yasutake, H., Lee, J. K., Hashimoto, A., Masuyama, K., Li, J., Kuramoto, Y., et al. (2021). Decreased YAP Activity Reduces Proliferative Ability in Human Induced Pluripotent Stem Cell of Duchenne Muscular Dystrophy Derived Cardiomyocytes. *Sci. Rep.* 11 (11), 10351. doi:10.1038/s41598-021-89603-8

Yazawa, M., Hsueh, B., Jia, X., Pasca, A. M., Bernstein, J. A., Hallmayer, J., et al. (2011). Using Induced Pluripotent Stem Cells to Investigate Cardiac Phenotypes in Timothy Syndrome. *Nature* 471 (471), 230–234. doi:10.1038/nature09855

## ACKNOWLEDGMENTS

We would like to thank all the members in laboratory for helpful discussion.

**Conflict of Interest:** The authors declare that the research was conducted in the absence of any commercial or financial relationships that could be construed as a potential conflict of interest.

frontiers in Cell and Developmental Biology

MINI REVIEW
published: 19 March 2020
doi: 10.3389/fcell.2020.00178

# A Brief Review of Current Maturation Methods for Human Induced Pluripotent Stem Cells-Derived Cardiomyocytes

*Razan Elfadil Ahmed[1], Tatsuya Anzai[1,2], Nawin Chanthra[1] and Hideki Uosaki[1]**

[1] *Division of Regenerative Medicine, Center for Molecular Medicine, Jichi Medical University, Shimotsuke, Japan,*
[2] *Department of Pediatrics, Jichi Medical University, Shimotsuke, Japan*

Cardiovascular diseases are the leading cause of death worldwide. Therefore, the discovery of induced pluripotent stem cells (iPSCs) and the subsequent generation of human induced pluripotent stem cell-derived cardiomyocytes (hiPSC-CMs) was a pivotal point in regenerative medicine and cardiovascular research. They constituted an appealing tool for replacing dead and dysfunctional cardiac tissue, screening cardiac drugs and toxins, and studying inherited cardiac diseases. The problem is that these cells remain largely immature, and in order to utilize them, they must reach a functional degree of maturity. To attempt to mimic *in vivo* environment, various methods including prolonging culture time, co-culture and modulations of chemical, electrical, mechanical culture conditions have been tried. In addition to that, changing the topology of the culture made huge progress with the introduction of the 3D culture that closely resembles the *in vivo* cardiac topology and overcomes many of the limitations of the conventionally used 2D models. Nonetheless, 3D culture alone is not enough, and using a combination of these methods is being explored. In this review, we summarize the main differences between immature, fetal-like hiPSC-CMs and adult cardiomyocytes, then glance at the current approaches used to promote hiPSC-CMs maturation. In the second part, we focus on the evolving 3D culture model – it's structure, the effect on hiPSC-CMs maturation, incorporation with different maturation methods, limitations and future prospects.

**Keywords: induced pluripotent stem cells, human induced pluripotent stem cells-derived cardiomyocytes, regenerative medicine, 3-dimensional culture, engineered heart tissue**

**Edited by:**
*Jong-Kook Lee,*
*Osaka University, Japan*

**Reviewed by:**
*Katriina Aalto-Setälä,*
*University of Tampere, Finland*
*Thomas Owen,*
*Imperial College London,*
*United Kingdom*

***Correspondence:**
*Hideki Uosaki*
*uosaki.hideki@jichi.ac.jp*

**Specialty section:**
*This article was submitted to Stem Cell Research, a section of the journal Frontiers in Cell and Developmental Biology*

**Received:** *13 January 2020*
**Accepted:** *03 March 2020*
**Published:** *19 March 2020*

**Citation:**
*Ahmed RE, Anzai T, Chanthra N and Uosaki H (2020) A Brief Review of Current Maturation Methods for Human Induced Pluripotent Stem Cells-Derived Cardiomyocytes. Front. Cell Dev. Biol. 8:178. doi: 10.3389/fcell.2020.00178*

## INTRODUCTION

The generation of induced pluripotent stem cells (iPSCs) forever changed the field of regenerative medicine, basic and translational biomedical researches (Takahashi et al., 2007). Human iPSCs became an appealing alternative to embryonic stem cells (Bilic and Izpisua Belmonte, 2012; Puri and Nagy, 2012). Since Yamanaka's breakthrough, many efficient protocols have been developed for generating cardiomyocytes derived from human iPSCs (hiPSC-CMs) (Yang et al., 2008; Elliott et al., 2011; Uosaki et al., 2011; Burridge et al., 2012, 2014; Minami et al., 2012; Dunn and Palecek, 2018).

One of the unresolved problems is that hiPSC-CMs remain largely immature when compared to human adult cardiomyocytes. Such immaturity hinders their usage on many aspects, e.g., pharmacological and toxicological screening (Sinnecker et al., 2014) and cardiovascular disease modeling (Jung and Bernstein, 2014; Yang et al., 2015). Transplanting human embryonic stem cell-derived cardiomyocytes (hESC-CMs) or non-human primate iPSC-CMs into non-human primates model of myocardial ischemia-reperfusion resulted in substantial remuscularization, but non-fatal ventricular arrhythmias were observed (Chong et al., 2014; Shiba et al., 2016), which could be a result of transplanting immature PSC-CMs that have automaticity. To address the issue of immaturity, many different approaches have been examined on enhancing the maturation of hiPSC-CMs.

In this review, we briefly list the main differences between immature, fetal-like hiPSC-CMs and adult cardiomyocytes (**Figure 1**). Then, we discuss the current methods used to promote hiPSC-CMs maturation (**Figure 2**). In the second part, we describe the details of the evolving 3D culture model – it's structure, the effect on hiPSC-CMs maturation, incorporation with different maturation methods, limitations, and future perspectives.

## COMPARISON OF hiPSC-CMs AND ADULT CARDIOMYOCYTES TO EVALUATE MATURITY

Researchers in the stem cell field agree that hiPSC-CMs are immature, but there is no consensus about how to evaluate their degree of maturation. Therefore, in addition to developing ways to increase iPSC-CMs maturity, methods on how to assess maturation are required. Here, we summarize characteristics of adult cardiomyocytes and differences to hiPSC-CMs (**Figure 1**).

### Morphology and Structure

It takes up to 10 years for cardiomyocytes to acquire adult phenotypes in structure and ploidy in a human heart (Peters et al., 1994; Bergmann et al., 2009; Vreeker et al., 2014). Adult cardiomyocytes are well-aligned, rod-like, multinucleated/tetraploid cells, with highly organized sarcomeres, well developed sarcoplasmic reticulum (SR) and transverse tubules (T-tubules) (Peters et al., 1994; Bergmann et al., 2009; Yang et al., 2014a), and have intercalated disks with mature mechanical and electrical junctions (Dhamoon and Jalife, 2005; Zwi et al., 2009; Ma et al., 2011; Kamakura et al., 2013; Vreeker et al., 2014; Denning et al., 2016). Such phenotypical maturation is still lacking in hiPSC-CMs, which tend to be small, mononucleated, rounded cells with disorganized sarcomere. Moreover, they have shorter sarcomeres, poorly developed SR, and no T-tubules (Yang et al., 2014a; Denning et al., 2016). Structural features can be used to evaluate the degree of hiPSC-CMs maturity because some of these features are characteristic to mature cardiomyocytes.

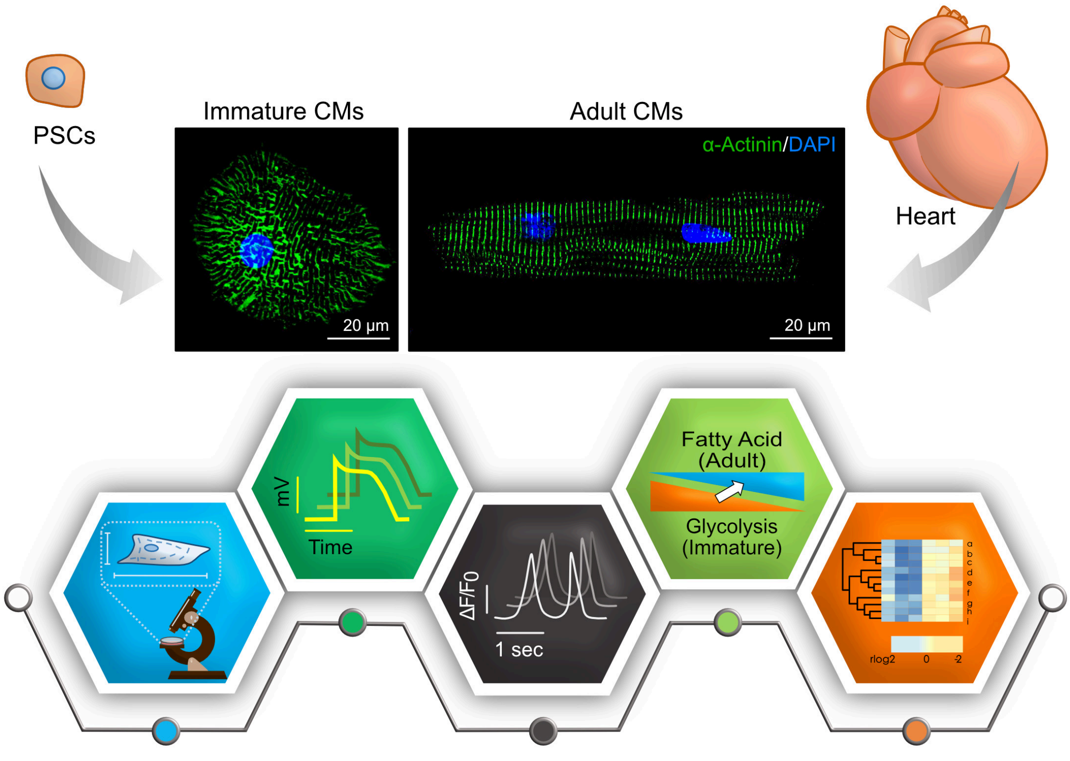

**FIGURE 1 |** Key features to characterize cardiomyocyte maturity. Compared to adult cardiomyocytes (CMs), many aspects – morphology and structure, electrophysiology, calcium handling, metabolism, and transcriptome – are different in immature PSC-CMs. Representative immunostainings of cardiomyocytes derived PSCs and adult mouse hearts are shown in upper panels (Green, α-actinin; Blue, DAPI). Pictograms shown in lower panels represent each aspect.

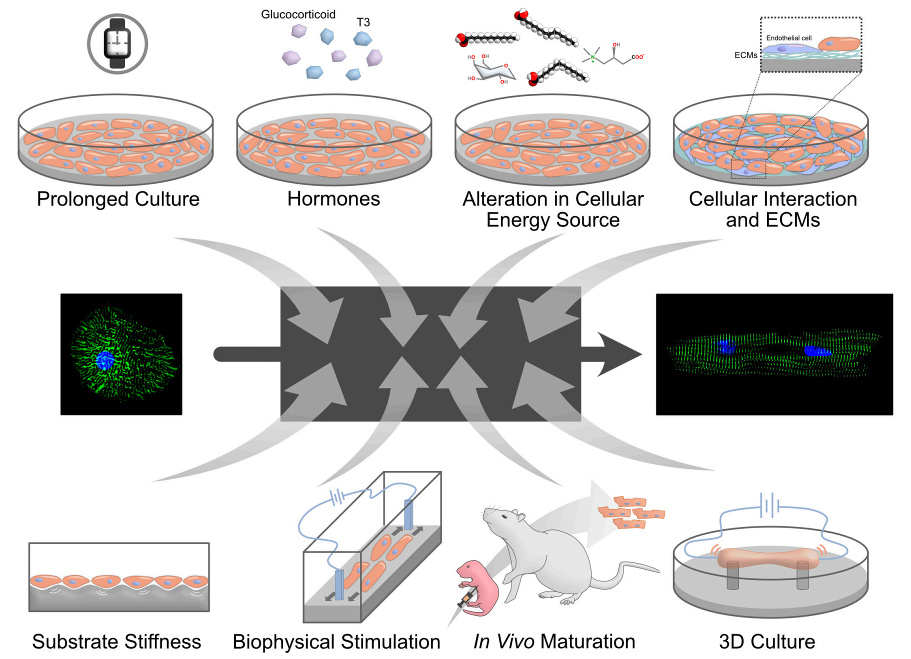

**FIGURE 2 |** Methods to mature PSC-CMs. Many different approaches to mature PSC-CMs have been proposed. However, it is largely unknown why these signals control cardiomyocyte maturation and how mature PSC-CMs can achieve as a result. A black box shown in the middle represents the unelucidated mechanisms.

## Physical and Electrophysiological Properties

Adult cardiomyocytes only beat when stimulated with a force around 40–80 $mN/mm^2$, conduction velocity around 60 cm/s and upstroke velocity about 150–350 V/s. In hiPSC-CMs, these parameters are around 0.08–4 $mN/mm^2$, 10–20 cm/s, and 10–50 V/s, consecutively (Denning et al., 2016). Moreover, hiPSC-CMs display mixed action potential (AP) morphologies that can be categorized as atrial, nodal, or ventricular-like AP (Ma et al., 2011). Although hiPSC-CMs generate important cardiac currents such as $I_{Na}$, $I_{Ca,L}$ $I_{to}$, $I_{Kr}$, and $I_{Ks}$, they lack $I_{K1}$ that is essential for stabilization of the resting potential (Dhamoon and Jalife, 2005; Hoekstra et al., 2012; Knollmann, 2013). This deficiency might be particularly important when hiPSC-CMs are used to study long QT syndrome. Human *ether-a-go-go* related gene (hERG) encode a subunit of $I_{Kr}$ channel, and mutation in hERG or blockade of $I_{Kr}$ cause long QT syndrome. Without $I_{K1}$, hiPSC-CMs rely on $I_{Kr}$ for the maximum diastolic potential (MDP) that is markedly depolarized with $I_{Kr}$ blockers (Doss et al., 2012). The other characteristic is the spontaneous beatings of hiPSC-CMs. $I_f$ current generated by HCN4, which is restricted to pacemaker cells *in vivo*, depolarize MDP and make hiPSC-CMs beat (Yanagi et al., 2007). Measuring the electrophysiological parameters and assessing the generation of $I_{K1}$ current is a promising tool that can be utilized to assess the maturation of hiPSC-CMs, though it would be technically challenging.

## Calcium Handling

In adult cardiomyocytes, T-tubules and SR are well developed to regulate $Ca^{2+}$ induced Ca release (CICR) and fast excitation-contraction coupling (ECC). The inflow of $Ca^{2+}$ via L-type channels triggers the release of $Ca^{2+}$ from the SR through the ryanodine receptor (RyR) channels (Bers, 2002). T-tubules, invagination of the cell membrane, near L-type $Ca^{2+}$ channel and RyR in adult cardiomyocytes. In the relaxation phase, $Ca^{2+}$ is returned to the SR through sarco/endoplasmic reticulum $Ca^{2+}$ ATPase (SERCA) and is extruded from the cell through the $Na^+$–$Ca^{2+}$ exchanger (NCX). The sharp and uniform increase of intracellular $Ca^{2+}$ concentration in adult cardiomyocytes is important for the synchronized contraction in multiple sarcomeres (Scuderi and Butcher, 2017; Steinhoff et al., 2017). In hiPSC-CMs, T-tubules are absent and SR is underdeveloped with low expression of SERCA and other key proteins. As a result, hiPSC-CMs rely on L-type channels for the increase of $Ca^{2+}$ and ECC is slow (Pesl et al., 2017; Veerman et al., 2017).

## Metabolism

In adult cardiomyocytes, mitochondria volume increases, and the oxidative capacity is increased, which represents to switch in metabolic substrates from glucose to fatty acid (Lopaschuk and Jaswal, 2010). To examine glycolysis and fatty acid oxidation, the oxygen consumption rate (OCR) and the extracellular acidification rate (ECAR) are often used, respectively (Rana et al., 2012). During early heart development, around 80% of energy is produced by glycolysis. When cardiomyocytes become mature, fatty acid β-oxidation increases and becomes a major source for energy production. In a rabbit, the metabolic switch occurs during early postnatal growth (Lopaschuk et al., 1991). As hiPSC-CMs remain immature, they rely on glycolysis rather than fatty acid β-oxidation (Rana et al., 2012; Kim et al., 2013; Kikuchi et al., 2015; Correia et al., 2017).

## Gene Expression

Identifying the genes involved in human cardiomyocytes maturation is still an ongoing process. But the overall expression pattern of maturation-related genes identified in mice and humans are mostly similar (DeLaughter et al., 2016; Uosaki and Taguchi, 2016). Isoform transitions of sarcomeric genes occur from fetal to adult period. Cardiac myosin heavy chain (*MHC*, also known as *MYH*) has two isoforms. These are α-isoform (α-*MHC*, also known as *MYH6*) and β-isoform (β-*MHC*, also known as *MYH7*). In adult cardiomyocytes, the β-isoform is predominant. To note, the isoform switch occurs from β-isoform to α-isoform in mouse hearts. Troponin I (TnI) has three isoforms [slow skeletal (ssTnI), fast skeletal (fsTnI), and cardiac (cTnI)] encoded by *TNNI1*, *TNNI2*, and *TNNI3*, respectively. In adult cardiomyocytes, cTnI is highly expressed although ssTnI is the primary isoform in hiPSC-CMs. Titin (*TTN*) has three major isoforms. These are N2B, N2BA and fetal cardiac titin (FCT). In adult cardiomyocytes, N2B is mainly expressed whereas N2BA is predominant in hiPSC-CMs (Yin et al., 2015; Denning et al., 2016). Moreover, hiPSC-CMs show low expression levels of important cardiac genes such as *SERCA2* (sarcoplasmic reticulum ATPase), *CAV3* (caveolin 3), *KCNH2* (potassium voltage-gated channel), and other adult cardiomyocytes genes (Karakikes et al., 2015; van den Berg et al., 2015; Denning et al., 2016).

To assess hiPSC-CMs maturation, measuring the *TNNI3* to *TNNI1* ratio is one way (Bedada et al., 2014). To achieve more precise measurement of maturation, transcriptome-based approaches were proposed, including a gene regulatory network-based (Uosaki et al., 2015) and a relative expression orderings-based scoring method (Chen et al., 2019). Single-cell transcriptome analysis could also predict the developmental ages of cardiomyocytes. However, most of these approaches are limited to mouse PSC-CMs as limited transcriptome data is available for full-spectrum of human developing hearts including late fetal and early postnatal periods (van den Berg et al., 2015; Kreipke et al., 2016; Tiburcy et al., 2017; Cardoso-Moreira et al., 2019). Thus, further work must be done to generate a valid, agreed upon, maturation index for hiPSC-CMs.

# CUES TO PROMOTE MATURATION OF hiPSC-CMs

In order to be able to fully utilize hiPSC-CMs for clinical or research purposes, especially for drug discoveries and disease modeling, they must acquire an adult-like maturation state. In this part, we discuss different approaches used to enhance the maturation of hiPSC-CMs (**Figure 2**).

## Prolonged Culture Time

It takes years for cardiomyocytes to fully mature *in vivo* (Vreeker et al., 2014), which prompted a hypothesis that prolonged culture time would promote maturation of hiPSC-CMs. To date, hiPSC-CMs were cultured up to a full year to test their maturity (Kamakura et al., 2013; Lundy et al., 2013; Lewandowski et al., 2018). With prolonged culture, hiPSC-CMs displayed more mature phenotypes in morphology (larger cell size), structure (myofibril density, alignment, microscopically visible sarcomere), and physiology (calcium handling and β-adrenergic response). The cells expressed maturation-related cardiac genes such as *MYH7* with isoform switch (Lundy et al., 2013; Lewandowski et al., 2018). Interestingly, extending the cultures to 180 days resulted in more tightly packed myofibrils with the appearance of mature Z-, A-, H-, and I-bands, but not M-bands. M-bands, a key feature of sarcomere structure, are finally developed after 360 days of culture (Kamakura et al., 2013). These results consolidate the fact that prolonged culture generates more mature cardiomyocytes. However, it poses a question if it is possible to yield cells mature enough in a realistic, and financially appropriate culture time frame.

## Biochemical Cues

### Hormones

Thyroid hormone, known to have a crucial role in cardiac development and cardiovascular physiology (Klein and Ojamaa, 2001), displayed strong enhancement of hiPSC-CM maturation (Yang et al., 2014b). Triiodothyronine (T3) treatment makes hiPSC-CMs bigger, more elongated morphology with longer sarcomeres. T3-treated hiPSC-CMs displayed increased mitochondrial activity and improved calcium handling along with higher contractile force.

Glucocorticoids are essential for maturation of fetal heart structure and function. Endogeneous glucocorticoids work by stimulating glucocorticoid receptor (GR) on fetal cardiomyocytes/vascular smooth muscle to promote myofibril assembly and organization (Rog-Zielinska et al., 2013, 2015). Adding glucocorticoid analog, dexamethasone, to T3 in culture further improve hiPSC-CMs maturation (Parikh et al., 2017).

These results highlight the importance of these chemical cues and call for studying more molecules and combinations that may further enhance maturation of cardiomyocytes.

### Alterations in Cellular Energy Source

A hallmark of postnatal cardiomyocyte maturation is switching their metabolism from glycolysis to fatty acid oxidation (Yang et al., 2019). Recently, the glucose-free and lactate-containing medium were identified to eliminate non-cardiomyocyte and enrich hiPSC-CMs (Tohyama et al., 2013; Burridge et al., 2014), while hiPSC-CMs are usually cultured in glucose-containing medium. Replacing glucose with galactose and fatty acids – more specifically, palmitate, oleic acid, linoleic acid, and carnitine – enhanced maturation of hiPSC-CMs (Correia et al., 2017; Nakano et al., 2017; Horikoshi et al., 2019; Yang et al., 2019). The switch of energy source not only increased mitochondrial number and metabolisms but also enhanced morphological, structural and physiological maturation. On the other hand, culturing hiPSC-CMs in high glucose medium inhibits their structural and functional maturation by promoting nucleotide biosynthesis (Nakano et al., 2017), which is attributed to a reduction of cardiac glucose uptake and increased nucleotide deprivation during late gestational and early postnatal stages.

## Cellular Interaction and Extracellular Matrices

Cells interact with each other through direct cellular contact or indirect paracrine factors secreted by the neighboring cells in a heart, and cellular interaction has been implicated in cardiac maturation (Talman and Kivelä, 2018; Yoshida et al., 2018; Abecasis et al., 2019). To mimic these cellular interactions *in vitro*, hiPSC-CMs were cocultured with non-cardiomyocytes, such as human mesenchymal stem cells (MSCs) and endothelial cells. Human MSCs secrete VEGF, bFGF, SDF-1, and GM-CSF to mediate differentiation and electrical coupling of hiPSC-CMs (Yoshida et al., 2018). In contrast, endothelial cells express extracellular matrices (ECMs; collagens I and III, fibronectin, thrombospondin-4) to increase sarcomere length of hiPSC-CMs (Abecasis et al., 2019). ECMs alone had some effects on enhancing structural and functional maturation of hiPSC-CMs (Chun et al., 2015; Herron et al., 2016; Ogasawara et al., 2017).

## Substrate Stiffness

Extracellular matrices regulate tissue stiffness, and the stiffness of a heart increases gradually *in vivo* as a result of collagen accumulation (Jacot et al., 2010). This process increases the ability of the heart to pump blood due to its increased stiffness. Compared to hearts (∼10 kPa), cell culture dishes are much stiffer (∼1 MPa), which prompted a hypothesis that soft matrices might be better for the maturation of hiPSC-CMs. Polydimethylsiloxane (PDMS), hydrogels or polyacrylamide (PAA) were often used to create such culture conditions. Soft surfaces (6∼10 kPa) tuned sarcomere tension and contractility, and hiPSC-CMs on it generated more force (0.1 μN) than those on a hard surface (35 kPa, 0.01–2 μN) (Ribeiro et al., 2015). PDMS and PAA are also used to regulate topology of cell morphology and forcing hiPSC-CMs into rectangular shape results in better maturation (Thavandiran et al., 2013; McCain et al., 2014; Ribeiro et al., 2015). In the agreement with this, the vascular structure also forces hiPSC-CMs in a rectangular shape and made them more mature (Vuorenpää et al., 2017).

## Biophysical Stimulation

Biophysical stimulation is absent under a standard culture condition. In a heart, cardiomyocytes are regularly exposed to electrical stimulation and mechanical stress. Applying a continuous electrical stimulation yielded hiPSC-CMs with rod-like morphology, enhanced cellular alignment, and more organized sarcomeres (Chan et al., 2013). Furthermore, subjecting combined synchronized electrical and mechanical stimulation on hiPSC-CM resulted in enhanced localization of N-cadherin toward cell membrane, sarcomere shortening, and reduced transmembrane calcium current, suggesting more mature phenotype (Kroll et al., 2017).

## *In vivo* Maturation

Instead of mimicking *in vivo* environment *in vitro*, an *in vivo* environment can be used to provide all necessary signals including unknown ones to hiPSC-CMs. There are some disagreements what developmental stages of the heart can be appropriate – neonate, adult, or adult heart after infarction (Funakoshi et al., 2016; Cho et al., 2017; Kadota et al., 2017), however, hiPSC-CMs *in vivo* are more matured than ones *in vitro*. Transplantation to neonatal hearts generated adult-like mature hiPSC-CMs within 2 months of transplantation, suggesting that the maturation speed is accelerated in a rat heart and it is defined by non-cell autonomous manner. Furthermore, hiPSC-CMs from a patient of arrhythmogenic right ventricular dysplasia/cardiomyopathy recapitulated disease phenotypes with the neonatal transplantation method (Cho et al., 2017).

# 3D CULTURE

Cells are aligned three-dimensionally *in vivo* rather than a monolayer. In the last decade, 3D culture methods have been advanced and become an appealing alternative to the conventional 2D monolayer culture for the maturation of hiPSC-CMs. As 3D tissues also resemble native cardiac architecture, 3D tissues of dilated cardiomyopathy hiPSC-CMs could recapitulate disease phenotypes that 2D cultures failed (Hinson et al., 2015). Here, we discuss the usefulness of 3D cultures on the maturation of hiPSC-CMs.

## General Concepts of 3D Culture

Conventional 2D cultures fail to recapitulate the complexity of the *in vivo* cellular crosstalk, tissue architectures, and extracellular microenvironments with forced and unwanted apical-basal polarity. On the other hand, 3D cultures have more similarity to the *in vivo* extracellular microenvironment, support better cellular interactions, and allows for biochemical and physical stimuli to reach the cells in an evenly distributed manner (Duval et al., 2017; Mirbagheri et al., 2019). In 3D cultures, hiPSC-CMs display structural, functional and metabolic maturation compared to that in 2D cultures (Huethorst et al., 2016; Lemoine et al., 2017; Correia et al., 2018; Ulmer et al., 2018). They show improved myofibrillar alignment and sarcolemma remodeling which led to better $Ca^{2+}$ handling (Silbernagel et al., 2020). Moreover, hiPSC-CMs in 3D culture exhibited faster maturation analyzed by transcriptome (Branco et al., 2019), while 2D cultures hinder the maturation or cause maturation arrest (Uosaki et al., 2015).

Different strategies are used to produce 3D cardiac tissues. One way is seeding hiPSC-CMs in to designed scaffolds or embedding them in hydrogel (Lemoine et al., 2017; Correia et al., 2018; Dattola et al., 2019; Silbernagel et al., 2020). To produce scaffold, photolithography is often used, however, it requires clean room and specialized equipment that are not often available for biomedical research labs (Hoang et al., 2018). 3D printing technologies have been evolving rapidly, and digital light processing (DLP)-based printing is now used to fabricate scaffolds or molds to embed cells in hydrogel directly in a cell culture dish (Ma et al., 2019). Another method is layering hiPSC-CMs into multi-layered cardiac tissue constructs, which successfully recapitulate Torsade de Pointes *in vitro* (Kawatou et al., 2017).

Overall, there is a growing effort to learn the appropriate technology and materials to design a reproducible, efficient and affordable 3D culture system, such advancement will be a great step toward the generation of mature, functional cardiomyocytes.

## Enhancing hiPSC-CMs Maturation in 3D Culture Systems

Although 3D cultures of hiPSC-CMs have great potential to make more matured cardiomyocytes, it is insufficient to do so by itself, and a combination of the above-mentioned maturation-promoting methods worked in 2D must be utilized within a 3D setting, which includes cell-cell interaction (e.g., fibroblasts) (Zhang et al., 2017; King et al., 2019; Valls-Margarit et al., 2019; Yan et al., 2019), hormones (Balistreri et al., 2017; Huang et al., 2020), and electrical and physiological stimulation. Below, we will provide a brief review of the electrical and physiological stimulation applied to 3D cultures to reach the ultimate goal.

### 3D Cultures With Biophysical Stimuli

One of the epoch-making studies was done by Nunes et al. (2013). Embedding hiPSC-CMs with collagen gel into PDMS channel to form a wire-like structure and exposing the tissues to electrical stimuli generate functionally more matured cardiac tissue. To further augment electrical conduction, electrically conductive silicon nanowires or carbon nanotubes were incorporated into hiPSC-CMs spheroids to form an electrically conductive environment (Tan et al., 2015; Roshanbinfar et al., 2019) that is later enhanced by the addition of an exogenous electrical stimulation (Richards et al., 2016). The regimens of electrical stimulation were explored by several groups to achieve T-tubule formation and positive force-frequency relationships (Hirt et al., 2014; Godier-Furnémont et al., 2015). More sophisticated stimulation has been explored, and a high-intensity training regimen of electrical current with gradually increasing frequency, from 2 to 6 Hz within 2 weeks, followed by another week of stimulation at 2 Hz, achieved hiPSC-CMs with adult-like gene expression, well-developed ultrastructure including T-tubule, better calcium handling and contraction force (Ronaldson-Bouchard et al., 2018).

In the mechanical aspect, passive stretch or application of afterload on 3D tissue of hiPSC-CMs (namely, engineered heart muscle or engineered heart tissue) promoted its structural and functional maturation (Abilez et al., 2018; Leonard et al., 2018). A passive stretch is enough to facilitate metabolic switches in hiPSC-CMs (Ulmer et al., 2018). Moderate afterloads are beneficial on cardiomyocyte maturation, while higher afterloads may be detrimental and cause pathological changes (Leonard et al., 2018). The combinations of both electrical and mechanical stimuli – either cyclic stretch or static stress – were also explored (Ruan et al., 2016; LaBarge et al., 2019). In such conditions, hiPSC-CMs displayed a more matured signature than a single stimulus.

## CONCLUSION AND FUTURE PROSPECTS

As we summarized, the maturity of hiPSC-CMs is getting better by numerous efforts. However, methods still need further improvement to reach the desired degree of maturity. Other aspects lacked in this field are to determine definitive maturity of hiPSC-CMs rather than relative measurements and some mechanistic insights why cells are maturing with particular stimuli. Transcriptome-based assay followed by bioinformatics would be one way to define the maturity and uncover mechanistic insights (Uosaki et al., 2015), though more transcriptome data of human hearts in late fetus and postnatal periods is required. As we noted, human cardiomyocytes require years to complete their maturation in a human heart (Vreeker et al., 2014). Therefore, a question remains to be elucidated if and how we can generate adult-like mature hiPSC-CMs at an affordable time and cost. In a specific condition *in vivo*, the maturation process is accelerated (Cho et al., 2017), thus, hopefully, the issue will be resolved in the near future.

## AUTHOR CONTRIBUTIONS

RA summarized the publications for this mini review and drafted the manuscript. RA, TA, and HU wrote the manuscript. RA and NC drew the figures. HU finalized the manuscript.

## FUNDING

This work was supported by Fund for the Promotion of Joint International Research [Fostering Joint International Research (B), 19KK0219] from Japan Society for the Promotion of Science, Takeda Science Foundation, and the Grant for Basic Research of the Japanese Circulation Society to HU.

## ACKNOWLEDGMENTS

We would like to thank all the members in Division of Regenerative Medicine, Center for Molecular Medicine, Jichi Medical University for helpful discussion.

## REFERENCES

Abecasis, B., Gomes-Alves, P., Rosa, S., Gouveia, P. J., Ferreira, L., Serra, M., et al. (2019). Unveiling the molecular crosstalk in a human induced pluripotent stem cell-derived cardiac model. *Biotechnol. Bioeng.* 116, 1245–1252. doi: 10.1002/bit.26929

Abilez, O. J., Tzatzalos, E., Yang, H., Zhao, M.-T., Jung, G., Zöllner, A. M., et al. (2018). Passive stretch induces structural and functional maturation of engineered heart muscle as predicted by computational modeling: structural and functional maturation of EHMs. *Stem Cells* 36, 265–277. doi: 10.1002/stem.2732

Balistreri, M., Davis, J. A., Campbell, K. F., Da Rocha, A. M., Treadwell, M. C., and Herron, T. J. (2017). Effect of glucose on 3D cardiac microtissues derived from human induced pluripotent stem cells. *Pediatr. Cardiol.* 38, 1575–1582. doi: 10.1007/s00246-017-1698-2

Bedada, F. B., Chan, S. S.-K., Metzger, S. K., Zhang, L., Zhang, J., Garry, D. J., et al. (2014). Acquisition of a quantitative, stoichiometrically conserved ratiometric marker of maturation status in stem cell-derived cardiac myocytes. *Stem Cell Rep.* 3, 594–605. doi: 10.1016/j.stemcr.2014.07.012

Bergmann, O., Bhardwaj, R. D., Bernard, S., Zdunek, S., Barnabé-Heider, F., Walsh, S., et al. (2009). Evidence for cardiomyocyte renewal in humans. *Science* 3, 98–102. doi: 10.1126/science.1164680

Bers, D. M. (2002). Cardiac excitation-contraction coupling. *Nature* 10, 198–205.

Bilic, J., and Izpisua Belmonte, J. C. (2012). Concise review: induced pluripotent stem cells versus embryonic stem cells: close enough or yet too far apart? *Stem Cells* 30, 33–41. doi: 10.1002/stem.700

Branco, M. A., Cotovio, J. P., Rodrigues, C. A. V., Vaz, S. H., Fernandes, T. G., Moreira, L. M., et al. (2019). Transcriptomic analysis of 3D cardiac differentiation of human induced pluripotent stem cells reveals faster cardiomyocyte maturation compared to 2D culture. *Sci. Rep.* 9:9229. doi: 10.1038/s41598-019-45047-9

Burridge, P. W., Keller, G., Gold, J. D., and Wu, J. C. (2012). Production of de novo cardiomyocytes: human pluripotent stem cell differentiation and direct reprogramming. *Cell Stem Cell* 10, 16–28. doi: 10.1016/j.stem.2011.12.013

Burridge, P. W., Matsa, E., Shukla, P., Lin, Z. C., Churko, J. M., Ebert, A. D., et al. (2014). Chemically defined generation of human cardiomyocytes. *Nat. Methods* 11, 855–860. doi: 10.1038/nmeth.2999

Cardoso-Moreira, M., Halbert, J., Valloton, D., Velten, B., Chen, C., Shao, Y., et al. (2019). Gene expression across mammalian organ development. *Nature* 571, 505–509. doi: 10.1038/s41586-019-1338-5

Chan, Y.-C., Ting, S., Lee, Y.-K., Ng, K.-M., Zhang, J., Chen, Z., et al. (2013). Electrical stimulation promotes maturation of cardiomyocytes derived from human embryonic stem cells. *J. Cardiovasc. Trans. Res.* 6, 989–999. doi: 10.1007/s12265-013-9510-z

Chen, R., He, J., Wang, Y., Guo, Y., Zhang, J., Peng, L., et al. (2019). Qualitative transcriptional signatures for evaluating the maturity degree of pluripotent stem cell-derived cardiomyocytes. *Stem Cell Res. Ther.* 10:113. doi: 10.1186/s13287-019-1205-1

Cho, G.-S., Lee, D. I., Tampakakis, E., Murphy, S., Andersen, P., Uosaki, H., et al. (2017). Neonatal transplantation confers maturation of PSC-derived cardiomyocytes conducive to modeling cardiomyopathy. *Cell Rep.* 18, 571–582. doi: 10.1016/j.celrep.2016.12.040

Chong, J. J. H., Yang, X., Don, C. W., Minami, E., Liu, Y.-W., Weyers, J. J., et al. (2014). Human embryonic-stem-cell-derived cardiomyocytes regenerate non-human primate hearts. *Nature* 510, 273–277. doi: 10.1038/nature13233

Chun, Y. W., Balikov, D. A., Feaster, T. K., Williams, C. H., Sheng, C. C., Lee, J.-B., et al. (2015). Combinatorial polymer matrices enhance in vitro maturation of human induced pluripotent stem cell-derived cardiomyocytes. *Biomaterials* 67, 52–64. doi: 10.1016/j.biomaterials.2015.07.004

Correia, C., Koshkin, A., Duarte, P., Hu, D., Carido, M., Sebastião, M. J., et al. (2018). 3D aggregate culture improves metabolic maturation of human pluripotent stem cell derived cardiomyocytes. *Biotechnol. Bioeng.* 115, 630–644. doi: 10.1002/bit.26504

Correia, C., Koshkin, A., Duarte, P., Hu, D., Teixeira, A., Domian, I., et al. (2017). Distinct carbon sources affect structural and functional maturation of cardiomyocytes derived from human pluripotent stem cells. *Sci. Rep.* 7:8590. doi: 10.1038/s41598-017-08713-4

Dattola, E., Parrotta, E. I., Scalise, S., Perozziello, G., Limongi, T., Candeloro, P., et al. (2019). Development of 3D PVA scaffolds for cardiac tissue engineering and cell screening applications. *RSC Adv.* 9, 4246–4257. doi: 10.1039/c8ra08187e

DeLaughter, D. M., Bick, A. G., Wakimoto, H., McKean, D., Gorham, J. M., Kathiriya, I. S., et al. (2016). Single-cell resolution of temporal gene expression during heart development. *Dev. Cell.* 39, 480–490. doi: 10.1016/j.devcel.2016.10.001

Denning, C., Borgdorff, V., Crutchley, J., Firth, K. S. A., George, V., Kalra, S., et al. (2016). Cardiomyocytes from human pluripotent stem cells: from laboratory curiosity to industrial biomedical platform. *Biochim. Biophys. Acta* 1863(7 Pt B), 1728–1748. doi: 10.1016/j.bbamcr.2015.10.014

Dhamoon, A. S., and Jalife, J. (2005). The inward rectifier current (IK1) controls cardiac excitability and is involved in arrhythmogenesis. *Heart Rhythm* 2, 316–324. doi: 10.1016/j.hrthm.2004.11.012

Doss, M. X., Diego, J. M. D., Goodrow, R. J., Wu, Y., Cordeiro, J. M., Nesterenko, V. V., et al. (2012). Maximum diastolic potential of human induced pluripotent stem cell-derived cardiomyocytes depends critically on IKr. *PLoS One* 5:e40288. doi: 10.1371/journal.pone.0040288

Dunn, K. K., and Palecek, S. P. (2018). Engineering scalable manufacturing of high-quality stem cell-derived cardiomyocytes for cardiac tissue repair. *Front. Med.* 24:110. doi: 10.3389/fmed.2018.00110

Duval, K., Grover, H., Han, L.-H., Mou, Y., Pegoraro, A. F., Fredberg, J., et al. (2017). Modeling physiological events in 2D vs. 3D cell culture. *Physiology* 32, 266–277. doi: 10.1152/physiol.00036.2016

Elliott, D. A., Braam, S. R., Koutsis, K., Ng, E. S., Jenny, R., Lagerqvist, E. L., et al. (2011). NKX2-5eGFP/w hESCs for isolation of human cardiac progenitors and cardiomyocytes. *Nat. Methods* 8, 1037–1040. doi: 10.1038/nmeth.1740

Funakoshi, S., Miki, K., Takaki, T., Okubo, C., Hatani, T., Chonabayashi, K., et al. (2016). Enhanced engraftment, proliferation, and therapeutic potential in heart using optimized human iPSC-derived cardiomyocytes. *Sci. Rep.* 6:19111. doi: 10.1038/srep19111

Godier-Furnémont, A. F. G., Tiburcy, M., Wagner, E., Dewenter, M., Lämmle, S., El-Armouche, A., et al. (2015). Physiologic force-frequency response in engineered heart muscle by electromechanical stimulation. *Biomaterials* 60, 82–91. doi: 10.1016/j.biomaterials.2015.03.055

Herron, T. J., Rocha, A. M. D., Campbell, K. F., Ponce-Balbuena, D., Willis, B. C., Guerrero-Serna, G., et al. (2016). Extracellular matrix-mediated maturation of human pluripotent stem cell-derived cardiac monolayer structure and electrophysiological function. *Circ. Arrhythm. Electrophysiol.* 9:e003638. doi: 10.1161/CIRCEP.113.003638

Hinson, J. T., Chopra, A., Nafissi, N., Polacheck, W. J., Benson, C. C., Swist, S., et al. (2015). Titin mutations in iPS cells define sarcomere insufficiency as a cause of dilated cardiomyopathy. *Science* 349, 982–986. doi: 10.1126/science.aaa5458

Hirt, M. N., Boeddinghaus, J., Mitchell, A., Schaaf, S., Börnchen, C., Müller, C., et al. (2014). Functional improvement and maturation of rat and human engineered heart tissue by chronic electrical stimulation. *J. Mol. Cell Cardiol.* 74, 151–161. doi: 10.1016/j.yjmcc.2014.05.009

Hoang, P., Wang, J., Conklin, B. R., Healy, K. E., and Ma, Z. (2018). Generation of spatial-patterned early-developing cardiac organoids using human pluripotent stem cells. *Nat. Protoc.* 13, 723–737. doi: 10.1038/nprot.2018.006

Hoekstra, M., Mummery, C. L., Wilde, A. A. M., Bezzina, C. R., and Verkerk, A. O. (2012). Induced pluripotent stem cell derived cardiomyocytes as models for cardiac arrhythmias. *Front. Physiol.* 3:346. doi: 10.3389/fphys.2012.00346

Horikoshi, Y., Yan, Y., Terashvili, M., Wells, C., Horikoshi, H., Fujita, S., et al. (2019). Fatty acid-treated induced pluripotent stem cell-derived human cardiomyocytes exhibit adult cardiomyocyte-like energy metabolism phenotypes. *Cells* 8:E1095. doi: 10.3390/cells8091095

Huang, C. Y., Peres Moreno Maia-Joca, R., Ong, C. S., Wilson, I., DiSilvestre, D., Tomaselli, G. F., et al. (2020). Enhancement of human iPSC-derived cardiomyocyte maturation by chemical conditioning in a 3D environment. *J. Mol. Cell. Cardiol.* 138, 1–11. doi: 10.1016/j.yjmcc.2019.10.001

Huethorst, E., Hortigon, M., Zamora-Rodriguez, V., Reynolds, P. M., Burton, F., Smith, G., et al. (2016). Enhanced human-induced pluripotent stem cell derived cardiomyocyte maturation using a dual microgradient substrate. *ACS Biomater Sci. Eng.* 2, 2231–2239. doi: 10.1021/acsbiomaterials.6b00426

Jacot, J. G., Martin, J. C., and Hunt, D. L. (2010). Mechanobiology of cardiomyocyte development. *J Biomech.* 43, 93–98. doi: 10.1016/j.jbiomech.2009.09.014

Jung, G., and Bernstein, D. (2014). hiPSC modeling of inherited cardiomyopathies. *Curr. Treat Options Cardiovasc. Med.* 16:320. doi: 10.1007/s11936-014-0320-7

Kadota, S., Pabon, L., Reinecke, H., and Murry, C. E. (2017). *In vivo* maturation of human induced pluripotent stem cell-derived cardiomyocytes in neonatal and adult rat hearts. *Stem Cell Rep.* 8, 278–289. doi: 10.1016/j.stemcr.2016.10.009

Kamakura, T., Makiyama, T., Sasaki, K., Yoshida, Y., Wuriyanghai, Y., Chen, J., et al. (2013). Ultrastructural maturation of human-induced pluripotent stem cell-derived cardiomyocytes in a long-term culture. *Circ. J.* 77, 1307–1314. doi: 10.1253/circj.cj-12-0987

Karakikes, I., Ameen, M., Termglinchan, V., and Wu, J. C. (2015). Human induced pluripotent stem cell-derived cardiomyocytes: insights into molecular, cellular, and functional phenotypes. *Circ. Res.* 117, 80–88. doi: 10.1161/CIRCRESAHA.117.305365

Kawatou, M., Masumoto, H., Fukushima, H., Morinaga, G., Sakata, R., Ashihara, T., et al. (2017). Modelling Torsade de pointes arrhythmias in vitro in 3D human iPS cell-engineered heart tissue. *Nat. Commun.* 8:1078. doi: 10.1038/s41467-017-01125-y

Kikuchi, C., Bienengraeber, M., Canfield, S., Koopmeiner, A., Schäfer, R., Bosnjak, Z. J., et al. (2015). Comparison of cardiomyocyte differentiation potential between type 1 diabetic donor- and nondiabetic donor-derived induced pluripotent stem cells. *Cell Transplant.* 24, 2491–2504. doi: 10.3727/096368914X685762

Kim, C., Wong, J., Wen, J., Wang, S., Wang, C., Spiering, S., et al. (2013). Studying arrhythmogenic right ventricular dysplasia with patient-specific iPSCs. *Nature* 494, 105–110. doi: 10.1038/nature11799

King, O., Kermani, F., Wang, B., Kit-Anan, W., Fourre, J., Randi, A. M., et al. (2019). Endothelial cell regulation of excitation-contraction coupling in induced pluripotent stem cell derived myocardium. *Biophys. J.* 116:153a. doi: 10.1016/j.bpj.2018.11.850

Klein, I., and Ojamaa, K. (2001). Thyroid hormone and the cardiovascular system. *N. Engl. J. Med.* 344, 501–509.

Knollmann, B. C. (2013). Induced pluripotent stem cell-derived cardiomyocytes: boutique science or valuable arrhythmia model? *Circ. Res.* 112, 969–976. doi: 10.1161/CIRCRESAHA.112.300567

Kreipke, R., Wang, Y., Miklas, J. W., Mathieu, J., and Ruohola-Baker, H. (2016). Metabolic remodeling in early development and cardiomyocyte maturation. *Semin. Cell Dev. Biol.* 52, 84–92. doi: 10.1016/j.semcdb.2016.02.004

Kroll, K., Chabria, M., Wang, K., Häusermann, F., Schuler, F., and Polonchuk, L. (2017). Electro-mechanical conditioning of human iPSC-derived cardiomyocytes for translational research. *Prog. Biophys. Mol. Biol.* 130(Pt B), 212–222. doi: 10.1016/j.pbiomolbio.2017.07.003

LaBarge, W., Mattappally, S., Kannappan, R., Fast, V. G., Pretorius, D., Berry, J. L., et al. (2019). Maturation of three-dimensional, hiPSC-derived cardiomyocyte spheroids utilizing cyclic, uniaxial stretch and electrical stimulation. *PLoS One* 14:e0219442. doi: 10.1371/journal.pone.0219442

Lemoine, M. D., Mannhardt, I., Breckwoldt, K., Prondzynski, M., Flenner, F., Ulmer, B., et al. (2017). Human iPSC-derived cardiomyocytes cultured in 3D engineered heart tissue show physiological upstroke velocity and sodium current density. *Sci. Rep.* 7, 1–11. doi: 10.1038/s41598-017-05600-w

Leonard, A., Bertero, A., Powers, J. D., Beussman, K. M., Bhandari, S., Regnier, M., et al. (2018). Afterload promotes maturation of human induced pluripotent stem cell derived cardiomyocytes in engineered heart tissues. *J. Mol. Cell Cardiol.* 118, 147–158. doi: 10.1016/j.yjmcc.2018.03.016

Lewandowski, J., Rozwadowska, N., Kolanowski, T. J., Malcher, A., Zimna, A., Rugowska, A., et al. (2018). The impact of in vitro cell culture duration on the maturation of human cardiomyocytes derived from induced pluripotent stem cells of myogenic origin. *Cell Transplant.* 27, 1047–1067. doi: 10.1177/0963689718779346

Lopaschuk, G. D., and Jaswal, J. S. (2010). Energy metabolic phenotype of the cardiomyocyte during development, differentiation, and postnatal maturation. *J. Cardiovasc. Pharmacol.* 56, 130–140. doi: 10.1097/FJC.0b013e3181e74a14

Lopaschuk, G. D., Spafford, M. A., and Marsh, D. R. (1991). Glycolysis is predominant source of myocardial ATP production immediately after birth. *Am. J. Physiol. Heart Circulat. Physiol.* 261, H1698–H1705.

Lundy, S. D., Zhu, W.-Z., Regnier, M., and Laflamme, M. A. (2013). Structural and functional maturation of cardiomyocytes derived from human pluripotent stem cells. *Stem Cells Dev.* 22, 1991–2002. doi: 10.1089/scd.2012.0490

Ma, J., Guo, L., Fiene, S. J., Anson, B. D., Thomson, J. A., Kamp, T. J., et al. (2011). High purity human-induced pluripotent stem cell-derived cardiomyocytes: electrophysiological properties of action potentials and ionic currents. *Am. J. Physiol. Heart Circ. Physiol.* 301, H2006–H2017. doi: 10.1152/ajpheart.00694.2011

Ma, X., Dewan, S., Liu, J., Tang, M., Miller, K. L., Yu, C., et al. (2019). 3D printed micro-scale force gauge arrays to improve human cardiac tissue maturation and enable high throughput drug testing. *Acta Biomater.* 95, 319–327. doi: 10.1016/j.actbio.2018.12.026

McCain, M. L., Yuan, H., Pasqualini, F. S., Campbell, P. H., and Parker, K. K. (2014). Matrix elasticity regulates the optimal cardiac myocyte shape for contractility. *Am. J. Physiol. Heart Circulat. Physiol.* 306, H1525–H1539. doi: 10.1152/ajpheart.00799.2013

Minami, I., Yamada, K., Otsuji, T. G., Yamamoto, T., Shen, Y., Otsuka, S., et al. (2012). A small molecule that promotes cardiac differentiation of human pluripotent stem cells under defined, cytokine- and xeno-free conditions. *Cell Rep.* 2, 1448–1460. doi: 10.1016/j.celrep.2012.09.015

Mirbagheri, M., Adibnia, V., Hughes, B. R., Waldman, S. D., Banquy, X., and Hwang, D. K. (2019). Advanced cell culture platforms: a growing quest for emulating natural tissues. *Mater Horiz.* 6, 45–71. doi: 10.1039/c8mh00803e

Nakano, H., Minami, I., Braas, D., Pappoe, H., Wu, X., Sagadevan, A., et al. (2017). Glucose inhibits cardiac muscle maturation through nucleotide biosynthesis. Yelon D, editor. *eLife.* 6:e29330. doi: 10.7554/eLife.29330

Nunes, S. S., Miklas, J. W., Liu, J., Aschar-Sobbi, R., Xiao, Y., Zhang, B., et al. (2013). Biowire: a platform for maturation of human pluripotent stem cell–derived cardiomyocytes. *Nat. Methods.* 10, 781–787.

Ogasawara, T., Okano, S., Ichimura, H., Kadota, S., Tanaka, Y., Minami, I., et al. (2017). Impact of extracellular matrix on engraftment and maturation of pluripotent stem cell-derived cardiomyocytes in a rat myocardial infarct model. *Sci. Rep.* 7, 1–8. doi: 10.1038/s41598-017-09217-x

Parikh, S. S., Blackwell, D. J., Gomez-Hurtado, N., Frisk, M., Wang, L., Kim, K., et al. (2017). Thyroid and glucocorticoid hormones promote functional T-tubule development in human-induced pluripotent stem cell-derived cardiomyocytes. *Circ. Res.* 121, 1323–1330. doi: 10.1161/CIRCRESAHA.117.311920

Pesl, M., Pribyl, J., Caluori, G., Cmiel, V., Acimovic, I., Jelinkova, S., et al. (2017). Phenotypic assays for analyses of pluripotent stem cell-derived cardiomyocytes. *J. Mol. Recognit.* 30:e2602. doi: 10.1002/jmr.2602

Peters, N. S., Severs, N. J., Rothery, S. M., Lincoln, C., Yacoub, M. H., and Green, C. R. (1994). Spatiotemporal relation between gap junctions and fascia adherens junctions during postnatal development of human ventricular myocardium. *Circulation* 90, 713–725. doi: 10.1161/01.cir.90.2.713

Puri, M. C., and Nagy, A. (2012). Concise review: embryonic stem cells versus induced pluripotent stem cells: the game is on. *Stem Cells* 30, 10–14. doi: 10.1002/stem.788

Rana, P., Anson, B., Engle, S., and Will, Y. (2012). Characterization of human-induced pluripotent stem cell–derived cardiomyocytes: bioenergetics and utilization in safety screening. *Toxicol. Sci.* 130, 117–131. doi: 10.1093/toxsci/kfs233

Ribeiro, A. J. S., Ang, Y.-S., Fu, J.-D., Rivas, R. N., Mohamed, T. M. A., Higgs, G. C., et al. (2015). Contractility of single cardiomyocytes differentiated from pluripotent stem cells depends on physiological shape and substrate stiffness. *Proc. Natl. Acad. Sci. U.S.A.* 112, 12705–12710. doi: 10.1073/pnas.1508073112

Richards, D. J., Tan, Y., Coyle, R., Li, Y., Xu, R., Yeung, N., et al. (2016). Nanowires and electrical stimulation synergistically improve functions of hiPSC cardiac spheroids. *Nano Lett.* 16, 4670–4678. doi: 10.1021/acs.nanolett.6b02093

Rog-Zielinska, E. A., Craig, M.-A., Manning, J. R., Richardson, R. V., Gowans, G. J., Dunbar, D. R., et al. (2015). Glucocorticoids promote structural and functional maturation of foetal cardiomyocytes: a role for PGC-1α. *Cell Death Differ.* 22, 1106–1116. doi: 10.1038/cdd.2014.181

Rog-Zielinska, E. A., Thomson, A., Kenyon, C. J., Brownstein, D. G., Moran, C. M., Szumska, D., et al. (2013). Glucocorticoid receptor is required for foetal heart maturation. *Hum. Mol. Genet.* 22, 3269–3282. doi: 10.1093/hmg/ddt182

Ronaldson-Bouchard, K., Ma, S. P., Yeager, K., Chen, T., Song, L., Sirabella, D., et al. (2018). Advanced maturation of human cardiac tissue grown from pluripotent stem cells. *Nature* 556, 239–243. doi: 10.1038/s41586-018-0016-3

Roshanbinfar, K., Mohammadi, Z., Sheikh-Mahdi Mesgar, A., Dehghan, M. M., Oommen, O. P., Hilborn, J., et al. (2019). Carbon nanotube doped pericardial matrix derived electroconductive biohybrid hydrogel for cardiac tissue engineering. *Biomater. Sci.* 7, 3906–3917. doi: 10.1039/c9bm00434c

Ruan, J.-L., Tulloch, N. L., Razumova, M. V., Saiget, M., Muskheli, V., Pabon, L., et al. (2016). Mechanical stress conditioning and electrical stimulation promote contractility and force maturation of induced pluripotent stem cell-derived human cardiac tissue. *Circulation* 134, 1557–1567. doi: 10.1161/circulationaha.114.014998

Scuderi, G. J., and Butcher, J. (2017). Naturally engineered maturation of cardiomyocytes. *Front. Cell Dev. Biol.* 5:50. doi: 10.3389/fcell.2017.00050

Shiba, Y., Gomibuchi, T., Seto, T., Wada, Y., Ichimura, H., Tanaka, Y., et al. (2016). Allogeneic transplantation of iPS cell-derived cardiomyocytes regenerates primate hearts. *Nature* 538, 388–391. doi: 10.1038/nature19815

Silbernagel, N., Körner, A., Balitzki, J., Jaggy, M., Bertels, S., Richter, B., et al. (2020). Shaping the heart: structural and functional maturation of iPSC-cardiomyocytes in 3D-micro-scaffolds. *Biomaterials* 227:119551. doi: 10.1016/j.biomaterials.2019.119551

Sinnecker, D., Laugwitz, K.-L., and Moretti, A. (2014). Induced pluripotent stem cell-derived cardiomyocytes for drug development and toxicity testing. *Pharmacol. Ther.* 143, 246–252. doi: 10.1016/j.pharmthera.2014.03.004

Steinhoff, G., Nesteruk, J., Wolfien, M., Große, J., Ruch, U., Vasudevan, P., et al. (2017). Stem cells and heart disease – brake or accelerator? *Adv. Drug Deliv. Rev.* 120, 2–24. doi: 10.1016/j.addr.2017.10.007

Takahashi, K., Tanabe, K., Ohnuki, M., Narita, M., Ichisaka, T., Tomoda, K., et al. (2007). Induction of pluripotent stem cells from adult human fibroblasts by defined factors. *Cell* 131, 861–872. doi: 10.1016/j.cell.2007.11.019

Talman, V., and Kivelä, R. (2018). Cardiomyocyte-endothelial cell interactions in cardiac remodeling and regeneration. *Front. Cardiovasc. Med.* 5:101. doi: 10.3389/fcvm.2018.00101

Tan, Y., Richards, D., Xu, R., Stewart-Clark, S., Mani, S. K., Borg, T. K., et al. (2015). Silicon nanowire-induced maturation of cardiomyocytes derived from human induced pluripotent stem cells. *Nano Lett.* 15, 2765–2772. doi: 10.1021/nl502227a

Thavandiran, N., Nunes, S. S., Xiao, Y., and Radisic, M. (2013). Topological and electrical control of cardiac differentiation and assembly. *Stem Cell Res. Ther.* 4:14. doi: 10.1186/scrt162

Tiburcy, M., Hudson, J. E., Balfanz, P., Schlick, S., Meyer, T., Chang Liao, M.-L., et al. (2017). Defined engineered human myocardium with advanced maturation for applications in heart failure modeling and repair. *Circulation* 135, 1832–1847. doi: 10.1161/CIRCULATIONAHA.116.024145

Tohyama, S., Hattori, F., Sano, M., Hishiki, T., Nagahata, Y., Matsuura, T., et al. (2013). Distinct metabolic flow enables large-scale purification of mouse and human pluripotent stem cell-derived cardiomyocytes. *Cell Stem Cell* 12, 127–137. doi: 10.1016/j.stem.2012.09.013

Ulmer, B. M., Stoehr, A., Schulze, M. L., Patel, S., Gucek, M., Mannhardt, I., et al. (2018). Contractile work contributes to maturation of energy metabolism in hiPSC-derived cardiomyocytes. *Stem Cell Rep.* 10, 834–847. doi: 10.1016/j.stemcr.2018.01.039

Uosaki, H., Cahan, P., Lee, D. I., Wang, S., Miyamoto, M., Fernandez, L., et al. (2015). Transcriptional landscape of cardiomyocyte maturation. *Cell Rep.* 13, 1705–1716. doi: 10.1016/j.celrep.2015.10.032

Uosaki, H., Fukushima, H., Takeuchi, A., Matsuoka, S., Nakatsuji, N., Yamanaka, S., et al. (2011). Efficient and scalable purification of cardiomyocytes from human embryonic and induced pluripotent stem cells by VCAM1 surface expression. Prosper F, editor. *PLoS One* 18:e23657. doi: 10.1371/journal.pone.0023657

Uosaki, H., and Taguchi, Y. (2016). Comparative gene expression analysis of mouse and human cardiac maturation. *Genomics Proteomics Bioinformatics* 14, 207–215. doi: 10.1016/j.gpb.2016.04.004

Valls-Margarit, M., Iglesias-García, O., Di Guglielmo, C., Sarlabous, L., Tadevosyan, K., Paoli, R., et al. (2019). Engineered macroscale cardiac constructs elicit human myocardial tissue-like functionality. *Stem Cell Rep.* 13, 207–220. doi: 10.1016/j.stemcr.2019.05.024

van den Berg, C. W., Okawa, S., Chuva de Sousa Lopes, S. M., van Iperen, L., Passier, R., Braam, S. R., et al. (2015). Transcriptome of human foetal heart compared with cardiomyocytes from pluripotent stem cells. *Development* 142, 3231–3238. doi: 10.1242/dev.123810

Veerman, C. C., Mengarelli, I., Lodder, E. M., Kosmidis, G., Bellin, M., Zhang, M., et al. (2017). Switch from fetal to adult SCN5A isoform in human induced pluripotent stem cell-derived cardiomyocytes unmasks the cellular phenotype of a conduction disease-causing mutation. *J. Am. Heart Assoc.* 6:e005135. doi: 10.1161/JAHA.116.005135

Vreeker, A., van Stuijvenberg, L., Hund, T. J., Mohler, P. J., Nikkels, P. G. J., and van Veen, T. A. B. (2014). Assembly of the cardiac intercalated disk during Pre- and postnatal development of the human heart. Goumans MJ, editor. *PLoS One* 9:e94722. doi: 10.1371/journal.pone.0094722

Vuorenpää, H., Penttinen, K., Heinonen, T., Pekkanen-Mattila, M., Sarkanen, J.-R., Ylikomi, T., et al. (2017). Maturation of human pluripotent stem cell derived cardiomyocytes is improved in cardiovascular construct. *Cytotechnology* 69, 785–800. doi: 10.1007/s10616-017-0088-1

Yan, Y., Bejoy, J., Xia, J., Griffin, K., Guan, J., and Li, Y. (2019). Cell population balance of cardiovascular spheroids derived from human induced pluripotent stem cells. *Sci. Rep.* 9, 1–12. doi: 10.1038/s41598-018-37686-1

Yanagi, K., Takano, M., Narazaki, G., Uosaki, H., Hoshino, T., Ishii, T., et al. (2007). Hyperpolarization-activated cyclic nucleotide-gated channels and T-Type calcium channels confer automaticity of embryonic stem cell-derived cardiomyocytes. *Stem Cells* 25, 2712–2719. doi: 10.1634/stemcells.2006-0388

Yang, C., Al-Aama, J., Stojkovic, M., Keavney, B., Trafford, A., Lako, M., et al. (2015). Concise review: cardiac disease modeling using induced pluripotent stem cells. *Stem Cells* 33, 2643–2651. doi: 10.1002/stem.2070

Yang, L., Soonpaa, M. H., Adler, E. D., Roepke, T. K., Kattman, S. J., Kennedy, M., et al. (2008). Human cardiovascular progenitor cells develop from a KDR+ embryonic-stem-cell-derived population. *Nature* 453, 524–528. doi: 10.1038/nature06894

Yang, X., Pabon, L., and Murry, C. E. (2014a). Engineering adolescence: maturation of human pluripotent stem cell-derived cardiomyocytes. *Circ Res.* 31, 511–523. doi: 10.1161/circresaha.114.300558

Yang, X., Rodriguez, M., Pabon, L., Fischer, K. A., Reinecke, H., Regnier, M., et al. (2014b). Tri-iodo-l-thyronine promotes the maturation of human cardiomyocytes-derived from induced pluripotent stem cells. *J. Mol. Cell Cardiol.* 72, 296–304. doi: 10.1016/j.yjmcc.2014.04.005

Yang, X., Rodriguez, M. L., Leonard, A., Sun, L., Fischer, K. A., Wang, Y., et al. (2019). Fatty acids enhance the maturation of cardiomyocytes derived from human pluripotent stem cells. *Stem Cell Rep.* 13, 657–668. doi: 10.1016/j.stemcr.2019.08.013

Yin, Z., Ren, J., and Guo, W. (2015). Sarcomeric protein isoform transitions in cardiac muscle: a journey to heart failure. *Biochim. Biophys. Acta* 1852, 47–52. doi: 10.1016/j.bbadis.2014.11.003

Yoshida, S., Miyagawa, S., Fukushima, S., Kawamura, T., Kashiyama, N., Ohashi, F., et al. (2018). Maturation of human induced pluripotent stem cell-derived cardiomyocytes by soluble factors from human mesenchymal stem cells. *Mol. Ther.* 26, 2681–2695. doi: 10.1016/j.ymthe.2018.08.012

Zhang, W., Kong, C. W., Tong, M. H., Chooi, W. H., Huang, N., Li, R. A., et al. (2017). Maturation of human embryonic stem cell-derived cardiomyocytes (hESC-CMs) in 3D collagen matrix: effects of niche cell supplementation and mechanical stimulation. *Acta Biomater.* 49, 204–217. doi: 10.1016/j.actbio.2016.11.058

Zwi, L., Caspi, O., Arbel, G., Huber, I., Gepstein, A., Park, I.-H., et al. (2009). Cardiomyocyte differentiation of human induced pluripotent stem cells. *Circulation* 13, 1513–1523. doi: 10.1161/circulationaha.109.868885

**Conflict of Interest:** The authors declare that the research was conducted in the absence of any commercial or financial relationships that could be construed as a potential conflict of interest.

frontiers
in Cell and Developmental Biology

BRIEF RESEARCH REPORT
published: 22 April 2020
doi: 10.3389/fcell.2020.00268

# Comparative Transcriptome Landscape of Mouse and Human Hearts

*Tatsuya Anzai*[1,2]*, Takanori Yamagata*[2] *and Hideki Uosaki*[1]*

[1] *Division of Regenerative Medicine, Center for Molecular Medicine, Jichi Medical University, Shimotsuke, Japan,*
[2] *Department of Pediatrics, Jichi Medical University, Shimotsuke, Japan*

Transcriptome landscape of organs from mice and humans offers perspectives on the process of how organs develop and the similarity and diversity in each organ between the species. Among multi-species and multi-organ dataset, which was previously generated, we focused on the mouse and human dataset and performed a reanalysis to provide a more specific perspective on the maturation of human cardiomyocytes. First, we examined how organs diversify their transcriptome during development across and within two species. We unexpectedly identified that ribosomal genes were differentially expressed between mice and humans. Second, we examined the corresponding ages of organs in mice and humans and found that the corresponding developmental ages did not match throughout organs. Mouse hearts at P0–3 and human hearts at 18–19 wpc showed the most proximity in the regard of the transcriptome. Third, we identified a novel set of maturation marker genes that are more consistent between mice and humans. In contrast, conventionally used maturation marker genes only work well with mouse hearts. Finally, we compared human pluripotent stem cell-derived cardiomyocytes (PSC-CMs) in maturation-enhanced conditions to human fetal and adult hearts and revealed that human PSC-CMs only expressed low levels of the potential maturation marker genes. Our findings provide a novel foundation to study cardiomyocyte maturation and highlight the importance of studying human samples rather than relying on a mouse time-series dataset.

**Keywords: cardiomyocyte maturation, transcriptome, comparative transcriptome, maturation marker, ribosome**

OPEN ACCESS

***Edited by:***
*Jong-Kook Lee,*
*Osaka University, Japan*

***Reviewed by:***
*Masamichi Ito,*
*The University of Tokyo, Japan*
*Gonzalo del Monte Nieto,*
*Monash University, Australia*

****Correspondence:***
*Hideki Uosaki*
*uosaki.hideki@jichi.ac.jp*

***Specialty section:***
*This article was submitted to Stem Cell Research, a section of the journal Frontiers in Cell and Developmental Biology*

***Received:*** *13 January 2020*
***Accepted:*** *30 March 2020*
***Published:*** *22 April 2020*

***Citation:***
*Anzai T, Yamagata T and Uosaki H (2020) Comparative Transcriptome Landscape of Mouse and Human Hearts. Front. Cell Dev. Biol. 8:268. doi: 10.3389/fcell.2020.00268*

## INTRODUCTION

Understanding the transcriptome landscape of mouse developing hearts provided a compass to navigate how cardiomyocyte mature *in vivo* and a foundation to determine the maturity of mouse pluripotent stem cell-derived cardiomyocytes (PSC-CMs) cultured *in vitro* (Uosaki et al., 2015). Single-cell RNA-sequencing added the details on cell-type specific, spatiotemporal developmental programs in mice hearts, although it lacked fully-matured adult cardiomyocytes in the analysis (DeLaughter et al., 2016). The maturation of cardiomyocytes is a continuous process from early embryo to adult, but the maturation of PSC-CMs arrested at the late-embryonic stage (Uosaki et al., 2015), which demanded more information on cardiomyocyte maturation during postnatal maturation. Due to the limited availability of human heart samples at late-embryos to early ages, only transcriptome datasets of fetal and adult human hearts were evaluated in the past (Kuppusamy et al., 2015; Uosaki and Taguchi, 2016). Although many genes shared distinct expression patterns from fetus to adult in mouse and human hearts (Uosaki and Taguchi, 2016), the expression kinetics of maturation-related genes during the entire maturation process in human hearts were largely unknown.

Recently, time series of the transcriptome for six mammals and a bird, with seven organs, were conducted and provided from the other group (Cardoso-Moreira et al., 2019). While the dataset still lacks late-embryonic human samples, it offers the most complete dataset of human organs from early embryos to adults. Here, we hypothesized that detailed analyses of the dataset could reveal not only how the transcriptome of human hearts progresses but also the expression kinetics of maturation-related genes. In this study, we reanalyzed the dataset to obtain more accurate information about the transcriptome landscape of mice and humans, especially in hearts from embryonic to adult stage and determined expression kinetics of maturation-related genes in human hearts.

## MATERIALS AND METHODS

### Data Sets

The datasets analyzed for this study can be found in E-MTAB-6798 (mouse)[1] and E-MTAB-6814 (human)[2]. We used normalized data with reads per kilobase per million mapped reads (RPKM) in the repository. For the analysis of gene expressions in PSC-CMs, we obtained read counts data from GSE62913[3] and normalized to transcripts per million reads (TPM).

### Bioinformatics Analysis

We performed most of the analyses using the statistical software R version 3.6.1 (R Core Team, 2016). To identify orthologs, we used biomaRt and homologene (Durinck et al., 2009; Mancarci, 2018). For the data analysis, we first performed principal component analysis (PCA) with logarithmically converted data [log(RPKM + 1)] using prcomp function in R. To generate graphs and plots, we used ggplot2 (Wickham, 2016). For the 3D plots, we used plotly for R (Sievert, 2020) and exported as hypertext markup language (HTML, **Supplementary Data S1–S9**). To define developmental stages, we used k-means clustering and designated samples in each organ to five clusters unless noted otherwise. To identify differentially expressed genes (DEGs) in multigroup comparison settings, we used edgeR and performed generalized linear model and likelihood ratio test (GLM-LRT) (Robinson et al., 2010; McCarthy et al., 2012). Genes with false discovery rate (FDR) $< 0.01$, $P$-value $< 0.01$, log2 fold changes $> 1$, and log2 averaged RPKM $> 3$ were considered as DEGs. DEGs were further clustered using c-means fuzzy clustering with Mfuzz (Futschik and Carlisle, 2005; Kumar and Futschik, 2007). Genes with membership score $> 0.5$ are considered as members of a cluster. For gene ontology (GO) analysis, we used clusterProfiler and DOSE (Yu et al., 2012, 2015). We used cut-offs of 0.1 for both $P$-value and $Q$-value, and the FDR (also known as BH) adjustment was applied to adjust $P$-value. Top five GO terms with the lowest $P$-value were reported though some of them were not significantly enriched. To draw a gene-concept network, cnetplot function in enrichplot package was used. To define a candidate marker gene for maturation from the gene clusters 1 and 4 (upregulated in adults compared to embryos), we set criteria of RPKM $> 100$ in both mouse and human adult heart with $> 10$-fold changes when compared the adult to early embryonic hearts.

## RESULTS

### Global Transcriptome Analysis Comparing Organ Scale Maturation

Gene expression time series for six mammals and a bird, with seven organs, were performed in the previous study by the other group (Cardoso-Moreira et al., 2019). In this study, we aimed to perform a reanalysis of the dataset to obtain a more focused perspective on the transcriptome landscape, especially in hearts. As the most basic biomedical researches are conducted with mouse models, we decided to focus only on mouse and human rather than all seven species, which would allow us to translate the knowledge with mice into human researches. First, we examined the comparative transcriptome between humans and mice throughout the seven organs. To directly compare the human and mouse dataset, we curated 16,831 genes with 1:1 ortholog in mouse and human using biomaRt and homologene. Then, we performed PCA using all of the orthologs. While PC1 separated the samples based on the germ layer as previously shown, PC2 differentiated the samples by species (**Figure 1A** and **Supplementary Data S1**). This notion was unexpected as we expected organ-to-organ variations are more distinctive than species differences. With the combination of PC1, 3, and 4, the samples were distinguished by organs and developmental stages (**Figure 1B** and **Supplementary Data S2**). Clearer separations were observed with combinations of PC1 to PC3 in the PCA plots within single species (**Supplementary Data S3**, **S4**). To ask what makes human and mouse different in the transcriptome landscape, we performed GO analysis. Interestingly, GO term "structural constituent of ribosome" was highly enriched in both positively (human-specific) and negatively (mouse-specific) weighted genes responsible for PC2-axis (**Figure 1C**), however, the member genes enriched in the GO term for each species were distinctive. This result implicates ribosomal function might distinguish mice and humans regardless of organs.

### Developmental Stage Correspondences of Each Organ

Next, we aimed to define the corresponding developmental stages of each organ between mice and humans. For embryonic

---

[1] https://www.ebi.ac.uk/arrayexpress/experiments/E-MTAB-6798/

[2] https://www.ebi.ac.uk/arrayexpress/experiments/E-MTAB-6814/

[3] https://www.ncbi.nlm.nih.gov/geo/query/acc.cgi?acc=GSE62913

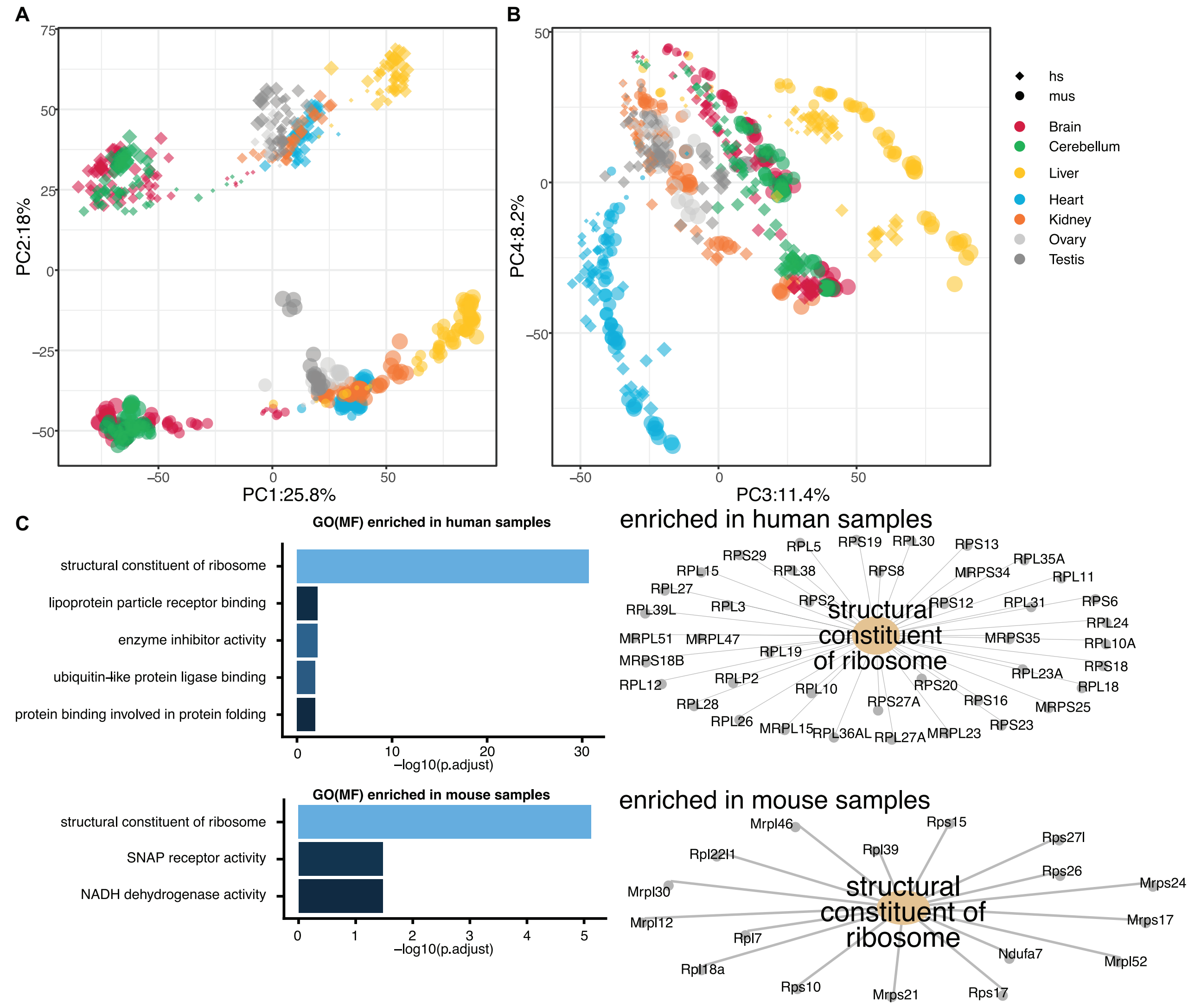

**FIGURE 1 |** Global transcriptome analysis of seven organs from mouse and human. **(A,B)** Principal component analysis (PCA) of seven organs from mouse and human. Sizes of dots indicate ages of samples [small dot, young; big dot, old. Ages ranging 4 weeks post conception (wpc)–senior of human and embryonic day (E) 9.5–postnatal (P) 63 of mouse]. Shapes of dots indicate species [diamond, human (hs); circle, mouse (mus)]. Color of each point indicates organs (red, brain; green, cerebellum; yellow, liver; blue, heart; orange, kidney; light gray, ovary; dark gray, testis). Principal component (PC) 1, 3, and 4 distinguish the organs while PC2 separate mouse and human. **(C)** Gene ontology (GO) analysis of PC2 axis. Top five GO terms for molecular function (MF) enriched in human and mouse organs are shown as bar graphs (left). In both mouse and human, GO term "structural constituent of ribosome" was highly enriched, though the enriched genes were different as shown in gene-concept networks. SNAP, synaptosomal-associated protein; NADH, nicotinamide adenine dinucleotide.

development, the Carnegie stages are often used (de Bakker et al., 2016). However, it is unknown if each organ developed the same manner in a body between humans and mice. To unveil this, we performed the PCAs of individual organs. As we expect, PC1 and PC2 are major explanatory variables of species and developmental stages, respectively, in most of the organs except testes (**Figure 2A**, **Supplementary Figure S1**, and **Supplementary Data S5–S9**). Proximity in a PCA plot indicates transcriptional similarity among samples. With *k-mean* clustering, we classified each organ of mouse and human to five clusters. Although the phylotypic stage in the developmental hourglass model is considered at the mid-embryonic stage (Irie and Kuratani, 2011), PCA plots of individual organs displayed more proximity at some point around birth. Interestingly, the time of the most proximate varies organ-to-organ. For example, human hearts at 19 weeks post conception (wpc) were closest to mouse hearts at postnatal day (P) 0–3 (**Figure 2A** and **Supplementary Data S5**). In contrast, human kidneys at 10–20 wpc and livers at 19–20 wpc were closest to mouse counterparts at P3–P14 and E17.5, respectively (**Supplementary Figures S1A,B** and **Supplementary Data S6, S7**). When brains and cerebellums from mouse and human were analyzed altogether, they had similar trajectory up to the late embryonic-neonatal stage and differentiated to more specific to brain or cerebellum later (**Supplementary Figure S1C** and **Supplementary Data S8**). Moreover, both mouse and human testes displayed sudden transcriptional changes at the adolescent stages (**Supplementary Figure S1D** and **Supplementary Data S9**). These results indicate that every organ has a different developmental speed.

## Differentially Expressed Genes in Heart

The heart is a major target organ for us. We previously demonstrated that the developmental stages of mouse PSC-CMs can be accurately predicted using the microarray-based dataset (Uosaki et al., 2015). However, due to the lack of compatibility across platforms of microarray and limited dataset of human hearts, it is unable to use the method to human PSC-CMs. We also demonstrated that mouse and human transcriptomes change similarly from embryo to adult (Uosaki and Taguchi, 2016), while no time-course study was performed at that point. Here, we examined the transcriptome data of mouse and human hearts to show the trajectory of transcriptome changes in mouse and human hearts. As we demonstrated that there is a specific time-point that an organ from mouse and human becomes more similar than the other time-points. Thus, we identified DEGs among three clusters – the earliest developmental clusters (E10.5–11.5 of the mouse hearts; 4–7 wpc of the humans), the closest clusters in between (P0–3 for mouse hearts; 18–19 wpc of humans), and the most aged clusters (P14–63 of mouse hearts; neonate–old mid age of humans). We identified more than 6,000 genes are differentially expressed at least one comparison among the clusters in both mouse and human hearts (**Figure 2B** and **Supplementary Figures S2A–C**). Among them, 3,267 genes were overlapped in mouse and human DEGs of hearts (**Figure 2B**). To test if expression trajectory is similar during heart development in mouse and human, we clustered the common DEGs of hearts using c-means fuzzy clustering. We identified six DEG clusters in mouse hearts (**Figure 2C**), which included steadily increased to adult (cluster 1), adult heart-specific (cluster 4), steadily decreased (clusters 3 and 6), early embryonic heart-specific (cluster 5), and transient upregulation (cluster 2). We also identified 6 DEG clusters in human hearts (**Figure 2D**), however, we found gene cluster upregulated in the postnatal-adult hearts (cluster 4) instead of adult heart-specific. Next, we asked if identified clusters shares genes. To test this, we compared genes in clusters 1 and 4 (upregulated in adults compared to embryos), cluster 2 (transiently upregulated), and clusters 3, 5, and 6 (downregulated in adults). Upregulated or downregulated genes were largely shared in mouse and human (**Figure 2E**), while genes in cluster 2 were almost distinct. To determine gene functions of upregulated or downregulated genes, we performed GO analysis on commonly upregulated or downregulated genes in adult mouse and human hearts. GO analysis revealed that genes enriched in adult hearts were related to mitochondrial activities, such as electron transfer and Nicotinamide adenine dinucleotide (NADH) dehydrogenase activity (**Supplementary Figure S3A**). In contrast, cell division-related genes were highly enriched in downregulated genes (**Supplementary Figure S3A**), which is consistent with our previous study (Uosaki et al., 2015). Next, we examined cluster 2s to determine what define the difference in transiently upregulated genes. In mouse hearts (**Supplementary Figure S3B**), extracellular matrix related GO terms are enriched in the genes specifically expressed in mouse cluster 2. In contrast, no GO term for molecular function (MF) were significantly enriched in human (**Supplementary Figure S3C**). GO terms for biological process (BP) enriched in the genes of human cluster 2 were related cardiac function (e.g., cardiac muscle cell action potential).

## Marker Genes for Cardiomyocyte Maturation

To apply this analysis to human PSC-CMs or cardiomyocyte maturation, identifying maturation markers would help. As most of such markers were identified or used based on the knowledge of mouse development, little is known for usefulness in human studies. Thus, we aimed to identify candidate genes for maturation markers of cardiomyocytes from the commonly upregulated DEGs. The medians of the common genes (479 genes, **Figure 2E**) in clusters 1 and 4 were 34.0 and 36.6 RPKM at the adult stage in mouse and human, respectively (**Supplementary Figure S4A**). To select highly expressed genes in adult hearts, we used 100 RPKM in both mouse and adult hearts as the minimum expressions. Next, we examined fold changes between the developmental stages (**Supplementary Figures S4B–H**) or between the species (**Supplementary Figure S4I**). Most of the genes showed less than 10-fold changes in any comparison between the stages. 10-fold changes between adult and early embryonic hearts in one species yielded 100-fold changes in the other species (**Supplementary Figure S4I**), and the genes with 10-fold upregulation in adult from early embryonic hearts include most of the genes that were upregulated in a later stage compared to earlier stages (**Supplementary Figures S4B–H**). Overall, 43 genes were selected as potential maturation marker genes, which showed fold changes of at least 10 times from the early embryos to adults and higher expression levels (> 100 RPKM) in both mice and human adult hearts (**Supplementary Figures S5, S6** and **Figure 3A**). Considering the expression levels and the consistency throughout the samples and species, we narrow down to 12 genes (**Figure 3A**). *MB*, *CKM*, *COX6A2, COX7A1, FABP3, and TCAP* were promising candidates for maturation markers as they reached more than 1,000 RPKM in adults, which would be high enough for making a fluorescent marker as well. TNNI3, a conventionally used marker, also displayed the same profile (**Figure 3B**). We examined nine conventionally used markers for cardiomyocyte maturation, including isoform switches (*MYH7* to 6, *TNNI1* to 3) to ask if these markers are reliable for human (van den Berg et al., 2015; Karakikes et al., 2015; Denning et al., 2016; Ahmed et al., 2020). All but *Kcnh2* displayed expected gene expression profiles in mouse hearts. In contrast, only *CAV3* and *TNNI3* showed consistent profiles as maturation markers for human cardiomyocytes. The expression kinetics of candidate genes varies in mouse and human: some genes (e.g., *MB* and *RPL3L*) started to express earlier in human hearts than mouse hearts at the corresponding stage but others

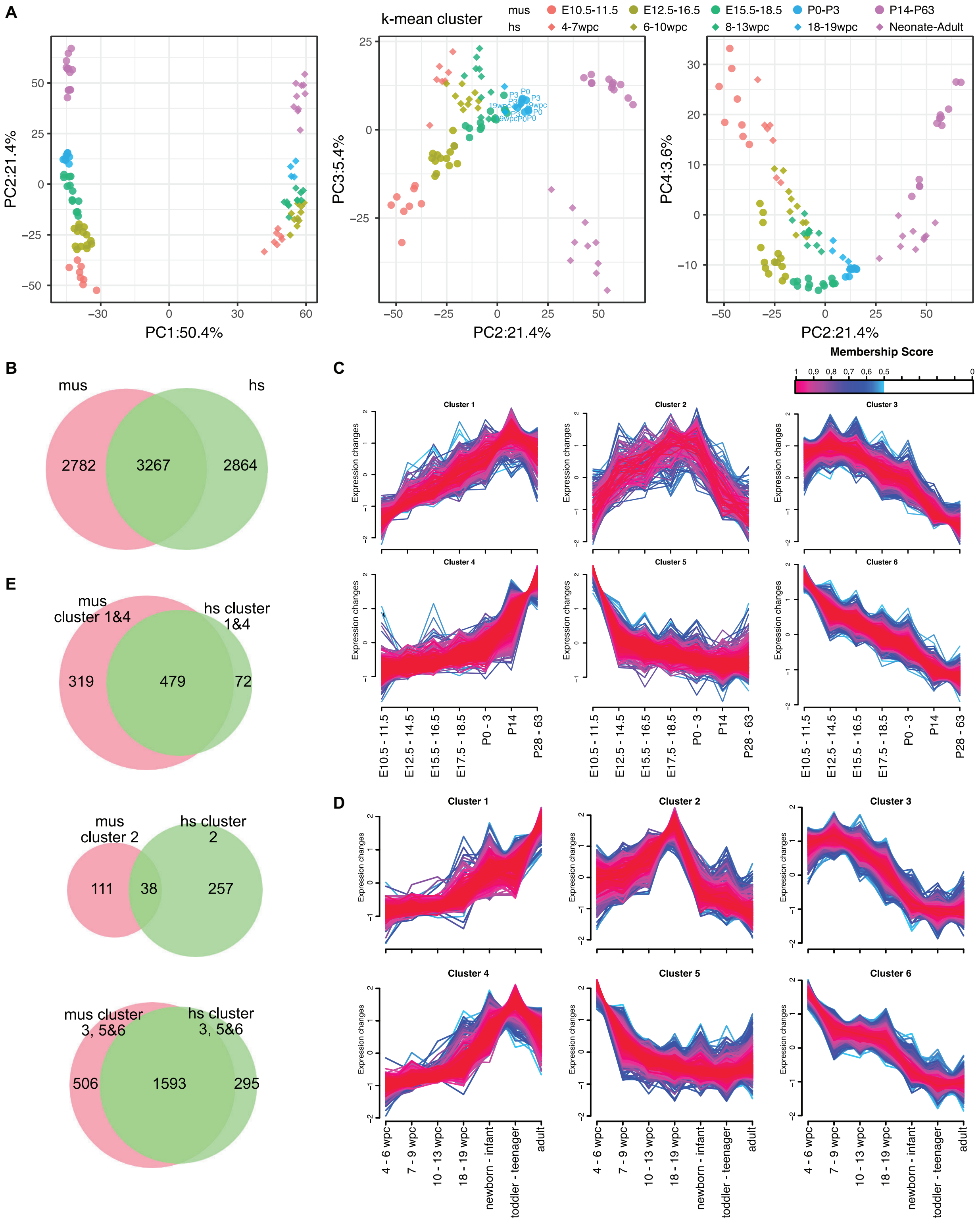

**FIGURE 2 |** Expression dynamics of DEGs during the maturation in hearts. **(A)** PCA of hearts from mouse and human. Shapes of dots represent species [diamond, human (hs); circle, mouse (mus)]. Color represents corresponding ages based on k-mean clusters as shown in figure. Ages shown in PCA plots indicate the ages of each point that is the closest dots between mouse and human. **(B)** Venn diagram of differentially expressed genes (DEGs) in mouse (mus) and human (hs). **(C,D)** Fuzzy clustering of DEGs in mouse **(C)** and human **(D)** with membership score of at least 0.5. Color indicates membership score of each gene in a cluster. **(E)** Venn diagrams of member genes in mouse and human. Gene clusters upregulated in adult (cluster 1 and 4), temporally upregulated (cluster 2), and downregulated in adult (cluster 3, 5, and 6) are shown.

were rather expressed later (e.g., *CKM* and *MGP*). These findings support that the novel set of maturation marker genes can be more reliable than the current set of marker genes.

## Expression of Marker Genes in PSC-CMs

To ask if the candidate maturation markers could dictate maturation of PSC-CMs, we reanalyzed an RNA-seq dataset include human fetal and adult hearts and PSC-CMs with maturation-enhanced conditions (Kuppusamy et al., 2015). In the previous study, PSC-CMs were cultured for 1 year or treated with Let-7 overexpression vector to enhance the maturation. Among 9 conventional markers or the genes the authors used (**Figure 4A**), *MYH7*, *ATP2A2*, *CAV3*, *TNNI3*, *TNNT2*, and *SCN5A* were upregulated from fetal ventricles to adult hearts, and *TNNI1* was downregulated. In PSC-CMs, *CAV3*, *TNNT2*, and *SCN5A* along with *KCNH2*, *RYR2*, and *PLN* were upregulated in maturation enhanced condition compared to control, although the expression of *CAV3* and *TNNI3* were relatively low and comparable to the fetal hearts. Low expression of *MYH7* and increased expression of *TNNI1* might indicate PSC-CMs in the maturation-enhanced condition remained in the fetal stages. Next, we examined the expression of the potential novel set of maturation markers (**Figures 4B,C**). *PERM1* was not found in the dataset, which leaves 42 genes including *TNNI3*. Among 41 genes, *XIRP2* was the only genes expressed at the level of adult hearts in PSC-CMs with the maturation-enhanced conditions. The rest was the level of fetal hearts or lower than that, even after upregulation. The genes expressed from earlier stages of human hearts (e.g., *CASQ2*, *LPL*, and *LRRC2*) displayed relatively higher expression in fetal ventricles and in PSC-CMs with the maturation-enhanced conditions. Taken together, the maturation-enhanced conditions could indeed increase maturation-related genes, but the overall maturation status remained in the fetal stages.

# DISCUSSION

## Identification of Maturation Markers

Cardiomyocyte maturation arrests at an immature state *in vitro*, and discovering a new method to generate mature PSC-CMs is a huge point of emphasis for the last decade (Uosaki et al., 2015; Cho et al., 2017; Ronaldson-Bouchard et al., 2018) after efficient differentiation methods were developed (Uosaki et al., 2011; Tohyama et al., 2013; Burridge et al., 2014). Since cardiomyocyte maturation is generally examined with physiological properties, and/or structural and morphological features, studying mechanisms of maturation is inefficient and little is understood. Moreover, some studies compared gene expression of PSC-CMs and adult human cardiomyocytes with a selected set of genes (Yang et al., 2014a; Karakikes et al., 2015), however, the selection of such genes is based on mouse expression profiles and the expression kinetics of the maturation marker genes during human heart development were unknown. In this study, we discovered a potential novel set of marker genes for maturation, which have similar kinetics in both humans and mice (**Figure 3A**). In addition, the commonly used marker genes displayed expected profiles in mice, however, they did not have the same dynamics or clearness in humans (**Figure 3B**). Recently, we developed a fluorescent reporter line for cardiomyocyte maturation (Chanthra et al., 2020). We inserted red fluorescent protein (RFP) into 3’ end of *Myom2* locus to fuse RFP with Myom2 and demonstrated that RFP positive PSC-CMs were more mature than RFP negative cells. We also demonstrated that the isoform-specific effects of laminin on cardiomyocyte maturation. Physiological and morphological analysis revealed Myom2-RFP PSC-CMs resembled postnatal cardiomyocytes, suggesting that 100 RPKM might be enough to detect fluorescence from the endogenous locus, though it must be validated individually. Generating reliable fluorescent reporter lines based on the novel maturation markers would further facilitate researches on cardiomyocyte maturation, and the maturation marker genes we identified in this study can be a candidate to generate them.

## Implication to Disease Modeling With Human PSC-CMs

As we demonstrated, the expressions of the potential maturation-marker genes were remained low in PSC-CMs even after 1-year cultures. Successful cardiac disease models with immature PSC-CMs would be limited to some diseases that display phenotypes from the very early stages of life as the immature PSC-CMs have distinct electrophysiological properties including calcium handling and metabolisms from adult cardiomyocytes (Yang et al., 2014a; Ahmed et al., 2020). Thus, challenges are still generating more mature PSC-CMs to recapture the disease phenotypes of late-onset cardiac diseases. There have been many attempts to achieve this goal with prolonged culture, electrical and mechanical stimulation, hormones and extracellular matrices (Kamakura et al., 2013; Lundy et al., 2013; Nunes et al., 2013; Yang et al., 2014b; Ronaldson-Bouchard et al., 2018; Chanthra et al., 2020), and some of them seemed more successful. However, it is difficult to compare one to the others because there is no definitive evaluation method of cardiomyocyte maturation. With our novel set of potential marker genes, we might be able to develop more accurate methods to define the maturity of PSC-CMs; the methods can be a fluorescent reporter or targeted RNA-seq of the marker genes.

## The Expression Kinetics of Maturation Markers

The overall transcriptome trajectory highlighted that mouse and human hearts are more similar at P0–3 and 18–19 wpc, respectively. Upregulated genes in the course are largely identical and involve in mitochondrial function. These findings are particularly interesting because mitochondria activity turns glycolysis to fatty acid β-oxidation postnatally (Lopaschuk et al., 1992). Although the overall transcriptome of P0–3 mouse hearts is more similar to that of 18–19 wpc human hearts (**Figure 2A**), expression kinetics of individual maturation marker genes are different. For instance, *Ckm* and *Nrap* start to express in embryonic mouse hearts at E15.5–16.5 and E12.5–14.5,

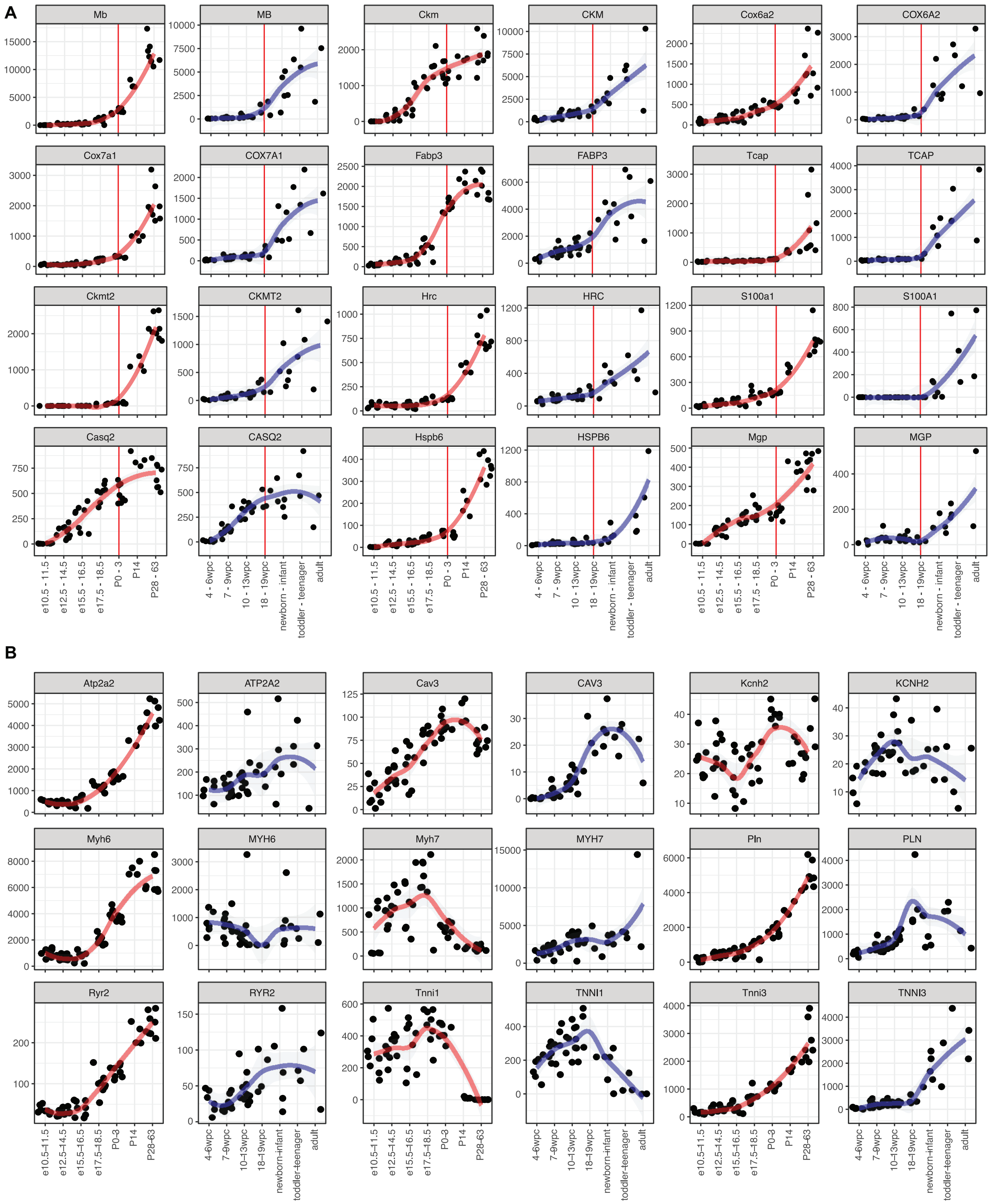

**FIGURE 3 |** Expression kinetics of the potential maturation marker genes. **(A,B)** Time course gene expression profiles. Mouse (left side) and human (right side) data is shown side-by-side. A red (for mouse) or blue (for human) line indicates local regression curve using locally estimated scatterplot smoothing (LOESS). **(A)** Candidate marker genes identified in this study. Red vertical lines indicate P0-3 in mouse and 18–19 wpc in human, which are considered as the same developmental stage. **(B)** Marker genes used in other literatures.

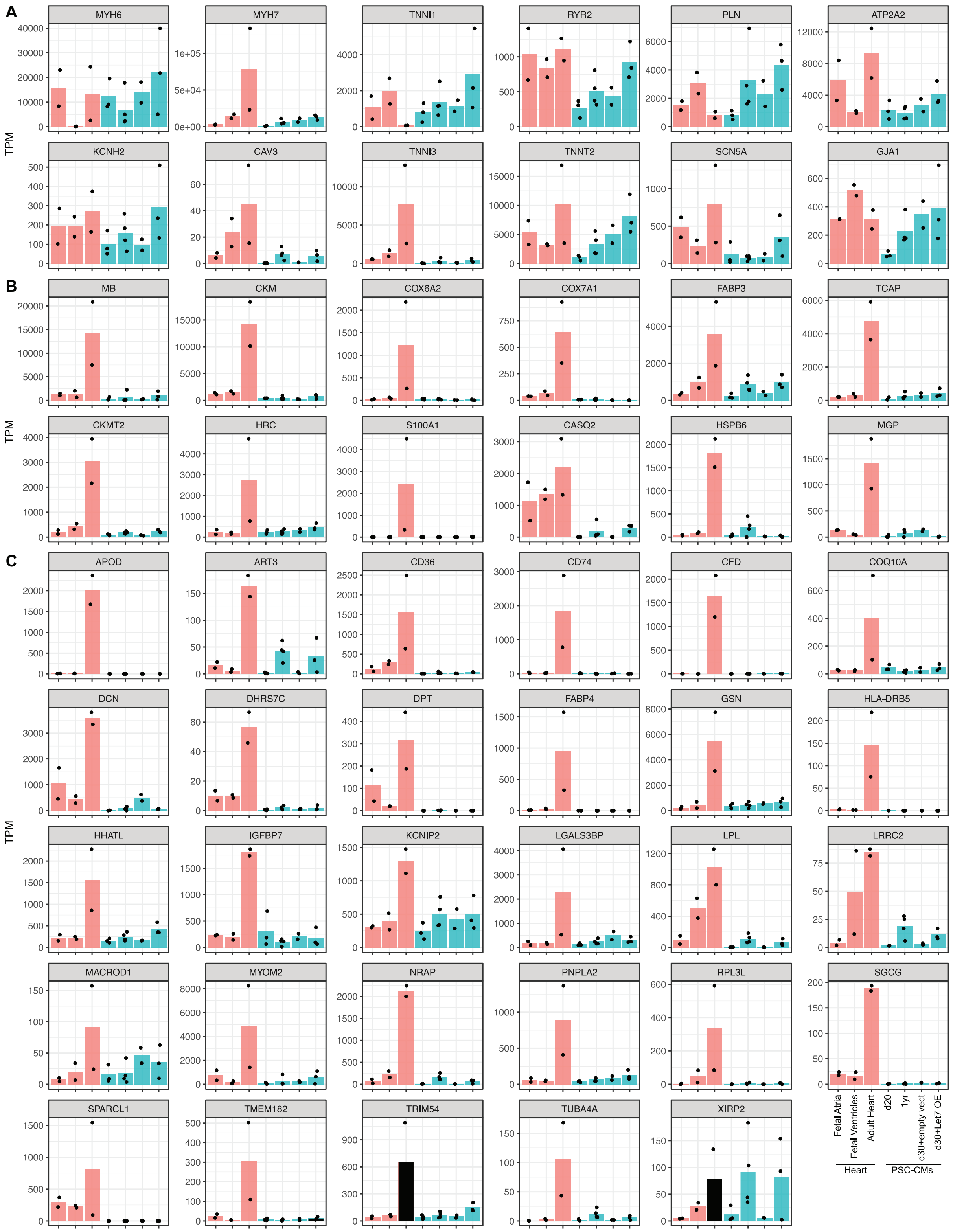

**FIGURE 4 |** Expressions of the maturation marker genes in PSC-CMs. Graphs of the candidate maturation marker gene expressions in human fetal and adult hearts and PSC-CMs. PSC-CMs at day 20 and day 30 with empty vectors are considered as immature while those at 1 year and d30 with Let7 overexpression vector (OE) are considered as more matured. **(A)** Common maturation marker genes including the isoform switch and the genes used in the original study. **(B)** Top 12 and **(C)** the rest of the candidate maturation marker genes identified in this study. Bars are shown in the mean of transcripts per million reads (TPM) and each dot indicates TPM of each sample.

respectively, while their expression becomes evident at 18–19 wpc in human hearts. Moreover, *Ckmt2*, a mitochondrial gene, expressed only after P14 in mouse hearts, but its expression starts mid-gestation in human hearts. These findings suggest that mitochondria might become more active in human fetal hearts.

### Ribosomes Might Define Mouse and Human Differences

The size of somite is determined by the periodic expressions of genes, which is called "segmentation clock." The oscillation periods are species-specific and regulated not only by sequence differences in the involved genes but also by species-specific cell-autonomous differences in biochemical reaction parameters (Chu et al., 2019; Matsuda et al., 2019; Diaz-Cuadros et al., 2020). We unexpectedly revealed that the members of ribosomal genes are differentially expressed in mice and humans. Since ribosomes translate mRNA to proteins, the expression differences in ribosome genes can be a major determinant of the differences in the speed of the segmentation clock. It requires further researches to fully understand how biochemical reaction parameters are different in mice and humans, including protein synthesis rates (Li et al., 2014).

## DATA AVAILABILITY STATEMENT

The datasets analyzed in this study can be found in the E-MTAB-6798, E-MTAB-6814, GSE62913.

## AUTHOR CONTRIBUTIONS

TA and HU conducted bioinformatics analyses and wrote the manuscript. TY provided necessary supervision.

## FUNDING

This study was mainly supported by Fund for the Promotion of Joint International Research [Fostering Joint International Research (B), 19KK0219] from Japan Society for the Promotion of Science (to HU). HU was also supported by Takeda Science Foundation, and the Grant for Basic Research of the Japanese Circulation Society.

## ACKNOWLEDGMENTS

We would like to thank the lab members in Division of Regenerative Medicine at Jichi Medical University for helpful discussions.

## SUPPLEMENTARY MATERIAL

The Supplementary Material for this article can be found online at: https://www.frontiersin.org/articles/10.3389/fcell.2020.00268/full#supplementary-material

## REFERENCES

Ahmed, R. E., Anzai, T., Chanthra, N., and Uosaki, H. (2020). A brief review of current maturation methods for human induced pluripotent stem cells-derived cardiomyocytes. *Front. Cell Dev. Biol* doi: 10.3389/fcell.2020.00178 [Epub ahead of print].

Burridge, P. W., Matsa, E., Shukla, P., Lin, Z. C., Churko, J. M., Ebert, A. D., et al. (2014). Chemically defined generation of human cardiomyocytes. *Nat. Methods* 11, 855–860. doi: 10.1038/nmeth.2999

Cardoso-Moreira, M., Halbert, J., Valloton, D., Velten, B., Chen, C., Shao, Y., et al. (2019). Gene expression across mammalian organ development. *Nature* 571, 505–509. doi: 10.1038/s41586-019-1338-5

Chanthra, N., Abe, T., Miyamoto, M., Sekiguchi, K., Kwon, C., Hanazono, Y., et al. (2020). A novel fluorescent reporter system identifies laminin-511/521 as potent regulators of cardiomyocyte maturation. *Sci. Rep.* 10:4249. doi: 10.1038/s41598-020-61163-3

Cho, G. S., Lee, D. I., Tampakakis, E., Murphy, S., Andersen, P., Uosaki, H., et al. (2017). Neonatal transplantation confers maturation of PSC-derived cardiomyocytes conducive to modeling cardiomyopathy. *Cell Rep.* 18, 571–582. doi: 10.1016/j.celrep.2016.12.040

Chu, L. F., Mamott, D., Ni, Z., Bacher, R., Liu, C., Swanson, S., et al. (2019). An in vitro human segmentation clock model derived from embryonic stem cells. *Cell Rep.* 28, 2247–2255.e5. doi: 10.1016/j.celrep.2019.07.090

de Bakker, B. S., de Jong, K. H., Hagoort, J., de Bree, K., Besselink, C. T., de Kanter, F. E., et al. (2016). An interactive three-dimensional digital atlas and quantitative database of human development. *Science* 354:aag0053. doi: 10.1126/science.aag0053

DeLaughter, D. M., Bick, A. G., Wakimoto, H., McKean, D., Gorham, J. M., Kathiriya, I. S., et al. (2016). Single-cell resolution of temporal gene expression during heart development. *Dev. Cell* 39, 480–490. doi: 10.1016/j.devcel.2016.v10.001

Denning, C., Borgdorff, V., Crutchley, J., Firth, K. S., George, V., Kalra, S., et al. (2016). Cardiomyocytes from human pluripotent stem cells: from laboratory curiosity to industrial biomedical platform. *Biochim. Biophys. Acta* 1863, 1728–1748. doi: 10.1016/j.bbamcr.2015.10.014

Diaz-Cuadros, M., Wagner, D. E., Budjan, C., Hubaud, A., Tarazona, O. A., Donelly, S., et al. (2020). In vitro characterization of the human segmentation clock. *Nature* 580, 113–118. doi: 10.1038/s41586-019-1885-9

Durinck, S., Spellman, P. T., Birney, E., and Huber, W. (2009). Mapping identifiers for the integration of genomic datasets with the R/bioconductor package biomaRt. *Nat. Protoc.* 4, 1184–1191. doi: 10.1038/nprot.2009.97

Futschik, M. E., and Carlisle, B. (2005). Noise-robust soft clustering of gene expression time-course data. *J. Bioinform. Comput. Biol.* 3, 965–988. doi: 10.1142/s0219720005001375

Irie, N., and Kuratani, S. (2011). Comparative transcriptome analysis reveals vertebrate phylotypic period during organogenesis. *Nat. Commun.* 2, 248. doi: 10.1038/ncomms1248

Kamakura, T., Makiyama, T., Sasaki, K., Yoshida, Y., Wuriyanghai, Y., Chen, J., et al. (2013). Ultrastructural maturation of human-induced pluripotent stem cell-derived cardiomyocytes in a long-term culture. *Circ. J.* 77, 1307–1314. doi: 10.1253/circj.cj-12-0987

Karakikes, I., Ameen, M., Termglinchan, V., and Wu, J. C. (2015). Human induced pluripotent stem cell-derived cardiomyocytes: insights into molecular, cellular, and functional phenotypes. *Circ. Res.* 117, 80–88. doi: 10.1161/CIRCRESAHA.117.305365

Kumar, L., and Futschik, E. M. (2007). Mfuzz: a software package for soft clustering of microarray data. *Bioinformation* 2, 5–7. doi: 10.6026/97320630002005

Kuppusamy, K. T., Jones, D. C., Sperber, H., Madan, A., Fischer, K. A., Rodriguez, M. L., et al. (2015). Let-7 family of microRNA is required for maturation and adult-like metabolism in stem cell-derived cardiomyocytes. *Proc. Natl. Acad. Sci. U.S.A.* 112, E2785–E2794. doi: 10.1073/pnas.1424042112

Li, G. W., Burkhardt, D., Gross, C., and Weissman, J. S. (2014). Quantifying absolute protein synthesis rates reveals principles underlying allocation of cellular resources. *Cell* 157, 624–635. doi: 10.1016/j.cell.2014.02.033

Lopaschuk, G. D., Collins-Nakai, R. L., and Itoi, T. (1992). Developmental changes in energy substrate use by the heart. *Cardiovasc. Res.* 26, 1172–1180. doi: 10.1093/cvr/26.12.1172

Lundy, S. D., Zhu, W. Z., Regnier, M., and Laflamme, M. A. (2013). Structural and functional maturation of cardiomyocytes derived from human pluripotent stem cells. *Stem Cells Dev.* 22, 1991–2002. doi: 10.1089/scd.2012.0490

Mancarci, O. (2018). *Homologene*: Quick Access to Homology Information. Available online at: https://CRAN.R-project.org/package=homologene (accessed November 27, 2019).

Matsuda, M., Hayashi, H., Garcia-Ojalvo, J., Yoshioka-Kobayashi, K., Kageyama, R., Yamanaka, Y., et al. (2019). Species-specific oscillation periods of human and mouse segmentation clocks are due to cell autonomous differences in biochemical reaction parameters. *bioRxiv* [Preprint]. doi: 10.1101/650648

McCarthy, D. J., Chen, Y., and Smyth, G. K. (2012). Differential expression analysis of multifactor RNA-seq experiments with respect to biological variation. *Nucleic Acids Res.* 40, 4288–4297. doi: 10.1093/nar/gks042

Nunes, S. S., Miklas, J. W., Liu, J., Aschar-Sobbi, R., Xiao, Y., Zhang, B., et al. (2013). Biowire: a platform for maturation of human pluripotent stem cell–derived cardiomyocytes. *Nat. Methods* 10, 781–787. doi: 10.1038/nmeth.2524

R Core Team (2016). *R: A Language and Environment for Statistical Computing*. Vienna: R Foundation for Statistical Computing.

Robinson, M. D., McCarthy, D. J., and Smyth, G. K. (2010). EdgeR: a bioconductor package for differential expression analysis of digital gene expression data. *Bioinformatics* 26, 139–140. doi: 10.1093/bioinformatics/btp616

Ronaldson-Bouchard, K., Ma, S. P., Yeager, K., Chen, T., Song, L., Sirabella, D., et al. (2018). Advanced maturation of human cardiac tissue grown from pluripotent stem cells. *Nature* 556, 239–243. doi: 10.1038/s41586-018-0016-3

Sievert, C. (2020). *Interactive Web-Based Data Visualization With R, Plotly, and Shiny*. Boca Raton, FL: CRC Press, Taylor and Francis Group, 2020. Available online at: https://plotly-r.com

Tohyama, S., Hattori, F., Sano, M., Hishiki, T., Nagahata, Y., Matsuura, T., et al. (2013). Distinct metabolic flow enables large-scale purification of mouse and human pluripotent stem cell-derived cardiomyocytes. *Cell Stem Cell* 12, 127–137. doi: 10.1016/j.stem.2012.09.013

Uosaki, H., Cahan, P., Lee, D. I., Wang, S., Miyamoto, M., Fernandez, L., et al. (2015). Transcriptional landscape of cardiomyocyte maturation. *Cell Rep.* 13, 1705–1716. doi: 10.1016/j.celrep.2015.10.032

Uosaki, H., Fukushima, H., Takeuchi, A., Matsuoka, S., Nakatsuji, N., and Yamanaka, S. (2011). Efficient and scalable purification of cardiomyocytes from human embryonic and induced pluripotent stem cells by VCAM1 surface expression. *PLoS One* 6:e23657. doi: 10.1371/journal.pone.0023657

Uosaki, H., and Taguchi, Y. H. (2016). Comparative gene expression analysis of mouse and human cardiac maturation. *Genomics Proteomics Bioinform.* 14, 207–215. doi: 10.1016/j.gpb.2016.04.004

van den Berg, C. W., Okawa, S., Chuva de Sousa Lopes, S. M., van Iperen, L., Passier, R., Braam, S. R., et al. (2015). Transcriptome of human foetal heart compared with cardiomyocytes from pluripotent stem cells. *Development* 142, 3231–3238. doi: 10.1242/dev.123810

Wickham, H. (2016). *Ggplot2: Elegant Graphics for Data Analysis*. New York, NY: Springer-Verlag.

Yang, X., Pabon, L., and Murry, C. E. (2014a). Engineering adolescence: maturation of human pluripotent stem cell–derived cardiomyocytes. *Circ. Res.* 114, 511–523. doi: 10.1161/CIRCRESAHA.114.300558

Yang, X., Rodriguez, M., Pabon, L., Fischer, K. A., Reinecke, H., Regnier, M., et al. (2014b). Tri-iodo-l-thyronine promotes the maturation of human cardiomyocytes-derived from induced pluripotent stem cells. *J. Mol. Cell. Cardiol.* 72, 296–304. doi: 10.1016/j.yjmcc.2014.04.005

Yu, G., Wang, L. G., Han, Y., and He, Q. Y. (2012). Cluster profiler: an R package for comparing biological themes among gene clusters. *OMICS* 16, 284–287. doi: 10.1089/omi.2011.0118

Yu, G., Wang, L. G., Yan, G. R., and He, Q. Y. (2015). DOSE: an R/bioconductor package for disease ontology semantic and enrichment analysis. *Bioinformatics* 31, 608–609. doi: 10.1093/bioinformatics/btu684

**Conflict of Interest:** The authors declare that the research was conducted in the absence of any commercial or financial relationships that could be construed as a potential conflict of interest.

frontiers
in Cell and Developmental Biology

METHODS
published: 15 May 2020
doi: 10.3389/fcell.2020.00309

# Endothelial Progenitor Cells Produced From Human Pluripotent Stem Cells by a Synergistic Combination of Cytokines, Small Compounds, and Serum-Free Medium

*Simon Farkas[1], Pavel Simara[1,2], Daniela Rehakova[2], Lenka Veverkova[3] and Irena Koutna[1,2]**

*[1] Department of Histology and Embryology, Theoretical Departments, Faculty of Medicine, Masaryk University, Brno, Czechia, [2] International Clinical Research Center, St. Anne's University Hospital Brno, Brno, Czechia, [3] I. Surgery Department, St. Anne's University Hospital Brno, Brno, Czechia*

**Edited by:**
*Jong-Kook Lee,*
*Osaka University, Japan*

**Reviewed by:**
*Yuuki Shimizu,*
*Nagoya University, Japan*
*Kyoko Hidaka,*
*The University of Kitakyushu, Japan*

***Correspondence:**
*Irena Koutna*
*qkoutna@mail.muni.cz;*
*qkoutna@gmail.com*

**Specialty section:**
*This article was submitted to Stem Cell Research, a section of the journal Frontiers in Cell and Developmental Biology*

**Received:** *21 October 2019*
**Accepted:** *07 April 2020*
**Published:** *15 May 2020*

**Citation:**
*Farkas S, Simara P, Rehakova D, Veverkova L and Koutna I (2020) Endothelial Progenitor Cells Produced From Human Pluripotent Stem Cells by a Synergistic Combination of Cytokines, Small Compounds, and Serum-Free Medium. Front. Cell Dev. Biol. 8:309. doi: 10.3389/fcell.2020.00309*

Human pluripotent stem cells (hPSCs) are a promising source of autologous endothelial progenitor cells (EPCs) that can be used for the treatment of vascular diseases. However, this kind of treatment requires a large amount of EPCs. Therefore, a highly efficient, robust, and easily reproducible differentiation protocol is necessary. We present a novel serum-free differentiation protocol that exploits the synergy of multiple powerful differentiation effectors. Our protocol follows the proper physiological pathway by differentiating EPCs from hPSCs in three phases that mimic *in vivo* embryonic vascular development. Specifically, hPSCs are differentiated into (i) primitive streak, which is subsequently turned into (ii) mesoderm, which finally differentiates into (iii) EPCs. This differentiation process yields up to 15 differentiated cells per seeded hPSC in 5 days. Endothelial progenitor cells constitute up to 97% of these derived cells. The experiments were performed on the human embryonic stem cell line H9 and six human induced pluripotent stem cell lines generated in our laboratory. Therefore, robustness was verified using many hPSC lines. Two previously established protocols were also adapted and compared to our synergistic three-phase protocol. Increased efficiency and decreased variability were observed for our differentiation protocol in comparison to the other tested protocols. Furthermore, EPCs derived from hPSCs by our protocol expressed the high-proliferative-potential EPC marker CD157 on their surface in addition to the standard EPC surface markers CD31, CD144, CD34, KDR, and CXCR4. Our protocol enables efficient fully defined production of autologous endothelial progenitors for research and clinical applications.

**Keywords: hiPSC, hESC, hPSC, mesoderm, endothelial progenitors, differentiation, protocol**

## INTRODUCTION

According to the World Health Organization, ischemic heart disease and stroke have been two major causes of death worldwide for the last 15 years. It is therefore very desirable to find an efficient treatment for such devastating diseases. Both diseases are often the result of worn-out and/or damaged endothelial cells (ECs). Replacement of dysfunctional ECs with healthy young ECs seems to be a logical solution that will be applicable in the foreseeable future. However, it is first necessary to determine which subtype of ECs is best suited for this job, and second, we have to produce this subtype of ECs in high-enough numbers to treat the aforementioned diseases. Last but not least, this cell production needs to be both robust and standardized, if it is to be ever widely used in clinical practice.

Endothelial cells form the linings of blood and lymphatic vessel lumens. They have regulatory roles in physiological processes, such as maintaining vascular tone and homeostasis; they participate in angiogenesis and vasculogenesis, and they mediate interactions of the vessel wall with blood elements (Carmeliet, 2000). The ECs most commonly found in the human vasculature are mature ECs such as human saphenous vein ECs (HSVECs) and human umbilical vein ECs (HUVECs), which can be harvested from umbilical cords, as their name suggests. Mature ECs highly express the surface pan-endothelial markers CD31 and CD144. CD34 and kinase insert domain receptor (KDR), which are mostly associated with the progenitor status of ECs, can also be expressed on the surface of mature ECs, although their expression is dim to none. Endothelial cells grow in cobblestone formation and have proliferative capacity. Nonetheless, mature ECs lack angiogenic and vasculogenic properties, which significantly reduces their potential use in regenerative medicine.

Endothelial progenitor cell (EPC) is a general term for a group of cells defined by high surface expression of the markers CD31, CD144, CD34, and KDR in the entirety of their populations. This group contains primitive ECs with improved angiogenic and vasculogenic properties (Cheng et al., 2013; Patel et al., 2013, 2017; Lee et al., 2015; Shafiee et al., 2018). These primitive ECs, also known as late EPCs or endothelial colony-forming cells (ECFCs), are derived from mesoderm, and they have the ability to proliferate and to differentiate into mature ECs. They grow in cobblestone formation such as mature ECs, and they cannot be distinguished from these cells by light microscopy. A significant fraction of ECFCs expresses C-X-C chemokine receptor type 4 (CXCR4/CD184) on their surface in addition to other EPC surface markers (Joo et al., 2015; Kang et al., 2015). While CXCR4 is not expressed in mesoderm, it is later expressed in some of its progeny, including ECFC. Presence of CXCR4 on the cell surface improves homing capabilities, which is desirable property in progenitor cells. Endothelial colony-forming cells contain a subpopulation of very proliferative, angiogenic, and vasculogenic cells, which are referred to as high-proliferative-potential (HPP) ECFCs. This subpopulation was recently discovered to express bone marrow stromal cell antigen 1 (CD157/BST-1) on their surface, unlike any other endothelial population reported so far (Wakabayashi et al., 2018). Because of their properties, ECFCs and HPP-ECFCs are ideal candidates for use in regenerative medicine.

More than 150 clinical trials are currently being conducted on ECFCs, mainly to treat myocardial infarction and peripheral vascular disease (Chong et al., 2016). Such treatments require vast amounts of ECFCs to be successful. However, ECFCs from blood vessels or peripheral blood can only be obtained in limited numbers, which makes it impossible to expand them to sufficient numbers without compromising their proliferative potential. To overcome these hurdles, human pluripotent stem cells (hPSCs) can be differentiated into endothelium. Attempts at efficient *in vitro* endothelial differentiation of hPSCs have been conducted for at least 10 years (Choi et al., 2009; Park et al., 2010; Vodyanik et al., 2010; Joo et al., 2011; Li et al., 2011; Tatsumi et al., 2011; Adams et al., 2013; Prasain et al., 2014; Sahara et al., 2014; Zhang et al., 2014; Bao et al., 2015; Patsch et al., 2015; Sriram et al., 2015; Kitajima et al., 2016; Ye et al., 2016; Harding et al., 2017; Olmer et al., 2018; Suknuntha et al., 2018; Zhao et al., 2018). This strategy has the potential to ensure a consistent and unlimited source of ECFCs for *in vitro* studies and regenerative medicine. There are two major approaches to endothelial differentiation of hPSCs. First, embryoid body-based differentiation may be used, but it is a time-consuming and relatively inefficient method of endothelial derivation (Li et al., 2011; Adams et al., 2013). Second, monolayer differentiation is a more feasible approach, with higher efficiency in a shorter time. There are multiple monolayer differentiation protocols that vary in both medium and cytokine supplement (Park et al., 2010; Joo et al., 2011; Tatsumi et al., 2011; Orlova et al., 2014; Prasain et al., 2014; Sahara et al., 2014; Bao et al., 2015; Patsch et al., 2015; Sriram et al., 2015; Kitajima et al., 2016; Harding et al., 2017; Zhao et al., 2018). Most monolayer protocols use single-cell seeding, small-clump seeding using ethylenediaminetetraacetic acid (EDTA), or larger-clump seeding using a needle. In general, clump-based differentiation protocols have higher differentiation efficiency than single-cell–based protocols. Unfortunately, clump-based protocols have very low reproducibility as they are highly dependent on the individual skill of the operator, and they make it harder to quantify the number of cells used. In contrast, single-cell protocols enable usage of more precise amounts of cells, which makes them potentially more suitable for standardized procedures, should their lower efficiency be resolved. A highly efficient, robust and standardized protocol is necessary in order to differentiate large-enough amounts of ECFCs from hPSCs, to satisfy the needs of regenerative medicine. We hypothesized that the best way to produce these ECFCs is by a differentiation protocol that replicates the three most important naturally occurring steps of embryonic endothelial differentiation. These steps are as follows: (i) rise of the primitive streak from the epiblast, (ii) differentiation of the primitive streak into mesoderm, and (iii) differentiation of the mesoderm into blood islands (a population of endothelial progenitors). To efficiently replicate these steps *in vitro*, we used known effectors of endothelial differentiation (Sahara et al., 2014; Patsch et al., 2015; Sriram et al., 2015; Kempf et al., 2016) in a novel synergistic strategy.

Our new protocol has three phases, and the unique medium composition in each phase drives the transition of hPSCs first

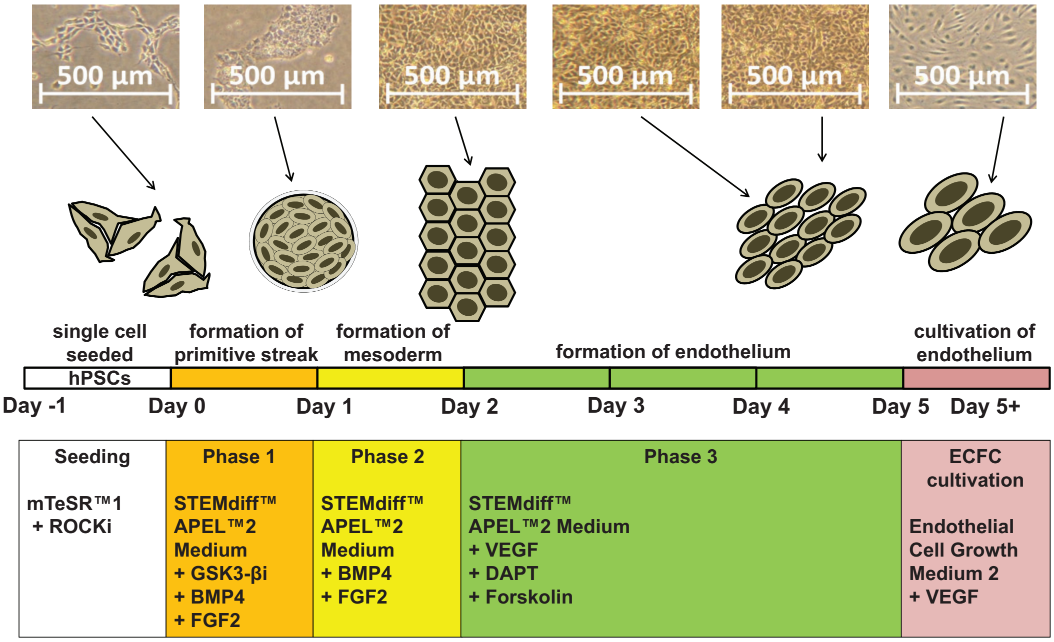

| Seeding | Phase 1 | Phase 2 | Phase 3 | ECFC cultivation |
|---|---|---|---|---|
| mTeSR™1<br>+ ROCKi | STEMdiff™ APEL™2 Medium<br>+ GSK3-βi<br>+ BMP4<br>+ FGF2 | STEMdiff™ APEL™2 Medium<br>+ BMP4<br>+ FGF2 | STEMdiff™ APEL™2 Medium<br>+ VEGF<br>+ DAPT<br>+ Forskolin | Endothelial Cell Growth Medium 2<br>+ VEGF |

**FIGURE 1 |** Schematic description of our synergistic three-phase differentiation protocol. Representative photographs of the hiPSC line CBIA-50 differentiated by our three-phase protocol and schematic description of this differentiation protocol. Human pluripotent stem cells (hPSCs) are seeded in single-cell format and then differentiated into endothelium in three phases. Lastly, the derived ECFCs are further cultivated.

to the primitive streak and then to KDR$^+$ mesoderm and finally to primitive endothelium (**Figure 1**). With our synergistic three-phase protocol, we were able to differentiate all seven hPSC lines used in this study into endothelium in only 5 days, with very high efficiency under standardized and fully described conditions. The derived endothelium fitted the description of HPP-ECFCs. To our knowledge, this is the most robust endothelial differentiation experiment conducted up to this point, given that the hPSCs used included a human embryonic stem cell (hESC) line and six human induced pluripotent stem cell (hiPSC) lines created by three different methods from multiple donor cell types. Therefore, our synergistic three-phase protocol is fully replicable and highly efficient and produces cells that fit the most recent profile of endothelial progenitors (HPP-ECFCs).

# MATERIALS AND EQUIPMENT

## Cytokines and Small Compounds

1. Y-27632 2HCl (ROCK1 inhibitor; Selleckchem, Houston, TX, United States, S1049);
2. CP21R7 [glycogen synthase kinase 3 beta (GSK3-β) inhibitor; Selleckchem, S7954];
3. BMP4 (Peprotech, Rocky Hill, NJ, United States, 120-05ET);
4. FGF2 (Peprotech, 100-18B);
5. VEGF$_{165}$ (Peprotech, 100-20);
6. DAPT–γ-secretase inhibitor (Sigma–Aldrich, St. Louis, MO, United States, D5942-5MG);
7. Forskolin (Sigma–Aldrich, F3917-10MG).

## Other Reagents and Media

1. mTeSR1$^{TM}$ (STEMCELL Technologies, Vancouver, BC, Canada, 85850);
2. Corning Matrigel matrix (Corning, Corning, NY, United States, 354277);
3. TrypLE$^{TM}$ Express (1×; Thermo Fisher Scientific, Waltham, MA, United States, 12604021);
4. STEMdiff$^{TM}$ APEL$^{TM}$2 (STEMCELL Technologies, 5270);
5. Fibronectin (Sigma–Aldrich, F0895-5MG);
6. Endothelial cell growth medium 2 (PromoCell, Heidelberg, Germany, C-22011);
7. Phosphate-buffered saline (PBS), pH 7.4 without phenol red, calcium or magnesium (Thermo Fisher Scientific, 10010056);
8. UltraPure$^{TM}$ 0.5M EDTA, pH 8.0 (Thermo Fisher Scientific, 15575020);
9. Bovine serum albumin (BSA; Sigma, A4503);
10. ZellShield® (Minerva Biolabs, Berlin, Germany);
11. DMEM/F-12, no glutamine (Thermo Fisher Scientific, 21331020).

## Florescence-Activated Cell Sorting Antibodies and Low-Density Lipoprotein

Combine two different types of antibodies (APC-conjugated + PE-conjugated antibodies) per sample if possible.

1. Anti-CD31 antibody (allophycocyanin [APC] conjugated; AC128; Miltenyi Biotec, Bergisch Gladbach, Germany, 130-092-652);

2. Anti-CD34 antibody (phycoerythrin [PE] conjugated; AC136; Miltenyi Biotec, 130-081-002);
3. Anti-CD144 antibody (PE conjugated; REA199; Miltenyi Biotec, 130-100-708); alternatively, the APC- conjugated variant may be used for convenience;
4. Anti-KDR antibody (PE conjugated; ES8-20E6; Miltenyi Biotec, 130-093-598);
5. Anti-CXCR4 antibody (APC conjugated; REA649; Miltenyi Biotec, 130-098-357);
6. Anti-CD157 antibody (APC conjugated; REA465; Miltenyi Biotec, 130-106-982);
7. Dil-labeled and acetylated (Dil-Ac)-LDL (Alpha Diagnostics, San Antonio, TX, United States, LDLA16-N-1).

## Equipment and Software

1. BD FACS Canto II flow cytometer (Becton–Dickinson, Heidelberg, Germany);
2. BD FACSDiva analysis software (Becton–Dickinson);
3. Flowing software (Cell Imaging Core, Turku Centre for Biotechnology, Turku, Finland);
4. CD31 MicroBead Kit (Miltenyi Biotec, 130-091-935);
5. CD144 MicroBead Kit (Miltenyi Biotec, 130-097-857);
6. MiniMACS$^{TM}$ Separator (Miltenyi Biotec, 130-042-102);
7. MS Column (Miltenyi Biotec, 130-042-201).

## Media Recipes

1. hPSC cultivation medium: mTeSR-1 medium;
2. Predifferentiation medium: mTeSR-1 medium and 10 ng/mL Y-27632 2HCl (ROCK1 inhibitor);
3. Phase 1 medium: STEMdiff APEL2, 3 μM CP21R7 (GSK3 -β inhibitor), 25 ng/mL BMP4, and 50 ng/mL FGF2;
4. Phase 2 medium: STEMdiff APEL2, 25 ng/mL BMP4 and 50 ng/mL FGF2;
5. Phase 3 medium: STEMdiff APEL2, 200 ng/mL $VEGF_{165}$, 10 μM DAPT, and 2 μM forskolin;
6. ECFC cultivation medium: endothelial cell growth medium 2 and 50 ng/mL $VEGF_{165}$.

Notes: To prevent contamination, all media used in the experiment contained Zell Shield (Minerva Biolabs) in a 1:100 ratio (according to manufacturer instructions). All supplements were mixed with their respective media according to manufacturer instructions.

## Dish Coating

Dishes for hPSC cultivation and differentiation: ice-cold Matrigel was mixed with ice-cold DMEM2/F-12, no glutamine according to manufacturer instructions (Corning, 354277; the exact ratio was LOT dependent). Dishes were coated at 1 mL/10 cm$^2$ and left at room temperature for at least 1 h prior to use.

Dishes for somatic ECs and derived ECFCs: Refrigerated (8°C) fibronectin was mixed with refrigerated (8°C) PBS at a 1:40 ratio. Dishes were coated at 1 mL/10 cm$^2$ (2.5 μg/cm$^2$) and left at room temperature for at least 1 h prior to use.

## Cultures of hPSCs Used to Test Efficiency and Robustness of the Protocol

The six hiPSC lines used were generated and characterized in our laboratory (Simara et al., 2014; Tesarova et al., 2016), and the hESC H9 (WA09) line was bought from WiCell Research Institute (Madison, WI, United States). The hPSC cultures were maintained long term in hPSC cultivation medium on hPSC cultivation dishes according to instructions from their respective manufacturers (STEMCELL Technologies 85850 and Corning 354277).

### hPSC ID, Stem Cell Type, Source Cell Type, and Reprogramming Methods

1. H9 (WA09), hESC, human embryo, no reprogramming method;
2. CBIA-3, hiPSC, CD34$^+$ blood progenitor, Sendai virus;
3. CBIA-7, hiPSC, human adult dermal fibroblasts, episomal vector;
4. CBIA-19, hiPSC, HUVECs, episomal vector;
5. CBIA-37, hiPSC, HSVECs, episomal vector;
6. CBIA-50, hiPSC, HUVECs, StemRNA-NM$^{TM}$ Reprogramming Kit;
7. CBIA-58, hiPSC, HSVECs, StemRNA-NM$^{TM}$ Reprogramming Kit.

### Somatic Endothelial Cells Used in the Experiment

1. HUVEC1—cell line pooled from multiple donors and bought from Thermo Fisher Scientific;
2. HUVEC2—cell line isolated from single donor in our laboratory;
3. C2—a HSVEC line from single donor isolated in our laboratory.

# PROCEDURES

## Predifferentiation (Up to Day -1)

Maintain the hPSC cultures in hPSC cultivation medium on hPSC cultivation dishes for at least three passages prior to differentiation. Upon reaching 70 to 80% confluence, add 10 ng/mL Y-27632 2HCl to the medium for at least 1 h. After this exposure to Y-27632 2HCl, dissociate hPSCs into single cells using TrypLE according to the manufacturer instructions. Seed the dissociated cells at a density of 40,000 cells/cm$^2$ and culture them in predifferentiation medium for 1 day (day -1).

## Phase 1 (Day 0)

Remove predifferentiation medium and wash cells with PBS. Remove PBS and add phase 1 medium, using 1 mL/10 cm$^2$ of culture dish, and culture the cells in these conditions for 1 day.

## Phase 2 (Day 1)

Exchange phase 1 medium for phase 2 medium, using 2 mL/10 cm$^2$ of culture dish, and culture the cells in these conditions for 1 day.

## Optional Mesoderm Verification (Day 2)

On day 2, collect adherent differentiating cells by TrypLE and analyze them by florescence-activated cell sorting (FACS) for the mesoderm-specific marker KDR and the endoderm-specific marker CXCR4. KDR should be highly expressed, whereas CXCR4 should have no or only dim expression in a small portion of the cell population, as exemplified in **Figure 3A**.

## Phase 3 (Days 2–4)

Exchange phase 2 medium for phase 3 medium on day 2, using 2 mL/10 $\text{cm}^2$ of culture. On days 3 and 4, replace old phase 3 medium with fresh phase 3 medium.

## End of Differentiation (Day 5)

On day 5, collect adherent differentiated cells by TrypLE and analyze a fraction of them by FACS for the endothelial surface markers CD31, CD144, CD34, and KDR (**Figure 2D**). Cell cultures with $\geq$85% expression of either CD31 or CD144 can be seeded without any separation. If the expression of both CD31 and CD144 in derived cells is <85%, separation by magnetic-activated cell sorting (MACS) for the marker CD31 or CD144 is necessary prior to seeding. Next, seed the differentiated cells at a density of 10,000 cells/$\text{cm}^2$ on dishes for derived ECFCs and cultivate them in 2 mL ECFC cultivation medium/$\text{cm}^2$.

## Cultivation of Derived Cells Postdifferentiation

Exchange ECFC cultivation medium every other day and passage the cells using TrypLE when they reach 90% confluence. In all subsequent passages, seed at a density of 7,000 cells/$\text{cm}^2$.

## Analysis of Derived Cells

Analyze derived cells by FACS after the first passage in order to verify the purity and quality of the cells. Use markers CD31 and/or CD144 to analyze purity and CD34, KDR, CXCR4, and CD157 to determine the ECFC character of the cells (**Figure 3A**). After three passages, the endothelial character of the derived cells can be further verified by measuring low-density lipoprotein (LDL) uptake and by conducting a tube formation assay, as described below.

Incubate the derived cells with 10 mg/mL Dil-Ac-LDL for 4 h and then harvest them as a single-cell suspension using TrypLE and resuspend them in 300 μL PBS containing 0.5% BSA and 2 mM EDTA. Analyze this suspension by FACS (**Figure 3C**).

Coat a 96-well microplate for angiogenesis (Ibidi, Planegg, Germany) with 25 μL/well Matrigel and incubate it at 37°C for 1 h. Seed the derived cells at densities of 5,000, 10,000, and 15,000 cells/well in endothelial cell growth medium 2 supplemented with 50 ng/mL $\text{VEGF}_{165}$ (50 μL/well) and incubate in a 37°C incubator with a 5% $\text{CO}_2$ atmosphere for 24 h to allow tubes to form. Analyze tube formation by light microscopy (**Figure 3D**).

## Additional Information

All media exchanges in the experiment were conducted at room temperature. All cells were cultured in an incubator at 37°C with a high humidity and a 5% $\text{CO}_2$ atmosphere. Representative images of predifferentiation hPSCs, the entire differentiation process, and postdifferentiation derived cells can be seen in **Figure 2**.

## Notes on FACS Analysis

Resuspend pellet of single cells in PBS containing 0.5% BSA and 2 mM EDTA. Use 100 μL of PBS/BSA/EDTA mixture per sample. Use at least 30,000 living cells per sample in order to get at least 10,000 relevant events during your FACS analysis. Combine two different types of antibodies (APC-conjugated + PE-conjugated antibodies) per sample if possible. Incubate the mixture with fluorochrome-conjugated antibodies for 15 min at 4°C. You can either use the manufacturer-recommended amount of antibodies or a reduced amount, for example, 3 to 4 μL instead of 10 μL or 1 μL instead of 2 μL. This reduction of antibody volume is possible because manufacturer-recommended amounts of antibodies are set for 1 million or more cells per sample, whereas a much smaller sample is sufficient. After incubation with antibodies, add 1 mL of refrigerated PBS per sample and centrifuge at 300 × *g* for 3 min at 4°C. Remove the supernatant and add 300 μL of refrigerated PBS to the pellet. Ideally, analyze it as soon as possible. If necessary, samples can last in this state for up to 2 h. Pipet or vortex the mixture for a few seconds prior to analysis.

## Notes on MACS Analysis

Resuspend pellet of single cells in PBS containing 0.5% BSA and 2 mM EDTA. The same PBS/BSA/EDTA mixture can be used for FACS and MACS. For example, prepare 1 mL of the PBS/BSA/EDTA mixture and then use 3 × 100 μL of it for FACS (for the unstained control, anti–CD31-APC + anti–CD34-PE and anti–CD144-APC + anti–KDR-PE experiments) and 700 μL of it for MACS. From this point on, follow the MACS instructions of the manufacturer. Skip MACS when either CD31 or CD144 expression is $\geq$85% (**Figure 2D**).

## Advice

In addition to your main sample(s), seed one or two additional small format dishes, for example, 12-well size. Use cells from these 12-well dishes for FACS analysis by the end of days 2 and 5. In our experience, the efficiency of differentiation is dependent on the cell line of source hPSCs (**Supplementary Figures S1–S3**). Variability between different samples of the same hPSC line is negligible. Therefore, the results of FACS analysis from a smaller sample can be used to determine whether MACS is necessary for a larger sample.

# EXPECTED RESULTS

We employed previously identified effectors of differentiation (Tan et al., 2013; Sahara et al., 2014; Patsch et al., 2015; Sriram et al., 2015; Kempf et al., 2016) into a synergistic three-phase differentiation protocol (**Figure 1**). With this synergistic approach, we were able to differentiate hPSCs into mesoderm with up to 93% surface expression of KDR and low expression

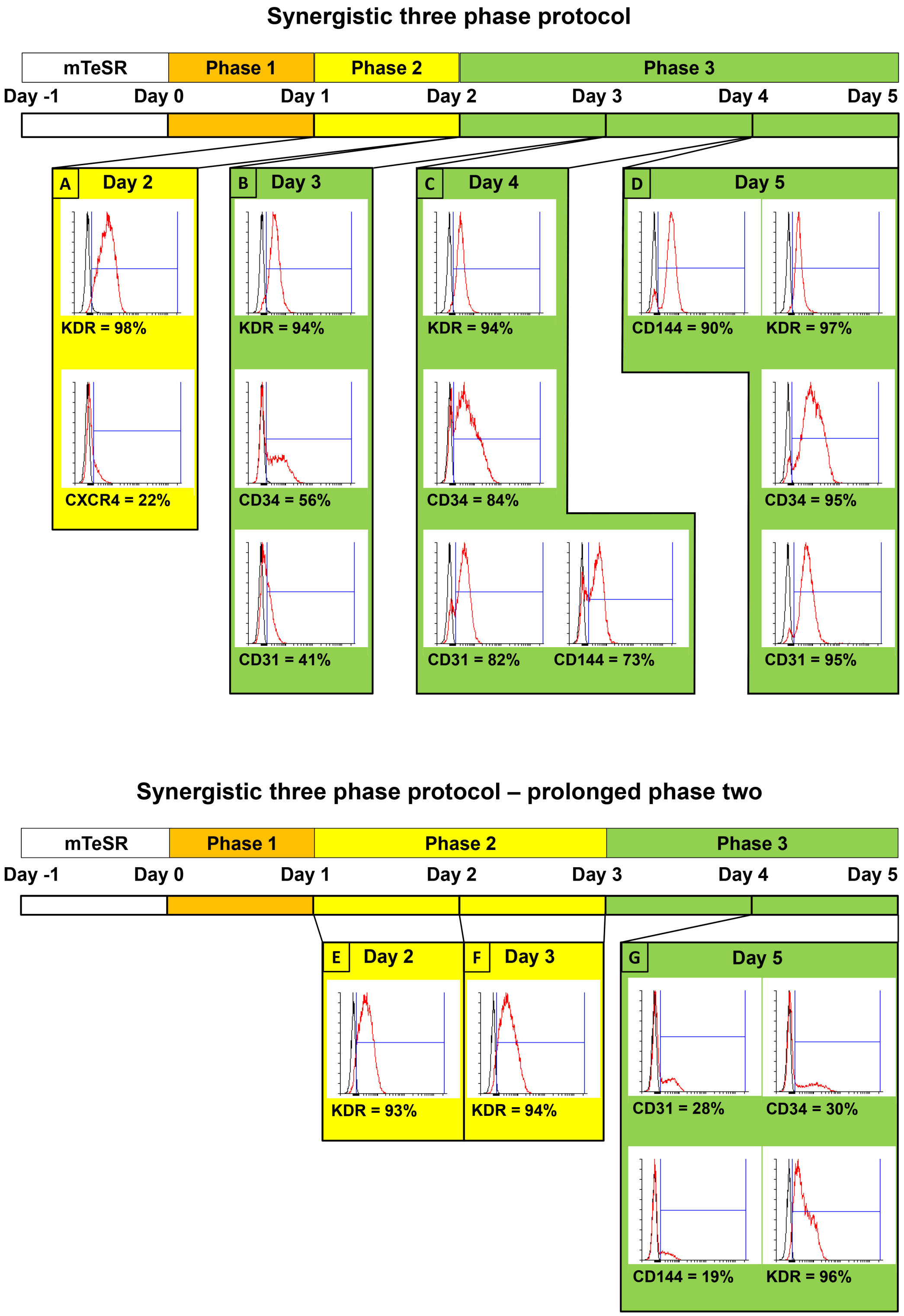

**FIGURE 2 |** Comparison of surface marker expressions between two variants of synergistic three-phase protocol, including simplified schemes of both variants. Both variants were tested using the CBIA-50 hiPSC line. The first variant is the one that is fully described in this article. Stage 2 lasts for only 1 day, whereas stage 3 lasts for 3 days. **(A)** KDR is expressed on the surface of 98% of cells, whereas CXCR4 is dimly expressed on 22% of cells by day 2 of differentiation. **(B–D)** KDR remains highly expressed during phase 3 of differentiation (94–97%), and other endothelial markers start to emerge by day 3 and gradually increase until they reach very high expression (90%–95%) by day 5 of differentiation. **(B)** Second variant of our protocol, in which both phases 2 and 3 last for 2 days. **(E,F)** Similar to the previous variant, KDR is expressed on 94% of cells on days 2 and 3. **(G)** By the end of phase 3 on day 5 of differentiation, the KDR expression is slightly reduced to 87%. More importantly, other endothelial markers, CD31, CD34, and CD144, have expression of only 28, 30, and 19%, respectively.

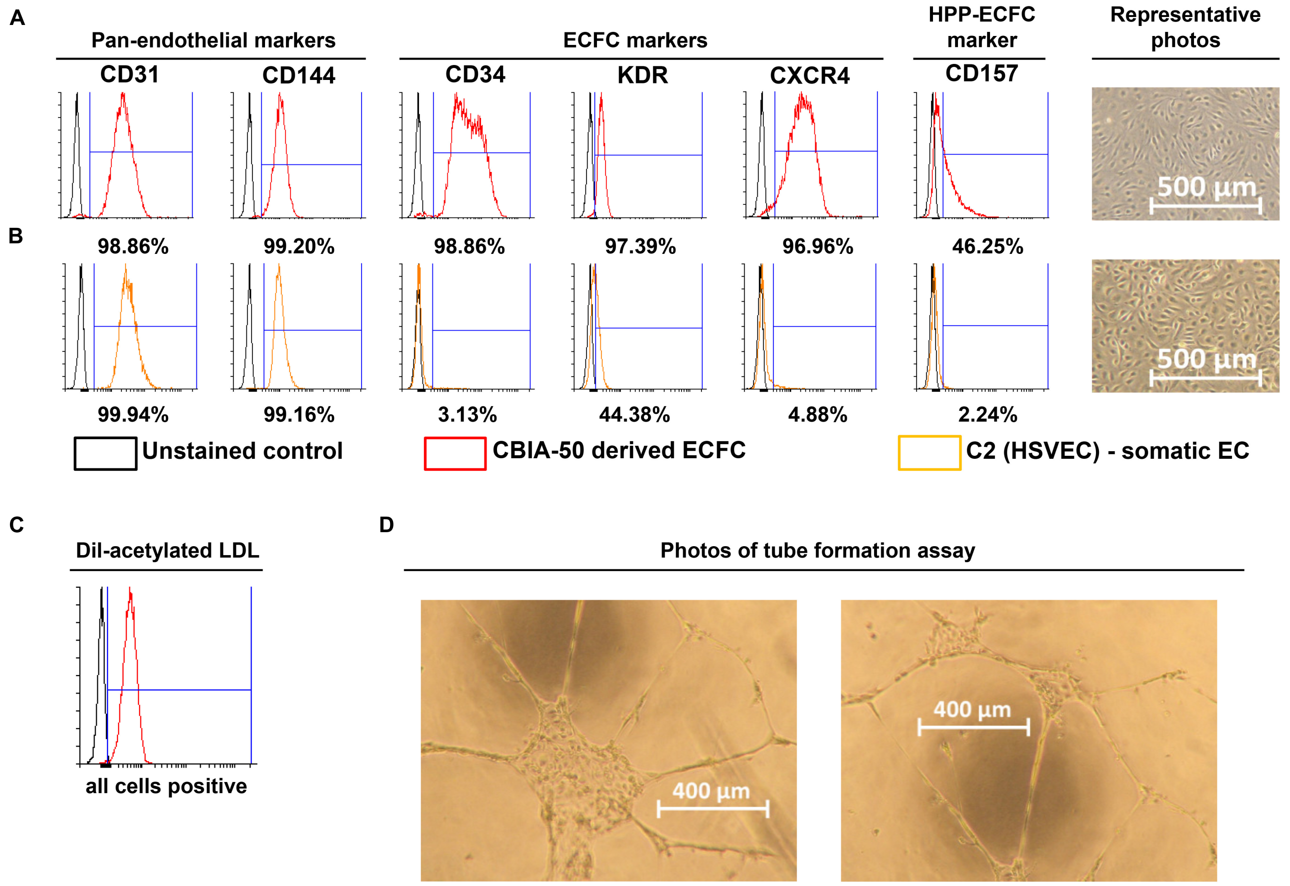

**FIGURE 3 |** Characterization of cells derived by our synergistic three-phase protocol and their comparison with somatic endothelial cells (ECs). Representative flow cytometry histogram overlays represent the surface expression of CD31, CD144, CD34, KDR, CXCR4, and CD157 and uptake of Dil-labeled and acetylated low-density lipoprotein (Dil-ac-LDL). **(A)** CBIA-50–derived ECFCs by the end of the first passage; ECFCs were obtained by passaging CBIA-50–derived cells, analyzed in **Figure 2D**, by day 5 of differentiation without separation. **(B)** Human saphenous vein EC cell line C2 by the end of passage 7; this cell line was harvested and characterized in our laboratory. **(A,B)** Morphology of confluent cells shows similar phenotype in both cell lineages shown. Both cell lines have similar CD31 expression but the CBIA-50–derived cells have much higher expression of markers CD34, KDR, CXCR4, and CD157 than the HSVEC line C2. **(C)** Uptake of Dil-ac-LDL by CBIA-50–derived cells in passage 3 was analyzed by flow cytometry, and the entire population was positive. **(D)** CBIA-50–derived cells formed tubes on Matrigel.

of CXCR4 by day 2 (**Figure 2A**). During the mesoderm–endothelial transition, the expression of markers CD34, CD31, and CD144 progressively increased. Specifically, on day 3, some cells were strongly expressing CD34 and dimly coexpressing CD31 in addition to overall expression of KDR (**Figure 2B**). On day 4, approximately 80% of all cells expressed CD31, CD34, and CD144 on their surface in addition to overall expression of KDR (**Figure 2C**). Finally, by the end of differentiation on day 5, endothelium with up to 97% surface expression of endothelial markers was present (**Figure 2D**). By the end of the first passage, differentiated ECFCs had high surface expression of the ECFC markers CXCR4, CD34, and KDR and the HPP-ECFC marker CD157 in addition to the standard pan-endothelial surface markers CD31 and CD144 (**Figure 3A**). We compared derived ECFCs to the somatic HSVEC line C2 derived in our laboratory. Expression of pan-endothelial markers was similar in both cell types, but expression of all the ECFC markers was much lower in the HSVECs than in the derived ECFCs (**Figure 3B**). CXCR4, CD34, and KDR are often highly expressed on the surface of ECFCs (Joo et al., 2015; Kang et al., 2015), which highlights the ECFC character of our hPSC-derived cells. Even more interestingly, it was recently discovered that CD157 is present on the surface of all HPP-ECFCs (a rare subpopulation of ECFCs), but it was missing on standard ECFCs and mature ECs *in vivo* (Wakabayashi et al., 2018). High expression of CD157 on the surface of endothelium derived using our protocol therefore suggests the HPP-ECFC character of these cells. Additionally, our cells had cobblestone morphology when observed by light microscopy (**Figures 3A**, **4I**), the entirety of their population took up Dil-Ac-LDL (**Figure 3C**), and they formed tubes on Matrigel (**Figure 3D**).

Intrigued by this, we decided to compare gene expression in our derived cells in passages 0 (cells by the day 5 of differentiation), 1, and 2 to hPSCs and HUVECs via quantitative

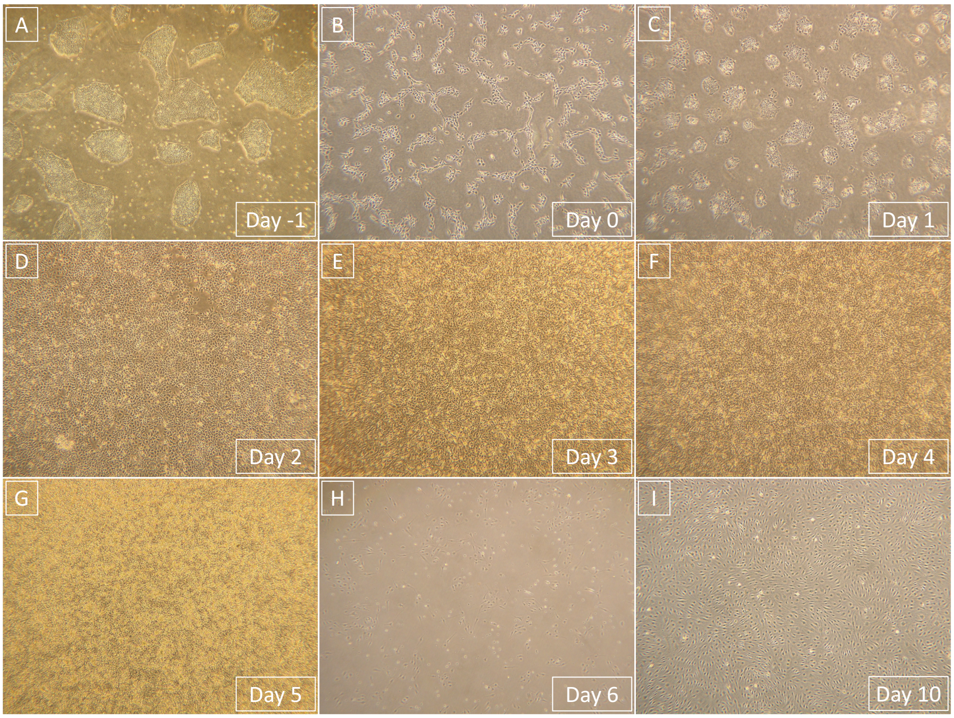

**FIGURE 4 |** Representative light microscopy photographs that show the entire process of differentiation from hPSCs to derived ECFCs. Magnification in all images is 40×. **(A)** hPSCs prior to single-cell seeding. **(B)** hPSCs 1 day after the single-cell seeding. **(C)** Primitive streak that formed from hPSCs after 1-day exposure to phase 1 medium. **(D)** Mesoderm that formed from primitive streak after 1-day exposure to phase 2 medium. **(E)** Endothelium that started to form from mesoderm after 1-day exposure to phase 3 medium. **(F)** Endothelium continuously formed after 2-day exposure to phase 3 medium. **(G)** Endothelium is fully formed and ready to be processed after 3-day exposure to phase 3 medium. **(H)** Derived ECFCs at the beginning of the first passage 1 day after seeding. **(I)** Confluent-derived ECFCs by the end of the first passage; confluence was mostly achieved 4 days after initial seeding.

polymerase chain reaction (**Figure 5**). We chose some of the genes that were previously linked to CD157-positive ECFCs (Wakabayashi et al., 2018), specifically FOXO1, FOXP1, MYC, FOSL2, ATF3, SOX4, and SOX7. In addition, we measured expression of ETV2, which can induce endothelial differentiation on its own, and NOS, which is marker of mature endothelial functionality. Expression of FOXP1, MYC, FOSL2, ATF3, and NOS gradually increased from pluripotent stem cells, through derived cells to mature HUVEC (**Figures 5A–E**). Expression of SOX4, a marker of pluripotency, gradually decreased from hPSCs, through derived cells to mature HUVECs (**Figure 5F**). ETV2 was more expressed in both hPSCs and derived cells than in HUVECs; interestingly, at passage 0, it was overexpressed by an order of magnitude in comparison to other passages of the derived cells and pluripotent stem cells (**Figure 5G**). FOXO1 had higher expression in derived cells by passage 2 than in all other tested cells (**Figure 5H**). Finally, SOX7 was more expressed in all derived cells than in pluripotent stem cells and HUVECs (**Figure 5I**).

We decided to compare the efficiency and robustness of our protocol with two previously published protocols that involve only some of the differentiation effectors used in our protocol (Sahara et al., 2014; Patsch et al., 2015). Differences between our protocol and these two protocols are detailed in **Table 1**. Briefly these two protocols involve two phases of differentiation: (i) hPSC to mesoderm and (ii) mesoderm to endothelium. They both utilize N-2 Supplement (100×) + B-27 Supplement (50×) along with either Gibco$^{TM}$ Neurobasal$^{TM}$ Medium (Thermo Fisher Scientific) and DMEM2 (Patsch et al., 2015) or only DMEM2 (Sahara et al., 2014) in phase 1 of differentiation and StemPro-34 serum-free medium (SFM; 1×) (Thermo Fisher Scientific) in phase 2 (i.e., two variants hereafter referred to as N2B27 + StemPro). They mainly differ from one another in their phase 2 usage of 2 μM forskolin with a high dosage of 200 ng/mL VEGF$_{165}$ (Patsch et al., 2015) or 10 μM DAPT with a more conservative dose of 50 ng/mL VEGF$_{165}$ (Sahara et al., 2014), respectively. Efficiency of differentiation was measured by FACS analysis of cell cultures on day 5 of differentiation. Our synergistic three-phase protocol had >90% expression of the markers CD31, CD34, CD144, and KDR (**Figure 6A**). The high VEGF + forskolin protocol had 36 to 69% expression for markers CD31, CD34, CD144, and KDR (**Figure 6B**). The DAPT protocol had 27 to 68% expression for markers CD31, CD34, CD144, and KDR (**Figure 6C**). For both the high VEGF + forskolin protocol and the DAPT protocol, most of the deviation was between different cell lines used; there was only a small deviation between pairs of samples of the same cell line (**Supplementary Figures S1–S3**). We concluded that the efficiency of these two protocols is generally lower and more cell line–dependent than the efficiency of our synergistic protocol. Additionally, there

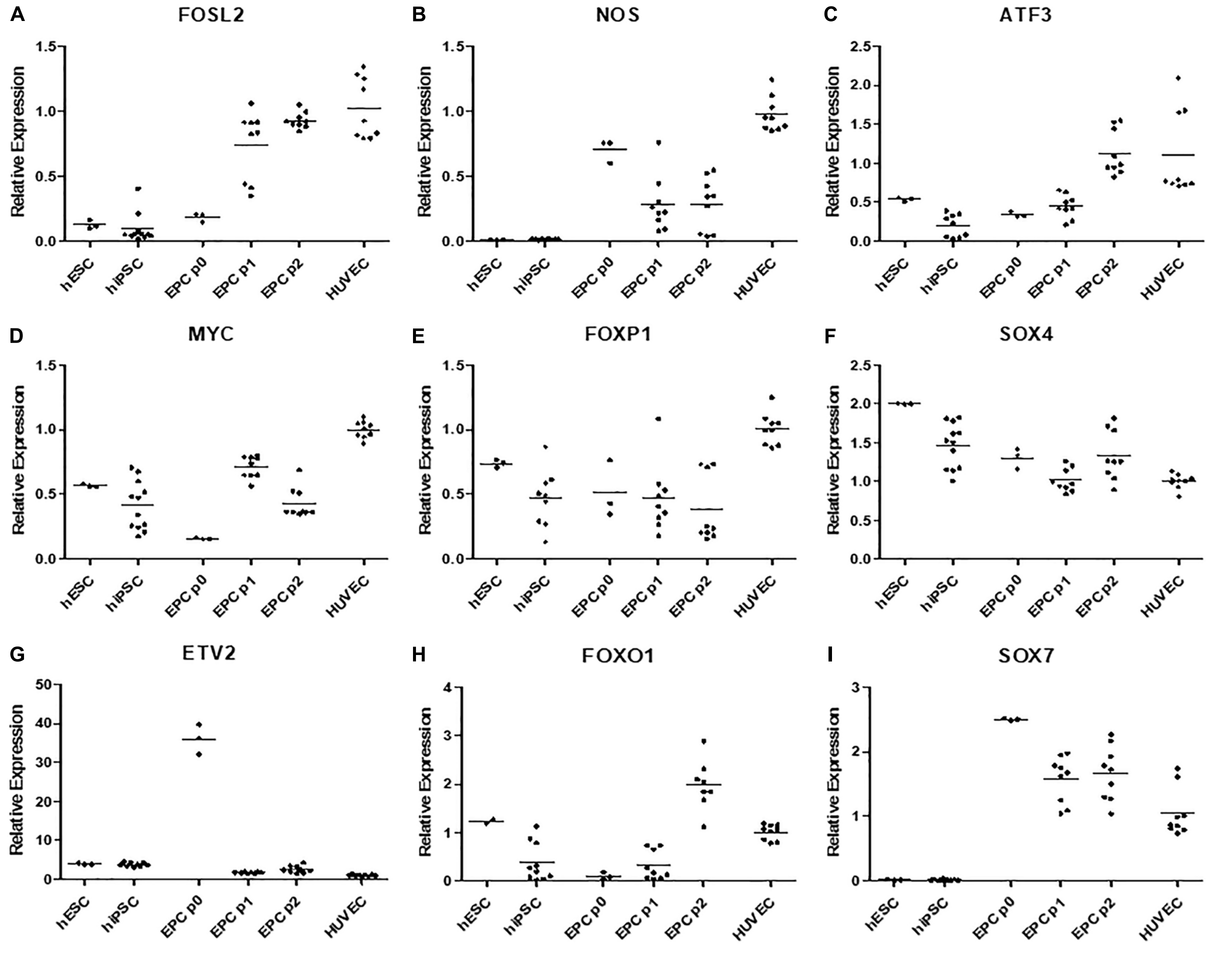

**FIGURE 5 | (A)** Gene FOSL2 has low expression in both hPSC types, its expression is higher in p0 derived cells and peaks in later passages of these cells and HUVECs. **(B)** Gene NOS have negligible expression in hPSCs, it is expressed in derived cells, however highest expression is recorded in HUVECs. **(C)** Gene ATF3 has low expression in hPSCs and passage 0–1 derived cells, its expression is high in passage 2 of derived endothelium and in HUVECs. **(D)** Gene MYC is moderately expressed hPSCs and passage 1 and 2 of derived cells, surprisingly its expression is low in passage 0 of derived cells and highes in HUVECs. **(E)** Gene FOXP1 was highly expressed in HUVECs and moderately expressed in all other cell types. **(F)** Expression of SOX4 gradually decreased from hPSCs to derived cells and HUVECs. **(G)** Gene ETV2 had the lowest expression in HUVECS multiple times higher expression in all other cell types and order of magnitude higher expression in p0 derived cells. **(H)** FOXO1 was moderately expressed in hESCs and HUVECs, highly expressed in p2 derived cells and it had low expression in hiPSCs and p0 and p1 derived cells. **(I)** SOX7 had negligible expression in all hPSCs high expression in p0 derived cells, gradually lower expression in following passages 1 and two and moderate expression in HUVECs.

was heterogeneity in the differentiation process itself when N2B27 + StemPro media were used. Sometimes, when N2B27 medium was exchanged for StemPro medium (**Supplementary Figure S6**), the entire monolayer cell population lost adherence to the surface only to adhere back to the surface later as a sphere-shaped structure. Endothelial cells then sprouted from this sphere-shaped structure in a root-like manner (**Supplementary Figure S6**). In some cases, this did not happen at all; instead, some parts of the monolayer mesoderm population eventually transformed into endothelium. However, when our synergistic three-phase protocol, which employs STEMdiff APEL2 medium, was used, cells grew in a monolayer, and the vast majority of them reliably turned into endothelium in an orderly and predictable manner (**Figures 4B–G**). Finally, certain elements of the differentiation process (such as the volume of the medium or whether the differentiation medium should be refreshed daily) were not fully described in the articles describing the two previous N2B27 + StemPro protocols (Sahara et al., 2014; Patsch et al., 2015). In contrast, we are describing each step of differentiation in full detail, which should help with the adaptation of our protocol in different laboratories.

Furthermore, we tested the robustness of our synergistic three-phase protocol on multiple hPSC lines comprising an hESC line and six hiPSC lines derived using virus, episomal vector, and mRNA induction techniques. Our protocol required no additional individual optimization for specific hPSC lines in order to achieve, on average, high differentiation efficiency (85%–94%) (**Figure 7** and **Supplementary Figure S4**). In addition, the tested hPSC lines tended to achieve high-enough endothelial surface marker expression to entirely exclude the need for cell

**TABLE 1 |** Description of basic properties of our synergistic three-phase differentiation protocol and protocols developed by Patsch et al. (2015) (nicknamed high VEGF + forskolin protocol in our article) and Sahara et al. (2014) (nicknamed DAPT protocol in our article).

| **Protocol** | **Duration of differentiation** | **Primitive streak and mesoderm differentiated by separate media (precision of differentiation)** | **Derived cells tested for standard surface markers** | **Cytokines used in each stage of differentiation: primitive streak = PS, mesoderm = M, endothelium = E** | **Media used in each stage of differentiation: primitive streak = PS, mesoderm = M, endothelium = E** | **Number of hPSC lines tested (robustness)** | **Average percentage of successfully differentiated cells (efficiency)** | **Precise single cell seeding density/media volumes defined (reproducibility and standardization)** |
|---|---|---|---|---|---|---|---|---|
| Our synergistic three phase protocol (Farkas et al.) | 5 days | Yes | CD31, CD34, CD144, KDR | PS: CP21R7, BMP4, FGF2 M: BMP4, FGF2 E: high concentration VEGF165, DAPT, Forskolin | PS: STEMdiff APEL2 M: STEMdiff APEL2 E: STEMdiff APEL2 | 7 | 85–94% for CD31, CD34, CD144, KDR | Yes – 400 000 cells per pm35 well*/yes – 1 ml per pm35 well in stage 1, 2 ml per well in stage 2 and three |
| Patsch et al., 2015 (original article results) | 5 days | No | CD31, CD144, vWF | M: BMP4, CP21R7 E: high concentration VEGF165, Forskolin | M: N2B27 + Neurobasal medium E: StemPro34 | 4 | 70.1 % CD144 | 370000–470000/No |
| Patsch et al., 2015 (our test results) | 5 days | No | CD31, CD34, CD144, KDR | M: BMP4, CP21R7 E: high concentration VEGF165, Forskolin | M: N2B27 + Neurobasal medium E: StemPro34 | 2 | 49–61% for CD31, CD34, CD144, KDR | Yes – 400 000 cells per pm35 well */yes 3 ml per pm35 well in each stage, no refreshment of medium – most efficient method we tested |
| Sahara et al., 2014 (original article results) | 5 days | No | CD31, CD34, CD144, KDR | M: BMP4, CP21R7 E: VEGF165, DAPT | M: N2B27 + Neurobasal medium + DMEM-F12 E: StemPro34 | 4 | 50% CD31 + CD144 | No/No |
| Sahara et al., 2014 (our test results) | 5 days | No | CD31, CD34, CD144, KDR | M: BMP4, CP21R7 E:VEGF165, DAPT | M: N2B27 + Neurobasal medium + DMEM-F12 E: StemPro34 | 2 | 44–54% for CD31, CD34, CD144, KDR | Yes – 400 000 cells per pm35 well* /yes 3 ml per pm35 well in each stage, no refreshment of medium – most efficient method we tested |

*Table includes relevant properties such as duration, precision, robustness, efficiency, reproducibility and standardization of differentiation, tested surface markers, cytokines, and media used in each stage of differentiation. Table includes information from both original articles written by their respective authors and our tests separately. *pm35 dish 10* $cm^2$.

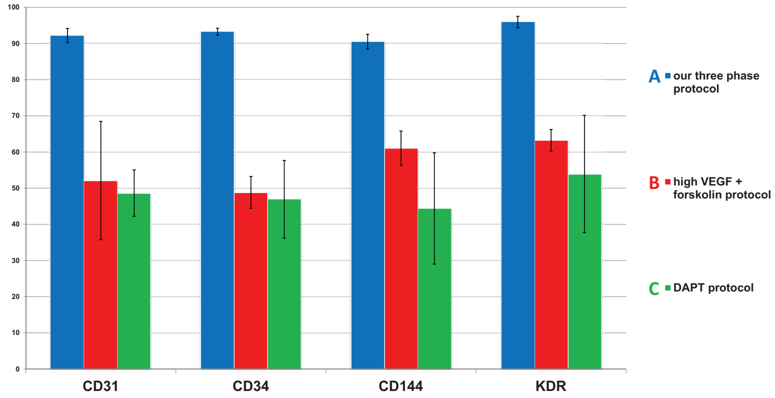

**FIGURE 6 |** Comparison of mean endothelial surface marker expression levels between our synergistic three-phase protocol and two N2B27 + StemPro protocols (high VEGF + forskolin protocol and DAPT protocol). Mean and standard deviation values were obtained from biological duplicates of differentiation experiments using CBIA-37 and CBIA-50 cell lines on day 5 of differentiation. Analysis was conducted via flow cytometry. The mean expression of surface markers CD31, CD144, CD34, and KDR was **(A)** 90% to 96% for our protocol, **(B)** 49% to 63% for the high VEGF + forskolin protocol, and **(C)** 44% to 54% for the DAPT protocol. Variability in the surface marker expression was lower for our protocol than the other tested protocols, as shown by the standard deviations.

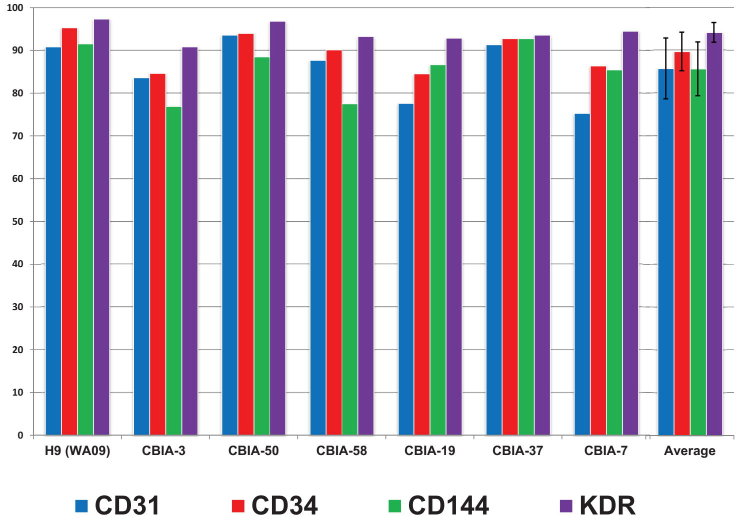

**FIGURE 7 |** Surface marker expression of cells differentiated by synergistic three-phase protocol from multiple hPSC lines by day 5 of differentiation along with the mean and standard deviation values across all hPSC lines used. The hESC line used was H9 (WA09), and the six hiPSC lines used were CBIA-3, CBIA-50, CBIA-58, CBIA-19, CBIA-37, and CBIA-7. Analysis of surface markers CD31, CD34, CD144, and KDR was conducted via flow cytometry. Expression of these markers ranged between 75% and 97%. Mean expression of these markers was between 85 and 94%.

separation. This considerably increased final yields, as when magnetic separation was applied it resulted in up to 50% loss of cells positive for the selected marker. As a result, the final differentiation efficiency is up to 1,500% (one stem cell gives rise to up to 15 differentiated cells) without using any separation method.

## TROUBLESHOOTING

### Potential Problem 1

Expression of both surface markers CD31 and CD144 is <85% on cells by day 5 of differentiation.

### Solutions to Potential Problem 1

Try seeding your hPSCs at higher densities, for example, 45,000 or 50,000/cm$^2$. Make sure your hPSCs are above passage 15; if you want to be totally safe, use hPSCs at passage 20 or higher. Cultivate your cells in mTeSR-1 (or a similar commercial medium if you have prior positive experience with it) in dishes coated with Matrigel (or a similar matrix) for at least three passages prior to single-cell seeding for differentiation. Make sure that your hPSCs have a healthy karyotype. Ideally, use hiPSCs below passage 30; do not use hiPSCs above passage 40 unless you are certain they are in perfect condition (related to karyotype, genomic mutations, and epigenetics). If none of this advice works for you, either use MACS to separate the derived cells or try using a different hPSC line.

## Potential Problem 2

Expression of pan-endothelial markers CD31 and CD144 is $<97\%$ in derived ECFCs by the end of the first passage.

## Solution to Potential Problem 2

Cultivate the cells for one more passage. If the expression does not increase, use MACS to separate the cells, employing microbeads against either CD31 or CD144.

## Potential Problem 3

Derived ECFCs do not express CD157 on their surface.

## Solution to Potential Problem 3

Try your anti-CD157 antibody against ECFCs derived from a different hPSC line to ensure that the antibody actually works. If the antibody functions correctly, it is likely that the hPSCs used to derive the first ECFCs have some issue with their karyotype.

# DISCUSSION

We created our synergistic protocol by employing multiple effectors of endothelial differentiation that were previously used and studied separately (Tan et al., 2013; Sahara et al., 2014; Patsch et al., 2015; Sriram et al., 2015; Kempf et al., 2016) to reliably generate ECFCs in large numbers. Therefore, our synergistic protocol involves a different medium for each of the three phases of differentiation. A schematic description of the entire differentiation process is shown in **Figure 1** and representative photos of entire procedure from pre-differentiation to post-differentiation state are shown in **Figures 4A–I**. A comparison of our protocol with many protocols cited in this article is shown in **Table 2**. During phase 1, a primitive streak was induced from hPSCs by a high dosage of a GSK3-β inhibitor in a low volume of medium (Tan et al., 2013; Kempf et al., 2016). The efficiency of this process was further increased by adding the cytokine BMP4, which primes the primitive streak toward $KDR^+$ mesoderm (Orlova et al., 2014; Sahara et al., 2014; Patsch et al., 2015; Sriram et al., 2015) and the cytokine FGF2, which increases the proliferation of the forming mesoderm (Sriram et al., 2015). During phase 2, the GSK3-β inhibitor is omitted as prolonged exposure to this inhibitor differentiates the primitive streak into definitive endoderm instead of mesoderm (Tan et al., 2013). Again, BMP4 was used to ensure the differentiation of the primitive streak into mesoderm, whereas FGF2 supported the proliferation of the new mesoderm. During phase 3, mesoderm was differentiated into endothelium by a high dosage of VEGF-$A_{165}$. Forskolin (a positive regulator of cAMP and protein kinase A) was added to the medium in order to maximize the effect of VEGF-$A_{165}$ by increasing the expression of its receptors, Neuropilin 1 and KDR (Yamamizu et al., 2009; Patsch et al., 2015). Finally, the Notch signaling inhibitor DAPT was utilized to promote the proliferation of newly forming ECFCs and simultaneously prevent their maturation during phase 3 of differentiation (Sahara et al., 2014). This procedure resulted in an almost pure population of endothelial progenitors by the end of differentiation (**Figures 2D**, **6A**, **7**). After one passage, the derived ECs fitted the profile of HPP-ECFCs when compared to the somatic HSVEC line (**Figure 3**). Finally, when gene expressions of hPSCs, derived ECs in passages 0 to 2 and HUVECs in passages 3 to 4 were compared, the derived ECs were mostly intermediate between hPSCs and HUVECs in their gene expression. In case of FOSL2, ATF3, MYC, NOS, and FOXP1, their expressions gradually increased from hPSCs to endothelium. SOX4 behaved exactly opposite as its expression gradually decreased from hPSCs to endothelium. There were notable exceptions to this general behavior. Expression of ETV2 that was already elevated in hPSCs spiked by the end of differentiation and then stayed elevated in derived ECs in comparison to HUVECs; this implies key role of ETV2 in endothelial differentiation. Expression of SOX7 was negligible in hPSCs but elevated in all derived ECs in comparison to HUVECs. FOXO1 had lower expression in derived ECs in passages 0 and 1 but elevated expression by passage 2 in comparison to both hPSCs and HUVECs. These results suggest endothelial characteristics of the derived cells but of less mature type than cells such as HUVECs.

Interestingly, when phase 2 (mesoderm) of our differentiation process was prolonged by 1 day, KDR expression was high and similar on both days 2 (**Figure 3E**) and 3 (**Figure 4F**). However, this did not translate into increased final endothelial differentiation efficiency. Surprisingly, by day 5 of differentiation, the expression of the endothelial markers CD31, CD34, and CD144 was significantly decreased (**Figure 3G**) in comparison to the standard version of our protocol (**Figure 3D**) involving only 1 day of phase 2. To explain this behavior, we hypothesize that mesoderm needs to be driven toward endothelium very soon after its appearance in order to avoid spontaneous differentiation toward different cell types. Additionally, it seems that the potential for endothelial differentiation precedes the actual appearance of mesoderm with KDR on its surface. In other words, the majority of cells (including $KDR^-$ cells of the primitive streak) are sufficiently primed toward mesoderm by day 2 of differentiation when our medium is used. Therefore, the phase 3 (endothelial differentiation) medium cannot disturb the eventual differentiation of these cells toward $KDR^+$ mesoderm. During phase 3, already present $KDR^+$ mesoderm differentiates to endothelial progenitors, whereas $KDR^-$ cells mature into $KDR^+$ mesoderm and then follow the aforementioned fate.

Next, we compared the synergistic effect of our protocol with the effects of two other previously published protocols (Sahara et al., 2014; Patsch et al., 2015) that use only some of the compounds and cytokines used in our protocol. We found that the efficiency of differentiation was higher for our protocol (**Figure 6A**) in comparison to the other two protocols (**Figures 6B,C**). Additionally, the variability in differentiation efficiency between two different hPSC lines

**TABLE 2 |** Description of basic properties of our synergistic three-phase differentiation protocol and other monolayer differentiation protocols cited in this article.

| Protocol | Duration of differentiation | Primitive streak and mesoderm differentiated by separate media (precision of differentiation) | Derived cells tested for standard surface markers | Derived cells tested for advanced progenitor markers or properties | Derived cells tested by tube forming assay/ LDL uptake | Number of hPSC lines tested (robustness) | Percentage of successfully differentiated cells/derived cells yield per pm35 (efficiency) | Precise single cell seeding density / media volumes defined (reproducibility and standardization) | Cytokines or media used require individualized dosage for different PSC lines (reproducibility and standardization) |
|---|---|---|---|---|---|---|---|---|---|
| Our synergistic three phase protocol (Farkas et al.) | 5 days | Yes | CD31, CD34, CD144, KDR | Surface markers CXCR4, CD157 | Yes/Yes | 7 | 85–94% CD31, CD34, CD144, KDR/up to 6 million cells | Yes/Yes | No |
| Patsch et al., 2015 | 5 days | No | CD31, CD144, vWF | *In vivo* test on mice, transcriptome | Yes/Yes | 4 | 70.1% CD144/ up to 8 million cells | No/No | No |
| Sahara et al., 2014 | 5 days | No | CD31, CD34, CD144, KDR | PCR array, lack of CD14, single cell assay, proliferation assay | Yes/No | 4 | 50% CD31 + CD144 | No/No | No |
| Sriram et al., 2015 | 5 days | Yes | CD31, CD34, KDR | Surface markers CXCR4, NRP1, migration assay, *in vivo* test in mice | Yes/Yes | 2 (only hESC, no hiPSC) | 90–95% CD31, CD34, KDR | No/No | No |
| Prasain et al., 2014 | 12 days | No | CD31, CD144, KDR | Surface marker NRP1, colony forming test, *in vivo* test on mice | Yes/No | 4 | Illegible but sorting necessary/3750 cells | No/Yes | No |
| Park et al., 2010 | 10–15 days + sorting +12 days | No | CD31, CD34, CD105 | Colony forming, *in vivo* test on mice | Yes/Yes | 2 | 10–16% CD31 + CD34/not mentioned | No/No | Yes |
| Harding et al., 2017 | 4–10 days | No | CD31, CD144, CD34 (negative) | No | Yes/Yes | 2 | 67.8% CD31+CD144- day 4/further manual separation | No/No | Yes |
| Orlova et al., 2014 | 10–11 days | No | CD31, CD105, CD73, CD144, KDR | *In vivo* test in zebra fish, gene expression | Yes/No | 3 | 19.9%/not mentioned | No/Yes | No |
| Tatsumi et al., 2011 | 5 days | No | CD31, CD34, CD144, KDR | No | Yes/Yes | 4 | 20%/1.2 million cells | No/No | No |
| Bao et al., 2015 | 5 days | No | CD31, CD34, CD144, vWF | No | Yes/Yes | 6 | 24.45 %CD31, CD34/not mentioned | No/No | Yes |

*Table includes relevant properties such as duration, precision, robustness, efficiency, reproducibility and standardization of differentiation, tested surface markers, tested progenitor properties, LDL uptake, and tube assay. Table includes information from original articles written by their respective authors.*

was lower with our protocol than with the other two protocols (**Figure 6**). Variability in differentiation efficiency between pairs of samples from the same hPSC line was very low for all protocols used (**Supplementary Figures S1–S3**). Additionally, cells differentiated by our protocol behaved in a very orderly and predictable manner during the differentiation process (**Figures 4B–G**). Surprisingly, all N2B27 + StemPro protocols that we tested behaved rather unpredictably during the mesoderm–endothelium transition. Specifically, sometimes when N2B27 medium was exchanged for StemPro medium, all the cells lost adherence to surface only to adhere later as one big clump (**Supplementary Figures S5, S6**). We actually tested a version of our protocol that used N2B27 and StemPro instead of STEMdiff APEL2 medium (data not shown), and while the differentiation efficiency was higher than that of the other two N2B27 + StemPro protocols (Sahara et al., 2014; Patsch et al., 2015), the same issues with variability of differentiation efficiency and adherence were present for all three protocols. Because of this, we believe the issues with adherence and variability are mostly due to transition from N2B27 medium to StemPro medium, not due to differences in the small compounds and cytokines. Therefore, we assume that our synergistic three-phase protocol results in predictable behavior and low variability due to the use of STEMdiff APEL2 medium, whereas the high efficiency of differentiation is the result of synergy between the timing of each step, the cytokines, and the small compounds.

In conclusion, our synergistic three-phase protocol differentiates hPSCs into ECFC-like cells via KDR$^+$ mesoderm, with higher efficiency, reproducibility, and robustness than other tested protocols. We proved this by successful differentiation of the hESC H9 line and six hiPSC lines derived using the three most common induction techniques (virus, episomal vector, and mRNA). Finally, the differentiated cells expressed the HPP-ECFC surface marker CD157 in addition to the standard pan-endothelial and ECFC markers. Therefore, our protocol is a promising asset in the effort to develop standardized regenerative medicine.

## DATA AVAILABILITY STATEMENT

All datasets generated for this study are included in the article/**Supplementary Material**.

## AUTHOR CONTRIBUTIONS

SF co-conceptualized the study, designed the differentiation protocol, drafted the manuscript, performed all cell culture, data collection, analysis and interpretation of results related to the differentiation protocol and following progenitor cultivation, and approved the final manuscript. PS was responsible for derivation, analysis and quality control of hiPSC lines CBIA-3, CBIA-7, CBIA-19, and CBIA-37 used in the differentiation protocol, provision of editorial support, and approval of the final manuscript. DR was responsible for derivation, analysis and quality control of hiPSC lines CBIA-50 and CBIA-58 used in the differentiation protocol, provision of editorial support, and approval of the final manuscript. LV provided tissue necessary for primary cell culture cultivation, further derivation of hiPSC lines from the cell cultures, provision of editorial support, and approved the final manuscript. IK co-conceptualized and supervised the study, provided editorial support, and approved the final manuscript.

## FUNDING

This study was generously supported by the Czech Health Research Council (16-31501A), the European Social Fund, and the European Regional Development Fund Project MAGNET (no. CZ.02.1.01/0.0/0.0/15_003/0000492).

## SUPPLEMENTARY MATERIAL

The Supplementary Material for this article can be found online at: https://www.frontiersin.org/articles/10.3389/fcell.2020.00309/full#supplementary-material

## REFERENCES

Adams, W. J., Zhang, Y., Cloutier, J., Kuchimanchi, P., Newton, G., Sehrawat, S., et al. (2013). Functional vascular endothelium derived from human induced pluripotent stem cells. *Stem Cell Rep.* 1, 105–113. doi: 10.1016/j.stemcr.2013.06.007

Bao, X., Lian, X., Dunn, K. K., Shi, M., Han, T., Qian, T., et al. (2015). Chemically-defined albumin-free differentiation of human pluripotent stem cells to endothelial progenitor cells. *Stem Cell Res.* 15, 122–129. doi: 10.1016/j.scr.2015.05.004

Carmeliet, P. (2000). Mechanisms of angiogenesis and arteriogenesis. *Nat. Med.* 6, 389–395. doi: 10.1038/74651

Cheng, C.-C., Chang, S.-J., Chueh, Y.-N., Huang, T.-S., Huang, P.-H., Cheng, S.-M., et al. (2013). Distinct angiogenesis roles and surface markers of early and late endothelial progenitor cells revealed by functional group analyses. *BMC Genomics* 14:182. doi: 10.1186/1471-2164-14-182

Choi, K.-D., Yu, J., Smuga-Otto, K., Salvagiotto, G., Rehrauer, W., Vodyanik, M., et al. (2009). Hematopoietic and endothelial differentiation of human induced pluripotent stem cells. *Stem Cells* 27, 559–567. doi: 10.1634/stemcells.2008-0922

Chong, M. S. K., Ng, W. K., and Chan, J. K. Y. (2016). Concise review: endothelial progenitor cells in regenerative medicine: applications and challenges: endothelial progenitors in regenerative medicine. *Stem Cells Transl. Med.* 5, 530–538. doi: 10.5966/sctm.2015-0227

Harding, A., Cortez-Toledo, E., Magner, N. L., Beegle, J. R., Coleal-Bergum, D. P., Hao, D., et al. (2017). Highly efficient differentiation of endothelial cells from pluripotent stem cells requires the MAPK and the PI3K pathways: the MAPK and PI3K pathways in endothelial fate. *Stem Cells* 35, 909–919. doi: 10.1002/stem.2577

Joo, H. J., Kim, H., Park, S.-W., Cho, H.-J., Kim, H.-S., Lim, D.-S., et al. (2011). Angiopoietin-1 promotes endothelial differentiation from embryonic stem cells and induced pluripotent stem cells. *Blood* 118, 2094–2104. doi: 10.1182/blood-2010-12-323907

Joo, H. J., Song, S., Seo, H.-R., Shin, J. H., Choi, S.-C., Park, J. H., et al. (2015). Human endothelial colony forming cells from adult peripheral blood have enhanced sprouting angiogenic potential through up-regulating VEGFR2 signaling. *Int. J. Cardiol.* 197, 33–43. doi: 10.1016/j.ijcard.2015.06.013

Kang, S. N., Park, C., Kim, S. M., Park, K. W., Park, B. J., Han, D. K., et al. (2015). Effect of stromal cell derived factor-1α release from heparin-coated Co-Cr stent substrate on the recruitment of endothelial progenitor cells. *Macromol. Res.* 23, 1159–1167. doi: 10.1007/s13233-015-4002-z

Kempf, H., Olmer, R., Haase, A., Franke, A., Bolesani, E., Schwanke, K., et al. (2016). Bulk cell density and Wnt/TGFbeta signalling regulate mesendodermal patterning of human pluripotent stem cells. *Nat. Commun.* 7:13602. doi: 10.1038/ncomms13602

Kitajima, K., Nakajima, M., Kanokoda, M., Kyba, M., Dandapat, A., Tolar, J., et al. (2016). GSK3β inhibition activates the CDX/HOX pathway and promotes hemogenic endothelial progenitor differentiation from human pluripotent stem cells. *Exp. Hematol.* 44, 68.e10–74.e10. doi: 10.1016/j.exphem.2015.09.007

Lee, J. H., Lee, S. H., Choi, S. H., Asahara, T., and Kwon, S.-M. (2015). The sulfated polysaccharide fucoidan rescues senescence of endothelial colony-forming cells for ischemic repair. *Stem Cells* 33, 1939–1951. doi: 10.1002/stem.1973

Li, Z., Hu, S., Ghosh, Z., Han, Z., and Wu, J. C. (2011). Functional characterization and expression profiling of human induced pluripotent stem cell- and embryonic stem cell-derived endothelial cells. *Stem Cells Dev.* 20, 1701–1710. doi: 10.1089/scd.2010.0426

Olmer, R., Engels, L., Usman, A., Menke, S., Malik, M. N. H., Pessler, F., et al. (2018). Differentiation of human pluripotent stem cells into functional endothelial cells in scalable suspension culture. *Stem Cell Rep.* 10, 1657–1672. doi: 10.1016/j.stemcr.2018.03.017

Orlova, V. V., van den Hil, F. E., Petrus-Reurer, S., Drabsch, Y., ten Dijke, P., and Mummery, C. L. (2014). Generation, expansion and functional analysis of endothelial cells and pericytes derived from human pluripotent stem cells. *Nat. Protoc.* 9, 1514–1531. doi: 10.1038/nprot.2014.102

Park, S.-W., Koh, Y. J., Jeon, J., Cho, Y.-H., Jang, M.-J., Kang, Y., et al. (2010). Efficient differentiation of human pluripotent stem cells into functional CD34+ progenitor cells by combined modulation of the MEK/ERK and BMP4 signaling pathways. *Blood* 116, 5762–5772. doi: 10.1182/blood-2010-04-280719

Patel, J., Seppanen, E., Chong, M. S. K., Yeo, J. S. L., Teo, E. Y. L., Chan, J. K. Y., et al. (2013). Prospective surface marker-based isolation and expansion of fetal endothelial colony-forming cells from human term placenta. *Stem Cells Transl. Med.* 2, 839–847. doi: 10.5966/sctm.2013-0092

Patel, J., Seppanen, E. J., Rodero, M. P., Wong, H. Y., Donovan, P., Neufeld, Z., et al. (2017). Functional definition of progenitors versus mature endothelial cells reveals key SoxF-dependent differentiation process. *Circulation* 135, 786–805. doi: 10.1161/CIRCULATIONAHA.116.024754

Patsch, C., Challet-Meylan, L., Thoma, E. C., Urich, E., Heckel, T., O'Sullivan, J. F., et al. (2015). Generation of vascular endothelial and smooth muscle cells from human pluripotent stem cells. *Nat. Cell Biol.* 17, 994–1003. doi: 10.1038/ncb3205

Prasain, N., Lee, M. R., Vemula, S., Meador, J. L., Yoshimoto, M., Ferkowicz, M. J., et al. (2014). Differentiation of human pluripotent stem cells to cells similar to cord-blood endothelial colony–forming cells. *Nat. Biotechnol.* 32, 1151–1157. doi: 10.1038/nbt.3048

Sahara, M., Hansson, E. M., Wernet, O., Lui, K. O., Später, D., and Chien, K. R. (2014). Manipulation of a VEGF-Notch signaling circuit drives formation of functional vascular endothelial progenitors from human pluripotent stem cells. *Cell Res.* 24, 820–841. doi: 10.1038/cr.2014.59

Shafiee, A., Patel, J., Hutmacher, D. W., Fisk, N. M., and Khosrotehrani, K. (2018). Meso-endothelial bipotent progenitors from human placenta display distinct molecular and cellular identity. *Stem Cell Rep.* 10, 890–904. doi: 10.1016/j.stemcr.2018.01.011

Simara, P., Tesarova, L., Padourova, S., and Koutna, I. (2014). Generation of human induced pluripotent stem cells using genome integrating or non-integrating methods. *Folia Biol.* 60:6.

Sriram, G., Tan, J. Y., Islam, I., Rufaihah, A. J., and Cao, T. (2015). Efficient differentiation of human embryonic stem cells to arterial and venous endothelial cells under feeder- and serum-free conditions. *Stem Cell Res. Ther.* 6:261. doi: 10.1186/s13287-015-0260-5

Suknuntha, K., Tao, L., Brok-Volchanskaya, V., D'Souza, S. S., Kumar, A., and Slukvin, I. (2018). Optimization of synthetic mRNA for highly efficient translation and its application in the generation of endothelial and hematopoietic cells from human and primate pluripotent stem cells. *Stem Cell Rev. Rep.* 14, 525–534. doi: 10.1007/s12015-018-9805-1

Tan, J. Y., Sriram, G., Rufaihah, A. J., Neoh, K. G., and Cao, T. (2013). Efficient derivation of lateral plate and paraxial mesoderm subtypes from human embryonic stem cells through GSKi-mediated differentiation. *Stem Cells Dev.* 22, 1893–1906. doi: 10.1089/scd.2012.0590

Tatsumi, R., Suzuki, Y., Sumi, T., Sone, M., Suemori, H., and Nakatsuji, N. (2011). Simple and eighly efficient method for production of endothelial cells from human embryonic stem cells. *Cell Transplant* 20, 1423–1430. doi: 10.3727/096368910X547444

Tesarova, L., Simara, P., Stejskal, S., and Koutna, I. (2016). The aberrant DNA methylation profile of human induced pluripotent stem cells is connected to the reprogramming process and is normalized during in vitro culture. *PLoS One* 11:e0157974. doi: 10.1371/journal.pone.0157974

Vodyanik, M. A., Yu, J., Zhang, X., Tian, S., Stewart, R., Thomson, J. A., et al. (2010). A mesoderm-derived precursor for mesenchymal stem and endothelial cells. *Cell Stem Cell* 7, 718–729. doi: 10.1016/j.stem.2010.11.011

Wakabayashi, T., Naito, H., Suehiro, J., Lin, Y., Kawaji, H., Iba, T., et al. (2018). CD157 marks tissue-resident endothelial stem cells with homeostatic and regenerative properties. *Cell Stem Cell* 22, 384.e6–397.e6. doi: 10.1016/j.stem.2018.01.010

Yamamizu, K., Kawasaki, K., Katayama, S., Watabe, T., and Yamashita, J. K. (2009). Enhancement of vascular progenitor potential by protein kinase A through dual induction of Flk-1 and Neuropilin-1. *Blood* 114, 3707–3716. doi: 10.1182/blood-2008-12-195750

Ye, L., Tan, S.-H., Su, L.-P., and Cook, S. (2016). Three-dimensional scaffolds for efficient arterial endothelial cell differentiation from human induced pluripotent stem cells. *J. Am. Coll. Cardiol.* 67:2291. doi: 10.1016/S0735-1097(16)32292-6

Zhang, S., Dutton, J. R., Su, L., Zhang, J., and Ye, L. (2014). The influence of a spatiotemporal 3D environment on endothelial cell differentiation of human induced pluripotent stem cells. *Biomaterials* 35, 3786–3793. doi: 10.1016/j.biomaterials.2014.01.037

Zhao, H., Zhao, Y., Li, Z., Ouyang, Q., Sun, Y., Zhou, D., et al. (2018). FLI1 and PKC co-activation promote highly efficient differentiation of human embryonic stem cells into endothelial-like cells. *Cell Death Dis.* 9:131. doi: 10.1038/s41419-017-0162-9

**Conflict of Interest:** The authors declare that the research was conducted in the absence of any commercial or financial relationships that could be construed as a potential conflict of interest.

frontiers
in Cell and Developmental Biology

ORIGINAL RESEARCH
published: 23 June 2020
doi: 10.3389/fcell.2020.00440

# Contractility of Induced Pluripotent Stem Cell-Cardiomyocytes With an *MYH6* Head Domain Variant Associated With Hypoplastic Left Heart Syndrome

**Min-Su Kim[1], Brandon Fleres[2], Jerrell Lovett[2], Melissa Anfinson[3], Sai Suma K. Samudrala[3], Lauren J. Kelly[2], Laura E. Teigen[2], Matthew Cavanaugh[2], Maribel Marquez[4], Aron M. Geurts[4], John W. Lough[3], Michael E. Mitchell[1], Robert H. Fitts[2] and Aoy Tomita-Mitchell[1,5]***

*[1] Division of Pediatric Cardiothoracic Surgery, Department of Surgery, Medical College of Wisconsin, Herma Heart Institute, Milwaukee, WI, United States, [2] Department of Biological Sciences, Marquette University, Milwaukee, WI, United States, [3] Department of Cell Biology, Neurobiology and Anatomy, Medical College of Wisconsin, Milwaukee, WI, United States, [4] Department of Physiology, Medical College of Wisconsin, Milwaukee, WI, United States, [5] Department of Biomedical Engineering, Medical College of Wisconsin, Milwaukee, WI, United States*

**Edited by:**
*Shinsuke Yuasa,*
*Keio University, Japan*

**Reviewed by:**
*Shijun Hu,*
*Soochow University, China*
*Beth Pruitt,*
*University of California, Santa Barbara, United States*
*Masamichi Ito,*
*The University of Tokyo, Japan*

***Correspondence:**
*Aoy Tomita-Mitchell*
*amitchell@mcw.edu*

**Specialty section:**
*This article was submitted to Stem Cell Research, a section of the journal Frontiers in Cell and Developmental Biology*

**Received:** *14 January 2020*
**Accepted:** *11 May 2020*
**Published:** *23 June 2020*

**Citation:**
*Kim M-S, Fleres B, Lovett J, Anfinson M, Samudrala SSK, Kelly LJ, Teigen LE, Cavanaugh M, Marquez M, Geurts AM, Lough JW, Mitchell ME, Fitts RH and Tomita-Mitchell A (2020) Contractility of Induced Pluripotent Stem Cell-Cardiomyocytes With an MYH6 Head Domain Variant Associated With Hypoplastic Left Heart Syndrome. Front. Cell Dev. Biol. 8:440. doi: 10.3389/fcell.2020.00440*

Hypoplastic left heart syndrome (HLHS) is a clinically and anatomically severe form of congenital heart disease; however, its etiology remains largely unknown. We previously demonstrated that genetic variants in the *MYH6* gene are significantly associated with HLHS. Additionally, induced pluripotent stem cell-derived cardiomyocytes (iPSC-CMs) from an HLHS-affected family trio (affected parent, unaffected parent, affected proband) carrying an *MYH6*-R443P head domain variant demonstrated dysmorphic sarcomere structure and increased compensatory *MYH7* expression. Analysis of iPSC-CMs derived from the HLHS trio revealed that only beta myosin heavy chain expression was observed in CMs carrying the *MYH6*-R443P variant after differentiation day 15 (D15). Functional assessments performed between D20-D23 revealed that *MYH6*-R443P variant CMs contracted more slowly (40 ± 2 vs. 47 ± 2 contractions/min, $P < 0.05$), shortened less (5.6 ± 0.5 vs. 8.1 ± 0.7% of cell length, $P < 0.05$), and exhibited slower shortening rates (19.9 ± 1.7 vs. 28.1 ± 2.5 μm/s, $P < 0.05$) and relaxation rates (11.0 ± 0.9 vs. 19.7 ± 2.0 μm/s, $P < 0.05$). Treatment with isoproterenol had no effect on iPSC-CM mechanics. Using CRISPR/Cas9 gene editing technology, introduction of the R443P variant into the unaffected parent's iPSCs recapitulated the phenotype of the proband's iPSC-CMs, and conversely, correction of the R443P variant in the proband's iPSCs rescued the cardiomyogenic differentiation, sarcomere organization, slower contraction ($P < 0.05$) and decreased velocity phenotypes ($P < 0.0001$). This is the first report to identify that cardiac tissues from HLHS patients with *MYH6* variants can exhibit sarcomere disorganization in atrial but not ventricular tissues. This new discovery was not unexpected, since *MYH6* is expressed predominantly in the postnatal atria in humans. These findings demonstrate the feasibility of employing patient-derived iPSC-CMs, in combination with patient cardiac tissues, to gain mechanistic insight into how genetic variants can lead to HLHS. Results from this study suggest that decreased contractility of CMs due to sarcomere disorganization in the atria may effect hemodynamic changes preventing development of a normal left ventricle.

**Keywords: HLHS, hypoplastic left heart syndrome, iPSC-cardiomyocytes, *MYH6*, contractility, CRISPR/Cas9, sarcomere**

## INTRODUCTION

Hypoplastic left heart syndrome (HLHS) is a severe form of congenital heart disease (CHD) characterized by atresia/stenosis of the aortic and mitral valves, and severe hypoplasia of the left ventricle and aorta (Noonan and Nadas, 1958). HLHS affects more than one in every 4000 live births (Mai et al., 2019). Evidence supporting a genetic basis for HLHS includes observations of familial clustering, high heritability, and its occurrence with specific chromosomal disorders such as Turner and Jacobsen syndromes (Tomita-Mitchell et al., 2016; Lara et al., 2017; Yagi et al., 2018). HLHS exhibits complex genetic inheritance along with an increased frequency of bicuspid aortic valve (BAV) and coarctation of the aorta (CoA) in relatives of HLHS patients (Hinton et al., 2007, 2009). Variants in genes such as *GJA1* (Dasgupta et al., 2001), *NKX2.5* (Elliott et al., 2003), *NOTCH1* (Garg et al., 2005; McBride et al., 2008; Hrstka et al., 2017; Yang et al., 2017), and *MYH6* (Theis et al., 2015; Tomita-Mitchell et al., 2016), as well as observations of syndromic or rare copy number variants (CNVs) in cardiomyogenic genes (Grossfeld, 2007; Grossfeld et al., 2009; Tomita-Mitchell et al., 2012; Warburton et al., 2014; Glidewell et al., 2015) have been associated with HLHS. We previously reported that rare variants in *MYH6* (alpha myosin heavy chain; α-MHC) were observed in 10% of HLHS patients, and that cardiac transplant-free survival was reduced in HLHS subjects containing *MYH6* variants in comparison with HLHS patients without *MYH6* variants. Furthermore, cardiac tissue from *MYH6* variant carriers exhibited significant upregulation of sarcomere genes, including *ACTA1* (actin alpha 1), *MYL2* (myosin light chain 2), *TNNT2* (cardiac troponin T), and the *MYH6* homolog *MYH7*, which encodes the beta-myosin heavy chain (β-MHC) isoform. Using cardiomyocytes (CMs) derived from induced pluripotent stem cells (iPSCs) obtained from an HLHS patient carrying an *MYH6*-R443P variant, we discovered that sarcomere structure was dysmorphic (Tomita-Mitchell et al., 2016).

Two myosin heavy chain proteins (α-MHC and β-MHC) are expressed in the human heart. During development, α-MHC is expressed in both the primitive atrium and ventricle until gestational day 35, after which its expression continually decreases in the ventricle (Wessels et al., 1990, 1991). In contrast, β-MHC expression gradually increases in the ventricles throughout gestation and this expression pattern persists throughout adult stages, so that β-MHC is the predominant ventricular isoform, while α-MHC is the predominant atrial isoform in adults (Cummins and Lambert, 1986; Reiser et al., 2001). We previously noted that *MYH6* mRNA strongly predominates during the earliest stages of *in vitro* cardiomyogenesis in H1 human embryonic stem cells wherein *MYH6* comprises ∼99% of total MHC transcripts in differentiation day 8 (D8) cultures, and declines to ∼86% at D14 (Kim et al., 2015). This likely reflects a prominent role for α-MHC in nascent myocyte development that may be disrupted by *MYH6* variants associated with HLHS.

Fetal heart development relies on proper blood flow, as signaling pathways responsive to shear stress and pressure-related strain both affect cardiac chamber formation. The prevailing hypothesis is that HLHS pathophysiology stems from impaired blood flow through the left ventricle (LV) during cardiogenesis (Fishman et al., 1978; Gruber and Epstein, 2004; deAlmeida et al., 2007). Our findings are consistent with this, as disruptions in an atrial protein such as α-MHC would alter ventricular preload with consequent defective expansion and/or differentiation of cardiomyocytes resulting in a dysmorphic and dysfunctional ventricle (Hove et al., 2003; Burggren et al., 2004; Hierck et al., 2008; McCain and Parker, 2011; Santhanakrishnan and Miller, 2011; Lee et al., 2016; McCormick and Tzima, 2016; Hoog et al., 2018). This is further supported by studies of weak atrium (*wea*) zebrafish, which harbor *myh6* mutations and exhibit defects in both cardiac chambers, including defective atrial contraction along with abnormal sarcomere organization and an underdeveloped ventricle (Berdougo et al., 2003).

Current non-invasive imaging methods allow detection of HLHS as early as 16 weeks gestational age (Friedberg et al., 2009; Galindo et al., 2009), long after the fetal heart is formed and septated at 7–8 weeks. The primitive heart, expressing only *MYH6*, begins beating even earlier, during the third week of development. Thus, the pathological changes associated with HLHS are likely present long before we are able to detect them. Given these limitations, developmental defects such as HLHS are often investigated using murine models. However, the chamber-specific MHC expression in rodents is the opposite of humans, making them an unsuitable option for our studies. Here we studied human cardiac tissue and patient-specific iPSC-CMs to identify structural characteristics of atrial and ventricular tissue of HLHS patients and contractile properties of human iPSC-CMs with an *MYH6* variant. The latter permitted us to monitor early stages of cardiomyogenesis in CMs of HLHS patients *in vitro*. Our hypothesis is that the *MYH6* variant iPSC-CMs exhibit depressed extent and velocity of shortening that can be rescued by correcting the variant in proband-iPSCs using Clustered Regularly Interspaced Short Palindromic Repeats (CRISPR)/Cas9 gene editing. Importantly, we show the feasibility of employing iPSC-CMs to ascertain functional consequences of the *MYH6*-R443P variant, demonstrating that changes in the myosin isoforms confer contractile limitations.

# MATERIALS AND METHODS

## Study Participants

Study subjects have been previously described (Tomita-Mitchell et al., 2016). All subjects provided written informed consent, and procedures were approved by the MCW Institutional Review Board and conformed to the principles in the Declaration of Helsinki.

## Gene Editing iPSC Lines

### Guide RNA and ssODN Design

All CRISPRs were designed as previously described (Mitzelfelt et al., 2017). Briefly, CRISPR target sites within 30 bps of the single nucleotide polymorphism (SNP) *MYH6*-R443P were identified using ZiFiT Targeter (Version 4.2). Three guide RNAs were cloned into pX330-U6-Chimeric_BB-CBh-hSpCas9 (Addgene, Cambridge, MA, United States) to introduce *MYH6*-R443P into the heart healthy parent's iPSCs. CRISPR efficiency was determined using the Cel-1 surveyor assay in HEK293 cells. The variant *MYH6*-R443P was flanked approximately 60 bp on either side by single strand oligonucleotides (ssODNs) (**Table 1**). Silent mutations were incorporated to prevent re-cutting by Cas9 by disrupting the target sequence. An additional AAVS1 locus was targeted for incorporation of GFP-puromycin resistance using the AAVS1 Safe Harbor TALE-Nuclease kit (SBI, Palo Alto, CA, United States).

To correct the *MYH6*-R443P variant in proband iPSCs, we designed CRISPR targets (**Table 1**) to align with the variant allele and purchased synthesized RNA (AltR CRISPR-Cas9 cr RNA, Integrated DNA Technologies, Coralville, IA, United States), RFP-labeled repetitive sequence (AltR CRISPR-Cas9 tracr RNA, Integrated DNA Technologies, Coralville, IA, United States) and purified Cas9 enzyme (40 Um/U1). Additionally, we designed and validated a CRISPR targeting the AAVS1 locus to introduce a puromycin resistance cassette (Integrated DNA Technologies, Coralville, IA, United States).

**TABLE 1 |** Oligonucleotides used for gene editing, sequencing, and genotyping.

| | |
|---|---|
| **CRISPR guide RNAs** | |
| *MYH6*-R443P introduction | tgagaagatgttcaactgga |
| *MYH6*-R443P correction | gacgcccatcaacgccaccc |
| *AAVS1* locus | gtcaccaatcctgtccctag |
| **ssODNs** | |
| *MYH6*-R443P introduction | ccagcgatgtccaggactcctatgaagtactggcgtggctgcttggtctccagggtggcgttgatgggcgtcaccatccaattgaacatcttctcatacactgccttggccagagccccgatggagtagtacacctgctgc |
| *MYH6*-R443P correction | ctctggccaaggcagtgtatgagaagatgttcaactggatggtgacgcgcatcaacgcgacgctggagaccaagcagccacgccagtacttcataggagtcctggacatcgctggcttcg |
| **PCR primers for genotyping (5′∼3′)** | |
| F-*MYH6*-R443P locus | ggcaacgagtatgtcaccaa |
| R-*MYH6*-R443P locus | ctttgtctggatggcagagg |
| **Allele-specific SNP genotyping (5′∼3′)** | |
| Reference probe | FAM-tggtgacgcgcat |
| Variant probe | VIC-atggtgacgcccat |
| F-*MYH6*-R443P locus | aaggcagtgtatgagaagatgttca |
| R-*MYH6*-R443P locus | aagtactggcgtggctgctt |

### Transfecting iPSCs

Prior to transfection, iPSCs were pretreated for 3–4 h with 5 μM Rho-associated kinase (ROCK) inhibitor (Y27632, Stemgent, Lexington, MA, United States), dissociated with accutase (Thermo Fisher Scientific, Waltham, MA, United States) to ensure single cell suspension, and transferred to an electroporation cuvette. For each transfection (D0), 1 μg of the gene-specific CRISPRs, 80 μM of the relevant ssODN, 1 μg of each of the two AAVS1-specific cassettes, and 1 μg AAVS1 donor plasmid were added to 100 μl P4 solution (Lonza, Basel, Switzerland) and electroporated using program CB-150 on a 4D Nucleofector$^{TM}$ (Lonza, Basel, Switzerland) into iPSCs ($1 \times 10^6$ cells/transfection). iPSCs from each transfection were then seeded into one well of a geltrex-coated 24-well plate ($5 \times 10^5$ cells/cm$^2$) for recovery in mTeSR1 supplemented with 5 μM ROCK inhibitor. The following day (D1), iPSCs were cultured with mTeSR1. Two days post-transfection (D2), iPSCs from one well of 24-well plate were sub-cultured at a clonal density ($\sim 5 \times 10^4$ cells/cm$^2$) into all wells of a 6-well plate pre-seeded with mitomycin C-treated mouse embryonic fibroblast (MEF) feeder cells (Thermo Fisher Scientific, Waltham, MA, United States) in human ESC medium. ESC medium was comprised of Knockout DMEM (Thermo Fisher Scientific, Waltham, MA, United States) supplemented with 20% Knockout Serum Replacement (Thermo Fisher Scientific, Waltham, MA, United States), MEM-NEAA (Thermo Fisher Scientific, Waltham, MA, United States), 2 mM L-glutamine (Thermo Fisher Scientific, Waltham, MA, United States), Penicillin/Streptomycin, 0.1 mM β-mercaptoethanol (Sigma-Aldrich, St. Louis, MO, United States), 10 ng/ml human basic fibroblast growth factor (bFGF, Cell Signaling, Danvers, MA, United States), 50 ng/ml L-ascorbic acid (Sigma-Aldrich, St. Louis, MO, United States) and 5 μM ROCK inhibitor. Medium was changed 2 days later (D4) to ESC medium without ROCK inhibitor. Five days post-seeding (D5), medium was changed to puromycin (0.5 g/ml)-supplemented MEF-conditioned medium with bFGF and L-ascorbic acid, which was replaced every 2 days for 1 week. Following maintenance (∼D12), distinct colonies (∼1 mm diameter) were manually transferred to a single well of a 24-well plate pre-coated with geltrex in mTeSR1 medium plus ROCK inhibitor without MEFs. Following genotyping (see below), clones were expanded to a geltrex-coated well of a 12-well plate in mTeSR1 plus ROCK inhibitor and further expanded and frozen in mFreSR freezing medium (STEMCELL Technologies, Vancouver, BC, Canada). Isolated CRISPRed iPSC lines were frequently sub-cloned to ensure homogeneity of the population.

### Allele-Specific SNP Genotyping and Sanger Sequencing

To isolate genomic DNA from iPSCs, 30 μl Quick Extract Solution (Epicentre, Madison, WI, United States) was added to each cell pellet and incubated for 15 min at 65°C, followed by 5 min at 95°C. PCR was carried out using gene-specific primers

(**Table 1**), and 2 μl of PCR product were used for further allele-specific SNP genotyping with Quantstudio7 (Thermo Fisher Scientific, Waltham, MA, United States). After confirmation of gene edit, ∼100 ng of PCR product was treated with Exosap-IT (Thermo Fisher Scientific, Waltham, MA, United States) and sent to Retrogen (San Diego, CA, United States) for Sanger sequencing. Clones that were positive for iPSCs containing the edited *MYH6*-R443P gene were sequenced at the conserved region in *MYH7* as well to check the CRISPR's off-target activity.

## Cardiomyocyte Differentiation of iPSCs

Induced pluripotent stem cell (iPSC) lines were generated from dermal fibroblasts donated by HLHS probands and their parents. Fibroblasts were reprogrammed to pluripotent stem cells using Sendai reprogramming as previously described (Tomita-Mitchell et al., 2016). Pluripotency was confirmed with morphological appearance and % of cells exhibiting Oct4-positive immunostaining (99–100%). The cells were karyotypically normal and had the ability to differentiate into multiple lineages (definitive endoderm and cardiomyogenic mesoderm) (Tomita-Mitchell et al., 2016). In short, iPSCs were maintained in a hypoxic incubator at 5% $CO_2$ and 4% $O_2$. All experiments were performed on cells during passages 10–50. One day prior to inducing cardiomyocyte (CM) differentiation, the iPSCs were seeded at a cell density of $>1 \times 10^5/\text{cm}^2$ on a 10 $\mu$g/cm$^2$ geltrex-coated (Thermo Fisher Scientific, Waltham, MA, United States) tissue culture dish. The cells were cultured in mTeSR1 medium (STEMCELL Technologies, Vancouver, BC, Canada) supplemented with 5 μM ROCK inhibitor. The cells were induced with 10 μM CHIR99021 (Stemgent, Lexington, MA, United States) and 10 ng/ml Activin-A (R&D Systems, Minneapolis, MN, United States) in insulin-free RPMI/B27 (Thermo Fisher Scientific, Waltham, MA, United States). On D3, the medium was exchanged for insulin-free RPMI/B27 with 5 μM IWP (Tocris, Bristol, United Kingdom). Starting at D7, at 2-day intervals the medium was changed to RPMI/B27 with insulin (Thermo Fisher Scientific, Waltham, MA, United States). Cultures were evaluated for % of cardiac troponin T (cTnT) positive cells via flow cytometry and MHC (MF20) expression by immunostaining. The cardiomyocytes were either frozen at D15, or were sub-cultured between D10–D15 after dissociation into single cells with 0.25% trypsin; specifically, cells centrifuged at 1,000 rpm for 5 min were either frozen at a density of $>2 \times 10^6$ in cryovials with 10% DMSO and 90% FBS, or were re-plated at a density of $2 \times 10^4$–$5 \times 10^4/\text{cm}^2$ on a geltrex-coated 12 cm$^2$ round cover glass for single cell-based contractility studies, or at $>5 \times 10^4/\ \text{cm}^2$ for automated contractility video analysis (Pulse Video Analysis, Dana solutions, Palo Alto, CA, United States).

## Cardiomyocyte Sarcomere-Immunostaining

The iPSC-CMs and tissues were co-immunostained with anti-sarcomeric α-actinin (AF594) (Abcam, Cambridge, MA, United States) to image sarcomere organization, and anti-MHC monoclonal MF20 (AF488) (DSHB, University of Iowa, Iowa City, IA, United States) to inform myocyte identity. Sarcomeres in iPSC-CMs were visualized with a Nikon inverted fluorescent microscope at 400x.

## Contractility of iPSC-CMs

All the contractile experiments with iPSC-CMs were conducted in a non-biased blinded fashion. Contractile data were collected from iPSC-CMs at differentiation days D20, D27, D34, and D41. Experiments were conducted over 3 days such that D20 includes D20-D23, D27 (D27–D30), D34 (D34–D37), and D41 (D41–D43). The iPSC-CMs were transferred to a recording chamber containing 1 mM $Ca^{2+}$ Tyrode's solution (35°C) mounted on the stage of an inverted microscope (Nikon TE2000). Spontaneously contracting iPSCs were visualized at 40x and contractile events recorded using a MyoCam-S video 250 Hz camera and a CFA300 cell framing adapter (IonOptix, Boston, MA, United States). The left and right edges of iPSC-CMs were defined and contractions per minute (CPM), shortening (μm), % cell shortening, and rates of shortening and relaxation (μm/second) were measured using the IonWizard image detection program (IonOptix, Boston, MA, United States). Ten cells on a 12 cm$^2$ round cover glass were evaluated for 10 contractions each. For a subset of D20 iPSC-CMs, the same parameters were determined for responses to 1 and 2 Hz stimulation or to 1 μM isoproterenol. As an alternative method, an automated contractility software[1] (Dana solution, Palo Alto, CA, United States) (Maddah et al., 2014, 2015) was used to study videos of contracting iPSC-CMs.

## Action Potentials of iPSC-CMs

Action potentials of iPSC-CMs were obtained with microelectrodes (50–70 MΩ) filled with 2.7 M KCl and 10 mM HEPES and recorded at 35°C using Clampex9.2 software (Axon Instruments, Axoclamp-2A, San Jose, CA, United States). For each iPSC-CM measured, the lowest membrane potential (referred to as diastolic potential), threshold potential, peak spike potential, and action potential duration were averaged from 5 action potentials per cell. Action potential duration ($APD_{90}$) was defined as the time (ms) from the start of the action potential until membrane potential returned to 10% of its peak height.

## Calcium Transients of iPSC-CMs

The iPSC-CMs were plated on an 18 mm$^2$ round cover glass at D15. At D20, the iPSC-CMs were incubated for 45 min at 35°C in 0.5 mM $Ca^{2+}$ Tyrode's solution containing 2.5 μM of Fura-2 AM (Invitrogen, Carlsbad, CA, United States). Then, cover glasses were inserted into a quick-release chamber (RC-49MFS, Warner Instruments, Hamden, CT, United States) bathed in 1 mM $Ca^{2+}$ Tyrode's solution at 35°C. Whole cell $Ca^{2+}$ transients were recorded using Fura-2 AM as described previously (Wang and Fitts, 2018). Briefly, Fura-2 AM was excited at 340 and 380 nm switching between wavelengths with a LAMBDA DG4 (Sutter Instrument, Novato, CA, United States) and the fluorescence emission measured at 510 nm. To determine the $Ca^{2+}$ transient rate of rise and fall and the peak amplitude, the ratio was analyzed with IonWizard and data were expressed as ratio units (peak

---

[1] https://www.pulsevideoanalysis.com/

amplitude) and ratio units/s (rate of transient rise and fall). Ten $Ca^{2+}$ transients were averaged for every iPSC-CM.

## Protein Expression Analysis of iPSC-CMs

### Sample Preparation

Following contractile studies, iPSC-CMs were scraped from cover glasses into 1 mM $Ca^{2+}$ Tyrode's solution and centrifuged for 5 min at 16,100 × *g*. The pellet of iPSC-CMs was collected in 10 μl SDS sample buffer (10% SDS, 23 mM EDTA, 50% glycerol, 0.4% bromophenol blue, and 5.1% β-mercaptoethanol, pH 6.8) and stored at −80°C until studied.

### Silver Staining

MHC composition was determined by silver staining 5% SDS-PAGE gels as previously described (Sundberg et al., 2018). Briefly, gels were run for 28–30 h at 4°C to separate α-MHC and β-MHC, and ImageJ (National Institutes of Health) was used to quantify protein expression. Samples were also run for 1 h at 150 V on 12% precast polyacrylamide gels using a Mini-PROTEAN Electrophoresis Cell (Bio-Rad, Hercules, CA, United States) and silver stained to examine lower molecular weight proteins.

### Western Blotting

Diluted samples were run on a 4–15% gradient gel for 1 h at 150 V and transferred to a 0.2 μm nitrocellulose membrane using a Mini Trans-Blot cell (Bio-Rad, Hercules, CA, United States) at 100 V for 50 min. The gel was run in Tris-glycine running buffer and transferred with running buffer containing 20% methanol. Following transfer, membranes were blocked for 3 h in 5% non-fat dry milk in TBS-0.1% Tween pH 7.6 (TBST) and probed with primary antibodies overnight at 4°C. Primary antibodies for MHC (MF20, 1:800, DSHB), GAPDH (ab181602, 1:1,000, Abcam, Cambridge, United Kingdom), and ventricular myosin light chain-2 (MLC2v) (7C9, 1:2,000, Fisher Scientific, Hampton, NH, United States) were diluted in 5% non-fat dry milk in TBST. Then, the blots were incubated with horseradish peroxidase-conjugated secondary antibodies (sc-516132, 1:6,500, Santa Cruz Biotechnology; NBP2-30347H, 1:6,500, Novus Biologicals; G-21234, 1:1,600, Fisher Scientific, Hampton, NH, United States) in 5% non-fat dry milk in TBST for 1 h at room temperature. Protein expression was detected on autoradiography film (Hyblot CL, Fisher Scientific, Hampton, NH, United States) by chemiluminescence. ImageJ (National Institutes of Health) was used for densiometric analysis and protein expression was normalized to GAPDH.

## Tissue Sarcomere-Immunostaining

### Tissue Sample Preparation

A total of 27 samples from atrial and ventricular tissues were examined, including two 4-day old neonatal atrial tissues, one from an HLHS subject without an *MYH6* variant and one from an HLHS subject with the *MYH6*-R443P variant. The 25 non-neonatal tissues were from subjects between 227 days to 24-years old. These samples were divided into three study groups: control (non-HLHS CHDs and structurally normal cardiac control), HLHS subjects without an *MYH6* variant, and HLHS subjects with an *MYH6* variant. In each study group, when available, we included atrial and ventricular tissues. In all cases, the samples were pieces of tissue dissected and phenotyped at the time of surgery. They were snap frozen immediately after removal from the patient. Some tissues came at the time of heart implantation, and some came from the time of reparative surgery.

### Tissue Immunostaining

Cryo-sections (10 μm) of the frozen tissues were prepared. The tissues were co-immunostained with anti-sarcomeric α-actinin (AF594) (Abcam, Cambridge, MA, United States) to image sarcomere organization, and anti-MHC monoclonal MF20 (AF488) (DSHB, University of Iowa) to inform myocyte identity. Sarcomeres in tissue sections and iPSC-CMs were visualized with Structured Illumination Microscopy (SIM) at 1000x magnification.

## Statistical Analyses

### Characterization of Gene-Edited iPSC-CMs

Significant differences between two groups were analyzed through an unpaired two-tailed Student's *t*-test using Excel (Microsoft). If the data were not normally distributed, comparisons were made using the non-parametric Wilcoxon signed-rank test. Statistical significance was set at $P < 0.05$.

### Contractile Studies

When necessary, data were transformed to meet assumptions of normality and homogeneity of variance. For the time course study, a two-way ANOVA was performed to compare iPSC-CM contractility of wild-type (WT) vs. variant (VAR; *MYH6*-R443P) at timepoints D20, D27, D34, and D41. *Post hoc* pair-wise comparisons were performed using Tukey's test. All subsequent studies (action potentials, contractile responses to stimulation, isoproterenol, and $Ca^{2+}$ transient recordings) were restricted to D20. Data were analyzed with a one-way ANOVA, except for stimulation data, which were analyzed with a two-way ANOVA. Statistics were performed using Minitab v18.1 with significance set at $P < 0.05$.

# RESULTS

## CRISPR/Cas9 Gene Edited iPSC-CMs

### Insertion of the *MYH6*-R443P Variant Into the Heart Healthy Parent's iPSCs Results in Expression of the Proband's Sarcomere Phenotype

Using CRISPR/Cas9 gene editing, the *MYH6*-R443P variant was introduced into the heart healthy parent's iPSCs, generating CRISPRed control wild-type (WTcc) lines, as well as lines having one allele (inserted +/VAR) or both alleles inserted (inserted VAR/VAR). The CRISPR target site has one base-pair mismatch, and the sequences of both *MYH6* (**Figure 1A**) and its close homologue *MYH7* (**Supplementary Figure S1**) were confirmed in CRISPRed iPSCs with Sanger sequencing for any off-target effects. The experiments performed in VAR-inserted cells were obtained with only one line per genotype. Following cellular expansion and verification of

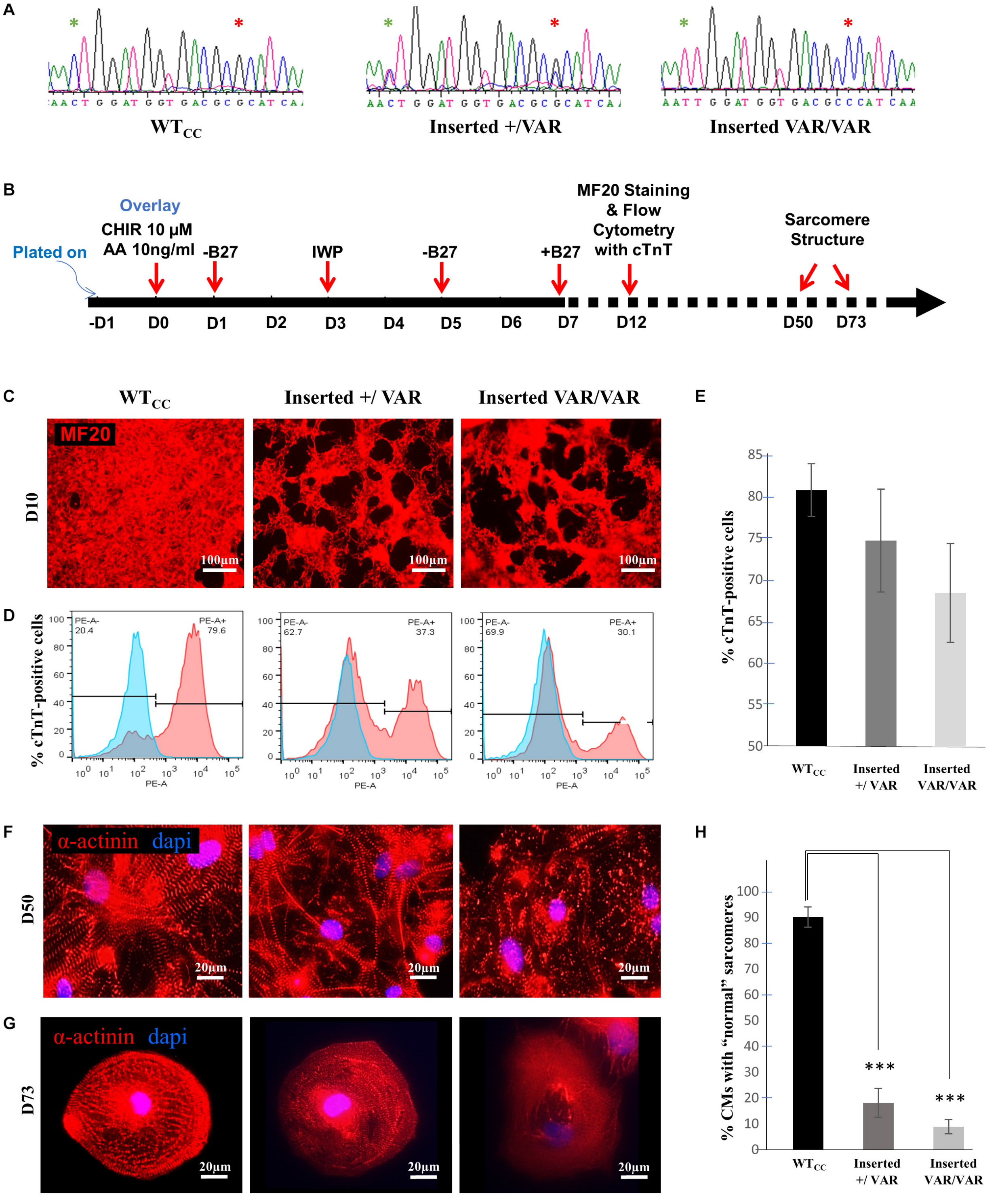

**FIGURE 1 |** *MYH6*-R443P VAR-inserted iPSC-CMs recapitulate phenotypes of patient-specific iPSC-CMs. **(A)** Sequences at the *MYH6*-R443 locus in VAR-inserted lines. * is R443 locus and * is locus for silencing mutation. **(B)** Scheme for differentiating CMs using small molecule Gsk3 inhibitor (CHIR99021) with Activin-A and Wnt inhibitor (IWP). **(C)** Representative immunostaining of VAR-inserted iPSC-CMs with MF20 at D12. **(D)** Representative flow cytometry of cardiac troponin T (cTnT) positive cells in CRISPRed iPSC-CMs at D12. **(E)** Flow cytometry of cells cultured in parallel with those in **(D)**, showing % cTnT-positive cells in VAR-inserted iPSC-CMs at D10-15. Data were compiled from 16 replicates in each cell type and 5 separate experiments. **(F)** Sarcomeres are dysmorphic in VAR-introduced iPSC-CMs as compared to $WT_{CC}$. α-actinin immunostaining (red) is seen in high density cultures at D50. **(G)** Comparative sarcomere organization in single cell iPSC-CMs isolated after sub-culturing at a low density at D69-D73. **(H)** % of cells with normal organized sarcomeres in both VAR-inserted iPSC-CMs, +/VAR and VAR/VAR in parallel to those in **(G)**. WTcc, CRISPRed control wild-type; +/VAR, *MYH6*-R443P heterozygous inserted; VAR/VAR, *MYH6*-R443P homozygous inserted. Values are means ± SE. Student's *t*-test (two-tailed, equal variance), $^{***}P < 0.0005$.

genotype, iPSCs representing WTcc, inserted +/VAR and inserted VAR/VAR were induced to undergo cardiomyogenic differentiation as we previously described (Kim et al., 2015) (depicted in **Figure 1B**). The efficiency of cardiomyogenic differentiation during D10–D15 was reduced in both the inserted +/VAR and inserted VAR/VAR iPSC-CMs determined by MF20 immunostaining (**Figure 1C**) and flow cytometry assessment of % cTnT-positive cells (**Figures 1D,E**). We also evaluated sarcomere structure in iPSC-CMs at later stages of differentiation in both mass cultured CMs at D50 (**Figure 1F**) and individual CMs isolated from the culture at D73 (**Figure 1G**). Over 100 isolated iPSC-CMs of each line were judged for dysmorphic sarcomere organization at D69 and D73 (**Figure 1H**). "Normal" iPSC-CMs exhibit crisp and elongated ladders with wide Z-bands. Dysmorphic iPSC-CMs are characterized by more than 50% of the myocyte area displaying blurred α-actinin staining and/or sarcomeric ladders with punctate or truncated deposits of α-actinin (**Figures 1G,H**). iPSC-CMs with the *MYH6*-R443P variant were substantially disorganized in both the inserted +/VAR and inserted VAR/VAR compared to WTcc-CMs.

### Correction of the *MYH6*-R443P Variant in iPSCs Normalizes the Proband's Sarcomere Phenotype

Using CRISPR-Cas9, we corrected the *MYH6*-R443P variant (corrected WT) in the proband's iPSCs (**Figure 2A**). This improved the efficiency of cardiomyogenic differentiation as assessed by MF20 immunostaining (**Figure 2B**) and by flow cytometric quantitation of the % of cTnT-positive cells (**Figures 2C,D**). Perhaps most notable was the appearance of the sarcomeres, which were relatively disorganized in CRISPRed control proband (Probandcc) iPSC-CMs expressing the R443P variant (**Figure 2E**, left) and became organized upon correction in corrected WT iPSC-CMs (**Figure 2E**, right).

## Contractility of iPSC-CMs From WT, VAR, and *MYH6*-R443P CRISPRed Lines

Contractile data were collected from WT (heart healthy parent wild-type) and VAR (proband with the *MYH6*-R443P variant) iPSC-CMs at time points D20, D27, D34, and D41 (**Supplementary Table S1**). WT iPSC-CMs showed a higher percent shortening and relaxation rate at D20 compared to VAR. However, by D27, there were no significant differences in contractile parameters except values for contraction rate per minute (CPM), which was higher in WT iPSC-CMs (**Supplementary Table S1**). This indicates that the primary difference in contractile parameters between WT and VAR manifests at relatively early stages. Consequently, the focus of our study shifted to a detailed examination of D20 cells. At D20, the extent of shortening (μm), the % shortening, and the rates of shortening and relaxation were higher in WT iPSC-CMs in comparison with VAR (**Table 2**). In **Figure 3A**, the best-fit lines demonstrate the measurement of maximal cell shortening and relaxation rates. For this cell, we measured the following parameters: CPM (WT, 57.2 and VAR, 45.7), shortening (WT, 2.9 μm and VAR, 2.4 μm), percent shortening (WT, 6.7% and VAR, 4.3%), rate of shortening (WT, 28.3 μm/s and VAR 23.2 μm/s) and rate of relaxation (WT, 22.5 μm/s and VAR, 17.4 μm/s). Addition of 1 μM isoproterenol had no effect on iPSC-CMs mechanics of either cell type. However, both cell types responded to 1 Hz stimulation, contracting at 60 ± 4 (WT) and 64 ± 4 (VAR), and while CPM increased further with 2 Hz stimulation, neither cell type was able to respond at 2 Hz (WT, 73 ± 6 and VAR, 76 ± 8). The amplitude of the $Ca^{2+}$ transient was higher in WT compared to the VAR (**Figure 3B**) cells, but no differences were observed in the rate of rise or fall of the transient (**Supplementary Table S2**). Isoproterenol had no effect on the amplitude of the $Ca^{2+}$ transient in either cell type but did increase the rate of rise and fall of the transient in the VAR (**Supplementary Table S2**). **Figure 3C** shows representative action potentials for WT and VAR at D20, followed by a 5 s recording from the same cell. The $APD_{90}$ for these cells are 298 and 300 ms for WT and VAR, respectively.

Contractile data revealed that *MYH6*-R443P variant-inserted iPSC-CMs contracted more slowly, while the % shortening as well as the rates of shortening and relaxation were not different between the WTcc vs. inserted +/VAR and inserted VAR/VAR iPSC-CMs (**Table 3** and **Supplementary Table S3**). All three of the CRISPRed genotypes responded to 1 and 2 Hz stimulation, but the inserted VAR/VAR iPSC-CMs had a higher CPM compared to WTcc at 2 Hz (**Supplementary Table S3**). The inserted VAR/VAR iPSC-CMs also had a greater shortening rate compared to the inserted +/VAR iPSC-CMs at 1 Hz but not 2 Hz. There were no differences in the $Ca^{2+}$ transients of the WTcc, inserted +/VAR and inserted VAR/VAR iPSC-CMs (**Supplementary Table S4**). The mean action potential characteristics for the WT, VAR, WTcc, inserted +/VAR and inserted VAR/VAR were not different (**Table 4**). This is important as it demonstrates that neither the variant nor the CRISPR technology altered the electrical properties of the sarcolemma membrane.

In mass cell cultures, using a separate automated contractility software (see section "Materials and Methods" for details), we also analyzed velocity of corrected WT iPSC-CMs at D20-D22. With this analysis, we obtained similar results as single-cell studies. Corrected WT iPSC-CMs exhibit faster contraction (**Figure 4A**, $P < 0.05$) and increased velocity (**Figure 4B**, $P < 0.0001$) compared to Probandcc iPSC-CMs.

## Protein Expression of Typical Muscle Proteins

Both α-MHC and β-MHC were present in WT iPSC-CMs throughout the time course of D15-D34, while VAR iPSC-CMs showed the presence of only β-MHC after D15 (**Figure 5A**). The 12% SDS gel (**Supplementary Figure S2**) shows that both cell types contain multiple proteins known to exist in cardiac muscle, including actin and MLC2v. Western blot analyses confirmed the presence of MHC and MLC2v in all iPSC-CM samples and densitometric analyses found no difference between cell types in the expression of either total MHC (both α- and β- isoforms of MHC) or MLC2v (**Figure 5B**).

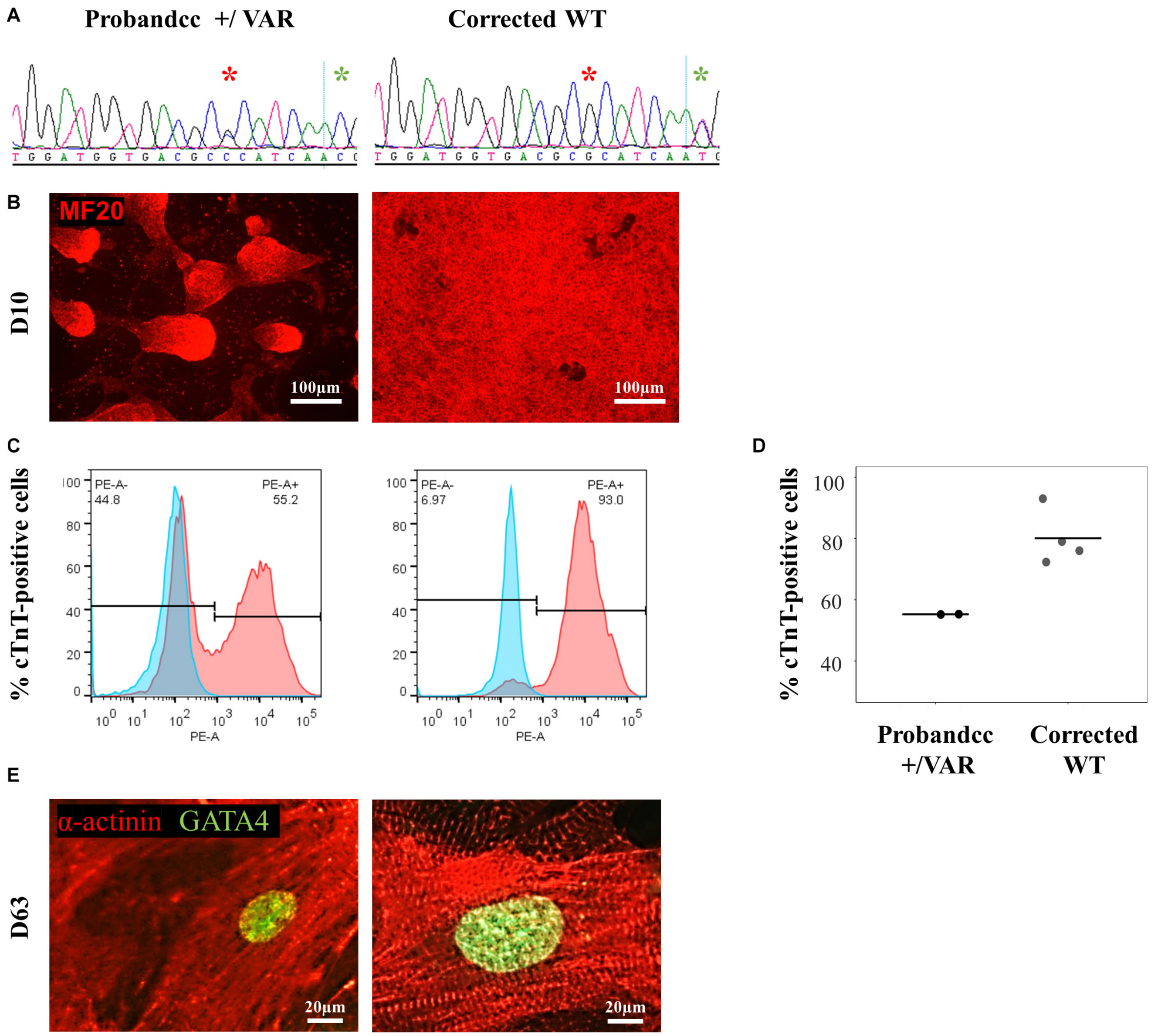

**FIGURE 2 |** *MYH6*-R443P VAR-corrected iPSC-CMs rescues the phenotype of proband iPSC-CMs. **(A)** Sequences at the *MYH6*-R443P locus in corrected line. * is the R443 locus and * is the locus for a silencing mutation. **(B)** Representative immunostaining of VAR-corrected iPSC-CMs with MF20 (red) at D10. **(C)** Representative flow cytometry of cardiac troponin T (cTnT) positive cells in corrected iPSC-CMs at D12. **(D)** Flow cytometry of cells cultured in parallel with those in **(C)**, showing % cTnT-positive cells at D10. Each dot is a technical replicate (Probandcc $n = 2$ and corrected WT $n = 4$). **(E)** Sarcomeres appear more "normal" in corrected WT iPSC-CMs compared to Probandcc iPSC-CMs. α-actinin immunostaining is seen in red and GATA4 in green in high density cultures at D63. Probandcc, CRISPRed control proband; corrected WT, CRISPRed and corrected *MYH6*-R443P variant.

**TABLE 2 |** Summary of contractile differences between WT and VAR iPSC-CMs at D20.

| | CPM | Shortening (µm) | Percentage of shortening (%) | Shortening rate (µm/s) | Relaxation rate (µm/s) |
|---|---|---|---|---|---|
| WT | 47 ± 2 | 2.9 ± 0.2 | 8.1 ± 0.7 | 28.1 ± 2.5 | 19.7 ± 2.0 |
| VAR *MYH6*-R443P | 40 ± 2* | 2.3 ± 0.2* | 5.6 ± 0.5* | 19.9 ± 1.7* | 11.0 ± 0.9* |

*For CPM measurements, n = 36 and 35 for WT and VAR, respectively. Ten contractions for each cell were averaged to give a single value for the contractile parameter. Only cells shortening inward from both edges were analyzed for shortening, % shortening, and rates of shortening/relaxation. CPM, contraction per minute; WT, heart-healthy parent wild-type; VAR, proband with MYH6-R443P. Values are means ± SE. One-way ANOVA, *P < 0.05.*

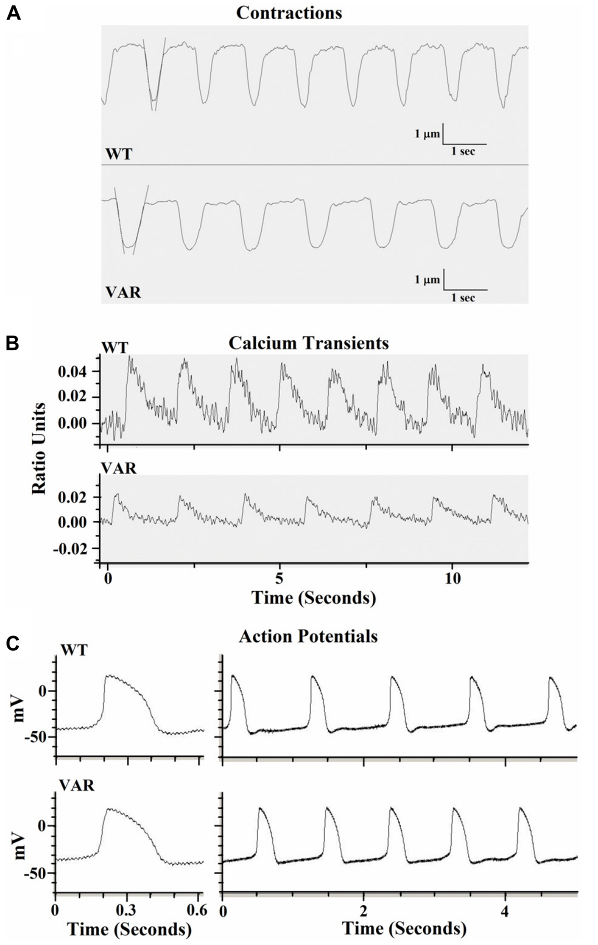

**FIGURE 3 |** Representative traces of contractile properties of single iPSC-CMs at D20. **(A)** Spontaneously contracting WT and VAR single iPSC-CMs. Best-fit lines are shown to demonstrate the measurement of maximal cell shortening and relaxation rates (IonOptix). **(B)** Representative calcium transients of WT and VAR single iPSC-CMs **(C)** Representative action potentials of WT and VAR single iPSC-CMs, followed by a 5 s recording from the same cell. CPM, contraction per minute; WT, heart-healthy parent wild-type; VAR, proband with *MYH6*-R443P.

## Sarcomere Organization in Patient Cardiac Tissues

We observed a dysmorphic sarcomere phenotype in cardiac tissues from HLHS subjects with *MYH6* variants. Detailed sample information is listed in **Table 5** and **Supplementary Table S5**. We also identified combined annotation dependent depletion (CADD) scores for variant pathogenicity for all the *MYH6* variants (GRCh38-v1.6 for SNP and GRCh38-v1.3 for deletion): 26.5 for *MYH6*-R443P (**Figure 6I**), 25.9 for *MYH6*-K849- (**Figure 6J**), 33 for *MYH6*-E1503V (**Figure 6K**), and 22.9 for *MYH6*-S385L/25.2 for M436V compound heterozygous variant (**Figure 6L**; Rentzsch et al., 2019).

Sarcomeres in the atria and ventricles of healthy (**Figures 6A–D**) and HLHS tissues without *MYH6* variants (**Figures 6E–H** and **Supplementary Figures S4A–D,G**) were organized except two samples, which are further described below. This was also the case in atrial tissues of other CHD subjects, including Ebstein's Anomaly (**Figure 6A**) and Dextrocardia (**Figure 6B**). The organized sarcomere structure in HLHS patients without the *MYH6* variant is clearly seen by comparing the atrial tissue in **Figure 6E** with the ventricular tissue in **Figure 6M**, both obtained at the time of surgery from the same HLHS subject. Notably, 3 of the 4 atrial tissues from HLHS subjects possessing the *MYH6* variant (**Figures 6I–L**) exhibited poor sarcomere organization, while ventricular tissues showed normal structure (**Figures 6Q,R**). Sarcomeres in atrial tissues from HLHS subjects with *MYH6* variants are absent, or if detectable are disorganized [**Figure 6I** (*MYH6*-R443P), **Figure 6J** (*MYH6*-K849-), **Figure 6K** (*MYH6*-E1503V)]. The *MYH6*-R443P variant is in the head domain whereas *MYH6*-K849- and *MYH6*-E1503V are in the tail domain. The atrial and the ventricular tissues in **Figures 6J,R** are from a HLHS patient with *MYH6*- K849-, while the atrial and the ventricular tissues in **Figures 6K,Q** are from a HLHS patient with *MYH6*-E1503V. At the neonatal stage, sarcomeres are organized in both atrial tissues from HLHS patients with and without *MYH6* variants (**Supplementary Figure S3**). The atrial restriction of this sarcomere phenotype corresponds to the predominance of *MYH6* expression in the atria after the neonatal stage. The samples in **Supplementary Figure S3B** were from the same HLHS patient with *MYH6*-R443P (**Figure 6I**). Additional samples exhibited disrupted sarcomeres in HLHS subjects without an *MYH6* variant, one carrying a *Dystrophin* hemizygous variant (*DMD*-I228N, scaled CADD-score 26.6) (**Supplementary Figure S4E**) while the other HLHS subject did not reveal any sarcomere gene variants from whole exome sequencing (**Supplementary Figure S4F**).

## DISCUSSION

HLHS etiology remains incomplete, in part due to its diverse phenotype and complex genetic inheritance, as well as

**TABLE 3 |** Summary of contractile differences between WTcc and VAR-inserted iPSC-CMs at D20.

| | *n* | CPM | Shortening (µm) | Percentage of shortening (%) | Shortening rate (µm/s) | Relaxation rate (µm/s) |
|---|---|---|---|---|---|---|
| WTcc | 60 | 66 ± 6 | 1.9 ± 0.09 | 5.1 ± 0.34 | 16.8 ± 1.23 | 10.9 ± 0.59 |
| Inserted +/VAR | 54 | 34 ± 2* | 1.8 ± 0.12† | 4.6 ± 0.35 | 15.3 ± 1.04 | 11.6 ± 0.70 |
| Inserted VAR/VAR | 59 | 37 ± 2* | 2.2 ± 0.14 | 4.2 ± 0.27 | 19.1 ± 1.50 | 13.0 ± 1.05 |

*Ten contractions were averaged for each cell (n). Only cells shortening inward from both edges were analyzed. CPM, contraction per minute; WTcc, CRISPRed control wild-type; +/VAR, MYH6-R443P heterozygous inserted; VAR/VAR, MYH6-R443P homozygous inserted. Values are means ± SE. One-way ANOVA, $P < 0.05$. *Denotes significant difference from WTcc. †Denotes significant difference from Inserted VAR/VAR.*

**TABLE 4 |** Summary of action potentials at D20.

| | *n* | Diastolic potential (mV) | Threshold potential (mV) | $APD_{90}$ (ms) | Spike potential (mV) |
|---|---|---|---|---|---|
| WT | 37 | −40 ± 1 | −34 ± 1 | 269 ± 15 | 19 ± 2 |
| VAR *MYH6*-R443P | 37 | −37 ± 2 | −34 ± 2 | 258 ± 8 | 16 ± 1 |
| $WT_{CC}$ | 10 | −38 ± 2 | −34 ± 3 | 269 ± 23 | 20 ± 2 |
| Inserted +/VAR | 24 | −31 ± 2 | −29 ± 2 | 337 ± 17 | 18 ± 2 |
| Inserted VAR/VAR | 14 | −35 ± 4 | −32 ± 4 | 315 ± 24 | 27 ± 4 |

*Each iPSC-CM's diastolic potential, threshold potential, $APD_{90}$, and spike potential were determined from the average of five different action potentials. $APD_{90}$, time in ms for potential to return to 10% of initial (i.e., most negative) potential. WT, heart-healthy parent wild-type; VAR, proband with MYH6-R443P; WTcc, CRISPRed control wild-type; +/VAR, MYH6-R443P heterozygous inserted; VAR/VAR, MYH6-R443P homozygous inserted. Values are means ± SE. One-way ANOVA, $P < 0.05$.*

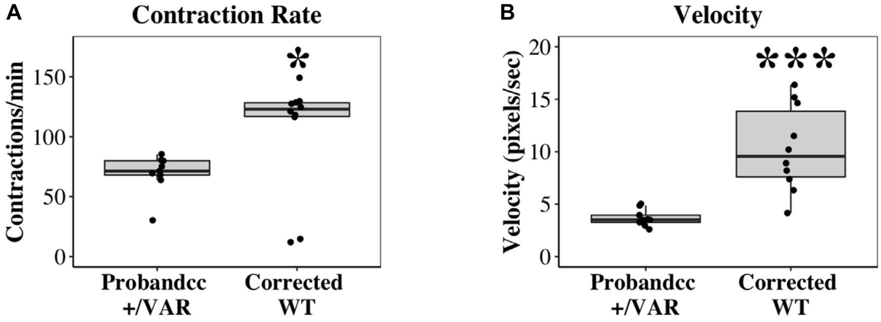

**FIGURE 4 |** Contractile differences between Probandcc and corrected WT iPSC-CMs at D20-D22. **(A)** Contraction rate and **(B)** Velocity of iPSC-CMs were recorded at D20-D22 using an automated contractility software with four technical replicates for each genotype (Probandcc *n* = 9 and corrected WT *n* = 10). Probandcc, CRISPRed control proband; corrected WT, CRISPRed and corrected *MYH6*-R443P variant. The lines in the box plots indicate median, with maximum and minimum calculated values shown as whiskers. Each dot is a technical replicate. Wilcoxon signed-rank test, $^{*}P < 0.05$ and $^{***}P < 0.001$.

environmental factors. To understand the molecular and cellular mechanisms of HLHS, we investigated patient-specific HLHS etiology using an iPSC-CM model and examined cardiac tissue from HLHS patients with sarcomere immunostaining. To further demonstrate the impact of the *MYH6*-R443P variant on HLHS, we used CRISPR/Cas9 gene editing to generate isogenic controls. Insertion of the *MYH6*-R443P variant into the heart healthy parent's iPSCs recapitulated the dysmorphic sarcomere phenotype (**Figure 1**) and contractile dysfunction (compare **Tables 2**, **3**). Correcting the *MYH6*-R443P variant in the proband's iPSCs rescued the phenotypes of decreased CM differentiation efficiency, dysmorphic sarcomeres, and abnormal CPM and velocity (**Figure 4**).

Based on functional analysis of iPSC-CMs with the *MYH6*-R443P variant, the primary contractile defects were reduced CPM, impaired cell shortening (expressed as a % of cell length), and decreased rates of shortening and relaxation. These defects occurred early (by D20) and likely resulted from reduced development of the SR including the SERCA pump and the increased expression of the slow β-MHC isoform in the variant iPSC-CMs (**Figure 5A**). The reduced SR SERCA pump activity would explain the slower relaxation rates in the VAR. Regarding contraction rate, the β-MHC isoform is known to have a lower ATPase activity which limits cross-bridge cycle speed, and skeletal fibers containing this isoform are 3–4 times slower than α-MHC fast fibers (Schluter and Fitts, 1994; Fitts, 2008). The reduced contractile function in the *MYH6*-R443P variant compared to WT iPSC-CMs at D20 may be due to delayed development, as by D27 there were no differences in the contractility between the WT and VAR. Beyond D27, the loss of difference between cell types in contractile function was likely at least in part due to delayed development of the VAR particularly the SR. This is best demonstrated by the relaxation rate where at D20 the WT was twofold higher but by D27 the VAR relaxation rate had increased to match the WT (**Supplementary Table S1**). Despite no differences in shortening rate between WT and VAR past D20, the β-MHC content remained high in the VAR from D21 through D34 (**Figure 5**). We know iPSC-CMs are immature at D20, which may explain why cell contractility was not increased by adrenergic stimulation with isoproterenol (**Supplementary Table S2**). This lack of response most likely indicates immaturity of the sarcoplasmic reticulum, but also could indicate lack of the ß1 receptor on the surface membrane (Pillekamp et al., 2012).

The *MYH6*-R443P variant showed a reduced amplitude of the $Ca^{2+}$ transients upon activation compared to WT, but both showed diminished $Ca^{2+}$ release compared to adult rat ventricular cardiac cells (Wang and Fitts, 2017). It is likely that the reduced $Ca^{2+}$ release relates to lower sarcoplasmic reticulum content and not to differences in surface membrane activation, as the recorded action potentials were identical between the WT and VAR. Differences in membrane excitability at D20 were noted, indicated by lower CPM in the VAR compared to the WT. Since the lowest membrane potential (referred to as diastolic potential)

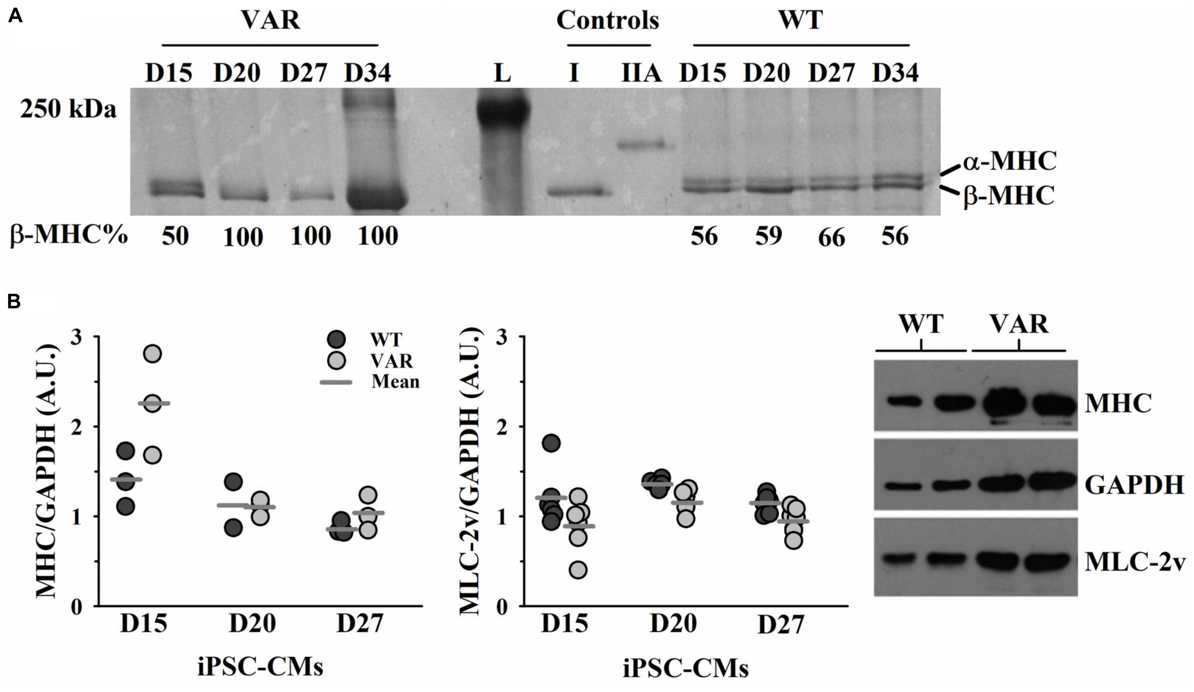

**FIGURE 5 |** Upregulation of β-MHC in VAR at D15-D34. **(A)** Silver stained 5% SDS PAGE gel with each lane corresponding to the differentiation days and % of β-MHC expression listed beneath, as determined by densitometric analysis. **(B)** Protein expression in WT and VAR at D15, D20 and D27, as determined by densitometric analysis. Left: WT and VAR expression of MHC (*left*) and MLC2v (*right*), normalized to GAPDH. Values are means ± SEM of three technical replicates for each day and cell type. Right: Representative Western blot showing MHC, MLC2v, and GAPDH expression in WT and VAR at D20. L, ladder; I, type I skeletal muscle fiber; IIA, type IIA skeletal muscle fiber; WT, heart-healthy parent wild-type; VAR, proband with *MYH6*-R443P.

and the threshold potential were not different between cell types, this suggests that the rate of spontaneous depolarization to threshold may have been faster in the WT. However, our recordings did not show an obvious difference in the rate of depolarization to threshold between cell types (**Figure 3** and **Table 4**). This may be because the difference is too small for detection during the single-cell level experiments performed at D20. Sorting out differences between the WT and VAR iPSC-CMs

**TABLE 5 |** Tissue characteristics for **Figure 6**.

| Sample label | Tissue source | Patient age (years) | Clinical diagnosis | *MYH6* genotype | Transplantation age |
|---|---|---|---|---|---|
| A | Left atrium | 1 – 5 | Ebstein's anomaly | WT | N/A |
| B | Left atrium | 1 – 5 | Dextrocardia | WT | N/A |
| C | Inter atrial septum | 20 – 25 | Structurally normal | WT | N/A |
| D | Left atrium | 1 – 5 | Structurally normal | WT | N/A |
| E | Left atrium | 10 - 15 | HLHS | WT | At the same time of tissue sage |
| F | Left atrium | 1 – 5 | HLHS | WT | At the same time of tissue sage |
| G | Right atrium | 1 – 5 | HLHS | WT | N/A |
| H | Atrium (unknown side) | 1 – 5 | HLHS | WT | N/A |
| I | Left atrium | 1 – 5 | HLHS | R443P | N/A |
| J | Left atrium | 1 – 5 | HLHS | K849- | At the same time of tissue sage |
| K | Left atrium | 10 - 15 | HLHS | E1503V | At the same time of tissue sage |
| L | Atrial septum | 1 – 5 | HLHS | S385L and M436V | N/A |
| M | Ventricle | 10 – 15 | HLHS | WT | At the same time of tissue sage |
| N | Right ventricle | 0 – 1 | HLHS | WT | N/A |
| O | Ventricle | 10 – 15 | HLHS | WT | N/A |
| P | Right ventricle | 0 – 1 | HLHS | WT | N/A |
| Q | Right ventricle | 10 – 15 | HLHS | E1503V | Later than tissue age |
| R | Apex | 1 – 5 | HLHS | K849- | At the same time of tissue sage |

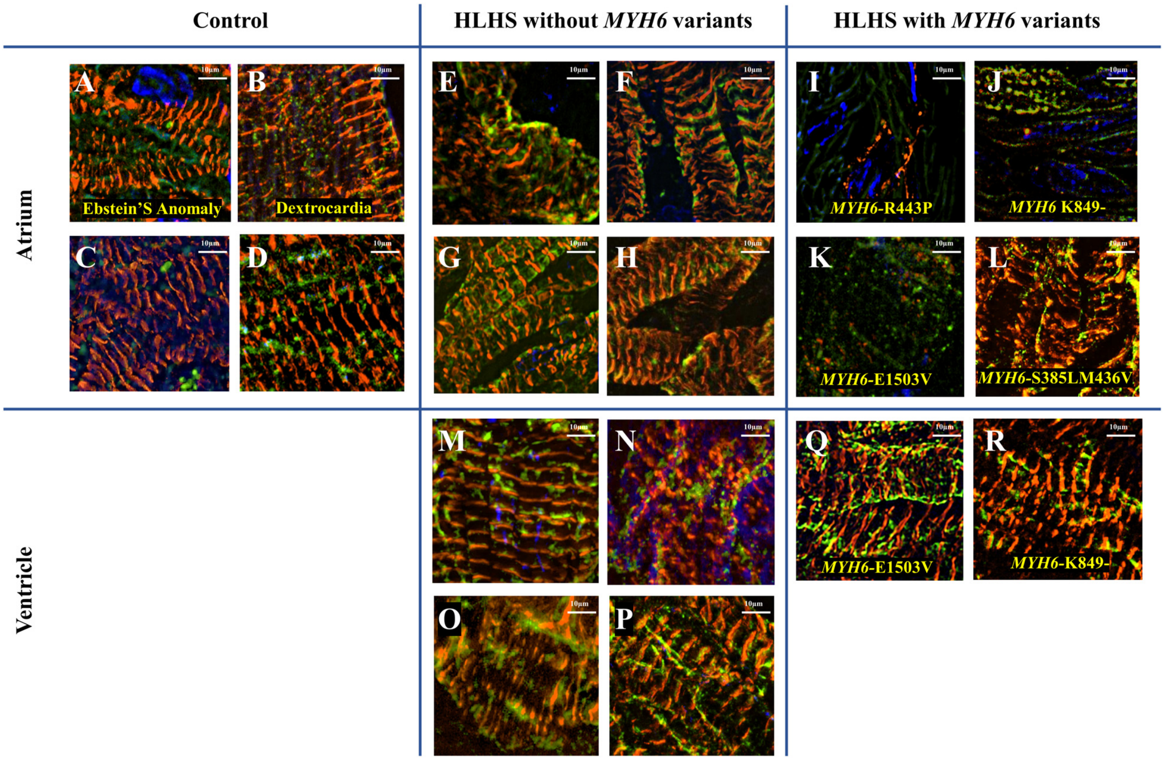

**FIGURE 6 |** Dysmorphic sarcomeres were observed in atrial tissues from HLHS patients with *MYH6* variants, but not in ventricles. Sarcomeric α-actinin is in red, MF20 in green and dapi in blue. **(A–D)** Atrial tissues from HLHS free patients without *MYH6* variants. **(E–H)** Atrial tissues from HLHS patients without *MYH6* variants. **(I–L)** Atrial tissues from HLHS patients with *MYH6* variants. **(M–P)** Ventricular tissues from HLHS patients without *MYH6* variants. **(Q,R)** Ventricular tissues from HLHS patients with *MYH6* variants.

will require additional studies of organelle function (particularly the sarcoplasmic reticulum and myofilaments).

The basic contractile unit of striated (cardiac and skeletal) muscle is the sarcomere, a highly ordered structure containing contractile and regulatory proteins. Disruptions in sarcomere proteins have been implicated in many cardiac diseases (Redwood et al., 1999; Seidman and Seidman, 2001; Richard et al., 2003; Laing and Nowak, 2005). Here, we observed dysmorphic sarcomeres in tissues from HLHS patients with certain *MYH6* variants and these changes were phenocopied in iPSC-CMs generated from a HLHS patient with the *MYH6*-R443P variant. Sarcomere disorganization in cardiac tissues from three out of four HLHS patients with *MYH6* variants was observed in atrial but not in ventricular tissues (**Figure 6**). This result was expected as α-MHC protein expression is predominantly in the postnatal atria in humans. Likely, the *in vivo* contractile dysfunction is mainly in the atria, with the hypoplastic ventricular phenotype representing a developmental response resultant from diminished inflow pulsatility. Adding to the idea that poorly organized sarcomeres might contribute to the development of HLHS, atrial tissues from a HLHS patient with a costameric variant in *Dystrophin* (*DMD*) also showed sarcomere disruption (**Supplementary Figure S4E**). Furthermore, we observed that variants with the highest scaled CADD-scores: *MYH6*-R443P (26.5), *MYH6*-K849- (25.9), *MYH6*-E1503V (33) and *DMD*-I288N (26.6) had the most apparent disruptions in sarcomere structure in atrial tissues *ex vivo*. One limitation was lack of paired controls, however tissue samples showed convincing evidence of abnormalities (**Figure 6**).

Investigating HLHS etiology requires a physiological system of electrically and mechanically connected iPSC-CMs. One concern with employing iPSCs is the clonal variability; to reduce variability, we conducted all experiments multiple times (as indicated in each figure legend) in a non-biased, blinded fashion. A WT line was always differentiated along with experimental lines to compare differences among cell types at each differentiation stage. Additionally, isogenic *MYH6*-R443P cell lines were created using CRISPR/Cas9 gene editing and these lines recapitulated the phenotypes of patient-specific *MYH6*-R443P iPSC-CMs. An additional limitation is the heterogenous population of iPSC-CMs, including both atrial and ventricular cells. There are MLC-2a, MLC-2v, as well as double-positive iPSC-CMs in our cultures upon immunostaining at D31-D35 (data not shown). As our protein expression (**Figure 5**) and automated contractility assays (**Figure 4**) were analyzed in masse, they may underestimate the true heterogeneity of our cells. While we have a relatively pure population of cTnT positive CMs that express our cardiac gene of interest, *MYH6*, single-cell analyses similar to those completed by other groups may help further clarify their composition (Weber et al., 2016).

Despite being relatively immature, iPSC-CMs expressing the *MYH6*-R443P allele showed morphological and physiological differences from WT. iPSC-CMs could be used for clinical applications such as pharmacological drug testing, but these applications require mature CMs. A number of strategies have been employed to promote the maturity of iPSC-CMs, including: the administration of biochemical agents [adrenergic receptor agonists, Triiodothyronine (Yang et al., 2014b; Jackman et al., 2018), insulin-like growth factor 1 or microRNA (mir1 or mir208)], altering substrate stiffness or utilizing molds for cell-patterning (Ribeiro et al., 2015, 2016, 2017; Carson et al., 2016; Jung et al., 2016), application of mechanical stimuli (Hirt et al., 2014), and co-culture with different cell types to mimic human tissue, including bioengineering of 3D tissue (Yang et al., 2014a; Ronaldson-Bouchard et al., 2018). iPSC-CM maturation can then be confirmed using a multiparametric quality assessment, including gene expression profiling and structural, electrophysiological, and contractile measurements (Sheehy et al., 2014).

We showed contractile and sarcomere organization differences between WT and *MYH6*-R443P iPSC-CMs, however, how the early stage CM-phenotype affects cardiac morphogenesis *in vivo* and how this phenotype progresses to adulthood is complex and not understood. To investigate this progression *in vivo* it may be beneficial to use an animal model in parallel with iPSC-CMs. While murine models have opposite chamber-specific expression of *Myh6* and *Myh7*, zebrafish may be a suitable alternative for studying *MYH6*-associated CHD despite having a two-chambered heart. Importantly, zebrafish chamber-specific MHC expression is the same as humans. The phenotype of weak atrium (*wea*) *myh6*-mutant zebrafish exhibits a hypoplastic ventricle (Berdougo et al., 2003).

Our study proposes a new potential mechanism for the development of HLHS related to *MYH6*-R443P: sarcomere disorganization likely causes decreased atrial contractility and results in hypoplastic left ventricular development. The failing structural and contractile changes of the atrial sarcomere may effect hemodynamic changes that prevent the development of a normal left ventricle and downstream structures including the mitral valve, the aortic valve and the aorta. In addition, postnatally, atrial dysfunction due to sarcomere disorganization in single ventricle patients may result in decreased atrial kick, which would be expected to lead to heart failure over time. Further studies are needed to test potential ways to correct these contractile changes. It is possible that drugs targeting contractility may be able to alleviate some of the contractile changes due to the *MYH6*-R443P variant. Ultimately, we may be able to alter the developmental pathways and minimize or prevent the development of *MYH6* variant associated HLHS.

## DATA AVAILABILITY STATEMENT

All datasets generated for this study are included in the article/**Supplementary Material**. Additional raw data will be made available by the authors, without undue reservation, to any qualified researcher.

## ETHICS STATEMENT

This study is in accordance with the principles outlined in the Declaration of Helsinki and institutionally approved research (IRB) protocols by the Children's Hospital of Wisconsin (CHW, Milwaukee, WI, United States). Subjects were consented through the CHD Tissue Bank (IRB #CHW 06/229, GC 300) and the Wisconsin Pediatric Cardiac Registry (IRB #CHW 09/91, GC 889), IRB-approved research databases housed at CHW prior to inclusion in the study. Both biorepositories provided all cardiac tissue as well as iPSCs, from patients and family members, with associated clinical outcome variables.

## AUTHOR CONTRIBUTIONS

AT-M and RF designed and directed the project. AT-M, RF, MEM, JWL, and AG were involved in planning and supervising the work. M-SK, RF, BF, JL, MC, MA, SS, LK, LT, and MM processed the experimental data, performed the analysis, and interpreted the data. M-SK took the lead in writing manuscript with support from AT-M, RF, BF, JL, LK, LT, MM, MA, and SS. All authors discussed the results and commented on the manuscript.

## FUNDING

This work was supported by Advancing a Healthier Wisconsin Endowment at the Medical College of Wisconsin Grant, Clinical and Translational Science Institute from the National Institutes of Health (NIH) CTSA award: UL1TR001436, Greater Milwaukee Foundation and the Little Hearts for Life Foundation, the Medical College of Wisconsin's Department of Surgery, and the Herma Heart Institute/Children's Research Institute.

## ACKNOWLEDGMENTS

We thank the families, physicians, and clinical care team of the Herma Heart Institute from CHW, Mary Krolikowski for tremendous IRB support, the outstanding cardiothoracic surgical team including M. E. Barnes, J. L. Dunham-Ingle, T. A. Fehrenbacher, M. R. Madrzak, L. E. May, D. Semerda, R. G. Smith, and the operating room staff for making this study possibly. We gratefully acknowledge M. Goetsch, H.-L. Liang, and L. Armitage for helpful support and the excellent technical assistance from the Children's Research Institute (CRI) Pathology Core. We also thank M. Gryzbowski for expertise that enabled use of CRISPR/Cas9 technique.

## SUPPLEMENTARY MATERIAL

The Supplementary Material for this article can be found online at: https://www.frontiersin.org/articles/10.3389/fcell.2020.00440/full#supplementary-material

## REFERENCES

Berdougo, E., Coleman, H., Lee, D. H., Stainier, D. Y., and Yelon, D. (2003). Mutation of weak atrium/atrial myosin heavy chain disrupts atrial function and influences ventricular morphogenesis in zebrafish. *Development* 130, 6121–6129. doi: 10.1242/dev.00838

Burggren, W., Khorrami, S., Pinder, A., and Sun, T. (2004). Body, eye, and chorioallantoic vessel growth are not dependent on cardiac output level in day 3-4 chicken embryos. *Am. J. Physiol. Regul. Integr. Comp. Physiol.* 287, R1399–R1406. doi: 10.1152/ajpregu.00086.2004

Carson, D., Hnilova, M., Yang, X., Nemeth, C. L., Tsui, J. H., Smith, A. S., et al. (2016). Nanotopography-induced structural anisotropy and sarcomere development in human cardiomyocytes derived from induced pluripotent stem cells. *ACS Appl. Mater. Interfaces* 8, 21923–21932. doi: 10.1021/acsami.5b11671

Cummins, P., and Lambert, S. J. (1986). Myosin transitions in the bovine and human heart. A developmental and anatomical study of heavy and light chain subunits in the atrium and ventricle. *Circ. Res.* 58, 846–858. doi: 10.1161/01.res.58.6.846

Dasgupta, C., Martinez, A. M., Zuppan, C. W., Shah, M. M., Bailey, L. L., and Fletcher, W. H. (2001). Identification of connexin43 (alpha1) gap junction gene mutations in patients with hypoplastic left heart syndrome by denaturing gradient gel electrophoresis (DGGE). *Mutat. Res.* 479, 173–186. doi: 10.1016/s0027-5107(01)00160-9

deAlmeida, A., McQuinn, T., and Sedmera, D. (2007). Increased ventricular preload is compensated by myocyte proliferation in normal and hypoplastic fetal chick left ventricle. *Circ. Res.* 100, 1363–1370. doi: 10.1161/01.RES.0000266606.88463.cb

Elliott, D. A., Kirk, E. P., Yeoh, T., Chandar, S., McKenzie, F., Taylor, P., et al. (2003). Cardiac homeobox gene NKX2-5 mutations and congenital heart disease: associations with atrial septal defect and hypoplastic left heart syndrome. *J. Am. Coll. Cardiol.* 41, 2072–2076.

Fishman, N. H., Hof, R. B., Rudolph, A. M., and Heymann, M. A. (1978). Models of congenital heart disease in fetal lambs. *Circulation* 58, 354–364. doi: 10.1161/01.cir.58.2.354

Fitts, R. H. (2008). The cross-bridge cycle and skeletal muscle fatigue. *J. Appl. Physiol.* 104, 551–558. doi: 10.1152/japplphysiol.01200.2007

Friedberg, M. K., Silverman, N. H., Moon-Grady, A. J., Tong, E., Nourse, J., Sorenson, B., et al. (2009). Prenatal detection of congenital heart disease. *J. Pediatr.* 155, 26–31, 31.e1. doi: 10.1016/j.jpeds.2009.01.050

Galindo, A., Nieto, O., Villagra, S., Graneras, A., Herraiz, I., and Mendoza, A. (2009). Hypoplastic left heart syndrome diagnosed in fetal life: associated findings, pregnancy outcome and results of palliative surgery. *Ultrasound Obstet. Gynecol.* 33, 560–566. doi: 10.1002/uog.6355

Garg, V., Muth, A. N., Ransom, J. F., Schluterman, M. K., Barnes, R., King, I. N., et al. (2005). Mutations in NOTCH1 cause aortic valve disease. *Nature* 437, 270–274. doi: 10.1038/nature03940

Glidewell, S. C., Miyamoto, S. D., Grossfeld, P. D., Clouthier, D. E., Coldren, C. D., Stearman, R. S., et al. (2015). Transcriptional impact of rare and private copy number variants in hypoplastic left heart syndrome. *Clin. Transl. Sci.* 8, 682–689. doi: 10.1111/cts.12340

Grossfeld, P. (2007). Hypoplastic left heart syndrome: new insights. *Circ. Res.* 100, 1246–1248. doi: 10.1161/01.RES.0000268192.20525.c2

Grossfeld, P., Ye, M., and Harvey, R. (2009). Hypoplastic left heart syndrome: new genetic insights. *J. Am. Coll. Cardiol.* 53, 1072–1074. doi: 10.1016/j.jacc.2008.12.024

Gruber, P. J., and Epstein, J. A. (2004). Development gone awry: congenital heart disease. *Circ. Res.* 94, 273–283. doi: 10.1161/01.RES.0000116144.43797.3B

Hierck, B. P., Van der Heiden, K., Poelma, C., Westerweel, J., and Poelmann, R. E. (2008). Fluid shear stress and inner curvature remodeling of the embryonic heart. Choosing the right lane! *ScientificWorldJournal* 8, 212–222. doi: 10.1100/tsw.2008.42

Hinton, R. B. Jr., Martin, L. J., Tabangin, M. E., Mazwi, M. L., Cripe, L. H., and Benson, D. W. (2007). Hypoplastic left heart syndrome is heritable. *J. Am. Coll. Cardiol.* 50, 1590–1595. doi: 10.1016/j.jacc.2007.07.021

Hinton, R. B., Martin, L. J., Rame-Gowda, S., Tabangin, M. E., Cripe, L. H., and Benson, D. W. (2009). Hypoplastic left heart syndrome links to chromosomes 10q and 6q and is genetically related to bicuspid aortic valve. *J. Am. Coll. Cardiol.* 53, 1065–1071. doi: 10.1016/j.jacc.2008.12.023

Hirt, M. N., Boeddinghaus, J., Mitchell, A., Schaaf, S., Bornchen, C., Muller, C., et al. (2014). Functional improvement and maturation of rat and human engineered heart tissue by chronic electrical stimulation. *J. Mol. Cell. Cardiol.* 74, 151–161. doi: 10.1016/j.yjmcc.2014.05.009

Hoog, T. G., Fredrickson, S. J., Hsu, C. W., Senger, S. M., Dickinson, M. E., and Udan, R. S. (2018). The effects of reduced hemodynamic loading on morphogenesis of the mouse embryonic heart. *Dev. Biol.* 442, 127–137. doi: 10.1016/j.ydbio.2018.07.007

Hove, J. R., Koster, R. W., Forouhar, A. S., Acevedo-Bolton, G., Fraser, S. E., and Gharib, M. (2003). Intracardiac fluid forces are an essential epigenetic factor for embryonic cardiogenesis. *Nature* 421, 172–177. doi: 10.1038/nature01282

Hrstka, S. C., Li, X., Nelson, T. J., and Wanek Program Genetics Pipeline Group (2017). NOTCH1-dependent nitric oxide signaling deficiency in hypoplastic left heart syndrome revealed through patient-specific phenotypes detected in bioengineered cardiogenesis. *Stem Cells* 35, 1106–1119. doi: 10.1002/stem.2582

Jackman, C., Li, H., and Bursac, N. (2018). Long-term contractile activity and thyroid hormone supplementation produce engineered rat myocardium with adult-like structure and function. *Acta Biomater.* 78, 98–110. doi: 10.1016/j.actbio.2018.08.003

Jung, G., Fajardo, G., Ribeiro, A. J., Kooiker, K. B., Coronado, M., Zhao, M., et al. (2016). Time-dependent evolution of functional vs. remodeling signaling in induced pluripotent stem cell-derived cardiomyocytes and induced maturation with biomechanical stimulation. *FASEB J.* 30, 1464–1479. doi: 10.1096/fj.15-280982

Kim, M. S., Horst, A., Blinka, S., Stamm, K., Mahnke, D., Schuman, J., et al. (2015). Activin-A and Bmp4 levels modulate cell type specification during CHIR-induced cardiomyogenesis. *PLoS One* 10:e0118670. doi: 10.1371/journal.pone.0118670

Laing, N. G., and Nowak, K. J. (2005). When contractile proteins go bad: the sarcomere and skeletal muscle disease. *Bioessays* 27, 809–822. doi: 10.1002/bies.20269

Lara, D. A., Ethen, M. K., Canfield, M. A., Nembhard, W. N., and Morris, S. A. (2017). A population-based analysis of mortality in patients with Turner syndrome and hypoplastic left heart syndrome using the Texas Birth Defects Registry. *Congenit. Heart Dis.* 12, 105–112. doi: 10.1111/chd.12413

Lee, J., Fei, P., Packard, R. R., Kang, H., Xu, H., Baek, K. I., et al. (2016). 4-Dimensional light-sheet microscopy to elucidate shear stress modulation of cardiac trabeculation. *J. Clin. Invest.* 126, 1679–1690. doi: 10.1172/JCI83496

Maddah, M., Heidmann, J. D., Mandegar, M. A., Walker, C. D., Bolouki, S., Conklin, B. R., et al. (2015). A non-invasive platform for functional characterization of stem-cell-derived cardiomyocytes with applications in cardiotoxicity testing. *Stem Cell Rep.* 4, 621–631. doi: 10.1016/j.stemcr.2015.02.007

Maddah, M., Shoukat-Mumtaz, U., Nassirpour, S., and Loewke, K. (2014). A system for automated, noninvasive, morphology-based evaluation of induced pluripotent stem cell cultures. *J. Lab. Autom.* 19, 454–460. doi: 10.1177/2211068214537258

Mai, C. T., Isenburg, J. L., Canfield, M. A., Meyer, R. E., Correa, A., Alverson, C. J., et al. (2019). National population-based estimates for major birth defects, 2010-2014. *Birth Defects Res.* 111, 1420–1435. doi: 10.1002/bdr2.1589

McBride, K. L., Riley, M. F., Zender, G. A., Fitzgerald-Butt, S. M., Towbin, J. A., Belmont, J. W., et al. (2008). NOTCH1 mutations in individuals with left ventricular outflow tract malformations reduce ligand-induced signaling. *Hum. Mol. Genet.* 17, 2886–2893. doi: 10.1093/hmg/ddn187

McCain, M. L., and Parker, K. K. (2011). Mechanotransduction: the role of mechanical stress, myocyte shape, and cytoskeletal architecture on cardiac function. *Pflugers Arch.* 462, 89–104. doi: 10.1007/s00424-011-0951-4

McCormick, M. E., and Tzima, E. (2016). Pulling on my heartstrings: mechanotransduction in cardiac development and function. *Curr. Opin. Hematol.* 23, 235–242. doi: 10.1097/MOH.0000000000000240

Mitzelfelt, K. A., McDermott-Roe, C., Grzybowski, M. N., Marquez, M., Kuo, C. T., Riedel, M., et al. (2017). Efficient precision genome editing in iPSCs via genetic co-targeting with selection. *Stem Cell Rep.* 8, 491–499. doi: 10.1016/j.stemcr.2017.01.021

Noonan, J. A., and Nadas, A. S. (1958). The hypoplastic left heart syndrome; an analysis of 101 cases. *Pediatr. Clin. North Am.* 5, 1029–1056.

Pillekamp, F., Haustein, M., Khalil, M., Emmelheinz, M., Nazzal, R., Adelmann, R., et al. (2012). Contractile properties of early human embryonic stem cell-derived cardiomyocytes: beta-adrenergic stimulation induces positive chronotropy and lusitropy but not inotropy. *Stem Cells Dev.* 21, 2111–2121. doi: 10.1089/scd.2011.0312

Redwood, C. S., Moolman-Smook, J. C., and Watkins, H. (1999). Properties of mutant contractile proteins that cause hypertrophic cardiomyopathy. *Cardiovasc. Res.* 44, 20–36. doi: 10.1016/s0008-6363(99)00213-8

Reiser, P. J., Portman, M. A., Ning, X. H., and Schomisch Moravec, C. (2001). Human cardiac myosin heavy chain isoforms in fetal and failing adult atria and ventricles. *Am. J. Physiol. Heart Circ. Physiol.* 280, H1814–H1820. doi: 10.1152/ajpheart.2001.280.4.H1814

Rentzsch, P., Witten, D., Cooper, G. M., Shendure, J., and Kircher, M. (2019). CADD: predicting the deleteriousness of variants throughout the human genome. *Nucleic Acids Res.* 47, D886–D894. doi: 10.1093/nar/gky1016

Ribeiro, A. J. S., Schwab, O., Mandegar, M. A., Ang, Y. S., Conklin, B. R., Srivastava, D., et al. (2017). Multi-imaging method to assay the contractile mechanical output of micropatterned human iPSC-Derived cardiac myocytes. *Circ. Res.* 120, 1572–1583. doi: 10.1161/CIRCRESAHA.116.310363

Ribeiro, A. J., Ang, Y. S., Fu, J. D., Rivas, R. N., Mohamed, T. M., Higgs, G. C., et al. (2015). Contractility of single cardiomyocytes differentiated from pluripotent stem cells depends on physiological shape and substrate stiffness. *Proc. Natl. Acad. Sci. U.S.A.* 112, 12705–12710. doi: 10.1073/pnas.1508073112

Ribeiro, A. J., Denisin, A. K., Wilson, R. E., and Pruitt, B. L. (2016). For whom the cells pull: Hydrogel and micropost devices for measuring traction forces. *Methods* 94, 51–64. doi: 10.1016/j.ymeth.2015.08.005

Richard, P., Charron, P., Carrier, L., Ledeuil, C., Cheav, T., Pichereau, C., et al. (2003). Hypertrophic cardiomyopathy: distribution of disease genes, spectrum of mutations, and implications for a molecular diagnosis strategy. *Circulation* 107, 2227–2232. doi: 10.1161/01.CIR.0000066323.15244.54

Ronaldson-Bouchard, K., Ma, S. P., Yeager, K., Chen, T., Song, L., Sirabella, D., et al. (2018). Advanced maturation of human cardiac tissue grown from pluripotent stem cells. *Nature* 556, 239–243. doi: 10.1038/s41586-018-0016-3

Santhanakrishnan, A., and Miller, L. A. (2011). Fluid dynamics of heart development. *Cell Biochem. Biophys.* 61, 1–22. doi: 10.1007/s12013-011-9158-8

Schluter, J. M., and Fitts, R. H. (1994). Shortening velocity and ATPase activity of rat skeletal muscle fibers: effects of endurance exercise training. *Am. J. Physiol.* 266(6 Pt 1), C1699–C1713. doi: 10.1152/ajpcell.1994.266.6.C1699

Seidman, J. G., and Seidman, C. (2001). The genetic basis for cardiomyopathy: from mutation identification to mechanistic paradigms. *Cell* 104, 557–567. doi: 10.1016/s0092-8674(01)00242-2

Sheehy, S. P., Pasqualini, F., Grosberg, A., Park, S. J., Aratyn-Schaus, Y., and Parker, K. K. (2014). Quality metrics for stem cell-derived cardiac myocytes. *Stem Cell Rep.* 2, 282–294. doi: 10.1016/j.stemcr.2014.01.015

Sundberg, C. W., Hunter, S. K., Trappe, S. W., Smith, C. S., and Fitts, R. H. (2018). Effects of elevated H(+) and Pi on the contractile mechanics of skeletal muscle fibres from young and old men: implications for muscle fatigue in humans. *J. Physiol.* 596, 3993–4015. doi: 10.1113/jp276018

Theis, J. L., Zimmermann, M. T., Evans, J. M., Eckloff, B. W., Wieben, E. D., Qureshi, M. Y., et al. (2015). Recessive MYH6 mutations in hypoplastic left heart with reduced ejection fraction. *Circ. Cardiovasc. Genet.* 8, 564–571. doi: 10.1161/CIRCGENETICS.115.001070

Tomita-Mitchell, A., Mahnke, D. K., Struble, C. A., Tuffnell, M. E., Stamm, K. D., Hidestrand, M., et al. (2012). Human gene copy number spectra analysis in congenital heart malformations. *Physiol. Genomics* 44, 518–541. doi: 10.1152/physiolgenomics.00013.2012

Tomita-Mitchell, A., Stamm, K. D., Mahnke, D. K., Kim, M. S., Hidestrand, P. M., Liang, H. L., et al. (2016). Impact of MYH6 variants in hypoplastic left heart syndrome. *Physiol. Genomics* 48, 912–921. doi: 10.1152/physiolgenomics.00091.2016

Wang, X., and Fitts, R. H. (2017). Ventricular action potential adaptation to regular exercise: role of beta-adrenergic and KATP channel function. *J. Appl. Physiol.* 123, 285–296. doi: 10.1152/japplphysiol.00197.2017

Wang, X., and Fitts, R. H. (2018). Effects of regular exercise on ventricular myocyte biomechanics and KATP channel function. *Am. J. Physiol. Heart Circ. Physiol.* 315, H885–H896. doi: 10.1152/ajpheart.00130.2018

Warburton, D., Ronemus, M., Kline, J., Jobanputra, V., Williams, I., Anyane-Yeboa, K., et al. (2014). The contribution of de novo and rare inherited copy number changes to congenital heart disease in an unselected sample of children with conotruncal defects or hypoplastic left heart disease. *Hum. Genet.* 133, 11–27. doi: 10.1007/s00439-013-1353-9

Weber, N., Schwanke, K., Greten, S., Wendland, M., Iorga, B., Fischer, M., et al. (2016). Stiff matrix induces switch to pure beta-cardiac myosin heavy chain expression in human ESC-derived cardiomyocytes. *Basic Res. Cardiol.* 111:68.

Wessels, A., Vermeulen, J. L., Viragh, S., and Moorman, A. F. (1990). The ontogenesis of myosin heavy chain isoforms in the developing human hearta. *Ann. N. Y. Acad. Sci.* 588, 461–464. doi: 10.1111/j.1749-6632.1990.tb13264.x

Wessels, A., Vermeulen, J. L., Viragh, S., Kalman, F., Lamers, W. H., and Moorman, A. F. (1991). Spatial distribution of "tissue-specific" antigens in the developing human heart and skeletal muscle. II. An immunohistochemical analysis of myosin heavy chain isoform expression patterns in the embryonic heart. *Anat. Rec.* 229, 355–368. doi: 10.1002/ar.1092290309

Yagi, H., Liu, X., Gabriel, G. C., Wu, Y., Peterson, K., Murray, S. A., et al. (2018). The genetic landscape of hypoplastic left heart syndrome. *Pediatr. Cardiol.* 39, 1069–1081. doi: 10.1007/s00246-018-1861-4

Yang, C., Xu, Y., Yu, M., Lee, D., Alharti, S., Hellen, N., et al. (2017). Induced pluripotent stem cell modelling of HLHS underlines the contribution of dysfunctional NOTCH signalling to impaired cardiogenesis. *Hum. Mol. Genet.* 26, 3031–3045. doi: 10.1093/hmg/ddx140

Yang, X., Pabon, L., and Murry, C. E. (2014a). Engineering adolescence: maturation of human pluripotent stem cell-derived cardiomyocytes. *Circ. Res.* 114, 511–523. doi: 10.1161/CIRCRESAHA.114.300558

Yang, X., Rodriguez, M., Pabon, L., Fischer, K. A., Reinecke, H., Regnier, M., et al. (2014b). Tri-iodo-l-thyronine promotes the maturation of human cardiomyocytes-derived from induced pluripotent stem cells. *J. Mol. Cell. Cardiol.* 72, 296–304. doi: 10.1016/j.yjmcc.2014.04.005

**Conflict of Interest:** AT-M and MEM are cofounders of TAI Diagnostics (Milwaukee, WI, United States), a biotechnology company involved in transplant diagnostics, and members of its scientific advisory board.

The remaining authors declare that the research was conducted in the absence of any commercial or financial relationships that could be construed as a potential conflict of interest.

frontiers
in Cell and Developmental Biology

ORIGINAL RESEARCH
published: 28 July 2020
doi: 10.3389/fcell.2020.00536

# Ultrarapid Delayed Rectifier $K^+$ Channelopathies in Human Induced Pluripotent Stem Cell-Derived Cardiomyocytes

***Sarah Hilderink*[1], *Harsha D. Devalla*[1], *Leontien Bosch*[1], *Ronald Wilders*[1]* and *Arie O. Verkerk*[1,2]**

*[1] Department of Medical Biology, Amsterdam UMC, University of Amsterdam, Amsterdam, Netherlands, [2] Department of Experimental Cardiology, Amsterdam UMC, University of Amsterdam, Amsterdam, Netherlands*

Atrial fibrillation (AF) is the most common cardiac arrhythmia. About 5–15% of AF patients have a mutation in a cardiac gene, including mutations in *KCNA5*, encoding the $K_V1.5$ α-subunit of the ion channel carrying the atrial-specific ultrarapid delayed rectifier $K^+$ current ($I_{Kur}$). Both loss-of-function and gain-of-function AF-related mutations in *KCNA5* are known, but their effects on action potentials (APs) of human cardiomyocytes have been poorly studied. Here, we assessed the effects of wild-type and mutant $I_{Kur}$ on APs of human induced pluripotent stem cell-derived cardiomyocytes (hiPSC-CMs). We found that atrial-like hiPSC-CMs, generated by a retinoic acid-based differentiation protocol, have APs with faster repolarization compared to ventricular-like hiPSC-CMs, resulting in shorter APs with a lower AP plateau. Native $I_{Kur}$, measured as current sensitive to 50 μM 4-aminopyridine, was 1.88 ± 0.49 (mean ± SEM, $n = 17$) and 0.26 ± 0.26 pA/pF ($n = 17$) in atrial- and ventricular-like hiPSC-CMs, respectively. In both atrial- and ventricular-like hiPSC-CMs, $I_{Kur}$ blockade had minimal effects on AP parameters. Next, we used dynamic clamp to inject various amounts of a virtual $I_{Kur}$, with characteristics as in freshly isolated human atrial myocytes, into 11 atrial-like and 10 ventricular-like hiPSC-CMs, in which native $I_{Kur}$ was blocked. Injection of $I_{Kur}$ with 100% density shortened the APs, with its effect being strongest on the AP duration at 20% repolarization ($APD_{20}$) of atrial-like hiPSC-CMs. At $I_{Kur}$ densities < 100% (compared to 100%), simulating loss-of-function mutations, significant AP prolongation and raise of plateau were observed. At $I_{Kur}$ densities > 100%, simulating gain-of-function mutations, $APD_{20}$ was decreased in both atrial- and ventricular-like hiPSC-CMs, but only upon a strong increase in $I_{Kur}$. In ventricular-like hiPSC-CMs, lowering of the plateau resulted in AP shortening. We conclude that a decrease in $I_{Kur}$, mimicking loss-of-function mutations, has a stronger effect on the AP of hiPSC-CMs than an increase, mimicking gain-of-function mutations, whereas in ventricular-like hiPSC-CMs such increase results in AP shortening, causing their AP morphology to become more atrial-like. Effects of native $I_{Kur}$ modulation on atrial-like hiPSC-CMs are less pronounced than effects of virtual $I_{Kur}$ injection because $I_{Kur}$ density of atrial-like hiPSC-CMs is substantially smaller than that of freshly isolated human atrial myocytes.

**Keywords: atrial fibrillation, cardiac differentiation, dynamic clamp, human pluripotent stem cells, ion channels, *KCNA5*, $K_V$1.5, ultrarapid delayed rectifier potassium current**

***Edited by:***
*Jong-Kook Lee,*
*Osaka University, Japan*

***Reviewed by:***
*Haibo Ni,*
*University of California, Davis,*
*United States*
*Andrea Barbuti,*
*University of Milan, Italy*

****Correspondence:***
*Ronald Wilders*
*r.wilders@amsterdamumc.nl*

***Specialty section:***
*This article was submitted to Stem Cell Research, a section of the journal Frontiers in Cell and Developmental Biology*

***Received:*** *31 March 2020*
***Accepted:*** *08 June 2020*
***Published:*** *28 July 2020*

***Citation:***
*Hilderink S, Devalla HD, Bosch L, Wilders R and Verkerk AO (2020) Ultrarapid Delayed Rectifier $K^+$ Channelopathies in Human Induced Pluripotent Stem Cell-Derived Cardiomyocytes. Front. Cell Dev. Biol. 8:536. doi: 10.3389/fcell.2020.00536*

## INTRODUCTION

Worldwide, the prevalence of atrial fibrillation (AF) is around 1–2% (Potpara and Lip, 2011). Mutations in cardiac genes account for onset of 5–15% of AF cases (Darbar et al., 2003; Potpara and Lip, 2011). Mutations in *KCNA5* are associated with AF, although rare (Feghaly et al., 2018). *KCNA5* encodes the pore-forming α-subunit $K_V1.5$ of the channel carrying the ultrarapid delayed rectifier $K^+$ current ($I_{Kur}$) (Fedida et al., 1993; Wang et al., 1993). In the human heart, $K_V1.5$ and the mRNA encoding $K_V1.5$ are both highly expressed in the atria (Ellinghaus et al., 2005; Gaborit et al., 2007), whereas expression of $K_V1.5$ is very low in both endocardial and epicardial ventricular tissue (Mays et al., 1995; Gaborit et al., 2007) and expression of mRNA encoding $K_V1.5$ is also low (Kääb et al., 1998; Gaborit et al., 2007). Accordingly, in their voltage clamp experiments on isolated human atrial and subepicardial ventricular myocytes, Amos et al. (1996) could not observe an $I_{Kur}$-like current in their ventricular myocytes, in contrast to their atrial myocytes. $I_{Kur}$ activates rapidly upon depolarizations to membrane potentials positive to −50 mV and is responsible for the early repolarization in human atrial action potentials (APs) (Wang et al., 1993; Amos et al., 1996; Wettwer et al., 2004; Li et al., 2008).

Both loss-of-function and gain-of-function mutations in *KCNA5* have been identified in patients with AF (Olson et al., 2006; Yang et al., 2009, 2010; Christophersen et al., 2013; Hayashi et al., 2015; Tian et al., 2015). Loss-of-function mutations in *KCNA5* are supposed to increase susceptibility to AF by prolonging the AP duration (APD) of atrial myocytes, which may eventually result in early afterdepolarizations (EADs) (Yang et al., 2009; Hayashi et al., 2015). Indeed, *in vitro* electrophysiological studies where $I_{Kur}$ was blocked, representing complete *KCNA5* loss-of-function mutations, resulted in prolonged APDs and presence of EADs (Olson et al., 2006). EADs as a consequence of prolonged APDs have also been observed in *in silico* studies on loss-of-function *KCNA5* mutations (Colman et al., 2017; Ni et al., 2017).

Gain-of-function mutations, on the other hand, are presumed to cause AF by shortening the effective refractory period (ERP) of the atrial AP, facilitating re-entry wavelets in the atria (Nattel, 2002; Christophersen et al., 2013). This hypothesis is supported by *in silico* studies, which demonstrated that increased $I_{Kur}$ density, representing gain-of-function mutations, resulted in a shortened APD and arrhythmogenesis in human atrial tissue (Colman et al., 2017; Ni et al., 2017).

Although the *in silico* studies are instrumental in determining the potential effect of both loss-of-function and gain-of-function mutations in *KCNA5*, detailed electrophysiological studies of the *KCNA5* mutations in human cardiomyocytes are limited. Human induced pluripotent stem cell cardiomyocytes (hiPSC-CMs) have become a highly suitable tool to study cardiac ion channelopathies and their electrophysiology (Zhang et al., 2011; Hoekstra et al., 2012; Verkerk et al., 2017). Over time, the technique of cardiomyocyte differentiation has advanced, facilitating the generation of distinct atrial- and ventricular-like hiPSC-CM populations (Zhang et al., 2011; Devalla et al., 2015; Devalla and Passier, 2018). In the present study, we employed dynamic clamp to investigate the effects of loss-of-function and gain-of-function mutations in *KCNA5* in both atrial- and ventricular-like hiPSC-CMs.

## MATERIALS AND METHODS

### hiPSC-CM Differentiation

hiPSC-CMs were generated from the control LUMC0099iCTRL04 hiPSC line, which was derived from human fibroblasts extracted through skin biopsies from of a Caucasian woman. The LUMC0099iCTRL04 line is registered in the Human Pluripotent Stem Cell Registry (Seltmann et al., 2016), which contains all details pertaining to its generation and characterization (hPSCreg, 2019). hiPSC clones showing stem cell morphology were characterized for pluripotency marker expression and differentiation potential to hiPSC-CMs in BPEL medium (Ng et al., 2008) containing activin-A, BMP4, and CHIR99021 (Devalla et al., 2016). After 3 days, this medium was replaced by BPEL medium containing XAV939 (Tocris Biosciences) for ventricular differentiation (Ng et al., 2008; Devalla et al., 2016). To differentiate hiPSC-CMs to atrial-like hiPSC-CMs, 1 μM all-trans retinoic acid (RA) was added (Devalla et al., 2015). Twenty days after differentiation, hiPSC-CMs were dissociated with TrypLE Select (Life Technologies), and plated at a low density ($\approx 7.5 \times 10^4$ cells) on Matrigel coated coverslips in BPEL medium (Devalla et al., 2016).

### Patch-Clamp Measurements

#### Data Acquisition

Electrophysiological recordings were performed 4–13 days post dissociation from spontaneously beating single hiPSC-CMs. RA-treated hiPSC-CMs displaying a short, pulse-like beating pattern and non-RA-treated hiPSC-CMs with a contraction-like beating pattern were selected for data acquisition. APs and $I_{Kur}$ were recorded at 36–37°C with the perforated patch-clamp technique using an Axopatch 200B amplifier (Molecular Devices, Sunnyvale, CA, United States). Data acquisition and analysis were performed with custom software. Signals were low-pass filtered with a cut-off frequency of 2 kHz and digitized at 40 and 5 kHz for AP and $I_{Kur}$ recordings, respectively. Cell membrane capacitance ($C_m$, in pF) was calculated by dividing the time constant of the decay of capacitive transient when hyperpolarized by 5 mV from −40 mV in voltage clamp by series resistance. $C_m$ of atrial- and ventricular-like hiPSC-CMs was 16.4 ± 2.3 pF (mean ± SEM, $n = 28$), and 19.2 ± 2.5 pF ($n = 27$), respectively ($t$-test, N.S.). Patch pipettes with a resistance of ≈2.0 MΩ were pulled from borosilicate glass (Harvard Apparatus) and filled with solution containing (in mM): 125 K-gluconate, 20 KCl, 5 NaCl, 0.44 Amphotericin-B, 10 HEPES; pH set to 7.2 (KOH). Cells were superfused with modified Tyrode's solution containing (in mM): 140 NaCl, 5.4 KCl, 1.8 $CaCl_2$, 1.0 $MgCl_2$, 5.5 D-glucose, 5 HEPES; pH set to 7.4 (NaOH). All potentials were corrected for the estimated liquid junction potential of −15 mV (Barry and Lynch, 1991).

## Action Potential Recordings

APs were elicited at 1 Hz by 3-ms, ≈1.2 × threshold current pulses through the patch pipette. The AP parameters analyzed were resting membrane potential (RMP, in mV), maximum upstroke velocity ($dV/dt_{max}$, in V/s), AP amplitude (APA, in mV), AP duration at 20, 50, and 90% repolarization ($APD_{20}$, $APD_{50}$, and $APD_{90}$, respectively, in ms), and AP plateau amplitude (APPlatA, in mV), derived from the membrane potential ($V_m$) at 50 ms after the time of $dV/dt_{max}$.

## Native $I_{Kur}$ Recordings

Native $I_{Kur}$ was activated by 200-ms voltage clamp steps from −50 to +50 mV. A 50-ms prepulse to 0 mV was applied to activate and inactivate remaining transient membrane currents. Series resistance was compensated by ≥ 80%. $I_{Kur}$ was measured as the current sensitive to 50 μM 4-aminopyridine (4-AP) (Wang et al., 1993; Caballero et al., 2010), and was normalized to $C_m$ to calculate current density (in pA/pF).

## Dynamic Clamp

Although inward rectifier $K^+$ current ($I_{K1}$) is not necessarily low in hiPSC-CMs (Horváth et al., 2018), hiPSC-CMs tend to lack $I_{K1}$, which is responsible for stabilizing the RMP of atrial and ventricular myocytes, and thus show spontaneous activity (Dhamoon and Jalife, 2005; Hoekstra et al., 2012; Verkerk et al., 2017). The RMP of our atrial- and ventricular-like hiPSC-CMs was stabilized and set at a regular hyperpolarized value using the dynamic clamp technique (Wilders, 2006). A virtual Kir2.1-based $I_{K1}$, with a standard peak current density of 2 pA/pF, was injected into the hiPSC-CMs and this $I_{K1}$ was computed in real time, based on the acquired $V_m$, following the approach of Meijer van Putten et al. (2015). Accordingly, the mathematical equation for $I_{K1}$ reads

$$I_{K1} = 0.12979 \times \left( \frac{V_m - E_K}{1.0 + e^{(0.093633 \times (V_m + 72))}} \right)$$

In this equation, in which the rectification properties of $I_{K1}$ are implemented through a Boltzmann equation, $I_{K1}$ is in pA/pF and $V_m$ is in mV. $E_K$ is the Nernst potential for potassium, which amounts to −86.9 mV in our experimental setting.

The effect of the injection of this virtual $I_{K1}$ is illustrated in **Figure 1**, which shows the APs of typical atrial-like and ventricular-like hiPSC-CMs in the absence and presence of this virtual $I_{K1}$ (top panels) and the associated injected current (bottom panels), which consists of this $I_{K1}$ and a short inward stimulus current. A virtual Kir2.1-based $I_{K1}$, characteristic for human ventricular myocytes (Wang et al., 1998), was used in both atrial- and ventricular-like hiPSC-CMs because a more 'atrial-like' $I_{K1}$ in hiPSC-CMs results in a substantial current during early repolarization due to its reduced rectification (Meijer van Putten et al., 2015; Verkerk et al., 2017; Fabbri et al., 2019), and we wanted to prevent a prominent overlap and potential interference of $I_{K1}$ and $I_{Kur}$ during the course of an action potential.

The dynamic clamp technique was also used to provide our atrial- and ventricular-like hiPSC-CMs with a virtual wild-type or mutant $I_{Kur}$, as illustrated in **Figure 2**. Like $I_{K1}$, $I_{Kur}$ was computed in real time, based on the acquired value of $V_m$. $I_{Kur}$ was formulated as detailed in Section "$I_{Kur}$ Equations" below. Virtual $I_{Kur}$ was injected into atrial- and ventricular-like hiPSC-CMs with a fully activated conductance of 12.5, 25, 50, and 75% of its wild-type value to mimic loss-of-function mutations, and 125, 150, 175, and 200% of its wild-type value to mimic gain-of-function mutations.

## $I_{Kur}$ Equations

To compute $I_{Kur}$ in our dynamic clamp system, $I_{Kur}$ equations of the comprehensive human atrial myocyte model by Maleckar et al. (2009) were used. These equations were also adopted by Grandi et al. (2011) in their human atrial action potential and $Ca^{2+}$ model and read:

$$I_{Kur} = g_{Kur} \times a_{ur} \times i_{ur} \times (V - E_K)$$

$$da_{ur}/dt = (a_{ur,\infty} - a_{ur}) / \tau_{aur}$$

$$di_{ur}/dt = (i_{ur,\infty} - i_{ur}) / \tau_{iur}$$

$$a_{ur,\infty} = \frac{1.0}{\left[1.0 + e^{-\left(V + \frac{6.0}{8.6}\right)}\right]}$$

$$i_{ur,\infty} = \frac{1.0}{\left[1.0 + e^{\left(V + \frac{7.5}{10.0}\right)}\right]}$$

$$\tau_{aur} = \frac{0.009}{\left[1.0 + e^{\left(V + \frac{5.0}{12.0}\right)}\right]} + 0.0005$$

$$\tau_{iur} = \frac{0.59}{\left[1.0 + e^{\left(V + \frac{60.0}{10.0}\right)}\right]} + 3.05$$

In these equations, the dimensionless Hodgkin and Huxley-type activation and inactivation gating variables, ranging between 0 and 1, are denoted by $a_{ur}$ and $i_{ur}$, respectively, whereas $I_{Kur}$ (in pA/pF), $g_{Kur}$ (in nS/pF), V (in mV), $E_K$ (in mV), and t (in s) denote the ultrarapid delayed rectifier outward $K^+$ current, its fully activated conductance, the membrane potential, the $K^+$ reversal potential, and the time, respectively. The steady-state values of $a_{ur}$ and $i_{ur}$ are denoted by $a_{ur,\infty}$ and $i_{ur,\infty}$, respectively, and the associated time constants by $\tau_{aur}$ (in s) and $\tau_{iur}$ (in s), respectively. As in the models by Maleckar et al. (2009) and Grandi et al. (2011), a default value of 0.045 nS/pF was used for $g_{Kur}$. Of note, Maleckar et al. (2009) based this value on experimental data on $I_{Kur}$ density in human atrial myocytes.

# Statistical Analysis

Data are presented as mean ± SEM. Statistical analysis was carried out with SigmaStat 3.5 software (Systat Software, Inc., San Jose, CA, United States). Native $I_{Kur}$ density of atrial- and ventricular-like hiPSC-CMs was compared with an independent samples *t*-test. Two-way repeated measures ANOVA followed by the Student–Newman–Keuls *post hoc* test was used for

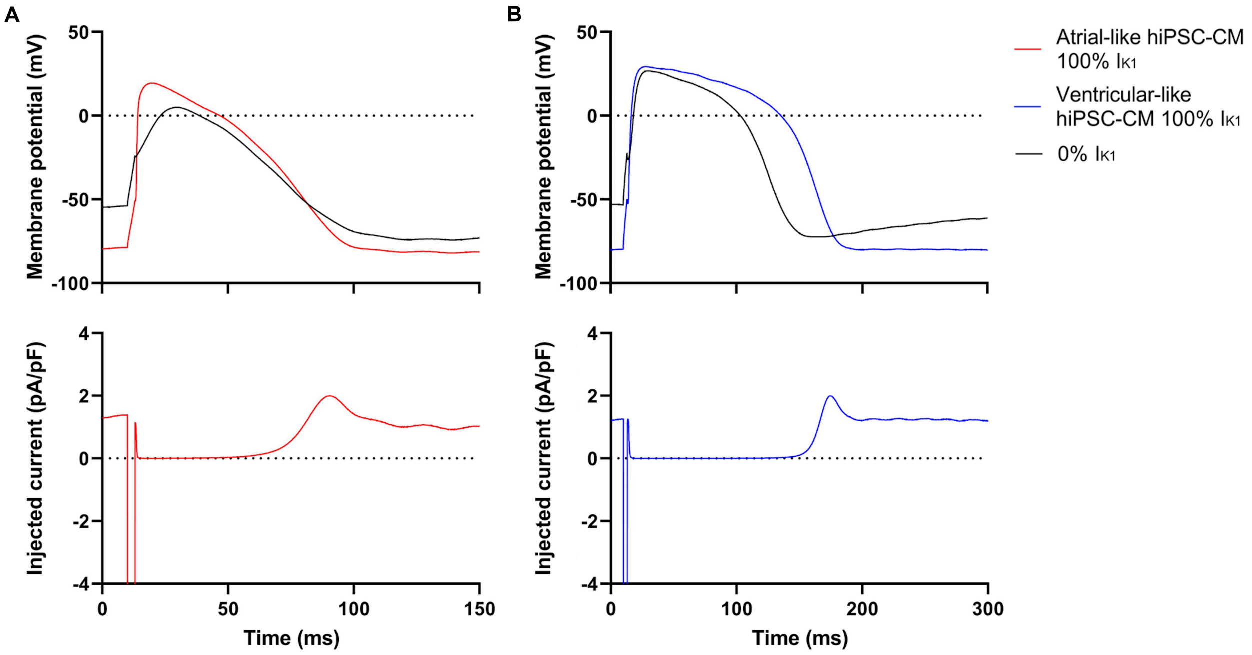

**FIGURE 1 |** Typical action potentials (APs) of atrial- and ventricular-like hiPSC-CM with and without $I_{K1}$ injection. **(A)** Superimposed APs (top panel) of an atrial-like hiPSC-CM in absence (black line) and presence (red line) of 100% virtual $I_{K1}$ injected through dynamic clamp and associated injected current (bottom panel) consisting of stimulus current and 0% or 100% virtual $I_{K1}$. **(B)** Superimposed APs and associated injected current of a ventricular-like hiPSC-CM. APs elicited at 1 Hz by a 3-ms stimulus of 100 pA. Note difference in time scale between panels **(A,B)**.

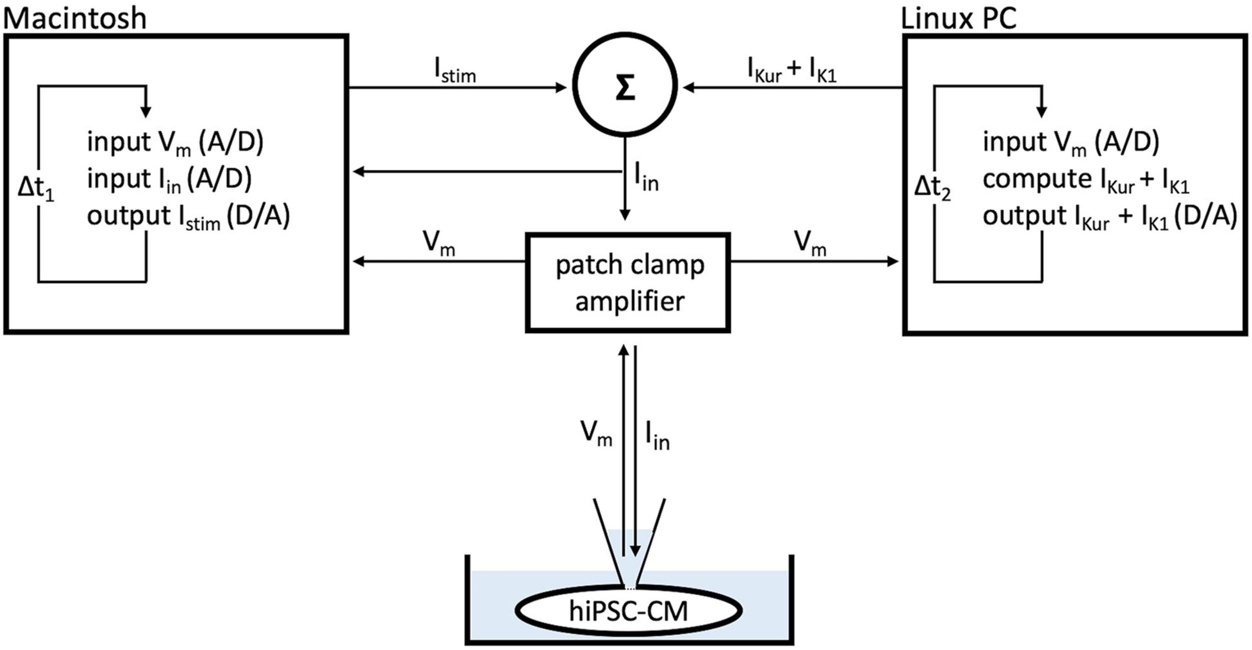

**FIGURE 2 |** Dynamic clamp setup. Ultrarapid delayed rectifier $K^+$ current ($I_{Kur}$) and inward rectifier potassium current ($I_{K1}$) were computed in real time on a PC running the Linux operating system and Real-Time Experiment Interface (RTXI) software (Patel et al., 2017), based on the acquired membrane potential ($V_m$) of the human induced pluripotent stem cell-derived cardiomyocyte (hiPSC-CM). Data were recorded on an Apple Macintosh computer using custom software to visualize and control the experiment. The sum of the stimulus current ($I_{stim}$), $I_{K1}$, and $I_{Kur}$ resulted in the current that was injected into the hiPSC-CM ($I_{in}$). Sample rates were 30 kHz ($\Delta t_1$ = 33.33 μs) and 20 kHz ($\Delta t_2$ = 50 μs).

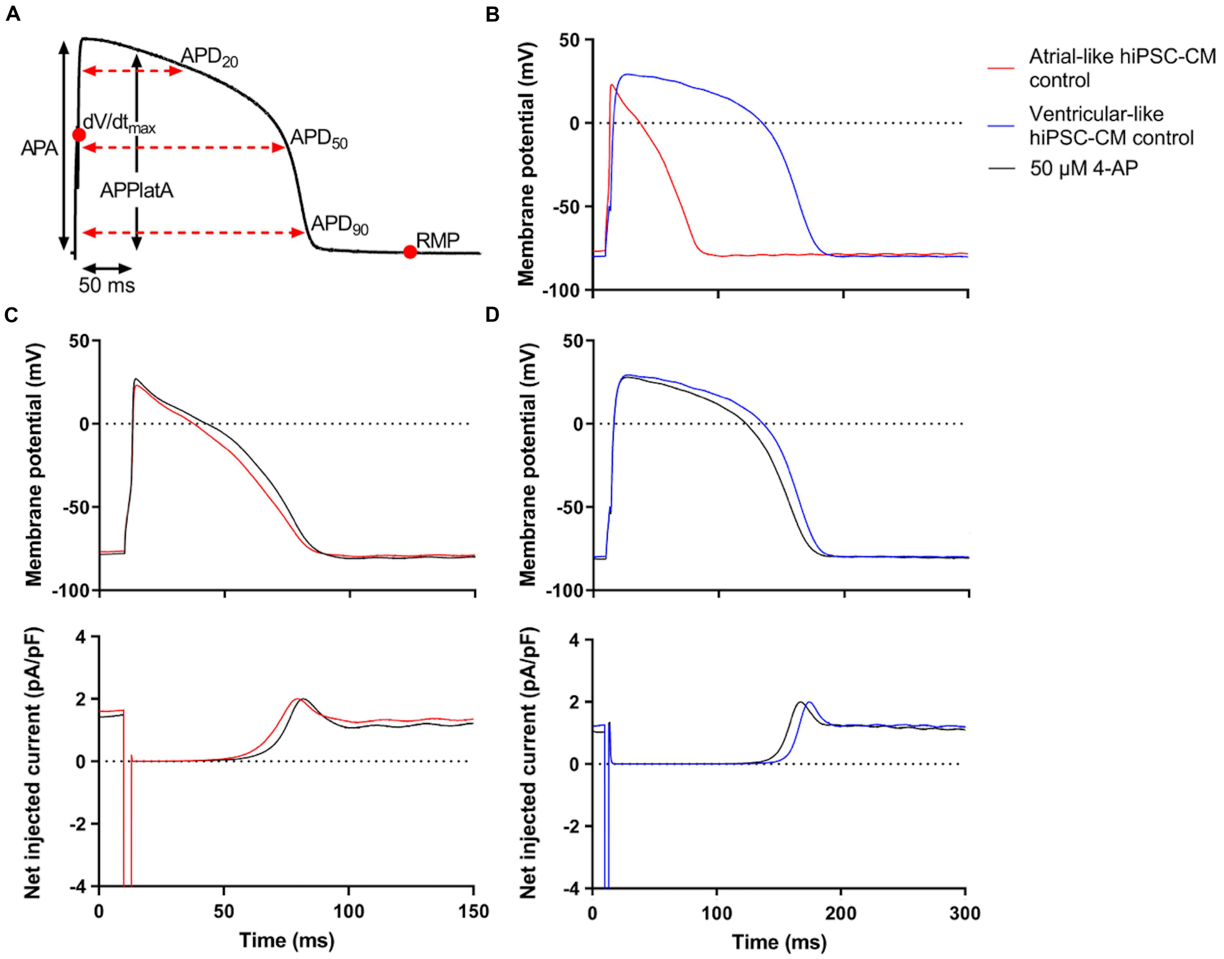

**FIGURE 3 |** Control atrial- and ventricular-like hiPSC-CM APs. **(A)** AP parameters used for analysis: resting membrane potential (RMP), maximum upstroke velocity ($dV/dt_{max}$), AP amplitude (APA), AP duration at 20, 50, and 90% repolarization ($APD_{20}$, $APD_{50}$, and $APD_{90}$, respectively), and AP plateau amplitude at 50 ms after reaching $dV/dt_{max}$ (APPlatA). **(B)** Superimposed typical APs of an atrial-like hiPSC-CM (red line) and a ventricular-like hiPSC-CM (blue line). **(C)** Superimposed APs (top panel) and associated net current consisting of stimulus current and virtual $I_{K1}$ injected through dynamic clamp (bottom panel) of an atrial-like hiPSC-CM in absence (red line) and presence of 50 μM 4-aminopyridine (4-AP) (black line). **(D)** Superimposed APs (top panel) and associated net injected current (bottom panel) of a ventricular-like hiPSC-CM. APs elicited at 1 Hz by a 3-ms stimulus of 100 pA. Note difference in time scale between panels **(C,D)**.

comparing AP parameters of atrial- and ventricular-like hiPSC-CMs in absence or presence of 4-AP. One-way repeated measures ANOVA followed by the Student–Newman–Keuls *post hoc* test was used for comparing the effect of injecting virtual $I_{Kur}$ at various densities into atrial- and ventricular-like hiPSC-CMs. $P < 0.05$ was considered statistically significant.

# RESULTS

## Atrial- and Ventricular-Like hiPSC-CM APs

APs were recorded from single atrial- and ventricular-like hiPSC-CMs that showed spontaneous beating upon visual inspection, clearly indicating a healthy and myocardial status. APs were elicited at 1 Hz and virtual $I_{K1}$ was injected into the cells, based on the approach of Meijer van Putten et al. (2015), to stabilize the RMP and set it at a regular hyperpolarized value. **Figure 3B** shows typical atrial- and ventricular-like hiPSC-CM APs. AP parameters, as illustrated in **Figure 3A**, are summarized in **Table 1**. Atrial-like hiPSC-CMs repolarize faster than ventricular-like APs, resulting in a significantly shorter $APD_{20}$, $APD_{50}$, and $APD_{90}$. The ventricular-like APs have a prominent plateau phase at relatively positive potentials, in contrast with the atrial-like hiPSC-CMs that show a less prominent plateau phase at less positive potentials, if any plateau at all. Consequently, APPlatA was significantly smaller in atrial-like hiPSC-CMs and thus appeared a strong tool to distinguish between atrial-like and ventricular-like hiPSC-CMs. APA and $dV/dt_{max}$ did not differ between the atrial- and ventricular-like hiPSC-CMs, but RMP was less negative in ventricular-like hiPSC-CMs.

Next, the cells were superfused with 50 μM 4-AP to block intrinsic $I_{Kur}$. **Figures 3C,D**, top panels, show typical atrial- and ventricular-like hiPSC-CMs in absence (red and blue lines,

**TABLE 1 |** AP parameters of atrial- and ventricular-like hiPSC-CMs in absence and presence of 4-AP.

| | Atrial-like hiPSC-CMs (*n* = 11) | | Ventricular-like hiPSC-CMs (*n* = 10) | |
|---|---|---|---|---|
| | **Baseline** | **4-AP** | **Baseline** | **4-AP** |
| RMP (mV) | −81.31 ± 0.43 | −80.83 ± 0.65 | −75.52 ± 1.69$^{*}$ | −74.92 ± 1.71$^{\#}$ |
| $dV/dt_{max}$ (V/s) | 74.54 ± 13.10 | 76.47 ± 13.41 | 83.70 ± 20.21 | 94.33 ± 24.43 |
| APA (mV) | 96.61 ± 2.66 | 98.33 ± 1.44 | 105.61 ± 3.69 | 104.59 ± 3.88 |
| $APD_{20}$ (ms) | 35.86 ± 4.35 | 38.13 ± 4.69 | 77.73 ± 11.59$^{*}$ | 68.68 ± 10.67$^{\ddagger\#}$ |
| $APD_{50}$ (ms) | 60.99 ± 5.55 | 65.05 ± 5.38 | 127.93 ± 19.67$^{*}$ | 119.41 ± 18.09$^{\ddagger\#}$ |
| $APD_{90}$ (ms) | 81.27 ± 6.37 | 86.76 ± 5.92$^{\dagger}$ | 155.01 ± 21.49$^{*}$ | 147.68 ± 20.38$^{\ddagger\#}$ |
| APPlatA (mV) | 53.61 ± 5.25 | 60.53 ± 4.53$^{\dagger}$ | 89.61 ± 4.51$^{*}$ | 89.42 ± 4.30$^{\#}$ |

*Data are AP parameters (mean ± SEM) of APs elicited at 1 Hz in absence (baseline) and presence of 50 μM 4-aminopyridine (4-AP).* $^{*}$*$P < 0.05$ atrial- vs. ventricular-like hiPSC-CMs (baseline);* $^{\dagger}$*$P < 0.05$ 4-AP vs. baseline of atrial-like hiPSC-CMs;* $^{\ddagger}$*$P < 0.05$ 4-AP vs. baseline of ventricular-like hiPSC-CMs;* $^{\#}$*$P < 0.05$ atrial- vs. ventricular-like hiPSC-CMs (4-AP).*

respectively) and presence of 4-AP (black lines). The associated injected currents, which each consist of $I_{K1}$ and the 3-ms stimulus current applied at 10 ms, are displayed in the bottom panels of **Figures 3C,D**. In atrial-like hiPSC-CMs, $I_{Kur}$ blockade resulted in a significantly increased $APD_{90}$ and APPlatA, while other AP parameters were unaffected (**Table 1**). In contrast, in ventricular-like hiPSC-CMs, $APD_{20}$, $APD_{50}$ and $APD_{90}$ were significantly decreased upon $I_{Kur}$ blockade (**Table 1**). The small AP shortening likely results from a time effect rather than a drug effect because $I_{Kur}$ is virtually absent in our ventricular-like hiPSC-CMs. Comparing atrial- with ventricular-like APs during $I_{Kur}$ blockade, most AP parameters still differ significantly, except APA and $dV/dt_{max}$.

## Native $I_{Kur}$

Native $I_{Kur}$ density in atrial- and ventricular-like hiPSC-CMs was quantified during 200-ms depolarizing voltage clamp steps as the current sensitive to 50 μM 4-AP. **Figure 4A** shows typical examples in an atrial-like (red trace) and a ventricular-like hiPSC-CM (blue trace). On average, $I_{Kur}$ density in atrial-like hiPSC-CMs was significantly larger than in ventricular-like hiPSC-CMs, with densities of 1.88 ± 0.49 ($n = 17$) and 0.26 ± 0.26 ($n = 17$) pA/pF, respectively (**Figure 4B**).

If the voltage clamp protocol of **Figure 4A** is repeated in computer simulations with the Maleckar et al. (2009) human atrial myocyte model (Wilders, 2018), an $I_{Kur}$ density of 5.45 pA/pF is obtained. We regard the latter as a realistic value for human atrial myocytes since Maleckar et al. (2009) based the characteristics of their model $I_{Kur}$ on experimental data on $I_{Kur}$ from isolated human atrial myocytes.

## Effects of Baseline Virtual $I_{Kur}$ on APs of Atrial- and Ventricular-Like hiPSC-CMs

Next, we studied the effects of a virtual $I_{Kur}$ on APs of atrial and ventricular-like hiPSC-CMs using dynamic clamp. In the human heart, $I_{Kur}$ is highly atrial-specific (Ellinghaus et al., 2005; Gaborit et al., 2007). However, the dynamic clamp technique allowed us to inject a virtual $I_{Kur}$ in both atrial- and ventricular-like hiPSC-CMs and thus assess to which extent this made their action potential morphology become similar. In either case, 4-AP (50 μM) was present to ensure that any native $I_{Kur}$ was blocked (Wang et al., 1993) and from here on we name this condition 0% $I_{Kur}$. First, we injected a virtual $I_{Kur}$ as implemented in the Maleckar et al. (2009) human atrial myocyte model, i.e., with the aforementioned 5.45 pA/pF density at +50 mV, which we here consider as 100% density.

**Figures 5A,B**, top panels, show typical examples of APs recorded from atrial- and ventricular-like hiPSC-CM at 0% (red and blue lines, respectively) and 100% $I_{Kur}$ (black lines). The injected current, which now consists of $I_{K1}$, 0% or 100% $I_{Kur}$, and a short stimulus current, is shown in the middle panels of **Figures 5A,B**. The average effects on the AP parameters of 11 atrial- and 10 ventricular-like hiPSC-CMs appear as the bars at 0% and 100% $I_{Kur}$ in **Figures 6A–H**, **7A–F**, in which each of the AP parameters is expressed as a percentage of its value obtained at 100% $I_{Kur}$. Injection of $I_{Kur}$ shortened the AP of both atrial- and ventricular-like hiPSC-CMs, while the AP plateau was suppressed (**Figures 5**, **6**). $dV/dt_{max}$ was unaltered in both atrial- and ventricular-like hiPSC-CMs, but in atrial-like hiPSC-CMs RMP was significantly more negative and APA significantly larger in absence than in presence of $I_{Kur}$ (**Figure 7**). The small 1.2% difference in RMP, equivalent to a 1.0-mV hyperpolarization, is likely a false positive because injection of various amounts of $I_{Kur}$ did not affect the RMP in either atrial-like or ventricular-like hiPSC-CMs (see below).

The phase plane plots of **Figures 5C,D** show the injected currents of the middle panels of **Figures 5A,B** plotted against the associated membrane potentials of the APs shown in the top panels of **Figures 5A,B**. The start and the end of the negative depolarizing current that flows during the stimulus are indicated by downward and upward vertical arrows, respectively. The black loops of the phase plane plots clearly show that $I_{Kur}$ is a repolarizing current that is already activated during the 3-ms stimulus and stays active until repolarization reaches −40 to −50 mV and the black traces 'fuse' with the red and blue traces of the action potentials without $I_{Kur}$ (horizontal arrows). At these negative potentials, $I_{Kur}$ becomes small because of both deactivation—rather than inactivation, which is much slower—and diminishing driving forces. The maximum $I_{Kur}$ during the atrial-like AP is slightly larger compared to the ventricular-like AP because in this particular example the atrial-like AP reaches a higher peak than the ventricular-like AP, which results in a larger driving force for $I_{Kur}$.

## Effects of $I_{Kur}$ Loss-of-Function Mutations in Atrial- and Ventricular-Like hiPSC-CMs

Next, we studied the effects of loss-of-function mutations in *KCNA5*, resulting in a decrease in $I_{Kur}$. Therefore, we decreased the fully activated conductance of the virtual $I_{Kur}$ conductance to 75, 50, 25, and 12.5% of its control value. **Figure 8** shows typical examples of the effects on the APs of atrial- and ventricular-like hiPSC-CMs. The average changes

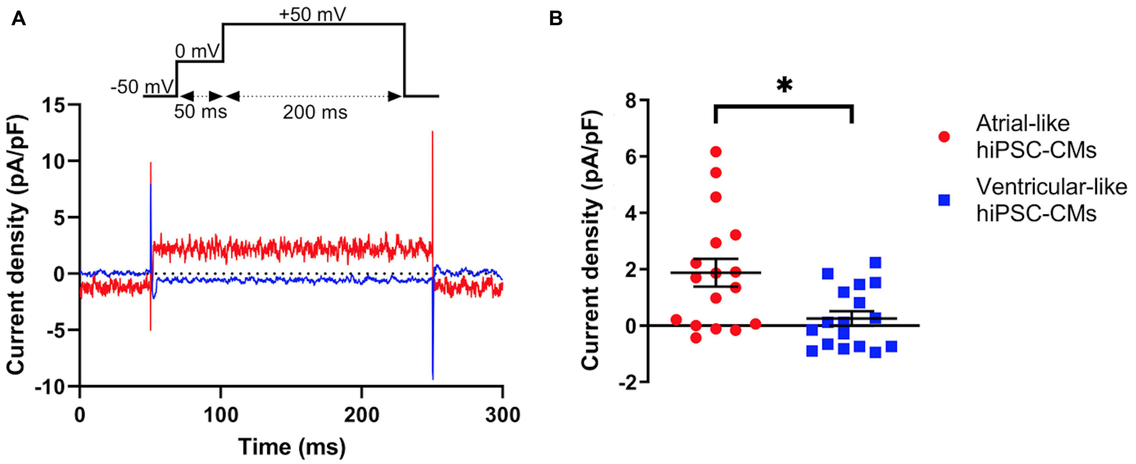

**FIGURE 4 |** Density of $I_{Kur}$ measured as 50 μM 4-AP-sensitive current. **(A)** Typical 4-AP-sensitive currents in an atrial- and a ventricular-like hiPSC-CM (red and blue traces, respectively) upon 200-ms depolarizing voltage clamp steps to +50 mV from a holding potential of −50 mV. **(B)** $I_{Kur}$ density in 17 atrial- and 17 ventricular-like hiPSC-CMs. $^{*}P < 0.05$.

in AP parameters are shown in **Figures 6**, **7**. In both atrial- and ventricular-like hiPSC-CMs, APD$_{20}$, APD$_{50}$, and APD$_{90}$ significantly increased upon a reduction in $I_{Kur}$ (**Figures 6A–F**). However, while the increase in APD$_{90}$ in atrial-like APs is only present upon severe $I_{Kur}$ reduction, APD$_{90}$ prolongation in ventricular-like APs is already present at a mild reduction (**Figures 6E,F**). APPlatA was significantly increased in both atrial- and ventricular-like APs (**Figures 6G,H**). RMP and dV/dt$_{max}$ were unaffected (**Figures 7A–D**), whereas a slight increase in APA was observed, but only in atrial-like hiPSC-CMs at severe reductions of $I_{Kur}$ (**Figures 7E,F**).

## Effects of $I_{Kur}$ Gain-of-Function Mutations in Atrial- and Ventricular-Like hiPSC-CMs

Finally, we studied the effects of gain-of-function mutations in *KCNA5*, resulting in an increase in $I_{Kur}$. Therefore, we increased the fully activated conductance of the virtual $I_{Kur}$ conductance to 125, 150, 175, and 200% of its control value. **Figure 9** shows typical examples of the effects on the APs of atrial- and ventricular-like hiPSC-CMs. The average changes in AP parameters are shown in **Figures 6**, **7**. In both atrial- and ventricular-like hiPSC-CMs, APD$_{20}$ and APD$_{50}$ significantly shortened, but only when $I_{Kur}$ was strongly increased (**Figures 6A–D**). APD$_{90}$ was significantly reduced in ventricular-like, but not in atrial-like hiPSC-CMs (**Figures 6E,F**). APPlatA only showed a significant decrease in ventricular-like hiPSC-CMs (**Figures 6G,H**). Other AP parameters were unaffected upon increases in $I_{Kur}$ (**Figure 7**).

# DISCUSSION

Overall, the APs of our atrial-like hiPSC-CMs were substantially shorter and had a lower AP plateau than those of our ventricular-like hiPSC-CMs, in qualitative agreement with previous studies on atrial- and ventricular-like hiPSC-CMs (Marczenke et al., 2017; Verkerk et al., 2017; Argenziano et al., 2018; Cyganek et al., 2018; Lemme et al., 2018; Veerman et al., 2019). There are some quantitative differences in AP parameters with previous studies, but these are likely due to differences in cell lines, differences in differentiation protocols, absence or presence of $I_{K1}$ injection, and a different definition of AP plateau amplitude. The differences in AP parameters of our atrial- and ventricular-like hiPSC-CMs would have been even larger if we had supplied our atrial-like hiPSC-CMs with a more atrial-specific $I_{K1}$, as not only observed in human heart (Wang et al., 1998), but also in canine, murine and sheep heart (Dhamoon et al., 2004; Panama et al., 2007; Cordeiro et al., 2015). Of note, Fabbri et al. (2019) recently published a detailed *in silico* study of the effects of several $I_{K1}$ formulations on AP duration of hiPSC-CMs.

Maximum sustained native $I_{Kur}$ density was larger in our atrial-like hiPSC-CMs than in our ventricular-like hiPSC-CMs. Yet, with a value of 1.88 ± 0.49 pA/pF at +50 mV, the $I_{Kur}$ density of our atrial-like hiPSC-CMs was small in comparison with that of freshly isolated human atrial myocytes, for which Amos et al. (1996) observed a density of 5.1 ± 0.3 pA/pF for peak $I_{Kur}$ and 4.7 ± 0.2 pA/pF for late $I_{Kur}$ during a 300-ms voltage clamp step to +40 mV at 22°C (114 cells, 32 hearts). Therefore, we decided to block native $I_{Kur}$ and use dynamic clamp to study the effects of $I_{Kur}$, using a virtual $I_{Kur}$ with characteristics, including its density, based on observations made in freshly isolated human atrial myocytes.

Due to the relatively low native $I_{Kur}$ density of our atrial- and ventricular-like hiPSC-CMs, it was not surprising that blockade of $I_{Kur}$ by 4-AP had only minor effects on AP parameters. When native $I_{Kur}$ was replaced with virtual $I_{Kur}$ with 100% density, similar to $I_{Kur}$ density in freshly isolated human atrial myocytes, more pronounced effects on AP parameters were observed. In atrial-like hiPSC-CMs, APD$_{20}$ shortened substantially, whereas APD$_{50}$ shortened only moderately and APD$_{90}$ even less so. In ventricular-like hiPSC-CMs, on the other hand, not only

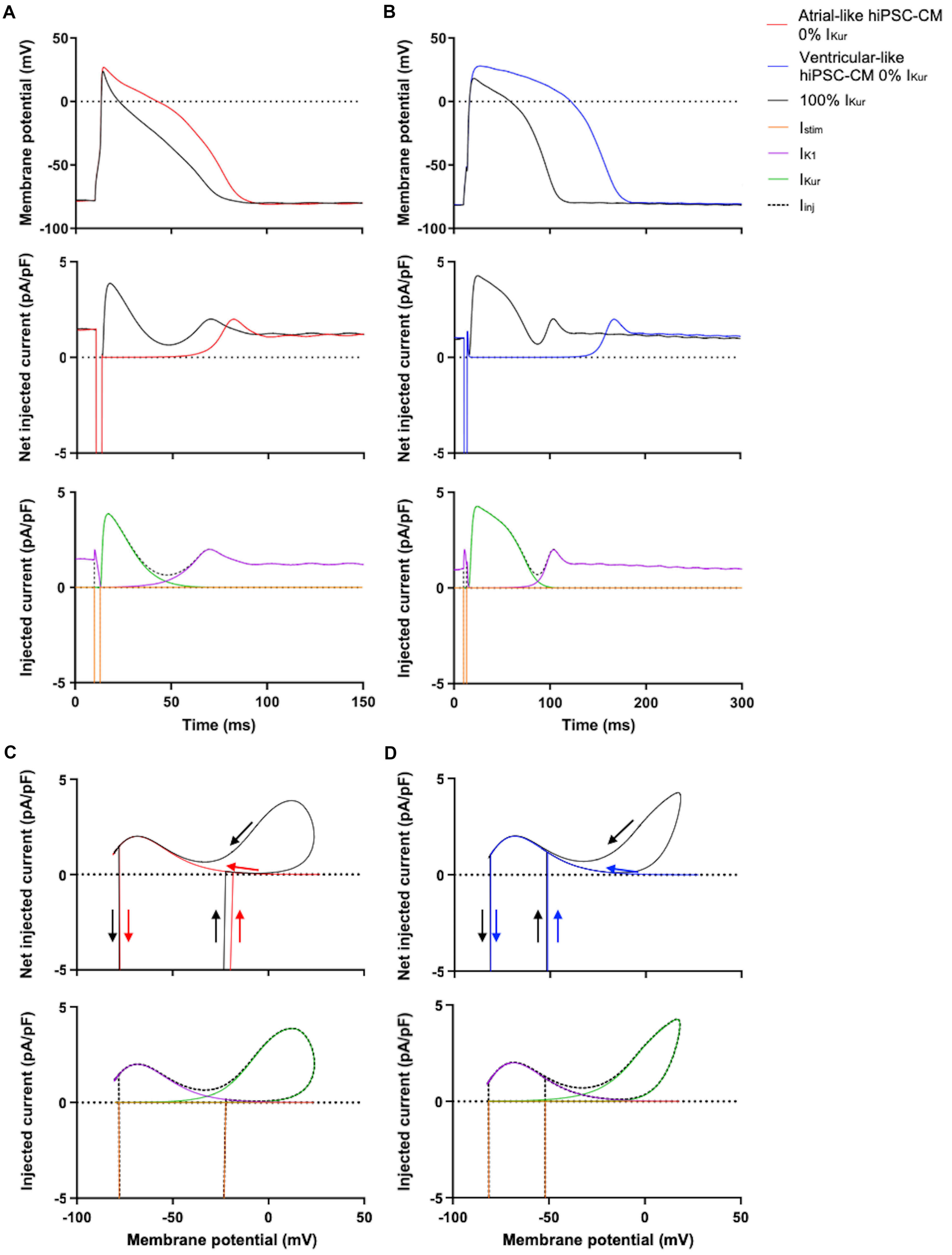

**FIGURE 5 |** Effect of injection of 100% virtual $I_{Kur}$ through dynamic clamp on APs of atrial- and ventricular-like hiPSC-CMs. **(A)** Superimposed APs (top panel) of an atrial-like hiPSC-CM at 0% (red line) and 100% virtual $I_{Kur}$ (black line) and associated net injected current (middle panel), consisting of $I_{K1}$, 0% or 100% $I_{Kur}$, and a short stimulus current, as shown in the bottom panel in case of 100% $I_{Kur}$. **(B)** Superimposed APs (top panel), associated net injected current (middle panel), and its individual components in case of 100% $I_{Kur}$ (bottom panel) of a ventricular-like hiPSC-CM. **(C,D)** Phase plane plots (top panel) of the action potentials and injected currents of panels **(A,B)** with their individual components in case of 100% $I_{Kur}$ (bottom panel). APs elicited at 1 Hz by a 3-ms stimulus of 100 pA. Note difference in time scale between panels **(A,B)**.

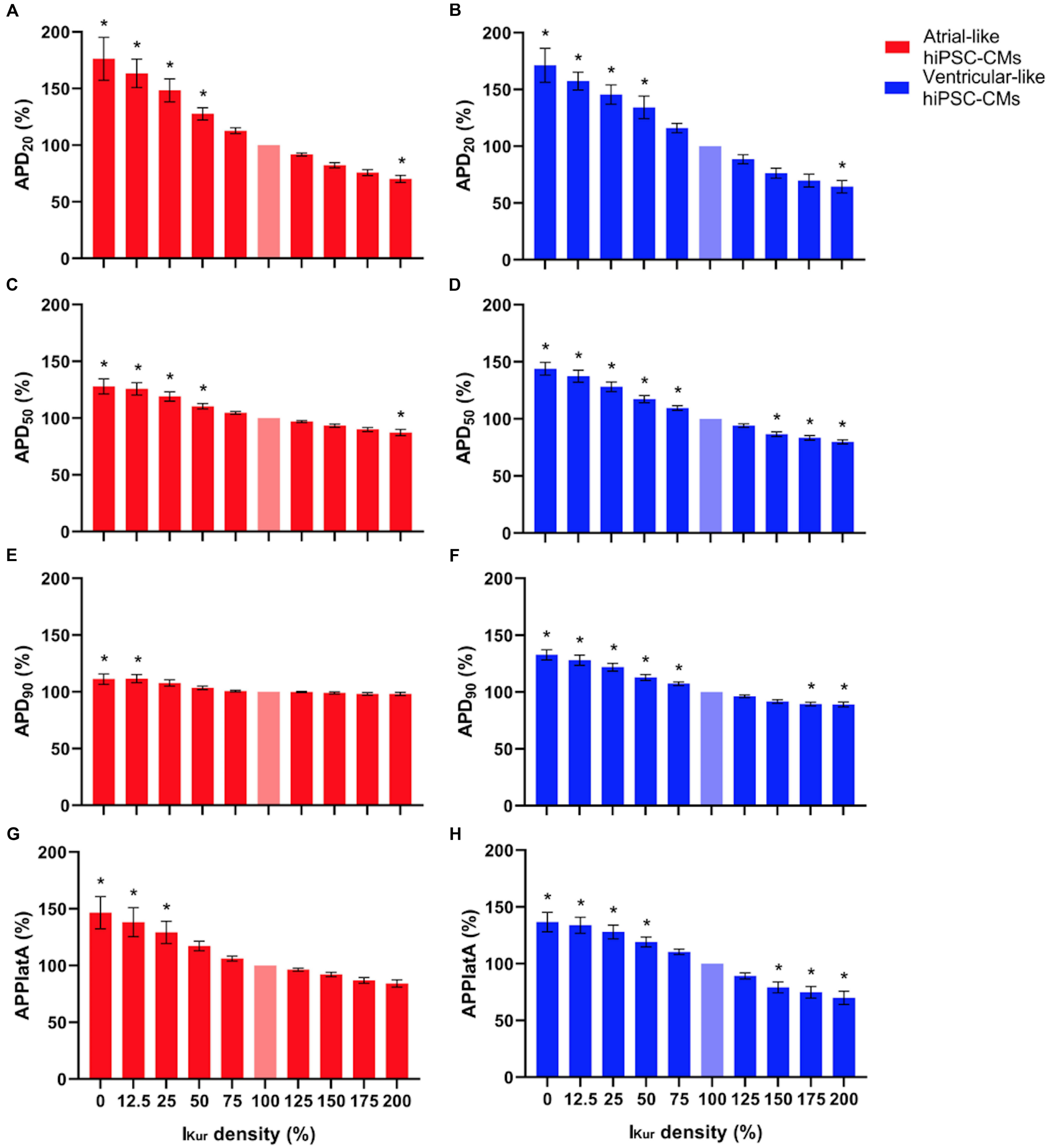

**FIGURE 6 | (A,B)** $APD_{20}$, **(C,D)** $APD_{50}$, **(E,F)** $APD_{90}$, and **(G,H)** APPlatA of atrial- and ventricular-like hiPSC-CMs (left and right panels, respectively) at virtual $I_{Kur}$ densities ranging from 0 to 200%. AP parameters are expressed as percentage relative to their value at 100% $I_{Kur}$ density (bleached bars). Data from 11 atrial- and 10 ventricular-like hiPSC-CMs. *$P < 0.05$.

$APD_{20}$, but also $APD_{50}$ and $APD_{90}$ shortened substantially upon injection of virtual $I_{Kur}$. The more pronounced effect on APD in ventricular-like hiPSC-CMs is likely related to the longer and more positive AP plateau potentials leading to more functional consequences of $I_{Kur}$. The observed decrease in $APD_{20}$ was accompanied by a lowering of the AP plateau in both atrial- and ventricular-like hiPSC-CMs.

We only performed experiments at a pacing rate of 1 Hz and not at higher pacing rates. Therefore, we were unable to confirm that the relative contribution of $I_{Kur}$ to AP repolarization

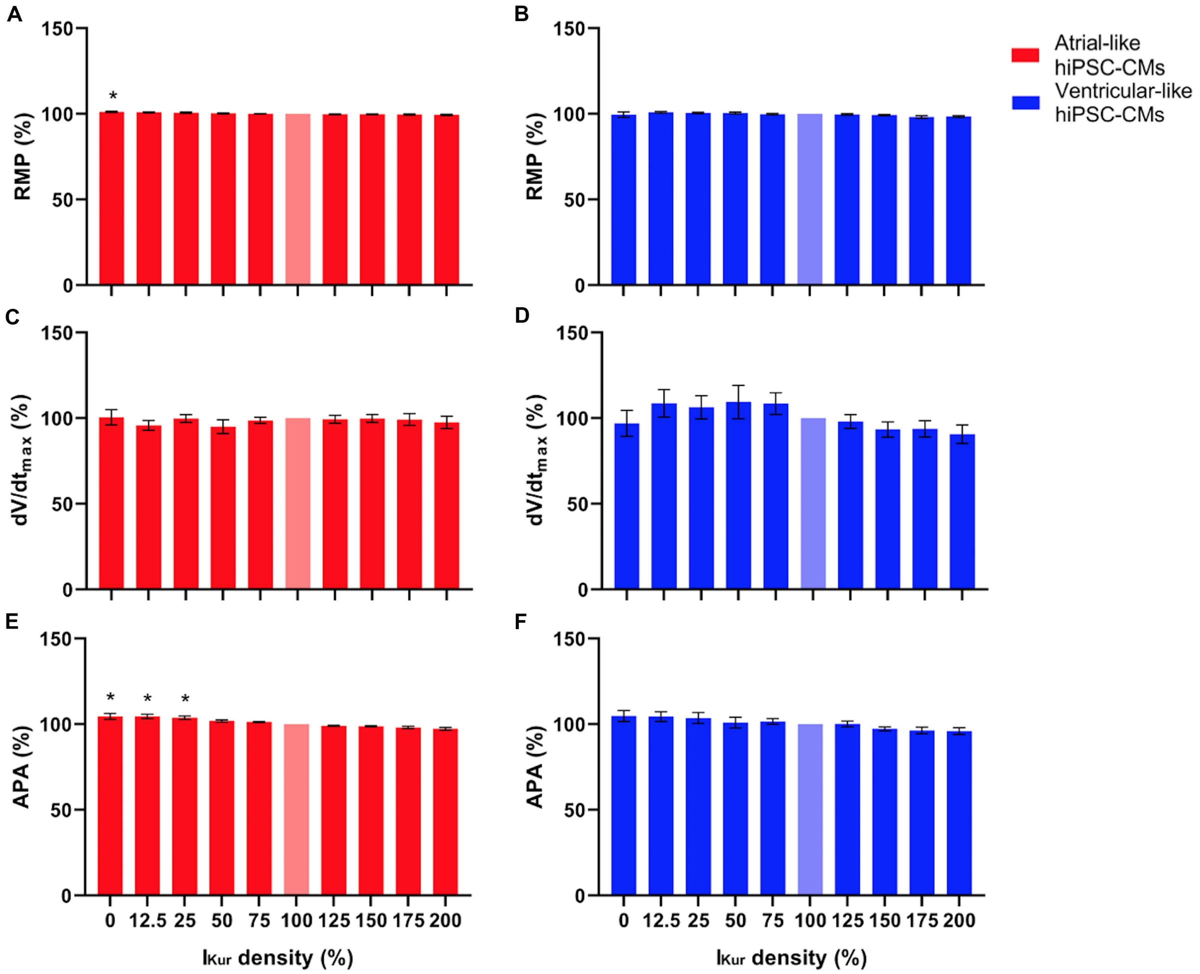

**FIGURE 7 | (A,B)** RMP, **(C,D)** dV/dt$_{max}$, and **(E,F)** APA of atrial- and ventricular-like hiPSC-CMs (left and right panels, respectively) at virtual $I_{Kur}$ densities ranging from 0 to 200%. AP parameters are expressed as percentage relative to their value at 100% $I_{Kur}$ density (bleached bars). Data from 11 atrial- and 10 ventricular-like hiPSC-CMs. *$P < 0.05$.

increases with increasing pacing rate (Ford et al., 2016; Aguilar et al., 2017). Aguilar et al. (2017) carried out comprehensive computer simulations with the Courtemanche et al. (1998) human atrial myocyte model, in which the $I_{Kur}$ formulation was updated in accordance with the experimental observations on $I_{Kur}$ inactivation by Feng et al. (1998). They found that $I_{Kur}$ did not inactivate significantly at high pacing rates and, consequently, the contribution of $I_{Kur}$ to repolarization was mainly determined by its (fast) activation kinetics. Accordingly, rate-dependent changes in $I_{Kur}$ were largely determined by changes in action potential morphology. In computer simulations with the Maleckar et al. (2009) model, on which we based our $I_{Kur}$ formulation, we made similar observations (data not shown). We aim to test the rate dependence of the effects of $I_{Kur}$ on AP repolarization in future experiments on hiPSC-CMs.

In both atrial- and ventricular-like hiPSC-CMs, simulation of loss-of-function mutations through lowering of the virtual $I_{Kur}$ density from 100% to 12.5–75% of its control value, resulted in prolongation of the AP and raise of its plateau, in line with the differences in AP parameters that were observed between 0 and 100% $I_{Kur}$. Marczenke et al. (2017) found that knock-out of *KCNA5* in hiPSC-CMs, representing a complete loss-of-function, may result in the development of EADs, which, however, were not observed in the present study, likely due to our higher pacing frequency. At $I_{Kur}$ densities > 100%, simulating gain-of-function mutations, effects on AP parameters were somewhat less pronounced. In both atrial- and ventricular-like hiPSC-CMs, APD$_{20}$ was only significantly decreased upon an increase in $I_{Kur}$ density to 200%. A significant lowering of the AP plateau, together with AP shortening, was only observed in ventricular-like hiPSC-CMs.

Although the sustained native $I_{Kur}$ density at +50 mV was small in our atrial-like hiPSC-CMs (1.88 ± 0.49 pA/pF, $n = 17$), it was still significantly larger than in our ventricular-like hiPSC-CMs (0.26 ± 0.26 pA/pF, $n = 17$). Within our atrial-like hiPSC-CM population we noted cells lacking $I_{Kur}$ (**Figure 4B**), although atrial-like hiPSC-CM generation using retinoic acid has been shown to generate 90–95% atrial-like hiPSC-CMs

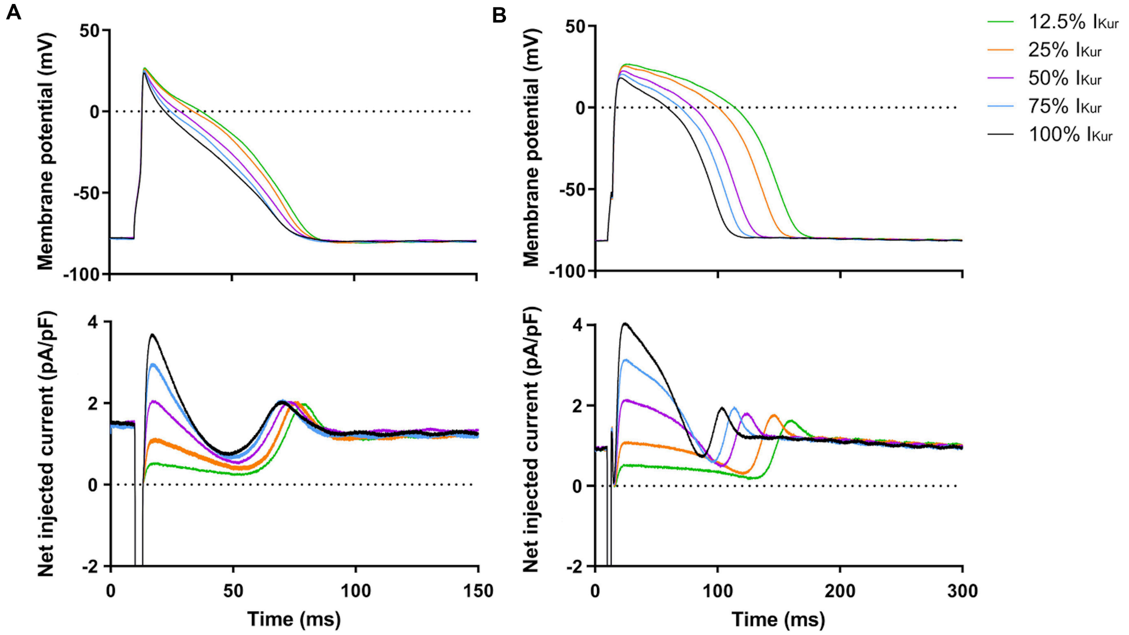

**FIGURE 8 |** Effect of $I_{Kur}$ loss-of-function mutations on APs of atrial- and ventricular-like hiPSC-CMs. **(A)** Superimposed APs of an atrial-like hiPSC-CM upon injection of 12.5–100% virtual $I_{Kur}$ through dynamic clamp and associated injected current (bottom panel), consisting of $I_{K1}$, 12.5–100% $I_{Kur}$, and a short stimulus current. **(B)** Superimposed APs (top panel) and associated injected current (bottom panel) of a ventricular-like hiPSC-CM. APs elicited at 1 Hz by a 3-ms stimulus of 100 pA. Note difference in time scale between panels **(A,B)**.

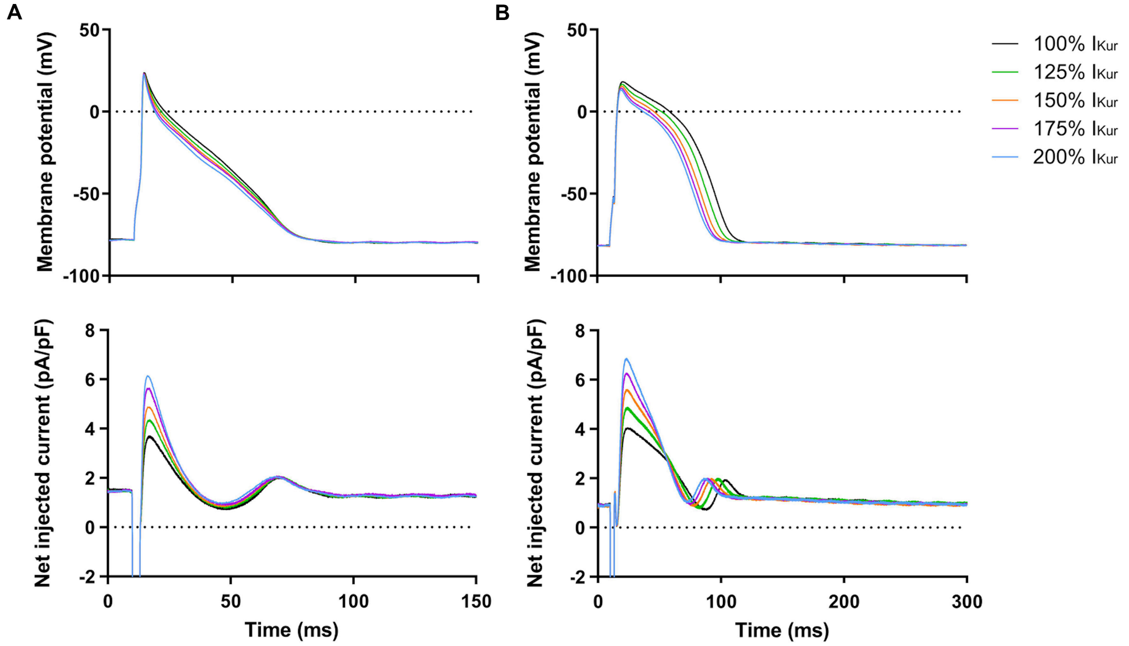

**FIGURE 9 |** Effect of $I_{Kur}$ gain-of-function mutations on APs of atrial- and ventricular-like hiPSC-CMs. **(A)** Superimposed APs of an atrial-like hiPSC-CM upon injection of 100–200% virtual $I_{Kur}$ through dynamic clamp and associated injected current (bottom panel), consisting of $I_{K1}$, 100–200% $I_{Kur}$, and a short stimulus current. **(B)** Superimposed APs (top panel) and associated injected current (bottom panel) of a ventricular-like hiPSC-CM. APs elicited at 1 Hz by a 3-ms stimulus of 100 pA. Note difference in time scale between panels **(A,B)**.

(Cyganek et al., 2018), with the rest being sinus- or ventricular-like hiPSC-CMs. Since hiPSC-CMs display an immature phenotype, it is possible that not all atrial-like hiPSC-CMs have developed $I_{Kur}$ densities large enough to be detected as 4-AP sensitive current in a voltage clamp setting. Our recorded $I_{Kur}$ densities are lower than those of the only other known quantification of $I_{Kur}$ density in atrial- and ventricular-like hiPSC-CMs (Kaplan et al., 2016). In the study by Kaplan et al. (2016), which has only been published in abstract form, the sustained $I_{Kur}$ density at +50 mV amounted to 3.71 ± 0.55 pA/pF ($n$ = 5) in atrial-like hiPSC-CMs, which was significantly larger than that of ventricular-like hiPSC-CMs (1.00 ± 0.10 pA/pF, $n$ = 16). To distinguish between the two types of hiPSC-CMs based on $I_{Kur}$ densities would require further investigation, although the available data suggest a trend of a significantly larger $I_{Kur}$ density in atrial-like hiPSC-CMs.

Of note, all AP parameters of our atrial- and ventricular-like hiPSC-CMs except $dV/dt_{max}$ and APA were not only different under control conditions, but also upon blockade of $I_{Kur}$ by 4-AP, indicating that the two types of hiPSC-CMs are not only different in their level of $K_v1.5$ expression, as determined by $I_{Kur}$ density, and suggesting that differences in membrane currents other than $I_{Kur}$ also contribute to the observed differences in AP parameters. This result is in line with previous findings by both Marczenke et al. (2017) and Lemme et al. (2018), who found that knock-out of *KCNA5* or $I_{Kur}$ blockade by 4-AP in atrial-like hiPSC-CMs did not result in completely ventricular-like APs. These findings are, however, to some extent at odds with those by Kaplan et al. (2016), who noticed that the APs of their atrial-like hiPSC-CMs took on a ventricular-like shape when treated with 4-AP, which strongly suggested that $I_{Kur}$ is the major determinant of atrial action potential morphology. Conversely, they observed that injection of a virtual $I_{Kur}$ in ventricular-like hiPSC-CMs, employing the dynamic clamp technique using oocytes expressing a cloned $K_v1.5$ current, resulted in APs similar to those of atrial-like hiPSC-CMs. Apart from the studies by Kaplan et al. (2016), Marczenke et al. (2017), and Lemme et al. (2018), data on $I_{Kur}$ in hiPSC-CMs are limited and the electrophysiology of $I_{Kur}$ in atrial- and ventricular-like hiPSC-CMs remains largely unknown.

Apart from demonstrating a link between altered $I_{Kur}$ density and changes in AP parameters, $I_{Kur}$ has now been quantified in both atrial- and ventricular-like hiPSC-CMs. Thus, the present study provides additional data toward a complete characterization of individual membrane currents in hiPSC-CMs. Moreover, our study illustrates the potentials of dynamic clamp experiments on hiPSC-CMs, allowing manipulation of characteristics of the injected current in real time, thus facilitating direct, systematic, and efficient testing of changes in those characteristics. In the context of studying drug effects, including effects of anti-AF drugs, dynamic clamp may prove useful in the identification of potential drug targets and in testing model-based hypotheses (Ortega et al., 2018). For instance, dynamic clamp experiments on atrial-like hiPSC-CMs with $I_{Kur}$ based on specific loss- or gain-of-function mutations in *KCNA5* can be utilized to assess the cellular effects of these mutations as well as effects of dedicated pharmacological treatment through modulation of $I_{Kur}$. Ultimately, this may lead to mutation-specific treatment of AF.

## DATA AVAILABILITY STATEMENT

The raw data supporting the conclusions of this article will be made available by the authors, without undue reservation.

## AUTHOR CONTRIBUTIONS

SH designed and performed the experiments, analyzed the data, and drafted the manuscript. HD cultured the hiPSC line and developed the procedures to generate atrial-like and ventricular-like hiPSC-CMs. LB prepared the hiPSC-CMs used for electrophysiology in the present study. AV and RW designed the study, interpreted the data, and drafted, edited, and approved the manuscript.

## FUNDING

Dr. Harsha D. Devalla is supported by a ZonMW and Hartstichting MKMD grant (114021512).

## REFERENCES

Aguilar, M., Feng, J., Vigmond, E., Comtois, P., and Nattel, S. (2017). Rate-dependent role of $I_{Kur}$ in human atrial repolarization and atrial fibrillation maintenance. *Biophys. J.* 112, 1997–2010. doi: 10.1016/j.bpj.2017.03.022

Amos, G. J., Wettwer, E., Metzger, F., Li, Q., Himmel, H. M., and Ravens, U. (1996). Differences between outward currents of human atrial and subepicardial ventricular myocytes. *J. Physiol.* 491, 31–50. doi: 10.1113/jphysiol.1996.sp021194

Argenziano, M., Lambers, E., Hong, L., Sridhar, A., Zhang, M., Chalazan, B., et al. (2018). Electrophysiologic characterization of calcium handling in human induced pluripotent stem cell-derived atrial cardiomyocytes. *Stem Cell Rep.* 10, 1867–1878. doi: 10.1016/j.stemcr.2018.04.005

Barry, P. H., and Lynch, J. W. (1991). Liquid junction potentials and small cell effects in patch-clamp analysis. *J. Membr. Biol.* 121, 101–117. doi: 10.1007/BF01870526

Caballero, R., De la Fuente, M. G., Gómez, R., Barana, A., Amorós, I., Dolz-Gaitón, P., et al. (2010). In humans, chronic atrial fibrillation decreases the transient outward current and ultrarapid component of the delayed rectifier current differentially on each atria and increases the slow component of the delayed rectifier current in both. *J. Am. Coll. Cardiol.* 55, 2346–2354. doi: 10.1016/j.jacc.2010.02.028

Christophersen, I. E., Olesen, M. O., Liang, B., Andersen, M. A., Larsen, A. P., Nielsen, J. B., et al. (2013). Genetic variation in *KCNA5*: impact on the atrial-specific potassium rectifier current $I_{Kur}$ in patients with lone atrial fibrillation. *Eur. Heart J.* 34, 1517–1525. doi: 10.1093/eurheartj/ehs442

Colman, M. A., Ni, H., Liang, B., Schmidt, N., and Zhang, H. (2017). *In silico* assessment of genetic variation of *KCNA5* reveals multiple mechanisms of human atrial arrhythmogenesis. *PLoS Comput. Biol.* 13:e1005587. doi: 10.1371/journal.pcbi.1005587

Cordeiro, J. M., Zeina, T., Goodrow, R., Kaplan, A. D., Thomas, L. M., Nesterenko, V. V., et al. (2015). Regional variation of the inwardly rectifying potassium current in the canine heart and the contributions to differences in action potential repolarization. *J. Mol. Cell. Cardiol.* 84, 52–60. doi: 10.1016/j.yjmcc.2015.04.010

Courtemanche, M., Ramirez, R. J., and Nattel, S. (1998). Ionic mechanisms underlying human atrial action potential properties: insights from a mathematical model. *Am. J. Physiol.* 275, H301–H321. doi: 10.1152/ajpheart.1998.275.1.H301

Cyganek, L., Tiburcy, M., Sekeres, K., Gerstenberg, K., Bohnenberger, H., Lenz, C., et al. (2018). Deep phenotyping of human induced pluripotent stem cell–derived atrial and ventricular cardiomyocytes. *JCI Insight* 3:e99941. doi: 10.1172/jci.insight.99941

Darbar, D., Herron, K. J., Ballew, J. D., Jahangir, A., Gersh, B. J., Shen, W. K., et al. (2003). Familial atrial fibrillation is a genetically heterogeneous disorder. *J. Am. Coll. Cardiol.* 41, 2185–2192. doi: 10.1016/S0735-1097(03)00465-0

Devalla, H. D., Gélinas, R., Aburawi, E. H., Beqqali, A., Goyette, P., Freund, C., et al. (2016). *TECRL*, a new life-threatening inherited arrhythmia gene associated with overlapping clinical features of both LQTS and CPVT. *EMBO Mol. Med.* 8, 1390–1408. doi: 10.15252/emmm.201505719

Devalla, H. D., and Passier, R. (2018). Cardiac differentiation of pluripotent stem cells and implications for modeling the heart in health and disease. *Sci. Transl. Med.* 10:eaah5457. doi: 10.1126/scitranslmed.aah5457

Devalla, H. D., Schwach, V., Ford, J. W., Milnes, J. T., El-Haou, S., Jackson, C., et al. (2015). Atrial-like cardiomyocytes from human pluripotent stem cells are a robust preclinical model for assessing atrial-selective pharmacology. *EMBO Mol. Med.* 7, 394–410. doi: 10.15252/emmm.201404757

Dhamoon, A. S., and Jalife, J. (2005). The inward rectifier current ($I_{K1}$) controls cardiac excitability and is involved in arrhythmogenesis. *Heart Rhythm* 2, 316–324. doi: 10.1016/j.hrthm.2004.11.012

Dhamoon, A. S., Pandit, S. V., Sarmast, F., Parisian, K. R., Guha, P., Li, Y., et al. (2004). Unique Kir2.x properties determine regional and species differences in the cardiac inward rectifier $K^+$ current. *Circ. Res.* 94, 1332–1339. doi: 10.1161/01.RES.0000128408.66946.67

Ellinghaus, P., Scheubel, R. J., Dobrev, D., Ravens, U., Holtz, J., Huetter, J., et al. (2005). Comparing the global mRNA expression profile of human atrial and ventricular myocardium with high-density oligonucleotide arrays. *J. Thoracic Cardiovasc. Surg.* 129, 1383–1390. doi: 10.1016/j.jtcvs.2004.08.031

Fabbri, A., Goversen, B., Vos, M. A., van Veen, T. A. B., and de Boer, T. P. (2019). Required $G_{K1}$ to suppress automaticity of iPSC-CMs depends strongly on $I_{K1}$ model structure. *Biophys. J.* 117, 2303–2315. doi: 10.1016/j.bpj.2019.08.040

Fedida, D., Wible, B., Wang, Z., Fermini, B., Faust, F., Nattel, S., et al. (1993). Identity of a novel delayed rectifier current from human heart with a cloned $K^+$ channel current. *Circ. Res.* 73, 210–216. doi: 10.1161/01.RES.73.1.210

Feghaly, J., Zakka, P., London, B., MacRae, C. A., and Refaat, M. M. (2018). Genetics of atrial fibrillation. *J. Am. Heart Assoc.* 7:e009884. doi: 10.1161/JAHA.118.009884

Feng, J., Xu, D., Wang, Z., and Nattel, S. (1998). Ultrarapid delayed rectifier current inactivation in human atrial myocytes: properties and consequences. *Am. J. Physiol.* 275, H1717–H1725. doi: 10.1152/ajpheart.1998.275.5.H1717

Ford, J., Milnes, J., El Haou, S., Wettwer, E., Loose, S., Matschke, K., et al. (2016). The positive frequency-dependent electrophysiological effects of the $I_{Kur}$ inhibitor XEN-D0103 are desirable for the treatment of atrial fibrillation. *Heart Rhythm* 13, 555–564. doi: 10.1016/j.hrthm.2015.10.003

Gaborit, N., Le Bouter, S., Szuts, V., Varro, A., Escande, D., Nattel, S., et al. (2007). Regional and tissue specific transcript signatures of ion channel genes in the non-diseased human heart. *J. Physiol.* 582, 675–693. doi: 10.1113/jphysiol.2006.126714

Grandi, E., Pandit, S. V., Voigt, N., Workman, A. J., Dobrev, D., Jalife, J., et al. (2011). Human atrial action potential and $Ca^{2+}$ model: sinus rhythm and chronic atrial fibrillation. *Circ. Res.* 109, 1055–1066. doi: 10.1161/CIRCRESAHA.111.253955

Hayashi, K., Konno, T., Tada, H., Tani, S., Liu, L., Fujino, N., et al. (2015). Functional characterization of rare variants implicated in susceptibility to lone atrial fibrillation. *Circulation* 8, 1095–1104. doi: 10.1161/CIRCEP.114.002519

Hoekstra, M., Mummery, C. L., Wilde, A. A. M., Bezzina, C. R., and Verkerk, A. O. (2012). Induced pluripotent stem cell derived cardiomyocytes as models for cardiac arrhythmias. *Front. Physiol.* 3:346. doi: 10.3389/fphys.2012.00346

Horváth, A., Lemoine, M. D., Löser, A., Mannhardt, I., Flenner, F., Uzun, A. U., et al. (2018). Low resting membrane potential and low inward rectifier potassium currents are not inherent features of hiPSC-derived cardiomyocytes. *Stem Cell Rep.* 10, 822–833. doi: 10.1016/j.stemcr.2018.01.012

hPSCreg (2019). *LUMCi004-A*. Available online at: https://hpscreg.eu/cell-line/LUMCi004-A (accessed March 31, 2020).

Kääb, S., Dixon, J., Duc, J., Ashen, D., Näbauer, M., Beuckelmann, D. J., et al. (1998). Molecular basis of transient outward potassium current downregulation in human heart failure: a decrease in Kv4.3 mRNA correlates with a reduction in current density. *Circulation* 98, 1383–1393. doi: 10.1161/01.CIR.98.14.1383

Kaplan, A. D., Rasmusson, R. L., and Bett, G. C. L. (2016). Ionic basis of repolarization of atrial and ventricular specific cell types derived from human induced pluripotent stem cells. *Biophys. J.* 110(Suppl. 1), 343a. doi: 10.1016/j.bpj.2015.11.1848

Lemme, M., Ulmer, B. M., Lemoine, M. D., Zech, A. T. L., Flenner, F., Ravens, U., et al. (2018). Atrial-like engineered heart tissue: an *in vitro* model of the human atrium. *Stem Cell Rep.* 11, 1378–1390. doi: 10.1016/j.stemcr.2018.10.008

Li, G.-R., Wang, H.-B., Qin, G.-W., Jin, M.-W., Tang, Q., Sun, H.-Y., et al. (2008). Acacetin, a natural flavone, selectively inhibits human atrial repolarization potassium currents and prevents atrial fibrillation in dogs. *Circulation* 117, 2449–2457. doi: 10.1161/CIRCULATIONAHA.108.769554

Maleckar, M. M., Greenstein, J. L., Giles, W. R., and Trayanova, N. A. (2009). $K^+$ current changes account for the rate dependence of the action potential in the human atrial myocyte. *Am. J. Physiol. Heart Circ. Physiol.* 297, H1398–H1410. doi: 10.1152/ajpheart.00411.2009

Marczenke, M., Piccini, I., Mengarelli, I., Fell, J., Röpke, A., Seebohm, G., et al. (2017). Cardiac subtype-specific modeling of $K_v1.5$ ion channel deficiency using human pluripotent stem cells. *Front. Physiol.* 8:469. doi: 10.3389/fphys.2017.00469

Mays, D. J., Foose, J. M., Philipson, L. H., and Tamkun, M. M. (1995). Localization of the Kv1.5 $K^+$ channel protein in explanted cardiac tissue. *J. Clin. Investig.* 96, 282–292. doi: 10.1172/JCI118032

Meijer van Putten, R. M. E., Mengarelli, I., Guan, K., Zegers, J. G., Van Ginneken, A. C. G., Verkerk, A. O., et al. (2015). Ion channelopathies in human induced pluripotent stem cell derived cardiomyocytes: a dynamic clamp study with virtual $I_{K1}$. *Front. Physiol.* 6:7. doi: 10.3389/fphys.2015.00007

Nattel, S. (2002). New ideas about atrial fibrillation 50 years on. *Nature* 415, 219–226. doi: 10.1038/415219a

Ng, E. S., Davis, R., Stanley, E. G., and Elefanty, A. G. (2008). A protocol describing the use of a recombinant protein-based, animal product-free medium (APEL) for human embryonic stem cell differentiation as spin embryoid bodies. *Nat. Protoc.* 3, 768–776. doi: 10.1038/nprot.2008.42

Ni, H., Adeniran, I., and Zhang, H. (2017). *In-silico* investigations of the functional impact of *KCNA5* mutations on atrial mechanical dynamics. *J. Mol. Cell. Cardiol.* 111, 86–95. doi: 10.1016/j.yjmcc.2017.08.005

Olson, T. M., Alekseev, A. E., Liu, X. K., Park, S., Zingman, L. V., Bienengraeber, M., et al. (2006). $K_v1.5$ channelopathy due to *KCNA5* loss-of-function mutation causes human atrial fibrillation. *Hum. Mol. Genet.* 15, 2185–2191. doi: 10.1093/hmg/ddl143

Ortega, F. A., Grandi, E., Krogh-Madsen, T., and Christini, D. J. (2018). Applications of dynamic clamp to cardiac arrhythmia research: role in drug target discovery and safety pharmacology testing. *Front. Physiol.* 8:1099. doi: 10.3389/fphys.2017.01099

Panama, B. K., McLerie, M., and Lopatin, A. N. (2007). Heterogeneity of $I_{K1}$ in the mouse heart. *Am. J. Physiol. Heart Circ. Physiol.* 293, H3558–H3567. doi: 10.1152/ajpheart.00419.2007

Patel, Y. A., George, A., Dorval, A. D., White, J. A., Christini, D. J., and Butera, R. J. (2017). Hard real-time closed-loop electrophysiology with the Real-Time eXperiment Interface (RTXI). *PLoS Comput. Biol.* 13:e1005430. doi: 10.1371/journal.pcbi.1005430

Potpara, T. S., and Lip, G. Y. H. (2011). Lone atrial fibrillation: what is known and what is to come. *Int. J. Clin. Pract.* 65, 446–457. doi: 10.1111/j.1742-1241.2010.02618.x

Seltmann, S., Lekschas, F., Müller, R., Stachelscheid, H., Bittner, M.-S., Zhang, W., et al. (2016). hPSCreg—the human pluripotent stem cell registry. *Nucleic Acids Res.* 44, D757–D763. doi: 10.1093/nar/gkv963

Tian, L., Liu, G., Wang, L., Zheng, M., and Li, Y. (2015). KCNA5 gene polymorphism associate with idiopathic atrial fibrillation. *Int. J. Clin. Exp. Med.* 8, 9890–9896.

Veerman, C. C., Mengarelli, I., Koopman, C. D., Wilders, R., Van Amersfoorth, S. C., Bakker, D., et al. (2019). Genetic variation in *GNB5* causes bradycardia by augmenting the cholinergic response via increased acetylcholine-activated potassium current ($I_{K,ACh}$). *Dis. Models Mech.* 12:dmm037994. doi: 10.1242/dmm.037994

Verkerk, A. O., Veerman, C. C., Zegers, J. G., Mengarelli, I., Bezzina, C. R., and Wilders, R. (2017). Patch-clamp recording from human induced pluripotent stem cell-derived cardiomyocytes: improving action potential characteristics through dynamic clamp. *Int. J. Mol. Sci.* 18:1873. doi: 10.3390/ijms18091873

Wang, Z., Fermini, B., and Nattel, S. (1993). Sustained depolarization-induced outward current in human atrial myocytes: evidence for a novel delayed rectifier $K^+$ current similar to $K_v1.5$ cloned channel currents. *Circ. Res.* 73, 1061–1076. doi: 10.1161/01.RES.73.6.1061

Wang, Z., Yue, L., White, M., Pelletier, G., and Nattel, S. (1998). Differential distribution of inward rectifier potassium channel transcripts in human atrium versus ventricle. *Circulation* 98, 2422–2428. doi: 10.1161/01.cir.98.22.2422

Wettwer, E., Hála, O., Christ, T., Heubach, J. F., Dobrev, D., Knaut, M., et al. (2004). Role of $I_{Kur}$ in controlling action potential shape and contractility in the human atrium: influence of chronic atrial fibrillation. *Circulation* 110, 2299–2306. doi: 10.1161/01.CIR.0000145155.60288.71

Wilders, R. (2006). Dynamic clamp: a powerful tool in cardiac electrophysiology. *J. Physiol.* 576, 349–359. doi: 10.1113/jphysiol.2006.115840

Wilders, R. (2018). Cellular mechanisms of sinus node dysfunction in carriers of the *SCN5A*-E161K mutation and role of the H558R polymorphism. *Front. Physiol.* 9:1795. doi: 10.3389/fphys.2018.01795

Yang, T., Yang, P., Roden, D. M., and Darbar, D. (2010). Novel KCNA5 mutation implicates tyrosine kinase signaling in human atrial fibrillation. *Heart Rhythm* 7, 1246–1252. doi: 10.1016/j.hrthm.2010.05.032

Yang, Y., Li, J., Lin, X., Yang, Y., Hong, K., Wang, L., et al. (2009). Novel KCNA5 loss-of-function mutations responsible for atrial fibrillation. *J. Hum. Genet.* 54, 277–283. doi: 10.1038/jhg.2009.26

Zhang, Q., Jiang, J., Han, P., Yuan, Q., Zhang, J., Zhang, X., et al. (2011). Direct differentiation of atrial and ventricular myocytes from human embryonic stem cells by alternating retinoid signals. *Cell Res.* 21, 579–587. doi: 10.1038/cr.2010.163

**Conflict of Interest:** The authors declare that the research was conducted in the absence of any commercial or financial relationships that could be construed as a potential conflict of interest.

frontiers
in Cell and Developmental Biology

ORIGINAL RESEARCH
published: 12 August 2020
doi: 10.3389/fcell.2020.00772

# IP3R-Mediated Compensatory Mechanism for Calcium Handling in Human Induced Pluripotent Stem Cell-Derived Cardiomyocytes With Cardiac Ryanodine Receptor Deficiency

*Xiaojing Luo[1]†, Wener Li[1]†, Karolina Künzel[1], Sarah Henze[2], Lukas Cyganek[2,3], Anna Strano[1], Mareike S. Poetsch[1], Mario Schubert[1] and Kaomei Guan[1,2]**

*[1] Institute of Pharmacology and Toxicology, Technische Universität Dresden, Dresden, Germany, [2] Clinic for Cardiology and Pneumology, Universitätsmedizin Göttingen, Göttingen, Germany, [3] DZHK (German Center for Cardiovascular Research), Partner Site Göttingen, Göttingen, Germany*

In adult cardiomyocytes (CMs), the type 2 ryanodine receptor (RYR2) is an indispensable Ca$^{2+}$ release channel that ensures the integrity of excitation-contraction coupling, which is fundamental for every heartbeat. However, the role and importance of RYR2 during human embryonic cardiac development are still poorly understood. Here, we generated two human induced pluripotent stem cell (iPSC)-based *RYR2* knockout (RYR2$^{-/-}$) lines using the CRISPR/Cas9 gene editing technology. We found that RYR2$^{-/-}$-iPSCs could differentiate into CMs with the efficiency similar to control-iPSCs (Ctrl-iPSCs); however, the survival of iPSC-CMs was markedly affected by the lack of functional RYR2. While Ctrl-iPSC-CMs exhibited regular Ca$^{2+}$ handling, we observed significantly reduced frequency and intense abnormalities of Ca$^{2+}$ transients in RYR2$^{-/-}$-iPSC-CMs. Ctrl-iPSC-CMs displayed sensitivity to extracellular Ca$^{2+}$ ([Ca$^{2+}$]$_o$) and caffeine in a concentration-dependent manner, while RYR2$^{-/-}$-iPSC-CMs showed inconsistent reactions to [Ca$^{2+}$]$_o$ and were insensitive to caffeine, indicating there is no RYR2-mediated Ca$^{2+}$ release from the sarcoplasmic reticulum (SR). Instead, compensatory mechanism for calcium handling in RYR2$^{-/-}$-iPSC-CMs is partially mediated by the inositol 1,4,5-trisphosphate receptor (IP3R). Similar to Ctrl-iPSC-CMs, SR Ca$^{2+}$ refilling in RYR2$^{-/-}$-iPSC-CMs is mediated by SERCA. Additionally, RYR2$^{-/-}$-iPSC-CMs showed a decreased beating rate and a reduced peak amplitude of L-type Ca$^{2+}$ current. These findings demonstrate that RYR2 is not required for CM lineage commitment but is important for CM survival and contractile function. IP3R-mediated Ca$^{2+}$ release is one of the major compensatory mechanisms for Ca$^{2+}$ cycling in human CMs with the RYR2 deficiency.

**Keywords: ryanodine receptor 2, induced pluripotent stem cell-derived cardiomyocytes, CRISPR/Cas9, calcium handling, inositol 1,4,5-trisphosphate receptor**

OPEN ACCESS

***Edited by:***
*Shinsuke Yuasa,*
*Keio University, Japan*

***Reviewed by:***
*Keiko Uchida,*
*Keio University, Japan*
*Yoshinori Yoshida,*
*Kyoto University, Japan*
*Masafumi Yano,*
*Yamaguchi University, Japan*
*Mihaela Gherghiceanu,*
*Victor Babes National Institute of Pathology (INCDVB), Romania*

****Correspondence:***
*Kaomei Guan*
*kaomei.guan@tu-dresden.de*

*†These authors have contributed equally to this work*

***Specialty section:***
*This article was submitted to Stem Cell Research, a section of the journal Frontiers in Cell and Developmental Biology*

***Received:*** *13 January 2020*
***Accepted:*** *22 July 2020*
***Published:*** *12 August 2020*

***Citation:***
*Luo X, Li W, Künzel K, Henze S, Cyganek L, Strano A, Poetsch MS, Schubert M and Guan K (2020) IP3R-Mediated Compensatory Mechanism for Calcium Handling in Human Induced Pluripotent Stem Cell-Derived Cardiomyocytes With Cardiac Ryanodine Receptor Deficiency. Front. Cell Dev. Biol. 8:772. doi: 10.3389/fcell.2020.00772*

## INTRODUCTION

The type 2 ryanodine receptor (RYR2) represents the major sarcoplasmic reticulum (SR) $Ca^{2+}$ release channel in adult cardiomyocytes (CMs). It plays an essential role in excitation-contraction coupling, a process by which an electrical signal is converted into a single contraction (Eisner et al., 2017). Upon spontaneous depolarization of membrane potential, voltage-dependent L-type calcium channels (LTCC) are activated, which cause the influx of a small amount of external $Ca^{2+}$ into the cytosol. The $Ca^{2+}$ signal is then sensed and amplified by the $Ca^{2+}$-sensitive RYR2. The opening of RYR2 causes a substantial release of $Ca^{2+}$ from the SR into the cytosol and thus elevates intracellular $Ca^{2+}$ levels. In the end, the binding of $Ca^{2+}$ to troponin promotes sliding of thick and thin filaments, which results in cardiac contraction (Eisner et al., 2017).

A growing number of studies highlight the importance of RYR2 for the precise functionality of the adult heart. An inducible cardiac-specific *Ryr2* knockout (*Ryr2*$^{-/-}$) mouse model claimed that RYR2 plays a non-redundant role in the control of heart rate and rhythmicity (Bround et al., 2012). An in-frame deletion of exon-3 in the *Ryr2* gene in the mouse (Ex3-del$^{+/-}$) was associated with bradycardia and death. However, Ex3-del$^{+/-}$ mice did not display some clinical phenotypes of patients with the RYR2 exon-3 deletion, including catecholaminergic polymorphic ventricular tachycardia (Liu et al., 2014).

In the early stage of embryonic heart development in mice, $Ca^{2+}$ homeostasis is regulated not only by RYR2 but also by LTCC and inositol 1,4,5-trisphosphate receptor (IP3R) (Takeshima et al., 1998; Rosemblit et al., 1999; Kapur and Banach, 2007; Sasse et al., 2007). Ryr2$^{-/-}$ mice possess the ability of repetitive $Ca^{2+}$ signals and rhythmic contractions at embryonic day E9.5 (Takeshima et al., 1998), when LTCC and IP3R may be responsible for the early $Ca^{2+}$ cycling (Liu et al., 2002; Kockskamper et al., 2008; Xie et al., 2018). However, as the development of the embryo proceeds, the importance of $Ca^{2+}$ cycling via SR increases progressively (Liu et al., 2002). Ryr2$^{-/-}$ mice died of cardiac arrest around embryonic day E10 with irregular arranged myocardium and trabeculae (Takeshima et al., 1998).

To date, studies on the expression and function of RYR2 during early embryonic cardiac development are limited to investigations using mouse Ryr2$^{-/-}$ models and mouse embryonic stem cell-derived CMs (mESC-CMs) (Takeshima et al., 1998; Liu et al., 2002; Yang et al., 2002; Fu et al., 2006; Kapur and Banach, 2007; Sasse et al., 2007; Xie et al., 2018). The major challenge to study the origin and development of human embryonic cardiac myocytes is the limitation of a reliable human cell model, which can be used for long-term culture experiments. The appearance of human induced pluripotent stem cell (iPSC) technology has shown its great potential to solve this challenge (Takahashi et al., 2007; Yu et al., 2007). In the iPSC approach, adult somatic cells can be efficiently reprogrammed into pluripotent stem cells by ectopic expression of a set of transcription factors (Takahashi and Yamanaka, 2006). Based on this revolutionary finding, researchers have established the generation of human iPSCs and the efficient differentiation of these cells into iPSC-CMs (Itzhaki et al., 2011; Lian et al., 2013; Cyganek et al., 2018). Previous studies have demonstrated that both RYR2 and IP3R are involved in calcium handling in human ESC- and iPSC-derived CMs (Satin et al., 2008; Itzhaki et al., 2011). However, our knowledge about how these two signaling pathways are cooperated during human embryonic cardiac growth is still not sufficient.

In this study, we used iPSC technology in combination with the CRISPR/Cas9 gene editing technique to investigate the role of RYR2 in differentiation, development, and function of human iPSC-CMs. We hypothesized that the generated RYR2$^{-/-}$-iPSC-CMs exhibit morphological and physiological abnormalities, providing insights into the function of RYR2 during human embryonic heart development.

## MATERIALS AND METHODS

### Culture and Maintenance of iPSCs

Human iPSC lines iWTD2.1 and iBM76.1 were used in this study as controls (Ctrl-iPSCs), which were generated from dermal fibroblasts and mesenchymal stem cells from two healthy donors, respectively, using the STEMCCA lentivirus system, and characterized as previously described (Streckfuss-Bomeke et al., 2013; Cyganek et al., 2018). The study was approved by the Ethics Committee of the University Medical Center Göttingen (approval number: 21/1/11), and carried out in accordance with the approved guidelines. Human iPSCs were cultured in chemically defined E8 medium (Thermo Fischer Scientific) on Geltrex- (Thermo Fischer Scientific) coated cell culture plates at 37°C with 5% $CO_2$. The E8 medium was changed daily and cells at ∼85% confluency were passaged using Versene (Thermo Fischer Scientific).

### Generation of RYR2$^{-/-}$-iPSC Lines Using CRISPR/Cas9-Mediated Genome Editing

In order to generate homozygous RYR2 knockout (RYR2$^{-/-}$) iPSC lines, two guide RNAs (gRNAs) were designed and inserted into the CRISPR/Cas9 plasmid (Sigma-Aldrich), respectively (**Supplementary Figure 1A**). While gRNA1 (ACGAACTCTTCGTAGTCGAGGG) targets exon 90 (g.741541-741563) of the *RYR2* gene, gRNA2 (CCTAGCCTGGTATATGACTATG) targets exon 99 (g.763747-763768). For transfection using the Amaxa Nucleofector II device (Lonza), $2 \times 10^6$ iPSCs were collected and re-suspended in a mixture of 82 μl Nucleofector solution and 18 μl supplement 1 (Nucleofector kit 1/2, Lonza) containing 4 μg plasmid. One day after transfection, GFP$^+$ cells were sorted and seeded on Geltrex-coated 96-well plates at a density of $1 \times 10^3$ cells/well for expansion. The genomic DNA from the colonies was isolated and purified using the automated Maxwell 16 cell DNA purification kit (Promega) according to the manufacturer's instruction. For genomic DNA sequencing, the DNA sequence of RYR2 was initially amplified by PCR using the appropriate primer set (**Supplementary Table 1A**). DNA sequencing of PCR products from CRISPR/Cas9-edited clones was performed by a commercial sequencing facility (Seqlab, Göttingen).

To characterize the pluripotency of the CRISPR/Cas9-edited $RYR2^{-/-}$-iPSCs, reverse transcription-PCR analysis, immunofluorescence staining, and spontaneous differentiation *in vitro* were carried out using standard protocols as described earlier (Streckfuss-Bomeke et al., 2013). For detailed description, please see the **Supplementary Material**.

## Directed Differentiation of iPSCs Into Cardiomyocytes

Directed differentiation of Ctrl- and $RYR2^{-/-}$-iPSCs into CMs (Ctrl-iPSC-CMs, $RYR2^{-/-}$-iPSC-CMs, respectively) was induced by modulating WNT signaling as previously described (Lian et al., 2013; Cyganek et al., 2018). Briefly, when monolayer cultures of iPSCs on 12-well plates reached 80–90% confluency, differentiation was initiated by changing the E8 medium to cardio differentiation medium, which was composed of RPMI 1640 with Glutamax and HEPES (Thermo Fischer Scientific), 0.5 mg/ml human recombinant albumin (Sigma-Aldrich) and 0.2 mg/ml L-ascorbic acid 2-phosphate (Sigma-Aldrich). Cells were first treated with 4 μM of the GSK3β inhibitor CHIR99021 (Millipore) for 48 h and then with 5 μM of the WNT signaling inhibitor IWP2 (Millipore) for additional 48 h. Afterward, cells were cultured in cardio differentiation medium for another 4 days. From day 8, cells were cultivated in cardio culture medium containing RPMI 1640 with Glutamax and HEPES, supplemented with 2% B27 (Thermo Fischer Scientific). At day 20, beating iPSC-CMs were detached from the plate by incubating with 2 ml of 1 mg/ml collagenase B (Worthington Biochemical), dissolved in cardio culture medium, for 1 h at 37°C. Floating iPSC-CM sheet was gently transferred into a falcon tube and dissociated with 3 ml of 0.25% Trypsin/EDTA (Thermo Fischer Scientific) for 8 min at 37°C. Digestion was stopped by adding the double volume of the cardio digestion medium (80% cardio culture medium, 20% FCS, and 2 μM Thiazovivin). Cells were centrifuged at 200 g for 5 min, re-suspended in cardio digestion medium, and replated into Geltrex-coated 6-well plates at a density of 800,000 cells/well. Afterward, iPSC-CMs were cultured in cardio culture medium until 90 days.

## Time-Dependent Proliferation Analysis and Cell Viability Assay of iPSC-CMs

To investigate the proliferation of iPSC-CMs during long-term culture, both Ctrl- and $RYR2^{-/-}$-iPSC-CMs were replated at a fixed density of 800,000 cells/well at day 20 post differentiation. Cell number was determined weekly for 10 weeks until CMs reached the age of 90 days. CMs from two randomly selected wells of one differentiation experiment were detached, dissociated, and quantified by counting the cell numbers with a hemocytometer and taking the average.

To assess the metabolic activity of iPSC-CMs, the MTT (3-(4,5-dimethylthiazol-2-yl)-2,5-diphenyl tetrasodium bromide) assay was performed according to the manufacturer's instructions (MTT Kit CT02, Millipore). Briefly, iPSC-CMs at week 8 after replating were seeded in 48-well plates at a density of 60,000 cells per well, and cultured for another 2 weeks. Afterwards, 50 μg/ml MTT dissolved in 200 μl cardio culture medium was added onto the cells, which were then incubated at 37°C for 2 h. Reaction was stopped by the addition of 200 μl isopropanol supplemented with 0.04 M HCl. Samples were incubated and shaken (300 rpm) for 10 min at room temperature (RT). Absorbance of the formazan at 570 and 630 nm was measured using a plate reader (Biotek Synergy HTX). Cell viability was determined as absorbance (570–630 nm) and normalized to control group.

## Immunofluorescence Staining of iPSC-CMs

Ctrl- and $RYR2^{-/-}$-iPSC-CMs grown on glass coverslips were fixed with 4% paraformaldehyde (PFA; Carl Roth), blocked with 1% bovine serum albumin (BSA; Sigma-Aldrich), and permeabilized with 0.1% Triton X-100 (Carl Roth). Immunofluorescence staining was performed overnight using the following primary antibodies: anti-α-actinin (1:500; mouse monoclonal, IgG1, Sigma-Aldrich), anti-Ki67 (1:400; rabbit polyoclonal, abcam), anti-IP3R (1:100; rabbit polyclonal, Merck Millipore, used for all three subtypes of IP3R), and anti-RYR2 (1:500; rabbit polyclonal, HPA020028; Sigma-Aldrich, used for the full length of RYR2). Afterward, cells were washed three times with PBS and incubated with the corresponding secondary antibodies (1:1000; anti-rabbit Alexa fluor 546, Invitrogen; anti-rabbit Alexa fluor 488, Invitrogen; anti-mouse Alexa fluor 546, Invitrogen; anti-mouse Alexa fluor 488, Invitrogen) for 1 h at RT. Nuclei were co-stained with 4',6-diamidino-2-phenylindole (DAPI; 0.4 μg/ml; Sigma-Aldrich). Documentation was performed using fluorescence microscopy (Carl Zeiss).

## Western Blot

Both Ctrl- and $RYR2^{-/-}$-iPSC-CMs (90 days old) were scraped off from the culture plates and cell pellets were snap-frozen into liquid nitrogen and stored at –80°C. For cell lysis, frozen cell pellets were resuspended in lysis buffer containing 20 mM Tris/HCl (pH 7.4), 200 mM NaCl, 1 mM $Na_3VO_4$, 20 mM NaF, 1% IGEPAL CA-630 (Sigma-Aldrich), 1 mM dithiothreitol (Roth), PhosSTOP phosphatase inhibitor (Roche), and cOmplete$^{TM}$ protease inhibitor (Roche). After incubation for 30 min on ice, lysates were centrifuged and protein concentration was determined using the Pierce BCA protein assay kit (Thermo Fisher Scientific) according to the manufacturer's instructions. A total amount of 40 μg protein lysate mixed with SDS loading buffer and DPBS in a volume of 20 μl was denatured for 30 min at 37°C. Afterward, samples were run on a 6–15% polyacrylamide gel with a 5% stacking gel at 250 mA for around 1–2 h and then transferred to PVDF membranes using the Wet/Tank blotting system. Unspecific binding sites on the membrane were blocked with 1% BSA in TBS with 0.1% Tween 20 (TBS-T) or with 5% non-fat dry milk in TBS-T for 1 h at RT. Membranes were incubated with primary antibodies overnight at 4°C. The following primary antibodies were used: anti-RYR2 (1:500; rabbit polyclonal; SAB4502707; Sigma-Aldrich, used for the detection of both the full-length and the truncated RYR2), anti-RYR2 (1:1000; mouse monoclonal, IgG1, MA3-916 C3-33; Thermo Fisher Scientific Pierce antibodies used for the detection of the full length of RYR2), anti-IP3R (1:750; rabbit polyclonal), anti-SERCA2A (sarco/endoplasmic reticulum $Ca^{2+}$-ATPase type 2A; 1:1000; mouse monoclonal, IgG2a, Thermo Fisher Scientific), anti-NCX1 (sodium-calcium exchanger type 1; 1:1000; mouse monoclonal, IgG2b, Novus), anti-$Ca_v$1.2 (voltage-dependent L-type calcium channel alpha 1C subunit; 1:200; mouse monoclonal, IgG2b, abcam), anti-α-actinin (1:1000; mouse monoclonal, IgG1), anti-eukaryotic elongation factor 2 (EEF2; 1:50,000; rabbit polyclonal, IgG, abcam), anti-cardiac troponin T (cTNT; 1:1000; rabbit polyclonal, IgG, abcam), and anti-GAPDH (glyceraldehyde 3-phosphate dehydrogenase; 1:5000; rabbit polyclonal, Thermo Fisher Scientific). The membranes were then incubated with HRP-conjugated goat anti-mouse or anti-rabbit secondary antibodies (1:10,000; Thermo Fisher Scientific) for 1 h at RT. Afterwards, membranes were washed three times with TBS-T. Antigens of interest were detected by chemiluminescence (ECL; GE Healthcare) and visualized using the ChemiDoc MP system. Quantification was performed by calculating the signal intensity with Image Lab software (Bio-Rad).

To detect protein degradation, Ctrl-, A3 and A5 $RYR2^{-/-}$-iPSC-CMs (90 days old) were stimulated with 100 nM isoprenaline (Sigma-Aldrich) for 6 h and stepwise treated with the proteasome and calpain inhibitor MG132 (10 μM for 24 h; Sigma-Aldrich) and the autophagy inhibitor bafilomycin A1 (BafA1; 100 nM for 6 h; Sigma-Aldrich) before the cell pellets were collected.

## Reverse Transcription-PCR Analysis

For gene expression analysis, Ctrl-iPSCs, CRISPR-edited A3 and A5 $RYR2^{-/-}$-iPSCs as well as 90-day-old Ctrl- and $RYR2^{-/-}$-iPSC-CMs were washed three times with PBS and cell pellets were collected, snap-frozen into liquid nitrogen, and stored at –80°C. Isolation and purification of total RNA were performed using the SV total RNA isolation system (Promega) in accordance to the manufacturer's instructions. First strand cDNA synthesis was performed using MULV reverse transcriptase (Thermo Fisher Scientific) and Oligo d(T)16 primer (Thermo Fisher Scientific). The expression level of *SOX2, OCT4, NANOG, LIN28*, and *FOXD3* were assessed in Ctrl- and CRISPR-edited iPSC lines by reverse transcription-PCR using the GoTaq DNA polymerase (Promega). In addition, the expression level of *RYR2*, *IP3R1*, *IP3R2*, *CACNA1C*, *TNNT2*, and *ACTN2* were assessed in Ctrl and $RYR2^{-/-}$-iPSC-CMs. GAPDH was used as an internal control. Primer sequences, annealing temperature, and cycles used for reverse transcription-PCR analyses are listed in **Supplementary Table 1B**.

## Calcium Spark Measurement of iPSC-CMs

For calcium spark recordings, spontaneously beating Ctrl- and $RYR2^{-/-}$-iPSC-CMs (around 80-day-old) were dissociated, replated on Geltrex-coated coverslips at a density of 200,000 cells per 6-well and then allowed to recover for at least 10 days in cardio culture medium. Before measurement, cells were loaded with the fluorescent calcium indicator 5 μM fluo-4/AM (Thermo Fisher Scientific) and 0.02% [w/v] pluronic F-127 (Thermo Fisher Scientific) in Tyrode's solution containing (in mM): NaCl 140, KCl 5.4, $CaCl_2$ 1.8, $MgCl_2$ 1, HEPES 10, and glucose 10 (pH adjusted to 7.3 with NaOH) for 30 min at RT. Following incubation, the indicator-containing solution was removed and cells were washed twice, and incubated for additional 10 min to allow de-esterification of the indicator. To detect $Ca^{2+}$ sparks, both Ctrl- and $RYR2^{-/-}$-iPSC-CMs were pre-treated with 100 nM isoprenaline for 10 min before starting the recordings. Recordings were obtained using a LSM 710 confocal microscopy system in line scan mode (512 pixels, 45 μm, 1057.7 Hz, 20,000 cycles). Cells were incubated in Tyrode's solution at RT and field stimulated at 0.25 Hz for at least 20 s to bring the cytosolic calcium concentration to a steady state. Fluo-4 was excited at 488 nm and emitted fluorescence was captured at 490–540 nm. Quantification of $Ca^{2+}$ sparks was performed using the SparkMaster plugin of ImageJ (NIH) and several key parameters were determined: spark frequency (events per 100 μm per second), amplitude ($\Delta F/F_0$), full duration at half maximum (FDHM), full width at half maximum (FWHM), and SR $Ca^{2+}$ leak per cell (spark frequency × amplitude × FDHM × FWHM). As fixed criteria, sparks with minimal amplitude of 0.2 $\Delta F/F_0$, minimal width of 0.7 μm, and minimal duration of 7 ms were selected for detailed analysis.

## Calcium Transient Measurement of iPSC-CMs

Both Ctrl- and $RYR2^{-/-}$-iPSC-CMs around day 80 were dissociated and replated on coverslips at a density of 200,000 cells/well. Cells were allowed to recover for at least 10 days post-replating. For measurement, cells were loaded with Fura-2 (Thermo Fisher Scientific) at a final concentration of 5 μM in cardio culture medium for 30 min at 37°C and washed twice with the medium. Prior to measurement, cells were incubated for 10 min to enable complete de-esterification of intracellular Fura-2. Intracellular $Ca^{2+}$ events were recorded using a 40 × objective on an Olympus IX70 microscope fitted with an IonOptix system (Ionoptix, Milton, MA) at 35°C. Samples were excited at 340 and 380 nm with a switching frequency of 200 Hz and the emitted fluorescence was collected at 510 nm. The cytosolic $Ca^{2+}$ level was measured as the ratio of fluorescence at 340 and 380 nm (340/380 nm).

Spontaneous whole-cell $Ca^{2+}$ transients were recorded in normal Tyrode's solution containing (in mM): NaCl 138, KCl 4, $CaCl_2$ 1.8, $MgCl_2$ 1, $NaH_2PO_4$ 0.33, HEPES 10, and glucose 10 (pH adjusted to 7.3 with NaOH). To normalize the $Ca^{2+}$ transient frequency, Ctrl- and $RYR2^{-/-}$-iPSC-CMs were field-stimulated using a MyoPacer (Ionoptix, Milton, MA) at a pacing frequency of 0.5 Hz (6 V, 10 ms). Monotonic transient analysis was performed using the LabChart Pro software (ADInstrument) and the following parameters were determined: peak amplitude of $Ca^{2+}$ transients (the Fura-2 ratio at systole subtracted by the Fura-2 ratio at diastole), decay rate (tau), as well as duration and frequency of $Ca^{2+}$ transients.

Calcium sensitivity analysis was performed as described previously (Jiang et al., 2007). Briefly, Ctrl- and $RYR2^{-/-}$-iPSC-CMs loaded with Fura-2 were first exposed to 0 mM $Ca^{2+}$ Tyrode's solution until no spontaneous $Ca^{2+}$ transient was detected and then continuously perfused with Tyrode's solution containing $Ca^{2+}$ of increasing concentrations (0, 0.1, 0.2, 0.3, 0.5, 1.0, and 2.0 mM). In the end, caffeine (10 mM; Sigma-Aldrich) was applied to confirm the activity of RYR2.

To examine the caffeine-induced $Ca^{2+}$ release in iPSC-CMs, cells loaded with Fura-2 were washed with depolarization solution containing (in mM): NaCl 112, KCl 30, $CaCl_2$ 1.8, $MgCl_2$ 1, $NaH_2PO_4$ 0.33, HEPES 10, and glucose 10 (pH adjusted to 7.3 with NaOH). Cytosolic $Ca^{2+}$ level was measured before and after continuous addition of caffeine with increasing concentrations (from 0.025 to 5.0 mM).

To investigate the role of IP3R-mediated $Ca^{2+}$ release in $Ca^{2+}$ handling of iPSC-CMs, spontaneous $Ca^{2+}$ transients were recorded before and after the application of the IP3R antagonists 2-aminoethoxydiphenyl borate (2-APB, 20 μM; Tocris) and Xestospongin C (XeC, 1 μM; abcam). To determine the contribution of SERCA-mediated SR $Ca^{2+}$ uptake to $Ca^{2+}$ cycling in iPSC-CMs, spontaneous $Ca^{2+}$ transients were recorded before and after the application of the SERCA inhibitor thapsigargin (5 μM; Millipore). The changes of $Ca^{2+}$ transient amplitude and frequency caused by the addition of these inhibitors were determined.

For these experiments, we used an imaging chamber (RC-47FSLP, Warner instruments), which is furnished with a field stimulation and a built-in aspiration port. For fluid control, a 12-valve superfusion system (DAD-VM, ALA Scientific Instruments) combined with a multi-tube pre-heater (MPRE8, Cell MicroControls) was used, which together allows a gentle, rapid, and direct solution change around the measured cells. The overflow solution was removed via the aspiration port by suction with a peristaltic pump (minipuls 3, Gilson).

## Patch-Clamp Recording of iPSC-CMs

Ctrl- and $RYR2^{-/-}$-iPSC-CMs around day 80 were enzymatically singularized into single cells and seeded on coverslips at a density of 30,000 cells per 3.5-cm dish. Whole-cell patch-clamp recording of single cells was conducted using an EPC10 amplifier (HEKA Elektronik), controlled by the PatchMaster software (HEKA Elektronik). Series resistance was compensated by 85%. Pipette potentials ($V_{Pip}$) were corrected for liquid junction potentials. All experiments were performed at RT. Action potential (AP) measurement was performed under current-clamp mode without any current injection in RPMI 1640 basal medium using the pipette solution containing (in mM): $K_D$-gluconate 100, KCl 60, MgATP 4, NaGTP 0.3, $Na_2$-phosphocreatine 5, and HEPES 10 (pH adjusted to 7.2 with KOH). Voltage-clamp measurement of L-type calcium current ($I_{CaL}$) was conducted in an extracellular solution containing (in mM): NMDG-Cl 140, $CaCl_2$ 1.8, $MgCl_2$ 1, HEPES 10, and glucose 10 (pH adjusted to 7.3 with HCl) and a pipette solution containing (in mM): CsCl 110, TEA-Cl 20, $MgCl_2$ 5, EGTA 10, HEPES 10, and $Na_2ATP$ 2 (pH adjusted to 7.2 with CsOH). To elicit $I_{CaL}$, cells were clamped for 600 ms from the holding potential of –90 mV to test potentials between 70 and –80 mV in steps of –10 mV. The basic cycle length was 3 s.

## Statistical Analysis

Results are presented as mean ± standard error of the mean (SEM). Statistical analysis was performed using GraphPad Prism 5 software with student's *t*-test, the one-way ANOVA with the Dunnett's multiple comparison test or the two-way ANOVA with Sidak's correction for comparison of more groups and conditions. Results were considered statistically significant when the *P*-value was <0.05 ($^*P < 0.05$, $^{**}P < 0.01$, $^{***}P < 0.001$, $^{****}P < 0.0001$).

# RESULTS

## Loss of *RYR2* Leads to the Increased Death of $RYR2^{-/-}$-iPSC-CMs

To edit the *RYR2* gene, gRNA1 and gRNA2 were designed to target exon 90 (**Figure 1A**) and exon 99 (**Supplementary Figure 1B**) of *RYR2*, respectively. The success of the CRISPR/cas9 gene editing was screened by DNA sequencing (**Figures 1B,C** and **Supplementary Figures 1C,D**). The experiments revealed that the CRISPR/Cas9-targeted clone A3 had a homozygous deletion of one nucleotide (c.12230delC, exon 90), which resulted in a shift of the open reading frame. Consequently, the edited *RYR2* gene in A3 clone obtained a premature termination codon (PTC) in the cytosolic domain of RYR2 (L4077Sfs*25) (**Figure 1C**), leading to a lack of the sequence encoding transmembrane domain, which forms the channel pore. Clone A5 showed homozygous deletion of eight nucleotides (c.14159-14166del, exon 99), leading to a PTC (W4721Dfs*8; **Supplementary Figure 1D**), and the loss of three transmembrane helical sections and the pore-forming region.

A3 and A5 $RYR2^{-/-}$-iPSC lines were analyzed for their pluripotency. Both cell lines were positive for the human pluripotency markers OCT4, SOX2, LIN28, NANOG, TRA-1-60, and SSEA4 as demonstrated by immunostaining (**Supplementary Figure 1E**), similar to their parental Ctrl-iPSCs (Cyganek et al., 2018). In addition, both A3 and A5 $RYR2^{-/-}$-iPSC lines expressed several pluripotency genes, such as *SOX2, OCT4, NANOG, LIN28*, and *FOXD3* similar to the Ctrl-iPSCs (**Supplementary Figure 1F**). Differentiation potential of the edited iPSC lines *in vitro* was studied using the embryoid body-mediated differentiation method. Both A3 and A5 $RYR2^{-/-}$-iPSCs differentiated into derivatives of three embryonic germ layers, as detected by the expression of genes encoding α-fetoprotein (*AFP*), cardiac troponin T (*TNNT2*), and synaptophysin (*SYP*) (**Supplementary Figure 1G**). Notably, the embryoid bodies formed from A3 and A5 $RYR2^{-/-}$-iPSCs grew slower than those from Ctrl-iPSCs and revealed smaller sizes (data not shown).

Importantly, using the standard directed differentiation protocol, both A3 and A5 $RYR2^{-/-}$-iPSCs were able to be successfully differentiated into spontaneously beating CMs ($RYR2^{-/-}$-iPSC-CMs; **Supplementary Videos 1, 2**) similar to Ctrl-iPSCs (**Supplementary Video 3**). The percentage of cTNT-positive CMs at day 20 post differentiation of $RYR2^{-/-}$-iPSCs (A3: 96.7 ± 0.5%, *n* = 3; A5: 96.6 ± 0.4%, *n* = 3) was similar to that of Ctrl-iPSCs (97.7 ± 0.8%, *n* = 3; **Supplementary Figure 2A**).

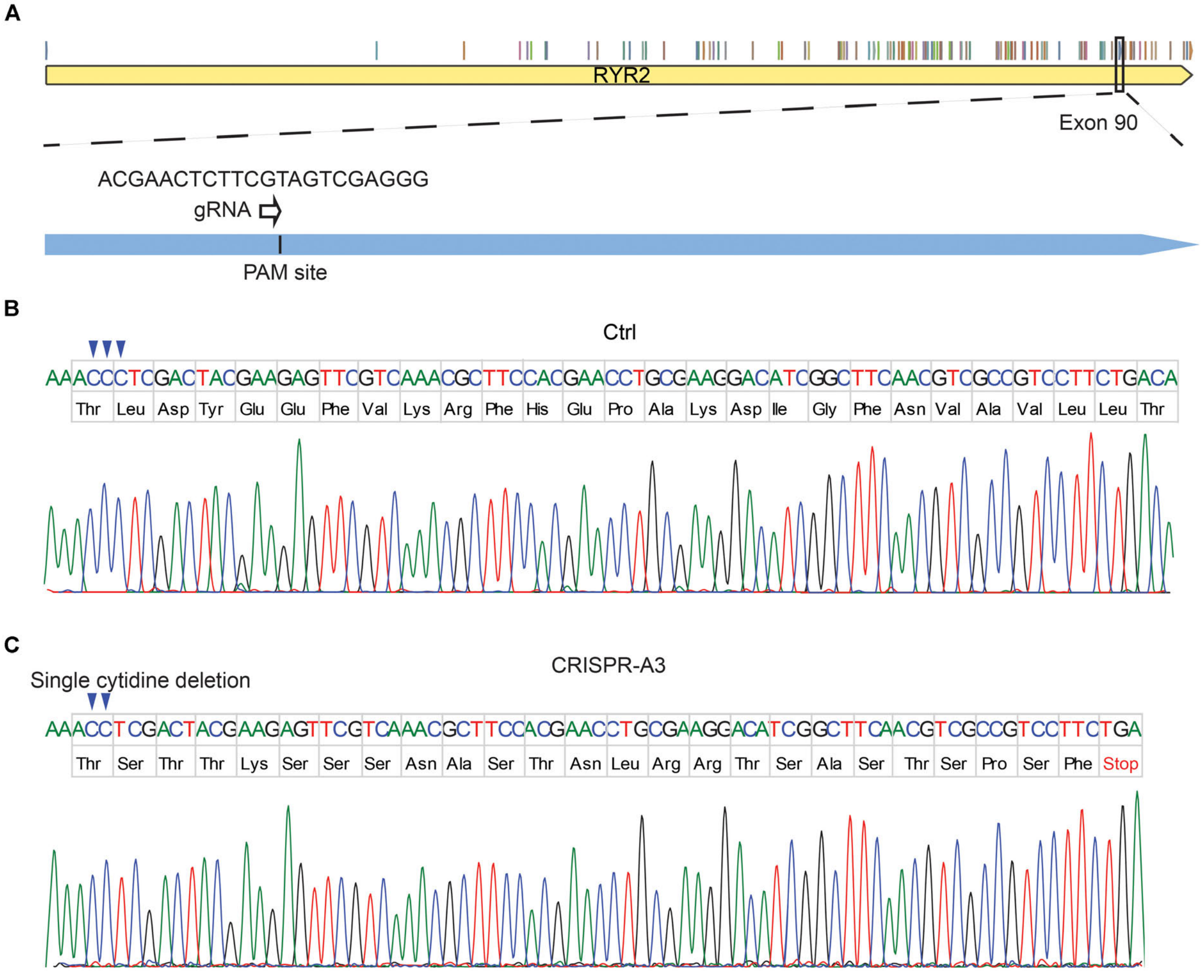

**FIGURE 1 |** Generation of human homozygous RYR2 knockout iPSCs (RYR2$^{-/-}$-iPSCs). **(A)** Illustration of the *RYR2* locus and gRNA1 designed for CRISPR/Cas9-mediated gene editing in exon 90 of *RYR2*. **(B,C)** DNA sequencing of Ctrl- **(B)** and CRISPR/Cas9-edited A3 RYR2$^{-/-}$-iPSC lines **(C)**. The A3 RYR2$^{-/-}$-iPSC line displayed a single homozygous cytidine deletion in the *RYR2* gene, which resulted in a premature termination codon (PTC).

These results indicate that loss of RYR2 does not alter the early cardiac commitment of iPSCs and the differentiation efficiency into CMs.

Although RYR2$^{-/-}$-iPSC-CMs could be cultivated for up to 3 months and remained a high percentage of cTNT-positive cells similar to the Ctrl group (Ctrl: 98.4 ± 0.2%, $n = 3$; A3: 96.8 ± 2.4%, $n = 3$; A5: 96.7 ± 0.4%, $n = 3$; **Supplementary Figure 2B**), they grew differently with higher number of floating cells and signs of cell death in comparison to Ctrl-iPSC-CMs (**Figures 2A,B** and **Supplementary Figures 2C,D**) during long-term culture. To analyze the survival and proliferation rate during long-term culture, both Ctrl- and RYR2$^{-/-}$-iPSC-CMs were replated at a fixed density of 0.8 million cells/well on day 20 post differentiation. No significant difference in cell numbers was observed between Ctrl- and A3 RYR2$^{-/-}$-iPSC-CMs during the first five weeks after replating. However, while Ctrl-iPSC-CMs revealed a steady increase in their number until week 8 and remained stable afterward, RYR2$^{-/-}$-iPSC-CMs showed no increase in their number. At week 10, the number of Ctrl-iPSC-CMs quadrupled to 3.2 ± 0.3 million cells/well, and the number of RYR2$^{-/-}$-iPSC-CMs only increased to 1.4 ± 0.3 million cells/well, $P < 0.0001$ (**Figure 2C**). To analyze whether RYR2$^{-/-}$-iPSC-CMs have a lower proliferation capacity, Ctrl- and RYR2$^{-/-}$-iPSC-CMs at week 8 post replating were double immunostained for sarcomeric α-actinin and Ki67, a marker of cell proliferation. The percentage of proliferating CMs was quantified as the number of Ki67-positive nuclei divided by the total number of nuclei. The number of Ki67-positive cells was comparable in Ctrl- and RYR2$^{-/-}$-iPSC-CMs (Ctrl: 3.9 ± 0.4%; A3-RYR2$^{-/-}$: 4.6 ± 0.3%; A5-RYR2$^{-/-}$: 3.6 ± 0.3%; **Figures 2D,F,G**), suggesting that the lower cell number in RYR2$^{-/-}$-iPSC-CMs at week 10 is not due to a change in the cell proliferation capacity. Next, we performed the MTT assay to compare the cellular metabolic activity of Ctrl- and RYR2$^{-/-}$-iPSC-CMs, which reflects the number of viable cells presented. The results showed a significant reduction of cell viability in RYR2$^{-/-}$-iPSC-CMs compared to Ctrl-CMs (**Figure 2E**).

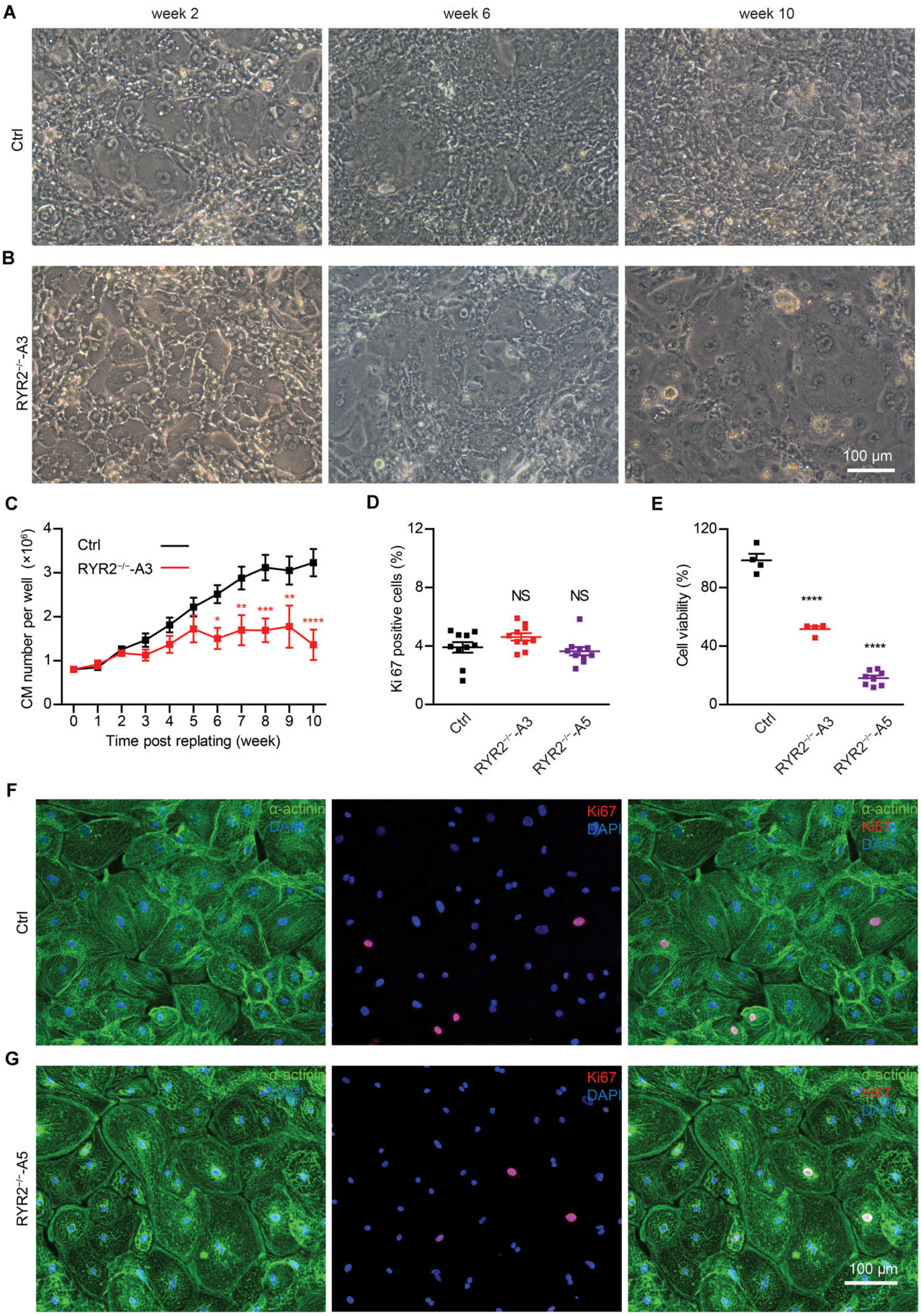

**FIGURE 2 |** Growth analysis of Ctrl- and $RYR2^{-/-}$-iPSC-CMs during long-term culture. **(A,B)** Bright-field images of Ctrl-iPSC-CMs **(A)** and A3 $RYR2^{-/-}$-iPSC-CMs **(B)** after replating at day 20 of differentiation. Ctrl-iPSC-CMs showed an increase in cell density from week 2 to week 10 post replating **(A)**, while $RYR2^{-/-}$-iPSC-CMs exhibited reduced cell density **(B)**. Scale bar, 100 μm. **(C)** Quantification of the cardiomyocyte numbers. Ctrl- and A3 $RYR2^{-/-}$-iPSC-CMs showed distinct growth curves during long-term cell culture. Ctrl-CMs from 2 different iPSC lines and 11 differentiation experiments (iBM76.1: $n = 6$ and iWTD2.1: $n = 5$) were analyzed. A3 $RYR2^{-/-}$-CMs from six differentiation experiments were used. $^{*}P < 0.05$, $^{**}P < 0.01$, $^{***}P < 0.001$, and $^{****}P < 0.0001$, $RYR2^{-/-}$ vs. Ctrl by using the two-way ANOVA with the Sidak's multiple comparison test. **(D)** Percentage of Ki67-positive CMs ($n = 10$ samples each for Ctrl, A3 and A5, $n = 300$–$400$ cells per sample counted). **(E)** Cell viability of Ctrl-, A3 and A5 $RYR2^{-/-}$-iPSC-CMs (Ctrl: $n = 4$ from two differentiation experiments; A3 $RYR2^{-/-}$: $n = 4$ from two differentiation experiments; A5 $RYR2^{-/-}$: $n = 8$ from two differentiation experiments). $^{****}P < 0.0001$ by using the one-way ANOVA with the Dunnett's multiple comparison test **(D,E)**. **(F,G)** Representative immunostaining of Ctrl- and $RYR2^{-/-}$-iPSC-CMs probing for Ki67 (red) and α-actinin (green). Cells were counterstained with DAPI (blue) to show the nucleus. Scale bar, 100 μm.

## Loss of RYR2 Does Not Affect the Expression of $Ca^{2+}$ Signaling-Associated Genes

To assess whether the RYR2 expression is lost in $RYR2^{-/-}$-iPSC-CMs, different anti-RYR2 antibodies were applied for western blot analysis. Whereas the mouse monoclonal anti-RYR2 antibody, produced by using canine cardiac Ryr2 as the immunogen, was used to detect the full-length protein of RYR2, the rabbit polyclonal anti-RYR2 antibody (SAB4502707) recognizes both the full-length and the truncated proteins by binding the N-terminal region before the PTC. Neither the full length nor the truncated proteins of RYR2 were detectable in A3 (**Figures 3A,B** and **Supplementary Figure 3A**) and A5 $RYR2^{-/-}$-iPSC-CMs (**Supplementary Figure 3B**), indicating the loss of functional RYR2 in A3 and A5 $RYR2^{-/-}$-iPSC-CMs. Immunofluorescence staining using anti-α-actinin and anti-RYR2 antibodies further confirmed the absence of RYR2 in A3 and A5 $RYR2^{-/-}$-iPSC-CMs (**Figure 3D**). However, the *RYR2* mRNA levels were not altered in A3 and A5 $RYR2^{-/-}$-iPSC-CMs compared to Ctrl-iPSC-CMs (**Figure 4A** and **Supplementary Figure 3C**). To investigate whether the absence of the truncated RYR2 in $RYR2^{-/-}$-iPSC-CMs might be the result of protein degradation, isoprenaline-stimulated Ctrl- and $RYR2^{-/-}$-iPSC-CMs were treated with MG132 (10 μM for 24 h) to inhibit the activity of the proteasome and with bafilomycin A1 (BafA1, 100 nM for 6 h) to inhibit the fusion of autophagosomes with lysosomes. Interference of the two major protein degradation pathways did not result in the detection of degraded RYR2 proteins in both A3 (**Figure 3C**) and A5 $RYR2^{-/-}$-iPSC-CMs (**Supplementary Figure 3D**), suggesting that nonsense-mediated mRNA decay leads to no translation of the truncated RYR2 protein in $RYR2^{-/-}$-iPSC-CMs.

Next, we evaluated the impact of loss of RYR2 on the expression of other cardiac $Ca^{2+}$ signaling-associated genes in $RYR2^{-/-}$-iPSC-CMs, such as genes encoding the cardiac IP3R types 1 and 2 (*IP3R1*, *IP3R2*) and the voltage-gated calcium channel subunit alpha-1C (*CACNA1C*). No tendency of increased or decreased expression of tested genes was observed in $RYR2^{-/-}$-iPSC-CMs in comparison to their corresponding Ctrl-iPSC-CMs (**Figure 4A** and **Supplementary Figure 3C**). However, as $RYR2^{-/-}$-iPSC-CMs remained the ability to spontaneously contract, we hypothesized that RYR2 may not be the only channel promoting intracellular calcium release. To verify potential compensatory mechanisms in response to loss of RYR2, we studied the expression of several $Ca^{2+}$-regulation related proteins. Consistent with *IP3R* mRNA levels, western blot analysis revealed no differences in IP3R protein expression in $RYR2^{-/-}$-iPSC-CMs compared to Ctrl-iPSC-CMs. In addition, we detected no significant changes in the protein expression of SERCA2A and NCX1 between Ctrl- and $RYR2^{-/-}$-iPSC-CMs (**Figures 4B–E**). To study the distribution of IP3R in iPSC-CMs, we conducted immunostaining by using antibodies against IP3R and sarcomeric α-actinin (**Figure 4F**). IP3R was expressed throughout the cytosol (**Figure 4F** middle) and partially co-localized with sarcomeric α-actinin (**Figure 4F** right). The perinuclear region displayed an intensive expression of IP3R. We did not observed differences in the distribution of IP3R between Ctrl- and $RYR2^{-/-}$-iPSC-CMs.

## Loss of RYR2 Results in Significant Reduction of Spontaneous Release of $Ca^{2+}$ Sparks in $RYR2^{-/-}$-iPSC-CMs

To determine functional consequences of the loss of RYR2, $Ca^{2+}$ sparks were measured in Ctrl- and $RYR2^{-/-}$-iPSC-CMs after pacing at 0.25 Hz, which were pre-treated with 100 nM isoprenaline to activate the β-adrenergic signaling and to promote the occurrence of $Ca^{2+}$ sparks. In Ctrl-iPSC-CMs, typical $Ca^{2+}$ sparks occurred randomly throughout the cell (**Figure 5A**). In contrast, $Ca^{2+}$ sparks appeared rarely in $RYR2^{-/-}$-iPSC-CMs (**Figure 5B**) and showed a significantly lower frequency with smaller amplitude ($\Delta F/F_0$) compared to Ctrl-iPSC-CMs (**Figure 5C**). Additionally, $RYR2^{-/-}$-iPSC-CMs showed significantly reduced FDHM and FWHM, indicating smaller sizes of the released $Ca^{2+}$ sparks in $RYR2^{-/-}$-iPSC-CMs compared to Ctrl-iPSC-CMs. This led to a 95.7 and 94.7% reduction of spontaneous SR $Ca^{2+}$ leak in A3 and A5 $RYR2^{-/-}$-iPSC-CMs, respectively, compared to Ctrl-iPSC-CMs (**Figure 5C**). These data indicate that RYR2 plays a major role in spontaneous $Ca^{2+}$ leak from the SR at diastole. The remaining but smaller $Ca^{2+}$ sparks detected in $RYR2^{-/-}$-iPSC-CMs suggest the existence of some other $Ca^{2+}$ regulatory channels, which may mediate $Ca^{2+}$ sparks independent of RYR2.

## $RYR2^{-/-}$-iPSC-CMs Show Abnormal $Ca^{2+}$ Transients Compared to Ctrl-iPSC-CMs

To further investigate whether normal $Ca^{2+}$ homeostasis was affected in $RYR2^{-/-}$-iPSC-CMs, spontaneous $Ca^{2+}$ transients were assessed. Although we detected spontaneous $Ca^{2+}$ transients in both Ctrl- and $RYR2^{-/-}$-iPSC-CMs (**Figure 5D**), 54.1 ± 6.1% of A3 and 65.7 ± 9.6% of A5 $RYR2^{-/-}$-iPSC-CMs showed abnormalities in $Ca^{2+}$ handling (**Figures 5E,F**). These irregularities were mainly detectable as highly frequent $Ca^{2+}$ release events at elevated diastolic $Ca^{2+}$ levels (**Figure 5E**), which were not observed in Ctrl-iPSC-CMs. Furthermore, $RYR2^{-/-}$-iPSC-CMs showed significantly lower diastolic $Ca^{2+}$ levels, but no significant differences in systolic $Ca^{2+}$ levels and peak amplitude of $Ca^{2+}$ transients in comparison to Ctrl-iPSC-CMs (**Figure 5G** and **Supplementary Figure 3E**). We also observed a significant decrease in the frequency of $Ca^{2+}$ transients and an increase in the duration of $Ca^{2+}$ transients in $RYR2^{-/-}$-iPSC-CMs compared to Ctrl-iPSC-CMs (**Figure 5G** and **Supplementary Figure 3E**), indicating that loss of RYR2 results in reduced but prolonged contraction-relaxation cycles. Moreover, the time constant (tau) during the decay of $Ca^{2+}$ transients was significantly increased in $RYR2^{-/-}$-iPSC-CMs compared to Ctrl-iPSC-CMs (**Figure 5G** and **Supplementary Figure 3E**). By applying a field stimulation, we normalized the $Ca^{2+}$ cycling of Ctrl- and $RYR2^{-/-}$-iPSC-CMs to 0.5 Hz. Paced $Ca^{2+}$ transients in A3 $RYR2^{-/-}$-iPSC-CMs revealed a comparable peak amplitude (**Figures 5H,I**). However, the diastolic level of $Ca^{2+}$ transients after pacing was much higher

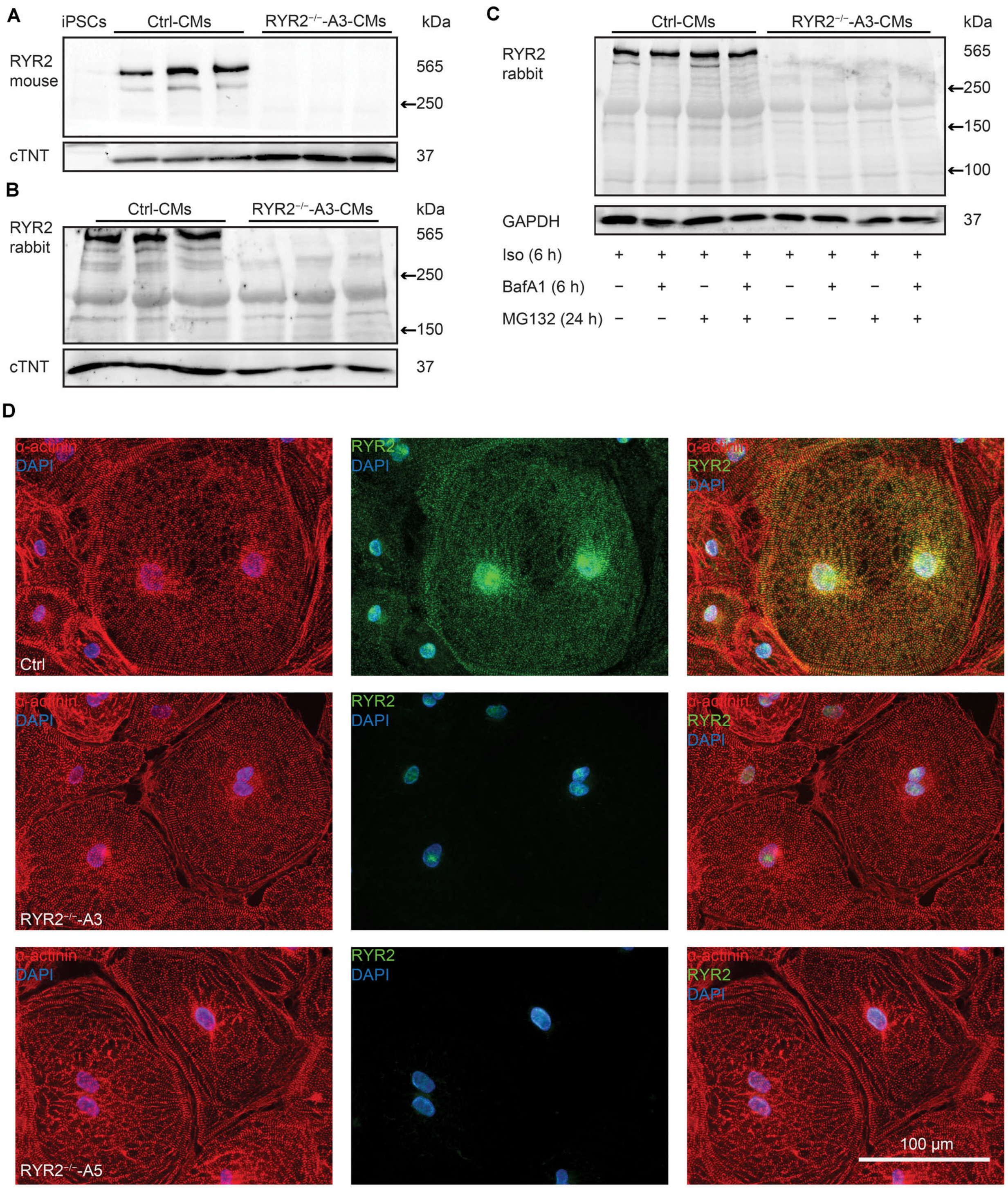

**FIGURE 3 |** Expression of RYR2 in 3-month-old Ctrl- and $RYR2^{-/-}$-iPSC-CMs. **(A)** Western blot analysis of the full-length RYR2 and cardiac troponin T (cTNT) in Ctrl- and A3 $RYR2^{-/-}$-iPSC-CMs (Ctrl: $n = 3$ and A3 $RYR2^{-/-}$: $n = 3$ independent differentiation experiments). **(B)** Western blot analysis showing protein expression of N-terminal RYR2 and cTNT in Ctrl- and A3 $RYR2^{-/-}$-iPSC-CMs (Ctrl: $n = 3$ and A3 $RYR2^{-/-}$: $n = 3$ independent differentiation experiments). **(C)** Representative western blot analysis of RYR2 in response to treatment with MG132 and/or Bafilomycin A (BafA1) in Ctrl- and $RYR2^{-/-}$-iPSC-CMs (Ctrl: $n = 3$, A3 $RYR2^{-/-}$: $n = 3$ independent differentiation experiments). No degraded RYR2 proteins were detected in $RYR2^{-/-}$-iPSC-CMs by inhibiting protein degradation with the proteasome and calpain inhibitor MG132 and the autophagy inhibitor BafA1. **(D)** Representative immunostaining of Ctrl- and $RYR2^{-/-}$-iPSC-CMs using antibodies against RYR2 (green) and α-actinin (red). The cells were counterstained with DAPI (blue) to show the nucleus. Scale bar, 100 μm.

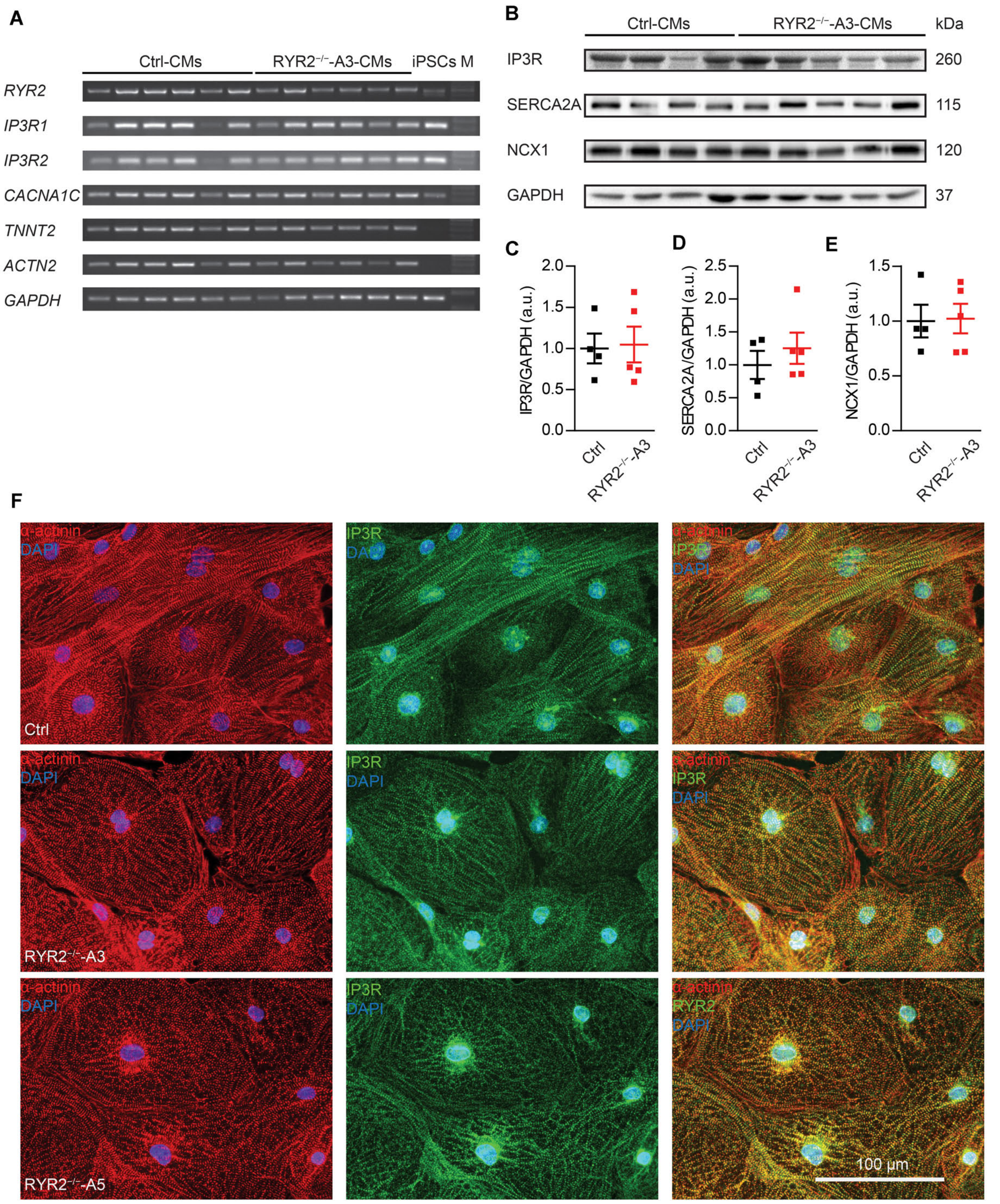

**FIGURE 4 |** Expression of markers involved in $Ca^{2+}$ signaling in $RYR2^{-/-}$-iPSC-CMs compared to Ctrl-iPSC-CMs. **(A)** Reverse transcription-PCR analyses showing mRNA expression of transcripts for $Ca^{2+}$ handling-related genes (*RYR2, IP3R1, IP3R2,* and *CACNA1C*), genes encoding sarcomeric proteins (*TNNT2* and *ACTN2*), and the housekeeping gene *GAPDH* in Ctrl- and A3 $RYR2^{-/-}$-iPSC-CMs (Ctrl: $n = 6$ and $RYR2^{-/-}$-A3: $n = 6$ different differentiation experiments). M: DNA molecular-weight size marker. **(B)** Western blot showing expression of $Ca^{2+}$ handling-associated proteins (IP3R, SERCA2A, and NCX1) in both Ctrl- and A3 $RYR2^{-/-}$-iPSC-CMs. **(C–E)** Scatter dot plot showing protein levels of IP3R **(C)**, SERCA2A **(D)**, and NCX1 **(E)** normalized to GAPDH between Ctrl- and A3 $RYR2^{-/-}$-iPSC-CMs (Ctrl: $n = 4$ and A3 $RYR2^{-/-}$: $n = 5$ different differentiation experiments). **(F)** Representative immunostaining of Ctrl- and $RYR2^{-/-}$-iPSC-CMs for IP3R (green) and α-actinin (red). Cells were counterstained with DAPI (blue). Scale bar, 100 μm.

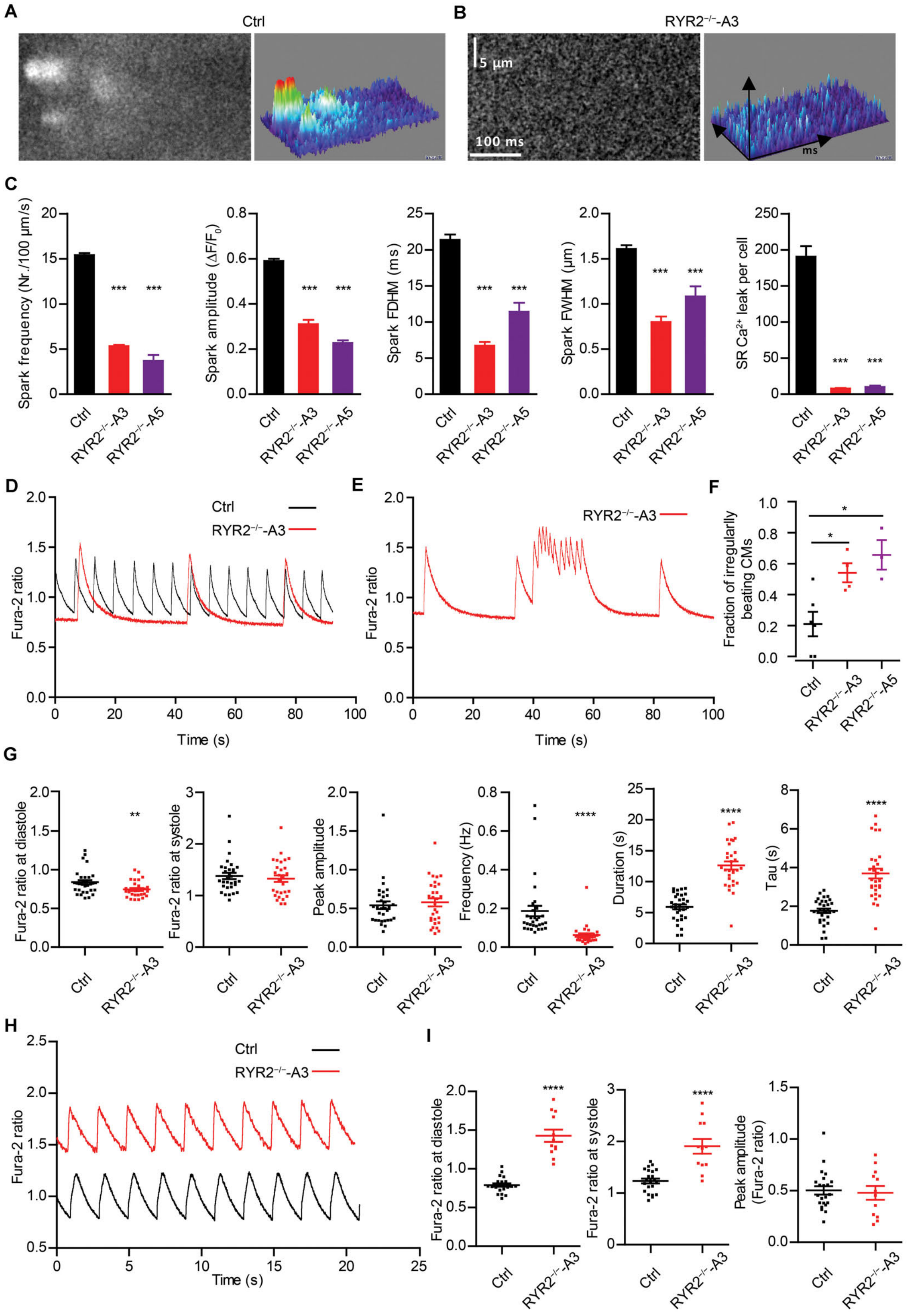

**FIGURE 5 |** Continued

**FIGURE 5 |** RYR2$^{-/-}$-iPSC-CMs showed defective Ca$^{2+}$ cycling. **(A,B)** Ca$^{2+}$ sparks in Ctrl- and A3 RYR2$^{-/-}$-iPSC-CMs during β-adrenergic stimulation. **(A)** Spontaneous Ca$^{2+}$ spark images in Ctrl-iPSC-CMs (**A**; $n_{cell}$ = 358, $n_{spark}$ = 1521) and A3 RYR2$^{-/-}$-iPSC-CMs (**B**; $n_{cell}$ = 21, $n_{spark}$ = 38) after treatment with 100 nM isoproterenol. Both Ctrl- and RYR2$^{-/-}$-iPSC-CMs were paced at 0.25 Hz. **(C)** Bar graphs summarize the key parameters of Ca$^{2+}$ sparks in mean ± SEM values for Ctrl- and RYR2$^{-/-}$-iPSC-CMs: spark frequency (100 $\mu m^{-1} s^{-1}$), amplitude ($\Delta F/F_0$), FDHM (ms), FWHM (μm) and relative SR Ca$^{2+}$ leak. For A5 RYR2$^{-/-}$-iPSC-CMs, $n_{cell}$ = 12, $n_{spark}$ = 20 were analyzed. ***$P < 0.001$ by using the one-way ANOVA with the Dunnett's multiple comparison test. **(D)** Representative Ca$^{2+}$ transients in spontaneously beating Ctrl- and A3 RYR2$^{-/-}$-iPSC-CMs. **(E)** Representative abnormal Ca$^{2+}$ transients in A3 RYR2$^{-/-}$-iPSC-CMs. **(F)** Fractions of irregularly beating Ctrl- and A3- and A5 RYR2$^{-/-}$-iPSC-CMs (Ctrl: CMs from six differentiation experiments; A3 RYR2$^{-/-}$: CMs from four differentiation experiments; A5 RYR2$^{-/-}$: CMs from three differentiation experiments. $n > 15$ cells per experiment). *$P < 0.05$ by using the one-way ANOVA with the Dunnett's multiple comparison test. **(G)** Scatter dot plot showing the diastolic Ca$^{2+}$ levels, systolic Ca$^{2+}$ levels, peak amplitude, frequency and duration of Ca$^{2+}$ transients, as well as the time constant during the decay of Ca$^{2+}$ transients (tau) in Ctrl- and A3 RYR2$^{-/-}$-iPSC-CMs (Ctrl: $n$ = 31 cells from five differentiation experiments; A3 RYR2$^{-/-}$: $n$ = 32 cells from three differentiation experiments). **(H)** Representative Ca$^{2+}$ transients in Ctrl- and A3 RYR2$^{-/-}$-iPSC-CMs under a normalized field stimulation at a pacing frequency of 0.5 Hz. **(I)** Scatter dot plot showing the diastolic Ca$^{2+}$ levels, systolic Ca$^{2+}$ levels and peak amplitude of paced Ca$^{2+}$ transients in Ctrl- and A3 RYR2$^{-/-}$-iPSC-CMs (Ctrl: $n$ = 22 cells from three differentiation experiments; A3 RYR2$^{-/-}$: $n$ = 12 cells from two differentiation experiments). **$P < 0.01$; ****$P < 0.0001$ RYR2$^{-/-}$ vs. Ctrl by using the unpaired Student's *t*-test.

in RYR2$^{-/-}$-iPSC-CMs than in non-paced RYR2$^{-/-}$-iPSC-CMs as well as in Ctrl-iPSC-CMs (**Figures 5H,I**). Together with the increased time constant of spontaneous Ca$^{2+}$ transients in RYR2$^{-/-}$-iPSC-CMs (**Figure 5G** and **Supplementary Figure 3E**), these data suggest that the efficiency of Ca$^{2+}$ removal from the cytosol either by reuptake into the SR or by pumping Ca$^{2+}$ out of the cell is lower in RYR2$^{-/-}$-iPSC-CMs than in Ctrl-iPSC-CMs.

## The Sensitivity of RYR2$^{-/-}$-iPSC-CMs to Extracellular Ca$^{2+}$ and to Caffeine Is Changed

To evaluate the relationship between extracellular Ca$^{2+}$ ($[Ca^{2+}]_o$) levels and the occurrence of Ca$^{2+}$ transients in iPSC-CMs, we measured Ca$^{2+}$ events under different $[Ca^{2+}]_o$ concentrations using the fluorescent Ca$^{2+}$ dye Fura-2 in combination with Ca$^{2+}$ imaging. To this end, spontaneously beating iPSC-CMs were first washed with Tyrode's solution containing no Ca$^{2+}$ until no spontaneous Ca$^{2+}$ transient was detectable. Afterward, cytosolic Ca$^{2+}$ changes were monitored in response to continuous perfusion with increasing Ca$^{2+}$ concentrations (from 0 to 2.0 mM) and addition of 10 mM caffeine at the end. To quantify the fraction of Ca$^{2+}$-oscillating cells for each condition, the number of iPSC-CMs, which displayed spontaneous Ca$^{2+}$ transients at each $[Ca^{2+}]_o$ concentration was determined. As shown in **Figure 6A**, no Ca$^{2+}$ transients in Ctrl-iPSC-CMs were detected with $[Ca^{2+}]_o$ lower than 0.5 mM. Raising $[Ca^{2+}]_o$ concentrations stepwise from 0.3 to 2.0 mM concomitantly increased the amplitude and frequency of Ca$^{2+}$ transients in Ctrl-iPSC-CMs (**Figures 6A,C**), as well as the fraction of Ca$^{2+}$-oscillating cells (**Figure 6D**). In contrast, RYR2$^{-/-}$-iPSC-CMs responded differently to increased $[Ca^{2+}]_o$ concentrations (**Figures 6B–D**). While 6 out of 16 A3 RYR2$^{-/-}$-iPSC-CMs did not display any Ca$^{2+}$ transients from 0.1 to 2 mM $[Ca^{2+}]_o$, the remaining 10 cells revealed Ca$^{2+}$ transients already at 0.1 or 0.2 mM $[Ca^{2+}]_o$ (**Figure 6B**). Similar results were observed in A5 RYR2$^{-/-}$-iPSC-CMs; 5 out of 12 cells showed no Ca$^{2+}$ transients under all conditions while the remaining 7 cells exhibited Ca$^{2+}$ transients already at 0.1 mM $[Ca^{2+}]_o$ (**Figure 6D**). Furthermore, both A3 and A5 RYR2$^{-/-}$-iPSC-CMs showed no caffeine-induced Ca$^{2+}$ release as observed in Ctrl-iPSC-CMs (**Figures 6A,B**), which confirms the absence of functional RYR2.

Caffeine, a pharmacological agonist of RYR2 (Porta et al., 2011), is commonly used to monitor RYR2-mediated Ca$^{2+}$ release. To determine the impact of loss of RYR2 in iPSC-CMs, we measured cytosolic Ca$^{2+}$ levels in Ctrl- and RYR2$^{-/-}$-iPSC-CMs before and after continuously supplementing caffeine with increasing concentrations (from 0.025 to 5.0 mM). As shown in **Figure 6E**, low concentration of caffeine (0.025 mM) resulted in a reduction of cytosolic Ca$^{2+}$ levels in Ctrl-iPSC-CMs, while the amplitudes of caffeine-induced Ca$^{2+}$ release progressively increased under the caffeine treatment at concentrations from 0.05 to 2.5 mM and declined at the concentration of 5 mM (**Figure 6F**). We believe that the decrease in caffeine-induced Ca$^{2+}$ release at 5 mM caffeine might be the result of depletion of internal Ca$^{2+}$ stores in the SR due to previous caffeine supplementation. In contrast to Ctrl-iPSC-CMs, caffeine treatment did not result in any change of cytosolic Ca$^{2+}$ levels in both A3 and A5 RYR2$^{-/-}$-iPSC-CMs (**Figures 6E,F**), indicating that no functional RYR2 is present in RYR2$^{-/-}$-iPSC-CMs and that Ca$^{2+}$ transients observed in RYR2$^{-/-}$-iPSC-CMs (**Figures 5D,E**, **6B**) are not caused by Ca$^{2+}$ release via RYR2, rather via other mechanisms.

## IP3R-Mediated Ca$^{2+}$ Release and SERCA-Mediated SR Ca$^{2+}$ Uptake Are Required for the Generation of Ca$^{2+}$ Transients in RYR2$^{-/-}$-iPSC-CMs

Given that RYR2$^{-/-}$-iPSC-CMs can spontaneously beat and release Ca$^{2+}$ sparks and Ca$^{2+}$transients without RYR2 protein expression, we believe that these cells possess an alternative Ca$^{2+}$ regulatory mechanism to compensate for the missing RYR2. IP3R-involved Ca$^{2+}$ signaling has been discovered to play an important role during the process of cardiac development (Rosemblit et al., 1999; Poindexter et al., 2001). Therefore, we studied the effect of IP3R blockade on Ca$^{2+}$ handling in iPSC-CMs. To this end, spontaneous Ca$^{2+}$ transients in Ctrl- and A3 RYR2$^{-/-}$-iPSC-CMs were measured before and after the application of 20 μM 2-APB. As shown in **Figures 7A–C**, 2-APB treatment for 500 s completely and reversibly blocked all Ca$^{2+}$ transients in 10 out of 14 tested A3 RYR2$^{-/-}$-iPSC-CMs (**Figures 7B,C**), while Ctrl-iPSC-CMs (10 out of

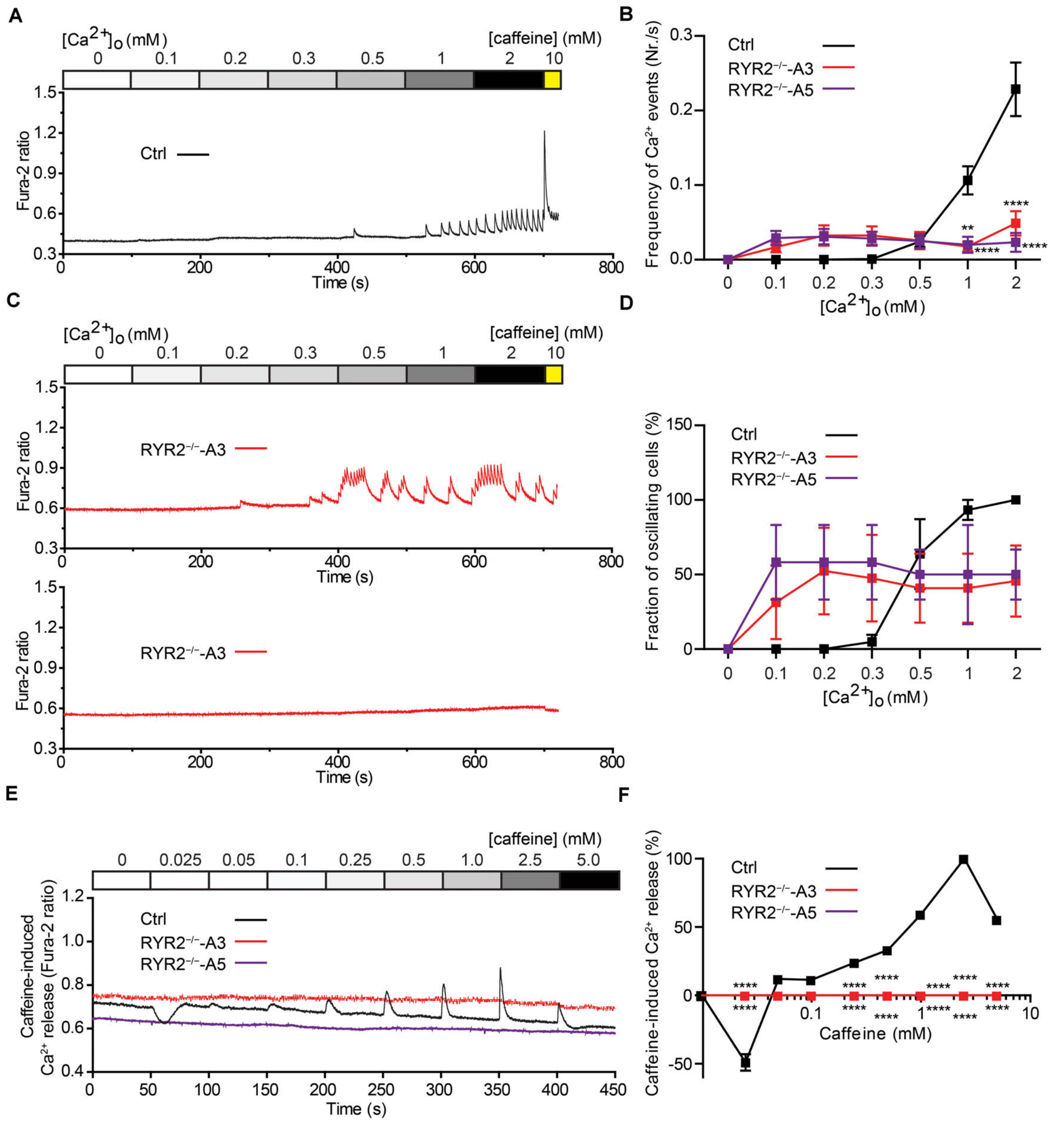

**FIGURE 6 |** Sensitivity of Ctrl- and $RYR2^{-/-}$-iPSC-CMs to extracellular calcium and caffeine. **(A,B)** Cytosolic $Ca^{2+}$ dynamics in Ctrl-iPSC-CMs **(A)** and A3 $RYR2^{-/-}$-iPSC-CMs **(B)** perfused with increasing concentrations of extracellular $Ca^{2+}$ ($[Ca^{2+}]_o$). Cytosolic $Ca^{2+}$ dynamics in A3 $RYR2^{-/-}$-iPSC-CMs **(B)** were inconsistent from cell to cell. **(C)** Frequency of $Ca^{2+}$ events detected in Ctrl- and $RYR2^{-/-}$-iPSC-CMs under different $[Ca^{2+}]_o$. **(D)** Percentage of CMs displaying $Ca^{2+}$ events under different $[Ca^{2+}]_o$ concentrations among the three groups (Ctrl: $n = 20$ cells from four differentiation experiments; A3 $RYR2^{-/-}$: $n = 15$ cells from three differentiation experiments; A5 $RYR2^{-/-}$: $n = 12$ cells from two differentiation experiments). **(E)** Representative traces of caffeine-induced $Ca^{2+}$ release in Ctrl- and $RYR2^{-/-}$-iPSC-CMs. **(F)** Relationship between $Ca^{2+}$ release and caffeine concentration in CMs from the two groups. The amplitude of each caffeine-induced $Ca^{2+}$ release was normalized to the maximum peak for each experiment (Ctrl: $n = 20$ cells from four differentiation experiments; A3 $RYR2^{-/-}$: $n = 6$ cells from two differentiation experiments; A5 $RYR2^{-/-}$: $n = 6$ cells from two differentiation experiments). $^{**}P < 0.01$, $^{****}P < 0.0001$ $RYR2^{-/-}$ vs. Ctrl by the two-way ANOVA with the Sidak's multiple comparison test.

13) displayed intensive but slightly smaller $Ca^{2+}$ transients (**Figures 7A,C**). Although 2-APB application decreased $Ca^{2+}$ transient amplitude in Ctrl-iPSC-CMs (**Figure 7D**), it did not reduce the beating frequency of these cells (**Figure 7E**). On the contrary, in A3 $RYR2^{-/-}$-iPSC-CMs, the amplitude and frequency of $Ca^{2+}$ transients during 2-APB treatment for 100∼300 s declined to 54.7 and 49.1%, respectively, whereas the inhibitory effects increased as treatment lasted longer (300–500 s): the amplitude and frequency decreased to 20.1 and 12.9%, respectively (**Figures 7D,E**). Previous studies reported that 2-APB is also a blocker of store-operated $Ca^{2+}$ entry independently of the function of IP3R (Iwasaki et al., 2001; Bootman et al., 2002).

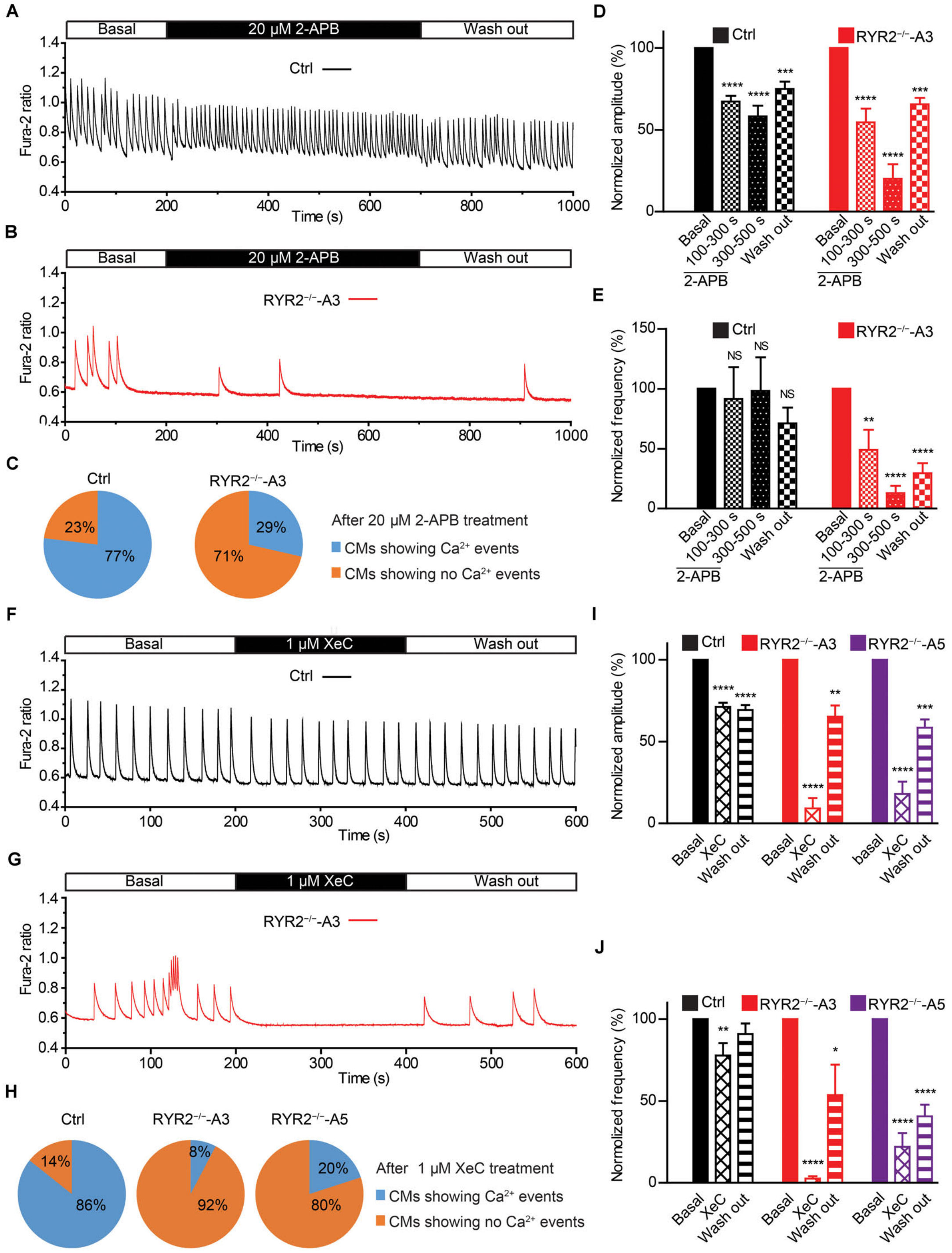

**FIGURE 7 |** Contributions of IP3R-mediated $Ca^{2+}$ release to spontaneous $Ca^{2+}$ transients in Ctrl- and $RYR2^{-/-}$-iPSC-CMs. **(A,B)** Representative cytosolic $Ca^{2+}$ dynamics in Ctrl- **(A)** and $RYR2^{-/-}$-iPSC-CMs **(B)** before and after the addition of IP3R antagonist 2-APB (20 μM), and after the washout of the drug. **(C)** Pie charts depict the percentage of cells maintaining $Ca^{2+}$ transients after the treatment with 2-APB for 500 s. **(D,E)** Changes of $Ca^{2+}$ transient amplitude **(D)** and frequency **(E)** after the treatment and the following removal of 2-APB, which were normalized to those from the same cell under the basal condition (Ctrl: $n = 13$ cells from three differentiation experiments; A3 $RYR2^{-/-}$: $n = 14$ cells from three differentiation experiments). **(F,G)** Representative cytosolic $Ca^{2+}$ dynamics in Ctrl- **(F)** and $RYR2^{-/-}$-iPSC-CMs **(G)** before and after the addition of IP3R inhibitor Xestospongin C (XeC;1 μM), and after the washout of the drug. **(H)** Pie charts depict the percentage of cells maintaining $Ca^{2+}$ transients after the treatment with XeC for 200 s. **(I,J)** Changes of $Ca^{2+}$ transient amplitude **(I)** and frequency **(J)** after the treatment and following the washout of XeC, which were normalized to those from the same cell under the basal condition (Ctrl: $n = 14$ cells from three differentiation experiments; A3 $RYR2^{-/-}$: $n = 13$ cells from three differentiation experiments; A5 $RYR2^{-/-}$: $n = 10$ cells from two differentiation experiments). $^{*}P < 0.05$; $^{**}P < 0.01$; $^{***}P < 0.001$;$^{****}P < 0.0001$ by using the one-way ANOVA with the Dunnett's multiple comparison test.

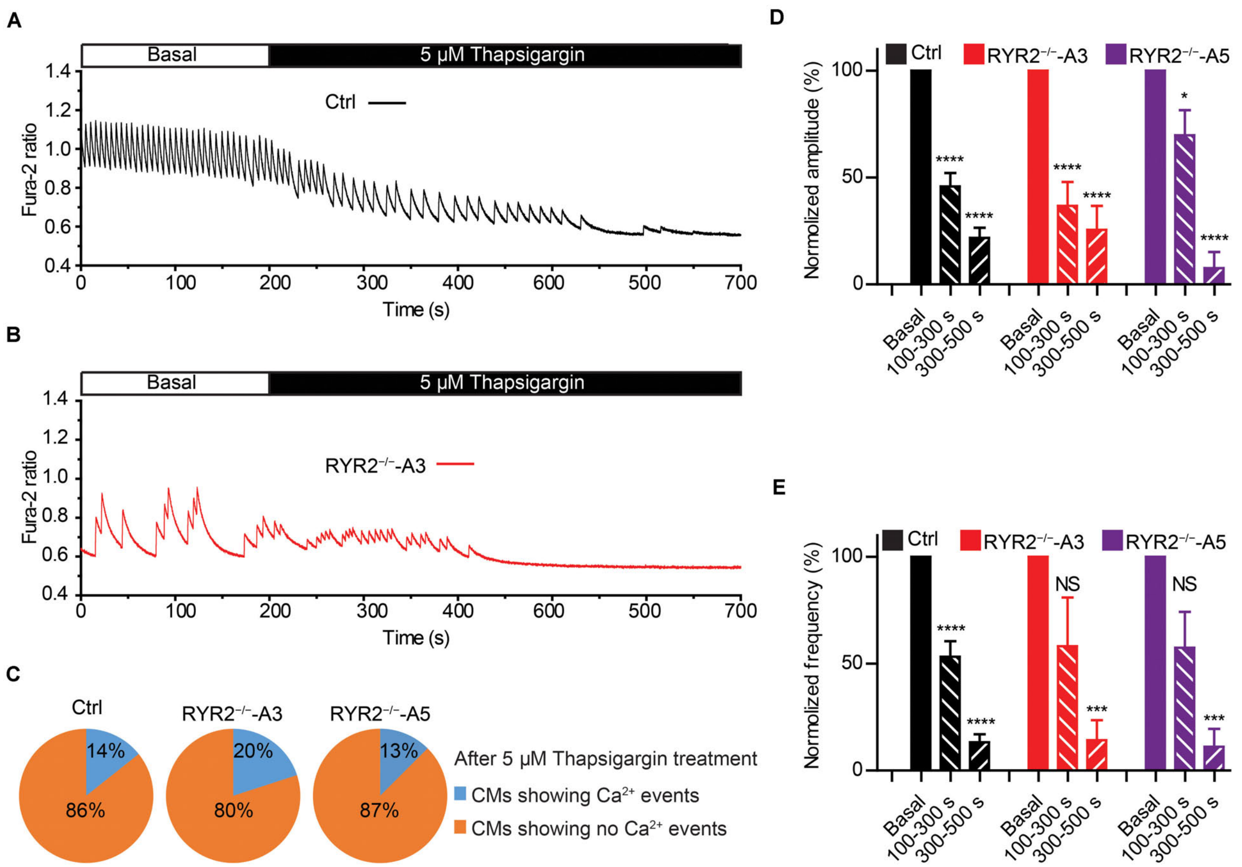

**FIGURE 8 |** Contributions of SERCA-mediated SR $Ca^{2+}$ uptake to spontaneous $Ca^{2+}$ transients in Ctrl- and RYR2$^{-/-}$-iPSC-CMs. **(A,B)** Representative cytosolic $Ca^{2+}$ dynamics in Ctrl- **(A)** and RYR2$^{-/-}$-iPSC-CMs **(B)** before and after the addition of SERCA inhibitor thapsigargin (5 µM). **(C)** Pie charts depict the percentage of cells maintaining $Ca^{2+}$ transients after the treatment with thapsigargin for 500 s. **(D,E)** Changes of $Ca^{2+}$ transient amplitude **(D)** and frequency **(E)** after the treatment with thapsigargin, which were normalized to those from the same cell under the basal condition. (Ctrl: $n = 14$ cells from three differentiation experiments; A3 RYR2$^{-/-}$: $n = 10$ cells from three differentiation experiments; A5 RYR2$^{-/-}$: $n = 8$ cells from two differentiation experiments). $^{*}P < 0.05$; $^{***}P < 0.001$; $^{****}P < 0.0001$ by using the one-way ANOVA with the Dunnett's multiple comparison test.

Therefore, we used the IP3R inhibitor Xestospongin C (XeC) to confirm our hypothesis. As shown in **Figures 7F–J**, the $Ca^{2+}$ transients in 12 out of 13 A3 and 8 out of 10 A5 RYR2$^{-/-}$-iPSC-CMs were completely and reversibly blocked after the addition of 1 µM XeC (**Figures 7G,H**), while the majority of Ctrl-iPSC-CMs (12 out of 14) still showed $Ca^{2+}$ transients (**Figures 7F,H**). Additionally, RYR2$^{-/-}$-iPSC-CMs showed a faster reaction to XeC (1 µM) than 2-APB (20 µM), as 200 s of XeC (1 µM) treatment was sufficient to block the $Ca^{2+}$ transients in these cells. These observations imply that an IP3-gated $Ca^{2+}$ pool is functional in iPSC-CMs, which is dominant in the modulation of $Ca^{2+}$ handling in RYR2$^{-/-}$-iPSC-CMs.

We next studied the contribution of another important $Ca^{2+}$ handling protein located on the SR membrane, namely SERCA. To this end, we recorded spontaneous $Ca^{2+}$ transients in Ctrl- and RYR2$^{-/-}$-iPSC-CMs before and after the application of 5 µM thapsigargin, a specific SERCA inhibitor. It turned out that thapsigargin treatment for 500 s was sufficient to block all $Ca^{2+}$ transients in most of Ctrl- (12 out of 14), A3 (8 out of 10) and A5 RYR2$^{-/-}$-iPSC-CMs (7 out of 8) in a time-dependent manner (**Figures 8A–E**). The amplitude and frequency of $Ca^{2+}$ transients in Ctrl-iPSC-CMs declined to 21.8 and 13.2%, respectively, during thapsigargin treatment for 300∼500 s, which was comparable with the changes found in RYR2$^{-/-}$-iPSC-CMs (**Figures 8D,E**). These findings indicate that the refilling of SR $Ca^{2+}$ content by SERCA pumps is the main mechanism in both Ctrl- and RYR2$^{-/-}$-iPSC-CMs with no significant differences.

## RYR2$^{-/-}$-iPSC-CMs Displayed Abnormal Action Potentials

It is well-known that LTCC are the main transporter for trans-sarcolemmal $Ca^{2+}$ influx responsible for the activation of RYR2. To understand whether loss of RYR2 function affects LTCC, we analyzed $I_{CaL}$ in Ctrl- and RYR2$^{-/-}$-iPSC-CMs. We found that $I_{CaL}$ density was significantly lower in RYR2$^{-/-}$-iPSC-CMs (**Figures 9A–D**). Compared to 3-month-old Ctrl-iPSC-CMs, both A3 and A5 RYR2$^{-/-}$-iPSC-CMs at the same age presented a reduction of peak current density at 0 mV by half (**Figure 9D**).

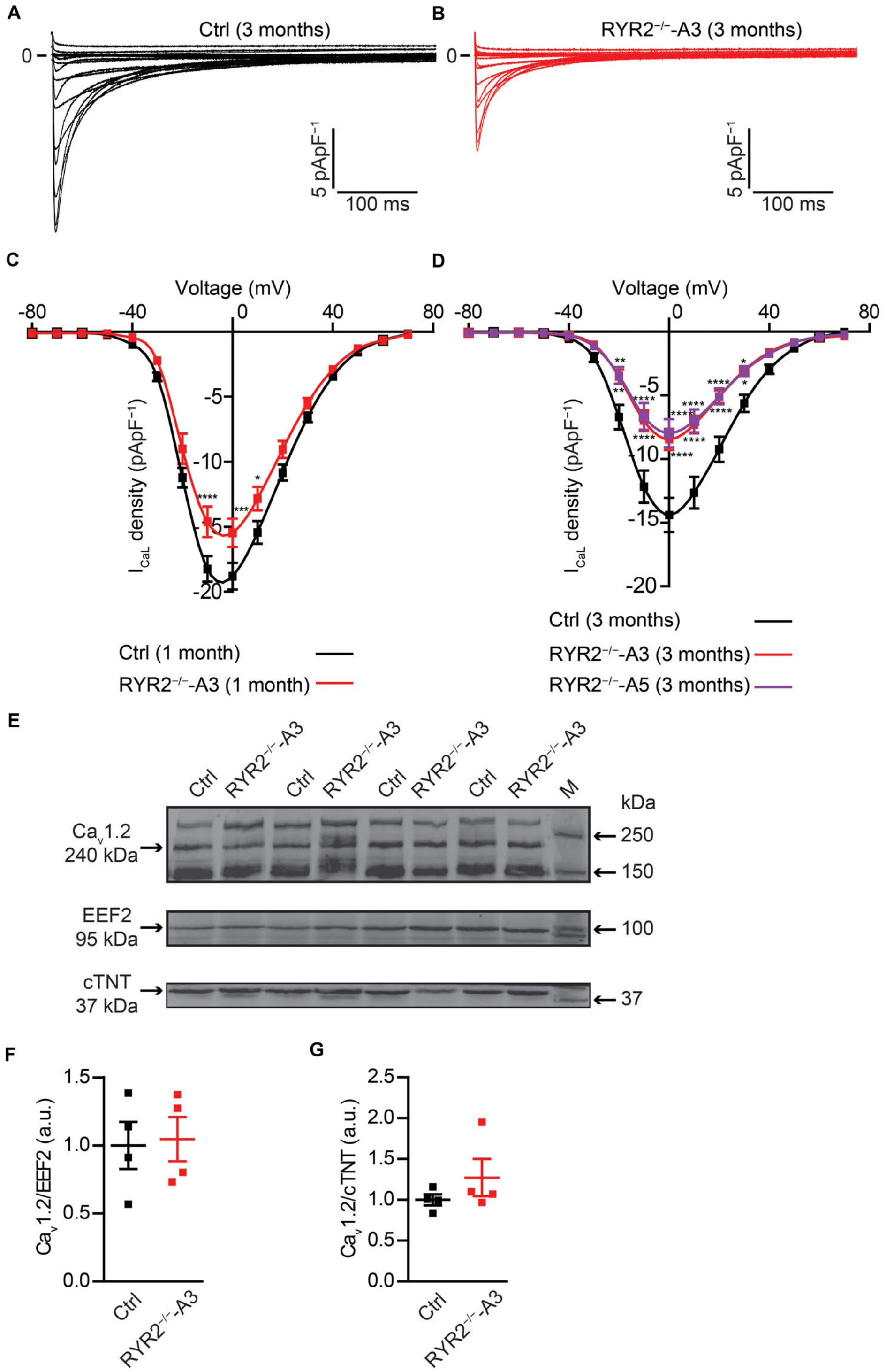

**FIGURE 9 |** Electrophysiological analysis of $I_{CaL}$ in Ctrl- and $RYR2^{-/-}$-iPSC-CMs. **(A,B)** Representative $I_{CaL}$ traces of 3-month-old Ctrl- **(A)** and A3 $RYR2^{-/-}$-iPSC-CMs **(B)**. **(C)** Average current-voltage (I–V) curves for peak $I_{CaL}$ in 1-month-old Ctrl- and $RYR2^{-/-}$-iPSC-CMs (Ctrl: $n = 12$ cells from three differentiation experiments; $RYR2^{-/-}$: $n = 15$ cells from two differentiation experiments). **(D)** Average current-voltage (I–V) curves for peak $I_{CaL}$ in 3-month-old Ctrl- and $RYR2^{-/-}$-iPSC-CMs (Ctrl: $n = 32$ cells from four differentiation experiments; A3 $RYR2^{-/-}$: $n = 24$ cells from three differentiation experiments; A5 $RYR2^{-/-}$: $n = 18$ cells from two differentiation experiments). $^*P < 0.05$; $^{**}P < 0.01$; $^{***}P < 0.001$; $^{****}P < 0.0001$ $RYR2^{-/-}$ vs. Ctrl by the two-way ANOVA with Sidak's multiple comparison test. **(E–G)** Western blot analysis of the voltage-dependent calcium channel alpha 1C subunit ($Ca_V1.2$) in Ctrl- and A3 $RYR2^{-/-}$-iPSC-CMs. Protein levels of $Ca_V1.2$ normalized to EEF2 **(F)** and cTNT **(G)** in Ctrl- and A3 $RYR2^{-/-}$-iPSC-CMs. Ctrl: $n = 4$ and A3 $RYR2^{-/-}$: $n = 4$ independent differentiation experiments.

No significant difference in *I-V* curve of $I_{CaL}$ between A3 and A5 $RYR2^{-/-}$-iPSC-CMs was detectable. In addition, a similar tendency was also found in 1-month-old $RYR2^{-/-}$-iPSC-CMs (**Figure 9C**). To investigate whether the loss of RYR2 has an effect on the protein expression of L-type $Ca^{2+}$ channel $Ca_v1.2$ in iPSC-CMs, we performed western blot analysis and found no differences between Ctrl- and $RYR2^{-/-}$-iPSC-CMs (**Figures 9E–G**). These data suggest that the modulation of the LTCC (for example, calmodulin binding, or phosphorylation) might be altered in $RYR2^{-/-}$-iPSC-CMs, leading to the inactivation of the channel or to a reduced open probability of the channel.

Calcium-induced calcium release is fundamental for excitation-contraction coupling, in which RYR2 plays an important role. To investigate if $RYR2^{-/-}$-iPSC-CMs are still able to generate cardiac action potentials (APs), we recorded APs of Ctrl- and $RYR2^{-/-}$-iPSC-CMs at single-cell level (**Figures 10A,B**) and analyzed main AP parameters, including resting membrane potential (RMP), AP amplitude (APA), upstroke velocity (Vmax), and AP frequency (**Figures 10C–F**). While Ctrl-iPSC-CMs showed regular spontaneous APs with typical ventricular-like AP morphology, APs in both A3 and A5 $RYR2^{-/-}$-iPSC-CMs remained mainly abnormal, as indicated by more positive RMP (**Figure 10C**), smaller APA (**Figure 10D**), reduced Vmax (**Figure 10E**), as well as lower and irregular beating frequency (**Figures 10B,F**).

## DISCUSSION

In this study, we have generated two iPSC-based *RYR2* knockout lines using the CRISPR/Cas9 gene-editing technology to study the physiological role of RYR2 in human iPSC-CMs. Our data reveal that (i) RYR2 is not essential for the early commitment of iPSCs into the cardiac lineage, while RYR2 is important for the viability and function of iPSC-CMs; (ii) RYR2-mediated $Ca^{2+}$ release is essential for the maintenance of normal $Ca^{2+}$ transients, which directly modulates the beating rate of iPSC-CMs; (iii) $Ca^{2+}$ handling in iPSC-CMs is sensitive to $[Ca^{2+}]_o$, which mainly depends on RYR2; (iv) in the absence of functional RYR2, $RYR2^{-/-}$-iPSC-CMs generate $Ca^{2+}$ sparks and transients via compensative IP3R-mediated pathway; and v) refilling of SR $Ca^{2+}$ store by SERCA pumps is required for the $Ca^{2+}$ cycling in $RYR2^{-/-}$-iPSC-CMs similar to Ctrl-iPSC-CMs. We conclude that SR $Ca^{2+}$ release via RYR2 is critical for the survival and whole-cell $Ca^{2+}$ handling of iPSC-CMs. When the function of RYR2 is lost, IP3R-mediated $Ca^{2+}$ release from the SR compensates the RYR2 function partially.

So far, the importance of RYR2 in developing fetal heart has mainly been investigated in animal models. As documented previously, the homozygous deletion of the mouse *Ryr2* gene is associated with embryonic cardiac arrest at around E10.5, even the looped heart tubes were formed at E8.5 and spontaneous heartbeat was observed at E9.5 (Takeshima et al., 1998). Cardiomyocyte-specific deletion of *Ryr2* in mice caused calpain-10 dependent programmed cell death *in vivo* (Bround et al., 2013). Moreover, homozygous deletion of exon-3 in mouse *Ryr2* gene led to embryonic lethality (Liu et al., 2014). In this study, we performed the first *in vitro* study to investigate the effect of homozygous knockout of *RYR2* on the survival and function of human iPSC-CMs that are structurally and functionally similar to human embryonic CMs (Kolanowski et al., 2017). Generated human $RYR2^{-/-}$-iPSCs retained stem cell morphology and pluripotency and were able to differentiate into spontaneously beating CMs, which is in line with the previous study using $Ryr2^{-/-}$mESCs (Yang et al., 2002). We detected no differences in the proliferation capacity of $RYR2^{-/-}$-iPSC-CMs compared to Ctrl-iPSC-CMs. However, $RYR2^{-/-}$-iPSC-CMs displayed a tremendously low cell viability during long-term culture, which resulted from increased cell death, indicating that RYR2 is critical for the survival of human embryonic CMs.

The most striking finding of the current study is that $RYR2^{-/-}$-iPSC-CMs developed an alternative mechanism for $Ca^{2+}$ handling to compensate for the missing of RYR2. In functional CMs, $Ca^{2+}$ enters the cell through LTCC and activates RYR2, which results in $Ca^{2+}$ release from the SR into the cytosol (Sham et al., 1995; Adachi-Akahane et al., 1996). It was reported that knockout of *Ryr2* in mESC-derived CMs resulted in the absence of $Ca^{2+}$ release from the SR and an increase of $I_{CaL}$ (Fu et al., 2006). Inhibition of SERCA by thapsigargin hardly affected the dynamics of $Ca^{2+}$ transients in both *Ryr2*$^{-/-}$ mESC-CMs and embryonic *Ryr2*$^{-/-}$ CMs (Liu et al., 2002; Guo and Yang, 2009). $Ca^{2+}$ transients and CM contraction in the early embryonic stage of the mouse were attained by a compensatory $Ca^{2+}$ influx into the cytosol via LTCC, accompanied by reduced $Ca^{2+}$ release-induced $Ca^{2+}$ channel inactivation (Liu et al., 2002; Guo and Yang, 2009). In contrast to these data, both 1- and 3-month-old $RYR2^{-/-}$-iPSC-CMs in the current study displayed reduced $I_{CaL}$, indicating that trans-sarcolemmal $Ca^{2+}$ influx via LTCC during each AP was lower in $RYR2^{-/-}$-iPSC-CMs compared to Ctrl-iPSC-CMs. Moreover, we noticed that treatment of iPSC-CMs with the SERCA inhibitor thapsigargin decreased the amplitude of $Ca^{2+}$ transients in both Ctrl- and $RYR2^{-/-}$-iPSC-CMs in a similar time-dependent manner, resulting in a complete inhibition of $Ca^{2+}$ transients over long time treatment. Therefore, we assume that the differences observed between human iPSC-CMs and mESC-CMs might be a result of different species. Interestingly, a recent study demonstrated that mitochondrial $Ca^{2+}$ flux modulates the spontaneous electrical activity in *Ryr2*$^{-/-}$ mESC-CMs, which depends on IP3R-mediated SR $Ca^{2+}$ release (Xie et al., 2018).

IP3R shares structural and functional similarities to RYRs. IP3-operated releasable $Ca^{2+}$ store has been demonstrated to be expressed and functional in human ESC- and iPSC-CMs (Satin et al., 2008; Sedan et al., 2008; Itzhaki et al., 2011). In our study, although IP3R gene and protein expression was not altered in $RYR2^{-/-}$-iPSC-CMs, we discovered an increased sensitivity to the IP3R inhibitors 2-APB and XeC in iPSC-CMs. Treatment of Ctrl-iPSC-CMs with 20 μM 2-APB or 1 μM XeC, respectively, showed minor or nearly no effect on the $Ca^{2+}$ transient frequency, while both inhibitors completely and reversibly blocked all $Ca^{2+}$ events in more than 70% $RYR2^{-/-}$-iPSC-CMs. These data demonstrate that the dependency of iPSC-CMs on IP3R-mediated $Ca^{2+}$ release is

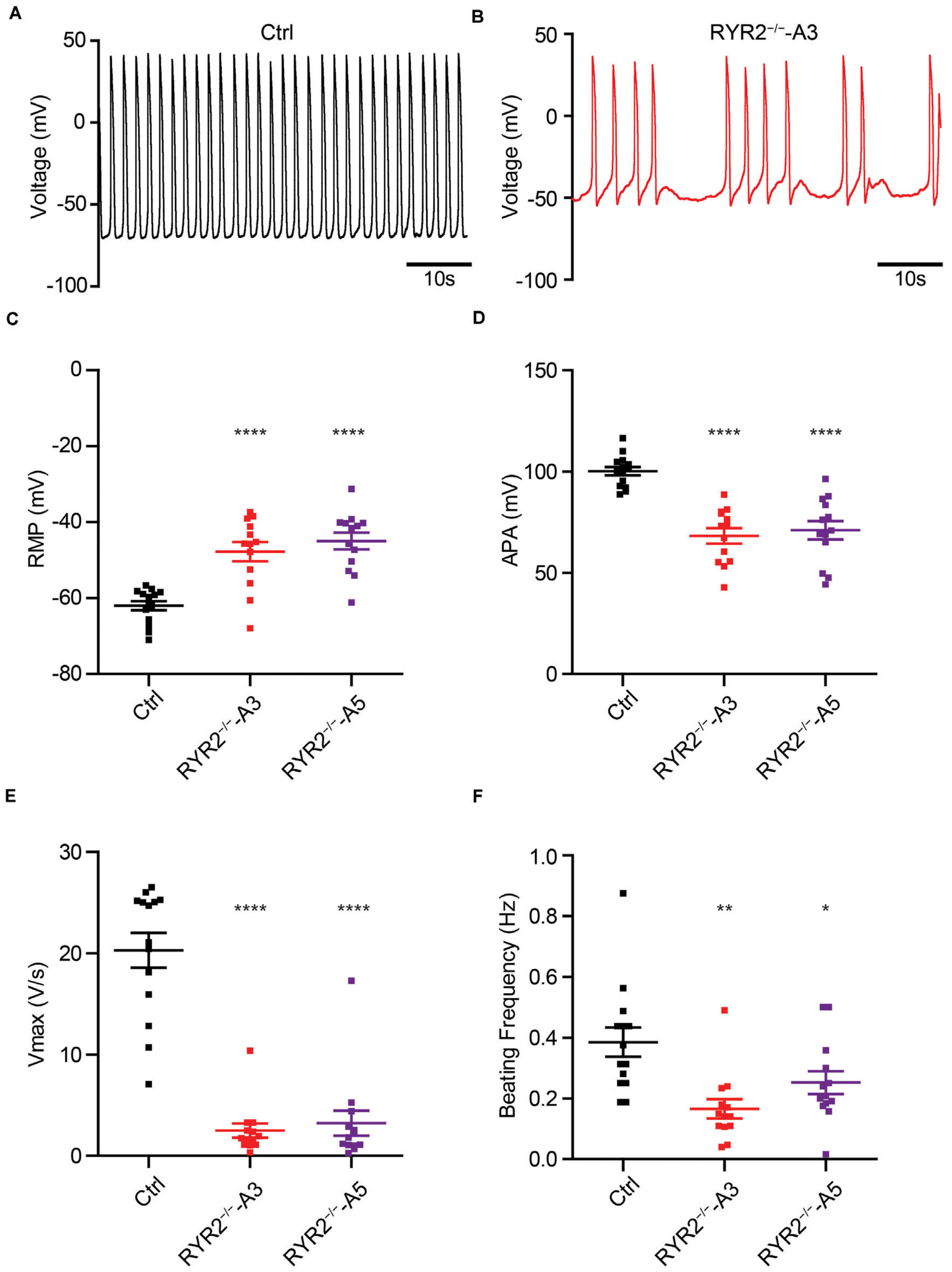

**FIGURE 10 |** Analysis of action potentials in Ctrl- and $RYR2^{-/-}$-iPSC-CMs. **(A,B)** Representative traces of APs revealed normal beating rhythm in Ctrl-iPSC-CMs **(A)** and arrhythmic beating in A3 $RYR2^{-/-}$-iPSC-CMs **(B)**. **(C–F)** Scatter dot plot comparing RMP **(C)**, APA **(D)**, maximal upstroke velocity $V_{max}$ **(E)**, and beating frequency **(F)** between Ctrl- and $RYR2^{-/-}$-iPSC-CMs (Ctrl: $n = 12$ cells from three differentiation experiments; A3 $RYR2^{-/-}$: $n = 13$ cells from two differentiation experiments; A5 $RYR2^{-/-}$: $n = 13$ cells from two differentiation experiments). $^*P < 0.05$; $^{**}P < 0.01$; $^{***}P < 0.001$; $^{****}P < 0.0001$ by the one-way ANOVA with the Dunnett's multiple comparison test.

significantly strengthened in the absence of functional RYR2. The finding of declined $Ca^{2+}$ transient amplitude in Ctrl-iPSC-CMs after 2-APB application is consistent with a previous report showing that IP3-releasable $Ca^{2+}$ pool contributes to whole-cell intracellular $Ca^{2+}$ transients in human iPSC-CMs (Itzhaki et al., 2011). To maintain sustainable $Ca^{2+}$ cycling, released $Ca^{2+}$ must be removed from the cytosol. In adult human CMs, 70% of cytosolic $Ca^{2+}$ during CM contraction is pumped back to the SR via SERCA to decrease intracellular $Ca^{2+}$ level and to regulate SR $Ca^{2+}$ load (Bers, 2002). SERCA-mediated $Ca^{2+}$ uptake is required for $Ca^{2+}$ handling in human iPSC-CMs (Itzhaki et al., 2011). These findings indicate that IP3R-mediated $Ca^{2+}$ release and SERCA-mediated SR $Ca^{2+}$ uptake are one of the major compensatory mechanisms for $Ca^{2+}$ handling in human CMs when the RYR2 function is lost. Future studies should investigate whether IP3R-dependent mitochondrial $Ca^{2+}$ flux modulates spontaneous electrical activity in human RYR2$^{-/-}$-iPSC-CMs and whether IP3R-mediated nuclear $Ca^{2+}$ signaling is involved in the activation of nuclear signal transduction for CM survival (Garcia and Boehning, 2017). Previous studies demonstrated that the store-operated calcium entry (SOCE) is present in embryonic cardiomyocytes and induces significant rise in $Ca^{2+}$ entry when the depletion of SR $Ca^{2+}$ stores occurs (Huang et al., 2006; Avila-Medina et al., 2018). In the future, it is also necessary to figure out whether SOCE plays an important role in $Ca^{2+}$ handling in human CMs lacking functional RYR2, either by abolishing the SOCE response with known SOCE inhibitors (BTP-2 and SKF-96365) or by targeted knockdown of Orai1 with RNAi in RYR2$^{-/-}$-iPSCs.

In the present study, we identified abnormalities of $Ca^{2+}$ transients in more than 50% of RYR2$^{-/-}$-iPSC-CMs. The abnormal $Ca^{2+}$ transients were found only in a small number of Ctrl-iPSC-CMs, which is consistent with the results of other studies (Maizels et al., 2017) and may be explained by an inhomogeneous maturity of iPSC-CMs (Ronaldson-Bouchard et al., 2018). Calcium spark, an elementary event of $Ca^{2+}$ release from SR, is believed to be mainly mediated by the spontaneous opening of one or a few RYR2 channels and contributes to the diastolic $Ca^{2+}$ levels. In RYR2$^{-/-}$-iPSC-CMs, β-adrenergic stimulation induced less generation of $Ca^{2+}$ sparks with smaller size and amplitude compared to Ctrl-iPSC-CMs. This might explain the lower diastolic $Ca^{2+}$ levels observed in spontaneously beating RYR2$^{-/-}$-iPSC-CMs. Furthermore, $Ca^{2+}$ transients in RYR2$^{-/-}$-iPSC-CMs showed a comparable peak amplitude, but longer duration and slower tau compared to Ctrl-iPSC-CMs, suggesting that a higher amount of $Ca^{2+}$ in one $Ca^{2+}$ transient are released from the SR in RYR2$^{-/-}$-iPSC-CMs. When RYR2$^{-/-}$-iPSC-CMs are paced at 0.5 Hz, $Ca^{2+}$ transients displayed comparable morphology and similar peak amplitude, but significantly elevated diastolic and systolic $Ca^{2+}$ levels compared to Ctrl-iPSC-CMs. These findings suggest that $Ca^{2+}$ cannot be removed rapidly and efficiently from the cytosol. Given that the SERCA-mediated refilling of SR $Ca^{2+}$ is not significantly affected in RYR2$^{-/-}$-iPSC-CMs, future studies should focus on the investigation of other mechanisms for $Ca^{2+}$ removal from the cytosol, especially the function of NCX. Previous studies have shown that the majority of $Ca^{2+}$ removal (about 75%) is accomplished by SERCA2A and by the sarcolemmal NCX (about 25%) in human cardiomyocytes. Further studies should focus on the investigation of the localization and activity of NCX in RYR2$^{-/-}$-iPSC-CMs.

Since $Ca^{2+}$ plays a critical role in the formation of $Ca^{2+}$ transients, which are instrumental for subsequent cardiac contraction, we investigated the relationship between $[Ca^{2+}]_o$ levels and $Ca^{2+}$ transients in iPSC-CMs with RYR2 deficiency. Our results revealed that 3-month-old iPSC-CMs are sensitive toward $[Ca^{2+}]_o$ at 0.5 mM or higher, with increased frequency and amplitude of $Ca^{2+}$ transients, as well as increased fraction of $Ca^{2+}$-oscillating cells in response to elevated $[Ca^{2+}]_o$. These findings indicate a $Ca^{2+}$ concentration dependent opening of RYR2 in iPSC-CMs, which is in line with the previous studies showing that human embryonic kidney (HEK) 293 cells expressing wild-type RYR2 displayed $Ca^{2+}$ oscillations under $[Ca^{2+}]_o$ at 0.3 mM or higher and in a concentration dependent manner (Jiang et al., 2007). In contrast, RYR2$^{-/-}$-iPSC-CMs reacted differently to the gradually increased $[Ca^{2+}]_o$ concentrations, showing $Ca^{2+}$ transients already at very low $[Ca^{2+}]_o$ concentrations (0.1–0.2 mM), suggesting the opening of IP3R occurred at lower intracellular $Ca^{2+}$ concentration than RYR2. In RYR2$^{-/-}$-iPSC-CMs, spontaneous $Ca^{2+}$ transients with lower frequency in comparison to Ctrl-iPSC-CMs were detected, which is in line with the observation in Ryr2$^{-/-}$ mESC-CMs (Fu et al., 2006). Our data support the hypothesis by Korhonen et al. (2010) demonstrating that the developing CMs might lose the capability to generate homogeneous $Ca^{2+}$ signals at a high frequency in response to the deficiency of the functional $Ca^{2+}$ release channel RYR2. AP measurements revealed that loss of RYR2 resulted in a lower beating frequency in comparison to Ctrl-iPSC-CMs. These data are consistent with studies performed in mESC-derived CMs, showing similar decline in the beating frequency of Ryr2$^{-/-}$ mESC-derived CMs (Yang et al., 2002). In addition, cardiomyocyte-specific loss of Ryr2 in mice resulted in arrhythmogenic events, such as bradycardia and tachycardia (Bround et al., 2012). As RYR2$^{-/-}$-iPSC-CM also displayed disturbances in the rhythmicity, manifesting bradycardia, we believe that RYR2 is a critical player in the regulation of heart rate.

Furthermore, our study provides the first comprehensive assessment regarding the sensitivity of iPSC-CMs to caffeine, a pharmacological agonist of cardiac RYR2 $Ca^{2+}$ release channels. Continuously exposing Ctrl-iPSC-CMs to caffeine with increasing concentrations resulted in a series of cytosolic $Ca^{2+}$ changes, while low concentration of caffeine (0.025 mM) decreased cytosolic $Ca^{2+}$ levels. Under the stimulation of 0.025 mM caffeine, HEK 293 cells expressing wild-type RYR2 presented a caffeine-induced $Ca^{2+}$ release (Liu et al., 2010; Roston et al., 2017). This difference may be caused by the different expression and assembling of $Ca^{2+}$ handling elements in HEK cells compared to iPSC-CMs. Interestingly, HEK 293 cells transfected with wild-type RYR2 alone or with wild-type and I4855M mutant RYR2 together showed a slight decrease of cytosolic $Ca^{2+}$ levels at 0.025 mM caffeine (Liu et al., 2010; Roston et al., 2017), which were normally considered an artifact. However, this phenomenon was not found in RYR2$^{-/-}$-iPSC-CMs, suggesting that the decrease of cytosolic

$Ca^{2+}$ levels might be related to RYR2 opening. We assume that such a low concentration of caffeine might result in a small amount of $Ca^{2+}$ release from the SR in Ctrl-iPSC-CMs, which might reach a threshold of NCX activation, leading to slow extrusion of calcium from the cytosol via NCX. Further study should be performed to investigate whether the NCX inhibitor can block the reduction of cytosolic $Ca^{2+}$ levels at a low concentration of caffeine in Ctrl-iPSC-CMs. Importantly, no changes in cytosolic $Ca^{2+}$ levels were detected in $RYR2^{-/-}$-iPSC-CMs treated with caffeine at low or high concentrations, which indicate that IP3R-mediated SR $Ca^{2+}$ release in $RYR2^{-/-}$-iPSC-CMs is not sensitive to caffeine.

## CONCLUSION

In conclusion, we generated two homozygous $RYR2^{-/-}$-iPSC lines with normal capacity to differentiate into spontaneously beating CMs. However, $RYR2^{-/-}$-iPSC-CMs in long-term culture showed enhanced cell death, indicating that RYR2 is critical for the survival but less important for the initiation of contraction of iPSC-CMs. Moreover, our study demonstrates that RYR2 plays a vital role in the maintenance of rhythmic heart beating and normal $Ca^{2+}$ handling. Loss of functional RYR2 strengthens the dependency of iPSC-CMs on IP3R-related pathway, which combines with SERCA pumps to make critical contributions to the $Ca^{2+}$ cycling in $RYR2^{-/-}$-iPSC-CMs. As RYR2 is crucial for the development and function of CMs, the availability of human $RYR2^{-/-}$-iPSC lines represent a useful tool for the *in vitro* study of early human heart development and molecular mechanism of $Ca^{2+}$ cycling in human CMs.

## DATA AVAILABILITY STATEMENT

All datasets generated for this study are included in the article/**Supplementary Material**.

## ETHICS STATEMENT

The studies involving the use of human induced pluripotent stem cells were reviewed and approved by the Ethics Committee of the University Medical Center Göttingen (approval number: 21/1/11), and carried out in accordance with the approved guidelines. The patients/participants provided their written informed consent to participate in this study.

## AUTHOR CONTRIBUTIONS

XL, WL, and KG conceived the study and designed experiments, contributed to interpretation of the data, and wrote the manuscript. XL, WL, KK, SH, LC, AS, MP, and MS performed experiments and acquisition of the data. XL, WL, KK, SH, AS, MS, and KG analyzed the data. All authors contributed to the article and approved the submitted version.

## FUNDING

The authors would like to express great appreciation to the E-Rare-3 grant (JTC 2015) and the DFG (GU 595/3-1 and SFB1002 A04 to KG) for the financial support of this work. This work was also supported by the Free State of Saxony and the European Union EFRE (SAB projects "PhänoKard," "HERMES," and "PhenoCor" to KG) and the DFG Project Number 288034826–IRTG 2251: Immunological and Cellular Strategies in Metabolic Disease.

## ACKNOWLEDGMENTS

We thank Jessie Pöche, Konstanze Fischer, Ying Ulbricht, Judith Müller, and Romy Kempe for their excellent technical assistances and Silke Tulok (CFCI TU Dresden) for assistance in LSM microscopy. We acknowledge the support of the Open Access Funding by the Publication Fund of the TU Dresden.

## SUPPLEMENTARY MATERIAL

The Supplementary Material for this article can be found online at: https://www.frontiersin.org/articles/10.3389/fcell.2020.00772/full#supplementary-material

## REFERENCES

Adachi-Akahane, S., Cleemann, L., and Morad, M. (1996). Cross-signaling between L-type Ca2+ channels and ryanodine receptors in rat ventricular myocytes. *J. Gen. Physiol.* 108, 435–454. doi: 10.1085/jgp.108.5.435

Avila-Medina, J., Mayoral-Gonzalez, I., Dominguez-Rodriguez, A., Gallardo-Castillo, I., Ribas, J., Ordonez, A., et al. (2018). The complex role of store operated calcium entry pathways and related proteins in the function of cardiac, skeletal and vascular smooth muscle cells. *Front. Physiol.* 9:257. doi: 10.3389/fphys.2018.00257

Bers, D. M. (2002). Cardiac excitation-contraction coupling. *Nature* 415, 198–205. doi: 10.1038/415198a

Bootman, M. D., Collins, T. J., Mackenzie, L., Roderick, H. L., Berridge, M. J., and Peppiatt, C. M. (2002). 2-aminoethoxydiphenyl borate (2-APB) is a reliable blocker of store-operated Ca2+ entry but an inconsistent inhibitor of InsP3-induced Ca2+ release. *FASEB J.* 16, 1145–1150. doi: 10.1096/fj.02-0037rev

Bround, M. J., Asghari, P., Wambolt, R. B., Bohunek, L., Smits, C., Philit, M., et al. (2012). Cardiac ryanodine receptors control heart rate and rhythmicity in adult mice. *Cardiovasc. Res.* 96, 372–380. doi: 10.1093/cvr/cvs260

Bround, M. J., Wambolt, R., Luciani, D. S., Kulpa, J. E., Rodrigues, B., Brownsey, R. W., et al. (2013). Cardiomyocyte ATP production, metabolic flexibility, and survival require calcium flux through cardiac ryanodine receptors in vivo. *J. Biol. Chem.* 288, 18975–18986. doi: 10.1074/jbc.M112.427062

Cyganek, L., Tiburcy, M., Sekeres, K., Gerstenberg, K., Bohnenberger, H., Lenz, C., et al. (2018). Deep phenotyping of human induced pluripotent stem cell-derived atrial and ventricular cardiomyocytes. *JCI Insight* 3:e99941. doi: 10.1172/jci.insight.99941

Eisner, D. A., Caldwell, J. L., Kistamas, K., and Trafford, A. W. (2017). Calcium and excitation-contraction coupling in the heart. *Circ. Res.* 121, 181–195. doi: 10.1161/CIRCRESAHA.117.310230

Fu, J. D., Li, J., Tweedie, D., Yu, H. M., Chen, L., Wang, R., et al. (2006). Crucial role of the sarcoplasmic reticulum in the developmental regulation of Ca2+ transients and contraction in cardiomyocytes derived from embryonic stem cells. *FASEB J.* 20, 181–183. doi: 10.1096/fj.05-4501fje

Garcia, M. I., and Boehning, D. (2017). Cardiac inositol 1,4,5-trisphosphate receptors. *Biochim. Biophys. Acta Mol. Cell Res.* 1864, 907–914. doi: 10.1016/j.bbamcr.2016.11.017

Guo, A., and Yang, H. T. (2009). Ca2+ removal mechanisms in mouse embryonic stem cell-derived cardiomyocytes. *Am. J. Physiol. Cell Physiol.* 297, C732–C741. doi: 10.1152/ajpcell.00025.2009

Huang, J., van Breemen, C., Kuo, K. H., Hove-Madsen, L., and Tibbits, G. F. (2006). Store-operated Ca2+ entry modulates sarcoplasmic reticulum Ca2+ loading in neonatal rabbit cardiac ventricular myocytes. *Am. J. Physiol. Cell Physiol.* 290, C1572–C1582. doi: 10.1152/ajpcell.00226.2005

Itzhaki, I., Rapoport, S., Huber, I., Mizrahi, I., Zwi-Dantsis, L., Arbel, G., et al. (2011). Calcium handling in human induced pluripotent stem cell derived cardiomyocytes. *PLoS One* 6:e18037. doi: 10.1371/journal.pone.0018037

Iwasaki, H., Mori, Y., Hara, Y., Uchida, K., Zhou, H., and Mikoshiba, K. (2001). 2-Aminoethoxydiphenyl borate (2-APB) inhibits capacitative calcium entry independently of the function of inositol 1,4,5-trisphosphate receptors. *Recept. Channels* 7, 429–439.

Jiang, D., Chen, W., Wang, R., Zhang, L., and Chen, S. R. (2007). Loss of luminal Ca2+ activation in the cardiac ryanodine receptor is associated with ventricular fibrillation and sudden death. *Proc. Natl. Acad. Sci. U.S.A.* 104, 18309–18314. doi: 10.1073/pnas.0706573104

Kapur, N., and Banach, K. (2007). Inositol-1,4,5-trisphosphate-mediated spontaneous activity in mouse embryonic stem cell-derived cardiomyocytes. *J. Physiol.* 581(Pt 3), 1113–1127. doi: 10.1113/jphysiol.2006.125955

Kockskamper, J., Zima, A. V., Roderick, H. L., Pieske, B., Blatter, L. A., and Bootman, M. D. (2008). Emerging roles of inositol 1,4,5-trisphosphate signaling in cardiac myocytes. *J. Mol. Cell Cardiol.* 45, 128–147. doi: 10.1016/j.yjmcc.2008.05.014

Kolanowski, T. J., Antos, C. L., and Guan, K. (2017). Making human cardiomyocytes up to date: derivation, maturation state and perspectives. *Int. J. Cardiol.* 241, 379–386. doi: 10.1016/j.ijcard.2017.03.099

Korhonen, T., Rapila, R., Ronkainen, V. P., Koivumaki, J. T., and Tavi, P. (2010). Local Ca2+ releases enable rapid heart rates in developing cardiomyocytes. *J. Physiol.* 588(Pt 9), 1407–1417. doi: 10.1113/jphysiol.2009.185173

Lian, X., Zhang, J., Azarin, S. M., Zhu, K., Hazeltine, L. B., Bao, X., et al. (2013). Directed cardiomyocyte differentiation from human pluripotent stem cells by modulating Wnt/beta-catenin signaling under fully defined conditions. *Nat. Protoc.* 8, 162–175. doi: 10.1038/nprot.2012.150

Liu, W., Yasui, K., Opthof, T., Ishiki, R., Lee, J. K., Kamiya, K., et al. (2002). Developmental changes of Ca(2+) handling in mouse ventricular cells from early embryo to adulthood. *Life Sci.* 71, 1279–1292. doi: 10.1016/s0024-3205(02)01826-x

Liu, Y., Wang, R., Sun, B., Mi, T., Zhang, J., Mu, Y., et al. (2014). Generation and characterization of a mouse model harboring the exon-3 deletion in the cardiac ryanodine receptor. *PLoS One* 9:e95615. doi: 10.1371/journal.pone.0095615

Liu, Z., Wang, R., Tian, X., Zhong, X., Gangopadhyay, J., Cole, R., et al. (2010). Dynamic, inter-subunit interactions between the N-terminal and central mutation regions of cardiac ryanodine receptor. *J. Cell Sci.* 123(Pt 10), 1775–1784. doi: 10.1242/jcs.064071

Maizels, L., Huber, I., Arbel, G., Tijsen, A. J., Gepstein, A., Khoury, A., et al. (2017). Patient-specific drug screening using a human induced pluripotent stem cell model of catecholaminergic polymorphic ventricular tachycardia type 2. *Circ. Arrhythm. Electrophysiol.* 10:e004725. doi: 10.1161/CIRCEP.116.004725

Poindexter, B. J., Smith, J. R., Buja, L. M., and Bick, R. J. (2001). Calcium signaling mechanisms in dedifferentiated cardiac myocytes: comparison with neonatal and adult cardiomyocytes. *Cell Calcium.* 30, 373–382. doi: 10.1054/ceca.2001.0249

Porta, M., Zima, A. V., Nani, A., Diaz-Sylvester, P. L., Copello, J. A., Ramos-Franco, J., et al. (2011). Single ryanodine receptor channel basis of caffeine's action on Ca2+ sparks. *Biophys. J.* 100, 931–938. doi: 10.1016/j.bpj.2011.01.017

Ronaldson-Bouchard, K., Ma, S. P., Yeager, K., Chen, T., Song, L., Sirabella, D., et al. (2018). Advanced maturation of human cardiac tissue grown from pluripotent stem cells. *Nature* 556, 239–243. doi: 10.1038/s41586-018-0016-3

Rosemblit, N., Moschella, M. C., Ondriasova, E., Gutstein, D. E., Ondrias, K., and Marks, A. R. (1999). Intracellular calcium release channel expression during embryogenesis. *Dev. Biol.* 206, 163–177. doi: 10.1006/dbio.1998.9120

Roston, T. M., Guo, W., Krahn, A. D., Wang, R., Van Petegem, F., Sanatani, S., et al. (2017). A novel RYR2 loss-of-function mutation (I4855M) is associated with left ventricular non-compaction and atypical catecholaminergic polymorphic ventricular tachycardia. *J. Electrocardiol.* 50, 227–233. doi: 10.1016/j.jelectrocard.2016.09.006

Sasse, P., Zhang, J., Cleemann, L., Morad, M., Hescheler, J., and Fleischmann, B. K. (2007). Intracellular Ca2+ oscillations, a potential pacemaking mechanism in early embryonic heart cells. *J. Gen. Physiol.* 130, 133–144. doi: 10.1085/jgp.200609575

Satin, J., Itzhaki, I., Rapoport, S., Schroder, E. A., Izu, L., Arbel, G., et al. (2008). Calcium handling in human embryonic stem cell-derived cardiomyocytes. *Stem Cells* 26, 1961–1972. doi: 10.1634/stemcells.2007-2591

Sedan, O., Dolnikov, K., Zeevi-Levin, N., Leibovich, N., Amit, M., Itskovitz-Eldor, J., et al. (2008). 1,4,5-Inositol trisphosphate-operated intracellular Ca(2+) stores and angiotensin-II/endothelin-1 signaling pathway are functional in human embryonic stem cell-derived cardiomyocytes. *Stem Cells* 26, 3130–3138. doi: 10.1634/stemcells.2008-0777

Sham, J. S., Cleemann, L., and Morad, M. (1995). Functional coupling of Ca2+ channels and ryanodine receptors in cardiac myocytes. *Proc. Natl. Acad. Sci. U.S.A.* 92, 121–125. doi: 10.1073/pnas.92.1.121

Streckfuss-Bomeke, K., Wolf, F., Azizian, A., Stauske, M., Tiburcy, M., Wagner, S., et al. (2013). Comparative study of human-induced pluripotent stem cells derived from bone marrow cells, hair keratinocytes, and skin fibroblasts. *Eur. Heart J.* 34, 2618–2629. doi: 10.1093/eurheartj/ehs203

Takahashi, K., Tanabe, K., Ohnuki, M., Narita, M., Ichisaka, T., Tomoda, K., et al. (2007). Induction of pluripotent stem cells from adult human fibroblasts by defined factors. *Cell* 131, 861–872. doi: 10.1016/j.cell.2007.11.019

Takahashi, K., and Yamanaka, S. (2006). Induction of pluripotent stem cells from mouse embryonic and adult fibroblast cultures by defined factors. *Cell* 126, 663–676. doi: 10.1016/j.cell.2006.07.024

Takeshima, H., Komazaki, S., Hirose, K., Nishi, M., Noda, T., and Iino, M. (1998). Embryonic lethality and abnormal cardiac myocytes in mice lacking ryanodine receptor type 2. *EMBO J.* 17, 3309–3316. doi: 10.1093/emboj/17.12.3309

Xie, A., Zhou, A., Liu, H., Shi, G., Liu, M., Boheler, K. R., et al. (2018). Mitochondrial Ca2+ flux modulates spontaneous electrical activity in ventricular cardiomyocytes. *PLoS One* 13:e0200448. doi: 10.1371/journal.pone.0200448

Yang, H. T., Tweedie, D., Wang, S., Guia, A., Vinogradova, T., Bogdanov, K., et al. (2002). The ryanodine receptor modulates the spontaneous beating rate of cardiomyocytes during development. *Proc. Natl. Acad. Sci. U.S.A.* 99, 9225–9230. doi: 10.1073/pnas.142651999

Yu, J., Vodyanik, M. A., Smuga-Otto, K., Antosiewicz-Bourget, J., Frane, J. L., Tian, S., et al. (2007). Induced pluripotent stem cell lines derived from human somatic cells. *Science* 318, 1917–1920. doi: 10.1126/science.1151526

**Conflict of Interest:** The authors declare that the research was conducted in the absence of any commercial or financial relationships that could be construed as a potential conflict of interest.

frontiers
in Cell and Developmental Biology

ORIGINAL RESEARCH
published: 13 August 2020
doi: 10.3389/fcell.2020.00761

# Propranolol Attenuates Late Sodium Current in a Long QT Syndrome Type 3-Human Induced Pluripotent Stem Cell Model

**Sayako Hirose[1], Takeru Makiyama[1]*, Dario Melgari[2,3], Yuta Yamamoto[1,4], Yimin Wuriyanghai[1], Fumika Yokoi[1], Suguru Nishiuchi[1], Takeshi Harita[1], Mamoru Hayano[1], Hirohiko Kohjitani[1], Jingshan Gao[1], Asami Kashiwa[1], Misato Nishikawa[5], Jie Wu[2,6], Jun Yoshimoto[7], Kazuhisa Chonabayashi[5], Seiko Ohno[4], Yoshinori Yoshida[5], Minoru Horie[2,8] and Takeshi Kimura[1]**

*[1] Department of Cardiovascular Medicine, Kyoto University Graduate School of Medicine, Kyoto, Japan, [2] Department of Cardiovascular and Respiratory Medicine, Shiga University of Medical Science, Otsu, Japan, [3] Institute of Cardiometabolism and Nutrition, Sorbonne University, Paris, France, [4] Department of Bioscience and Genetics, National Cerebral and Cardiovascular Center, Suita, Japan, [5] Center for iPS Cell Research and Application (CiRA), Institute for Integrated Cell-Material Sciences, Kyoto University, Kyoto, Japan, [6] Department of Pharmacology, Medical School of Xi'an Jiaotong University, Xi'an, China, [7] Department of Cardiology, Shizuoka Children's Hospital, Shizuoka, Japan, [8] Center for Epidemiologic Research in Asia, Shiga University of Medical Science, Otsu, Japan*

OPEN ACCESS

**Edited by:**
*Masayuki Yazawa,*
*Columbia University, United States*

**Reviewed by:**
*Yukiomi Tsuji,*
*Nagasaki University, Japan*
*Milena Bellin,*
*Leiden University Medical Center, Netherlands*

***Correspondence:**
*Takeru Makiyama*
*makiyama@kuhp.kyoto-u.ac.jp*

**Specialty section:**
*This article was submitted to Stem Cell Research, a section of the journal Frontiers in Cell and Developmental Biology*

***Received:*** *12 February 2020*
***Accepted:*** *20 July 2020*
***Published:*** *13 August 2020*

**Citation:**
*Hirose S, Makiyama T, Melgari D, Yamamoto Y, Wuriyanghai Y, Yokoi F, Nishiuchi S, Harita T, Hayano M, Kohjitani H, Gao J, Kashiwa A, Nishikawa M, Wu J, Yoshimoto J, Chonabayashi K, Ohno S, Yoshida Y, Horie M and Kimura T (2020) Propranolol Attenuates Late Sodium Current in a Long QT Syndrome Type 3-Human Induced Pluripotent Stem Cell Model. Front. Cell Dev. Biol. 8:761. doi: 10.3389/fcell.2020.00761*

**Background:** Long QT syndrome type 3 (LQT3) is caused by gain-of-function mutations in the *SCN5A* gene, which encodes the α subunit of the cardiac voltage-gated sodium channel. LQT3 patients present bradycardia and lethal arrhythmias during rest or sleep. Further, the efficacy of β-blockers, the drug used for their treatment, is uncertain. Recently, a large multicenter LQT3 cohort study demonstrated that β-blocker therapy reduced the risk of life-threatening cardiac events in female patients; however, the detailed mechanism of action remains unclear.

**Objectives:** This study aimed to establish LQT3-human induced pluripotent stem cells (hiPSCs) and to investigate the effect of propranolol in this model.

**Method:** An hiPSCs cell line was established from peripheral blood mononuclear cells of a boy with LQT3 carrying the *SCN5A*-N1774D mutation. He had suffered from repetitive torsades de pointes (TdPs) with QT prolongation since birth (QTc 680 ms), which were effectively treated with propranolol, as it suppressed lethal arrhythmias. Furthermore, hiPSCs were differentiated into cardiomyocytes (CMs), on which electrophysiological functional assays were performed using the patch-clamp method.

**Results:** N1774D-hiPSC-CMs exhibited significantly prolonged action potential durations (APDs) in comparison to those of the control cells (N1774D: 440 ± 37 ms vs. control: 272 ± 22 ms; at 1 Hz pacing; $p < 0.01$). Furthermore, N1774D-hiPSC-CMs presented gain-of-function features: a hyperpolarized shift of steady-state activation and increased late sodium current compared to those of the control cells. 5 μM propranolol shortened APDs and inhibited late sodium current in N1774D-hiPSC-CMs, but did not significantly affect in the control cells. In addition, even in the presence of intrapipette guanosine diphosphate βs (GDPβs), an inhibitor of G proteins, propranolol reduced late sodium current in N1774D cells. Therefore, these results suggested a unique inhibitory effect of propranolol on late sodium current unrelated to β-adrenergic receptor block in N1774D-hiPSC-CMs.

**Conclusion:** We successfully recapitulated the clinical phenotype of LQT3 using patient-derived hiPSC-CMs and determined that the mechanism, by which propranolol inhibited the late sodium current, was independent of β-adrenergic receptor signaling pathway.

**Keywords: long QT syndrome type 3, induced pluripotent stem cell, sodium channel, β blocker, arrhythmia**

## INTRODUCTION

Congenital long QT syndrome (LQT) is an inherited arrhythmogenic disease, associated with lethal arrhythmic events and sudden cardiac death. Patients with LQT are currently classified into over 15 genetic subtypes, and LQT1-3 accounts for approximately 90% of the genotyped patients, specifically: 40–55%, 30–45%, and 5–10% are LQT1, LQT2, and LQT3, respectively (Schwartz et al., 2012; Mizusawa et al., 2014). LQT1 and LQT2 are caused by loss-of-function mutations in *KCNQ1* and *KCNH2* genes, which encode cardiac slowly ($I_{Ks}$) and rapidly ($I_{Kr}$) activating delayed rectifier potassium channels, respectively (Moss et al., 2007; Shimizu et al., 2009). On the other hand, LQT3 is caused by gain-of function mutations in the *SCN5A* gene, which encodes cardiac voltage-gated sodium channels (Bennett et al., 1995).

A number of studies reported genotype-phenotype correlations among those three major genotypes (Moss et al., 2000; Schwartz et al., 2001; Priori et al., 2004; Hobbs et al., 2006), and genetic testing for patients with LQT is highly recommended for identifying carriers in the families and determining the appropriate choice of gene-specific treatment (Ackerman et al., 2011; Skinner et al., 2019). Patients with LQT1 and LQT2 suffer from cardiac events that occur during exercise or emotional stress (Schwartz et al., 2001, 2012). They are usually treated with β-blockers, as they are highly effective in reducing cardiac event and mortality rates (Schwartz et al., 2001; Priori et al., 2004). By contrast, patients with LQT3 experience cardiac events during rest or sleep (Schwartz et al., 2001, 2012), and β-blocker therapy has resulted less effective or even harmful in preventing those cardiac events, according to small cohort studies and the clinical features of LQT3 (Moss et al., 2000; Schwartz et al., 2001; Priori et al., 2004). Recently, a large clinical cohort study, which consisted of 406 patients with LQT3, demonstrated that β-blocker therapy reduced the number of cardiac events in female patients >1 year old (Wilde et al., 2016), thus β-blocker therapy has regained importance as an optimal medicine for LQT3. However, the pharmacological mechanism by which β-blockers benefit LQT3 patients is still unclear.

In the present study, we investigated the cellular mechanism by which β-blockers affected late sodium currents in human LQT3 cardiomyocytes (CMs). To this end, we established a human induced pluripotent stem cell line (hiPSCs) from a young male carrying *SCN5A*-N1774D genotype and whose repetitive torsades de pointes (TdPs) were effectively treated with propranolol. In N1774D-hiPSC-derived CMs, prolonged action potential durations (APDs) and increased late sodium current at baseline were attenuated after propranolol administration. More importantly, we determined that late sodium current inhibition by propranolol was unrelated to β-adrenergic receptor signaling pathway in the LQT3 hiPSC-CM model.

## MATERIALS AND METHODS

### Generation and Characterization of LQT3-hiPSCs

We collected peripheral blood mononuclear cells from a patient carrying *SCN5A*-N1774D after obtaining the written informed consent, and employed an integration-free method using episomal vectors to generate hiPSCs (Okita et al., 2013). We used three different patient-derived iPSCs clones in this study. As control hiPSCs lines, we used two different lines (201B7 and 253G1) generated from a healthy donor (Takahashi et al., 2007; Nakagawa et al., 2008). This study was approved by the Kyoto University ethics review broad and conformed to the principles of the Declaration of Helsinki.

The pluripotency of established LQT3-hiPSCs were assessed using immunostaining and teratoma assay (Yamamoto et al., 2017; Wuriyanghai et al., 2018). Briefly, the hiPSC colonies were fixed with 4% paraformaldehyde for 20 min at 4°C. The cells were permeabilized in 0.2% Triton X-100 (Nacalai Tesque, Kyoto, Japan) and blocked with 5% FBS. The samples were stained overnight at 4°C with the following primary antibodies: mouse monoclonal anti-OCT3/4 (1:50; Santa Cruz Biotechnology, Delaware, CA, United States), mouse monoclonal anti-SSEA4 (1:200; Santa Cruz Biotechnology), and mouse monoclonal anti-TRA 1–60 (1:200; Santa Cruz Biotechnology). The secondary antibody was donkey anti-mouse Alexa fluor 488 (1:1000, Invitrogen, Carlsbad, CA, United States). The nuclei were stained with DAPI (1:2000, Wako Pure Chemical Industries, Osaka, Japan). The specimens were observed under a fluorescence microscope (Biozero BZ-9000; KEYENCE, Osaka, Japan). For teratoma assay, the hiPSCs were injected into severe combined immunodeficiency disease scid/scid mice under the testis capsule. Tumor samples were surgically dissected at 8 weeks, fixed in 10% formalin and stained with hematoxylin and eosin. All animal experiments were performed in accordance with the "Guide for the Care and Use of Laboratory Animals" (2011) of the National Institutes of Health and the Regulation on Animal Experimentation at Kyoto University, and approved by Ethics Committee of Kyoto University.

## Cardiomyocyte Differentiation

Cardiomyocyte differentiation was induced with an embryoid body (EB) differentiation system as previously described (Yang et al., 2008; Wuriyanghai et al., 2018). The hiPSCs aggregated to form EBs and cultured in suspension for 20 days. On the 20th day of culture, EBs were dispersed into small clusters using collagenase B (Roche Diagnostics GmbH, Mannheim, Germany) and trypsin EDTA (Nacalai Tesque) and were plated onto 0.1% gelatin coated dishes. After day 20, hiPSC-CMs were maintained in DMEM/F12 with 2% fetal bovine serum, 2 mmol/L L-glutamine, 0.1 mmol/L non-essential amino acids, 0.1 mmol/L β-mercaptoethanol, 50 U/ml penicillin, and 50 μg/ml streptomycin. The medium was renewed every 2–3 days. Differentiated 6–8-week-old hiPSC-CMs were enzymatically dispersed into single cells using collagenase B and trypsin EDTA. The cells were plated on 0.1% gelatin coated glass cover slips. Patch-clamp experiments were performed 4–7 days after the procedures. Cardiac differentiation was performed more than five times with each hiPSCs clone and the data pooled from different lines or clones among the control and N1774D group were analyzed.

## Electrophysiological Assay

Electrophysiological assays were performed using the whole-cell patch-clamp technique with the Multiclamp 700B microelectrode amplifier and Axon Digidata 1440 digitizer hardware (Molecular Devices, San Jose, CA, United States), as described previously (Ma et al., 2011; Hayano et al., 2017; Wuriyanghai et al., 2018).

Action potentials (APs) were recorded with perforated patch-clamp in the current mode at a bath temperature of 36 ± 1°C. APs were evoked at a constant pacing rate of 1 Hz, with 5 ms depolarizing current injections of 50–200 pA. The external solution contained (in mM): 140 NaCl, 5.4 KCl, 1.8 $CaCl_2$, 1.0 $MgCl_2$, 10 HEPES, 10 Glucose, pH 7.40 (adjusted with NaOH) and pipette solution contained (in mM): 150 KCl, 5 EGTA, 5 MgATP, 10 HEPES, 5 NaCl, 2 $CaCl_2$ with pH of 7.2 and 300–500 μg/ml amphotericin B. The patch pipettes had a resistance of 3–6 MΩ. Ventricular-type action potentials were defined by the morphology of APs and the classification based on previous report (Matsa et al., 2011): a deep diastolic membrane potential ($<-50$ mV), a sharp systolic depolarization, a long plateau phase, and AP duration at 90% repolarization (action potential duration: $APD_{90}$)/APD at 50% repolarization ($APD_{50}$) ratio <1.4.

Sodium current was recorded at the bath temperature of 22–23°C using whole-cell voltage-clamp technique. Pipette resistances were between 0.8 and 1.8 MΩ, with access resistances of <5 MΩ. The extracellular bath solution contained (in mM): 137 NaCl, 100 TEA-Cl, 1.8 $CaCl_2$, 2 $MgCl_2$, 10 HEPES, 10 Glucose, 0.2 $NiCl_2$, 0.005 Nifedipine (pH was adjusted to 7.4 with CsOH). The intrapipette solution was contained (in mM): 5 NaCl, 70 CsCl, 40 CSAs, 2.0 $CaCl_2$, 10 EGTA, 10 HEPES, 5 MgATP, pH 7.3 (adjusted with $C_sOH$). The standard holding potential was −100 mV. Each protocol in detail is illustrated in the inset.

The current-voltage relationships were fit with the Boltzmann equation: $I = (V - V_{rev}) \times G_{max} \times [1 + \exp\ (V - V_{1/2})/k]^{-1}$, where $I$ is the peak sodium current during the test pulse potential $V$. The parameters estimated by the fitting are reversal potential ($V_{rev}$), maximum conductance ($G_{max}$), and slop factor ($k$). Steady-state availability was fit to the Boltzmann equation: $I/I_{\ max} = [1 + \exp\ (V - V_{1/2})/k]^{-1}$ to determine the membrane potential for $V_{1/2}$ (half-maximal inactivation) and $k$ (slop factor). $I_{\ max}$ is the maximum peak sodium current. Data for the time course of recovery from inactivation were fitted by a biexponential equation: $I(t)/I_{\ max} = A_f\ [1 - \exp(-t/\tau_f)] + A_s\ [1 - \exp(-t/\tau_s)]$, where $A_f$ and $A_s$ represent fractions of each components, respectively. Time course of entry into the slow inactivation state and development of closed-state inactivation were fitted with a single exponential equation: $I/I_{\ max} = y0 + A[1 - \exp(-t/\tau)]$, where the transfer rate of sodium channels from closed-state to inactivated closed-state without an intervening opening state was measured by a double pulse protocol. Time course for development of closed-state inactivation was fit with a single exponential equation, $I/I_{\ max} = y0 + A\ [1 - \exp(-t/\tau\ )]$.

Late sodium currents were recorded for 800 ms at −10 mV before and after 20 μM tetrodotoxin (TTX; Nacalai Tesque) application. The pipette solution contained (in mM): 5 NaCl, 70 CsCl, 40 $C_SAsp$, 10 EGTA, 10 HEPES, 5 MgATP, pH 7.3 (adjusted with CsOH).

To assess the effect of propranolol for APD and sodium current, recordings were performed before and after the administration of 5 μM propranolol hydrochloride (FUJIFILM Wako, Osaka, Japan).

## Statistics

Data are expressed as mean ± the standard error of measurement. Statistical comparisons were analyzed using appropriate student's $t$-test and paired $t$-tests. A $p$ value of $<0.05$ was considered statistically significant.

# RESULTS

## Clinical Patient Profile

The proband was a 1-day-old infant who exhibited severe bradycardia at 27 weeks of gestation (Kato et al., 2014). His surface electrocardiogram showed an extremely prolonged QT interval (QTc 680 ms) with functional atrio-ventricular block and repeated TdPs immediately after his birth. He was suspected of long QT syndrome and thus propranolol was administered to suppress TdPs. But the treatment was not enough to suppress the electrical storm. Therefore, mexiletine was added and, as a result, TdPs disappeared.

Additionally, genetic testing identified a heterozygous *SCN5A* mutation, named p. N1774D, confirming the diagnosis of LQT3. Therefore, treatment of the patient with propranolol was discontinued. However, TdPs recurred after its interruption, and thus propranolol administration was resumed, and as a consequence, TdPs immediately disappeared.

## Generation and Characterization of *SCN5A*-N1774D-hiPSCs

Patient-specific LQT3 hiPSCs were generated from the peripheral blood mononuclear cells of the pediatric patient carrying the *SCN5A*-N1774D mutation. *SCN5A*-N1774D-hiPSCs displayed characteristics of human embryonic stem cell morphology and expressed human pluripotency makers: OCT3/4, SSEA4, and TRA-1-60 (**Figure 1A**). To evaluate the pluripotency of the generated hiPSC line, teratoma formation assays were performed using scid/scid mice. The teratomas contained tissues derivatives of three germ layers: ectoderm, endoderm, and mesoderm (**Figure 1B**). Furthermore, the *SCN5A*-N1774D

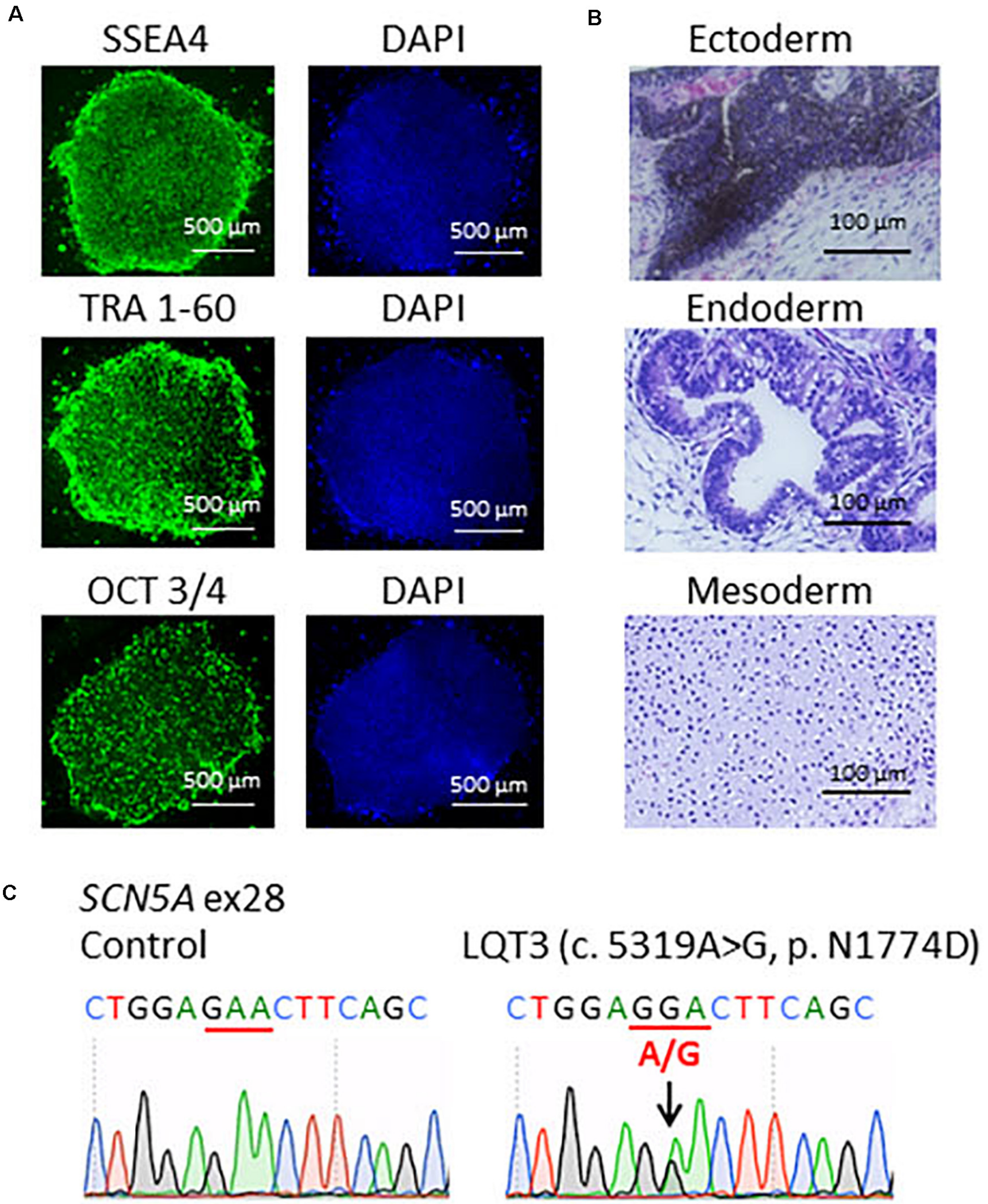

**FIGURE 1 |** Characterization of LQT3-hiPSCs. **(A)** Immunofluorescence staining for stem cells makers. LQT3-hiPSC colonies derived from the peripheral blood mononuclear cells of a patient with *SCN5A*-N1774D expressed pluripotency markers; SSEA4, TRA 1-60, and OCT 3/4. Blue (right) showed 40-6-diamidino-2-phenylindole (DAPI) staining of nuclei. Scale bars = 500 μm. **(B)** Hematoxylin-eosin staining of teratomas formed from LQT3-hiPSC showed differentiation of the cells into various tissue derived from all three germ layers: melanocytes (ectoderm), gut-like structures (endoderm), and cartilage tissue (mesoderm). **(C)** DNA sequences of the *SCN5A* gene identified in the control hiPSCs and LQT3 cells carrying N1774D heterozygous mutation in LQT3-hiPSCs, not control hiPSCs. Scale bars: 100 μm.

mutation (c.5319A > G) was confirmed in the patient-derived hiPSCs, but not identified in the control samples (**Figure 1C**).

## Prolonged APDs in N1774D-hiPSC-CMs

Action potentials of hiPSC-CMs were recorded using the current-clamp technique. **Figure 2A** shows typical ventricular-type APs. For this study, we measured APDs at 50% and 90% repolarization, $APD_{50}$ and $APD_{90}$, respectively, maximum diastolic potential, and AP amplitude.

Action potential durations in N1774D-hiPSC-CMs were significantly prolonged compared to those in control hiPSC-CMs at 1 Hz pacing ($APD_{50}$ and $APD_{90}$: N1774D-hiPSC-CMs, 440 ± 37 ms and 377 ± 33 ms, respectively, $n = 11$, vs. control, 272 ± 22 ms and 192 ± 18 ms, respectively, $n = 10$; $p < 0.01$; **Figure 2** and **Table 1**). However, no significant difference in other AP parameters was observed (**Table 1**).

## N1774D-hiPSC-CMs Exhibited Increased Late Sodium Current

The sodium channel currents in N1774D-hiPSC-CMs and control cells were recorded by using the voltage-clamp technique (**Figure 3** and **Table 2**). **Figure 3A** illustrates representative whole-cell current traces of N1774D-hiPSC-CMs and control cells. As shown in **Figure 3B**, the peak sodium current densities of N1774D-hiPSC-CMs were significantly increased, compared to those of the control cells (N1774D: −333 ± 62 pA/pF, $n = 15$ vs. control: −175 ± 33 pA/pF, $n = 15$; $p < 0.005$; **Table 2**). Moreover, the steady-state activation of sodium channels, shifted to more negative potentials by 13 mV in N1774D-hiPSC-CMs, compared to that of the control cells (**Figure 3C** and **Table 2**). No significant differences in the voltage dependence of inactivation and other kinetic properties were noted between control cells and N1774D-hiPSC-CMs.

Next, we measured the late sodium current for both cell lines. **Figure 4A** shows representative whole-cell sodium current traces from control and N1774D-hiPSC-CMs. The ratio of late/peak sodium current in N1774D-hiPSC-CMs was significantly increased compared with that in control cells (N1774D: 0.47 ± 0.04%, $n = 11$, vs. control, 0.04 ± 0.01%, $n = 5$; $p < 0.0001$; **Figure 4B**).

**TABLE 1 |** AP parameters at baseline and after administration of propranolol in control and N1774D-hiPSC-CMs at 1 Hz pacing.

| | Control | | N1774D | |
|---|---|---|---|---|
| | Baseline | Propranolol 5 μM | Baseline | Propranolol 5 μM |
| | (*N* = 11) | (*N* = 11) | (*N* = 10) | (*N* = 10) |
| RMP (mV) | −69.3 ± 2.9 | −67 ± 3.0 | −70.0 ± 2.4 | −69.9 ± 1.5 |
| MDP (mV) | −75.8 ± 2.9 | −72.7 ± 2.7 | −76.7 ± 3.3 | −74.9 ± 2.2 |
| APA (mV) | 114.4 ± 3.4 | 114.4 ± 3.1 | 120.4 ± 1.6 | 119.9 ± 1.5 |
| Max dV/dt (mV/ms) | 30.2 ± 3.7 | 36.2 ± 9.0 | 32.8 ± 4.4 | 31.8 ± 3.6 |
| $APD_{50}$ (ms) | 192 ± 18 | 178 ± 18$^{\dagger}$ | 377 ± 33$^{\#}$ | 268 ± 31$^{\dagger}$ |
| $APD_{90}$ (ms) | 272 ± 22 | 267 ± 26 | 440 ± 37$^{\#}$ | 332 ± 37$^{\dagger}$ |

*AP, action potential; RMP, resting membrane potential: The threshold potential at which the action potential is initiated; MDP, maximum diastolic potential; APA, AP amplitude; Max dV/dt, maximum rate of rise of the AP upstroke;* $APD_{50}$ *and* $APD_{90}$*, AP durations at 50% and 90%. The data pooled from different lines or clones among the control and N1774D group were analyzed. The number of experiments is indicated in parentheses. Data are showed as means ± standard error of measurement.* $^{\#}p < 0.01$ *vs. Control,* $^{\dagger}p < 0.01$ *vs. Baseline.*

## Propranolol Shortened APDs and Reduced Late Sodium Current in N1774D-hiPSC-CMs

We assessed the effect of propranolol on APDs and late sodium current using hiPSC-CMs. Propranolol shortened APDs in N1774D-hiPSC-CMs ($APD_{90}$: 440 ± 37 ms at baseline vs. 332 ± 37 ms after propranolol treatment, respectively, $n = 10$; at

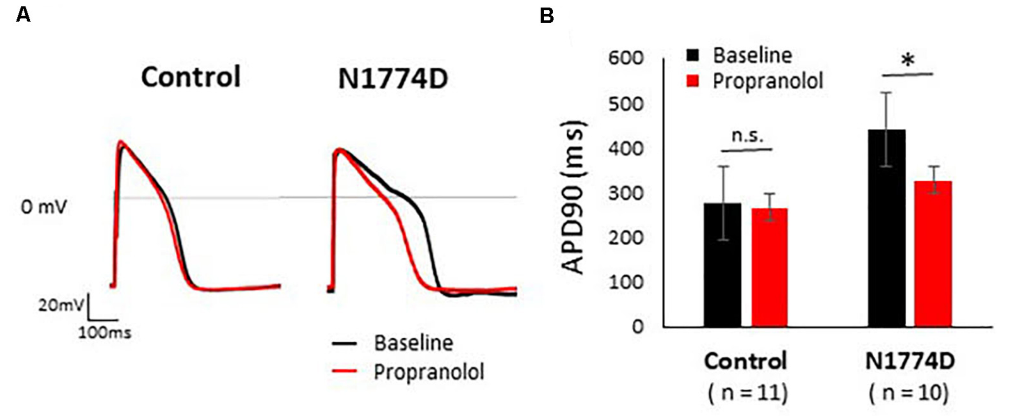

**FIGURE 2 |** Effect of propranolol on action potential recording in control and N1774D-hiPSC-CMs. **(A)** Representative traces of paced ventricular-type action potential (AP) at 1 Hz pacing at baseline (black line) and after the administration 5 μM propranolol (red line) in control (left) and N1774D-hiPSC-CMs (right). **(B)** Summarized data in effects of propranolol on AP duration of control and N1774D-hiPSC-CMs. The data pooled from different lines or clones among the control and N1774D group were analyzed. * $p < 0.001$, vs. control. $APD_{90}$ was measured at 90% repolarization ($APD_{90}$). $APD_{90}$ values in N1774D-hiPSC-CMs were significantly prolonged compared with those in control. Propranolol significantly shortened the values of $APD_{90}$ in N1774D-hiPSC-CMs. * $p < 0.001$, vs. baseline.

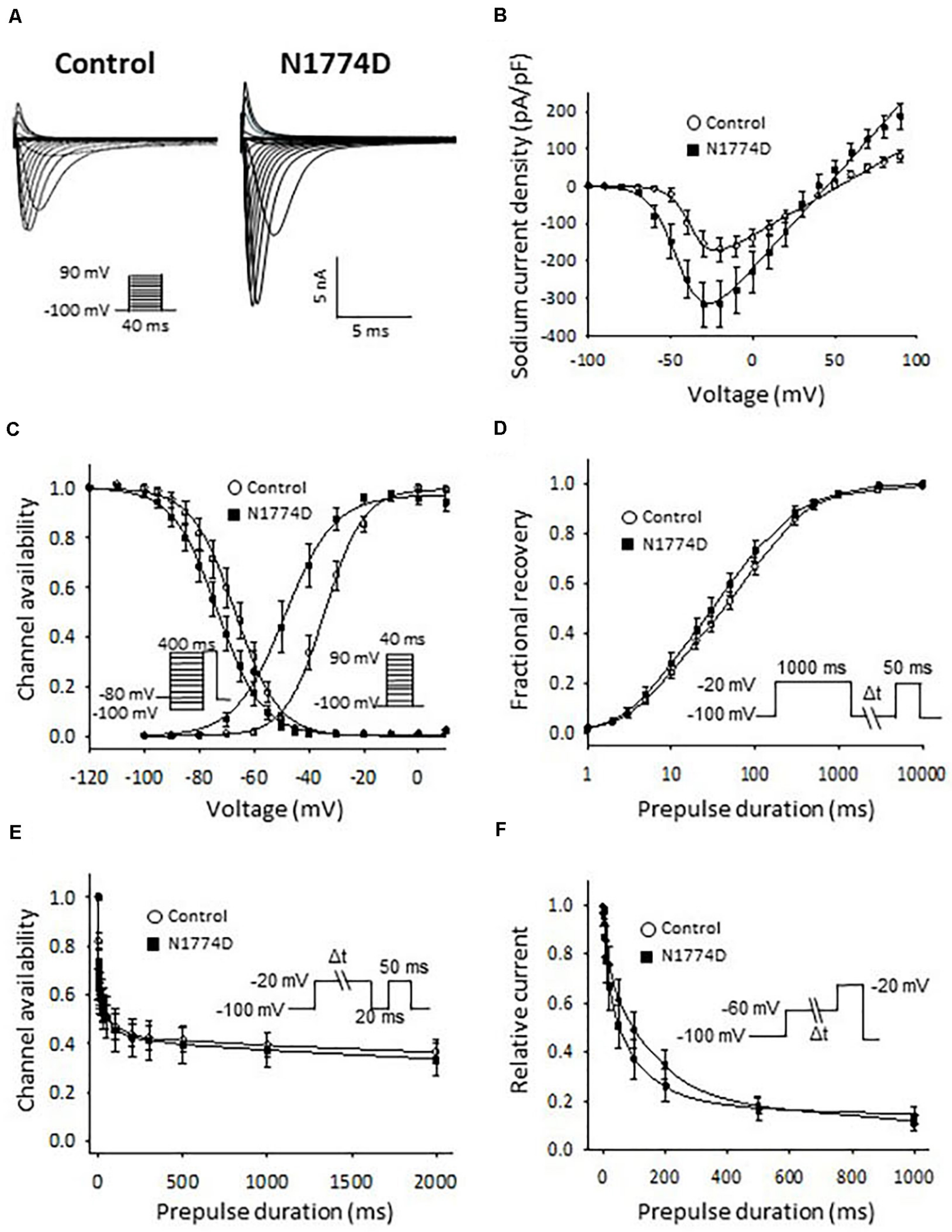

**FIGURE 3 |** Sodium current recordings and gating properties of sodium channels in hiPSC-CMs. **(A)** Representative traces of sodium currents in control and N1774D-hiPSC-CMs. The pulse protocol is shown in the inset. **(B)** Average current-voltage relationship for peak sodium current in control (*n* = 15, open circles) and N1774D channels (*n* = 15, closed squares). Data were fitted with the Boltzmann equation (see "Materials and Methods"). The currents were normalized to the cell capacitance to give a measure of peak current densities. The peak current densities were significantly lager in N1774D. **(C)** Voltage dependence of steady-state inactivation and activation in control and N1774D-hiPSC-CMs. Curves were fit using the Boltzmann equation. The activation curve negatively shifted by 13 mV. **(D)** Time course of recovery from inactivation was obtained by a double pulse potential shown in inset. Experimental data were fit to a biexponential. **(E)** Onset of slow inactivation. Time course of entry into the slow inactivation state was measured by a double pulse protocol shown in inset. Curves were fit with a shingle exponential equation. **(F)** Closed-state inactivation. The transfer rate of sodium channels from closed-state to inactivated closed-state without an intervening opening state was elicited with a double pulse protocol shown in inset. The data pooled from different lines or clones among the control and N1774D group were analyzed.

**TABLE 2 |** Biophysical properties in control and N1774D-hiPSC-CMs.

| | Control | N1774D |
|---|---|---|
| Peak $I_{Na}$ density | (*N* = 15) | (*N* = 15) |
| | −175 ± 33 | −333 ± 62$^{\dagger}$ |
| Steady-state activation | (*N* = 15) | (*N* = 15) |
| $V_{1/2}$ | −34.9 ± 1.6 | −47.7 ± 3.5$^{\dagger}$ |
| *k* | 5.6 ± 0.5 | 4.9 ± 0.3 |
| Steady-state fast inactivation | (*N* = 11) | (*N* = 12) |
| $V_{1/2}$ | −67.4 ± 2.5 | −73.2 ± 2.4 |
| *k* | 6.3 ± 0.2 | 6.7 ± 0.1 |
| Recovery from inactivation | (*N* = 12) | (*N* = 11) |
| $\tau_f$ (ms) | 21.5 ± 6.3 | 24.9 ± 4.8 |
| $\tau_s$ (ms) | 227.2 ± 42.4 | 236.8 ± 43.4 |
| Onset of slow inactivation | (*N* = 11) | (*N* = 8) |
| A | 0.47 ± 0.06 | 0.56 ± 0.07 |
| τ (ms) | 14.4 ± 4.0 | 22.9 ± 8.7 |
| Closed-state inactivation | (*N* = 10) | (*N* = 9) |
| A | 0.89 ± 0.02 | 0.84 ± 0.07 |
| τ (ms) | 123.1 ± 32.0 | 74.6 ± 17.4 |

*Data are expressed as means ± standard error of measurement. Parameters were calculated from fitting individual experiments illustrated in **Figure 3**. The data pooled from different lines or clones among the control and N1774D group were analyzed.* $^{\dagger}p < 0.01$ *vs. Control. A, fractional amplitude; τ, time constant;* $V_{1/2}$*, midpoint potential; k, slop factor, and n, number of tested cells, respectively.*

1 Hz pacing; $p < 0.01$; **Figure 2** and **Table 1**), but propranolol did not significantly affect APDs in the control cells ($APD_{90}$: 272 ± 22 ms at baseline vs. 267 ± 26 ms after propranolol treatment, respectively, $n = 11$; at 1 Hz pacing; $p = 0.15$; **Figure 2** and **Table 1**).

**Figure 5A** shows the representative traces of late sodium current at baseline and after administration of 5 μM propranolol to N1774D-hiPSC-CMs. Propranolol treatment decreased the ratio of late/peak sodium current by approximately 25%, from 0.53 ± 0.05 to 0.40 ± 0.06% ($n = 7$; $p < 0.001$; **Figure 5B**). These results suggested that propranolol attenuated late sodium current and thus shortened APDs in N1774D-hiPSC-CMs.

## Propranolol Directly Inhibited the Late Sodium Current in N1774D-hiPSC-CMs

Finally, to examine whether propranolol affected the sodium channels through G protein cascade or not, we recorded late sodium currents by using intrapipette guanosine diphosphate βs (GDPβs), a G protein inhibitor (**Figure 5C**). The late sodium current was significantly reduced by treatment with propranolol and 1 mM intrapipette GDPβs (baseline, 0.43 ± 0.07% vs. propranolol 0.28 ± 0.07%, $n = 8$; $p = 0.01$; **Figure 5D**). However, the reduction rate of late sodium current by propranolol treatment was not statistically different after addition of intrapipette GDPβs (without GDPβs: 24.7 ± 4.8% vs. with GDPβs: 30.9 ± 6.9%; $p = 0.48$; **Figure 5E**). Thus, propranolol directly blocked sodium channels and did not affect them via G protein pathway through β-adrenergic receptors.

Additionally, the suppression of late sodium current by propranolol was larger than that of the peak current whether in absence or presence of intrapipette GDPβs (**Figure 6**). No significant difference in the suppression rate of the peak and the late sodium currents were observed whether in absence or presence of GDPβs (**Figure 6**).

# DISCUSSION

## Patient-Specific iPSC-CMs as a Cell Model for Studying *SCN5A*-N1774D Associated LQT3

The efficacy of β-blockers has been controversial in patients with LQT3 (Moss et al., 2000; Schwartz et al., 2001; Priori et al., 2004). Recently, a large clinical study demonstrated the efficacy of β-blockers on patients with LQT3 (Wilde et al., 2016);

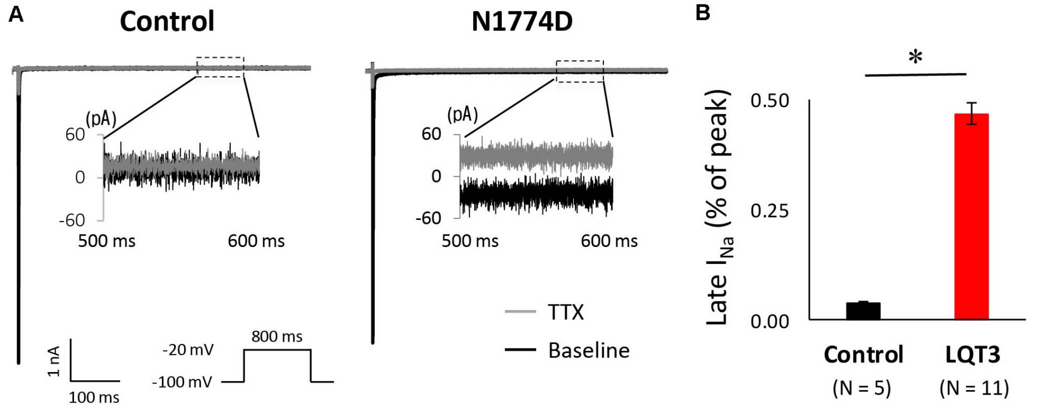

**FIGURE 4 |** Late sodium current in control and N1774D-hiPSC-CMs. **(A)** Representative traces of sodium currents in the absence (black line) and presence (gray line) of 20 μM tetrodotoxin (TTX). The used protocol is shown in the lower panel. Inset shows late sodium current between 500 and 600 ms. Tetrodotoxin-sensitive current was calculated by subtraction. **(B)** Mean late sodium current of control and N1774D channels. Late sodium current is presented as the percentage of late sodium current to peak sodium current. The data pooled from different lines or clones among the control and N1774D group were analyzed. The late sodium current was significantly increased. *$p < 0.001$, vs. control.

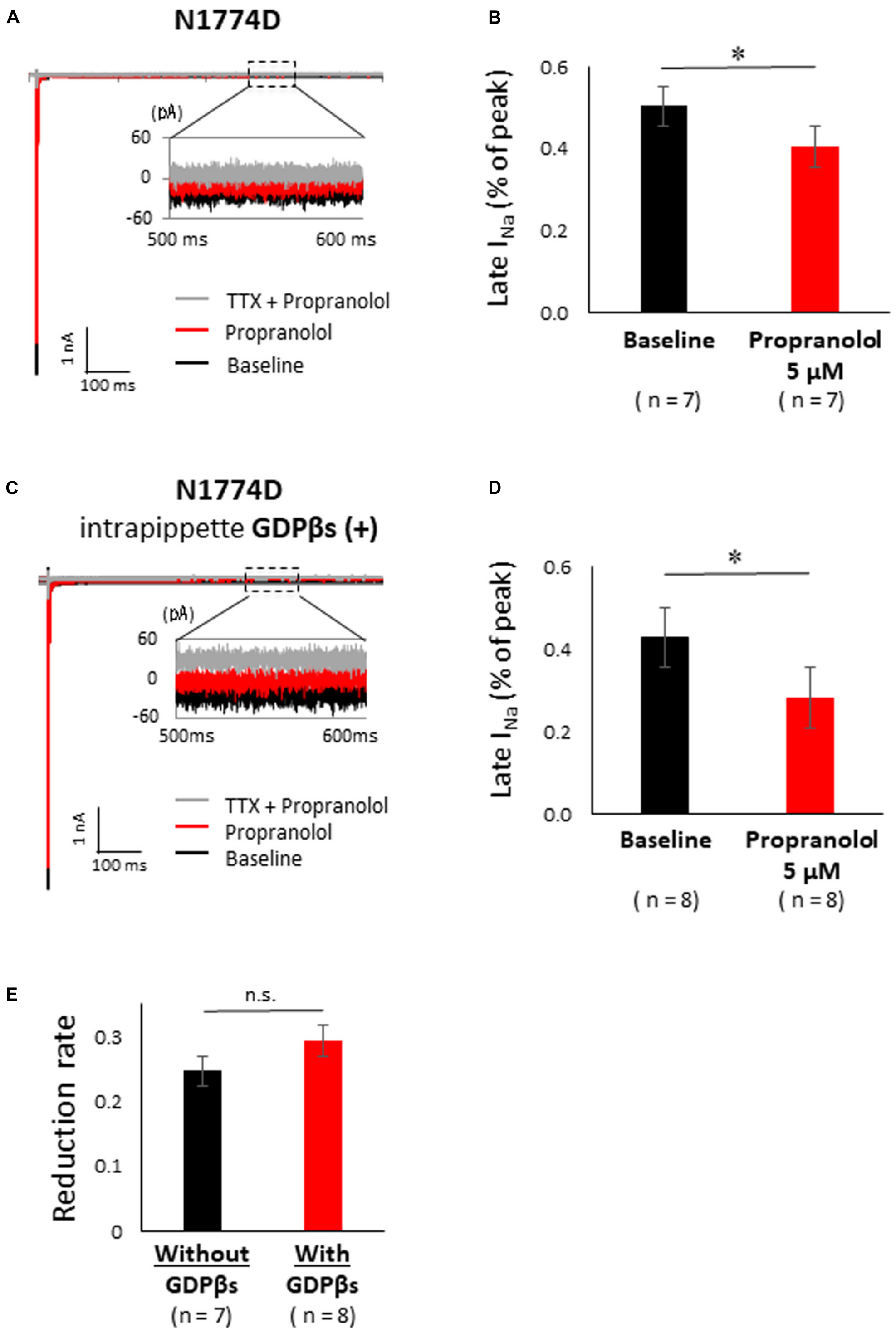

**FIGURE 5 |** Effect of propranolol on late sodium current in N1774-hiPSC-CMs. **(A)** Typical late sodium current traces recorded at baseline (black line), after 5 μM propranolol application (red line), and after the additional treatment with 20 μM tetrodotoxin (TTX) (gray line). **(B)** Statistical analysis of the effect of propranolol on late sodium current. The data pooled from different clones in N1774D-hiPSC-CMs were analyzed. Late sodium current was normalized to peak sodium current. Propranolol significantly reduced the ratio of late/peak sodium current. $^*p < 0.001$, vs. baseline. **(C)** Representative trace of late sodium current in the presence of intrapipette GDPβs. Black line is at baseline, red line is in the presence of 5 μM propranolol, and gray line is in the presence of 5 μM propranolol and 20 μM TTX. We recorded sodium currents in the presence of 5 μM propranolol following addition of 20 μM TTX after recording at baseline. **(D)** Summary of efficacy of propranolol on late sodium current after intrapipette GDPβs treatment. Propranolol significantly reduced the ratio of late/peak sodium current in the presence of intrapipette GDPβs. $^*p < 0.001$, vs. baseline. **(E)** Reduction rate of late sodium current with and without GDPβs. There is no significant difference between in the absence and the presence of intrapipette GDPβs. GDPβs, guanosine diphosphate βs; TTX, tetrodotoxin.

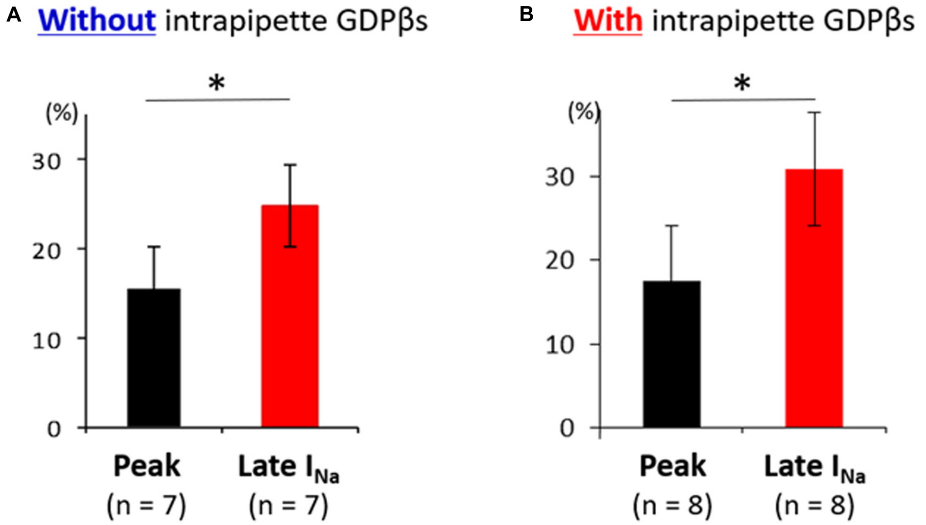

**FIGURE 6 |** Effect of propranolol on peak and late sodium current in N1774D-hiPSC-CMs. Effect of propranolol on peak and late sodium current in the absence **(A)** and the presence of intrapipette GDPβs **(B)**. The data pooled from different clones in N1774D-hiPSC-CMs were analyzed. **(A)** Without intrapipette GDPβs, the rate of reduction was larger in late sodium current compared to in peak sodium current. **(B)** In the presence of intrapipette GDPβs, the rate of reduction was also larger in late sodium current compared to in peak sodium current. $^*p < 0.001$, vs. peak sodium current.

however, the pharmacological mechanism of β-blockers in LQT3 remains unclear.

Recently, the iPSC technology enables us to analyze the disease-causing mechanism of inherited arrhythmia disorder using self-beating cardiomyocytes with the same genetic background as the patient, and several studies of hiPSC-based disease modeling of LQT3 have been reported (Davis et al., 2012; Fatima et al., 2013; Ma et al., 2013; Terrenoire et al., 2013; Spencer et al., 2014; Yoshinaga et al., 2019). To elucidate the mechanism, we established the LQT3-hiPSC-CM cell model from a patient carrying the *SCN5A*-N1774D mutation who was effectively treated with propranolol. In accordance with his clinical course, propranolol attenuated the increased of late sodium current and prolonged APDs in N1774D-hiPSC-CMs, compared to the control cells. In addition, by using GDPβs, an inhibitor of G proteins, we demonstrated that propranolol inhibited the late sodium current through a pathway other than β-adrenergic receptor signaling pathway. Thus, the efficacy and pharmacological mechanism of propranolol have never, to our knowledge, been hitherto elucidated in an LQT3-hiPSC-CM model.

In our previous report (Kato et al., 2014), we analyzed *SCN5A*-N1774D channels using a heterologous expression system in HEK 293 cells and determined that N1774D channels displayed increased peak sodium current densities (2.2 times), a hyperpolarized shift of steady-state activation curve by 7.9 mV, and increased late sodium current densities by 1.7 times, compared to those of wild-type channels. In our LQT3-hiPSC model, the steady-state activation curve was negatively shifted by 12.8 mV and the peak and late sodium current densities were 1.9 and 9.3 times greater, respectively, when compared to those of the control hiPSC-CMs (**Figures 2**, **3**). Considering that our hiPSCs carried the heterozygous *SCN5A*-N1774D mutation, the electrophysiological properties of hiPSC-CMs showed similar trends but different degrees of change in sodium channel kinetics to those of the heterologous expression system, possibly it might result from the differences between the two cell types.

## β-Blocker Therapy for Patients With LQT3

β-blocker therapy is effective for treatment of patients especially with LQT1 and LQT2, who experience cardiac events after adrenergic stimulation, such as exercise or emotional stress. In LQT1 and LQT2, β-blockers clinically reduce the rate of cardiac events and mortality (Moss et al., 2000; Schwartz et al., 2001; Priori et al., 2004). Therefore, based on the clinical evidence, β-blocker therapy is recommended as the first-line treatment for LQT1 and LQT2 (Priori et al., 2013).

In contrast, Schwartz et al. (2001) reported that the recurrence of syncope and death rates in patients with LQT3 were higher (50% and 17%, respectively, $n = 18$) than those with LQT1 and 2. Additionally, Priori et al. (2004) reported that 9 out of 28 (32%) LQT3 patients experienced a cardiac event while on β-blocker therapy at a rate four-fold higher than that of LQT1 patients. Even though the number of LQT3 patients enrolled in the study was small, β-blocker therapy in LQT3 was suggested to be ineffective in preventing fatal arrhythmias and even contraindicated or harmful due to the clinical feature of LQT3, that cardiac events mainly occur at rest, during sleep or bradycardia.

However, recently, the efficacy of β-blocker therapy was analyzed in a large multicenter LQT3 cohort study (Wilde et al., 2016). Wilde et al. (2016) investigated 406 LQT3 patients and demonstrated that β-blocker therapy reduced the risk of life-threatening cardiac events in female patients >1 year of age. In the present study, our patient suffered from repetitive TdPs since birth and propranolol was definitely effective in suppressing those events. Despite accumulating clinical evidence that β-blocker therapy might be beneficial to LQT3 patients, the underlying mechanism by which β-blockers suppress malignant ventricular arrhythmias remains mostly unclear. In our LQT3-hiPSC model, prolonged APDs at baseline were attenuated after propranolol administration (**Figure 5**), which was consistent with the clinical efficacy of β-blocker therapy in LQT3.

## Why Are β-Blockers Effective in Patients With LQT3?

### Cardiac Sodium Channel and β-Adrenergic Stimulation

Cardiac sodium channels are known to be modulated by β-adrenergic stimulation via phosphorylation sites on protein kinases A and C, PKA and PKC, respectively (Grant, 2009). In cardiac sodium channels, PKA activation increased the peak sodium current density and shifted both steady-state activation and inactivation to the hyperpolarized direction (Matsuda et al., 1992; Ono et al., 1993). On the contrary, PKC activation reduced peak sodium current densities and caused a negative shift of the steady-state inactivation curve (Valdivia et al., 2009).

PKA activation did not affect the late sodium current in wild-type sodium channels. On the other hand, in LQT3-related mutant sodium channels, PKA activation had little or no effect on Y1795C and Y1795H channels, but it enhanced the late sodium current in ΔKPQ, D1790G, R1623G, and V2016M channels (Chandra et al., 1999; Tateyama et al., 2003; Tsurugi et al., 2009; Chen et al., 2016).

In LQT3 mouse models, propranolol efficacy to prevent lethal arrhythmias has been contradictory. Fabritz et al. (2010) showed that chronic propranolol therapy did not suppress the carbachol-mediated ventricular arrhythmias, such as TdPs, in a heterozygous knock-in *SCN5A*-ΔKPQ LQT3 mice. On the other hand, Calvillo et al. (2014) reported that propranolol pretreatment prevented carbachol-mediated malignant ventricular tachyarrhythmias in the *SCN5A*-ΔKPQ LQT3 knock-in transgenic mice. Thus, the pharmacological mechanism of β-blockers in LQT3 mice and human cardiomyocytes derived from patients with LQT3 has remained uncertain until now. In the present study, we demonstrated that propranolol attenuated the prolonged APD, by reducing the late sodium current in the patient-derived LQT3-hiPSC-CMs, and provided new supportive evidence of its efficacy on LQT3 by using a human CM model.

### Propranolol Has an Inhibitory Effect on Sodium Channels but Not Through β-Adrenergic Receptor Blockade in an LQT3-hiPSC Model

Propranolol was previously reported to have a unique blocking effect on sodium channels, which was not identified in other β-blockers (Wang et al., 2010). In a heterologous expression system using HEK293 cells, only propranolol, not metoprolol or nadolol, blocked the cardiac sodium channels similar to local anesthetics, and not by acting as β-blockers (Wang et al., 2010). They also demonstrated that the block depends on a critical D4/S6 residue, F1760, involved in local anesthetic effects. In addition, Bankston and Kass (2010) demonstrated that propranolol decreased late sodium current in F1473C and ΔKPQ mutant channels. In this study, we showed no significant difference in the suppression rate of late sodium current by propranolol in presence, or not, of intrapipette GDPβs, an inhibitor of G proteins (**Figure 5E**). This was found to be consistent with the previous reports that propranolol has a sodium channel blocking effect through interfering with the cascade other than G protein cascades (Bankston and Kass, 2010; Wang et al., 2010).

Interestingly, Bankston and Kass (2010) also reported that propranolol within 40 nM to 40 μM range preferential inhibited late but not peak sodium currents. In this study, administration of 5 μM propranolol reduced late sodium current, but it slightly decreased peak sodium current (**Figure 6** and **Table 3**). Regarding the plasma concentration of propranolol, it was reported that there was wide inter-individual variation from 0.04 to 4 μM in peak plasma concentrations, and an increase in the dose up to plasma levels of approximately 0.4 μM was suggested when sufficient therapeutic effects were not achieved (Woosley et al., 1979). Unfortunately, the plasma concentration of propranolol in the patient in this study was not available, and we recorded APs and late sodium current with only 5 μM propranolol using hiPSC-CM model. In addition, we did not examine the effect of propranolol on the kinetics of sodium channel current, which was demonstrated in a heterologous expression system (Wang et al., 2010). Therefore, further examination is needed to reveal the detailed relationship between propranolol dose and the effects on electrophysiological properties in hiPSC-CMs.

## Study Limitations

In the present study, we did not employ the isogenic control line which will prove the phenotype is directly imputable to the mutation. In addition, we did not examine the efficacy of other

**TABLE 3 |** The change of peak and late sodium current after the administration of propranolol in N1774D-hiPSC-CMs.

| | Without GDPβs | | | With GDPβs | | | |
|---|---|---|---|---|---|---|---|
| | **Baseline (pA)** | **Propranolol 5 μM (pA)** | **Reduction rate (%)** | **Baseline (pA)** | **Propranolol 5 μM (pA)** | **Reduction rate (%)** | ***p* value** |
| Peak current | −11627 ± 2177 | −9857 ± 1933 | 15.6 ± 4.6 | −7779 ± 1035 | −6599 ± 1044 | 17.5 ± 3.3 | 0.74 |
| Late current | 61.9 ± 15.7 | 37.5 ± 8.3 | 24.7 ± 4.8 | 38.0 ± 8.6 | 19.3 ± 4.5 | 30.9 ± 6.9 | 0.48 |

*Data are expressed as means ± standard error of measurement. p value for vs. with GDPβs in reduction rate. The data pooled from different clones in N1774D-hiPSC-CMs were analyzed.*

β-blockers. Another limitation is that hiPSC-CM is an *in vitro* cellular model; therefore, it is impossible to assess the role of sympathetic nervous system. Clinically, left cardiac sympathetic denervation was reported to inhibit cardiac events in LQT3 patients (Schwartz et al., 2004), which indicated that β-blockers would have an antiarrhythmic effect by suppressing sympathetic nervous system in LQT3.

### Conclusion

We successfully recapitulated the LQT3 disease phenotype in the *SCN5A*-N1774D-hiPSC-CMs. Additionally, the propranolol efficacy and mode of action were demonstrated in this cell model. Specifically, propranolol blocked sodium channels by means of a unique mechanism unrelated to β-adrenergic signaling pathway, by preferentially inhibiting late rather than peak sodium current.

## DATA AVAILABILITY STATEMENT

The datasets generated for this study are available on request to the corresponding author.

## ETHICS STATEMENT

The studies involving human participants were reviewed and approved by the Ethics Committee of Kyoto University. Written informed consent to participate in this study was provided by the participants' legal guardian/next of kin. The animal study was reviewed and approved by Ethics Committee of Kyoto University.

## AUTHOR CONTRIBUTIONS

SH, TM, and MHo: conceptualization. SH and TM: methodology and writing – original draft. SH, TM, DM, JW, YYa, YW, FY, SN, TH, MHa, HK, JG, AK, MN, JY, and KC: investigation. TM, DM, MHa, and MHo: writing – review and editing. TM and MHo: funding acquisition. TM, SO, YYo, and MHo: resources. DM, SO, YYo, MHo, and TK: supervision. All authors contributed to the article and approved the submitted version.

## FUNDING

This work was supported by the JSPS KAKENHI (Grant Numbers JP16K09499 and JP19K08538 to TM), Suzuken Memorial Foundation (TK and TM), research grant from the Japan Agency for Medical Research and Development, AMED (Grant Number 19ek0109219h0003 to MHo and TM).

## ACKNOWLEDGMENTS

We would like to thank the proband and his family for their participation in this study. We are also grateful for Kyoko Yoshida for her technical assistance.

## REFERENCES

Ackerman, M. J., Priori, S. G., Willems, S., Berul, C., Brugada, R., Calkins, H., et al. (2011). HRS/EHRA expert consensus statement on the state of genetic testing for the channelopathies and cardiomyopathies this document was developed as a partnership between the Heart Rhythm Society (HRS) and the European Heart Rhythm Association (EHRA). *Heart Rhythm.* 8, 1308–1339. doi: 10.1016/j.hrthm.2011.05.020

Bankston, J. R., and Kass, R. S. (2010). Molecular determinants of local anesthetic action of beta-blocking drugs: implications for therapeutic management of long QT syndrome variant 3. *J. Mol. Cell Cardiol.* 48, 246–253. doi: 10.1016/j.yjmcc.2009.05.012

Bennett, P. B., Yazawa, K., Makita, N., and George, A. L. Jr. (1995). Molecular mechanism for an inherited cardiac arrhythmia. *Nature* 376, 683–685. doi: 10.1038/376683a0

Calvillo, L., Spazzolini, C., Vullo, E., Insolia, R., Crotti, L., and Schwartz, P. J. (2014). Propranolol prevents life-threatening arrhythmias in LQT3 transgenic mice: implications for the clinical management of LQT3 patients. *Heart Rhythm.* 11, 126–132. doi: 10.1016/j.hrthm.2013.10.029

Chandra, R., Chauhan, V. S., Starmer, C. F., and Grant, A. O. (1999). beta-Adrenergic action on wild-type and KPQ mutant human cardiac Na+ channels: shift in gating but no change in Ca2+:Na+ selectivity. *Cardiovasc. Res.* 42, 490–502. doi: 10.1016/s0008-6363(99)00042-5

Chen, J., Makiyama, T., Wuriyanghai, Y., Ohno, S., Sasaki, K., Hayano, M., et al. (2016). Cardiac sodium channel mutation associated with epinephrine-induced QT prolongation and sinus node dysfunction. *Heart Rhythm.* 13, 289–298. doi: 10.1016/j.hrthm.2015.08.021

Davis, R. P., Casini, S., van den Berg, C. W., Hoekstra, M., Remme, C. A., Dambrot, C., et al. (2012). Cardiomyocytes derived from pluripotent stem cells recapitulate electrophysiological characteristics of an overlap syndrome of cardiac sodium channel disease. *Circulation* 125, 3079–3091. doi: 10.1161/CIRCULATIONAHA.111.066092

Fabritz, L., Damke, D., Emmerich, M., Kaufmann, S. G., Theis, K., Blana, A., et al. (2010). Autonomic modulation and antiarrhythmic therapy in a model of long QT syndrome type 3. *Cardiovasc. Res.* 87, 60–72. doi: 10.1093/cvr/cvq029

Fatima, A., Kaifeng, S., Dittmann, S., Xu, G., Gupta, M. K., Linke, M., et al. (2013). The disease-specific phenotype in cardiomyocytes derived from induced pluripotent stem cells of two long QT syndrome type 3 patients. *PLoS One* 8:e83005. doi: 10.1371/journal.pone.0083005

Grant, A. O. (2009). Cardiac ion channels. *Circ. Arrhythm. Electrophysiol.* 2, 185–194. doi: 10.1161/CIRCEP.108.789081

Hayano, M., Makiyama, T., Kamakura, T., Watanabe, H., Sasaki, K., Funakoshi, S., et al. (2017). Development of a patient-derived induced pluripotent stem cell model for the investigation of SCN5A-D1275N-related cardiac sodium channelopathy. *Circ. J.* 81, 1783–1791. doi: 10.1253/circj.CJ-17-0064

Hobbs, J. B., Peterson, D. R., Moss, A. J., McNitt, S., Zareba, W., Goldenberg, I., et al. (2006). Risk of aborted cardiac arrest or sudden cardiac death during adolescence in the long-QT syndrome. *JAMA* 296, 1249–1254. doi: 10.1001/jama.296.10.1249

Kato, K., Makiyama, T., Wu, J., Ding, W. G., Kimura, H., Naiki, N., et al. (2014). Cardiac channelopathies associated with infantile fatal ventricular arrhythmias: from the cradle to the bench. *J. Cardiovasc. Electrophysiol.* 25, 66–73. doi: 10.1111/jce.12270

Ma, D., Wei, H., Zhao, Y., Lu, J., Li, G., Sahib, N. B., et al. (2013). Modeling type 3 long QT syndrome with cardiomyocytes derived from patient-specific induced pluripotent stem cells. *Int. J. Cardiol.* 168, 5277–5286. doi: 10.1016/j.ijcard.2013.08.015

Ma, J., Guo, L., Fiene, S. J., Anson, B. D., Thomson, J. A., Kamp, T. J., et al. (2011). High purity human-induced pluripotent stem cell-derived cardiomyocytes: electrophysiological properties of action potentials and ionic currents. *Am. J. Physiol. Heart Circ. Physiol.* 301, H2006–H2017. doi: 10.1152/ajpheart.00694.2011

Matsa, E., Rajamohan, D., Dick, E., Young, L., Mellor, I., Staniforth, A., et al. (2011). Drug evaluation in cardiomyocytes derived from human induced pluripotent stem cells carrying a long QT syndrome type 2 mutation. *Eur. Heart J.* 32, 952–962. doi: 10.1093/eurheartj/ehr073

Matsuda, J. J., Lee, H., and Shibata, E. F. (1992). Enhancement of rabbit cardiac sodium channels by beta-adrenergic stimulation. *Circ. Res.* 70, 199–207. doi: 10.1161/01.res.70.1.199

Mizusawa, Y., Horie, M., and Wilde, A. A. (2014). Genetic and clinical advances in congenital long QT syndrome. *Circ. J.* 78, 2827–2833. doi: 10.1253/circj.cj-14-0905

Moss, A. J., Shimizu, W., Wilde, A. A., Towbin, J. A., Zareba, W., Robinson, J. L., et al. (2007). Clinical aspects of type-1 long-QT syndrome by location, coding type, and biophysical function of mutations involving the KCNQ1 gene. *Circulation* 115, 2481–2489. doi: 10.1161/CIRCULATIONAHA.106.665406

Moss, A. J., Zareba, W., Hall, W. J., Schwartz, P. J., Crampton, R. S., Benhorin, J., et al. (2000). Effectiveness and limitations of beta-blocker therapy in congenital long-QT syndrome. *Circulation* 101, 616–623. doi: 10.1161/01.cir.101.6.616

Nakagawa, M., Koyanagi, M., Tanabe, K., Takahashi, K., Ichisaka, T., Aoi, T., et al. (2008). Generation of induced pluripotent stem cells without Myc from mouse and human fibroblasts. *Nat. Biotechnol.* 26, 101–106. doi: 10.1038/nbt1374

Okita, K., Yamakawa, T., Matsumura, Y., Sato, Y., Amano, N., Watanabe, A., et al. (2013). An efficient nonviral method to generate integration-free human-induced pluripotent stem cells from cord blood and peripheral blood cells. *Stem Cells* 31, 458–466. doi: 10.1002/stem.1293

Ono, K., Fozzard, H. A., and Hanck, D. A. (1993). Mechanism of cAMP-dependent modulation of cardiac sodium channel current kinetics. *Circ. Res.* 72, 807–815. doi: 10.1161/01.res.72.4.807

Priori, S. G., Napolitano, C., Schwartz, P. J., Grillo, M., Bloise, R., Ronchetti, E., et al. (2004). Association of long QT syndrome loci and cardiac events among patients treated with beta-blockers. *JAMA* 292, 1341–1344. doi: 10.1001/jama.292.11.1341

Priori, S. G., Wilde, A. A., Horie, M., Cho, Y., Behr, E. R., Berul, C., et al. (2013). HRS/EHRA/APHRS expert consensus statement on the diagnosis and management of patients with inherited primary arrhythmia syndromes: document endorsed by HRS, EHRA, and APHRS in May 2013 and by ACCF, AHA, PACES, and AEPC in June 2013. *Heart Rhythm.* 10, 1932–1963. doi: 10.1016/j.hrthm.2013.05.014

Schwartz, P. J., Crotti, L., and Insolia, R. (2012). Long-QT syndrome: from genetics to management. *Circ. Arrhythm. Electrophysiol.* 5, 868–877. doi: 10.1161/CIRCEP.111.962019

Schwartz, P. J., Priori, S. G., Cerrone, M., Spazzolini, C., Odero, A., Napolitano, C., et al. (2004). Left cardiac sympathetic denervation in the management of high-risk patients affected by the long-QT syndrome. *Circulation* 109, 1826–1833. doi: 10.1161/01.CIR.0000125523.14403.1E

Schwartz, P. J., Priori, S. G., Spazzolini, C., Moss, A. J., Vincent, G. M., Napolitano, C., et al. (2001). Genotype-phenotype correlation in the long-QT syndrome: gene-specific triggers for life-threatening arrhythmias. *Circulation* 103, 89–95. doi: 10.1161/01.cir.103.1.89

Shimizu, W., Moss, A. J., Wilde, A. A., Towbin, J. A., Ackerman, M. J., January, C. T., et al. (2009). Genotype-phenotype aspects of type 2 long QT syndrome. *J. Am. Coll. Cardiol.* 54, 2052–2062. doi: 10.1016/j.jacc.2009.08.028

Skinner, J. R., Winbo, A., Abrams, D., Vohra, J., and Wilde, A. A. (2019). Channelopathies that lead to sudden cardiac death: clinical and genetic aspects. *Heart Lung Circ.* 28, 22–30. doi: 10.1016/j.hlc.2018.09.007

Spencer, C. I., Baba, S., Nakamura, K., Hua, E. A., Sears, M. A., Fu, C. C., et al. (2014). Calcium transients closely reflect prolonged action potentials in iPSC models of inherited cardiac arrhythmia. *Stem Cell Rep.* 3, 269–281. doi: 10.1016/j.stemcr.2014.06.003

Takahashi, K., Tanabe, K., Ohnuki, M., Narita, M., Ichisaka, T., Tomoda, K., et al. (2007). Induction of pluripotent stem cells from adult human fibroblasts by defined factors. *Cell* 131, 861–872. doi: 10.1016/j.cell.2007.11.019

Tateyama, M., Rivolta, I., Clancy, C. E., and Kass, R. S. (2003). Modulation of cardiac sodium channel gating by protein kinase A can be altered by disease-linked mutation. *J. Biol. Chem.* 278, 46718–46726. doi: 10.1074/jbc.M308977200

Terrenoire, C., Wang, K., Tung, K. W., Chung, W. K., Pass, R. H., Lu, J. T., et al. (2013). Induced pluripotent stem cells used to reveal drug actions in a long QT syndrome family with complex genetics. *J. Gen. Physiol.* 141, 61–72. doi: 10.1085/jgp.201210899

Tsurugi, T., Nagatomo, T., Abe, H., Oginosawa, Y., Takemasa, H., Kohno, R., et al. (2009). Differential modulation of late sodium current by protein kinase A in R1623Q mutant of LQT3. *Life Sci.* 84, 380–387. doi: 10.1016/j.lfs.2009break01.001

Valdivia, C. R., Ueda, K., Ackerman, M. J., and Makielski, J. C. (2009). GPD1L links redox state to cardiac excitability by PKC-dependent phosphorylation of the sodium channel SCN5A. *Am. J. Physiol. Heart Circ. Physiol.* 297, H1446–H1452. doi: 10.1152/ajpheart.00513.2009

Wang, D. W., Mistry, A. M., Kahlig, K. M., Kearney, J. A., and Xiang, J. (2010). Propranolol blocks cardiac and neuronal voltage-gated sodium channels. *Front. Pharmacol.* 1:144. doi: 10.3389/fphar.2010.00144

Wilde, A. A., Moss, A. J., Kaufman, E. S., Shimizu, W., Peterson, D. R., Benhorin, J., et al. (2016). Clinical aspects of type 3 long-QT syndrome: an international multicenter study. *Circulation* 134, 872–882. doi: 10.1161/CIRCULATIONAHA.116.021823

Woosley, R. L., Kornhauser, D., Smith, R., Reele, S., Higgins, S. B., Nies, A. S., et al. (1979). Suppression of chronic ventricular arrhythmias with propranolol. *Circulation* 60, 819–827. doi: 10.1161/01.cir.60.4.819

Wuriyanghai, Y., Makiyama, T., Sasaki, K., Kamakura, T., Yamamoto, Y., Hayano, M., et al. (2018). Complex aberrant splicing in the induced pluripotent stem cell-derived cardiomyocytes from a patient with long QT syndrome carrying KCNQ1-A344Aspl mutation. *Heart Rhythm.* 15, 1566–1574. doi: 10.1016/j.hrthm.2018.05.028

Yamamoto, Y., Makiyama, T., Harita, T., Sasaki, K., Wuriyanghai, Y., Hayano, M., et al. (2017). Allele-specific ablation rescues electrophysiological abnormalities in a human iPS cell model of long-QT syndrome with a CALM2 mutation. *Hum. Mol. Genet.* 26, 1670–1677. doi: 10.1093/hmg/ddx073

Yang, L., Soonpaa, M. H., Adler, E. D., Roepke, T. K., Kattman, S. J., Kennedy, M., et al. (2008). Human cardiovascular progenitor cells develop from a KDR+ embryonic-stem-cell-derived population. *Nature* 453, 524–528. doi: 10.1038/nature06894

Yoshinaga, D., Baba, S., Makiyama, T., Shibata, H., Hirata, T., Akagi, K., et al. (2019). Phenotype-based high-throughput classification of long QT syndrome subtypes using human induced pluripotent stem cells. *Stem Cell Rep.* 13, 394–404. doi: 10.1016/j.stemcr.2019.06.007

**Conflict of Interest:** YYo owns stock in iPS Portal.

The remaining authors declare that the research was conducted in the absence of any commercial or financial relationships that could be construed as a potential conflict of interest.

frontiers
in Cell and Developmental Biology

ORIGINAL RESEARCH
published: 10 September 2020
doi: 10.3389/fcell.2020.542562

# Optimizing the Direction and Order of the Motion Unveiled the Ability of Conventional Monolayers of Human Induced Pluripotent Stem Cell-Derived Cardiomyocytes to Show Frequency-Dependent Enhancement of Contraction and Relaxation Motion

**Hiroko Izumi-Nakaseko[1], Koki Chiba[1], Mihoko Hagiwara-Nagasawa[1], Ayano Satsuka[2], Ai Goto[1], Yoshio Nunoi[1], Ryuichi Kambayashi[1], Akio Matsumoto[3], Yoshinori Takei[4], Yasunari Kanda[2], Atsuhiko T. Naito[5] and Atsushi Sugiyama[1,3,4]***

*[1] Department of Pharmacology, Faculty of Medicine, Toho University, Tokyo, Japan, [2] Division of Pharmacology, National Institute of Health Sciences, Kanagawa, Japan, [3] Department of Aging Pharmacology, Faculty of Medicine, Toho University, Tokyo, Japan, [4] Department of Translational Research & Cellular Therapeutics, Faculty of Medicine, Toho University, Tokyo, Japan, [5] Department of Physiology, Division of Cell Physiology, Graduate School of Medicine, Toho University, Tokyo, Japan*

**Edited by:**
*Masayuki Yazawa,*
*Columbia University, United States*

**Reviewed by:**
*Oscar J. Abilez,*
*Stanford University, United States*
*Josh Maxwell,*
*Emory University, United States*

***Correspondence:**
*Atsushi Sugiyama*
*atsushi.sugiyama@med.toho-u.ac.jp*

**Specialty section:**
*This article was submitted to Stem Cell Research, a section of the journal Frontiers in Cell and Developmental Biology*

**Received:** *13 March 2020*
**Accepted:** *19 August 2020*
**Published:** *10 September 2020*

**Citation:**
*Izumi-Nakaseko H, Chiba K, Hagiwara-Nagasawa M, Satsuka A, Goto A, Nunoi Y, Kambayashi R, Matsumoto A, Takei Y, Kanda Y, Naito AT and Sugiyama A (2020) Optimizing the Direction and Order of the Motion Unveiled the Ability of Conventional Monolayers of Human Induced Pluripotent Stem Cell-Derived Cardiomyocytes to Show Frequency-Dependent Enhancement of Contraction and Relaxation Motion. Front. Cell Dev. Biol. 8:542562. doi: 10.3389/fcell.2020.542562*

Contractility of the human heart increases as its beating rate is elevated, so-called positive force-frequency relationship; however, human induced pluripotent stem cell-derived cardiomyocytes (hiPSC-CMs) have been reported to exert a negative force-frequency relationship. We tested the hypothesis that the regulation of motion directions by electrical pacing and/or oxygen supply may improve the electro-mechanical properties of hiPSC-CMs monolayers. To better evaluate the spatial and temporal relationship between electrical excitation and contractile motion, we simultaneously observed the field potential and motion vector of hiPSC-CMs sheets. Under spontaneous contraction, although an electrical excitation originating from a region propagated unidirectionally over the cell sheet, contraction wave started from multiple sites, and relaxation wave was initiated from a geometric center of hiPSC-CMs sheet. During electrical pacing, contraction and relaxation waves were propagated from the stimulated site. Interestingly, the maximum contraction speed was more increased when the hiPSC-CMs sheet was stimulated at an area relaxation initiated under spontaneous condition. Furthermore, motion vector analysis demonstrated that "positive contraction velocity-frequency relationship" in contraction and "frequency-dependent enhancement of relaxation" were produced in the cell sheet by optimizing the direction and order of the contractile motion with pacing at the relaxation-initiating area. A close analysis of motion vectors along with field potential recording demonstrated that relaxation process consists of fast and slow phases, and suggest that intracellular $Ca^{2+}$

dynamics may be closely related to functions of $Ca^{2+}$-ATPase pump and $Na^{+}$-$Ca^{2+}$ exchangers. Namely, the slow relaxation phase occurred after the second peak of field potential, suggesting that the slow phase may be associated with extrusion of $Ca^{2+}$ by $Na^{+}$-$Ca^{2+}$ exchangers during repolarization. Increase of oxygen concentration from 20 to 95% as well as β-adrenergic stimulation with isoproterenol accelerated the fast relaxation, suggesting that it could depend on $Ca^{2+}$ uptake via $Ca^{2+}$-ATPase during the depolarization phase. The ratio of maximum contraction speed to field potential duration was increased by the β-adrenergic stimulation, indicating the elevated contraction efficiency per $Ca^{2+}$-influx. Thus, these findings revealed potential ability of conventional monolayers of hiPSC-CMs, which will help apply them to translational study filling the gap between physiological as well as pharmacological studies and clinical practice.

**Keywords: contraction velocity-frequency relationship, frequency-dependent enhancement of relaxation, human induced pluripotent stem cell-derived cardiomyocytes, field potential, motion vector**

## INTRODUCTION

Positive force-frequency relationship in ventricular muscle has been observed in guinea-pigs, rabbits and humans, which cannot be detected in mice or rats (Kurihara and Sakai, 1985; Pieske et al., 1999; Maier et al., 2000). Enhancement of twitch force occurs along with increasing sarcoplasmic reticulum (SR) $Ca^{2+}$ content in ventricular muscle (Kurihara and Sakai, 1985; Pieske et al., 1999; Maier et al., 2000). In a previous study using the human hearts, non-failing myocardium showed positive force-frequency relationship in twitch force in parallel with an increase of SR $Ca^{2+}$ content, but failing myocardium exerted negative force-frequency relationship in it with decreased SR $Ca^{2+}$ content (Pieske et al., 1999). Therefore, positive force-frequency relationship in contraction can be observed in matured and non-pathological human cardiomyocytes, which makes many researchers focus on the maturation of human induced pluripotent stem cell-derived cardiomyocytes (hiPSC-CMs) to mimic the physiology of the intact human heart. For this purpose, tissue engineering has been applied to facilitate hiPSC-CMs maturation; for example, hiPSC-CMs were mixed in hydrogel solution to prepare 3-dimentional tissue form, which were set on elastic pillars (Ronaldson-Bouchard et al., 2019), on the Biowire II (Feric et al., 2019), or in troughs of Tissue Train 6-well plates (Ruan et al., 2016). After the incubation under static stress and electrical pacing, they obtained the ability showing the positive force-frequency relationship in their twitch force together with changes including rod-shaped morphology and aligned sarcomeres (Ruan et al., 2016; Ronaldson-Bouchard et al., 2019; Feric et al., 2019). Since those experimental systems may be complex to perform, expensive and less versatile, and need hundreds of thousands to millions of hiPSC-CMs per engineered tissue, we adopted the monolayers of hiPSC-CMs which have been used to detect proarrhythmic and anti-arrhythmic potentials of a drug using extracellular field potential recordings (Ando et al., 2017; Izumi-Nakaseko et al., 2017a,b, 2018; Blinova et al., 2018). However, negative force-frequency relationships have been shown in the monolayers of hiPSC-CMs (Sasaki et al., 2018) possibly because of their random sarcomere alignment, the lack of transverse tubule or partially developed $Ca^{2+}$ handling (Yang et al., 2014).

In order to solve such problems in the engineered tissues and conventional monolayers of hiPSC-CMs as described above, we investigated the effects of electrophysiological and biochemical interventions on the conventional monolayers including the regulation of the contraction direction and oxygen tension. While oxygenation of culture medium by air is generally considered to be enough for the cell sheet to keep their basal physiological functions, it is unknown whether the oxygenation by air may be enough for hiPSC-CMs sheets particularly under higher frequency pacing and/or pharmacological β-adrenergic stimulation. In order to develop a method that can regulate the contractile direction, we first prepared mono-layered, high cell-density sheets of hiPSC-CMs set on the probe of the microelectrode-array system which can be paced via a set of two electrodes arbitrarily chosen from 64 electrodes (Izumi-Nakaseko et al., 2017b). Second, we combined microelectrode array measurement and motion vector analysis in order to evaluate the spatial and temporal relationships between electrical excitation and contractile motion propagating over the cell sheet, thus making it possible to study how the regulation of motion directions may improve the mechanophysiological property of hiPSC-CMs sheets. The motion vector analysis with a phase-contrast microscopy enables to observe the multi-directional motion in a cell sheet with high spatiotemporal resolution, which could indirectly provide the information of $Ca^{2+}$ dynamics in each cell, the electrical excitation waveform of sub-cell population, and the cell-to-cell mechanical interaction (Hayakawa et al., 2014; Sugiyama et al., 2019). Since the contraction velocity can be converted to the stretch velocity of the series elastic elements (Hill, 1938; Linke et al., 1999), the elevation of the contraction velocity would be linearly related to the increase of the contractile force in the cell sheet which adheres to the plastic material of the probe. Third, the effect of oxygen tension on the cell motion and field potential was analyzed at control as well as in the presence of 10 nM isoproterenol which would increase the oxygen demand. We propose that such currently used manipulations significantly improve the utility of the conventional monolayers of hiPSC-CMs for simultaneously assessing the inotropic and lusitropic actions of a chemical compound along with its electropharmacological property.

# MATERIALS AND METHODS

## Culture of hiPSC-CMs Sheets

Human iPSC-CMs (iCell® Cardiomyocytes, FUJIFILM Cellular Dynamics, Inc., Madison, WI, United States) had been incubated for 30∼32 days after differentiation, which were preserved in liquid $N_2$ (Ma et al., 2011). The cryopreserved hiPSC-CMs (iCell® Cardiomyocytes$^2$; FUJIFILM Cellular Dynamics, Inc.) were purchased and cultured as previously described (Izumi-Nakaseko et al., 2018). A volume of 2 μL of the cell suspension containing $1.5 \times 10^4$ cells/μL was plated onto 64-microelectrode array (MED probe; MED-P515A, Alpha MED Scientific Inc., Osaka, Japan) after having coated them with fibronectin. The culture medium (maintenance medium; FUJIFILM Cellular Dynamics, Inc.) around the probe was fully replaced with fresh one once a week. The cardiomyocytes were cultured for 3–5 days to form a cell sheet with spontaneous and synchronous electrical automaticity, which were used for experiments within 3 weeks. The age of hiPSC-CMs at the experiment was calculated as 44∼66 days old on the examination of pacing sites and 66∼70 days old on that with isoproterenol and oxygen concentration.

## Field Potential Recordings and Image Acquisitions

The hiPSC-CMs sheet was incubated in 1 mL of culture medium with 22 mm in diameter and 2.6 mm in depth at 37°C in a stage-top chamber set on the stage of a live cell imaging system, SI8000 (Sony Imaging Products & Solutions Inc., Tokyo, Japan), which was filled and equilibrated for > 30 min at 37°C with gas mixture of 95% air + 5% $CO_2$ (normal oxygen supply), or of 95% $O_2$ + 5% $CO_2$ (high oxygen supply) using a gas controller (INUM-MED-F1, TOKAI HIT Co., Ltd., Shizuoka, Japan). Then, the MED probe was connected to the amplifiers (MED-A64HE1S and MED-A64MD1, Alpha MED Scientific Inc.). The hiPSC-CMs sheet was electrically driven through a pair of neighboring electrodes selected from 64 ones. The stimulation pulses were biphasic, rectangular in shape, 12–50 μA in amplitude (about three times the threshold current) and of 0.4 ms duration, which were applied on the cell sheets in cycle lengths of 600–1,400 ms. In order to examine the effects of pacing sites on the cell sheet, we needed to choose the stimulation sites within 1,050 × 1,050 μm$^2$ of the microelectrode array, which was too small to necessarily set four edges. Thus, we selected the one pacing site where the threshold current was the lowest among the edges to reduce the damage of the cell sheets. Isoproterenol of 10 nM was applied to increase the oxygen demand of the cell sheet under each of the oxygen conditions. The rate-adapted field potential duration was assessed under a train of 15 stimuli at a cycle length of 600–1,400 ms before and after the drug treatment. Field potentials of the hiPSC-CMs sheet at 62 microelectrodes were acquired with high- and low-pass filters of 0.1 and 5 kHz, respectively. Field potentials were digitized at a sampling rate of 20 kHz with a MED64-Basic system (Alpha MED Scientific Inc.). Simultaneously, images of the cell sheet motion in the area of 1,365 × 1,365 μm$^2$ square were acquired with SI8000 (Sony Imaging Products & Solutions Inc.) at a frame rate of 150 Hz. Image acquisitions and microelectrode array recordings were synchronized using external triggering options of the MED64-Basic system.

## Drugs

(−)-Isoproterenol hydrochloride was purchased from Sigma-Aldrich Japan K.K. (Tokyo, Japan).

## Data Analyses

Field potential duration and excitation conduction were analyzed with Mobius software (Alpha MED Scientific Inc.) as previously described (Izumi-Nakaseko et al., 2018). Since the field potential duration was largely shortened by the initial several electrical pulses and gradually plateaued during the electrical pacing of 15 pulses, the traces from the 15th electrical stimulation were adopted for analysis. Motion vectors of cell sheet movements were extracted and analyzed by SI8000C Analyzer software (version 1.05.000; Sony Imaging Products & Solutions Inc.) (Hayakawa et al., 2014; Sugiyama et al., 2019). A region of interest (ROI) was set in two ways; (1) a whole observation area of 1,365 × 1,365 μm$^2$ square (Large ROI), and (2) multiple 200 × 200 μm$^2$ ones (Small ROIs). Contraction velocity of the hiPSC-CMs sheet gradually increased during electrical pacing, and it took about 5 s before the contraction velocity reached the new steady-state level. Based on this observation, motion vectors were analyzed $\geq$ 5 s after the start of electrical pacing in Large as well as Small ROIs to obtain the stable contractions. Axes for axial analysis of motion vectors in the Small ROIs were set based on the positions toward pacing sites. **Figure 1** illustrates the relationship among field potential waveform (top panel) and averaged motion speed changes without and with axial analysis (middle panels), postulated activity of $Na^+$-$Ca^{2+}$ exchanger and SERCA2a (bottom panel) with variables used in this study. Although "interval" as well as "duration" means the time interval between two points, we used these two terms in the same manner as described in the previous studies (Hayakawa et al., 2014; Izumi-Nakaseko et al., 2017a,b). Activities of $Ca^{2+}$ removal by $Na^+$-$Ca^{2+}$ exchanger and $Ca^{2+}$ uptake by SERCA2a are based on the information on the $Na^+$-$Ca^{2+}$ exchanger activity and intracellular $Ca^{2+}$ dynamics during an action potential, and $Ca^{2+}$ dependent SERCA activity in the rabbit ventricle (Bers, 1987; Shattock and Bers, 1989; Bassani et al., 1994). The ratio of maximum contraction speed toward field potential duration (maximum contraction speed/field potential duration) was calculated to estimate the contraction efficiency. To analyze the temporal relationship of the terminal points between repolarization and relaxation, interval was calculated by subtracting the field potential duration from either of the contraction-fast relaxation duration or contraction-slow relaxation duration at each pacing frequency.

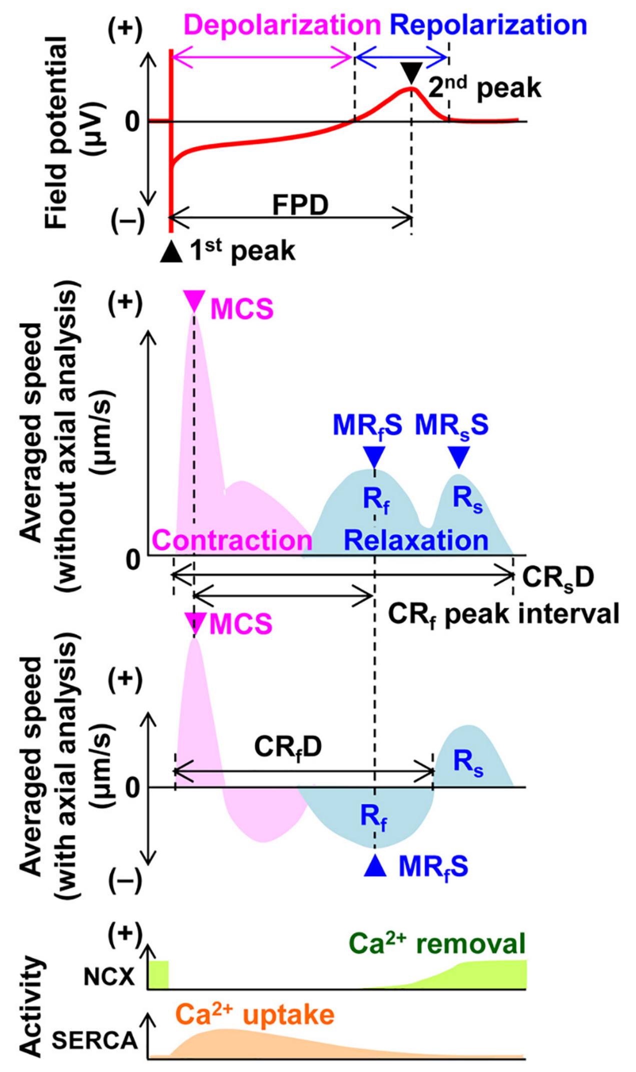

**FIGURE 1 |** Illustration of the field potential (top panel), motion velocity (middle 2 panels) and postulated activities of Na$^+$-Ca$^{2+}$ exchanger (NCX) and SERCA2a (SERCA) (bottom panel) of the human induced pluripotent stem cell-derived cardiomyocytes sheet during a cardiac cycle. The field potential includes the information of extracellular membrane potential of the cells and ion concentration changes by ion channel opening in the space surrounded by cells' membrane and the surface of the probe. The changes of motion velocity during contraction (pink) and relaxation (blue) are presented without (upper) and with axial analysis (lower), respectively. Activities of Ca$^{2+}$ removal by NCX and Ca$^{2+}$ uptake by SERCA are postulated using the information on the NCX activity and intracellular Ca$^{2+}$ dynamics during an action potential, and Ca$^{2+}$ dependent SERCA activity in the rabbit ventricle (Bers, 1987; Shattock and Bers, 1989; Bassani et al., 1994). FPD, field potential duration; MCS, maximum contraction speed; MR$_f$S, maximum fast-relaxation speed; MR$_s$S, maximum slow-relaxation speed; CR$_s$D, contraction-slow relaxation duration; CR$_f$ peak interval, contraction-fast relaxation peak interval; CR$_f$D, contraction-fast relaxation duration; R$_f$, fast relaxation phase; and R$_s$, slow relaxation phase.

Statistical analysis was performed with the software GraphPad Prism 6 (ver 6.03, GraphPad Software, Inc., La Jolla, CA, United States). Statistical significances within a parameter were assessed with one-way, repeated measures analysis of variance (ANOVA) followed by the uncorrected Fisher's least significant difference test for mean value comparison. Statistical significances before and after the treatment of the drugs were assessed with two-way, repeated measures ANOVA followed by the uncorrected Fisher's least significant difference test for mean value comparison. Data were presented as mean ± S.E.M. *P*-values $< 0.05$ were considered to be statistically significant.

## RESULTS

### The Effects of Electrical Pacing on the Field Potential, and the Contraction and Relaxation Processes of hiPSC-CMs Sheets

We prepared one layered, high cell-density sheets of hiPSC-CMs, and simultaneously recorded the field potentials and motion vectors to better understand electro-mechanical relationships in the cell sheets.

A spontaneous electrical excitation from a certain region propagated unidirectionally over the cell sheet (**Figure 2A** Spontaneous), which evoked contractions with various excitation-contraction intervals, forming a synchronous movement as shown in **Figure 2B** (Spontaneous a∼b, **Supplementary Videos S1, S2**). However, the maximal relaxation motion was observed around the center of the cell sheet (**Figure 2B**; see Spontaneous e∼g, **Supplementary Videos S1, S2**).

In order to investigate how the pacing positions can affect the excitation-contraction relationship, we electrically paced the cell sheet via the electrodes near the maximal relaxation region (**Figure 2A** MRR) or via those apart from MRR (**Figure 2A** Edge). The evoked excitation propagated uniformly from the pacing positions to the distal areas, whereas the contraction started around the pacing sites. Pacing the sheets around MRR made the starting area of contraction overlapped on MRR. The maximum contraction speed was higher under these pacing conditions than that under spontaneous one (**Figures 2B,C**, **Supplementary Videos S3, S4**). The maximum contraction speed was higher when the electrical stimuli were applied around MRR than around Edge (**Figure 2C**, see points "b"). In addition, there were fast and slow phases in contraction as well as in relaxation as shown in **Figure 2C**. Analysis with Small ROIs of 200 × 200 $\mu m^2$ square clarified that the vector directions of contraction and relaxation depended on the electrically paced sites as shown in vector direction histogram (**Figure 3**, **Supplementary Videos S5, S6**).

Representative traces of simultaneously obtained field potential waveform and averaged motion speed from whole observation area of 1,365 × 1,365 $\mu m^2$ square (Large ROI) under electrical pacing at 0.7, 1.0, and 1.4 Hz were overlaid in **Figure 4**. The relationships between the pacing frequency and either of the maximum contraction speed, maximum fast-relaxation speed, contraction-slow relaxation duration, field potential duration or contraction-fast relaxation peak interval are summarized

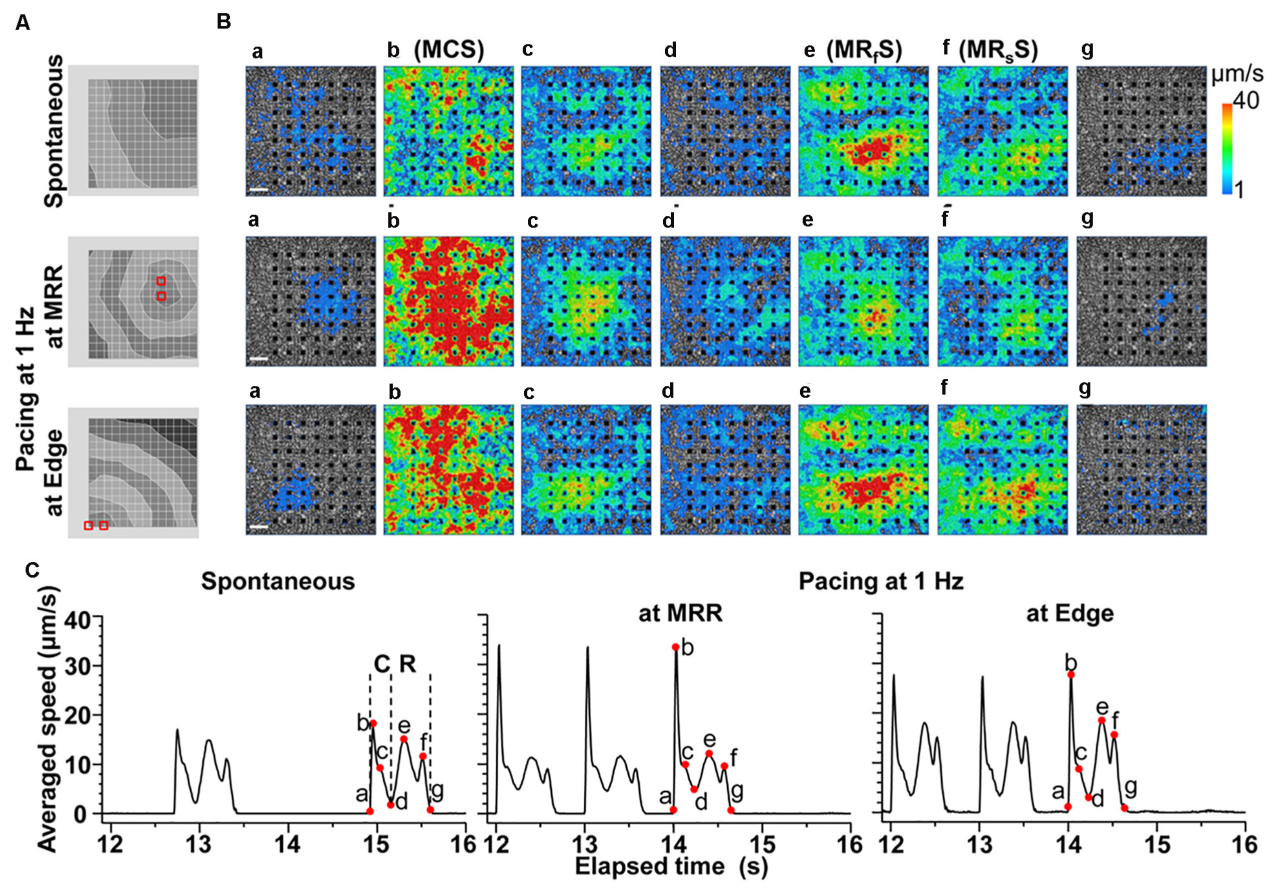

**FIGURE 2 |** Representative field potentials and motion vectors detected during contraction and relaxation phases of a human induced pluripotent stem cell-derived cardiomyocytes sheet during spontaneous activity, and electrical pacing around maximum relaxation region (MRR) or apart from MRR (Edge) under the mixed gas consisting of 95% $O_2$ + 5% $CO_2$. **(A)** Activation map of each excitation under spontaneous activity (Spontaneous, top), or under electrical pacing at MRR (middle) or Edge (bottom). Red squares indicate the pacing electrodes. The interval between isochrones is 1 ms. **(B)** The visualized velocity of cell motions on phase-contrast images of the cell sheet during contraction (a∼d) and relaxation (d∼g) under spontaneous activity (Spontaneous, top), or during electrical pacing at MRR (middle) or at Edge (bottom). White bars indicate 200 μm in length. **(C)** The representative traces of averaged speed under spontaneous activity (Spontaneous, left), or during electrical pacing at MRR (middle) or at Edge (right). These traces were obtained from whole observation area of 1,365 × 1,365 $\mu m^2$ square shown in panel B. The last 3 motions under electrical pacing consisting of 15 pulses at 1 Hz are shown (middle and right). Labels of "a" to "g" in panel B correspond to red points with "a" to "g" in panel C during contraction (C) and relaxation (R). Note that b, e and f represent the maximum speeds of contraction (MCS), fast relaxation (MR$_f$S), and slow relaxation (MR$_s$S), respectively.

in **Figure 5**. The conduction speeds during pacing at 1 Hz around MRR and Edge were calculated to be 0.19 ± 0.01 and 0.23 ± 0.02 m/s, respectively ($p < 0.05$) for the cell sheets of 44∼66 days old. Positive contraction velocity-frequency relationship was demonstrated in the maximum contraction speed which was higher in the pacing condition around MRR than around Edge (**Figure 5A** upper). The sheet also showed a frequency-dependent elevation of relaxation speed when the pacing was applied around Edge, which was not observed when it was done around MRR (**Figure 5A** lower). The field potential duration and contraction-slow relaxation duration were shortened in parallel in a frequency-dependent manner (**Figure 5B**). The field potential duration was shorter when paced around Edge than around MRR. The contraction-fast relaxation peak interval was also shortened in a frequency-dependent manner only when paced around Edge.

## Effects of Oxygen Supply on the Field Potential, and the Contraction and Relaxation Processes of hiPSC-CMs Sheets

Since it is unknown whether oxygenation of culture medium by air may be enough for the contractility of hiPSC-CMs sheets, we examined whether increasing oxygen supply could enhance the contraction and relaxation at control and in the presence of 10 nM isoproterenol using hiPSC-CMs sheets at the age of 66∼70 days old. As shown in **Figure 4**, two peaks of relaxation in averaged speed (fast and slow relaxations) were observed before and after the second peak of field potential waveform, respectively in the mixed gas of 95% $O_2$ + 5% $CO_2$. The relationships between the pacing frequency and either of contraction-slow relaxation duration, field potential

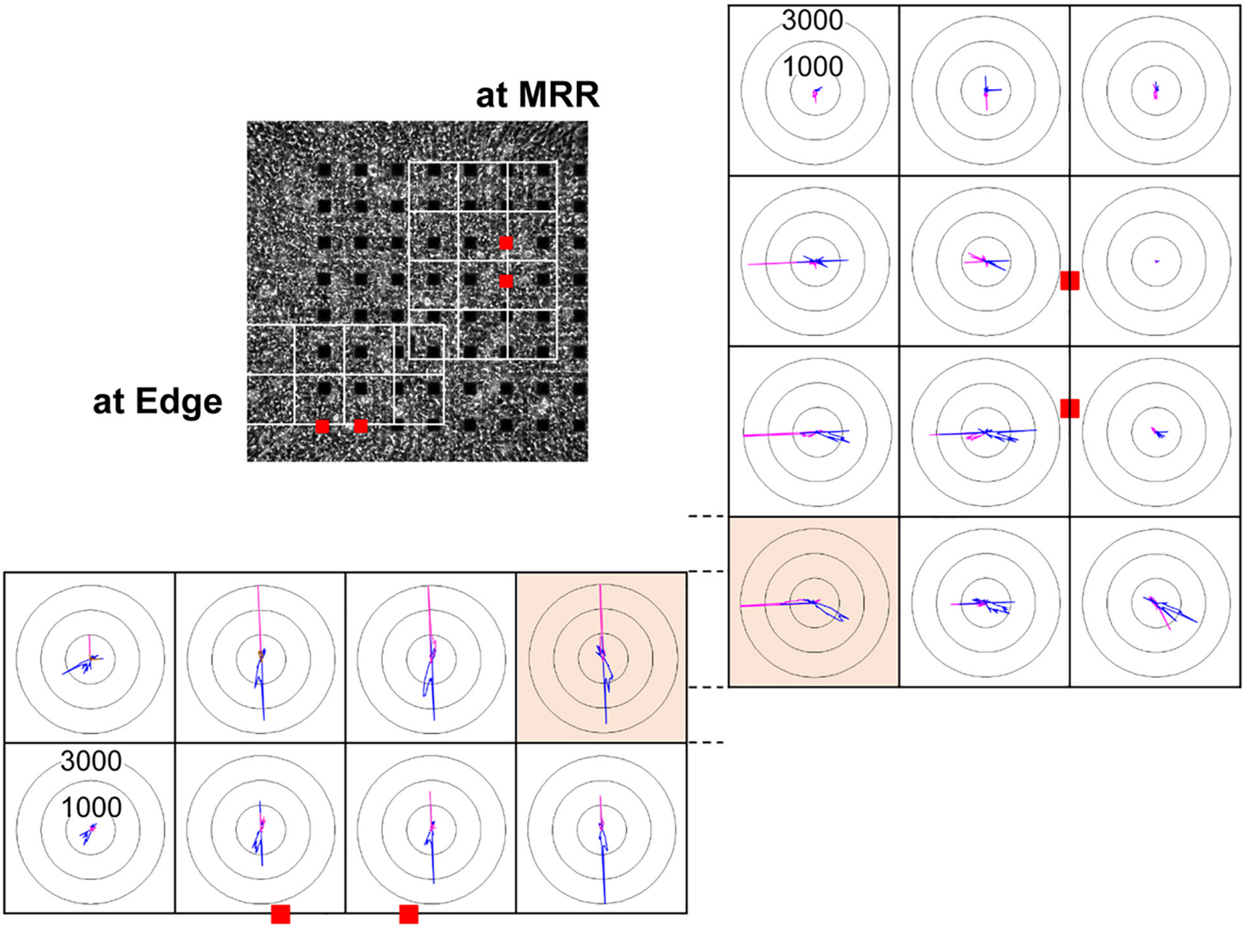

**FIGURE 3 |** Representative histogram of motion vector direction acquired from each of the small regions of interest (ROIs) consisting of 200 × 200 $\mu m^2$ square (white squares) from the same human induced pluripotent stem cell-derived cardiomyocytes sheet as that in **Figure 2**, when paced around maximum relaxation region (MRR, right) or apart from MRR (Edge, bottom) under the mixed gas consisting of 95% $O_2$ + 5% $CO_2$ are shown. Red squares indicate the positions of pacing electrodes on a phase-contrast image of the cell sheet (upper left panel). Each panel indicates the distribution of motion vectors detected during the contraction (pink) and relaxation phases (blue) in 360-degree under electrical pacing. The motion vectors during contraction and relaxation were extracted from the last 9 out of 15 excitations, and were sorted by the direction in every 2.5 degree. The numbers (1000 and 3000) indicate the number of vectors facing to an arbitrary direction. Highlighted small ROIs with bright orange color partially overlapped when paced at MRR and Edge. Note that their patterns of vector direction were quite different.

duration, contraction-fast relaxation peak interval, maximum contraction speed or maximum fast-relaxation speed extracted from Large ROI under the mixed gas of normal or high oxygen tension were summarized in **Figure 6**. In both gas conditions, contraction-slow relaxation duration, field potential duration and contraction-fast relaxation peak interval were shortened in a frequency-dependent manner. Ten nM of isoproterenol significantly shortened these parameters compared with those under pre-drug control conditions; and the extent of frequency-dependent shortening in the parameters was diminished but significant in the presence of isoproterenol (**Figures 6A,B**, upper). Isoproterenol shortened the field potential duration by about 200 ms at the frequency of 1Hz. Data at 0.71 and 0.83 Hz could not be obtained in the presence of isoproterenol because of accelerated spontaneous automaticity rate. Expression level of $\beta_1$ adrenoceptor in hiPSC-CMs at 44 days old of hiPSC-CMs was measured, which was about one third of the adult heart (**Supplementary Figure S1**). The conduction speed for the sheets of 66∼70 days old during pacing at 1 Hz with normal and high oxygen supply was calculated to be 0.22 ± 0.02 and 0.21 ± 0.03 m/s ($p$ = 0.61) in control, and 0.26 ± 0.02 and 0.24 ± 0.02 m/s ($p$ = 0.44) after 10 nM isoproterenol treatment, respectively. In both control conditions, the high oxygen supply made the frequency-dependent changes of contraction-slow relaxation duration and contraction-fast relaxation peak interval smaller compared with those under normal oxygen one (**Figures 6A,B**, Control, upper). As shown in **Figures 6A,B**, (lower), frequency-dependent increase of maximum contraction speed and maximum fast-relaxation speed was observed in control conditions under normal and high oxygen supply except for the maximum fast-relaxation speed under normal oxygen supply. Isoproterenol increased both of maximum contraction speed and maximum fast-relaxation speed significantly. The positive contraction velocity-frequency

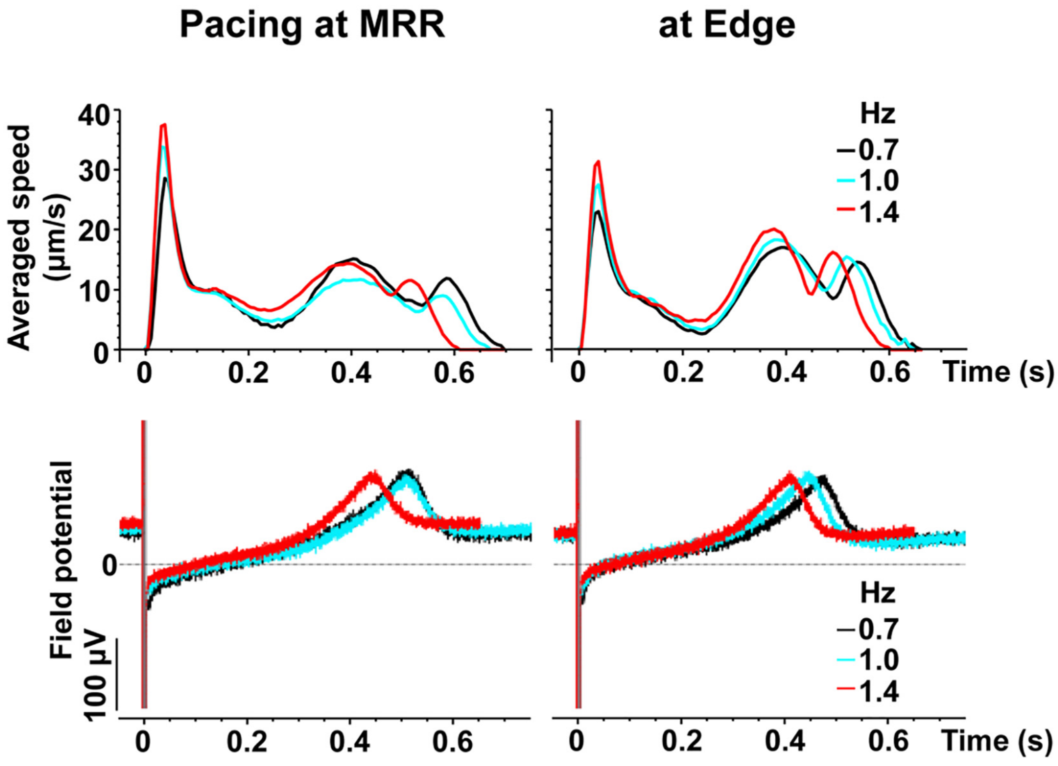

**FIGURE 4 |** Representative traces of simultaneously obtained averaged speed (upper) and field potential (lower) from the same human induced pluripotent stem cell-derived cardiomyocytes sheet as that in **Figure 2**, during pacing around maximum relaxation region (MRR, left) or apart from MRR (Edge, right) under the mixed gas consisting of 95% $O_2$ + 5% $CO_2$. The traces induced by 15th electrical stimulus at frequencies of 0.7 (black), 1 (blue) or 1.4 (red) Hz are superimposed.

relationship in contraction under high oxygen supply was more obvious than that under normal oxygen one.

To better analyze the fast relaxation phase, we adopted the axial analysis of motion vectors using Small ROIs (**Figure 1** middle). Representative traces of averaged speed and field potential waveforms recorded at control and in the presence of vehicle as well as 10 nM of isoproterenol under normal and high oxygen supply are shown in **Figure 7**, whereas the relationships between the pacing frequency and either of the field potential duration, contraction-fast relaxation duration, maximum contraction speed, maximum fast-relaxation speed, or maximum contraction speed/field potential duration under normal and high oxygen supply are summarized in **Figure 8**. The value by subtracting field potential duration from either of contraction-slow relaxation duration or contraction-fast relaxation duration is summarized at control (**Figure 9**, left) and in the presence of isoproterenol (**Figure 9**, right) under normal and high oxygen supply. The contraction-fast repolarization duration was shorter than the field potential duration in both gas conditions in control (**Figures 8A,B**, top), whereas high oxygen supply made the end point of fast relaxation phase occur much earlier from the 2nd peak of field potential than that under normal one (**Figure 9** lower left). Similarly, high oxygen supply made the end point of slow relaxation phase occur earlier behind the second peak of field potential than that under normal one (**Figure 9** upper left). The early-onset of the relaxation phase under high oxygen supply was declined by isoproterenol treatment (**Figure 9**, right). The positive contraction velocity-frequency relationship in maximum contraction speeds was observed under normal and high oxygen supply in the Small ROI analysis like Large ROI analysis at control (**Figure 8**, middle); moreover, the high oxygen supply enhanced the relationship. The contraction efficiency (maximum contraction speed/field potential duration) was increased by isoproterenol under normal and high oxygen supply (**Figure 8**, bottom). Meanwhile, isoproterenol elevated the maximum contraction speed in Large ROIs analysis at 1.00 and 1.25 Hz (**Figure 6**), which was diminished in Small ROIs analysis (**Figure 8**). Frequency-dependent enhancement of fast relaxation speed was observed under high oxygen supply in control (**Figure 8B**, left middle), which was not observed in the other conditions. Maximum fast-relaxation speed was increased by isoproterenol under normal and high oxygen supply (**Figures 8A,B**, middle).

## DISCUSSION

We demonstrated that a spontaneous electrical excitation originating from some region propagated over the cell sheet and formed a synchronous movement, but the initiation of mechanical contractions did not necessarily accord with the order of electrical excitations in the cell sheet of hiPSC-CMs

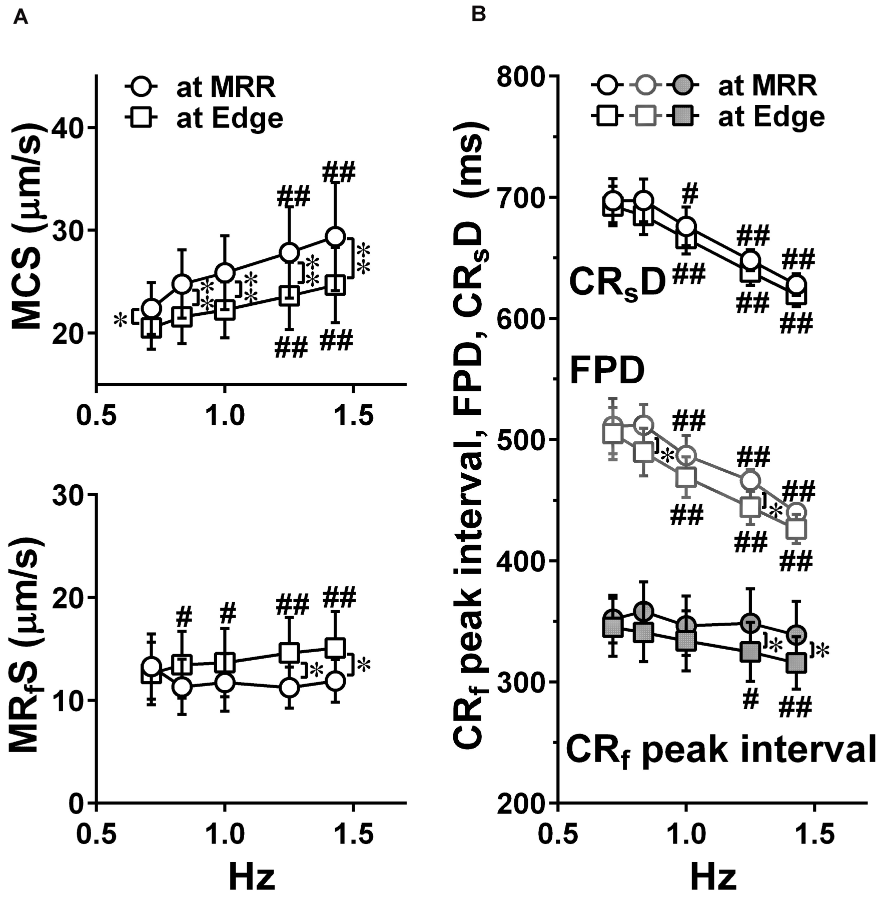

**FIGURE 5 |** Effects of pacing sites on the relationships between the pacing frequency and either of the maximum contraction speed (MCS, upper) and maximum fast-relaxation speed (MRfS, lower) **(A)**, the contraction-slow relaxation duration (CRsD; interval of "a" to "g" in **Figure 2C**), field potential duration, and contraction-fast relaxation peak interval (CRf peak interval; interval of "b" to "e" in **Figure 2C**) **(B)** in human induced pluripotent stem cell-derived cardiomyocytes sheets at the age ≥ 44 days old during pacing at MRR or Edge under the mixed gas consisting of 95% $O_2$ + 5% $CO_2$. Motion vectors were obtained from whole observation area. Data represent as mean ± S.E.M. (*n* = 5). Significant differences from the corresponding values at the lowest frequency of 0.7 Hz were indicated by $^{\#}p < 0.05$ and $^{\#\#}p < 0.01$. Significant differences between the values during pacing at two different sites were shown by $^{*}p < 0.05$ and $^{**}p < 0.01$.

(**Figure 2B**, "b" top). These findings indicate that the disorganized contractions would make the net contraction movement less great, and suggest that there might be large variability of the available $Ca^{2+}$ store in SR among the cells during slow automaticity. In addition, relaxation speed was high in the central area and the relaxation movement was propagated from central to peripheral within the cell sheets (**Figure 2B**, "e" top), indicating that $Ca^{2+}$ uptake rate to SR may be the fastest in the central. This finding also suggests that the central region may be passively stretched.

Next, we electrically paced the cell sheets in order to facilitate $Ca^{2+}$-loading to SR by increasing the excitation rate. Our results demonstrate that the contraction originated from the electrically stimulated regions during pacing (**Figure 2B**, "a" middle and bottom), and that the direction of contraction and relaxation motions varied depending on the paced sites (**Figure 3**). The conduction speed paced at 1 Hz was 0.19∼0.23 m/s for the cell sheets of 44∼66 days old (**Figure 2A**), which was lower limit of the intact human ventricle (0.2–0.3 m/sec) (Levy and Pappano, 2007). Moreover, when electrical pacing was applied at MRR, elevating the pacing frequency from 0.7 to 1.4 Hz increased the maximum contraction speed by + 27% ($p < 0.05$) (+ 39%/Hz) (**Figures 4**, **5**), indicating a positive contraction velocity-frequency relationship, which has not been reported before in conventional monolayers of hiPSC-CMs. Since the contraction velocity can be converted to the stretch velocity of the series elastic elements (Hill, 1938; Linke et al., 1999), the elevation of the contraction velocity would be linearly related to the increase of the contractile force in the cell sheet which adheres to the plastic material of the probe. Twitch force of human cardiac muscle strip preparation was shown to be linearly increased by + 71% when the stimulation frequency was changed from 0.25 to 3 Hz (+ 26%/Hz) (Pieske et al., 1999). Meanwhile, increase of atrial rate from spontaneous sinus automaticity (74 ± 8 bpm; 1.23 Hz) to that plus 25 bpm (102 ± 15 bpm; 1.7 Hz) and to that plus 50 bpm (134 ± 12 bpm; 2.23 Hz) was reported to linearly increase the left ventricular peak-positive dP/dt of the human *in situ* heart

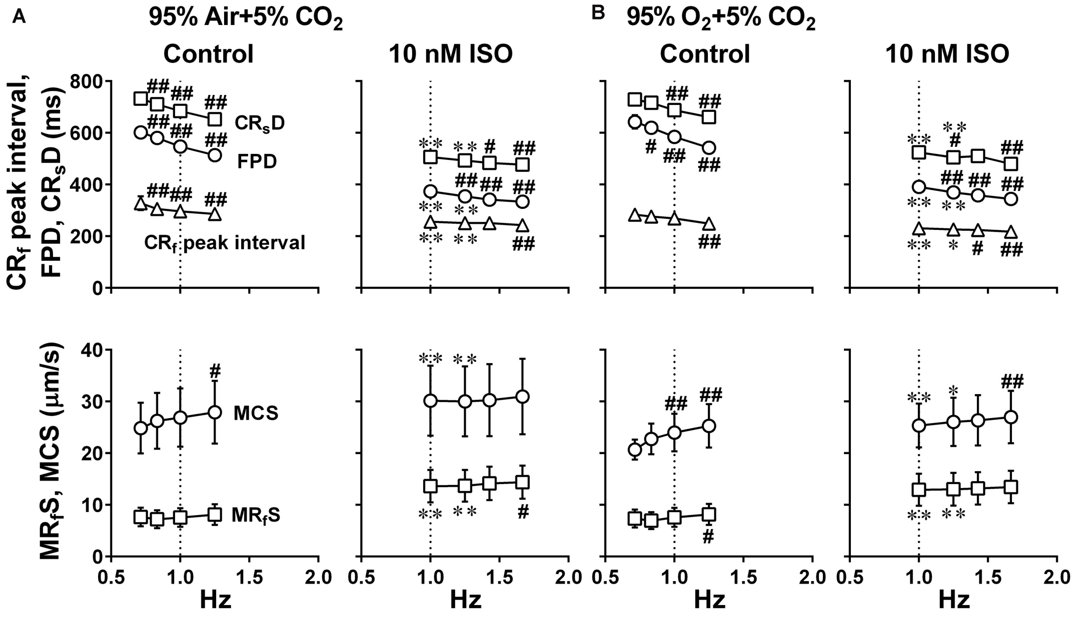

**FIGURE 6 |** Effects of the difference of oxygen tension; mixed gas of 95% air + 5% $CO_2$ **(A)** and 95% $O_2$ + 5% $CO_2$ **(B)**, on each of the variables of motion vectors and field potential waveforms obtained from the whole observation area (Large ROI) in human induced pluripotent stem cell-derived cardiomyocytes sheets at the age ≥ 66 days old. Summary of the relationships between the pacing frequency and either of the contraction-slow relaxation duration ($CR_SD$), field potential duration (FPD), contraction-fast relaxation peak interval ($CR_f$ peak interval) (upper panels), maximum contraction speed (MCS) or maximum fast-relaxation speed ($MR_fS$) (lower panels) is shown at control (Control) and in the presence of 10 nM isoproterenol (10 nM ISO). Each variable of motion vectors was obtained from whole observation area. Data represent as mean ± S.E.M. ($n$ = 5). Significant differences from the corresponding values at the lowest frequency of 0.7 Hz at control and 1 Hz in the presence of 10 nM isoproterenol are indicated by $^{\#}p < 0.05$ and $^{\#\#}p < 0.01$. Significant differences between the values at control and in the presence of 10 nM isoproterenol are shown by $^{*}p < 0.05$ and $^{**}p < 0.01$.

by + 19.4% and + 35.4%, respectively (+ 35.4%/Hz) (Feldman et al., 1988). Thus, the positive contraction velocity-frequency relationship of the contraction speed in the cell sheets could mimic positive force-frequency relationship shown in the human heart. In addition, when the pacing frequency was changed from 0.7 Hz to 1.4 Hz during pacing at Edge, the maximal contraction speed was less elevated by + 18% ($p < 0.05$) (+ 26%/Hz) than that during pacing at MRR (**Figure 5A**). Electrical excitation was propagated uniformly from electrically paced sites (**Figure 2A**), suggesting homogeneous distribution of connesxins throughout the cell sheet. Therefore, the connexin would have played a minor role in the observed differences induced by the change of pacing sites. Thus, regulation of the contractile direction by local electrical pacing could be critical to produce the positive contraction velocity-frequency relationship in the monolayers of hiPSC-CMs.

During electrical pacing at Edge, the maximum fast-relaxation speed was elevated (**Figure 5A** lower) in a frequency-dependent manner. Also, the contraction-slow relaxation duration and contraction-fast relaxation peak interval as well as field potential duration were shortened in a frequency-dependent manner except for contraction-fast relaxation peak interval paced at MRR (**Figure 5B**). Thus, by electrical pacing at Edge, we could induce the frequency-dependent enhancement of fast-relaxation speed along with early-onset of the fast-relaxation phase in the conventional monolayers of hiPSC-CMs. These results suggest that such a mechanism might be operated in the cell sheet that depolarization frequency-dependent $Ca^{2+}$/calmodulin-dependent kinase II (CaMKII) activation can enhance SERCA2a function via phosphorylation of phospholamban (Braun and Schulman, 1995; De Koninck and Schulman, 1998).

The slow relaxation phase occurred after the 2nd peak of field potential (**Figure 4**), suggesting that phase 3 repolarization may be associated with the slow relaxation. Since extrusion of $Ca^{2+}$ by $Na^{+}$-$Ca^{2+}$ exchangers is promoted as repolarization proceeds (Kimura et al., 1987; Bers, 2001; **Figure 1** bottom), the activity of $Na^{+}$-$Ca^{2+}$ exchangers may partly determine the duration and termination of the slow relaxation phase.

When paced at Edge, the contraction-fast relaxation peak interval (**Figure 5B**) was shortened and the maximum fast-relaxation speed (**Figure 5A** lower) was elevated in a frequency-dependent manner, which was not observed when paced at MRR. The fast relaxation would occur during plateau phase of action potential (**Figure 4**), indicating that the fast relaxation may be induced by $Ca^{2+}$ uptake via $Ca^{2+}$-ATPase, SERCA2a and/or plasma membrane $Ca^{2+}$-ATPase 4 (PMCA4). Since the maximum contraction speed was higher during pacing at MRR than at Edge (**Figure 5A** upper), basal SERCA2a activity could be higher around MRR than Edge, which could be explained by a previous report that cell-stretch can enhance SERCA2a activity by activating protein kinase G Iα

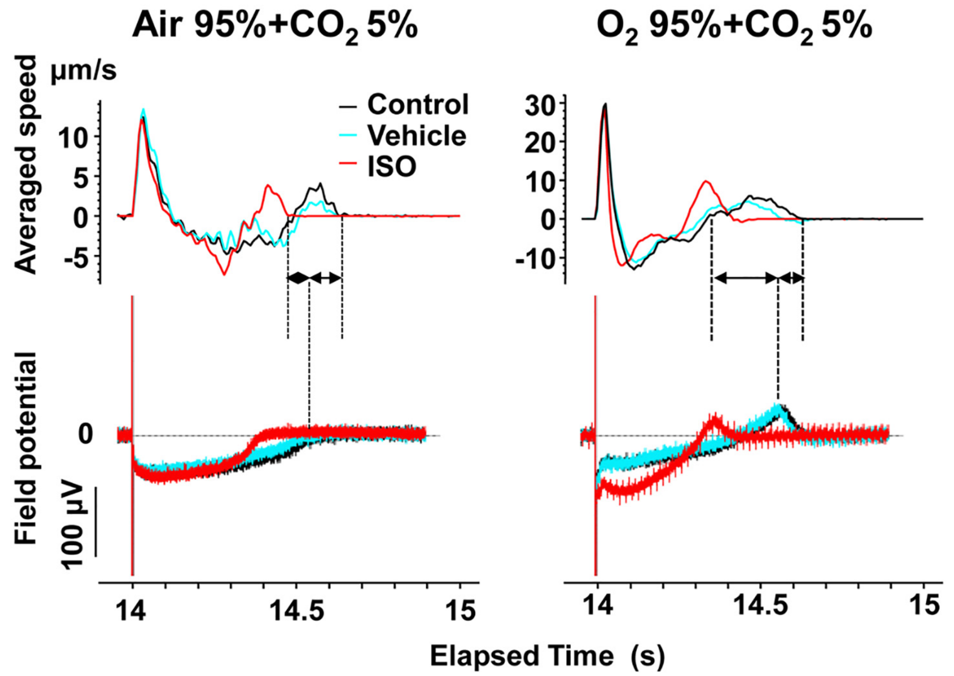

**FIGURE 7 |** Representative traces of simultaneously recorded averaged speed and field potential acquired from Small ROIs of 200 × 200 $\mu m^2$ of a human induced pluripotent stem cell-derived cardiomyocytes sheet. Traces of averaged speed and field potential induced by 15th electrical stimulus at 1 Hz are shown at control (Control, black), vehicle water (Vehicle; blue) and 10 nM isoproterenol (ISO, red) under the mixed gas conditions consisting of 95% air + 5% $CO_2$ (left) or 95% $O_2$ + 5% $CO_2$ (right). Dashed lines and solid arrows were prepared for the traces at control.

that phosphorylates phospholamban (Scotcher et al., 2016). Therefore, it is possible that stretch-enhanced SERCA2a activity in MRR could enhance the frequency-dependent increase of $Ca^{2+}$ storage and $Ca^{2+}$ release, which might have partly attenuated the relaxation motion despite of enhanced SERCA2a activity through depolarization frequency-dependent activation of CaMKII (Braun and Schulman, 1995; De Koninck and Schulman, 1998).

Air contains 20.93% of oxygen. When the culture medium is equilibrated with mixed gas consisting of 95% air + 5% $CO_2$ or 95% $O_2$ + 5% $CO_2$, their dissolved oxygen concentration is calculated to be 0.004 or 0.021 mL/mL $H_2O$ at 37°C, respectively, by using the Henry's law and Bunsen's absorption coefficient, giving the ratio of high/normal oxygen tension of 4.7. We adopted axial analysis on Small ROIs to examine the temporal relationships between the field potential and cell movement. There was no difference in the maximum contraction and fast-relaxation speeds at 0.7 Hz between both oxygen conditions at control (Control in **Figure 6** lower and **Figure 8** middle). Higher oxygen supply made the contraction velocity-frequency relationship and frequency-dependent elevation of fast-relaxation speed steeper, indicating that higher oxygen supply may have enhanced SERCA2a activity. Isoproterenol elevated the maximum contraction speed compared with control in the both oxygen conditions. Expression level of $\beta_1$ adrenoceptor in hiPSC-CMs at 44 days old was about one third of the adult heart (**Supplementary Figure S1**), which is in accordance with those described in a previous report (Wu et al., 2015), suggesting that $\beta_1$ adrenoceptor in the hiPSC-CMs at 66∼70 days old would actually contribute to the observed changes including the elevation of contraction and relaxation speeds by isoproterenol. However, its positive contraction velocity-frequency relationship was diminished or attenuated by isoproterenol (**Figure 6** lower and **Figure 8** middle). Furthermore, marked abbreviation of field potential duration was induced by isoproterenol (**Figures 6**, **8**, top), which would have decreased $Ca^{2+}$ influx via L-type $Ca^{2+}$ channels. In order to better evaluate the net effect of isoproterenol on contraction, we estimated the contraction efficiency by calculating the ratio of the maximum contraction speed to field potential duration, which unveiled the significant positive contraction velocity-frequency relationship under isoproterenol treatment (**Figure 8** bottom). When the positive contraction velocity-frequency relationship in the contraction efficiency was compared between control and isoproterenol conditions, higher oxygen supply made the relationship steeper.

The value of $CR_sD$–FPD under normal oxygen supply was not affected by the pacing frequencies, which was also observed with the presence of isoproterenol (**Figure 9** upper). Namely, there may be a strong causal relationship between the 2nd peak of field potential and the end point of the slow relaxation, suggesting that recovery of intracellular $Ca^{2+}$ might be highly regulated by $Na^+$-$Ca^{2+}$ exchangers which are up-regulated at resting potential (Kimura et al., 1987;

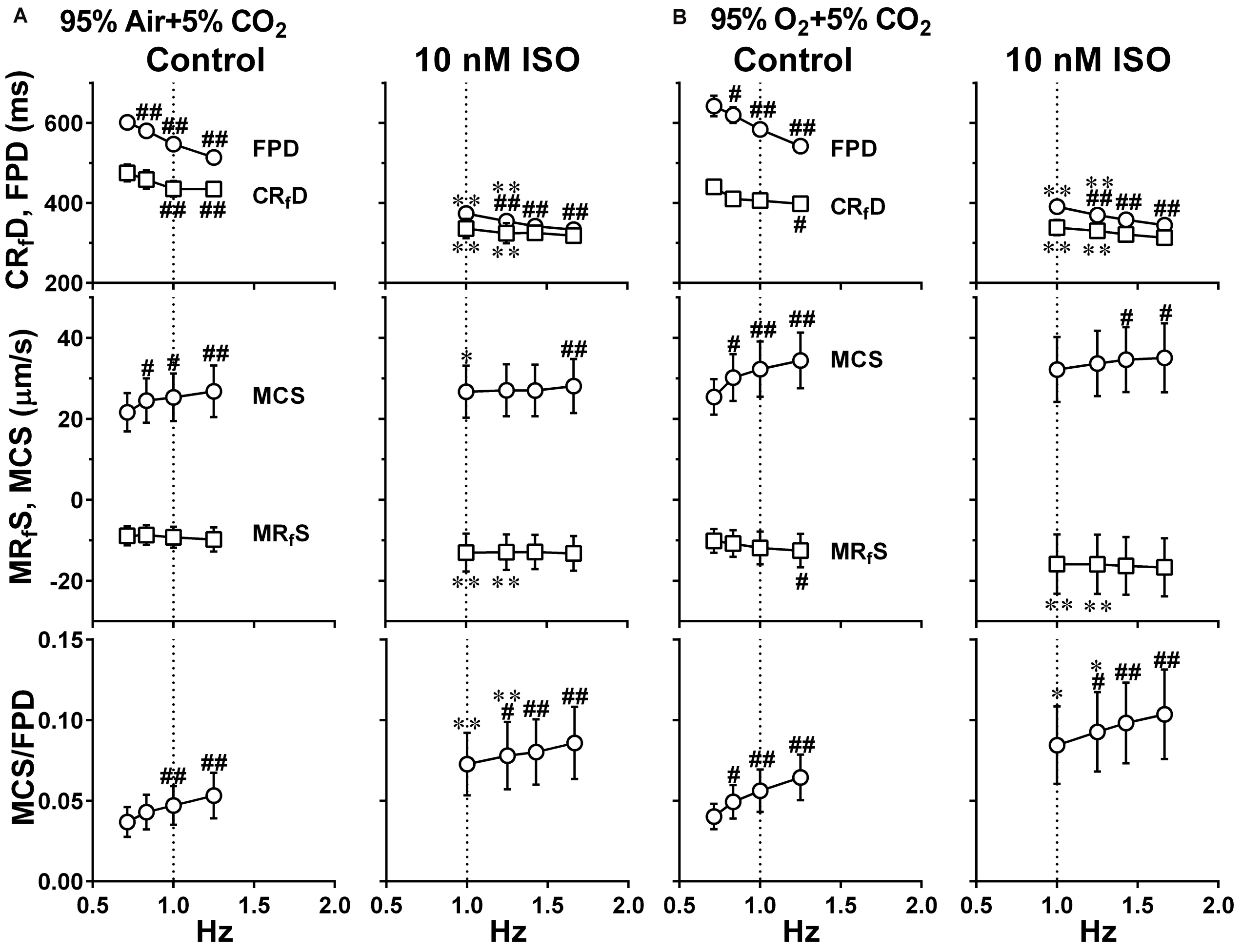

**FIGURE 8 |** Effects of the difference of oxygen tension; mixed gas of 95% air + 5% $CO_2$ **(A)** and 95% $O_2$ + 5% $CO_2$ **(B)**, on each of the variables of motion vectors and field potential waveforms acquired from Small ROIs of 200 × 200 $\mu m^2$. This data was obtained from the same human induced pluripotent stem cell-derived cardiomyocytes sheets at the age ≥ 66 days old as those used for obtaining the data shown in **Figure 6**. Summary of the relationships between the pacing frequency and either of the field potential duration (FPD), contraction-faster relaxation duration ($CR_fD$) (top panels), maximum contraction speed (MCS), maximum fast-relaxation speed ($MR_fS$) (middle panels) or maximum contraction speed/field potential duration (MCS/FPD) (bottom panels) is shown at control (Control) and in the presence of 10 nM isoproterenol (10 nM ISO). Data represent as mean ± S.E.M. ($n$ = 5). Significant differences from the corresponding values at the lowest frequency of 0.7 Hz (Control) or 1 Hz (ISO) are indicated by $^{\#}p < 0.05$ and $^{\#\#}p < 0.01$. Significant differences between the values at control and in the presence of 10 nM isoproterenol are shown by $^{*}p < 0.05$ and $^{**}p < 0.01$.

Bers, 2001; **Figure 1** bottom). Meanwhile, fast- and slow-relaxation terminated earlier with higher oxygen supply at control (**Figure 7** right; **Figure 9** left), indicating that higher oxygen supply could have improved SERCA2a activity (**Figure 1** bottom). However, $CR_sD$–FPD and $CR_fD$–FPD were gradually prolonged and shortened, respectively, by increasing the pacing frequency, and isoproterenol diminished the difference between the oxygen conditions (**Figure 8**), indicating that enhanced $Ca^{2+}$-mobilization would have delayed the relaxation.

We used a monolayer sheet consisting of 30,000 hiPSC-CMs which had been spontaneously excited and contracted until the experiments. Miniaturized cardiac tissue consisting of 2,000 hiPSC-CMs was reported to lack the positive force-frequency relationship (Huebsch et al., 2016). Meanwhile, it has been shown that engineered cardiac tissues exerted the positive force-frequency relationships in the twitch forces, but that they consisted of hundreds of thousands to millions of hiPSC-CMs and required static stress and/or frequency-escalated electrical pacing to facilitate their maturation (Ruan et al., 2016; Feric et al., 2019; Ronaldson-Bouchard et al., 2019). Thus, our protocol along with the monolayer sheets can be simple, less expensive, easy-to-construct and versatile, which could be used to study the physiology and pathophysiology of positive contraction velocity-frequency relationship in 2D model systems.

## LIMITATION

First, since we prepared the cell sheet by dropping a 2 μL of cell suspension onto the microelectrode array in the probe, the

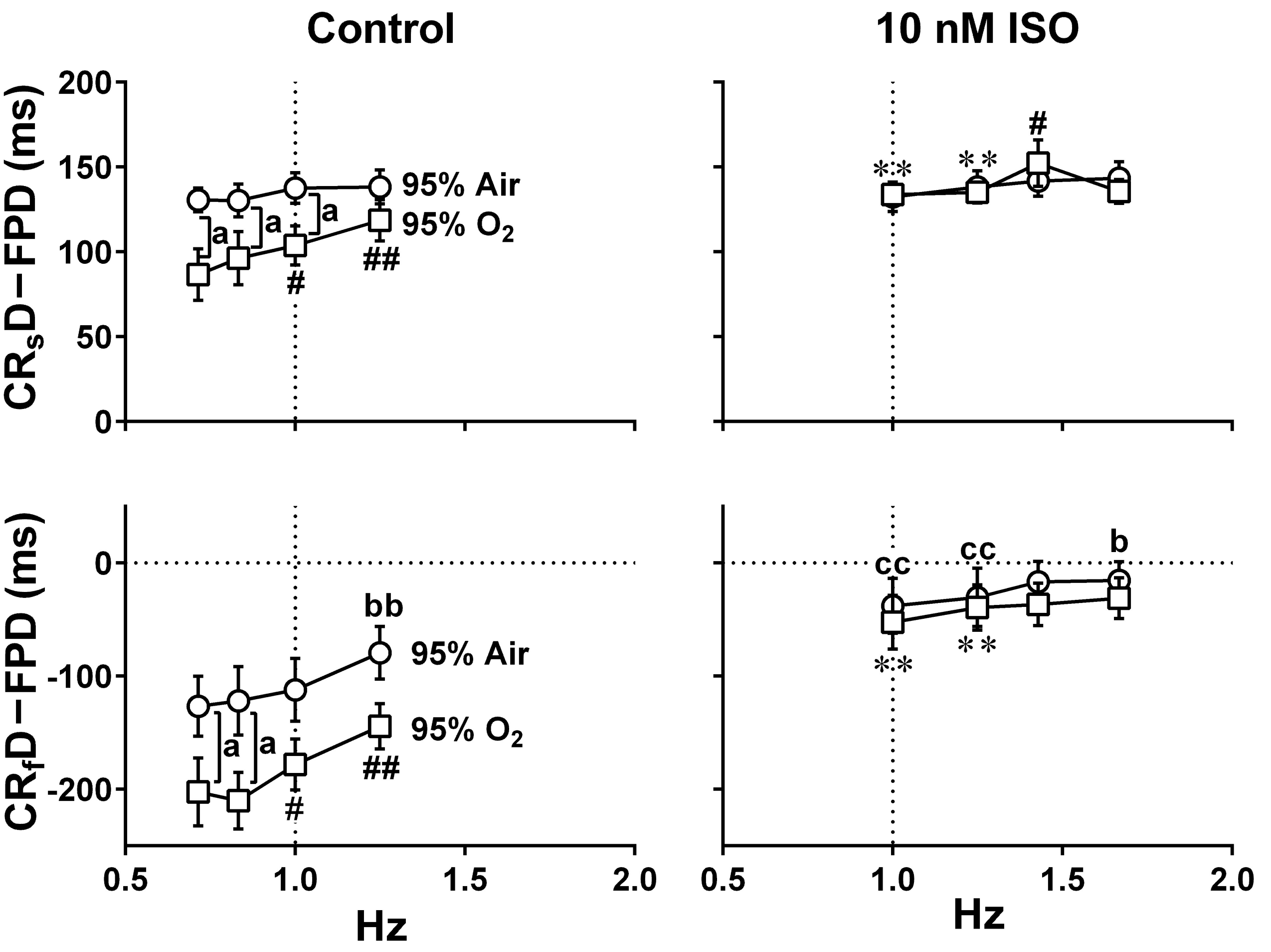

**FIGURE 9 |** The relationships between the pacing frequency and either of the temporal intervals obtained by subtracting the field potential duration from either of the contraction-slow relaxation duration (upper, $CR_sD–FPD$) or the contraction-fast relaxation duration (lower, $CR_fD–FPD$) are shown under the mixed gas conditions consisting of 95% air + 5% $CO_2$ (95% Air, circles) or 95% $O_2$ + 5% $CO_2$ (95% $O_2$, squares) at control (Control) or in the presence of 10 nM isoproterenol (10 nM ISO). The values of $CR_sD–FPD$ and $CR_fD–FPD$ were calculated from the data shown in **Figures 6**, **8**. Note that early-onset of the relaxation phase was induced by high oxygen supply. Data represent as mean ± S.E.M. (n = 5). Significant differences between the values under normal and high oxygen tensions are depicted by $^{a}p < 0.05$. Significant differences from the corresponding values at the lowest pacing frequency of 0.7 Hz (Control) or 1 Hz (ISO) are indicated by $^{b}p < 0.05$ and $^{bb}p < 0.01$ for 95% Air and by $^{\#}p < 0.05$ and $^{\#\#}p < 0.01$ for 95% $O_2$. Significant differences between the values at control and in the presence of 10 nM isoproterenol are shown by $^{cc}p < 0.01$ for 95% Air and by $^{**}p < 0.01$ for 95% $O_2$.

cell density in the central area of the cell sheet might be greater than those in peripheral ones. The surface area of the cell sheets was > 2 times greater than that of the observation window of 1,365 × 1,365 $\mu m^2$, possibly reducing the dispersion of the cell density within the window. The window included the central region of the cell sheet, where the 2nd peak amplitude of the field potential was higher, enabling to observe the area having the highest cell density within each cell sheet. Second, the number of experimental trials may not be sufficient for more reliable results with the variability associated with measurements in hiPSC-CMs; however, other researchers as well as we have provided the similar values in variables of field potential and motion vector to those in the current study using the cell sheets by 5∼7 trials (Hayakawa et al., 2014; Nakamura et al., 2014; Uesugi et al., 2014; Ando et al., 2017; Izumi-Nakaseko et al., 2017a,b; Isobe et al., 2018; Sugiyama et al., 2019). Thus, reliable results could be obtained by 5 experimental trials, although increasing the number of trials may further improve the reliability. Third, we used a single cell line that was commercially available, providing some possibility that the observations could be limited to this cell line. Although the cell line we adopted is one of the most widely used cell strains, other cell lines should be tested to verify our observations.

## CONCLUSION

We demonstrated that regulation of the motion directions in the conventional hiPSC-CMs monolayers enables to produce both "positive contraction velocity-frequency relationship" in contraction and "frequency-dependent enhancement of relaxation", which will become more obvious by increasing oxygen supply. We also clarified the spatial and temporal relationships between the electrical excitation and biphasic relaxation. Our findings might help interpret the drug-induced inotropic and lusitropic actions detected in hiPSC-CMs monolayers. Thus, currently adopted manipulation revealed potential ability of conventional monolayers of hiPSC-CMs, which will help apply them to translational study filling the gap between basic research and clinical practice.

## DATA AVAILABILITY STATEMENT

All datasets generated for this study are included in the article/**Supplementary Material**.

## AUTHOR CONTRIBUTIONS

HI-N and ASu supervised the project and designed the experiments. HI-N and ASa performed and analyzed the experiments. KC, MH-N, AG, YN, RK, AM, YT, YK, and AN provided technical support and discussions. HI-N and ASu wrote the manuscript. All authors reviewed the manuscript.

## FUNDING

This work was financially supported by JSPS KAKENHI Grant Number 17K08608 (to HI-N); AMED Grant JP18mk0104117 (to YK); AMED Grant 18am0101122j0002 (to AN and ASu); and Initiative for Realizing Diversity in the Research Environment (to HI-N).

## ACKNOWLEDGMENTS

The authors thank Ms. Yuri Ichikawa for technical assistance, Ms. Hikaru Tsuruoka, Ms. Yuka Mitsuhashi and Mr. Hibiki Tanigawa for data analysis, Mr. Keiichi Shirakawa for technical support for microelectrode array system, and Dr. Tomohiro Hayakawa and Ms. Hatsume Uno for technical support for motion vector assessment.

## SUPPLEMENTARY MATERIAL

The Supplementary Material for this article can be found online at: https://www.frontiersin.org/articles/10.3389/fcell.2020.542562/full#supplementary-material

## REFERENCES

Ando, H., Yoshinaga, T., Yamamoto, W., Asakura, K., Uda, T., Taniguchi, T., et al. (2017). A new paradigm for drug-induced torsadogenic risk assessment using human iPS cell-derived cardiomyocytes. *J. Pharmacol. Toxicol. Methods.* 84, 111–127. doi: 10.1016/j.vascn.2016.12.003

Bassani, J. W., Bassani, R. A., and Bers, D. M. (1994). Relaxation in rabbit and rat cardiac cells: species-dependent differences in cellular mechanisms. *J. Physiol.* 476, 279–293. doi: 10.1113/jphysiol.1994.sp020130

Bers, D. M. (1987). Mechanisms contributing to the cardiac inotropic effect of Na pump inhibition and reduction of extracellular Na. *J. Gen. Physiol.* 90, 479–504. doi: 10.1085/jgp.90.4.479

Bers, D. M. (2001). "Na/Ca exchange and the sarcolemmal Ca-pump," in *Excitation-Contraction Coupling and Cardiac Contractile Force*, 2nd Edn, (Norwell, MA: Kluwer Academic Publishers), 133–160. doi: 10.1007/978-94-010-0658-3_6

Blinova, K., Dang, Q., Millard, D., Smith, G., Pierson, J., Guo, L., et al. (2018). International multisite study of human-induced pluripotent stem cell-derived cardiomyocytes for drug proarrhythmic potential assessment. *Cell. Rep.* 24, 3582–3592. doi: 10.1016/j.celrep.2018.08.079

Braun, A. P., and Schulman, H. (1995). The multifunctional calcium/calmodulin-dependent protein kinase: from form to function. *Annu. Rev. Physiol.* 57, 417–445. doi: 10.1146/annurev.ph.57.030195.002221

De Koninck, P., and Schulman, H. (1998). Sensitivity of CaM kinase II to the frequency of Ca2+ oscillations. *Science* 279, 227–230. doi: 10.1126/science.279.5348.227

Feldman, M. D., Alderman, J. D., Aroesty, J. M., Royal, H. D., Ferguson, J. J., Owen, R. M., et al. (1988). Depression of systolic and diastolic myocardial reserve during atrial pacing tachycardia in patients with dilated cardiomyopathy. *J. Clin. Invest.* 82, 1661–1669. doi: 10.1172/JCI113778

Feric, N. T., Pallotta, I., Singh, R., Bogdanowicz, D. R., Gustilo, M., Chaudhary, K., et al. (2019). Engineered cardiac tissues generated in the biowire$^{TM}$ II: a platform for human-based drug discovery. *Toxicol. Sci.* 172, 89–97. doi: 10.1093/toxsci/kfz168

Hayakawa, T., Kunihiro, T., Ando, T., Kobayashi, S., Matsui, E., Yada, H., et al. (2014). Image-based evaluation of contraction-relaxation kinetics of human-induced pluripotent stem cell-derived cardiomyocytes: correlation and complementarity with extracellular electrophysiology. *J. Mol. Cell. Cardiol.* 77, 178–191. doi: 10.1016/j.yjmcc.2014.09.010

Hill, A. V. (1938). The heat of shortening and the dynamic constants of muscle. *Proc. Biol. Sci.* 126, 136–195. doi: 10.1098/rspb.1938.0050

Huebsch, N., Loskill, P., Deveshwar, N., Spencer, C. I., Judge, L. M., Mandegar, M. A., et al. (2016). Miniaturized iPS-cell-derived cardiac muscles for physiologically relevant drug response analyses. *Sci. Rep.* 6:24726. doi: 10.1038/srep24726

Isobe, T., Honda, M., Komatsu, R., and Tabo, M. (2018). Conduction and contraction properties of human iPS cell-derived cardiomyocytes: analysis by motion field imaging compared with the guinea-pig isolated heart model. *J. Toxicol. Sci.* 43, 93–506. doi: 10.2131/jts.43.493

Izumi-Nakaseko, H., Hagiwara-Nagasawa, M., Naito, A. T., Goto, A., Chiba, K., Sekino, Y., et al. (2018). Application of human induced pluripotent stem cell-derived cardiomyocytes sheets with microelectrode array system to estimate antiarrhythmic properties of multi-ion channel blockers. *J. Pharmacol. Sci.* 137, 372–378. doi: 10.1016/j.jphs.2018.07.011

Izumi-Nakaseko, H., Kanda, Y., Nakamura, Y., Hagiwara-Nagasawa, M., Wada, T., Ando, K., et al. (2017a). Development of correction formula for field potential duration of human induced pluripotent stem cell-derived cardiomyocytes sheets. *J. Pharmacol. Sci.* 135, 44–50. doi: 10.1016/j.jphs.2017.08.008

Izumi-Nakaseko, H., Nakamura, Y., Wada, T., Ando, K., Kanda, Y., Sekino, Y., et al. (2017b). Characterization of human iPS cell-derived cardiomyocyte sheets as a model to detect drug-induced conduction disturbance. *J. Toxicol. Sci.* 42, 183–192. doi: 10.2131/jts.42.183

Kimura, J., Miyamae, S., and Noma, A. (1987). Identification of sodium-calcium exchange current in single ventricular cells of guinea-pig. *J. Physiol.* 384, 199–222. doi: 10.1113/jphysiol.1987.sp016450

Kurihara, S., and Sakai, T. (1985). Effects of rapid cooling on mechanical and electrical responses in ventricular muscle of guinea-pig. *J. Physiol.* 361, 361–378. doi: 10.1113/jphysiol.1985.sp015650

Levy, M. N., and Pappano, A. J. (2007). *"Automaticity: Natural excitation of the heart" in Cardiovascular Physiology*, 9th Edn. Philadelphia, PA: Mosby, Inc, 33–54.

Linke, W. A., Rudy, D. E., Centner, T., Gautel, M., Witt, C., Labeit, S., et al. (1999). I-band titin in cardiac muscle is a three-element molecular spring and is critical for maintaining thin filament structure. *J. Cell. Biol.* 146, 631–644. doi: 10.1083/jcb.146.3.631

Ma, J., Guo, L., Fiene, S. J., Anson, B. D., Thomson, J. A., Kamp, T. J., et al. (2011). High purity human-induced pluripotent stem cell-derived cardiomyocytes: electrophysiological properties of action potentials and ionic currents. *Am. J. Physiol. Heart. Circ. Physiol.* 301, H2006–H2017. doi: 10.1152/ajpheart.00694.2011

Maier, L. S., Bers, D. M., and Pieske, B. (2000). Differences in Ca2+-handling and sarcoplasmic reticulum Ca2+-content in isolated rat and rabbit myocardium. *J. Mol. Cell. Cardiol.* 32, 2249–2258. doi: 10.1006/jmcc.2000.1252

Nakamura, Y., Matsuo, J., Miyamoto, N., Ojima, A., Ando, K., Kanda, Y., et al. (2014). Assessment of testing methods for drug-induced repolarization delay and arrhythmias in an iPS cell-derived cardiomyocyte sheet: multi-site validation study. *J. Pharmacol. Sci.* 124, 494–501. doi: 10.1254/jphs.13248fp

Pieske, B., Maier, L. S., Bers, D. M., and Hasenfuss, G. (1999). Ca2+ handling and sarcoplasmic reticulum Ca2+ content in isolated failing and nonfailing human myocardium. *Circ. Res.* 85, 38–46. doi: 10.1161/01.RES.85.1.38

Ronaldson-Bouchard, K., Ma, S. P., Yeager, K., Chen, T., Song, L., Sirabella, D., et al. (2019). Advanced maturation of human cardiac tissue grown from pluripotent stem cells. *Nature* 556, 239–243. doi: 10.1038/s41586-018-0016-3

Ruan, J. L., Tulloch, N. L., Razumova, M. V., Saiget, M., Muskheli, V., Pabon, L., et al. (2016). Mechanical stress conditioning and electrical stimulation promote contractility and force maturation of induced pluripotent stem cell-derived human cardiac tissue. *Circulation* 134, 1557–1567. doi: 10.1161/CIRCULATIONAHA.114.014998

Sasaki, D., Matsuura, K., Seta, H., Haraguchi, Y., Okano, T., and Shimizu, T. (2018). Contractile force measurement of human induced pluripotent stem cell-derived cardiac cell sheet-tissue. *PLoS One.* 13:e0198026. doi: 10.1371/journal.pone.0198026

Scotcher, J., Prysyazhna, O., Boguslavskyi, A., Kistamas, K., Hadgraft, N., Martin, E. D., et al. (2016). Disulfide-activated protein kinase G Iα regulates cardiac diastolic relaxation and fine-tunes the Frank-Starling response. *Nat. Commun.* 7:13187. doi: 10.1038/ncomms13187

Shattock, M. J., and Bers, D. M. (1989). Rat vs. rabbit ventricle: ca flux and intracellular Na assessed by ion-selective microelectrodes. *Am. J. Physiol.* 256, C813–C822. doi: 10.1152/ajpcell.1989.256.4.C813

Sugiyama, A., Hagiwara-Nagasawa, M., Kambayashi, R., Goto, A., Chiba, K., Naito, A. T., et al. (2019). Analysis of electro-mechanical relationship in human iPS cell-derived cardiomyocytes sheets under proarrhythmic condition assessed by simultaneous field potential and motion vector recordings. *J. Pharmacol. Sci.* 140, 317–320. doi: 10.1016/j.jphs.2019.07.006

Uesugi, M., Ojima, A., Taniguchi, T., Miyamoto, N., and Sawada, K. (2014). Low-density plating is sufficient to induce cardiac hypertrophy and electrical remodeling in highly purified human iPS cell-derived cardiomyocytes. *J. Pharmacol. Toxicol. Methods* 69, 177–188. doi: 10.1016/j.vascn.2013.11.002

Wu, H., Lee, J., Vincent, L. G., Wang, Q., Gu, M., Lan, F., et al. (2015). Epigenetic regulation of phosphodiesterases 2A and 3A underlies compromised β-adrenergic signaling in an iPSC model of dilated cardiomyopathy. *Cell. Stem. Cell.* 17, 89–100. doi: 10.1016/j.stem.2015.04.020

Yang, X., Pabon, L., and Murry, C. E. (2014). Engineering adolescence: maturation of human pluripotent stem cell-derived cardiomyocytes. *Circ. Res.* 114, 511–523. doi: 10.1161/CIRCRESAHA.114.300558

**Conflict of Interest:** The authors declare that the research was conducted in the absence of any commercial or financial relationships that could be construed as a potential conflict of interest.

frontiers
in Cell and Developmental Biology

REVIEW
published: 28 October 2020
doi: 10.3389/fcell.2020.550504

# Aortic “Disease-in-a-Dish”: Mechanistic Insights and Drug Development Using iPSC-Based Disease Modeling

*Hongorzul Davaapil, Deeti K. Shetty and Sanjay Sinha**

*Wellcome-MRC Cambridge Stem Cell Institute, Jeffrey Cheah Biomedical Centre, Cambridge, United Kingdom*

Thoracic aortic diseases, whether sporadic or due to a genetic disorder such as Marfan syndrome, lack effective medical therapies, with limited translation of treatments that are highly successful in mouse models into the clinic. Patient-derived induced pluripotent stem cells (iPSCs) offer the opportunity to establish new human models of aortic diseases. Here we review the power and potential of these systems to identify cellular and molecular mechanisms underlying disease and discuss recent advances, such as gene editing, and smooth muscle cell embryonic lineage. In particular, we discuss the practical aspects of vascular smooth muscle cell derivation and characterization, and provide our personal insights into the challenges and limitations of this approach. Future applications, such as genotype-phenotype association, drug screening, and precision medicine are discussed. We propose that iPSC-derived aortic disease models could guide future clinical trials via “clinical-trials-in-a-dish”, thus paving the way for new and improved therapies for patients.

**Keywords: induced pluripotent stem cell, aortic aneurysm, Marfan, Loeys-Dietz, vascular smooth muscle, disease-in-a-dish**

OPEN ACCESS

***Edited by:***
*Masayuki Yazawa,*
*Columbia University, United States*

***Reviewed by:***
*Zi-Bing Jin,*
*Capital Medical University, China*
*Christoph Schaniel,*
*Icahn School of Medicine at Mount Sinai, United States*

****Correspondence:***
*Sanjay Sinha*
*ss661@cam.ac.uk*

***Specialty section:***
*This article was submitted to Stem Cell Research, a section of the journal Frontiers in Cell and Developmental Biology*

***Received:*** *09 April 2020*
***Accepted:*** *08 October 2020*
***Published:*** *28 October 2020*

***Citation:***
*Davaapil H, Shetty DK and Sinha S (2020) Aortic “Disease-in-a-Dish”: Mechanistic Insights and Drug Development Using iPSC-Based Disease Modeling. Front. Cell Dev. Biol. 8:550504. doi: 10.3389/fcell.2020.550504*

## INTRODUCTION

Thoracic aortic disease usually proceeds silently until presenting suddenly with dissection or rupture (Pinard et al., 2019). Despite the frequently catastrophic and life-threatening consequences, there are no proven medical treatments for thoracic aortic disease beyond blood pressure control. Surgical replacement of the diseased section of aorta, either emergent or prophylactically, can be associated with significant morbidity and does not prevent disease progression or re-presentation in the non-replaced parts of the vessel. The lack of effective medical therapies has highlighted the

---

**Abbreviations:** α-SMA, α-smooth muscle actin; AT1R, Angiotensin II receptor, type 1; BAV, Bicuspid aortic valves; EB, Embryoid body; EC, Endothelial cell; ECM, Extracellular matrix; ESC, Embryonic stem cell; FC, Flow cytometry; HGP, Hutchison-Gilford progeria; IF, Immunofluorescence; iPSC, Induced pluripotent stem cell; KSR, Knock-out serum replacement; LDS, Loeys-Dietz syndrome; LM, Lateral plate mesoderm; MFS, Marfan syndrome; MMP, Matrix metalloproteinase; NC, Neural crest; NO, Nitric oxide; NR, Not reported; PM, Paraxial mesoderm; SMGM, Smooth Muscle Growth Medium; SM-MHC, Smooth muscle myosin heavy chain; SPC, Sphingosylphosphorylcholine; SVAS, Supravalvular aortic stenosis; TAAD, Thoracic aortic aneurysm and dissection; TEBV, Tissue-engineered blood vessel; TEVG, Tissue-engineered vascular graft; TGF, Transforming growth factor; TβRII, TGF-β receptor II; vEDS, Vascular Ehlers-Danlos syndrome; VSMC, Vascular smooth muscle cell.

critical need to define the mechanisms underlying aortic dilatation and dissection to inform the development of new treatments (Milewicz et al., 2005).

In contrast to abdominal aortic aneurysms, which have been shown to have links to inflammation and atherosclerosis, thoracic aortic aneurysms and disorders are frequently due to genetic factors (Humphrey et al., 2015; Pinard et al., 2019). A key question is to what extent the different genetic syndromes and disorders have common disease-causing pathways. The underlying mechanisms leading to aortic disease are still unclear despite the use of several mouse models; indeed, therapeutic discoveries made using the mouse models have not yet been shown to be effective in patients. Consequently, there is a pressing need for further studies and a wider range of model systems that may more fully predict a clinical response.

Through their seminal discovery of induced pluripotent stem cells (iPSCs), Takahashi and Yamanaka have bestowed the tools to now establish patient-derived complex models of human genetic diseases (Takahashi and Yamanaka, 2006). The power of this approach lies in the fact that these cells contain the patient's DNA, so exhibit both the causal genetic defects as well as the permissive genetic background that allows florid disease presentation. Furthermore, these cells represent a versatile and almost unlimited resource for the study of early disease processes and for drug discovery. Such is their potential utility for understanding and treating diseases that they have been referred to as "disease-in-a-dish" models (Tiscornia et al., 2011).

In this review we will critically discuss recent studies where iPSCs have been used to model thoracic aortic aneurysm and dissection (TAAD) disorders. Since these related disorders have already been reviewed in detail by others (Goldfinger et al., 2014; Michel et al., 2018), we will only briefly cover the diseases themselves and highlight the controversies and major questions that have emerged in this field. We will then devote the majority of this review to providing insights into the practical aspects, applications, strengths, and limitations of using iPSCs to model these conditions. Finally, we will explore potential future directions for this approach including precision medicine and "clinical-trials-in-a-dish."

# AORTOPATHIES, CURRENT SCIENTIFIC, AND CLINICAL CHALLENGES

## Thoracic Aortic Aneurysm and Dissection

Thoracic aortic aneurysm and dissections commonly occur sporadically or in association with bicuspid aortic valves (BAV). Single gene disorders also cause thoracic aortopathies, notably in genes encoding extracellular matrix (ECM) components, transforming growth factor (TGF)-β signaling, or vascular smooth muscle cell (VSMC) contractile machinery (Brownstein et al., 2018). Marfan syndrome (MFS), caused by mutations in *FBN1*, is the commonest and best studied genetic disease resulting in TAAD. Other syndromic disorders include Loeys-Dietz syndrome (LDS) and vascular Ehlers-Danlos syndrome (vEDS) which are caused by mutations in the TGF-β signaling cascade (Lindsay et al., 2012) and in *COL3A1* (Pepin et al., 2000), respectively. Mechanistically, it is likely that TAADs share common disease mechanisms. Improving our understanding of Mendelian genetic disorders is also likely to lead to effective treatments for sporadic and bicuspid valve-associated aortopathies.

Many TAAD disorders show considerable overlap in pathology with elevated matrix metalloproteinases (MMPs), elastin fiber breaks, proteoglycan, and glycosaminoglycan deposition and medial aortic VSMC loss, suggesting common final pathways for aneurysm development despite varying genetic causes. An intimal tear then leads to an influx of blood and medial dissection; a condition with a cumulative 1% mortality per hour if the dissection involves the ascending aorta – a type A dissection (Anagnostopoulos et al., 1972). This dramatic surgical emergency is due to the propensity of a type A dissection to progress retrogradely and involve the coronaries, leading to myocardial infarction, or the pericardium, leading to tamponade. The risk of dissection is in part a function of aneurysm size, although the correlation varies widely depending on the precise disease as well as other familial factors and co-morbidities such as the presence of hypertension. Notably, some disorders such as LDS or vEDS, can present with arterial dissection or rupture at relatively normal vessel dimensions (Pepin et al., 2000; Williams et al., 2007), emphasizing the need for additional prognostic markers to supplement cross-sectional imaging.

In this review, we use MFS as the exemplar for genetically mediated TAADs. We will discuss the biological controversies and clinical issues raised by MFS to illustrate the challenges in the management of patients with TAAD and areas where novel approaches may be helpful. MFS is an autosomal dominant, multi-system disease affecting approximately 1 in 5000 people, caused by mutations in the gene encoding fibrillin-1, a key connective tissue ECM protein (Dietz et al., 1991). Fibrillin-1 glycoproteins assemble into microfibrils, which have both structural and functional roles. These microfibrils provide elasticity and provide a template for elastin fiber formation, but can also regulate the bioavailability of growth factors, such as TGF-β (Chaudhry et al., 2007), and provide attachment motifs for cell-matrix interactions (Kielty et al., 1992; Bax et al., 2003).

The cardiovascular complications are potentially fatal, and affect men more strongly than women (Murdoch et al., 1972; Pyeritz and KcKusick, 1979). Patients can develop mitral valve prolapse and aortic regurgitation, with the significant complication being aortic dilatation. These aortic aneurysms typically form in the aortic root and arch, and predispose to rupture or dissection (Milewicz et al., 2005). As with other TAADs, VSMCs from MFS patients typically have high expression and activity of MMPs, elastic fiber fragmentation and VSMC death, which all lead to weakening of the aortic wall (Segura et al., 1998; Ikonomidis et al., 2006; Grewal and Gittenberger-de Groot, 2018). In addition, there is increased deposition of collagen and proteoglycans, which contributes to increased vessel stiffness (Andreotti et al., 1985; Cattell et al., 1994). Indeed, patients with MFS tend to have stiffer aortas compared to the general population (Jeremy et al., 1994; De Wit et al., 2013; Hannuksela et al., 2018).

Mouse models of MFS have been very useful to understand a variety of disease aspects. Two models are commonly reported in the literature – the *FBN1*$^{C1039G/+}$ (Judge et al., 2004) and *FBN1*$^{MgR/MgR}$ (Pereira et al., 1999) models which represent moderate and severe disease, respectively. In addition to powerful tools to dissect the genetics, mouse models allow for deep phenotypic and histological characterization. The different stages of disease progression can also be investigated, making murine models essential for understanding disease mechanisms. The findings from these disease models, in addition to their drawbacks, will be discussed further below.

Groups, including ours, have used iPSCs to investigate the pathology underlying MFS. Longaker and colleagues used a MFS embryonic stem cell (ESC) line as well as patient-derived iPSCs to show how antagonism of BMP signaling by TGF-β signaling impaired osteogenesis, leading to abnormal skeletogenesis (Quarto et al., 2012a,b). More recently, we used patient-derived iPSCs differentiated into VSMCs to recapitulate many aspects of vascular disease found in patients (Granata et al., 2017). This included increased MMP expression and cell death, fragmentation of ECM microfibrils, and reduced proliferation (**Figure 1**). Interestingly, when cells were exposed to cyclic mechanical stretch, the disease phenotype was further exaggerated, suggesting that there are abnormalities in mechanosensing/transduction, in line with current thinking about the mechanisms leading to disease progression. These disease features were rescued by using CRISPR-Cas9 mediated single nucleotide correction resulting in an isogenic normal control. iPSC-based models of other aortic diseases have also been developed, and are summarized in **Tables 1**, **2**. These models have successfully recapitulated key aspects of aortic diseases, and have enabled identification of potential disease mechanisms for further investigation.

## TGF-β Controversy – Cause or Consequence?

The TGF-β signaling pathway is crucial for normal VSMC function and it is a potent cytokine regulating proliferation, differentiation, extracellular matrix remodeling, and apoptosis (Guo, 2012). Activation of TGF-β receptors leads to canonical signaling through Smads but also non-canonical signaling through MAPKs (Zhang, 2017). Analysis of the lung of a severe mouse model of MFS, *FBN1*$^{mg\Delta}$, found increased activation of TGF-β (Neptune et al., 2003). Since treatment with a TGF-β neutralizing antibody rescued the lung phenotype, the Dietz lab hypothesized that the loss of microfibrils decreased the sequestration of TGF-β and in turn led to an increase in local TGF-β signaling. This line of thinking was supported by findings in the moderate *FBN1*$^{C1039G/+}$ murine model (Judge et al., 2004), where increased canonical TGF-β signaling was detected in the dilated aorta. Treatment with a TGF-β neutralizing antibody once again rescued the disease phenotype (Habashi et al., 2006), as did blockade of the angiotensin II receptor type 1 (AT1R) with losartan, which reduced TGF-β expression and non-canonical signaling (Lavoie et al., 2005; Rodríguez-Vita et al., 2005; Holm et al., 2011).

Given the dramatic results with losartan in mouse models of MFS, a series of clinical trials in patients commenced. An initial retrospective analysis of a pediatric cohort of MFS patients suggested promising results in slowing aortic dilatation (Brooke et al., 2008). Several randomized trials have now been carried out comparing losartan either to β-blocker or to placebo (Groenink et al., 2013; Lacro et al., 2014; Milleron et al., 2015; Teixido-Tura et al., 2018). Surprisingly, despite some early promise in small trials, the largest single randomized study has shown that losartan had no statistically significant improvement in children and young adult patients when compared to β-blockers (Lacro et al., 2014). Related to the findings in the initial retrospective analysis, this larger study found that the younger subjects were more responsive to treatment with losartan compared to the older cohort, suggesting that there may be an early therapeutic window for targeting angiotensin II signaling.

Subsequent evidence from mouse studies has indicated that the nature of TGF-β signaling in TAAD progression is complex, and may also confer a protective effect. Post-natal VSMC-specific deletion of TGF-β receptor II (TβRII; Hu et al., 2015) or treatment with a TGF-β neutralizing antibody (Wang et al., 2010) led to severe aortopathy. Indeed, crossing *FBN1*$^{C1039G/+}$ mice with a conditional knock-out for *Tgfbr2* exacerbated the aortic phenotype, indicating that TGF-β may have a protective effect (Li et al., 2014; Wei et al., 2017). *FBN1*$^{MgR/MgR}$ is a severe model for MFS (Pereira et al., 1999) in which treatment with losartan slightly improved lifespan, but did not have the same impact as in the moderate *FBN1*$^{C1039G/+}$ model (Xiong et al., 2012; Cook et al., 2015). In addition, treatment with a TGF-β neutralizing antibody was detrimental at P16, but beneficial at P45, indicative of a temporally dependent role for TGF-β in aneurysm formation (Cook et al., 2015). Other studies did not find any benefit of TGF-β or angiotensin II signaling inhibition in VSMCs (Angelov et al., 2017; Galatioto et al., 2018). Together, these lines of evidence indicate that the pathophysiology of MFS is more complex than just dysfunction of TGF-β signaling in VSMCs. The upregulation of TGF-β signaling in MFS may in part be a compensatory mechanism, rationalizing the increase observed in patients with severe aneurysm (Franken et al., 2013).

The losartan and TGF-β controversy indicates that further mechanistic validation is required when transitioning between mouse studies and patient treatment, particularly in the context of the human genome. While losartan was highly-effective and promising in a mouse model, its effectiveness was not matched in patients. This was potentially due to fundamental differences in the anatomy between murine and human aortas, but also due to the disparity between the dose required to elicit a response, and the dose deemed safe for human patients. Recently, another AT1R antagonist, irbesartan, was found to be effective in reducing aortic dilatation in children and young adults (Mullen et al., 2020). Although losartan and irbesartan both inhibit AT1R, irbesartan has greater bioavailability and a longer half-life, implying that the difference in outcome may be in part due to insufficient duration of action of losartan. In addition, while the mice used for the losartan studies were genetically homogeneous and

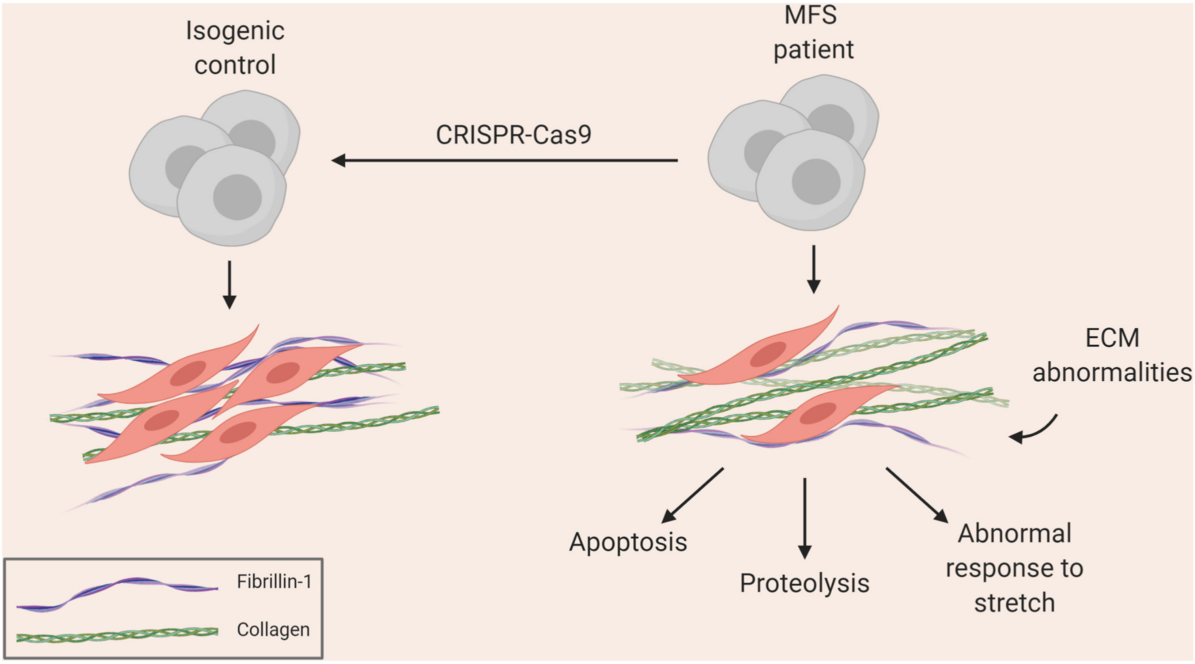

**FIGURE 1 |** Summary of aortic disease phenotype recapitulated in MFS iPSC model (Granata et al., 2017).

**TABLE 1 |** Overview of current aortic disease models.

| Disease model | Number of patient lines | Controls used (number of lines; clones) | Outcome |
|---|---|---|---|
| MFS Granata et al., 2017 | 2 | Healthy iPSC (3) Isogenic control (1) | Characterization of model; identification of disease mechanism |
| LDS Gong et al., 2020 | 1; mutation introduced into wild-type line | Healthy iPSC (1); isogenic to mutant line | Characterization of model; preliminary 3D model |
| BVS Jiao et al., 2016 | 2 | Healthy iPSC (2) | Characterization of model; identification of disease mechanism |
| SVAS Ge et al., 2012 | 1; 2 clones | Healthy iPSC (1; 2 clones) | Characterization of model; identification of disease mechanism |
| SVAS Kinnear et al., 2013 | 1; 4 clones | Healthy iPSC (1; 2 clones) | Characterization of model; identification of disease mechanism |
| SVAS Kinnear et al., 2020 | 5 | Healthy iPSC (3) | Further characterization of model; preliminary 3D model; drug screen |
| SVAS Dash et al., 2016 | 1 | Healthy iPSC (1) | Preliminary 3D model |
| HGP Zhang et al., 2014 | 2 | Healthy iPSC (1) | Characterization of model; identification of disease mechanism |
| HGP Liu et al., 2011 | 1 | Healthy iPSC (1) | Characterization of model; identification of disease mechanism |
| HGP Zhang et al., 2011 | 2 | Clinically normal parent iPSC (2) | Characterization of model |
| HGP Atchison et al., 2020 | 2 | Healthy iPSC (2) | Characterization of 3D model |

treated at the same age, the human patients introduced variability via their disease-causing mutations, genetic backgrounds and ages at treatment. Although animal models allow us to study various stages of disease and are still needed to assess potential therapeutic targets, this case has highlighted the need for an additional platform to assess the viability of mechanisms and treatments in a variety of patient lines before applying them in the clinic.

## Abnormalities in Mechanosensing

If excess TGF-β signaling is not causal in MFS, then what is? The contractile machinery of VSMCs is composed of thin and thick filaments that contain α-smooth muscle actin (α-SMA; *ACTA2*) and smooth muscle myosin heavy chain (SM-MHC; *MYH11*), respectively. In healthy conditions, once stress has been sensed via integrins (Martinez-Lemus et al., 2003), VSMCs can secrete various factors such as MMPs, TGF-β and angiotensin II to adapt the ECM and modulate VSMC phenotype to maintain blood pressure homeostasis (O'Callaghan and Williams, 2000). TAAD-causing mutations in *ACTA2* and *MYH11* disrupt their function (Zhu et al., 2006; Guo et al., 2007), suggesting that reduced VSMC contractility may be an underlying disease mechanism. In an iPSC model of LDS, where a mutation in *SMAD3* was created, the resulting VSMCs had decreased expression of contractile markers (Gong et al., 2020). Similarly, ECM mutations may disrupt the VSMC linkage to the matrix and ability to accurately sense wall stress. This is supported by electron microscopy images from MFS mice showing abnormally smooth elastic fibers due to reduced VSMC attachment (Bunton et al., 2001). It has therefore been proposed that abnormalities in mechanosensing, erroneous ECM remodeling and cellular response lead to aneurysm formation (Humphrey et al., 2015; Pinard et al., 2019). Another way in which mechanical forces may act could be by reduced vascular tone resulting in increased interstitial fluid leading to the formation of intramural edema and dissection (Mallat et al., 2016). This is supported by a study in rat abdominal aortic rings, where noradrenaline-stimulated VSMC contraction decreased hydraulic conductance (Chooi et al., 2017).

The mechanosensing hypothesis is supported by evidence from mouse models. Endothelial nitric oxide (NO)-mediated vasodilation exacerbated aortic aneurysm (Oller et al., 2017). In addition, treatment with calcium channel blockers as an alternative to current anti-hypertensive drugs also accelerated aneurysm formation in a model of MFS (Doyle et al., 2015). Post-natal *Tgfbr2* knock-out in mice led to decreased contractile gene expression and compaction in a collagen gel assay (Li et al., 2014). Further assessment of these mice found compromised aortic mechanical properties compared to controls, and treatment of these animals with rapamycin restored some of these mechanical properties and prevented pressure-induced delamination *in vitro* (Ferruzzi et al., 2016). Rapamycin has been shown to improve VSMC contractility (Martin et al., 2004), and has been used to rescue VSMC de-differentiation phenotypes, including *in vitro* disease models of supravalvular aortic stenosis (SVAS) and BAV/TAA (Kinnear et al., 2013; Jiao et al., 2016).

The relationship between inappropriate mechanosensing and TAAD formation is not yet fully understood. In addition to using animal models, iPSC-derived VSMCs could be used to investigate this hypothesis, as they can be genetically modified and stretched using various cell-stretching apparatus. We observed worsening of the disease phenotype upon cyclic stretch in our *in vitro* model of MFS (Granata et al., 2017), indicating that current protocols result in VSMCs sufficiently mature to be capable of mechanotransduction. Substrate stiffness is also something which can be explored – as mentioned above, the aortas of patients with TAADs tend to be stiffer. Combining iPSC-based models with hydrogels of varying stiffnesses could provide insights into the role of vessel wall stiffness in aortic disease.

### Understanding the Early Stages of Aortic Disease

Samples of diseased aortas can only be obtained from late-stage disease at the time of surgery, thus providing markers and mechanistic insight corresponding to severe TAADs only. From a therapeutic stand-point, investigating late-stage tissue provides limited information for developing novel therapies to prevent progression or identifying biomarkers for various stages of disease. Another challenge of using tissue from patients is the lack of appropriate controls. It is highly unlikely that researchers can obtain clinical samples of a healthy individual's aorta, but surgeons repairing a diseased aorta may collect biopsies from non-diseased sections, or at least from regions displaying no visible defects. However, such samples likely do not truly represent a healthy aorta, especially in the case of genetic disorders. Also, a region adjacent to the aneurysm could still exhibit defects in the ECM, signaling and response to mechanical stimuli. In addition, cytokines and growth factors in the circulation as well as local environmental cues may also contribute to the disease phenotype.

Early events in disease progression need to be better understood and characterized. As will be discussed further, there is significant variation in the disease presentation of MFS, even among individuals with the same causative mutation in *FBN1*. It is therefore difficult to predict from initial diagnosis whether disease progression will be mild or severe and this is a particular problem for sporadic cases with no family history. In addition, in disorders such as vEDS, patients do not tolerate surgery, with high post-operative mortality (Bergqvist et al., 2013). Consequently, treating patients at an early stage to prevent presentation or slow aneurysm growth would be ideal, and therefore understanding the early events in disease progression is critical.

These limitations may be circumvented by the use of iPSC-derived VSMCs. A virtually unlimited supply of cells can be generated from patient-derived iPSC lines along with genetically corrected isogenic controls. In our experience, both early and late events can be captured to some extent *in vitro*. For example, accumulation of disease phenotype with age is observed in the iPSC model of MFS. After differentiating MFS iPSCs to neural crest (NC)-derived VSMCs, we allow the cells to mature in serum for 30 days – during this time, the cells accrue a more severe phenotype in the dish, including increased proteolytic activity and apoptosis (Granata et al., 2017). We observed that NC-VSMCs at an earlier stage did not show the same intensity of disease characteristics, suggesting that, to an extent, we can mimic disease progression *in vitro*. We therefore suggest that iPSC-based models of VSMCs enable us to generate appropriate control cells and uncover events at various stages of disease progression.

### Conclusion

Thoracic aortic aneurysm and dissections are a group of disorders with life-threatening circumstances, and although surgical intervention has increased the mean life expectancy from 45 to 70 years in MFS (Milewicz et al., 2005), new medical treatments need to be urgently identified. Confounding results between mouse and clinical studies have emphasized the need for an additional assessment platform. iPSC-based modeling of aortic disease can be employed, where mechanistic and patient-specific information is used to direct future clinical trials and precision medicine. In the next section, we will discuss practical considerations for constructing a "disease-in-a-dish."

## PRACTICALITIES OF AORTIC DISEASE MODELING

### What do We Look for?

*In vitro* differentiation protocols are generally founded on developmental principles (Keller, 2005; Ayoubi et al., 2017).

For VSMC development, a huge body of work exists and as a detailed discussion is beyond the scope of this review, we refer the reader to excellent reviews written by others (Owens et al., 2004; Owens, 2007). Briefly, after endothelial cells (ECs) form a lumen mural cells are recruited and invested to stabilize the nascent vessel through various signaling axes, such as TGF-β, PDGF-BB, Notch and angiopoietin/Tie2 (Drake, 2003; Liu et al., 2009; Stenzel et al., 2009; Patel-Hett and D'Amore, 2011). This leads to the establishment of transcriptional modules, including SRF, GATA factors, and myocardin (Croissant et al., 1996; Manabe and Owens, 2001a; Chen et al., 2002; Nishida et al., 2002; Du et al., 2003). In addition, post-transcriptional processes, such as miR-143/145, have also been shown to contribute to this VSMC identity (Boucher et al., 2011). Finally, changes in the epigenome have been shown to allow binding of key transcription factors to their promoters, and lead to stabilization of this VSMC-specific gene expression, while still allowing for phenotypic plasticity depending on the integration of various inputs by the cells (Manabe and Owens, 2001b). Together, these processes lead to the stable expression of VSMC-specific gene expression. These markers of VSMCs can be used in stem cell-derived products to assess their identity and serve as a point for quality control.

An iPSC model is only as good as the differentiation protocol used. A variety of VSMC differentiation protocols exist and we have summarized those protocols that have been used in aortic disease modeling in **Table 2**; general VSMC differentiation protocols have been reviewed thoroughly by others (Ayoubi et al., 2017). When choosing a protocol to model aortic disease, there are a few parameters to consider. First, the length and nature of the protocol – older methods describe embryoid body (EB) differentiations, where aggregated stem cells spontaneously differentiate into the three germ layers, recapitulating events during development (Itskovitz-Eldor et al., 2000). From this point, VSMC fate can be induced. Differentiation through EBs requires precise control of cell aggregates, in respect of both size and homogeneity, as these can influence differentiation and yield (Messana et al., 2008), potentially due to cytokines and small molecules exerting their effects mainly on the surface layers (Sachlos and Auguste, 2008). Cell sorting by FACS could circumvent this issue, however, there are considerations for time and cell viability following sorting. Although methods have been developed to reduce variation in EB size and density, including the use of microwells, and micropatterned scaffolds (Bauwens et al., 2008; Mohr et al., 2010), the field has largely moved away from EBs to monolayer methods (Cheung et al., 2012; Mummery et al., 2012; Patsch et al., 2015; Palakkan et al., 2017). Generally, pluripotent stem cells grown as monolayer colonies are first directed toward a specific embryonic pathway, and then differentiated into VSMCs. This allows for more uniform delivery of factors guiding differentiation, as there are fewer considerations for factor diffusion and availability (Suchorska et al., 2017). Monolayer methods are also more amenable to large-scale production, due to their relative homogeneity compared to EBs, and do not necessarily require any cell sorting.

Another important consideration would be the presence of appropriate VSMC markers, indicative of maturation and contractility. With the possible exception of SM-MHC and smoothelin (*SMTN*), most VSMC markers can be expressed in other cell types under certain conditions (Alexander and Owens, 2012). Therefore, if the aim is to obtain relatively mature and contractile VSMCs, staining or flow cytometry of SM-MHC and/or smoothelin would be more appropriate ways of monitoring differentiation quality, rather than a less selective marker such as α-SMA. If opting for SM-MHC antibody staining, however, we caution readers to carefully assess the data – cross-reactivity of smooth muscle and non-muscle myosin heavy chains by polyclonal antibodies can confound interpretation of results and can lead to over-estimation of SM-MHC content (Rovner et al., 1986). It should be noted that *in vitro* differentiated cells can easily lose SM-MHC and smoothelin expression when exposed to serum (Alexander and Owens, 2012), so quality control to identify these VSMC markers should be performed prior to culture in serum. Furthermore, some patient-derived lines of familial TAADs may have mutations in VSMC contractile genes such as *MYH11* or *ACTA2*, so appropriate control lines, such as CRISPR-corrected isogenic lines, should be used in parallel in order to assess the quality of differentiations. In addition to marker expression, functional assays should also be performed. Identifying a protocol where the cells show VSMC-like responses, with rapid contraction, to vasoactive agonists such as carbachol would also be important to ensure that the correct cell type, or good differentiation, has been achieved. VSMC contraction should be noticeable on the scale of a few minutes, rather than hours (**Table 2**).

We appreciate that certain mutations will alter the expression of markers and function of resulting VSMCs. Care should be taken when establishing new disease models or lines to distinguish poor quality differentiations from genuine *in vitro* disease phenotypes. This may be particularly relevant in diseases or patient lines with mutations in genes affecting VSMC function, including the aforementioned *MYH11* or *ACTA2* mutations. In these cases, in addition to using gold standard isogenic controls, we strongly recommend careful and stringent quality control of the VSMC progenitor. This will reduce variability in the resulting VSMCs, and result in more consistent assessment of the disease phenotype.

## Maturity and Phenotype

Generating and analyzing contractile VSMCs is of crucial importance in recapitulating disease phenotypes. The importance of iPSC-derived maturity can be inferred firstly from the fact that TAADs are generally post-natal diseases rather than developmental. Moreover, with diseases related to VSMC de-differentiation, such as SVAS, restoration of full VSMC function and maturity *in vitro* would be an essential parameter of success for any new therapeutic. The inability of a differentiation protocol to yield mature VSMCs in control lines is likely to fatally compromise drug screening or testing with that protocol. In our experience, in addition to the specific protocol used, the contractile ability can be affected by user-dependent factors such as the seeding density during or after differentiation; these are important considerations as they contribute significantly to variation between differentiations, as will be highlighted below.

**TABLE 2 |** Summary of the differentiation protocols and parameters in aortic disease models.

| Protocol ref. | Use in disease modeling | Method | Length of VSMC induction | Media for VSMC induction | Markers of VSMCs detected | % Marker Expression | Contractility (time of assessment) | Lineage-specificity |
|---|---|---|---|---|---|---|---|---|
| Cheung et al., 2012, 2014; Serrano et al., 2019 | MFS Granata et al., 2017 | Monolayer through embryonic intermediates | 12 days and 30 days maturation | TGF-β (2 ng/ml) PDGF-BB (10 ng/ml); 10% FBS | *ACTA2, CNN1, TAGLN, SMTN MYH11* | >80% double-positive for *MYH11* and *CNN1* by FC | Carbachol (3 min) | NC, LM, and PM |
| Modification of Patsch et al., 2015 for CPC-VSMCs<br>Modification of Mica et al., 2013; Xiong et al., 2017 for NC-VSMCs | LDS Gong et al., 2020 | Monolayer through embryonic intermediates | For CPC-VSMCs: 6 days<br>For NC-VSMCs: 8 days | For CPC-VSMCs: TGF-β1 (2 ng/ml) PDGF-BB (10 ng/ml)<br>For NC-VSMCs: 20% KSR TGF-β (2 ng/ml) | *ACTA2, CNN1, TAGLN, SMTN MYH11* | Expression detected by qPCR and western blotting | Carbachol (30 min) | Cardiovascular progenitor cell (LM) and NC |
| Jiao et al., 2016 | BVS Jiao et al., 2016 | Monolayer through embryonic intermediates | 9 days | 15% KSR TGF-β (2 ng/ml) | *ACTA2, CNN1, TAGLN, MYH11* | >70% positive for *MYH11* by FC | Carbachol (30 min) | NC and PM |
| Xie et al., 2007 | SVAS Ge et al., 2012; Kinnear et al., 2013, 2020 | EB | 5–12 days | SMGM (Lonza); 5% FBS | *ACTA2, CNN1, TAGLN, MYOCD, MYLK, SMTN, MYH11* | 55% positive for *MYH11*; 97% positive for *ACTA2* by FC | Carbachol (30 min) | NR |
| Modification of Xie et al., 2007 | SVAS Dash et al., 2016 | EB | 17 days | SMGM-2 (Lonza); 0.5% FBS TGF-β (1 ng/ml) | *ACTA2, CNN1, TAGLN, ELN, MYH11* | 87% positive for *MYH11*; 75% positive for *ELN* by FC | Carbachol and KCl (15 min) | LM; inferred from cytokine response |
| Modification of Xie et al., 2007 | HGP Zhang et al., 2014 | EB | 42 days | SMGM (Lonza); 5% FBS | *ACTA2, CNN1, TAGLN* | >80% double positive for *ACTA2* and *CNN1* by FC | Angiotensin II (30 min) | NR |
| Liu et al., 2011 | HGP Liu et al., 2011 | Monolayer through CD34$^+$ progenitor | NR | SMGM-2 (Lonza) | *ACTA2, CNN1* | NR | NR | NR |
| Modification of Jeon et al., 2006 | HGP Zhang et al., 2011 | EB-derived mesenchymal stem cell (MSC) | 3 weeks | SPC (5 mM) TGF-β (2 ng/ml) | *ACTA2, CNN1, TAGLN, SMTN, MYH11* | 50–60% positive for *MYH11* by IF | Carbachol (60 min) | Mesoderm |
| Modification of Patsch et al., 2015 | HGP Atchison et al., 2020 | Monolayer through embryonic intermediate | 6 days | Activin A (2 ng/ml) PDGF-BB (10 ng/ml) Heparin (2 μg/ml) | *ACTA2, CNN1, MYH11* | >99% positive for *MYH11* by IF >90% positive for *ACTA2* and *CNN1* by FC | U46619 (10 min) | Mesoderm |

*MSC, Mesenchymal stem cell; KSR, Knock-out Serum Replacement; SMGM, Smooth Muscle Growth Medium; SPC, Sphingosylphosphorylcholine; FC, Flow Cytometry; IF, Immunofluorescence; and NR, not reported.*

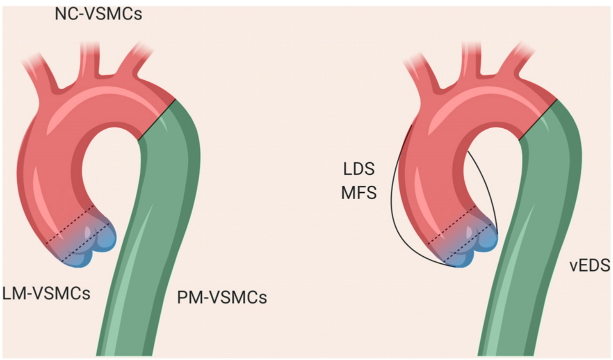

**FIGURE 2 |** The different regions of the thoracic aorta and their disease susceptibilities. The descending aorta comprises VSMCs from paraxial mesoderm, the aortic arch from neural crest, and the aortic root from lateral plate mesoderm. The boundary between the arch and descending aorta is clearly defined, whereas there is overlap between the VSMCs from NC and LM at the aortic root, as denoted by the dotted lines.

Vascular smooth muscle cell differentiation protocols can be further refined to improve the yield of contractile cells. In addition to reduction or replacement of serum in the maturation steps, small molecules can be introduced to improve yield of contractile VSMCs. Recently, a novel screening method was reported, where an *MYH11* reporter ESC line was used to screen over 4,000 compounds that may improve SM-MHC expression (Zhang et al., 2019). This screen identified RepSox, a modulator of Notch signaling, as improving VSMC contractility in differentiations using PDGF-BB and TGF-β. In addition to improvement in initial levels of SM-MHC, cells treated with RepSox also maintained high levels of SM-MHC for at least 8 weeks after derivation, suggesting that this may be a new and interesting direction for VSMC differentiation protocols.

## Lineages

The VSMCs comprising the aorta are derived from distinct embryonic lineages: the descending aorta is derived from paraxial mesoderm (PM), the ascending aorta and aortic arch from NC and the aortic root from lateral plate mesoderm (LM; Jiang et al., 2000; Wasteson et al., 2008; Harmon and Nakano, 2013; **Figure 2**). These different aortic regions seem to have distinct susceptibility to aortic diseases, including genetically-triggered aortopathies, suggesting that in addition to haemodynamics and wall structure, the embryonic lineage of the VSMC may be an important determinant for disease development and progression, [reviewed by (Majesky, 2007)]. In addition, the nature of the border between VSMCs of different lineages could be an important consideration; while there is a distinct boundary at the aortic isthmus between the PM- and NC-derived VSMCs (Nakamura et al., 2006), the transition between LM- and NC-VSMCs in the aortic root is not as well defined. Lineage-tracing experiments in mice have shown that there is a significant area of overlap between these lineages at the base of the aorta (Harmon and Nakano, 2013; Sawada et al., 2017). Indeed, it has been suggested that the differential response to cytokines and/or ECM composition between these overlapping or adjacent VSMC populations underpins the origins of aortic aneurysm and dissection (Topouzis and Majesky, 1996; Cheung et al., 2012), an hypothesis supported by recent work in mice (Angelov et al., 2017; MacFarlane et al., 2019). *Tgfbr2* deletion in VSMCs led to the development of thoracic aortic aneurysms, whereas treatment with a TGF-β neutralizing antibody resulted in abdominal aortic aneurysms (Angelov et al., 2017). Lineage tracking and sorting in a Loeys-Dietz mouse model showed a differential response of LM- and NC-derived VSMCs to TGF-β (MacFarlane et al., 2019).

As a result, protocols describing the derivation of VSMCs corresponding to the different regions of the aorta may be important to consider in order to accurately reflect the disease (Cheung et al., 2012; Patsch et al., 2015; Jiao et al., 2016; Gong et al., 2020). Our *in vitro* model of MFS showed differences in fibrillin-1 deposition and disease severity in VSMCs depending on embryonic origin, highlighting the importance of studying specific cohorts of VSMCs when modeling a "disease-in-a-dish" (Granata et al., 2017). A model of BAV has also demonstrated that NC-VSMCs, but not PM-VSMCs, from patients with BAV and TAA have defects in differentiation and contractile function (Jiao et al., 2016). Currently published iPSC models for SVAS, however, did not use lineage-specific protocols in their investigation (Ge et al., 2012; Kinnear et al., 2013, 2020). In a 3D model of SVAS, a lineage-specific protocol also was not used, although the investigators inferred lineage based on responsiveness to cytokines (Dash et al., 2016). Finally, in a recent iPSC-based model of LDS, NC-, and LM-VSMCs exhibited distinct defects relating to contractile marker expression and response to TGF-β depending on lineage (Gong et al., 2020), mirroring the *in vivo* findings (MacFarlane et al., 2019). These studies collectively echo the importance of using lineage-specific protocols wherever possible when modeling aortic disease.

## Contraction and Response to Stretch

VSMC contractility in response to agonists is an important indicator of maturity and this can be assayed in 2D and 3D systems. Contraction of VSMCs can be examined upon exposure to either ionophore compounds such as potassium chloride, ionomycin, or carbachol or peptide hormones such as angiotensin II. Angiotensin II activates AT1R, stimulating a cascade of G-coupled protein signaling or tyrosine phosphorylation triggering MAPK signaling followed by intracellular calcium release, which leads to contraction (Griendling et al., 1997; Touyz and Schiffrin, 1997). The extent of contraction can be investigated by comparing cell surface area before and after agonist stimulation, or more sophisticated methods involving live-imaging and/or force measurements can be employed (Gaio et al., 2016; Halaidych et al., 2019; van Meer et al., 2019). Importantly, routine examination of contractile response should be assayed in iPSC-derived VSMCs to ensure the consistency of differentiations.

In addition to being a functional benchmark, contraction has the ability to drive maturation. VSMCs contract to counterbalance hemodynamic forces as well as circumferential strain in blood vessels and, in response to these, maintain blood flow and pressure (Zulliger et al., 2004;

Alexander and Owens, 2012; Ahmadzadeh et al., 2019). Pulsatile stretch is interpreted by cells through intracellular signaling pathways leading to changes in proliferation, contraction, apoptosis, migration, and ECM remodeling (Haga et al., 2007). VSMC contraction does not only define the maturity of these cells, but the application of uniaxial mechanical forces using stretching platforms can itself induce functional differentiation of the nascent iPSC-derived VSMCs. Cyclic stretch is applied to VSMCs seeded on ECM-coated elastomer-bottomed culture plates and, over 6 to 48 h, the VSMCs align themselves based on the strain cues (Mantella et al., 2015). Stretched VSMCs have synchronized contraction and increased myocardin expression, indicative of enhanced contractility (Zhu et al., 2011; Raphel et al., 2012; Chiu et al., 2013; Qiu et al., 2013). It should be noted that uniaxial stretch promotes VSMC differentiation whereas equiaxial stretch has the opposite effect (Park et al., 2004) therefore the choice of method needs careful consideration.

Another mode of enhancing contractility is by the use of pulsatile flow, which has proved to be effective in improving both VSMC alignment and contractility in 2D as well as 3D culture systems (Shi and Tarbell, 2011). Cyclic stretch aided alignment of VSMCs and deposition of elastin as well as other ECM components such as collagen, which in turn enhanced tensile strength and elasticity of scaffolds, vascular rings and tissue engineered blood vessels (TEBVs) made of VSMCs and ECs (Solan et al., 2009; Cooper et al., 2014). Here, the stretched constructs demonstrated higher burst strength and elasticity compared to non-stretched counterparts, making them both more amenable for *in vivo* transplant and a more accurate disease model *in vitro*.

These simple 3D models are amenable to contractility assays and can supplement standard 2D *in vitro* systems. In addition, they offer the possibility to test VSMC interactions with other cell types such as ECs and fibroblasts (Jung et al., 2015; Ding-Yang et al., 2019). VSMCs embedded in collagen or Matrigel have been shown to reorganize and remodel their environment to more closely mimic *in vivo* ECM architecture (Song et al., 2001; van den Akker et al., 2012). Contraction can also be assayed in these 3D systems, which more closely resemble native blood vessels than 2D cultures. The collagen gel contraction assay is a typical one to assess functionality of VSMCs by measuring the reduction in gel area and has been applied to both primary and stem cell-derived VSMCs (Oishi et al., 2000; Sinha et al., 2006; van den Akker et al., 2012; Lee et al., 2019). Newer models employ the use of bioreactors for scale-up, and 3D hydrogel disks are prepared by mixing multiple cell types like VSMCs and ECs with collagen, and contraction assayed over 30 min to 1 h (Lin et al., 2019). Vascular rings, a 3D structure comprising VSMCs, can be created relatively quickly and changes in circumference or force generation can be assayed in response to contractile agonists (Bi et al., 2005; Dash et al., 2016). Dash and colleagues have successfully created rings using iPSC-derived VSMCs to create a preliminary 3D model of SVAS. Here, the vascular rings created from patient VSMCs exhibited reduced contractility, which was a similar finding to previously published 2D models of SVAS with the strength of analyzing collective force generation and contraction versus single cells in a monolayer (Ge et al., 2012; Kinnear et al., 2013).

An important consideration for aortic disease modeling is that the full of extent of VSMC dysfunction may not be evident in unstretched or unstimulated circumstances. For example, there may be defects in contraction or contractile responses which are critical for the disease phenotype which are not otherwise apparent. Subjecting cells to mechanical forces would emulate the *in vivo* strain, as well as triggering associated signaling pathways, such as the generation of physiological reactive oxygen species (Clempus and Griendling, 2006). This was recently highlighted by a study in vEDS mouse models, where the differences in collagen organization were only apparent after stretching (Dubacher et al., 2020). When developing new therapies for aortic disease, it is essential to ensure that the disease effect on VSMC contraction and mechanotransduction are sufficiently evaluated.

## Gene Editing to Create Isogenic Controls

With the advances in tools for gene editing, the use of isogenic controls is now the gold-standard in iPSC modeling. Many stem cell banks have catalogs of extensively-characterized healthy iPSC lines and these can be used as controls compared to patient lines. However, diseases such as MFS have high inter- and intra-familial variability – the same mutation in *FBN1* can result in varied disease presentations (Dietz et al., 1992). Consequently, gene editing, to provide a "corrected" wild-type version of the disease line, offers the significant advantage of an isogenic control line that has the same genetic background as the disease model but differs only by the few nucleotides that constitute the mutation. Although this approach is widely-used in many fields (Bassett, 2017), current aortic disease models mainly rely on healthy iPSC lines as controls (**Table 1**).

Of course, the gene editing tools used to correct a mutation can easily be used to create a mutation in an otherwise healthy control iPSC line. Several groups have used this approach to generate disease models without needing patient involvement (Paquet et al., 2016; Tidball et al., 2017; Frederiksen et al., 2019), including a recent model for LDS (Gong et al., 2020). Despite the obvious practical advantages of this strategy, we should sound a note of caution. If there is any variable expressivity of the mutation, then a permissive genetic background may be required for full disease manifestation *in vitro*, which unlike lines from patients with disease, is uncertain in healthy control iPSC lines. We predict that creating a patient mutation in a healthy line will not necessarily yield the same extent of cellular defects as the patient line. This will be particularly important for multi-variant disorders, but also when modeling disease from patients with milder clinical manifestations. In the case of the monogenic aortic diseases discussed here, genetic background likely plays an important role in influencing disease severity and presentation, as will be discussed later. In practical terms, in order to construct an accurate "disease-in-a-dish," we recommend the use of patient lines and genetically-engineered isogenic controls as the gold standard. Alternatively, wherever possible, iPSCs from unaffected family members could also be used as controls, which partly mitigates the differences in genetic backgrounds. In a model of Hutchison-Gilford progeria (HGP), researchers obtained unaffected parental fibroblasts in addition to patient lines from the Coriell Institute cell bank (Zhang et al., 2011); unfortunately, in this case, parents and patients were from different families.

### Conclusion

Many differentiation protocols exist for producing VSMCs and the choice of protocol can have important effects on the quality of disease modeling. This may be particularly pertinent in modeling aortic disease, as three lineages of VSMC are present in the aorta and may be involved with disease susceptibility, but also because aortopathies may result from improper VSMC function, such as abnormal proliferation and contractility. Once differentiated, iPSC-derived VSMCs provide a flexible system to address aspects of a disease – simple cell-based assays such as the assessment of proteolytic activity, proliferation, contractility, and response to mechanical stimuli can provide mechanistic insight. Lastly, gene editing tools allow researchers to create virtually any genetic modification in their patient-derived or healthy lines, creating opportunities to untangle issues such as the genotype-phenotype correlation in TAADs. Despite these advantages, there are a number of issues to be aware of which we will discuss next.

## LIMITATIONS OF CURRENT APPROACHES TO AORTIC DISEASE MODELING

### Production of Immature Cells

Cell maturity is a major consideration with iPSC-based modeling of aortic disease. Current iPSC differentiation protocols almost invariably result in cells which are closer to fetal VSMCs than to adult cells, as has been demonstrated in other fields (Mummery et al., 2012; Lundy et al., 2013; Hrvatin et al., 2014; Baxter et al., 2015). While this immaturity has been best characterized in cardiomyocyte and hepatic differentiation, a similar problem is likely to exist in VSMC differentiation; although the exact developmental stage, perhaps due to intrinsic VSMC plasticity (Alexander and Owens, 2012), is poorly characterized in most VSMC studies. Nevertheless, low levels of SM-MHC and smoothelin expression confirm that these iPSC-VSMCs are most likely to represent a fetal-like state. While this may be advantageous for developmental studies and disorders, caution is warranted for adult disease modeling and the potential drawbacks have been discussed earlier. It is possible to improve the maturity of the *in vitro* derived VSMCs using a range of strategies including EC co-culture (Collado et al., 2017), application of mechanical force (Park et al., 2004; Ghazanfari et al., 2009), small molecules or other growth factors such as TGF-β and retinoic acid (Martin et al., 2004; Yu et al., 2011; Wanjare et al., 2013; Zhang et al., 2019). Differentiation protocols continue to be refined, and protocols describing the derivation or indeed forward programming of adult-like VSMCs are eagerly awaited.

### *In vitro* Models: A Simplified System

Vascular smooth muscle cells grown in 2D monoculture provide a reductive snapshot of the disease. VSMCs in the aorta are normally in contact with adventitial fibroblasts, other VSMCs in the medial lamellae and ECs lining the lumen. ECs are also closely-associated with microfibrils via integrins, and like VSMCs can also secrete fibrillin-1, although the extent and functional significance of this has not been extensively characterized (Weber et al., 2002; Rossi et al., 2010). Intimal ECs experience direct shear stress and can modulate the function of VSMCs by releasing vasoconstrictors or relaxants (Lilly, 2014). Paracrine signaling and physical interactions between ECs and VSMCs are essential for vessel development and homeostasis of mature vessels, regulating tone, blood pressure, and response to injury (Lilly, 2014). For example, endothelial signaling of TGF-β and Notch regulates VSMC phenotype and differentiation (Domenga et al., 2004; Jakobsson and van Meeteren, 2013). VSMC monoculture therefore neglects these potentially important cellular interactions, limiting the information available from such systems.

While the majority of studies investigating aortopathies focus on VSMCs, abnormalities in EC function have also been reported. NO is produced from ECs and regulates vascular tone by inhibiting VSMC contraction. MFS thoracic aortas showed differential relaxation curves in response to endothelial NO compared to wild-type controls, whereas the response in the abdominal aorta was similar for MFS or control (Chung et al., 2007). A mouse model of TAAs found that NO is implicated in TAA disease progression, where various models of TAA, including MFS, had improved aortic phenotypes when treated with NO synthase inhibitor L-NAME (Oller et al., 2017). Recently, cell-specific deletion of the *AGTR1* was investigated in a severe model of MFS (Galatioto et al., 2018). The authors found that while there was no effect with VSMC-specific deletion of *AGTR1* on disease end-points, specific ablation in ECs improved survival and decreased aortic diameter. This study highlighted that there are differential responses of ECs and VSMCs to cytokines and growth factors. This characteristic could be an important consideration for *in vitro* drug screens and discovery; once an interesting target has been identified, the response of ECs should also be studied prior to validation *in vivo*, as ECs clearly impact the disease mechanism in MFS, and likely other TAADs. This can be done in a variety of ways – ECs and VSMCs can be assessed independently or in 2D co-culture, which provides a simple way of studying both cell types together (Fillinger et al., 1997; Hastings et al., 2007). After co-culture, ECs can be purified using magnetic beads coated with anti-CD31 allowing separate downstream analysis of ECs and VSMCs (Wallace et al., 2007).

Hemodynamic forces within the blood vessel influence VSMC phenotype and function. VSMCs are not normally exposed to luminal blood flow, but instead experience low transmural interstitial flow, with cells closer to the intima experiencing greater force (Shi and Tarbell, 2011). *In vitro*, flow was found to increase VSMC contraction (Civelek et al., 2002), and induces alignment of cells perpendicular to the direction of flow (Lee et al., 2002). Studies using VSMCs alone have conflicting reports on the effect of flow on VSMC phenotype (Papadaki et al., 1996; Ueba et al., 1997; Haga et al., 2007; Shi et al., 2010), possibly due to varied forces and culture conditions. However, when VSMCs and ECs are co-cultured with shear stress, VSMC phenotype was found to be more contractile and with gene expression signatures closer to that of primary cells (Tsai et al., 2009; Collado et al., 2017).

The power of a 3D approach in HGP has been illustrated by the use of TEBVs generated from patient-derived iPSCs (Atchison et al., 2017; Abutaleb and Truskey, 2020). These TEBVs recapitulated the disease phenotypes and helped to elucidate the role of both VSMCs and ECs in disease progression. Both vasoconstriction and dilation were affected and increased medial wall thickness, calcification and apoptosis were observed. Furthermore, this 3D model was used for drug testing, where they demonstrated that the rapamycin analog everolimus increased vasoreactivity and improved VSMC differentiation. Further refinement of this model using both iPSC-derived ECs and VSMCs demonstrated that ECs are likely responsible for the abnormal response to shear stress (Atchison et al., 2020). Together, these studies highlight the importance of contributions of ECs and shear stress to VSMC biology.

When investigating aortopathies, co-culture and/or 3D approaches could be considered. While these methods provide the possibility of analyzing cells in a more native-like state, they are also more complicated, time-consuming to set up and require careful construction. A blood vessel wall contains multiple cell types, with distinct interactions being critical for their proper function. Hence, consideration of the relative ratios of VSMC, ECs and fibroblasts is required, as these can impact a number of properties including ECM deposition and modulation of VSMC phenotype (Lilly, 2014; Kuwabara and Tallquist, 2017). The arrangement and orientation of these cell types should also be considered, such that the natural hierarchy of cells forming the vasculature is respected. Inappropriate integration of these cell types could be detrimental for building an accurate disease model, obscuring critical differences between control and disease models. Finally, as we’ll discuss below, generating large amounts of iPSC-derived VSMCs can by itself be a laborious and time-consuming task; additional differentiations to ECs or set-up to create 3D systems could be difficult to accommodate in large scale.

Despite efforts to improve fidelity of iPSC-based models, the same pitfalls for any *in vitro* model remain. They lack key features provided by *in vivo models*, including involvement of the immune system and integration of complex physiological networks. We would like to emphasize that these iPSC models do not replace *in vivo* studies; instead, they complement and can accelerate the study of disease by providing a flexible platform for testing and screening. We therefore propose that with the current limitations, simple VSMC-based assays and screens in 2D could identify interesting mechanisms and targets, which can then be tested in a more complex, *in vitro* system before transitioning to *in vivo* models.

## Scale-Up and Variability Issues

Hurdles facing iPSC-based disease modeling include difficulties in scaling up production of cells and variability between differentiations. There are physical limitations to manually culturing multiple lines of iPSCs and producing large amounts of cells. Currently, aortic disease modeling is done with a handful of patient lines and controls, with assays which don’t typically require large amounts of cells (**Table 1**). However, for modeling diseases using 3D methods, such as TEBVs or vascular rings, many millions of cells will be required. While we discussed the ability to create virtually any mutation in the lines, the sheer number of hours and hands required to culture many different cell lines could be inhibitory, let alone deriving large quantities from each line. VSMC-derivation protocols are currently multi-step procedures, which go through an intermediate or a VSMC precursor. In addition, protocols can also include a maturation step, where cells are cultured for up to a month to accrue their phenotype. As a result, when employing such protocols, a single line will yield four distinct cell-types to monitor and manage: iPSC, intermediate/precursor, immature VSMC and mature VSMC. In our experience, given the tiered nature of the VMSC differentiation protocols, creating good intermediates is essential to producing reliable and mature VSMCs, and their maintenance should not be neglected. The length of these protocols also means that there is more opportunity for variability in differentiations. Another complication is that different iPSC lines can also behave very differently, even among control or healthy iPSC lines; skill and experience are needed to ensure that all lines are appropriately handled during differentiation in order to reduce noise from interline variability. For example, a disease model line could have abnormal proliferation and the researcher must take this into account when deciding when to passage them.

How consistently can iPSCs be differentiated by the investigator, their colleagues or even other labs using the same protocol? Considerable variation in differentiations has been reported in various fields; for example, a multi-site analysis found substantial heterogeneity in neuronal differentiations between sites using the same lines and protocol (Volpato et al., 2018). Even within research groups, variation between lines and differentiations were observed for both EB and monolayer differentiations (Osafune et al., 2008; Hu et al., 2010). When studying the 9p21 vascular risk variant, multiple iPSC lines from the same patient or even the same line differentiated multiple times exhibited considerable transcriptional variability at both iPSC and VSMC stages (Lo Sardo et al., 2018). These findings underline the concern with regard to reproducibility of data. We certainly observe differences in VSMC differentiation between individuals in our group, stressing the influence the investigator has on the final outcome. Other researchers have also observed different levels of SM-MHC$^+$ cells using the same protocol or have had to modify the protocol to obtain sufficient maturity in their hands (Cheung et al., 2012; He et al., 2018; Trillhaase et al., 2018; Zhang et al., 2019). These differences could be due to the use of different iPSC lines, but are likely also impacted by variation imparted by the user. Current iPSC models of aortic disease are focused on severe models of disease. However, when modeling the effects of a milder mutation or variant, the effect of genotype may not be observed if the differentiations themselves are highly variable.

A common issue we'd like to highlight for many differentiation protocols is the use of non-chemically-defined media and coatings, such as serum or Matrigel, and the reliance on cytokines where different batches of these reagents may have varying effects on differentiated cells. Currently in disease modeling, serum is used to stimulate growth of VSMCs in various protocols after differentiation (**Table 2**), and high levels of serum are known to result in loss of contractile phenotype (Alexander and Owens, 2012). Aside from the use of Matrigel, a near chemically-defined protocol to generate VSMCs has been developed (Patsch et al., 2015) and modified protocols have recently been used to model HGP (Atchison et al., 2020) and LDS (Gong et al., 2020). In addition, many VSMC protocols rely on growth factors, such as TGF-β and PDGF-BB for differentiation. While these protocols do work, investigators should be wary of the numerous factors which may influence the efficacy of these cytokines, such as storage method and batch-to-batch variation. In the cardiac field, a protocol using entirely chemically-defined media to produce cardiomyocytes was developed by systematically assessing the necessity of individual factors (Burridge et al., 2014). Interestingly, they found that only three components were crucial for cardiomyocyte differentiation. This protocol resulted in improved consistency of differentiations in the 11 iPSC lines that were tested. In addition to ease and consistency, this approach could also enable researchers to scale-up production more than is possible using cytokine and xeno-containing formulations. Similar advances have been made in other fields (Erceg et al., 2008; Touboul et al., 2010) and would be beneficial in advancing aortic disease modeling.

It goes without saying that new protocols have to be carefully assessed and compared with tissue or primary cells to ensure that that the stem cell-derived product has the correct identity. With advances in the past decade, decreasing price and availability of large-scale experiments (Hasin et al., 2017), detailed comparisons can be performed to assess the quality and consistency of differentiation protocols. This was an approach demonstrated by Patsch et al. (2015), where they showed high correlation between their differentiated and primary VSMCs using both transcriptomics and metabolomics. In addition, high-throughput "omics" can be used to assess the consistency of differentiations (Paull et al., 2015), and single-cell RNA sequencing has been used to identify pivotal steps in differentiation protocols (Chu et al., 2016; Han et al., 2018). We predict that future iterations of protocols will utilize these tools to help direct and objectively assess the quality of differentiation protocols.

Alternative approaches, such as direct reprogramming and forward reprogramming, may circumvent the imperfect approximations of developmental pathways used for typical differentiation protocols, and reduce the number of intermediates required (**Figure 3A**). Work on direct reprogramming has been shown in various fields (Kelaini et al., 2014), including the derivation of cardiomyocytes from fibroblasts (Ieda et al., 2010). Forward reprogramming has been demonstrated to rapidly convert hESCs into neurons, skeletal myocytes, and oligodendrocytes by overexpressing key lineage-specific transcription factors (Pawlowski et al., 2017). These approaches in VSMCs have only recently been reported, and warrant further investigation (Yeung et al., 2017; Hirai et al., 2018). In addition, it may be challenging to produce the significant region-specific VSMCs using these strategies with our current limited understanding of the fundamental differences between VSMC from varying embryonic origins.

Until differentiation methods are refined, steps can be taken to improve reliability of current protocols with clearly-defined parameters for quality control at various stages. For example, stringent quality control should be performed after the derivation of an intermediate state before inducing cells toward a VSMC fate (Cheung et al., 2014); if the cells fail to meet the set criteria, they should not be used for further differentiation (**Figure 3C**). In addition, when VSMCs are produced, analysis of markers and/or function should be routinely assessed. These criteria should ideally be shared with collaborators in order to reduce the site-specific variability as described by Volpato et al. (2018). Furthermore, identification of novel surface markers exclusively expressed on contractile and mature VSMCs could be used for cell sorting and/or quality control. Lastly, wherever possible, the use of multiple iPSC clones from the same patient could also improve the signal-noise ratio, as different clones can themselves be highly variable (Lo Sardo et al., 2018; Popp et al., 2018).

Automated systems and machine learning could significantly reduce the input needed from the researcher when culturing multiple lines, improving consistency and enabling increased production. Automated iPSC culture systems have been developed and would present a solution to the workload and variability problems (Conway et al., 2015; Paull et al., 2015; **Figure 3B**). The method developed by Paull and colleagues describes the capacity to reprogram, expand and characterize hundreds of lines per month with significant reductions in reagent cost. In addition, transcriptomics analysis indicated that there was a significant reduction in variability in EB assays when compared to manual processing. This system was put to the test when iPSCs were differentiated into dopaminergic neurons using a 30-day protocol and the resulting cells maintained expected marker expression. This automated system was utilized by another group for cardiomyocyte differentiation, and found success with producing a maximum of $3 \times 10^9$ cardiomyocytes per batch (Denning et al., 2016). A recent method describing high-yield derivation of VSMCs based on an existing protocol (Patsch et al., 2015) was described, where VSMCs were derived in alginate hydrogel tubes (Lin et al., 2019). This method yielded $5 \times 10^8$ cells/ml in 10 days; as a result, bioengineering methods could rely on such advances for producing high numbers of cells.

The behavior of some patient lines with certain mutations can be tremendously divergent compared to control lines, requiring careful assessment from an experienced researcher to consider not only cell density, but also morphology, heterogeneity and survival. In our experience working with MFS patient iPSC lines, when deriving NC-VSMCs, the cells steadily exhibit more of the disease phenotype throughout the course of differentiation. They require much closer monitoring and the resulting differentiations can be more heterogeneous compared

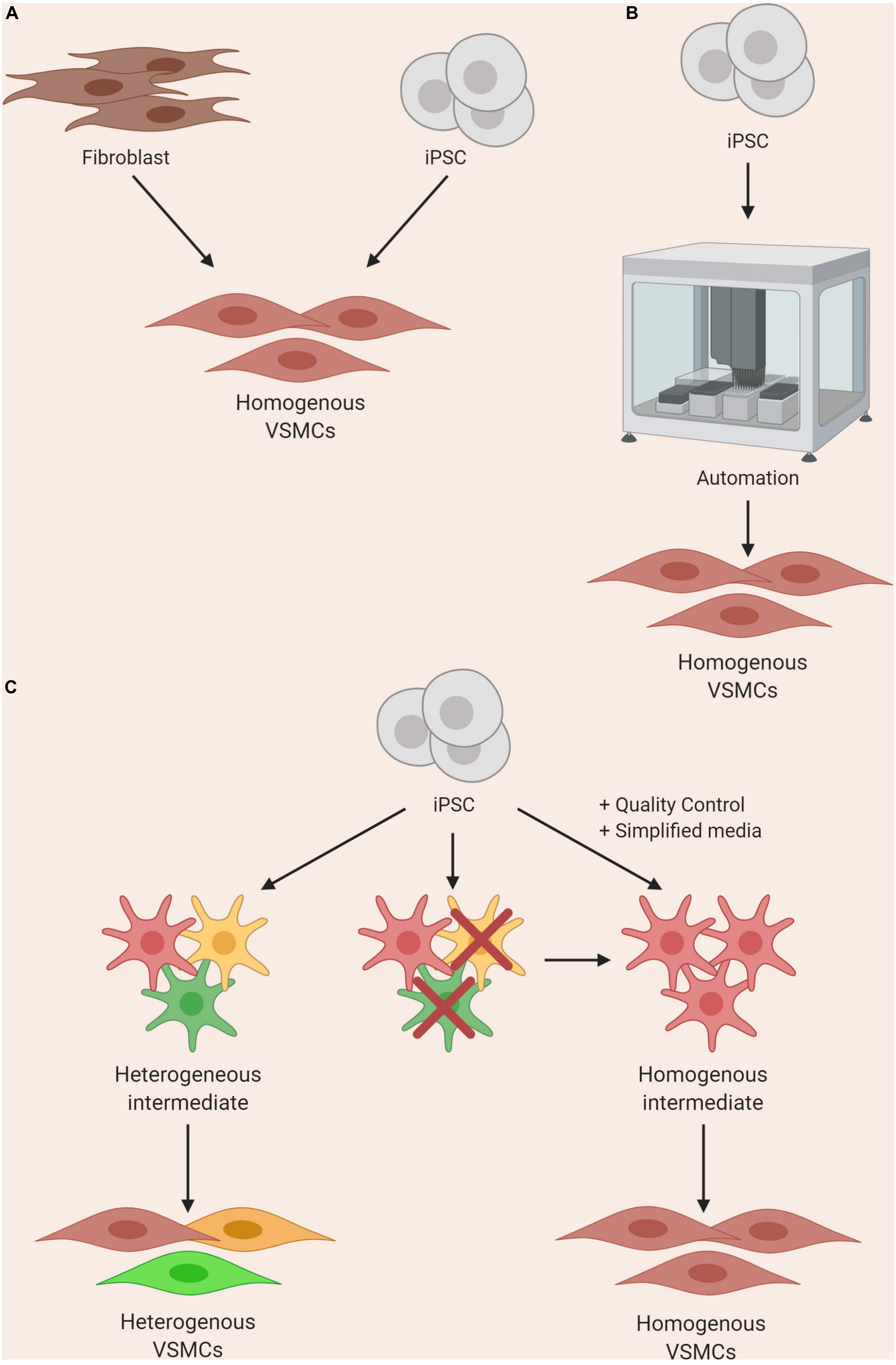

**FIGURE 3 |** Approaches to improving homogeneity of VSMC differentiations by using **(A)** direct or forward reprogramming methods, **(B)** automation, or **(C)** improved quality control and simplification of media components.

to controls, due to varied cell density caused by increased apoptosis and slower proliferation. Innovations in robotics and machine learning could overcome these bottlenecks. For example, machine learning has been developed to identify cells in phase contrast based on morphology alone without the need for molecular labeling (Kusumoto and Yuasa, 2019). This technology, in conjunction with modular automated systems, could be powerful for processing large numbers of iPSC lines, including cells derived from severely affected lines, as it could potentially remove the need for an experienced "eye" when culturing cells. However, at the moment, the protocols and technologies are not yet compatible with one another for robust, automated systems; the labor-intensive manual culture and differentiation of iPSC lines into VSMCs are current limitations for large-scale studies.

## Conclusion

Induced pluripotent stem cell-based modeling of aortic disease is still relatively new, with only a handful of papers describing disease models (**Table 1**). Despite the practical advantages of using this system, there are limitations. Most notably, the cells obtained from differentiation are not as mature as VSMCs in tissue due in part to absent mechanical cues, lack of contact with ECs and other physiological signals. In addition, without appropriate quality control, variability between differentiations can result in noisy and inconsistent data. Large-scale experiments involving multiple lines are difficult to perform as manual passaging and differentiation is required as a result of the complexity of certain protocols. In spite of this, we are certain that continued refinement of differentiation protocols and technological advances will be able to overcome these limitations to create valuable tools for understanding, preventing and treating aortopathies.

# POTENTIAL AND FUTURE DIRECTIONS

## Regenerative Medicine

The first engineered blood vessel was a relatively simple construct made from collagen and primary bovine VSMCs, which was then lined or coated with primary ECs and adventitial fibroblasts, respectively (Weinberg and Bell, 1986). Since then, efforts have been made to produce clinically-relevant TEBVs with the required mechanical specifications, as reviewed by (Kumar et al., 2011). Recently, tissue engineered vascular grafts (TEVGs; Carrabba and Madeddu, 2018; Song et al., 2018) and vasculature-on-a-chip (Kim et al., 2017) models have been developed to accommodate the gold standard properties of a transplantable graft using either self-assembling bioprinting technology or using natural or synthetic scaffolding (Konig et al., 2009; Wise et al., 2011). These models have the properties of a successful graft, such as an autologous endothelium, anti-thrombogenic properties and minimum integrity span of 21 months, with appropriate permeability, compliance, elastic modulus, and a minimum burst pressure of 1700 mmHg (Konig et al., 2009).

The use of TEVGs in regenerative medicine is still under development, with many groups innovating with novel ways to tackle the problems facing engineered grafts. For example, grafts comprising decellularized ECM on biodegradable scaffolds have been suggested to serve as readily available TEVGs; these have been tested in a variety of animals models (Dahl et al., 2011) and can exploit recent advances in 3D tissue printing to provide patient-specific grafts (Fukunishi et al., 2017; Best et al., 2018). Cell-free vessel grafts have been generated by allowing cells to secrete ECM for longer periods to more closely mimic the *in vivo* environment and are then decellularized (Lawson et al., 2016; Row et al., 2017). Furthermore, functionalization of TEVGs with biological signals such as the angiogenic cytokine VEGF have been shown to trigger *in situ* tissue endothelial regeneration (Koobatian et al., 2016). Although advances in traditional translational approaches for cardiac anomalies have paved the way for regenerative medicine, these TEVGs still suffer from a number of common issues including insufficient patency, integration, hemodynamics, immune-compatibility with the graft cell source and mechanical strength, as outlined by others (Pashneh-Tala et al., 2016; Matsuzaki et al., 2019; Skovrind et al., 2019).

Currently, if a TAAD patient's aorta dilatates sufficiently, prophylactic surgical intervention is required. iPSC-based systems raise the possibility of developing regenerative cell therapies for patients with aortic disease, where TEVGs can be produced from patient iPSCs. In addition, the availability of gene editing tools means that the TAAD-causing mutation(s) can be corrected in a patient's iPSCs. These, in turn, could be differentiated into VSMCs and developed into a healthy TEBV, to be used as an autologous bio-compatible graft. Furthermore, patient-derived iPSCs would provide immune-compatible grafts. These would be particularly useful in pediatric patients where cardiovascular grafts would ideally grow in line with the patient's normal growth and development (Sugiura et al., 2018). To our knowledge, there have been limited applications of iPSC-based TEVGs, let alone in the context of aortic disease. In one case at least, TEVGs demonstrated mechanical strength comparable to that of native veins; when implanted in rats, they showed sustained mechanical function and patency (Sundaram et al., 2014; Luo et al., 2020). While the application of iPSC-derived VSMCs in regenerative medicine for the treatment of aortic disease is attractive, we would like to caution that this represents a very labor-intensive task. We discussed earlier the current difficulties in obtaining large numbers of consistently-differentiated VSMCs. In addition, the approaches highlighted above would need to be tailored to each individual patient. In our experience, establishing and characterizing a new iPSC line can take weeks before differentiations can be started, which can themselves take up to a month before TEBV construction can begin. The timeline grows even longer if gene editing also has to be involved. As an alternative, haplotype matched/allogenic iPSCs, MSCs or ESCs could be used providing the advantage of well-defined VSMC differentiation protocols but without needing to develop individual lines and grafts specifically for each patient (Sundaram et al., 2014; Gui et al., 2016; Elliott et al., 2019; Luo et al., 2020). These can be prepared in a variety of formats, including printed, electrospun,or decellularized scaffold grafts. This approach could be developed even further by the use of lineage-specific protocols to create the closest approximation possible of on-demand TEVGs, catering to different matrix compositions.

## Prediction of Disease Severity and Phenotype-Genotype Correlation

Aortopathies have profound effects on the life quality of affected patients; not being able to know what the severity of the disease is can be an enormous burden. This is complicated by the lack of understanding of genotype-phenotype correlation in many TAADs – even within families, disease severity can vary significantly. This is even more difficult in sporadic cases, where there is no family history to infer prognosis from. The best solution at the moment is to monitor the patient's aorta by cross-sectional imaging, administer anti-hypertensives and intervene with surgery if the dilatation exceeds a threshold. However, what if we were able to predict the patient's disease severity and likely progression?

In MFS, there is high inter- and intra-familial variation in patients. *FBN1* is a large gene, encoded by 65 exons, with over 3,000 mutations identified to date (Collod-Béroud et al., 2003). Aside from neonatal MFS, there may be some broad genotype-phenotype correlation with *FBN1* mutations; in MFS, mutations in exons 24–32 or premature terminations are associated with a more severe disease outcome with cardiovascular complications (Faivre et al., 2007). Disease-causing mutations of *FBN1* can be categorized as dominant-negative or haploinsufficient. In dominant-negative forms, the mutant product interferes with normal microfibril formation or is mis-incorporated. Various studies in patient fibroblasts have found abnormalities with reduced synthesis, delayed intracellular processing, and secretion (Aoyama et al., 1994; Schrijver et al., 1999; Whiteman and Handford, 2003). Haploinsufficiency is typically caused by mis-sense or frameshift mutations; analysis of patient fibroblasts found a reduction in the mRNA levels of mutant fibrillin-1, and a disproportionately low amount of fibrillin-1 deposition (Schrijver et al., 2002). Large studies have concluded that mutations causing haploinsufficiency of fibrillin-1 resulted in a 2.5-fold increase in the risk of cardiovascular death compared to dominant-negative mutations (Franken et al., 2016), and that mutations involving cysteines tend to also result in more severe clinical presentations (Aubart et al., 2018).

Although these broad associations may explain in part some of the variation in disease severity observed between patients with different mutations, it is unclear what factors contribute to variation *within* families or between patients with the same mutation in different families. Variation in genetic background clearly plays a key role in the different expression of disease. However, identifying clear associations between genotype and phenotype can be challenging for rare diseases due to the statistical power needed to identify gene modifiers in population genomics. MFS is the most common TAAD, with an incidence for 1 in 5000, whereas diseases such as LDS and vEDS are even rarer. A small study in patients with TAAs identified that variants in *ADCK4* and *COL15A1* were associated with mild disease (Landis et al., 2017). Recent studies have shown that integrating multiple methods can overcome limitations of studying rare disorders (Aubart et al., 2018). Whole-exome sequencing and association studies in a large cohort of 1070 patient fibroblasts has identified interesting mutations and variants accompanying a more severe presentation of MFS (Aubart et al., 2018). Severe cases of MFS were associated with co-occurrence of another TAAD-causing mutation, including additional variants of *FBN1* or *SMAD3*. Interestingly, severe disease was also associated with mutations in *COL4A1*; variants of *COL4A1* have been reported in stroke and cerebral aneurysms (Lanfranconi and Markus, 2010). Three major modifier regions were identified, corresponding to loci encoding *ECE1*, *PRKG1* and *MMPs*.

iPSC-based modeling could help with severity prediction in two ways – first, by deepening our understanding of the genetic variants interacting with disease-causing mutations, and second, by potentially providing a platform with which to assess patient-specific disease severity. Whole-exome sequencing of a patient's genome could give clinicians an initial idea of the expected disease severity, based on the risk variants present. These identified variants could then be introduced into various iPSC lines to further underpin their role in modulating disease. This can be done in a variety of patient lines, isogenic controls and also in healthy iPSC lines. This approach was used in an investigation of metabolic disorders, where variants previously discovered using genome-wide association studies were investigated using patient iPSCs (Warren et al., 2017). From patient iPSCs, simple cell-based assays can be employed to construct a prediction of clinical severity in the patient. In the case of TAADs, this could be looking at proteolytic activity, abnormal ECM deposition or cell death. Guidelines for determining *in vitro* disease severity can be developed through iterative empirical testing until these *in vitro* benchmarks are sufficiently refined and can be robustly linked to clinical severity. This predictive tool could then be used in conjunction with clinical benchmarks to provide a more informed prognosis. Together, these methods could be used to predict the course of the disease and guide treatment for patients.

## Drug Screens and Precision Medicine

Patient-derived VSMCs can be subjected to drug testing to identify compounds which ameliorate function. The ease of assays in 2D culture systems makes it feasible to use multi-well formats, test their response to various drugs and analyze a range of readouts, including VSMC contraction, proliferation, and secretome. For example, multiple iPSC lines from a hypertensive pharmacogenomics cohort were differentiated to functional VSMCs and their responses to contractile agonists and inflammatory cytokine TNF-α were analyzed (Biel et al., 2015). This work established robust high throughput assays for pharmacogenomics studies, paving the way for future studies which may incorporate the use of isogenic controls. A recent report of a model for SVAS has used an iPSC model to test the effect of different classes and combinations of drugs, finding that mTOR inhibitor everolimus was the most effective at rescuing the disease phenotype (Kinnear et al., 2020). Interestingly, they found that combination therapy using everolimus and additional classes of drugs was not beneficial. As emphasized earlier, interesting drug targets identified from large-scale screening can then be tested in a more complex and physiological set-up, possibly incorporating shear stress and co-culture systems to better

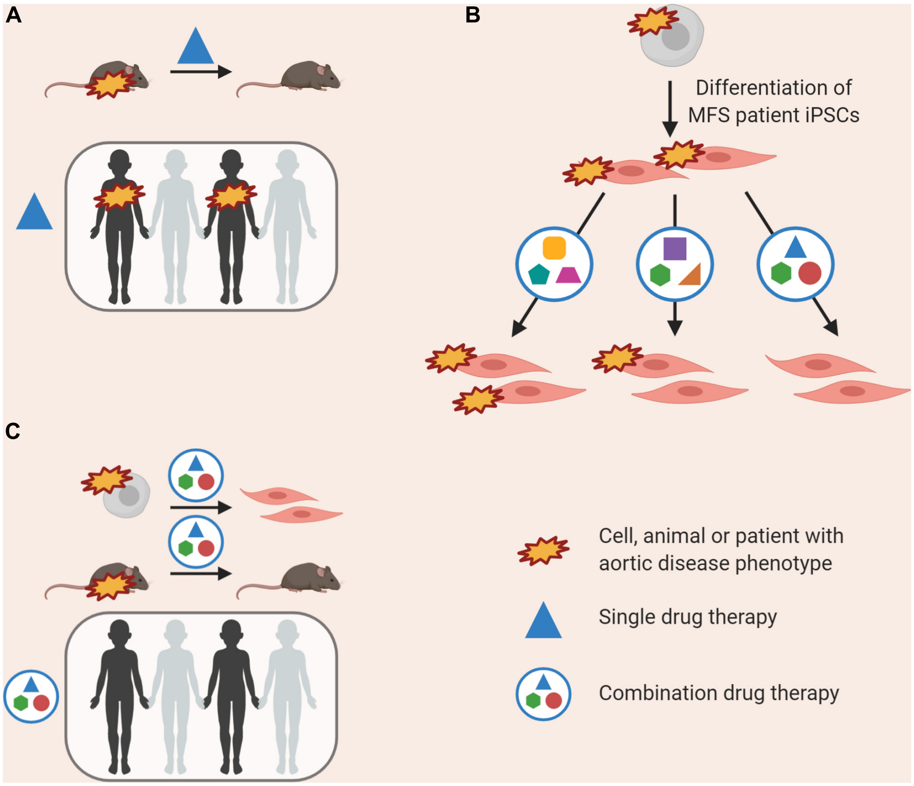

**FIGURE 4 |** Currently, successful use of a drug in animal models is the prerequisite for use in clinical trials **(A)**; this may lead to an amelioration in disease phenotype in some individuals, but not all. "Clinical-trials-in-a-dish" can be performed, where the effects of a combination of drugs at low doses is tested on patient-derived VSMCs, allowing us to target multiple de-regulated pathways **(B)**. This combination therapy could then be validated in rodent models prior to use in clinical trials, and may have an effect in more patients **(C)**.

mimic the aorta (Collado et al., 2017), preferably using lineage-specific cells where possible. Indeed, Atchison and colleagues have developed a 3D model of HGP from iPSC-derived VSMCs to test drug toxicology efficacy and dose response for various drugs (Atchison et al., 2017).

Thoracic aortic aneurysm and dissections are chronic and life-long conditions. Although establishing, characterizing, creating isogenic controls and finally differentiating new patient lines is a laborious task, drug testing and personalized medicine for diseases such as TAADs would be a worthwhile investment for the patient. With advances in automation, machine learning and refinement of existing protocols, we predict that this entire process of patient-specific drug screens and personalized medicine will be streamlined and simplified. Furthermore, developments in vascular 3D modeling to reduce costs, variability and intricacy may eventually allow for high-throughput drug screening in 3D. In addition to therapies and precision medicine, another way in which iPSC modeling could be beneficial would be to test for vascular toxicology. These sorts of studies have been performed in the cardiac field (Zhang et al., 2012; Florido et al., 2017; Sharma et al., 2017). Given that the cardiovascular complications of diseases such as MFS can be fatal, it may be worthwhile to undertake toxicology studies on additional drugs that could be detrimental to aortic health. For example, based on research focused on tendon rupture, the commonly used quinolone antibiotics are thought to cause connective tissue defects by upregulating MMP expression (Sendzik et al., 2010; Tsai et al., 2010). Their use in an animal model of TAAD (LeMaire et al., 2018) and susceptible patients (Daneman et al., 2015; Lee et al., 2015; Pasternak et al., 2018; Noman et al., 2019) is associated with a higher risk of complications and they are no longer recommended for patients with aortic disease. Both established and new drugs could be screened in iPSC models to identify those that pose risks to patients with aortopathies.

## "Clinical-Trials-in-a-Dish"

Induced pluripotent stem cell models can provide guidance for future clinical trials (**Figure 4**). In the case of the various losartan clinical trials, while some patients may have responded well to treatment with losartan, noise from non-responders would render such data non-significant despite the success in mice (**Figure 4A**). This may be due to the nature of mutation in *FBN1*, disease severity, genetic background, age of treatment or contribution from all of the above. Prior to a clinical trial, pre-screening patient-derived VSMCs to identify the pathways that are likely deregulated in the cohort, or conducting a preliminary trial *in vitro* before the full trial involving patients could be valuable (**Figure 4B**).

A multiplicity of signaling abnormalities has been found in MFS. We and others have identified that other non-canonical TGF-β signaling pathways are altered in MFS, including ERK and p38 (Carta et al., 2009; Habashi et al., 2011; Granata et al., 2017; Sato et al., 2018), and it is well-established that patient disease severity ranges widely. Other groups have identified a role for NO signaling contributing to the disease (Chung et al., 2007; Oller et al., 2017). How do we reconcile the multiple signaling abnormalities seen in this condition with disease pathophysiology? We propose that multiple pathways may be deregulated downstream of a single *FBN1* mutation and that these may also be deregulated to different extents. Using iPSC-derived VSMCs, “clinical-trials-in-a-dish” involving multiple drugs at tolerable, clinically-relevant concentrations can be employed before introducing the best combination in clinical trials (**Figure 4C**).

## CONCLUSION

There is no doubt that iPSCs and the ability to generate human disease models offer a powerful new weapon in our armamentarium against thoracic aortic diseases. In this review we have presented the current state-of-the-art and highlighted how this technology is being used to tackle critical questions in the field. A key strength of iPSC-based disease modeling is its link to individual patients, which encapsulates genetic variants or mutations in the context of a disease-susceptible genetic background. Rapid developments in differentiation protocols, including the ability to generate lineage specific VSMCs, have facilitated robust *in vitro* models. Together with ease of genetic modification, these models allow us to increasingly clearly delineate pathological mechanisms and carry out drug screening to develop much-needed new therapies for aortic disease.

We have tried in this review to offer our personal insights into the details and nuances of establishing iPSC-based *in vitro* disease models of aortopathies. We have also highlighted the challenges and limitations of such an approach, such as limited cell types and lack of 3D structure and blood flow, where appropriate. Despite the challenges, we are excited by the scientific and therapeutic opportunities presented by these model systems and particularly for future developments such as deeper genotype–phenotype analyses, vascular toxicology studies, “clinical trials-in-a-dish,” and precision medicine – potentially enabling better tailoring of therapy to individuals.

## AUTHOR CONTRIBUTIONS

HD, DS, and SS: writing, reviewing, and editing of manuscript. All authors contributed to the article and approved the submitted version.

## FUNDING

This work was supported by BHF Program Grant RG/17/5/32936 (HD and DS) and BHF Senior Fellowship FS/18/46/33663 (SS).

## ACKNOWLEDGMENTS

We thank the Wellcome-MRC Cambridge Stem Cell Institute for core support. We thank Dr. Peter Holt for helpful comments. Figures were created using BioRender.com.

## REFERENCES

Abutaleb, N. O., and Truskey, G. A. (2020). Human iPSCs stretch to improve tissue-engineered vascular grafts. *Cell Stem Cell* 26, 136–137. doi: 10.1016/j.stem.2020.01.011

Ahmadzadeh, H., Rausch, M. K., and Humphrey, J. D. (2019). Modeling lamellar disruption within the aortic wall using a particle-based approach. *Sci. Rep.* 9:15320.

Alexander, M. R., and Owens, G. K. (2012). Epigenetic control of smooth muscle cell differentiation and phenotypic switching in vascular development and disease. *Annu. Rev. Physiol.* 74, 13–40. doi: 10.1146/annurev-physiol-012110-142315

Anagnostopoulos, C. E., Prabhakar, M. J. S., and Kittle, C. F. (1972). Aortic dissections and dissecting aneurysms. *Am. J. Cardiol.* 30, 263–273. doi: 10.1016/0002-9149(72)90070-7

Andreotti, L., Bussotti, A., Cammelli, D., di Giovine, F., Sampognaro, S., Sterrantino, G., et al. (1985). Aortic connective tissue in ageing—a biochemical study. *Angiology* 36, 872–879. doi: 10.1177/000331978503601206

Angelov, S. N., Hu, J. H., Wei, H., Airhart, N., Shi, M., and Dichek, D. A. (2017). TGF-β (transforming growth factor-β) signaling protects the thoracic and abdominal aorta from angiotensin II-induced pathology by distinct mechanisms. *Arterioscler. Thromb. Vasc. Biol.* 37, 2102–2113. doi: 10.1161/ATVBAHA.117.309401

Aoyama, T., Francke, U., Dietz, H. C., and Furthmayr, H. (1994). Quantitative differences in biosynthesis and extracellular deposition of fibrillin in cultured fibroblasts distinguish five groups of Marfan syndrome patients and suggest distinct pathogenetic mechanisms. *J. Clin. Invest.* 94, 130–137. doi: 10.1172/JCI117298

Atchison, L., Abutaleb, N. O., Snyder-Mounts, E., Gete, Y., Ladha, A., Ribar, T., et al. (2020). iPSC-Derived endothelial cells affect vascular function in a tissue-engineered blood vessel model of hutchinson-gilford progeria syndrome. *Stem Cell Rep.* 14, 325–337. doi: 10.1016/j.stemcr.2020.01.005

Atchison, L., Zhang, H., Cao, K., and Truskey, G. A. (2017). A tissue engineered blood vessel model of hutchinson-gilford progeria syndrome using human iPSC-derived smooth muscle cells. *Sci. Rep.* 7:8168.

Aubart, M., Gazal, S., Arnaud, P., Benarroch, L., Gross, M.-S., Buratti, J., et al. (2018). Association of modifiers and other genetic factors explain Marfan syndrome clinical variability. *Eur. J. Hum. Genet.* 26, 1759–1772. doi: 10.1038/s41431-018-0164-9

Ayoubi, S., Sheikh, S. P., and Eskildsen, T. V. (2017). Human induced pluripotent stemcell-derived vascular smooth muscle cells: differentiation and therapeutic potential. *Cardiovasc. Res.* 113, 1282–1293. doi: 10.1093/cvr/cvx125

Bassett, A. R. (2017). Editing the genome of hiPSC with CRISPR/Cas9: disease models. *Mamm. Genome* 28, 348–364. doi: 10.1007/s00335-017-9684-9

Bauwens, C. L., Peerani, R., Niebruegge, S., Woodhouse, K. A., Kumacheva, E., Husain, M., et al. (2008). Control of human embryonic stem cell colony and aggregate size heterogeneity influences differentiation trajectories. *Stem Cells* 26, 2300–2310. doi: 10.1634/stemcells.2008-0183

Bax, D. V., Bernard, S. E., Lomas, A., Morgan, A., Humphries, J., Shuttleworth, C. A., et al. (2003). Cell adhesion to fibrillin-1 molecules and microfibrils is mediated by α5β1 and αvβ3 integrins. *J. Biol. Chem.* 278, 34605–34616. doi: 10.1074/jbc.M303159200

Baxter, M., Withey, S., Harrison, S., Segeritz, C. P., Zhang, F., Atkinson-Dell, R., et al. (2015). Phenotypic and functional analyses show stem cell-derived hepatocyte-like cells better mimic fetal rather than adult hepatocytes. *J. Hepatol.* 62, 581–589. doi: 10.1016/j.jhep.2014.10.016

Bergqvist, D., Björck, M., and Wanhainen, A. (2013). Treatment of vascular Ehlers-Danlos syndrome: a systematic review. *Ann. Surg.* 258, 257–261. doi: 10.1097/SLA.0b013e31829c7a59

Best, C., Strouse, R., Hor, K., Pepper, V., Tipton, A., Kelly, J., et al. (2018). Toward a patient-specific tissue engineered vascular graft. *J. Tissue Eng.* 9:2041731418764709. doi: 10.1177/2041731418764709

Bi, D., Nishimura, J., Niiro, N., Hirano, K., and Kanaide, H. (2005). Contractile properties of the cultured vascular smooth muscle cells. *Circ. Res.* 96, 890–897. doi: 10.1161/01.res.0000163018.66460.85

Biel, N. M., Santostefano, K. E., DiVita, B. B., El Rouby, N., Carrasquilla, S. D., Simmons, C., et al. (2015). Vascular smooth muscle cells from hypertensive patient-derived induced pluripotent stem cells to advance hypertension pharmacogenomics. *Stem Cells Transl. Med.* 4, 1380–1390. doi: 10.5966/sctm.2015-0126

Boucher, J. M., Peterson, S. M., Urs, S., Zhang, C., and Liaw, L. (2011). The miR-143/145 cluster is a novel transcriptional target of Jagged-1/Notch signaling in vascular smooth muscle cells. *J. Biol. Chem.* 286, 28312–28321. doi: 10.1074/jbc.M111.221945

Brooke, B. S., Habashi, J. P., Judge, D. P., Patel, N., Loeys, B., and Dietz, H. C. (2008). Angiotensin II blockade and aortic-root dilation in marfan's syndrome. *N. Engl. J. Med.* 358, 2787–2795. doi: 10.1056/NEJMoa0706585

Brownstein, A. J., Ziganshin, B. A., Kuivaniemi, H., Body, S. C., Bale, A. E., and Elefteriades, J. A. (2018). Genes associated with thoracic aortic aneurysm and dissection: an update and clinical implications. *Aorta* 6, 13–20. doi: 10.12945/j.aorta.2017.17.003

Bunton, T. E., Jensen Biery, N., Myers, L., Gayraud, B., Ramirez, F., and Dietz, H. C. (2001). Phenotypic alteration of vascular smooth muscle cells precedes elastolysis in a mouse model of Marfan syndrome. *Circ. Res.* 88, 37–43. doi: 10.1161/01.RES.88.1.37

Burridge, P. W., Matsa, E., Shukla, P., Lin, Z. C., Churko, J. M., Ebert, A. D., et al. (2014). Chemically defned generation of human cardiomyocytes. *Nat. Methods* 11, 855–860. doi: 10.1038/nMeth.2999

Carrabba, M., and Madeddu, P. (2018). Current strategies for the manufacture of small size tissue engineering vascular grafts. *Front. Bioeng. Biotechnol.* 6:41. doi: 10.3389/fbioe.2018.00041

Carta, L., Smaldone, S., Zilberberg, L., Loch, D., Dietz, H. C., Rifkin, D. B., et al. (2009). p38 MAPK is an early determinant of promiscuous Smad2/3 signaling in the aortas of fibrillin-1 (Fbn1)-null mice. *J. Biol. Chem.* 284, 5630–5636. doi: 10.1074/jbc.M806962200

Cattell, M. A., Hasleton, P. S., and Anderson, J. C. (1994). Glycosaminoglycan content is increased in dissecting aneurysms of human thoracic aorta. *Clin. Chim. Acta* 226, 29–46. doi: 10.1016/0009-8981(94)90100-7

Chaudhry, S. S., Cain, S. A., Morgan, A., Dallas, S. L., Shuttleworth, C. A., and Kielty, C. M. (2007). Fibrillin-1 regulates the bioavailability of TGFβ1. *J. Cell Biol.* 176, 355–367. doi: 10.1083/jcb.200608167

Chen, J., Kitchen, C. M., Streb, J. W., and Miano, J. M. (2002). Myocardin: a component of a molecular switch for smooth muscle differentiation. *J. Mol. Cell. Cardiol.* 34, 1345–1356. doi: 10.1006/jmcc.2002.2086

Cheung, C., Bernardo, A. S., Pedersen, R. A., and Sinha, S. (2014). Directed differentiation of embryonic origin-specific vascular smooth muscle subtypes from human pluripotent stem cells. *Nat. Protoc.* 9, 929–938. doi: 10.1038/nprot.2014.059

Cheung, C., Bernardo, A. S., Trotter, M. W. B., Pedersen, R. A., and Sinha, S. (2012). Generation of human vascular smooth muscle subtypes provides insight into embryological origing-dependent disease susceptibility. *Nat. Biotechnol.* 30, 165–173. doi: 10.1038/nbt.2107

Chiu, C.-Z., Wang, B.-W., and Shyu, K.-G. (2013). Effects of cyclic stretch on the molecular regulation of myocardin in rat aortic vascular smooth muscle cells. *J. Biomed. Sci.* 20:50. doi: 10.1186/1423-0127-20-50

Chooi, K. Y., Comerford, A., Sherwin, S. J., and Weinberg, P. D. (2017). Noradrenaline has opposing effects on the hydraulic conductance of arterial intima and media. *J. Biomech.* 54, 4–10. doi: 10.1016/j.jbiomech.2017.01.027

Chu, L. F., Leng, N., Zhang, J., Hou, Z., Mamott, D., Vereide, D. T., et al. (2016). Single-cell RNA-seq reveals novel regulators of human embryonic stem cell differentiation to definitive endoderm. *Genome Biol.* 17:173. doi: 10.1186/s13059-016-1033-x

Chung, A. W. Y., Au Yeung, K., Cortes, S. F., Sandor, G. G. S., Judge, D. P., Dietz, H. C., et al. (2007). Endothelial dysfunction and compromised eNOS/Akt signaling in the thoracic aorta during the progression of Marfan syndrome. *Br. J. Pharmacol.* 150, 1075–1083. doi: 10.1038/sj.bjp.0707181

Civelek, M., Ainslie, K., Garanich, J. S., and Tarbell, J. M. (2002). Smooth muscle cells contract in response to fluid flow via a Ca2+-independent signaling mechanism. *J. Appl. Physiol.* 93, 1907–1917. doi: 10.1152/japplphysiol.00988.2001

Clempus, R. E., and Griendling, K. K. (2006). Reactive oxygen species signaling in vascular smooth muscle cells. *Cardiovasc. Res.* 71, 216–225. doi: 10.1016/j.cardiores.2006.02.033

Collado, M. S., Cole, B. K., Figler, R. A., Lawson, M., Manka, D., Simmers, M. B., et al. (2017). Exposure of induced pluripotent stem cell-derived vascular endothelial and smooth muscle cells in coculture to hemodynamics induces primary vascular cell-like phenotypes. *Stem Cells Transl. Med.* 6, 1673–1683. doi: 10.1002/sctm.17-0004

Collod-Béroud, G., Le Bourdelles, S., Ades, L., Ala-Kokko, L., Booms, P., Boxer, M., et al. (2003). Update of the UMD-FBN1 mutation database and creation of an FBN1 polymorphism database. *Hum. Mutat.* 22, 199–208. doi: 10.1002/humu.10249

Conway, M. K., Gerger, M. J., Balay, E. E., O'Connell, R., Hanson, S., Daily, N. J., et al. (2015). Scalable 96-well plate based iPSC culture and production using a robotic liquid handling system. *J. Vis. Exp.* 99:e52755. doi: 10.3791/52755

Cook, J. R., Clayton, N. P., Carta, L., Galatioto, J., Chiu, E., Smaldone, S., et al. (2015). Dimorphic effects of transforming growth factor-β signaling during aortic aneurysm progression in mice suggest a combinatorial therapy for Marfan syndrome. *Arterioscler. Thromb. Vasc. Biol.* 35, 911–917. doi: 10.1161/ATVBAHA.114.305150

Cooper, J. L., Favreau, J. T., Gaudette, G. R., and Rolle, M. W. (2014). "Effects of cyclic stretch on three-dimensional vascular smooth muscle cell rings," in *Proceedings of the 2014 40th Annual Northeast Bioengineering Conference (NEBEC)*, Boston, MA, 1–2. doi: 10.1109/nebec.2014.6972762

Croissant, J. D., Kim, J. H., Eichele, G., Goering, L., Lough, J., Prywes, R., et al. (1996). Avian serum response factor expression restricted primarily to muscle cell lineages is required for α-actin gene transcription. *Dev. Biol.* 177, 250–264. doi: 10.1006/dbio.1996.0160

Dahl, S. L. M., Kypson, A. P., Lawson, J. H., Blum, J. L., Strader, J. T., Li, Y., et al. (2011). Readily available tissue-engineered vascular grafts. *Sci. Transl. Med.* 3:68ra9. doi: 10.1126/scitranslmed.3001426

Daneman, N., Lu, H., and Redelmeier, D. A. (2015). Fluoroquinolones and collagen associated severe adverse events: a longitudinal cohort study. *BMJ Open* 5:e010077. doi: 10.1136/bmjopen-2015-010077

Dash, B. C., Levi, K., Schwan, J., Luo, J., Bartulos, O., Wu, H., et al. (2016). Tissue-engineered vascular rings from human iPSC-derived smooth muscle cells. *Stem Cell Rep.* 7, 19–28. doi: 10.1016/j.stemcr.2016.05.004

De Wit, A., Vis, K., and Jeremy, R. W. (2013). Aortic stiffness in heritable aortopathies: relationship to aneurysm growth rate. *Hear. Lung Circ.* 22, 3–11. doi: 10.1016/j.hlc.2012.08.049

Denning, C., Borgdorff, V., Crutchley, J., Firth, K. S. A., George, V., Kalra, S., et al. (2016). Cardiomyocytes from human pluripotent stem cells: from laboratory curiosity to industrial biomedical platform. *Biochim. Biophys. Acta* 1863, 1728–1748. doi: 10.1016/j.bbamcr.2015.10.014

Dietz, H. C., Cutting, G. R., Pyeritz, R. E., Maslen, C. L., Sakai, L. Y., Corson, G. M., et al. (1991). Marfan syndrome caused by a recurrent de novo missense mutation in the fibrillin gene. *Nature* 352, 337–339. doi: 10.1038/352337a0

Dietz, H. C., Pyeritz, R. E., Puffenberger, E. G., Kendzior, R. J., Corson, G. M., Maslen, C. L., et al. (1992). Marfan phenotype variability in a family segregating a missense mutation in the epidermal growth factor-like motif of the Fibrillin Gene. *J. Clin. Invest.* 89, 1674–1680. doi: 10.1172/jci115766

Ding-Yang, T., Kuan-Lun, H., Jyong-Huei, L., Wei-Tien, C., and Shih-Kang, F. (2019). Abstract 595: constructing a tissue engineered blood vessel using a self-folding biodegradable hydrogel bilayer. *Arterioscler. Thromb. Vasc. Biol.* 39, A595–A595. doi: 10.1161/atvb.39.suppl_1.595

Domenga, V., Fardoux, P., Lacombe, P., Monet, M., Maciazek, J., Krebs, L. T., et al. (2004). Notch3 is required for arterial identity and maturation of vascular smooth muscle cells. *Genes Dev.* 18, 2730–2735. doi: 10.1101/gad.308904

Doyle, J. J., Doyle, A. J., Wilson, N. K., Habashi, J. P., Bedja, D., Whitworth, R. E., et al. (2015). A deleterious gene-by-environment interaction imposed by calcium channel blockers in Marfan syndrome. *eLife* 4:e08648. doi: 10.7554/eLife.08648

Drake, C. J. (2003). Embryonic and adult vasculogenesis. *Birth Defects Res. Part C Embryo Today* 69, 73–82. doi: 10.1002/bdrc.10003

Du, K. L., Ip, H. S., Li, J., Chen, M., Dandre, F., Yu, W., et al. (2003). Myocardin is a critical serum response factor cofactor in the transcriptional program regulating smooth muscle cell differentiation. *Mol. Cell. Biol.* 23, 2425–2437. doi: 10.1128/mcb.23.7.2425-2437.2003

Dubacher, N., Münger, J., Gorosabel, M. C., Crabb, J., Ksiazek, A. A., Caspar, S. M., et al. (2020). Celiprolol but not losartan improves the biomechanical integrity of the aorta in a mouse model of vascular Ehlers–Danlos syndrome. *Cardiovasc. Res.* 116, 457–465. doi: 10.1093/cvr/cvz095

Elliott, M. B., Ginn, B., Fukunishi, T., Bedja, D., Suresh, A., Chen, T., et al. (2019). Regenerative and durable small-diameter graft as an arterial conduit. *Proc. Natl. Acad. Sci. U.S.A.* 116, 12710–12719. doi: 10.1073/pnas.1905966116

Erceg, S., Laínez, S., Ronaghi, M., Stojkovic, P., Pérez-Aragó, M. A., Moreno-Manzano, V., et al. (2008). Differentiation of human embryonic stem cells to regional specific neural precursors in chemically defined medium conditions. *PLoS One* 3:e2122. doi: 10.1371/journal.pone.0002122

Faivre, L., Collod-Beroud, G., Loeys, B. L., Child, A., Binquet, C., Gautier, E., et al. (2007). Effect of mutation type and location on clinical outcome in 1,013 probands with Marfan syndrome or related phenotypes and FBN1 mutations: an international study. *Am. J. Hum. Genet.* 81, 454–466. doi: 10.1086/520125

Ferruzzi, J., Murtada, S. I., Li, G., Jiao, Y., Uman, S., Ting, M. Y. L., et al. (2016). Pharmacologically improved contractility protects against aortic dissection in mice with disrupted transforming growth factor-β signaling despite compromised extracellular matrix properties. *Arterioscler. Thromb. Vasc. Biol.* 36, 919–927. doi: 10.1161/ATVBAHA.116.307436

Fillinger, M. F., Sampson, L. N., Cronenwett, J. L., Powell, R. J., and Wagner, R. J. (1997). Coculture of endothelial cells and smooth muscle cells in bilayer and conditioned media models. *J. Surg. Res.* 67, 169–178. doi: 10.1006/jsre.1996.4978

Florido, R., Smith Karen, L., Cuomo Kimberly, K., and Russell Stuart, D. (2017). Cardiotoxicity from human epidermal growth factor receptor-2 (HER2) targeted therapies. *J. Am. Heart Assoc.* 6:e006915. doi: 10.1161/jaha.117.006915

Franken, R., Den Hartog, A. W., De Waard, V., Engele, L., Radonic, T., Lutter, R., et al. (2013). Circulating transforming growth factor-β as a prognostic biomarker in Marfan syndrome. *Int. J. Cardiol.* 168, 2441–2446. doi: 10.1016/j.ijcard.2013.03.033

Franken, R., Groenink, M., De Waard, V., Feenstra, H. M. A., Scholte, A. J., Van Den Berg, M. P., et al. (2016). Genotype impacts survival in Marfan syndrome. *Eur. Heart J.* 37, 3285–3290. doi: 10.1093/eurheartj/ehv739

Frederiksen, H. R., Holst, B., Mau-Holzmann, U. A., Freude, K., and Schmid, B. (2019). Generation of two isogenic iPSC lines with either a heterozygous or a homozygous E280A mutation in the PSEN1 gene. *Stem Cell Res.* 35:101403. doi: 10.1016/j.scr.2019.101403

Fukunishi, T., Best, C. A., Sugiura, T., Opfermann, J., Ong, C. S., Shinoka, T., et al. (2017). Preclinical study of patient-specific cell-free nanofiber tissue-engineered vascular grafts using 3-dimensional printing in a sheep model. *J. Thorac. Cardiovasc. Surg.* 153, 924–932. doi: 10.1016/j.jtcvs.2016.10.066

Gaio, N., Van Meer, B., Quirós Solano, W., Bergers, L., Van de Stolpe, A., Mummery, C., et al. (2016). Cytostretch, an organ-on-chip platform. *Micromachines* 7:120. doi: 10.3390/mi7070120

Galatioto, J., Caescu, C. I., Hansen, J., Cook, J. R., Miramontes, I., Iyengar, R., et al. (2018). Cell type-specific contributions of the angiotensin II type 1a receptor to aorta homeostasis and aneurysmal disease-brief report. *Arterioscler. Thromb. Vasc. Biol.* 38, 588–591. doi: 10.1161/ATVBAHA.117.310609

Ge, X., Ren, Y., Bartulos, O., Lee, M. Y., Yue, Z., Kim, K. Y., et al. (2012). Modeling supravalvular aortic stenosis syndrome with human induced pluripotent stem cells. *Circulation* 126, 1695–1704. doi: 10.1161/CIRCULATIONAHA.112.116996

Ghazanfari, S., Tafazzoli-Shadpour, M., and Shokrgozar, M. A. (2009). Effects of cyclic stretch on proliferation of mesenchymal stem cells and their differentiation to smooth muscle cells. *Biochem. Biophys. Res. Commun.* 388, 601–605. doi: 10.1016/j.bbrc.2009.08.072

Goldfinger, J. Z., Halperin, J. L., Marin, M. L., Stewart, A. S., Eagle, K. A., and Fuster, V. (2014). Thoracic aortic aneurysm and dissection. *J. Am. Coll. Cardiol.* 64, 1725–1739. doi: 10.1016/j.jacc.2014.08.025

Gong, J., Zhou, D., Jiang, L., Qiu, P., Milewicz, D. M., Eugene Chen, Y., et al. (2020). *In vitro* lineage-specific differentiation of vascular smooth muscle cells in response to SMAD3 deficiency. *Arterioscler. Thromb. Vasc. Biol.* 40, 1651–1663. doi: 10.1161/atvbaha.120.313033

Granata, A., Serrano, F., Bernard, W. G., McNamara, M., Low, L., Sastry, P., et al. (2017). An iPSC-derived vascular model of Marfan syndrome identifies key mediators of smooth muscle cell death. *Nat. Genet.* 49, 97–109. doi: 10.1038/ng.3723

Grewal, N., and Gittenberger-de Groot, A. C. (2018). Pathogenesis of aortic wall complications in Marfan syndrome. *Cardiovasc. Pathol.* 33, 62–69. doi: 10.1016/j.carpath.2018.01.005

Griendling, K. K., Ushio-Fukai, M., Lassègue, B., and Alexander, R. W. (1997). Angiotensin II signaling in vascular smooth muscle. *Hypertension* 29, 366–370. doi: 10.1161/01.hyp.29.1.366

Groenink, M., Den Hartog, A. W., Franken, R., Radonic, T., De Waard, V., Timmermans, J., et al. (2013). Losartan reduces aortic dilatation rate in adults with Marfan syndrome: a randomized controlled trial. *Eur. Heart J.* 34, 3491–3500. doi: 10.1093/eurheartj/eht334

Gui, L., Dash, B. C., Luo, J., Qin, L., Zhao, L., Yamamoto, K., et al. (2016). Implantable tissue-engineered blood vessels from human induced pluripotent stem cells. *Biomaterials* 102, 120–129. doi: 10.1016/j.biomaterials.2016.06.010

Guo, D. C., Pannu, H., Tran-Fadulu, V., Papke, C. L., Yu, R. K., Avidan, N., et al. (2007). Mutations in smooth muscle α-actin (ACTA2) lead to thoracic aortic aneurysms and dissections. *Nat. Genet.* 39, 1488–1493. doi: 10.1038/ng.2007.6

Guo, X. (2012). Transforming growth factor-β and smooth muscle differentiation. *World J. Biol. Chem.* 3, 41–52. doi: 10.4331/wjbc.v3.i3.41

Habashi, J. P., Doyle, J. J., Holm, T. M., Aziz, H., Schoenhoff, F., Bedja, D., et al. (2011). Angiotensin II type 2 receptor signaling attenuates aortic aneurysm in mice through ERK antagonism. *Science* 332, 361–365. doi: 10.1126/science.1192152

Habashi, J. P., Judge, D. P., Holm, T. M., Cohn, R. D., Loeys, B. L., Cooper, T. K., et al. (2006). Losartan, an AT1 antagonist, prevents aortic aneurysm in a mouse model of Marfan syndrome. *Scienc* 312, 117–121. doi: 10.1126/science.1124287

Haga, J. H., Li, Y.-S. J., and Chien, S. (2007). Molecular basis of the effects of mechanical stretch on vascular smooth muscle cells. *J. Biomech.* 40, 947–960. doi: 10.1016/j.jbiomech.2006.04.011

Halaidych, O. V., Cochrane, A., van den Hil, F. E., Mummery, C. L., and Orlova, V. V. (2019). Quantitative analysis of intracellular Ca 2+ release and contraction in hiPSC-derived vascular smooth muscle cells. *Stem Cell Rep.* 12, 647–656. doi: 10.1016/j.stemcr.2019.02.003

Han, X., Chen, H., Huang, D., Chen, H., Fei, L., Cheng, C., et al. (2018). Mapping human pluripotent stem cell differentiation pathways using high throughput single-cell RNA-sequencing. *Genome Biol.* 19:47.

Hannuksela, M., Johansson, B., and Carlberg, B. (2018). Aortic stiffness in families with inherited non-syndromic thoracic aortic disease. *Scand. Cardiovasc. J.* 52, 301–307. doi: 10.1080/14017431.2018.1546895

Harmon, A. W., and Nakano, A. (2013). Nkx2-5 lineage tracing visualizes the distribution of second heart field-derived aortic smooth muscle. *Genesis* 51, 862–869. doi: 10.1002/dvg.22721

Hasin, Y., Seldin, M., and Lusis, A. (2017). Multi-omics approaches to disease. *Genome Biol.* 18:83.

Hastings, N. E., Simmers, M. B., McDonald, O. G., Wamhoff, B. R., and Blackman, B. R. (2007). Atherosclerosis-prone hemodynamics differentially regulates endothelial and smooth muscle cell phenotypes and promotes pro-inflammatory priming. *Am. J. Physiol. Cell Physiol.* 293, 1824–1833. doi: 10.1152/ajpcell.00385.2007

He, J., Weng, Z., Wu, S. C. M., and Boheler, K. R. (2018). "Generation of induced pluripotent stem cells from patients with COL3A1 mutations and differentiation to smooth muscle cells for ECM-Surfaceome Analyses BT - The Surfaceome: methods and protocols," in *Methods in Molecular Biology*, Vol. 1722, eds K. R. Boheler and R. L. Gundry (New York, NY: Springer), 261–302. doi: 10.1007/978-1-4939-7553-2_17

Hirai, H., Yang, B., Garcia-Barrio, M. T., Rom, O., Ma, P. X., Zhang, J., et al. (2018). Direct reprogramming of fibroblasts into smooth muscle-like cells with defined transcription factors-brief report. *Arterioscler. Thromb. Vasc. Biol.* 38, 2191–2197. doi: 10.1161/ATVBAHA.118.310870

Holm, T. M., Habashi, J. P., Doyle, J. J., Bedja, D., Chen, Y., van Erp, C., et al. (2011). Noncanonical TGF-beta signaling contributes to aortic aneurysm progression in Marfan syndrome mice. *Science* 332, 332–361. doi: 10.1126/science.1192149

Hrvatin, S., O'Donnell, C. W., Deng, F., Millman, J. R., Pagliuca, F. W., DiIorio, P., et al. (2014). Differentiated human stem cells resemble fetal not adult, β cells. *Proc. Natl. Acad. Sci. U.S.A.* 111, 3038–3043. doi: 10.1073/pnas.1400709111

Hu, B. Y., Weick, J. P., Yu, J., Ma, L. X., Zhang, X. Q., Thomson, J. A., et al. (2010). Neural differentiation of human induced pluripotent stem cells follows developmental principles but with variable potency. *Proc. Natl. Acad. Sci. U.S.A.* 107, 4335–4340. doi: 10.1073/pnas.0910012107

Hu, J. H., Wei, H., Jaffe, M., Airhart, N., Du, L., Angelov, S. N., et al. (2015). Postnatal deletion of the type II transforming growth factor-β receptor in smooth muscle cells causes severe aortopathy in mice. *Arterioscler. Thromb. Vasc. Biol.* 35, 2647–2656. doi: 10.1161/ATVBAHA.115.306573

Humphrey, J. D., Schwartz, M. A., Tellides, G., and Milewicz, D. M. (2015). Role of mechanotransduction in vascular biology: focus on thoracic aortic aneurysms and dissections. *Circ. Res.* 116, 1448–1461. doi: 10.1161/CIRCRESAHA.114.304936

Ieda, M., Fu, J. D., Delgado-Olguin, P., Vedantham, V., Hayashi, Y., Bruneau, B. G., et al. (2010). Direct reprogramming of fibroblasts into functional cardiomyocytes by defined factors. *Cell* 142, 375–386. doi: 10.1016/j.cell.2010.07.002

Ikonomidis, J. S., Jones, J. A., Barbour, J. R., Stroud, R. E., Clark, L. L., Kaplan, B. S., et al. (2006). Expression of matrix metalloproteinases and endogenous inhibitors within ascending aortic aneurysms of patients with Marfan syndrome. *Circulation* 114, I–365–I–370. doi: 10.1161/CIRCULATIONAHA.105.000810

Itskovitz-Eldor, J., Schuldiner, M., Karsenti, D., Eden, A., Yanuka, O., Amit, M., et al. (2000). Differentiation of human embryonic stem cells into embryoid bodies compromising the three embryonic germ layers. *Mol. Med.* 6, 88–95. doi: 10.1007/bf03401776

Jakobsson, L., and van Meeteren, L. A. (2013). Transforming growth factor β family members in regulation of vascular function: in the light of vascular conditional knockouts. *Exp. Cell Res.* 319, 1264–1270. doi: 10.1016/j.yexcr.2013.02.015

Jeon, E. S., Moon, H. J., Lee, M. J., Song, H. Y., Kim, Y. M., Bae, Y. C., et al. (2006). Sphigosylphosphorylcholine induces differentiation of human mesenchymal stem cells into smooth-muscle-like through a TGF-β-dependent mechanism. *J. Cell Sci.* 119, 4994–5005. doi: 10.1242/jcs.03281

Jeremy, R. W., Huang, H., Hwa, J., McCarron, H., Hughes, C. F., and Richards, J. G. (1994). Relation between age, arterial distensibility, and aortic dilatation in the Marfan syndrome. *Am. J. Cardiol.* 74, 369–373. doi: 10.1016/0002-9149(94)90405-7

Jiang, X., Rowitch, D. H., Soriano, P., McMahon, A. P., and Sucov, H. M. (2000). Fate of the mammalian cardiac neural crest. *Development* 127, 1607–1616.

Jiao, J., Xiong, W., Wang, L., Yang, J., Qiu, P., Hirai, H., et al. (2016). Differentiation defect in neural crest-derived smooth muscle cells in patients with aortopathy associated with bicuspid aortic valves. *EBioMedicine* 10, 282–290. doi: 10.1016/j.ebiom.2016.06.045

Judge, D. P., Biery, N. J., Keene, D. R., Geubtner, J., Myers, L., Huso, D. L., et al. (2004). Evidence for a critical contribution of haploinsufficiency in the complex pathogenesis of Marfan syndrome. *J. Clin. Invest.* 114, 172–181. doi: 10.1172/jci20641

Jung, Y., Ji, H., Chen, Z., Fai Chan, H., Atchison, L., Klitzman, B., et al. (2015). Scaffold-free, human mesenchymal stem cell-based tissue engineered blood vessels. *Sci. Rep.* 5:15116. doi: 10.1038/srep15116

Kelaini, S., Cochrane, A., and Margariti, A. (2014). Direct reprogramming of adult cells: avoiding the pluripotent state. *Stem Cells Cloning* 7, 19–29. doi: 10.2147/SCCAA.S38006

Keller, G. (2005). Embryonic stem cell differentiation: emergence of a new era in biology and medicine. *Genes Dev.* 19, 1129–1155. doi: 10.1101/gad.1303605

Kielty, C. M., Whittaker, S. P., Grant, M. E., and Shuttleworth, C. A. (1992). Attachment of human vascular smooth muscle cells to intact microfibrillar assemblies of collagen VI and fibrillin. *J. Cell Sci.* 103, 445–451.

Kim, S., Kim, W., Lim, S., and Jeon, J. S. (2017). Vasculature-on-a-chip for in vitro disease models. *Bioengineering* 4:E8. doi: 10.3390/bioengineering4010008

Kinnear, C., Agrawal, R., Loo, C., Pahnke, A., Rodrigues, D. C., Thompson, T., et al. (2020). Everolimus rescues the phenotype of Elastin insufficiency in patient induced pluripotent stem cell-derived vascular smooth muscle cells. *Arterioscler. Thromb. Vasc. Biol.* 1325–1339. doi: 10.1161/ATVBAHA.119.313936

Kinnear, C., Chang, W. Y., Khattak, S., Hinek, A., Thompson, T., De Carvalho Rodrigues, D., et al. (2013). Modelling and rescue of the vascular phenotype of williams-beuren syndrome in patient induced pluripotent stem cells. *Stem Cells Transl. Med.* 2, 2–15. doi: 10.5966/sctm.2012-0054

Konig, G., McAllister, T. N., Dusserre, N., Garrido, S. A., Iyican, C., Marini, A., et al. (2009). Mechanical properties of completely autologous human tissue engineered blood vessels compared to human saphenous vein and mammary artery. *Biomaterials* 30, 1542–1550. doi: 10.1016/j.biomaterials.2008.11.011

Koobatian, M. T., Row, S., Smith, R. J. Jr., Koenigsknecht, C., Andreadis, S. T., and Swartz, D. D. (2016). Successful endothelialization and remodeling of a cell-free small-diameter arterial graft in a large animal model. *Biomaterials* 76, 344–358. doi: 10.1016/j.biomaterials.2015.10.020

Kumar, V. A., Brewster, L. P., Caves, J. M., and Chaikof, E. L. (2011). Tissue engineering of blood vessels: functional requirements, progress, and future challenges. *Cardiovasc. Eng. Technol.* 2, 137–148. doi: 10.1007/s13239-011-0049-3

Kusumoto, D., and Yuasa, S. (2019). The application of convolutional neural network to stem cell biology. *Inflamm. Regen.* 39, 1–7.

Kuwabara, J. T., and Tallquist, M. D. (2017). Tracking adventitial fibroblast contribution to disease: a review of current methods to identify resident fibroblasts. *Arterioscler. Thromb. Vasc. Biol.* 37, 1598–1607. doi: 10.1161/ATVBAHA.117.308199

Lacro, R. V., Dietz, H. C., Sleeper, L. A., Yetman, A. T., Bradley, T. J., Colan, S. D., et al. (2014). Atenolol versus losartan in children and young adults with Marfan's syndrome. *N. Engl. J. Med.* 371, 2061–2071. doi: 10.1056/NEJMoa1404731

Landis, B. J., Schubert, J. A., Lai, D., Jegga, A. G., Shikany, A. R., Foroud, T., et al. (2017). Exome sequencing identifies candidate genetic modifiers of syndromic and familial thoracic aortic aneurysm severity. *J. Cardiovasc. Transl. Res.* 10, 423–432. doi: 10.1007/s12265-017-9753-1

Lanfranconi, S., and Markus, H. S. (2010). COL4A1 mutations as a monogenic cause of cerebral small vessel disease: a systematic review. *Stroke* 41, 513–518. doi: 10.1161/STROKEAHA.110.581918

Lavoie, P., Robitaille, G., Agharazii, M., Ledbetter, S., Lebel, M., and Larivière, R. (2005). Neutralization of transforming growth factor-β attenuates hypertension and prevents renal injury in uremic rats. *J. Hypertens.* 23, 1895–1903. doi: 10.1097/01.hjh.0000182521.44440.c5

Lawson, J. H., Glickman, M. H., Ilzecki, M., Jakimowicz, T., Jaroszynski, A., Peden, E. K., et al. (2016). Bioengineered human acellular vessels for dialysis access in patients with end-stage renal disease: two phase 2 single-arm trials. *Lancet* 387, 2026–2034. doi: 10.1016/s0140-6736(16)00557-2

Lee, A. A., Graham, D. A., Dela Cruz, S., Ratcliffe, A., and Karlon, W. J. (2002). Fluid shear stress-induced alignment of cultured vascular smooth muscle cells. *J. Biomech. Eng.* 124, 37–43. doi: 10.1115/1.1427697

Lee, C.-C., Lee, M. G., Chen, Y.-S., Lee, S.-H., Chen, Y.-S., Chen, S.-C., et al. (2015). Risk of aortic dissection and aortic aneurysm in patients taking oral fluoroquinolone. *JAMA Intern. Med.* 175, 1839–1847. doi: 10.1001/jamainternmed.2015.5389

Lee, H. S., Yun, S. J., Ha, J. M., Jin, S. Y., Ha, H. K., Song, S. H., et al. (2019). Prostaglandin D(2) stimulates phenotypic changes in vascular smooth muscle cells. *Exp. Mol. Med.* 51:137. doi: 10.1038/s12276-019-0330-3

LeMaire, S. A., Zhang, L., Luo, W., Ren, P., Azares, A. R., Wang, Y., et al. (2018). Effect of ciprofloxacin on susceptibility to aortic dissection and rupture in mice. *JAMA Surg.* 153:e181804. doi: 10.1001/jamasurg.2018.1804

Li, W., Li, Q., Jiao, Y., Qin, L., Ali, R., Zhou, J., et al. (2014). Tgfbr2 disruption in postnatal smooth muscle impairs aortic wall homeostasis. *J. Clin. Invest.* 124, 755–767. doi: 10.1172/JCI69942

Lilly, B. (2014). We have contact: endothelial cell-smooth muscle cell interactions. *Physiology* 29, 234–241. doi: 10.1152/physiol.00047.2013

Lin, H., Qiu, X., Du, Q., Li, Q., Wang, O., Akert, L., et al. (2019). Engineered microenvironment for manufacturing human pluripotent stem cell-derived vascular smooth muscle cells. *Stem Cell Rep.* 12, 84–97. doi: 10.1016/j.stemcr.2018.11.009

Lindsay, M. E., Schepers, D., Bolar, N. A., Doyle, J. J., Gallo, E., Fert-Bober, J., et al. (2012). Loss-of-function mutations in TGFB2 cause a syndromic presentation of thoracic aortic aneurysm. *Nat. Genet.* 44, 922–927. doi: 10.1038/ng.2349

Liu, G. H., Barkho, B. Z., Ruiz, S., Diep, D., Qu, J., Yang, S. L., et al. (2011). Recapitulation of premature ageing with iPSCs from Hutchinson-Gilford progeria syndrome. *Nature* 472, 221–227. doi: 10.1038/nature09879

Liu, H., Kennard, S., and Lilly, B. (2009). NOTCH3 expression is induced in mural cells through an autoregulatory loop that requires Endothelial-expressed JAGGED1. *Circ. Res.* 104, 466–475. doi: 10.1161/CIRCRESAHA.108.184846

Lo Sardo, V., Chubukov, P., Ferguson, W., Kumar, A., Teng, E. L., Duran, M., et al. (2018). Unveiling the role of the most impactful cardiovascular risk locus through haplotype editing. *Cell* 175, P1796–1810.E20. doi: 10.1016/j.cell.2018.11.014

Lundy, S. D., Zhu, W. Z., Regnier, M., and Laflamme, M. A. (2013). Structural and functional maturation of cardiomyocytes derived from human pluripotent stem cells. *Stem Cells Dev.* 22, 1991–2002. doi: 10.1089/scd.2012.0490

Luo, J., Qin, L., Zhao, L., Gui, L., Ellis, M. W., Huang, Y., et al. (2020). Tissue-engineered vascular grafts with advanced mechanical strength from human iPSCs. *Cell Stem Cell* 26, 251–261.e8. doi: 10.1016/j.stem.2019.12.012

MacFarlane, E. G., Parker, S. J., Shin, J. Y., Ziegler, S. G., Creamer, T. J., Bagirzadeh, R., et al. (2019). Lineage-specific events underlie aortic root aneurysm pathogenesis in Loeys-Dietz syndrome. *J. Clin. Invest.* 129, 659–675. doi: 10.1172/JCI123547

Majesky, M. W. (2007). Developmental basis of vascular smooth muscle diversity. *Arterioscler. Thromb. Vasc. Biol.* 27, 1248–1258. doi: 10.1161/ATVBAHA.107.141069

Mallat, Z., Tedgui, A., and Henrion, D. (2016). Role of microvascular tone and extracellular matrix contraction in the regulation of interstitial fluid: implications for aortic dissection. *Arterioscler. Thromb. Vasc. Biol.* 36, 1742–1747. doi: 10.1161/ATVBAHA.116.307909

Manabe, I., and Owens, G. K. (2001a). CArG elements control smooth muscle subtype-specific expression of smooth muscle myosin *in vivo*. *J. Clin. Invest.* 107, 823–834. doi: 10.1172/JCI11385

Manabe, I., and Owens, G. K. (2001b). Recruitment of serum response factor and hyperacetylation of histones at smooth muscle-specific regulatory regions during differentiation of a novel P19-derived in vitro smooth muscle differentiation system. *Circ. Res.* 88, 1127–1134. doi: 10.1161/hh1101.091339

Mantella, L.-E. E., Quan, A., and Verma, S. (2015). Variability in vascular smooth muscle cell stretch-induced responses in 2D culture. *Vasc. Cell* 7:7.

Martin, K. A., Rzucidlo, E. M., Merenick, B. L., Fingar, D. C., Brown, D. J., Wagner, R. J., et al. (2004). The mTOR/p70 S6K1 pathway regulates vascular smooth muscle cell differentiation. *Am. J. Physiol. Cell Physiol.* 286, 507–517. doi: 10.1152/ajpcell.00201.2003

Martinez-Lemus, L. A., Wu, X., Wilson, E., Hill, M. A., Davis, G. E., Davis, M. J., et al. (2003). Integrins as unique receptors for vascular control. *J. Vasc. Res.* 40, 211–233. doi: 10.1159/000071886

Matsuzaki, Y., John, K., Shoji, T., and Shinoka, T. (2019). The evolution of tissue engineered vascular graft technologies: from preclinical trials to advancing patient care. *Appl. Sci.* 9:1274. doi: 10.3390/app9071274

Messana, J. M., Hwang, N. S., Coburn, J., Elisseeff, J. H., and Zhang, Z. (2008). Size of the embryoid body influences chondrogenesis of mouse embryonic stem cells. *J. Tissue Eng. Regen. Med.* 2, 499–506. doi: 10.1002/term

Mica, Y., Lee, G., Chambers, S. M., Tomishima, M. J., and Studer, L. (2013). Modeling neural crest induction, melanocyte specification, and disease-related pigmentation defects in hescs and patient-specific iPSCs. *Cell Rep.* 3, 1140–1152. doi: 10.1016/j.celrep.2013.03.025

Michel, J.-B., Jondeau, G., and Milewicz, D. M. (2018). From genetics to response to injury: vascular smooth muscle cells in aneurysms and dissections of the ascending aorta. *Cardiovasc. Res.* 114, 578–589. doi: 10.1093/cvr/cvy006

Milewicz, D. M., Dietz, H. C., and Miller, D. C. (2005). Treatment of aortic disease in patients with Marfan syndrome. *Circulation* 111, 150–157. doi: 10.1161/01.cir.0000155243.70456.f4

Milleron, O., Arnoult, F., Ropers, J., Aegerter, P., Detaint, D., Delorme, G., et al. (2015). Marfan Sartan: a randomized, double-blind, placebo-controlled trial. *Eur. Heart J.* 36, 2160–2166. doi: 10.1093/eurheartj/ehv151

Mohr, J. C., Zhang, J., Azarin, S. M., Soerens, A. G., de Pablo, J. J., Thomson, J. A., et al. (2010). The microwell control of embryoid body size in order to regulate cardiac differentiation of human embryonic stem cells. *Biomaterials* 31, 1885–1893. doi: 10.1016/j.biomaterials.2009.11.033

Mullen, M., Jin, X. Y., Child, A., Stuart, A. G., Dodd, M., Aragon-Martin, J. A., et al. (2020). Irbesartan in Marfan syndrome (AIMS): a double-blind, placebo-controlled randomised trial. *Lancet* 394, 2263–2270.

Mummery, C. L., Zhang, J., Ng, E. S., Elliott, D. A., Elefanty, A. G., and Kamp, T. J. (2012). Differentiation of human embryonic stem cells and induced pluripotent stem cells to cardiomyocytes: a methods overview. *Circ. Res.* 111, 344–358. doi: 10.1161/CIRCRESAHA.110.227512

Murdoch, J. L., Walker, B. A., Halpern, B. L., Kuzma, J. W., and McKusick, V. A. (1972). Life expectancy and causes of death in the Marfan syndrome. *N. Engl. J. Med.* 286, 804–808. doi: 10.1056/nejm197204132861502

Nakamura, T., Colbert, M. C., and Robbins, J. (2006). Neural crest cells retain multipotential characteristics in the developing valves and label the cardiac conduction system. *Circ. Res.* 98, 1547–1554. doi: 10.1161/01.RES.0000227505.19472.69

Neptune, E. R., Frischmeyer, P. A., Arking, D. E., Myers, L., Bunton, T. E., Gayraud, B., et al. (2003). Dysregulation of TGF-β activation contributes to pathogenesis in Marfan syndrome. *Nat. Genet.* 33, 407–411. doi: 10.1038/ng1116

Nishida, W., Nakamura, M., Mori, S., Takahashi, M., Ohkawa, Y., Tadokoro, S., et al. (2002). A triad of serum response factor and the GATA and NK families governs the transcription of smooth and cardiac muscle genes. *J. Biol. Chem.* 277, 7308–7317. doi: 10.1074/jbc.M111824200

Noman, A. T., Qazi, A. H., Alqasrawi, M., Ayinde, H., Tleyjeh, I. M., Lindower, P., et al. (2019). Fluoroquinolones and the risk of aortopathy: a systematic review and meta-analysis. *Int. J. Cardiol.* 274, 299–302. doi: 10.1016/j.ijcard.2018.09.067

O'Callaghan, C. J., and Williams, B. (2000). Mechanical strain-induced extracellular matrix production by human vascular smooth muscle cells: role of TGF-β1. *Hypertension* 36, 319–324. doi: 10.1161/01.HYP.36.3.319

Oishi, K., Itoh, Y., Isshiki, Y., Kai, C., Takeda, Y., Yamaura, K., et al. (2000). Agonist-induced isometric contraction of smooth muscle cell-populated collagen gel fiber. *Am. J. Physiol. Physiol.* 279, C1432–C1442. doi: 10.1152/ajpcell.2000.279.5.C1432

Oller, J., Méndez-Barbero, N., Ruiz, E. J., Villahoz, S., Renard, M., Canelas, L. I., et al. (2017). Nitric oxide mediates aortic disease in mice deficient in the metalloprotease Adamts1 and in a mouse model of Marfan syndrome. *Nat. Med.* 23, 200–212. doi: 10.1038/nm.4266

Osafune, K., Caron, L., Borowiak, M., Martinez, R. J., Fitz-Gerald, C. S., Sato, Y., et al. (2008). Marked differences in differentiation propensity among human embryonic stem cell lines. *Nat. Biotechnol.* 26, 313–315. doi: 10.1038/nbt1383

Owens, G. K. (2007). Molecular control of vascular smooth muscle cell differentiation and phenotypic plasticity. *Novartis Found. Symp.* 283, 174–191. doi: 10.1002/9780470319413.ch14

Owens, G. K., Kumar, M. S., and Wamhoff, B. R. (2004). Molecular regulation of vascular smooth muscle cell differentiation in development and disease. *Physiol. Rev.* 84, 767–801. doi: 10.1152/physrev.00041.2003

Palakkan, A. A., Nanda, J., and Ross, J. A. (2017). Pluripotent stem cells to hepatocytes, the journey so far. *Biomed. Rep.* 6, 367–373. doi: 10.3892/br.2017.867

Papadaki, M., McIntire, L. V., and Eskin, S. G. (1996). Effects of shear stress on the growth kinetics of human aortic smooth muscle cells *in vitro*. *Biotechnol. Bioeng.* 50, 555–561. doi: 10.1002/(sici)1097-0290(19960605)50:5<555::aid-bit10>3.0.co;2-i

Paquet, D., Kwart, D., Chen, A., Sproul, A., Jacob, S., Teo, S., et al. (2016). Efficient introduction of specific homozygous and heterozygous mutations using CRISPR/Cas9. *Nature* 533, 125–129. doi: 10.1038/nature17664

Park, J. S., Chu, J. S. F., Cheng, C., Chen, F., Chen, D., and Li, S. (2004). Differential effects of equiaxial and uniaxial strain on mesenchymal stem cells. *Biotechnol. Bioeng.* 88, 359–368. doi: 10.1002/bit.20250

Pashneh-Tala, S., MacNeil, S., and Claeyssens, F. (2016). The tissue-engineered vascular graft-past, present, and future. *Tissue Eng. Part B. Rev.* 22, 68–100. doi: 10.1089/ten.teb.2015.0100

Pasternak, B., Inghammar, M., and Svanström, H. (2018). Fluoroquinolone use and risk of aortic aneurysm and dissection: nationwide cohort study. *BMJ* 360:k678. doi: 10.1136/bmj.k678

Patel-Hett, S., and D'Amore, P. A. (2011). Signal transduction in vasculogenesis and developmental angiogenesis. *Int. J. Dev. Biol.* 55, 353–363. doi: 10.1387/ijdb.103213sp

Patsch, C., Challet-Meylan, L., Thoma, E. C., Urich, E., Heckel, T., O'Sullivan, J. F., et al. (2015). Generation of vascular endothelial and smooth muscle cells from human pluripotent stem cells. *Nat. Cell Biol.* 17, 994–1003. doi: 10.1038/ncb3205

Paull, D., Sevilla, A., Zhou, H., Hahn, A. K., Kim, H., Napolitano, C., et al. (2015). Automated, high-throughput derivation, characterization and differentiation of induced pluripotent stem cells. *Nat. Methods* 12, 885–892. doi: 10.1038/nmeth.3507

Pawlowski, M., Ortmann, D., Bertero, A., Tavares, J. M., Pedersen, R. A., Vallier, L., et al. (2017). Inducible and deterministic forward programming of human pluripotent stem cells into neurons, skeletal myocytes, and oligodendrocytes. *Stem Cell Rep.* 8, 803–812. doi: 10.1016/j.stemcr.2017.02.016

Pepin, M., Schwarze, U., Superti-Furga, A., and Byers, P. H. (2000). Clinical and genetic features of ehlers-danlos syndrome type IV, the vascular type. *N. Engl. J. Med.* 342, 673–680. doi: 10.1056/nejm200003093421001

Pereira, L., Lee, S. Y., Gayraud, B., Andrikopoulos, K., Shapiro, S. D., Bunton, T., et al. (1999). Pathogenetic sequence for aneurysm revealed in mice underexpressing fibrillin-1. *Proc. Natl. Acad. Sci. U.S.A.* 96, 3819–3823. doi: 10.1073/pnas.96.7.3819

Pinard, A., Jones, G. T., and Milewicz, D. M. (2019). Genetics of thoracic and abdominal aortic diseases. *Circ. Res.* 124, 588–606. doi: 10.1161/CIRCRESAHA.118.312436

Popp, B., Krumbiegel, M., Grosch, J., Sommer, A., Uebe, S., Kohl, Z., et al. (2018). Need for high-resolution Genetic Analysis in iPSC: results and lessons from the ForIPS consortium. *Sci. Rep.* 8:17201.

Pyeritz, R. E., and KcKusick, V. A. (1979). The Marfan Syndrome: diagnosis and Management. *N. Engl. J. Med.* 300, 772–777. doi: 10.1056/NEJM197904053001406

Qiu, J., Zheng, Y., Hu, J., Liao, D., Gregersen, H., Deng, X., et al. (2013). Biomechanical regulation of vascular smooth muscle cell functions: from in vitro to *in vivo* understanding. *J. R. Soc. Interface* 11:20130852. doi: 10.1098/rsif.2013.0852

Quarto, N., Leonard, B., Li, S., Marchand, M., Anderson, E., Behr, B., et al. (2012a). Skeletogenic phenotype of human Marfan embryonic stem cells faithfully phenocopied by patient-specific induced-pluripotent stem cells. *Proc. Natl. Acad. Sci. U.S.A.* 109, 215–220. doi: 10.1073/pnas.1113442109

Quarto, N., Li, S., Renda, A., and Longaker, M. T. (2012b). Exogenous activation of BMP-2 signaling overcomes TGFβ-mediated inhibition of osteogenesis in marfan embryonic stem cells and marfan patient-specific induced pluripotent stem cells. *Stem Cells* 30, 2709–2719. doi: 10.1002/stem.1250

Raphel, L., Talasila, A., Cheung, C., and Sinha, S. (2012). Myocardin overexpression is sufficient for promoting the development of a mature smooth muscle cell-like phenotype from human embryonic stem cells. *PLoS One* 7:e44052. doi: 10.1371/journal.pone.0044052

Rodríguez-Vita, J., Sánchez-López, E., Esteban, V., Rupérez, M., Egido, J., and Ruiz-Ortega, M. (2005). Angiotensin II activates the Smad pathway in vascular smooth muscle cells by a transforming growth factor-β-independent mechanism. *Circulation* 111, 2509–2517. doi: 10.1161/01.CIR.0000165133.84978.E2

Rossi, A., Gabbrielli, E., Villano, M., Messina, M., Ferrara, F., and Weber, E. (2010). Human microvascular lymphatic and blood endothelial cells produce fibrillin: deposition patterns and quantitative analysis. *J. Anat.* 217, 705–714. doi: 10.1111/j.1469-7580.2010.01306.x

Rovner, A. S., Murphy, R. A., and Owens, G. K. (1986). Expression of smooth muscle and nonmuscle myosin heavy chains in cultured vascular smooth muscle cells. *J. Biol. Chem.* 261, 14740–14745.

Row, S., Santandreu, A., Swartz, D. D., and Andreadis, S. T. (2017). Cell-free vascular grafts: recent developments and clinical potential. *Technology* 5, 13–20. doi: 10.1142/S2339547817400015

Sachlos, E., and Auguste, D. T. (2008). Embryoid body morphology influences diffusive transport of inductive biochemicals: a strategy for stem cell differentiation. *Biomaterials* 29, 4471–4480. doi: 10.1016/j.biomaterials.2008.08.012

Sato, T., Arakawa, M., Tashima, Y., Tsuboi, E., Burdon, G., Trojan, J., et al. (2018). Statins reduce thoracic aortic aneurysm growth in marfan syndrome mice via inhibition of the ras-induced ERK (Extracellular signal-regulated kinase) signaling pathway. *J. Am. Heart Assoc.* 7:e008543. doi: 10.1161/JAHA.118.008543

Sawada, H., Rateri, D. L., Moorleghen, J. J., Majesky, M. W., and Daugherty, A. (2017). Smooth muscle cells derived from second heart field and cardiac neural crest reside in spatially distinct domains in the media of the ascending aorta - brief report. *Arterioscler. Thromb. Vasc. Biol.* 37, 1722–1726. doi: 10.1161/ATVBAHA.117.309599

Schrijver, I., Liu, W., Brenn, T., Furthmayr, H., and Francke, U. (1999). Cysteine substitutions in epidermal growth factor-like domains of fibrillin-1: distinct effects on biochemical and clinical phenotypes. *Am. J. Hum. Genet.* 65, 1007–1020. doi: 10.1086/302582

Schrijver, I., Liu, W., Odom, R., Brenn, T., Oefner, P., Furthmayr, H., et al. (2002). Premature termination mutations in FBN1: distinct effects on differential allelic expression and on protein and clinical phenotypes. *Am. J. Hum. Genet.* 71, 223–237. doi: 10.1086/341581

Segura, A. M., Luna, R. E., Horiba, K., Stetler-Stevenson, W. G., McAllister, H. A., Willerson, J. T., et al. (1998). Immunohistochemistry of matrix metalloproteinases and their inhibitors in thoracic aortic aneurysms and aortic valves of patients with Marfan's syndrome. *Circulation* 98, II331–II337.

Sendzik, J., Shakibaei, M., Schäfer-Korting, M., Lode, H., and Stahlmann, R. (2010). Synergistic effects of dexamethasone and quinolones on human-derived tendon cells. *Int. J. Antimicrob. Agents* 35, 366–374. doi: 10.1016/j.ijantimicag.2009.10.009

Serrano, F., Bernard, W. G., Granata, A., Iyer, D., Steventon, B., Kim, M., et al. (2019). A novel human pluripotent stem cell-derived neural crest model of treacher collins syndrome shows defects in cell death and migration. *Stem Cells Dev.* 28, 81–100. doi: 10.1089/scd.2017.0234

Sharma, A., Burridge, P. W., McKeithan, W. L., Serrano, R., Shukla, P., Sayed, N., et al. (2017). High-throughput screening of tyrosine kinase inhibitor cardiotoxicity with human induced pluripotent stem cells. *Sci. Transl. Med.* 9:eaaf2584. doi: 10.1126/scitranslmed.aaf2584

Shi, Z. D., Abraham, G., and Tarbell, J. M. (2010). Shear stress modulation of smooth muscle cell marker genes in 2-D and 3-D depends on mechanotransduction by heparan sulfate Proteoglycans and ERK1/2. *PLoS One* 5:e12196. doi: 10.1371/journal.pone.0012196

Shi, Z.-D., and Tarbell, J. M. (2011). Fluid flow mechanotransduction in vascular smooth muscle cells and fibroblasts. *Ann. Biomed. Eng.* 39, 1608–1619. doi: 10.1007/s10439-011-0309-2

Sinha, S., Wamhoff, B. R., Hoofnagle, M. H., Thomas, J., Neppl, R. L., Deering, T., et al. (2006). Assessment of contractility of purified smooth muscle cells derived from embryonic stem cells. *Stem Cells* 24, 1678–1688. doi: 10.1634/stemcells.2006-0002

Skovrind, I., Harvald, E. B., Juul Belling, H., Jørgensen, C. D., Lindholt, J. S., and Andersen, D. C. (2019). Concise review: patency of small-diameter tissue-engineered vascular grafts: a meta-analysis of preclinical trials. *Stem Cells Transl. Med.* 8, 671–680. doi: 10.1002/sctm.18-0287

Solan, A., Dahl, S. L. M., and Niklason, L. E. (2009). Effects of mechanical stretch on collagen and cross-linking in engineered blood vessels. *Cell Transplant.* 18, 915–921. doi: 10.3727/096368909x471161

Song, H. H. G., Rumma, R. T., Ozaki, C. K., Edelman, E. R., and Chen, C. S. (2018). Vascular tissue engineering: progress, challenges, and clinical promise. *Cell Stem Cell* 22, 340–354. doi: 10.1016/j.stem.2018.02.009

Song, J., Rolfe, B. E., Hayward, I. P., Campbell, G. R., and Campbell, J. H. (2001). Reorganization of structural proteins in vascular smooth muscle cells grown in collagen gel and basement membrane matrices (Matrigel): a comparison with their in situ counterparts. *J. Struct. Biol.* 133, 43–54. doi: 10.1006/jsbi.2001.4327

Stenzel, D., Nye, E., Nisancioglu, M., Adams, R. H., Yamaguchi, Y., and Gerhardt, H. (2009). Peripheral mural cell recruitment requires cell-autonomous heparan sulfate. *Blood* 114, 915–924. doi: 10.1182/blood-2008-10-186239

Suchorska, W. M., Augustyniak, E., Richter, M., and Trzeciak, T. (2017). Comparison of four protocols to generate chondrocyte-like cells from human induced pluripotent stem cells (hiPSCs). *Stem Cell Rev. Rep.* 13, 299–308. doi: 10.1007/s12015-016-9708-y

Sugiura, T., Matsumura, G., Miyamoto, S., Miyachi, H., Breuer, C. K., and Shinoka, T. (2018). Tissue-engineered vascular grafts in children with congenital heart disease: intermediate term follow-up. *Semin. Thorac. Cardiovasc. Surg.* 30, 175–179. doi: 10.1053/j.semtcvs.2018.02.002

Sundaram, S., One, J., Siewert, J., Teodosescu, S., Zhao, L., Dimitrievska, S., et al. (2014). Tissue-engineered vascular grafts created from human induced pluripotent stem cells. *Stem Cells Transl. Med.* 3, 1535–1543. doi: 10.5966/sctm.2014-0065

Takahashi, K., and Yamanaka, S. (2006). Induction of pluripotent stem cells from mouse embryonic and adult fibroblast cultures by defined factors. *Cell* 126, 663–676. doi: 10.1016/j.cell.2006.07.024

Teixido-Tura, G., Forteza, A., Rodríguez-Palomares, J., González Mirelis, J., Gutiérrez, L., Sánchez, V., et al. (2018). Losartan versus Atenolol for prevention of aortic dilation in patients with Marfan syndrome. *J. Am. Coll. Cardiol.* 72, 1613–1618. doi: 10.1016/j.jacc.2018.07.052

Tidball, A. M., Dang, L. T., Glenn, T. W., Kilbane, E. G., Klarr, D. J., Margolis, J. L., et al. (2017). Rapid generation of human genetic loss-of-function iPSC lines by simultaneous reprogramming and gene editing. *Stem Cell Rep.* 9, 725–731. doi: 10.1016/j.stemcr.2017.07.003

Tiscornia, G., Vivas, E. L., and Belmonte, J. C. I. (2011). Diseases in a dish: modeling human genetic disorders using induced pluripotent cells. *Nat. Med.* 17, 1570–1576. doi: 10.1038/nm.2504

Topouzis, S., and Majesky, M. W. (1996). Smooth muscle lineage diversity in the chick embryo. Two types of aortic smooth muscle cell differ in growth and receptor-mediated transcriptional responses to transforming growth factor-β. *Dev. Biol.* 178, 430–445. doi: 10.1006/dbio.1996.0229

Touboul, T., Hannan, N. R. F., Corbineau, S., Martinez, A., Martinet, C., Branchereau, S., et al. (2010). Generation of functional hepatocytes from human embryonic stem cells under chemically defined conditions that recapitulate liver development. *Hepatology* 51, 1754–1765. doi: 10.1002/hep.23506

Touyz, R. M., and Schiffrin, E. L. (1997). Angiotensin II regulates vascular smooth muscle cell pH, contraction, and growth via tyrosine kinase–dependent signaling pathways. *Hypertension* 30, 222–229. doi: 10.1161/01.hyp.30.2.222

Trillhaase, A., Haferkamp, U., Rangnau, A., Märtens, M., Schmidt, B., Trilck, M., et al. (2018). Differentiation of human iPSCs into VSMCs and generation of VSMC-derived calcifying vascular cells. *Stem Cell Res.* 31, 62–70. doi: 10.1016/j.scr.2018.07.008

Tsai, M. C., Chen, L., Zhou, J., Tang, Z., Hsu, T. F., Wang, Y., et al. (2009). Shear stress induces synthetic-to-contractile phenotypic modulation in smooth muscle cells via peroxisome proliferator-activated receptor α/δ activations by prostacyclin released by sheared endothelial cells. *Circ. Res.* 105, 471–480. doi: 10.1161/CIRCRESAHA.109.193656

Tsai, W. C., Hsu, C. C., Chen, C. P. C., Chang, H. N., Wong, A. M. K., Lin, M. S., et al. (2010). Ciprofloxacin up-regulates tendon cells to express matrix metalloproteinase-2 with degradation of type i collagen. *J. Orthop. Res.* 29, 67–73. doi: 10.1002/jor.21196

Ueba, H., Kawakami, M., and Yaginuma, T. (1997). Shear stress as an inhibitor of vascular smooth muscle cell proliferation. *Arterioscler. Thromb. Vasc. Biol.* 17, 1512–1516. doi: 10.1161/01.atv.17.8.1512

van den Akker, J., Tuna, B. G., Pistea, A., Sleutel, A. J. J., Bakker, E. N. T. P., and van Bavel, E. (2012). Vascular smooth muscle cells remodel collagen matrices by long-distance action and anisotropic interaction. *Med. Biol. Eng. Comput.* 50, 701–715. doi: 10.1007/s11517-012-0916-6

van Meer, B. J., Krotenberg, A., Sala, L., Davis, R. P., Eschenhagen, T., Denning, C., et al. (2019). Simultaneous measurement of excitation-contraction coupling parameters identifies mechanisms underlying contractile responses of hiPSC-derived cardiomyocytes. *Nat. Commun.* 10:4325.

Volpato, V., Smith, J., Sandor, C., Ried, J. S., Baud, A., Handel, A., et al. (2018). Reproducibility of molecular phenotypes after long-term differentiation to human ipsc-derived neurons: a multi-site omics study. *Stem Cell Rep.* 11, 897–911. doi: 10.1016/j.stemcr.2018.08.013

Wallace, C. S., Strike, S. A., and Truskey, G. A. (2007). Smooth muscle cell rigidity and extracellular matrix organization influence endothelial cell spreading and adhesion formation in coculture. *Am. J. Physiol. Heart Circ. Physiol.* 293, 1978–1986. doi: 10.1152/ajpheart.00618.2007

Wang, Y., Ait-Oufella, H., Herbin, O., Bonnin, P., Ramkhelawon, B., Taleb, S., et al. (2010). TGF-β activity protects against inflammatory aortic aneurysm progression and complications in angiotensin II-infused mice. *J. Clin. Invest.* 120, 422–432. doi: 10.1172/JCI38136.422

Wanjare, M., Kuo, F., and Gerecht, S. (2013). Derivation and maturation of synthetic and contractile vascular smooth muscle cells from human pluripotent stem cells. *Cardiovasc. Res.* 97, 321–330. doi: 10.1093/cvr/cvs315

Warren, C. R., O'Sullivan, J. F., Friesen, M., Becker, C. E., Zhang, X., Liu, P., et al. (2017). Induced pluripotent stem cell differentiation enables functional validation of GWAS variants in metabolic disease. *Cell Stem Cell* 20, 547–557.e7. doi: 10.1016/j.stem.2017.01.010

Wasteson, P., Johansson, B. R., Jukkola, T., Breuer, S., Akydsurek, L. M., Partanen, J., et al. (2008). Developmental origin of smooth muscle cells in the descending aorta in mice. *Development* 135, 1823–1832. doi: 10.1242/dev.020958

Weber, E., Rossi, A., Solito, R., Sacchi, G., Agliano', M., and Gerli, R. (2002). Focal adhesion molecules expression and fibrillin deposition by lymphatic and blood vessel endothelial cells in culture. *Microvasc. Res.* 64, 47–55. doi: 10.1006/mvre.2002.2397

Wei, H., Hu, J. H., Angelov, S. N., Fox, K., Yan, J., Enstrom, R., et al. (2017). Aortopathy in a mouse model of Marfan syndrome is not mediated by altered transforming growth factor β signaling. *J. Am. Heart Assoc.* 6:e004968. doi: 10.1161/JAHA.116.004968

Weinberg, C. B., and Bell, E. (1986). A blood vessel model constructed from collagen and cultured vascular cells. *Science* 231, 397–400. doi: 10.1126/science.2934816

Whiteman, P., and Handford, P. A. (2003). Defective secretion of recombinant fragments of fibrillin-1: implications of protein misfolding for the pathogenesis of Marfan syndrome and related disorders. *Hum. Mol. Genet.* 12, 727–737. doi: 10.1093/hmg/ddg081

Williams, J. A., Loeys, B. L., Nwakanma, L. U., Dietz, H. C., Spevak, P. J., Patel, N. D., et al. (2007). Early surgical experience with loeys-dietz: a new syndrome of aggressive thoracic aortic aneurysm disease. *Ann. Thorac. Surg.* 83, S757–S763. doi: 10.1016/j.athoracsur.2006.10.091

Wise, S. G., Byrom, M. J., Waterhouse, A., Bannon, P. G., Weiss, A. S., and Ng, M. K. C. (2011). A multilayered synthetic human elastin/polycaprolactone hybrid vascular graft with tailored mechanical properties. *Acta Biomater.* 7, 295–303. doi: 10.1016/j.actbio.2010.07.022

Xie, C. Q., Zhang, J., Villacorta, L., Cui, T., Huang, H., and Chen, Y. E. (2007). A highly efficient method to differentiate smooth muscle cells from human embryonic stem cells [2]. *Arterioscler. Thromb. Vasc. Biol.* 27, 311–312. doi: 10.1161/ATVBAHA.107.154260

Xiong, W., Gong, J., Chen, Y. E., and Yang, B. (2017). Abstract 19200: a highly efficient in vitro smooth muscle cells differentiation system from human pluripotent stem cells-derived neural crest stem cells. *Circulation* 136:A19200.

Xiong, W., Meisinger, T., Knispel, R., Worth, J. M., and Baxter, B. T. (2012). MMP-2 Regulates Erk1/2 phosphorylation and aortic dilatation in Marfan syndrome. *Circ. Res.* 110, 92–101. doi: 10.1161/CIRCRESAHA.112.268268

Yeung, K. K., Bogunovic, N., Keekstra, N., Beunders, A. A. M., Pals, J., van der Kuij, K., et al. (2017). Transdifferentiation of human dermal fibroblasts to smooth muscle-like cells to study the effect of MYH11 and ACTA2 mutations in aortic aneurysms. *Hum. Mutat.* 38, 439–450. doi: 10.1002/humu.23174

Yu, K., Zheng, B., Han, M., and Wen, J. K. (2011). ATRA activates and PDGF-BB represses the SM22α promoter through KLF4 binding to, or dissociating from, its cis-DNA elements. *Cardiovasc. Res.* 90, 464–474. doi: 10.1093/cvr/cvr017

Zhang, H., Xiong, Z. M., and Cao, K. (2014). Mechanisms controlling the smooth muscle cell death in progeria via down-regulation of poly(ADP-ribose) polymerase 1. *Proc. Natl. Acad. Sci. U.S.A.* 111, E2261–E2270. doi: 10.1073/pnas.1320843111

Zhang, J., Lian, Q., Zhu, G., Zhou, F., Sui, L., Tan, C., et al. (2011). A human iPSC model of hutchinson gilford progeria reveals vascular smooth muscle and mesenchymal stem cell defects. *Cell Stem Cell* 8, 31–45. doi: 10.1016/j.stem.2010.12.002

Zhang, J., McIntosh, B. E., Wang, B., Brown, M. E., Probasco, M. D., Webster, S., et al. (2019). A human pluripotent stem cell-based screen for smooth muscle cell differentiation and maturation identifies inhibitors of Intimal hyperplasia. *Stem Cell Rep.* 12, 1269–1281. doi: 10.1016/j.stemcr.2019.04.013

Zhang, S., Liu, X., Bawa-Khalfe, T., Lu, L.-S., Lyu, Y. L., Liu, L. F., et al. (2012). Identification of the molecular basis of doxorubicin-induced cardiotoxicity. *Nat. Med.* 18, 1639–1642. doi: 10.1038/nm.2919

Zhang, Y. E. (2017). Non-Smad signaling pathways of the TGF-β family. *Cold Spring Harb. Perspect. Biol.* 9:a022129. doi: 10.1101/cshperspect.a022129

Zhu, J.-H., Chen, C.-L., Flavahan, S., Harr, J., Su, B., and Flavahan, N. A. (2011). Cyclic stretch stimulates vascular smooth muscle cell alignment by redox-dependent activation of Notch3. *Am. J. Physiol. Heart Circ. Physiol.* 300, H1770–H1780. doi: 10.1152/ajpheart.00535.2010

Zhu, L., Vranckx, R., Van Kien, P. K., Lalande, A., Boisset, N., Mathieu, F., et al. (2006). Mutations in myosin heavy chain 11 cause a syndrome associating thoracic aortic aneurysm/aortic dissection and patent ductus arteriosus. *Nat. Genet.* 38, 343–349. doi: 10.1038/ng1721

Zulliger, M. A., Rachev, A., and Stergiopulos, N. (2004). A constitutive formulation of arterial mechanics including vascular smooth muscle tone. *Am. J. Physiol. Circ. Physiol.* 287, H1335–H1343. doi: 10.1152/ajpheart.00094.2004

**Conflict of Interest:** The authors declare that the research was conducted in the absence of any commercial or financial relationships that could be construed as a potential conflict of interest.

frontiers
in Cardiovascular Medicine

REVIEW
published: 18 January 2021
doi: 10.3389/fcvm.2020.604581

# Mitochondrial Medicine: Genetic Underpinnings and Disease Modeling Using Induced Pluripotent Stem Cell Technology

*Parisa K. Kargaran*[1*†], *Diogo Mosqueira*[2*†] and *Tamas Kozicz*[3]

[1] *Department of Cardiovascular Medicine, Center for Regenerative Medicine, Mayo Clinic, Rochester, MN, United States,*
[2] *Division of Cancer & Stem Cells, Biodiscovery Institute, University of Nottingham, Nottingham, United Kingdom,*
[3] *Department of Clinical Genomics, Mayo Clinic, Rochester, MN, United States*

Mitochondrial medicine is an exciting and rapidly evolving field. While the mitochondrial genome is small and differs from the nuclear genome in that it is circular and free of histones, it has been implicated in neurodegenerative diseases, type 2 diabetes, aging and cardiovascular disorders. Currently, there is a lack of efficient treatments for mitochondrial diseases. This has promoted the need for developing an appropriate platform to investigate and target the mitochondrial genome. However, developing these therapeutics requires a model system that enables rapid and effective studying of potential candidate therapeutics. In the past decade, induced pluripotent stem cells (iPSCs) have become a promising technology for applications in basic science and clinical trials, and have the potential to be transformative for mitochondrial drug development. Engineered iPSC-derived cardiomyocytes (iPSC-CM) offer a unique tool to model mitochondrial disorders. Additionally, these cellular models enable the discovery and testing of novel therapeutics and their impact on pathogenic mtDNA variants and dysfunctional mitochondria. Herein, we review recent advances in iPSC-CM models focused on mitochondrial dysfunction often causing cardiovascular diseases. The importance of mitochondrial disease systems biology coupled with genetically encoded $NAD^+$/NADH sensors is addressed toward developing an *in vitro* translational approach to establish effective therapies.

**Keywords: human induced pluripotent stem cells, cardiomyocytes, regenerative medicine, mitochondrial disease, drug discovery, sonar sensor**

OPEN ACCESS

***Edited by:***
*Masayuki Yazawa,*
*Columbia University, United States*

***Reviewed by:***
*Yoshihiko Kakinuma,*
*Nippon Medical School, Japan*
*Joe Z. Zhang,*
*Stanford University, United States*

***Correspondence:**
*Parisa K. Kargaran*
*Kargaran.parisa@mayo.edu*
*Diogo Mosqueira*
*Diogo.Mosqueira@nottingham.ac.uk*

*†These authors have contributed equally to this work*

***Specialty section:***
*This article was submitted to Cardiovascular Biologics and Regenerative Medicine, a section of the journal Frontiers in Cardiovascular Medicine*

***Received:*** *09 September 2020*
***Accepted:*** *22 December 2020*
***Published:*** *18 January 2021*

***Citation:***
*Kargaran PK, Mosqueira D and Kozicz T (2021) Mitochondrial Medicine: Genetic Underpinnings and Disease Modeling Using Induced Pluripotent Stem Cell Technology. Front. Cardiovasc. Med. 7:604581. doi: 10.3389/fcvm.2020.604581*

## INTRODUCTION

Mitochondria are fundamental structures in eukaryotes since they play a dynamic role in cellular metabolism and are critical for ATP production. However, alterations in mitochondrial function can result in the generation of reactive oxygen species (ROS) and have been implicated in the pathogenesis of various diseases including cardiovascular disease, diabetes, cancer, and obesity (1). Thus, restoring mitochondrial dysfunction could offer a promising therapeutic approach for such prevalent diseases. This "mitochondrial medicine" requires a fundamental understanding of mitochondrial genetics, oxidative phosphorylation (OXPHOS), ion channels, mechanisms of ROS generation, and the role of mitochondria in the pathogenesis of disease.

Unlike nuclear DNA (nDNA), mitochondrial DNA (mtDNA) is present in multiple copies and is maternally inherited (2). The human mitochondrial genome is only 16.6 kb in size and contains 37 genes. 13 of the genes encode proteins of the OXPHOS complex and the remaining 24 (2 ribosomal, 22 tRNA-encoding) are used to translate proteins (2, 3). Since the discovery of mtDNA in 1963 (4), the importance of the mitochondrial genome has been greatly reinforced by numerous reports highlighting its involvement in several neuromuscular diseases (5–7). For example, mitochondrial gene deletions have been linked to myopathies and neuropathies (8) and certain mitochondrial DNA variants have been implicated in aging and senescence (8, 9).

The identification of pathogenic mtDNA variants has greatly expanded with the development of cutting-edge cell biology and next-generation sequencing techniques. Whole exome sequencing has shown that certain mitochondrial disorders are due to alterations in proteins involved in OXPHOS processes, or others needed for the assembly of these protein complexes (2, 10). While it is well documented that mitochondrial disease occurs in at least 1 in 5000 individuals, the prevalence of pathogenic mtDNA variants may be 1 in 200 as observed by umbilical cord blood screening from newborns, including the ten most common variants (11, 12). Phenotypically, mitochondrial diseases present with multisystem disorders, such as sensory organ failure, myopathies, cardiomyopathies, and neurodegeneration in the adult (13). However, their inheritance can be complex given mitochondrial variation.

Mitochondrial DNA varies in two distinct ways, which is commonly referred to as mitochondrial heterogeneity (14). There can be variation of mtDNA sequence within a single cell, termed heteroplasmy, and variation of mitochondria in different cells of the same organism. Importantly, mitochondrial heterogeneity is regulated via genetic and non-genetic (e.g., metabolic) mechanisms (14). Genetic sources of mitochondrial heterogeneity include changes in mtDNA copy number, mtDNA variants, and loss of mtDNA content mostly due to ROS (14, 15), which can impact the levels of mitochondrial RNA transcripts necessary for the respiratory output of the mitochondrion. The non-genetic mechanisms entail altered structure of electron transport chain (ETC) proteins and the mitochondrial network, disrupted composition of the mitochondrial membrane, and compromised membrane potential. These two mechanisms are inextricably linked. For example, altered transcription, a genetic mechanism of heterogeneity can impact respiratory output, a non-genetic mechanism of heterogeneity.

Interestingly, non-genetic mechanisms (e.g., metabolic state) can also impact the genetic state of a mitochondrion (including mtDNA content) when certain variants that alter mitochondrial structural or functional integrity are selectively targeted. This is possible due to the dynamic nature of the mitochondrial network, with fusion and fission events contributing to the turnover of mtDNA. Mitochondria may exhibit selective fusion and non-selective mitophagy (i.e., mitochondria that are not fused are more likely to undergo mitophagy). Reduced mitochondrial proton gradients may decrease fusion of these mitochondria and thus result in mitophagy. Therefore, if certain mtDNA variants are more likely to alter this gradient, they will be excluded by negative selection via reduced fusion and non-selective mitophagy, thereby promoting retention of variants that promote appropriate membrane potential integrity. Thus, the dynamic nature of the mitochondrial network can impact the mitochondrial genetic state (14, 16).

## MITOCHONDRIAL DISEASES CAUSED BY GENETIC DISRUPTION OF OXPHOS PROCESSES

Pathogenic mtDNA variants have been implicated in disease, as alterations in both mitochondrial and nuclear genes affect OXPHOS process of the mitochondrial respiratory chain (17). This is especially clear with variants that impact complex I (also termed NADH:ubiquinone oxidoreductase), which is the largest respiratory chain enzyme and a major contributor to mitochondrial disorders when disrupted (17). Complex I defects occur mainly due to variants in the 44 genes (both in nuclear or mitochondrial genomes) encoding subunits of the complex or proteins involved in its assembly (**Figure 1**). Examples of these can be seen in Leber hereditary optic neuropathy (LHON), Leigh syndrome and various other mitochondrial diseases. LHON is the most common mtDNA disorder and occurs as a result of homoplasmic variants in one of three genes encoding complex I subunits, m.11778G>A in NADH dehydrogenase 4 (ND4), m.3460G>A in ND1 and m.1448T>C in ND6. Leigh syndrome has also been associated with variants in genes encoding subunits of complex I (18, 19), (**Figure 1**). Secondary causes causing complex I dysfunction include variants in genes that encode proteins related to the complex's function, such as iron-sulfur cluster assembly and coenzyme Q10 synthesis (17).

Moreover, a great deal of phenotypic diversity is observed between different variants in mtDNA. For instance, the MT-ND4 variants m.11778G>A (p.Arg340His) and m.11777c>A (p.Arg340Ser) have different substitutions for the same amino acid, but are associated with LHON and Leigh syndrome, respectively (17). While in some cases the reason for this discrepancy is unclear (17), in others it may be linked with tissue-specific heteroplasmy as seen with the m.11777c>A (p.Arg340Ser) variant where heteroplasmy levels vary, with reduced variant levels in the brain compared to the skeletal muscle (20). Furthermore, similar phenotypic variation has been observed with NDUFS6 variants, whereby different variants result in a variety of phenotypes including lactic acidosis (c.344G>A), Leigh syndrome (c.3095G>A), and mitochondrial complex I deficiency (c.186+2T>A) (17, 21–23).

While over 250 distinct disease-causing variants have been identified in mtDNA (24), the most common point mutation

---

**Abbreviations:** iPSCs, induced pluripotent stem cells; CMs, Cardiomyocytes; iPSC-CM, induced pluripotent stem cell-derived cardiomyocyte; ESCs, embryonic stem cells; mtDNA, mitochondrial DNA; nDNA, nuclear DNA; MELAS, Mitochondrial encephalomyopathy, lactic acidosis, and stroke-like episodes; OXPHOS, Oxidative phosphorylation; ETC, Electron transport chain; ATP, Adenosine triphosphate; NADH, Nicotinamide adenine dinucleotide; SoNar, Sensor of NAD (H) redox.

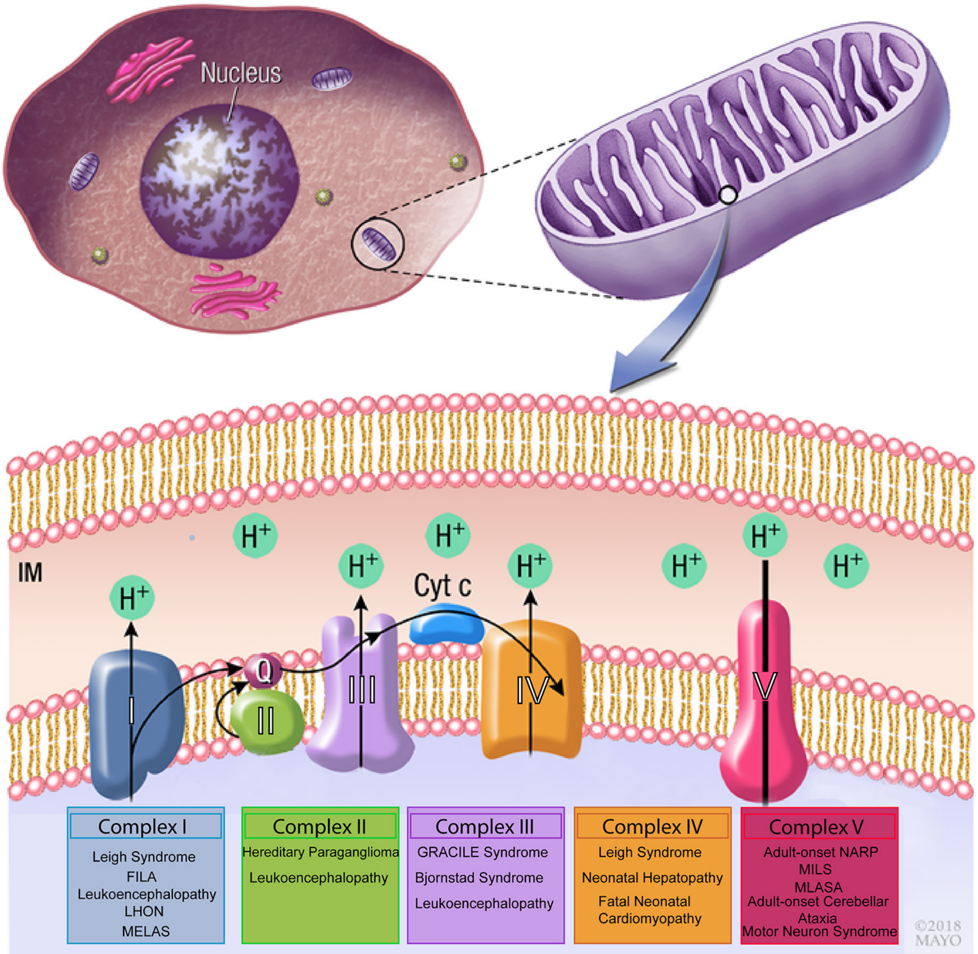

**FIGURE 1 |** Schematic drawing of the mitochondrial respiratory chain. Complex I, II, III, and IV are essential to generate a proton gradient that is utilized by the $F_0$-$F_1$-ATP synthase complex to generate ATP. Variants in mitochondrial genes involved in each of the complexes have been associated with neuromuscular disorders. FILA, Fatal infantile lactic acidosis; LHON, Leber hereditary optic neuropathy; MELAS, Mitochondrial encephalomyopathy, lactic acidosis, and stroke-like episodes; GRACILE, growth retardation, aminoaciduria, cholestasis, iron overload, lactic acidosis and early death; MILS, maternally inherited Leigh syndrome; MLASA, mitochondrial myopathy, lactic acidosis, and sideroblastic anemia.

results in an A to G transition at nucleotide 3243 in the tRNA Leu (UUR) gene with the recurrence of 16 in 100,000 people in northern Finland to a prevalence of 6.2 in 100,000 in Australia (18, 25). This variant typically exhibits high levels of heteroplasmy and causes mitochondrial encephalopathy, lactic acidosis, cardiomyopathy, and stroke-like episodes (MELAS), a multisystem disorder that primarily involves the brain, muscles and endocrine system (12, 26–28). It has also been associated with maternally inherited diabetes and deafness (MIDD) (28, 29). Other examples of common point mutations in mtDNA include A to G transition at nucleotide 8344 in tRNA Lys, which causes myoclonus epilepsy and ragged red fibers (MERRF) syndrome, along with the aforementioned T to G transversion at position 8993 in ATP6, resulting in neuropathy, ataxia, retinitis pigmentosa (NARP) and maternally inherited Leigh syndrome (MILS). All these three pathogenic variants are considered hallmarks of mitochondrial disorders that cover the range of morphological, biochemical, and clinical presentations associated with mitochondrial biology dysfunction (18).

In addition to neuromuscular disorders, mitochondrial dysfunction is associated with more common and complex pathologic conditions, including cardiac disease (30, 31), cancer (32), diabetes (33), Parkinson's disease (34), Alzheimer's disease (35), epilepsy (36), Huntington disease (37), and obesity (38, 39) (**Figure 2**). In particular, mtDNA variants and reduction in content have been widely involved in cardiac disorders (31, 40), as cardiomyocytes (CMs) have higher mtDNA copy number per diploid nuclear genome (41), given their dependence on OXPHOS to meet high energetic demands. It is therefore unsurprising that a deficiency of OXPHOS leads to mitochondrial dysfunction which can trigger cardiovascular disease (42).

Functional mitochondria are important for cardiomyocyte energy regulation, $Ca^{2+}$ homeostasis, and physiological

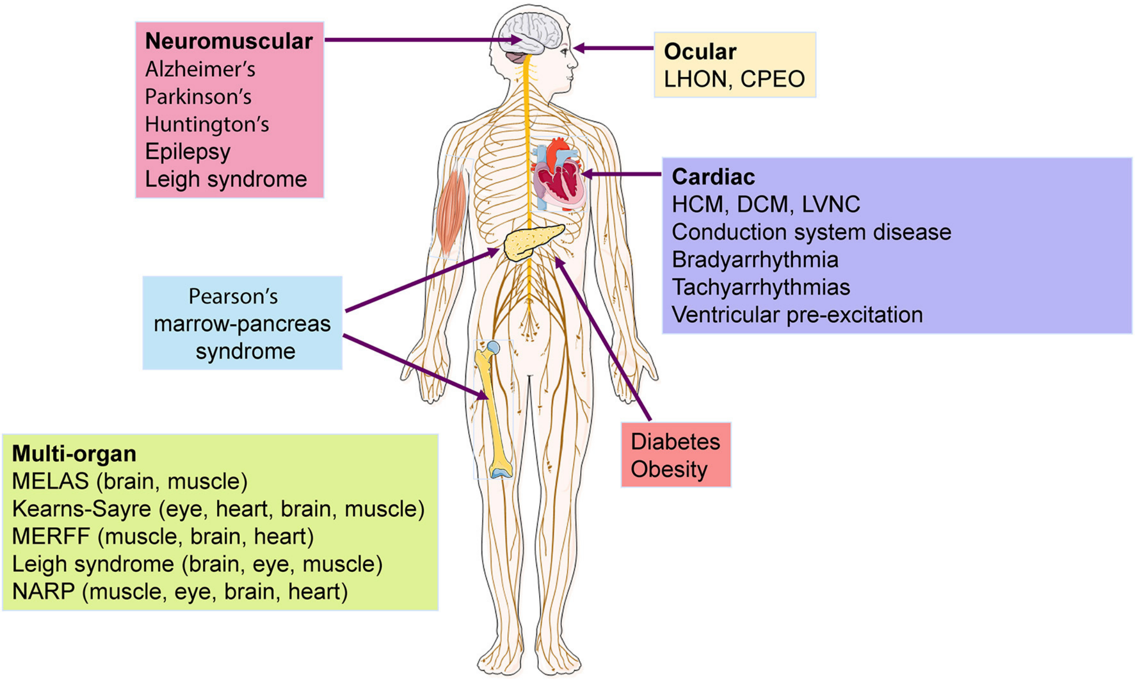

**FIGURE 2 |** Diseases and organs affected by mtDNA mutations. Several neuromuscular and cardiac disorders have been associated to mtDNA mutations, with some syndromes showing multisystemic incidence that affect mostly the brain, eye, and muscle. LHON, Leber hereditary optic neuropathy; CPEO, chronic progressive external ophthalmoplegia; HCM, hypertrophic cardiomyopathy; DCM, dilated cardiomyopathy; LVNC, left ventricular non-compaction; MELAS, mitochondrial encephalopathy, lactic acidosis, cardiomyopathy and stroke-like episodes ; MERFF, myoclonus epilepsy and ragged red fibers syndrome ; NARP, neuropathy, ataxia, retinitis pigmentosa.

inflammatory homeostasis. The role of cytosolic [$Ca^{2+}$] to activate cardiac muscle contraction and ATP production via mitochondria is well-established (43), as mitochondria maintain intracellular calcium homeostasis and match energetic demand through the mitochondrial calcium uniporter (MCU) channel. Importantly, *Mcu* knockout mice display no overt baseline phenotype and are protected against mitochondria $Ca^{2+}$ overload in an *in vivo* myocardial ischemia-reperfusion injury model, by preventing the activation of the mitochondrial permeability transition pore, decreasing infarct size, and preserving cardiac function (44). Additionally, *Mcu*$^{/}$ mice exhibit reduced contractile responsiveness to acute β-adrenergic receptor stimulation and in parallel are unable to activate mitochondrial dehydrogenases, displaying delayed matching of energy output to adrenergic or functional demand. These results support the hypothesis that MCU may be dispensable for homeostatic cardiac function but required to modulate $Ca^{2+}$- dependent metabolism during acute stress (44). Moreover, the deletion of *Mcu* greatly decreases susceptibility to mitochondrial permeability transition pore (MPTP) activation and thereby provides protection against necrotic cell death. Additional studies have revealed the relation between mitochondrial calcium content and cardiac dysfunction, suggesting a potential role for mitochondrial dysfunction in the pathophysiology of cardiac disorders, as reviewed in (45).

## DISEASE MODELING AND DRUG SCREENING OF MITOCHONDRIAL DISORDERS IMPACTING THE CARDIOVASCULAR SYSTEM

Common barriers and limitations in current drug discovery and development include the cost and low sensitivity of non-human animal models for the study of off-target toxicities (e.g., QT prolongation), and limited availability of human CMs (46). Due to genetic and physiological similarities to humans regarding the effect of mitochondrial dysfunction on post-mitotic tissues, mouse models have been extensively used to model mitochondrial disorders, being advantageous over cell lines and/or organoid cultures (47). In 1995 there were almost 50 mice strains expressing transgenes encoding mitochondrial proteins, with almost half of these being associated with mitochondrial diseases (47, 48). However, using mice as a model for mitochondrial dysfunction has considerable disadvantages as they require a high level of maintenance and do not always recapitulate human phenotypes, as shown by striking differences in muscle fiber excursion during walking, critical to model neuromuscular diseases such as Duchenne muscular dystrophy (49). Moreover, species-differences relative to human cardiac physiology include beating rate (typically slower in humans), energetics, myofilament configuration, myosin heavy chain isoform expression, presence of ion channels and electrophysiology, and $Ca^{2+}$ cycling (50). Thus, mice models may not be adequate for the early screening of a large number candidate compounds (47) to treat mitochondrial disorders.

As mtDNA variants impact preferentially in the heart, an abundant and physiologically-relevant platform to model cardiovascular diseases is needed. The clinical investigation and application of primary human CMs are further limited by donor cell availability and problematic isolation procedures (51). Given the lack of immortalized cardiomyocyte cell lines and the difficulty of obtaining appropriate animal models of advanced cardiac disease, development of new heart disease-specific therapeutics would benefit tremendously from advances in human induced pluripotent stem cell (hiPSC)-derived cardiomyocyte (CM) technologies. Importantly, these cells have overcome some of the limitations of animal models by providing a virtually infinite and physiologically-relevant source of CMs that have been extensively characterized *in vitro* in terms of molecular and functional features (52).

Molecular profiling of hiPSC differentiation into a CM lineage involves the serial activation of distinct genes that constitute the hallmark of normal cardiac development. *In vitro* differentiation initially is characterized by expression of (i) BRY and MIXL1 to form the mesoderm, (ii) MESP1, ISL1, and KDR to design cardiogenic mesoderm and (iii) NKX2.5, GATA4, TBX5, MEF2C, and HAND1/2 expressed in cardiac-specific progenitors stage (50). Finally, structural genes encoding for sarcomeric-related proteins such as MYL2, MYL7, MYH6, and TNNT2 are expressed in terminally differentiated CMs (50, 53–55). Altogether, the key goal for recapitulating cardiovascular development to boost differentiation efficiency is based on modulating signaling pathways such as Wnt, BMP, and Activin/Nodal/TGF-β (56–59). Therefore, the hiPSC-derived cardiac progenitor cells (CPCs), and CMs offer possible ways to address new drugs to market.

Moreover, a key feature of hiPSCs involves their patient-specific nature, thus providing a model system supporting personalized medicine approaches. The "patient-in-a-dish" from iPSCs approach has exhibited great potential to contribute to a better understanding of the exact pathological mechanisms of rare diseases (60). Further advances in hiPSC-CM technology have facilitated the study of pathophysiology and drug efficacy in 3D organoid environments with an expandable supply of cells from donor patients (61). This confers the benefits of using hiPSC-CMs but provides additional physiologically-relevant conditions experienced at the organ level. After screening candidate compounds using hiPSC-CM cells, *in vivo* testing can be pursued (61) on a more reduced number of drugs, thus limiting the risk and cost. This approach can address the limited applicability of mouse models for drug discovery by providing a translational system that enables screening of a large number of candidate compounds to treat mitochondrial diseases.

Overall, all of these desirable properties make pluripotent stem cell-based models a promising platform for drug testing and toxicology screening (46, 62–65). Additionally, hiPSC-CMs serve as a valuable model for pre-clinical screening of candidate anti-arrhythmic and anti-heart failure pharmacological agents, as well as studying the off–target cardiac toxicities of chemotherapeutic agents (66–68). However, there is still room for improvement of this cellular model as iPSC-derived lineages are typically immature relative to adult counterparts, and they fail to recapitulate multi-cellular organs with neurohormonal control (69). Nevertheless, there has been considerable progress in refining hiPSC-CM maturation (70), which have contributed significantly to cardiovascular research and has been applied to model several disorders. For example, hiPSC-CM have successfully modeled familial dilated cardiomyopathy (DCM) (71), catecholaminergic polymorphic ventricular tachycardia (CPVT) (72), and familial hypertrophic cardiomyopathy (HCM) (73). Thus, iPSC-CM technology greatly facilitates the study of genetic cardiovascular diseases, development of cardiovascular system, toxicological screening, drug discovery, and personalized cell-based therapy (50).

While these cardiomyopathy hiPSC-CM models focused mostly on mutations in sarcomeric genes that regulate cardiomyocyte contraction and calcium handling, a few have also showed energy depletion phenotypes due to mitochondrial dysfunction (74, 75). Importantly, hiPSC-CMs have also been harnessed to specifically model mitochondrial cardiomyopathies as these constitute phenocopies of HCM (40). Wang et al. derived a number of hiPSC lines from Barth syndrome patients showing frameshift or missense mutations in the Tafazzin (TAZ) gene (76). Human iPSC-CMs differentiated from these lines have demonstrated several disease phenotypes in comparison to healthy isogenic controls, such as reduced mitochondrial respiration activity, impaired sarcomere organization and decreased contractile stress generation in a tissue construct. These phenotypes were mechanistically linked with increased formation of ROS and immature cardiolipin.

Currently, most studies relating mutations in mtDNA to cardiovascular disorders rely on large-scale mitochondrial genetics to associate specific variants with patient cohorts exhibiting different cardiac phenotypes (31). While this approach is statistically robust, it lacks functional characterization of pathological phenotypes exhibited by cardiomyocytes *in vitro*, required to better understand disease progression and treatment. To the best of our knowledge, only one study characterized the impact of a mtDNA mutation that associated with HCM (77) in hiPSC-CMs. Li and colleagues have generated hiPSCs from HCM patients bearing the m.2336T>C mutation in the mitochondrial rRNA gene (MT-RNR2). When compared to unrelated healthy controls, diseased hiPSC-CM exhibited markedly lower levels of several mitochondrial proteins (MT-ND5, MT-CYB, MT-COX2, MT-ATP8), resulting in unstable 16S rRNA and ultrastructure defects in the mitochondria. Strikingly, these alterations led to several phenotypes characteristic of HCM, such as reduced ATP/ADP ratio and mitochondrial membrane potential as well as abnormal calcium handling (e.g., increased intracellular $Ca^{2+}$ levels). This study not only strongly supported causation of HCM by mtDNA mutations, but also overcame limitations associated with clinical studies showing varying tissue-specific heteroplasmy and susceptibilities to specific mtDNA mutations (78). Furthermore, our own studies related different *in vitro* phenotypic severities between hiPSC-CM lines bearing either the R453C-βMHC or the E99K-ACTC1 sarcomeric mutations with specific variants in mtDNA (79). This approach focused on coupling phenotypes of hiPSC-CMs with mtDNA sequencing is promising to unveil novel variants with potentially HCM-protective or aggravator function.

Remarkably, it is possible to generate iPSC-CMs clones representing a range of both healthy and diseased mtDNA for the study of mitochondrial disease. Moreover, producing independent subclones that have distinctive heteroplasmic mtDNA patterns in the context of native nuclear DNA enables deconvolution of authentic disease specific processes. For example, it has been previously demonstrated that MELAS-iPSC clones show a similar range of mtDNA heteroplasmy of the disease-causing variants as the original patient derived fibroblasts. Producing MELAS-iPSC clones with high and low levels of heteroplasmy and differentiating them along a cardiac lineage enabled direct comparison of genotype/phenotype relationships to investigate the impact of mutant mtDNA on MELAS patients (80). Additionally, our group has shown that iPSCs are capable of modeling intra- and inter-person variability stemming from different levels of heteroplasmy in mutant mtDNA between iPSC clones, including the functional consequences for mitochondrial respiration in iPSC-CMs (81). Overall, this results in a platform that be used to investigate pharmacological approaches for reducing the burden of mutant mtDNA. In addition, hiPSC-CM may also overcome the limitations of clinical mitochondrial genetic studies, where patient-derived samples are mostly collected from peripheral blood and therefore do not reflect the tissue-specific heteroplasmy showed by CMs [requiring clinically invasive procedures to harvest (78)].

Notwithstanding, hiPSC-CM technology is very recent and still needs to be further developed to become an ideal platform for the study of pharmacology, toxicology, pathogenesis, and cell-based therapy (60), although a number of methodological improvements have been published (82, 83). In particular, the investigation of mitochondrial diseases and recapitulation of mitochondrial dysfunction phenotypes will greatly benefit from metabolic maturation strategies. In fact, while the adult heart preferentially relies on fatty acid oxidation to sustain high energetic demands (84), hiPSC-CMs more closely resemble fetal heart metabolism by primarily depending on glycolysis (85). In order to bridge this gap, several hiPSC-CM maturation media were developed, consisting of supplementation with several fatty acids including palmitate, oleate and linoleic acid (86–88). Additionally, the inclusion in the media of fatty acid transporters into the mitochondria such as L-carnitine, or inhibition of lactate dehydrogenase A has further enhanced the switch from glycolysis to OXPHOS. Importantly, these different media formulations have consistently resulted in increased mitochondrial respiration capacities, mitochondrial content and cellular ATP levels, as well as functional improvement of cardiomyocyte calcium handling, ultrastructural features and contractility. Alternatively, transition from 2D monolayers to 3D aggregate cultures under agitation demonstrated changes in the transcriptome of hiPSC-CMs, leading to upregulation of genes involved in OXPHOS at the expense of glycolytic genes. These changes were reflected by lower glycolytic fluxes in 3D, accompanied by an increased TCA cycle activity, as measured by 13C-based metabolic flux analysis (89). Altogether, metabolic maturation strategies have effectively surpassed initial limitations associated with fetal-like metabolism of hiPSC-CMs.

Overall, this new technology will greatly complement current cell and animal models, and holds great promise in providing insight into the drug discovery, with new tools including biosensor photoproteins (90) and a strong predictive advantage for moving compounds into clinical practice (91).

## MITOCHONDRIAL MAINTENANCE AND NICOTINAMIDE ADENINE DINUCLEOTIDE ($NAD^+$) LEVELS

NADH, along with its oxidized form $NAD^+$, are fundamental cofactors in energy metabolism. $NAD^+$ in eukaryotic and prokaryotic cells is primarily synthesized from tryptophan or through the salvage pathway, which uses nicotinic acid and nicotinamide as precursors (92, 93). Since mitochondrial membranes have shown impermeability to $NAD^+$ and NADP, two major pools of $NAD^+$ and NADP in cells have been found, in the cytoplasm and mitochondria (94, 95). The cytosolic $NAD^+$/NADH redox cycling and homeostasis are maintained by transporting the cytosolic NADH into the mitochondria through the malate aspartate shuttle or the glycerol phosphate shuttle (96). Previous studies have reported that the total intracellular $NAD^+$: NADH ratio is about $3–10^4$. However, the ratio of the free $NAD^+$/NADH form is a more reliable indicator of cellular redox potential compared to the ratio of total $NAD^+$/NADH (97). Under the physiological conditions in typical eukaryotes, the cytosolic free $NAD^+$/NADH ratio is about 60–700 (98–100), while the ratio of mitochondrial $NAD^+$/NADH is between 4 and 10 (97, 98, 101). For example, in a mouse model of transverse aortic constriction (a model of pressure overload) the $NAD^+$/NADH ratio is around 2.75 (102). Investigation of cellular metabolism associated with $NAD^+$/NADH redox state is essential in both healthy and disease circumstances.

It has been well-established that increased levels of $NAD^+$ and sirtuin activation play a critical role in regulating mitochondrial homeostasis and lifespan (103). Sirtuins are a family of deacetylases that use $NAD^+$ as a cofactor and mediate mitochondrial homeostasis. For example, activation of SIRT1 and subsequent deacetylation and activation of peroxisome proliferator-activated receptor gamma coactivator-1alpha (PGC-1α), a coactivator of mitochondrial biogenesis, promotes increased ATP production. SIRT1 also activates forkhead box protein O1 (FOXO1) which increases fatty acid oxidation. Additionally, activation of SIRT3, a mitochondrial sirtuin, promotes fatty acid oxidation and is protective against reactive oxygen species. Given the role of NADH in oxidoreductive reactions of glycolysis, the Krebs cycle, fatty acid oxidation, and oxidative phosphorylation, alterations in NADH/$NAD^+$ can have broad metabolic effects (104, 105). In fact, a decreased $NAD^+$/NADH ratio is strongly associated with mitochondrial and age-related disorders including cancer, obesity, neurodegeneration, and diabetes (106–109). The level of $NAD^+$ decreases with age in multiple models including worms and rodents as well as human tissue

(107, 110–112). Research demonstrated that increasing the level of NAD$^+$ leads to NAD$^+$/sirtuin pathway activation and subsequent effects on multiple metabolic pathways. For example, treating the cytochrome *c* oxidase (COX) deficiency indicative of mitochondrial disorder with the AMPK agonist 5-aminoimidazole-4-carboxamide ribonucleotide (AICAR) partially rescued mitochondrial dysfunction and improved motor outcomes (113). Thus, regulation of mitochondrial metabolism via evolutionarily conserved NAD$^+$/sirtuin pathways presents a novel target for clinical trials.

Recent evidence suggests that NAD$^+$ and PARP inhibitors could be used to boost NAD$^+$ levels in cell culture and animal models (107). Moreover, additional work has shown that, in *Caenorhabditis elegans* and mice, α-amino-β-carboxymuconate-ε-semialdehyde decarboxylase (ACMSD) controls cellular NAD$^+$ levels. ACMSD is an enzyme that plays a role in *de novo* NAD$^+$ synthesis pathways by limiting spontaneous cyclization of α-amino-β-carboxymuconate-ε-semialdehyde. Interestingly, not only genetic inhibition of ACMSD but also the pharmacological inhibition of ACMSD increases *de novo* NAD$^+$ synthesis and sirtuin 1 activity (103), resulting in enhancement of mitochondrial function (103). Moreover, in addition to aging, an altered NAD$^+$/NADH ratio is observed in cardiac disease. Specifically, a decreased utilization of NADH may result in a reduced NAD$^+$/NADH ratio observed in failing hearts suggesting an inability to maintain NADH production due to mitochondrial dysfunction (12, 13, 114, 115). Both pharmacological and genetic attempts to increase NAD$^+$ levels and subsequently the NAD$^+$/NADH ratio have resulted in improved cardiac function in mouse models of heart failure (13, 115–117).

In 1924, Otto Warburg proposed that the energy in cancer cells is produced by a shift from oxidative phosphorylation to aerobic glycolysis (118), dramatically increasing the biosynthesis of macromolecules for rapid cell proliferation (32, 119, 120). Classical biochemical techniques including chromatography, mass spectrometry, enzymatic cycling assays, and nuclear magnetic response spectroscopy are not applicable methods for performing quantitative, high-throughput screening in real-time. As the NAD$^+$/NADH ratio plays a central role in all aspects of cellular metabolism, real time tracking of this metabolic state in living cells needs to be developed. Previous techniques relied upon the weak endogenous fluorescence of NADH, examined by single-proton or multiphoton excitation for measuring metabolic states of mitochondria (96, 97, 121, 122). However, these methods are plagued by innate disadvantages, including limited sensitivity and resultant cellular injury associated with ultraviolet irradiation (123). Because most of the NADPH fluorescence derives from the mitochondria, it is often challenging to identify and separate the bright mitochondrial signals from those emanating from the cytosol. Moreover, it is difficult to distinguish NADPH from NADH, as they are spectrally identical. Recently developed technology employing fluorescence lifetime imaging can quantitatively differentiate between the two cofactors based on the fact that bound NADH and bound NADPH acquires different fluorescence lifetimes inside the cell (123). Nevertheless, usage of fluorescence lifetime imaging is neither technically simple nor broadly applicable as it requires the separation of NADH and NADPH redox signaling without disrupting the samples on the addition of external probes.

Enzymatic cycling assays, chromatography and mass spectrometry are a few of the conventional methods that are often used to measure the intracellular NAD$^+$/NADH redox state (97). Additional limitations of these techniques involve the time required to conduct the assays, and their incompatibility with the study of spatiotemporal dynamics in single, intact cells, thereby making them unsuitable for quantitative, real-time high-throughput screening in living cells (97, 124, 125). To overcome the challenges of NAD$^+$/NADH dynamics analysis with subcellular resolution *in vivo*, we propose a new technology using a genetically encoded fluorescent sensor based on fluorescent proteins (FPs) with the ability to analyze NAD$^+$/NADH dynamics with subcellular resolution.

## LIVE MONITORING OF NAD$^+$/NADH REDOX STATE IN REAL TIME BY GENETICALLY ENCODED SENSOR TECHNOLOGY

Due to the limitations of conventional methods explored above, genetically encoded fluorescent sensors may present

**TABLE 1 |** SoNar has some key advantages for live cell monitoring of NAD$^+$/NADH compared to Frex and Peredox-mCherry.

| | Highlights | Limitations | Detected Signal |
|---|---|---|---|
| **Peredox-mCherry** | Modest brightness in cells<br>Aggregates in cytosol | Low dynamic range<br>Large gene<br>Not validated *in vivo* | NAD$^+$/NADH ratio* |
| **Frex** | Does not aggregate in cells<br>Moderate dynamic range | Minimal brightness in cells<br>Large gene | NADH |
| **SoNar** | High brightness in cells<br>High dynamic range<br>Small gene<br>Does not aggregate in cells<br>Validated *in vivo* | pH sensitive at 485 nm | NAD$^+$/NADH ratio |

**However, it is impacted by absolute NAD(H) levels.*

an adequate alternative for live monitoring of NAD$^+$/NADH redox state, supporting rapid and efficient metabolic chemical screening. Developing these sensors involves single-cell, real-time monitoring of multiple metabolic parameters (120). Recently, two independent groups have developed genetically encoded NADH sensors: Peredox and Frex (126, 127). In 2016, the Yang group described a second-generation genetically encoded biosensor for NAD$^+$/NADH, named Sensor of NAD (H) redox (SoNar) (128). All three sensors quantify NADH cellular levels or the NAD$^+$/NADH ratio through specific, non-covalent binding resulting in a conformational change that alters the fluorescent properties of the sensor. Since these proteins are genetically encoded and have intrinsic fluorescence without extraneous compounds, they can be easily introduced into live cells via DNA transfection and targeted to specific organelles. However, these proteins vary in their fluorescent properties. Notably, Frex and SoNar have two excitation peaks (97), enabling determination of ratiometric fluorescence. Thus, these can be used for detecting the NAD$^+$/NADH ratio given the differential effect of NAD$^+$ or NADH on the two excitation wavelengths. On the other hand, Frex can be used to detect NADH levels independent of sensor expression levels (97, 129). In contrast,

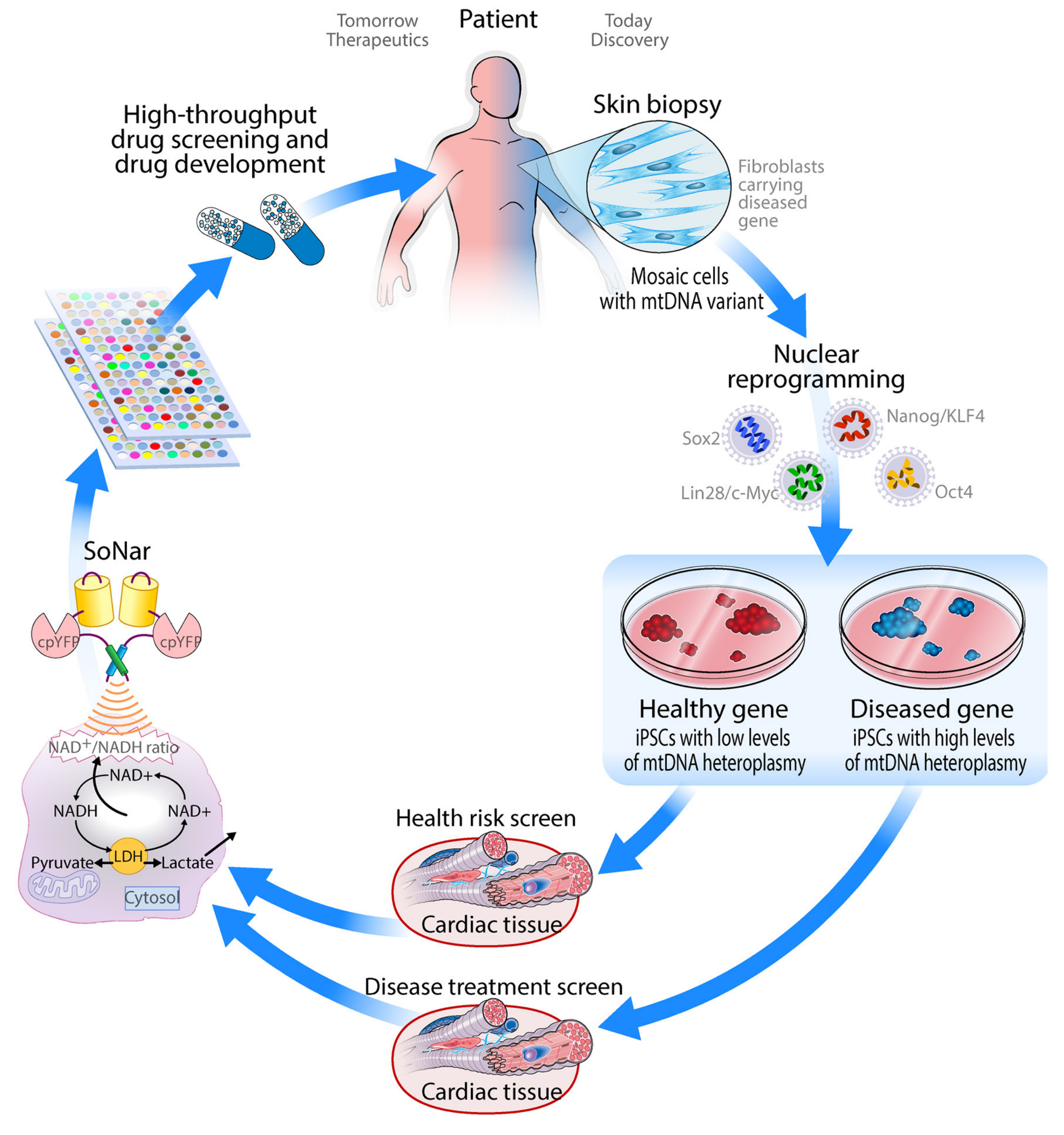

**FIGURE 3 |** Schematic drawing of how iPSC-derived cardiomyocytes can be applied as a drug screening platform for mitochondrial disorders.

Peredox must be made ratiometric by using fusing it with mCherry (97).

Compared to the first-generation sensors, SoNar provides a significant improvement for live cell $NAD^+$/NADH measurement (97) (**Table 1**). Given its shorter coding sequence, SoNar has a more intense fluorescence enabling its use for *in vivo* applications compared to Frex (128). SoNar has a wide dynamic range and high intensity fluorescence. It is rapidly responsive and thus suitable for tracking subtle changes of cellular metabolic and redox states *in vivo*. This sensor represents an improved reporter system for studying cell metabolism (130, 131) and compounds for drug discovery. In contrast to other available assays, which target a single protein or enzyme, SoNar is even capable of reporting several pathways affecting energy metabolism providing a more detailed insight into glycolysis and mitochondrial respiration (128). Previously, it was difficult to rigorously measure $NAD^+$/NADH levels in certain cancer lines. However, using SoNar, MDA-MB-468, U87, and H1299 cells, were shown to have a significantly reduced $NAD^+$/NADH cytosolic ratio (132).

However, the use of the SoNar sensor still poses a number of challenges. SoNar fluorescence may be impacted by changes in pH. While the chromophore responsible for fluorescence absorption at 420 nm is protonated and not sensitive to pH changes, the chromophore operating at 485 nm is normally deprotonated and responsive to changes in pH, which can trigger protonation and block fluorescence emission. This can be compensated by using absorption only at 420 nm, although this will impact the dynamic range of SoNar (97). Additionally, this sensor does not allow for the absolute quantification of NADH or $NAD^+$ but provides a measure of the $NAD^+$/NADH ratio, which is the key value that changes in disease state. Furthermore, the genetic construct encoding the sensor needs to be integrated into the host cell's genome, preventing its use for staining active live clinical samples (97). Nonetheless, this strategy can be harnessed to generate stable hiPSC reporter lines tracking $NAD^+$/NADH ratios that can then be differentiated into CMs to investigate metabolic cardiovascular disorders such as mitochondrial cardiomyopathies (133). This can be achieved by knocking-in the genetic construct into safe loci such as *AAVS1*, as previously demonstrated with genetically encoded calcium sensors (75). The properties of SoNar sensors, displaying high fluorescence intensity and dynamic range, are compatible with live imaging, enabling their application for high-content imaging, and/or for the measurement of overall signal intensity in a standard plate reader. Additionally, treatment with modulators of redox state in hiPSC-CMs such as hydrogen peroxide and DTT can be done to establish extremes of oxidation and reduction states of cellular $NAD^+$/NADH, respectively (134), leading to a more accurate quantification of the signal in the context of mitochondrial diseases where this ratio is disrupted (132). Moreover, these approaches can be multiplexed with existing platforms for evaluating mitochondrial respiration profiles in hiPSC-CMs such as the Seahorse assay (82), which is performed in 96-well plate format thereby facilitating high-throughput screening studies, in response to various energy sources or metabolic modulators such as perhexiline (51). This approach may also be incorporated in isogenic sets of patient-derived hiPSC lines with known mitochondrial diseases affected by mtDNA variants (79).

## CONCLUSIONS

Disruption of mitochondrial function is not only commonly observed in cardiovascular disorders but has also been proposed to underlie the pathology of disease progression (135), due to the high energetic demand of the heart and its cellular constituents. In turn, mitochondrial DNA variants have shown to cause phenocopies of cardiomyopathies (31), highlighting the close relationship between mitochondrial dysfunction and cardiovascular disease. Herein, we propose that human iPSC-derived cardiomyocytes provide a unique translational model system to advance understanding of mitochondrial pathogenic variants. These cellular models have the potential for not only investigating mitochondrial dysfunction caused by mtDNA variants (such as m.3243A>G involved in MELAS), but also as a drug screening platform for both mitochondrial and cardiovascular disorders. The genetically encoded fluorescent SoNar sensor that tracks $NAD^+$/NADH ratio provides a robust tool for quantifying the intracellular redox state and screening for small compounds that restore normal metabolic activity. Altogether, the combination of iPSC-CMs with the SoNar sensor is expected to transform the future treatment of metabolic and cardiovascular diseases by supporting the discovery of drugs treating these inextricably linked conditions (**Figure 3**). Finally, these cellular models can provide a platform for optimization of recently discovered tools to edit the mitochondrial genome (136), by offering a disease-relevant pathophysiology setting in the cardiac cell type of interest, more accurately recapitulating heart-specific heteroplasmy.

## AUTHOR CONTRIBUTIONS

PK conducted the literature search and compiled references into a cohesive draft. DM and TK carried out review, editing, and final approval of the manuscript.

## FUNDING

This work was supported by the Marriott Family Program. The authors would like to thank Dr. Frank J. Secreto and Dr. Timothy J. Nelson of the Todd and Karen Wanek Family Program for Hypoplastic Left Heart Syndrome at Mayo Clinic for valuable feedback and advice. DM was supported by National Center for the Replacement, Refinement, and Reduction of Animals in Research (NC3Rs: NC/S001808/1).

# REFERENCES

1. Koopman WJ, Willems PH, Smeitink JA. Monogenic mitochondrial disorders. *N Engl J Med.* (2012) 366:1132–41. doi: 10.1056/NEJMra1012478
2. Area-Gomez E, Schon EA. Mitochondrial genetics and disease. *J. Child Neurol.* (2014) 29:1208–15. doi: 10.1177/0883073814539561
3. Anderson S, Bankier AT, Barrell BG, de Bruijn MH, Coulson AR, Drouin J, et al. Sequence and organization of the human mitochondrial genome. *Nature.* (1981) 290:457–65. doi: 10.1038/290457a0
4. Nass S, Nass MMK. Intramitochondrial fibers with DNA characteristics. *IEnzymatic Other Hydrolytic Treatments.* (1963) 19:613–29. doi: 10.1083/jcb.19.3.613
5. Ephrussi B, Slonimski P. Yeast mitochondria: subcellular units involved in the synthesis of respiratory enzymes in yeast. *Nature.* (1955) 176:1207–8. doi: 10.1038/1761207b0
6. Wallace D, Singh G, Lott M, Hodge J, Schurr T, Lezza A, et al. Mitochondrial DNA mutation associated with Leber's hereditary optic neuropathy. *Science.* (1988) 242:1427–30. doi: 10.1126/science.3201231
7. Picard M, Wallace DC, Burelle Y. The rise of mitochondria in medicine. *Mitochondrion.* (2016) 30:105–16. doi: 10.1016/j.mito.2016.07.003
8. Holt IJ, Harding AE, Morgan-Hughes JA. Deletions of muscle mitochondrial DNA in patients with mitochondrial myopathies. *Nature.* (1988) 331:717–9. doi: 10.1038/331717a0
9. Wallace DC. Mitochondrial DNA mutations in disease and aging. *Environ Mol Mutagen.* (2010) 51:440–50. doi: 10.1002/em.20586
10. Calvo SE, Compton AG, Hershman SG, Lim SC, Lieber DS, Tucker EJ, et al. Molecular diagnosis of infantile mitochondrial disease with targeted next-generation sequencing. *Sci Translat Med.* (2012) 4:118ra110. doi: 10.1126/scitranslmed.3003310
11. Elliott HR, Samuels DC, Eden JA, Relton CL, Chinnery PF. Pathogenic mitochondrial DNA mutations are common in the general population. *Am J Human Genet.* (2008) 83:254–60. doi: 10.1016/j.ajhg.2008.07.004
12. DiMauro S, Schon EA, Carelli V, Hirano M. The clinical maze of mitochondrial neurology. *Nat Rev.* (2013) 9:429–44. doi: 10.1038/nrneurol.2013.126
13. DiMauro S, Hirano M, Schon EA. Approaches to the treatment of mitochondrial diseases. *Muscle Nerve.* (2006) 34:265–83. doi: 10.1002/mus.20598
14. Aryaman J, Johnston IG, Jones NS. Mitochondrial heterogeneity. *Front Genet.* (2019) 9:718. doi: 10.3389/fgene.2018.00718
15. Muftuoglu M, Mori MP, de Souza-Pinto. N. C. Formation and repair of oxidative damage in the mitochondrial DNA. *Mitochondrion.* (2014) 17:164–81. doi: 10.1016/j.mito.2014.03.007
16. Li M, Schröder R, Ni S, Madea B, Stoneking M. Extensive tissue-related and allele-related mtDNA heteroplasmy suggests positive selection for somatic mutations. *Proc Natl Acad Sci USA.* (2015) 112:2491–6. doi: 10.1073/pnas.1419651112
17. Rodenburg RJ. Mitochondrial complex I-linked disease. *Biochimica et Biophysica Acta.* (2016) 1857:938–45. doi: 10.1016/j.bbabio.2016.02.012
18. Schon EA, DiMauro S, Hirano M. Human mitochondrial DNA: roles of inherited and somatic mutations. *Nat Rev Genet.* (2012) 13:878–90. doi: 10.1038/nrg3275
19. Ghezzi D, Zeviani M. Human diseases associated with defects in assembly of OXPHOS complexes. *Essays Biochem.* (2018) 62:271–86. doi: 10.1042/EBC20170099
20. Deschauer M, Bamberg C, Claus D, Zierz S, Turnbull DM, Taylor RW. Late-onset encephalopathy associated with a C11777A mutation of mitochondrial DNA. *Neurology.* (2003) 60:1357–9. doi: 10.1212/01.WNL.0000055869.99975.4B
21. Kirby DM, Salemi R, Sugiana C, Ohtake A, Parry L, Bell KM, et al. NDUFS6 mutations are a novel cause of lethal neonatal mitochondrial complex I deficiency. *J Clin Invest.* (2004) 114:837–45. doi: 10.1172/JCI20683
22. Spiegel R, Shaag A, Mandel H, Reich D, Penyakov M, Hujeirat Y, et al. Mutated NDUFS6 is the cause of fatal neonatal lactic acidemia in Caucasus Jews. *Eur J Hum Genet.* (2009) 17:1200–3. doi: 10.1038/ejhg.2009.24
23. Ogawa E, Shimura M, Fushimi T, Tajika M, Ichimoto K, Matsunaga A, et al. Clinical validity of biochemical and molecular analysis in diagnosing Leigh syndrome: a study of 106 Japanese patients. *J Inherit Metab Dis.* (2017) 40:685–93. doi: 10.1007/s10545-017-0042-6
24. Tuppen HAL, Blakely EL, Turnbull DM, Taylor RW. Mitochondrial DNA mutations and human disease. *Biochimica et Biophysica Acta (BBA).* (2010) 1797:113–28. doi: 10.1016/j.bbabio.2009.09.005
25. Uusimaa J, Moilanen JS, Vainionp,ää L, Tapanainen P, Lindholm P, Nuutinen M, et al. Prevalence, segregation, and phenotype of the mitochondrial DNA 3243A>G mutation in children. *Annals Neurol.* (2007) 62:278–87. doi: 10.1002/ana.21196
26. Kaufmann P, Shungu DC, Sano MC, Jhung S, Engelstad K, Mitsis E, et al. Cerebral lactic acidosis correlates with neurological impairment in MELAS. *Neurology.* (2004) 62:1297–302. doi: 10.1212/01.WNL.0000120557.83907.A8
27. Yatsuga S, Povalko N, Nishioka J, Katayama K, Kakimoto N, Matsuishi T, et al. MELAS: a nationwide prospective cohort study of 96 patients in Japan. *Biochim et Biophys Acta.* (2012) 1820:619–24. doi: 10.1016/j.bbagen.2011.03.015
28. El-Hattab AW, Adesina AM, Jones J, Scaglia F. MELAS syndrome: clinical manifestations, pathogenesis, treatment options. *Mol Genet Metabol.* (2015) 116:4–12. doi: 10.1016/j.ymgme.2015.06.004
29. Hirano M, Pavlakis SG. Topical review: mitochondrial myopathy, encephalopathy, lactic acidosis, and strokelike episodes (MELAS): current concepts. *J Child Neurol.* (1994) 9:4–13. doi: 10.1177/088307389400900102
30. Hoppel CL, Tandler B, Fujioka H, Riva A. Dynamic organization of mitochondria in human heart and in myocardial disease. *Int J Biochem Cell Biol.* (2009) 41:1949–56. doi: 10.1016/j.biocel.2009.05.004
31. Bates MG, Bourke JP, Giordano C, d'Amati G, Turnbull DM, Taylor RW. (2012) Cardiac involvement in mitochondrial DNA disease: clinical spectrum, diagnosis, and management. *Eur Heart J.* 33:3023–33. doi: 10.1093/eurheartj/ehs275
32. Cairns RA, Harris IS, Mak TW. Regulation of cancer cell metabolism. *Nat Rev Cancer.* (2011) 11:85. doi: 10.1038/nrc2981
33. Sleigh A, Raymond-Barker P, Thackray K, Porter D, Hatunic M, Vottero A, et al. Mitochondrial dysfunction in patients with primary congenital insulin resistance. *J Clin Invest.* (2011) 121:2457–61. doi: 10.1172/JCI46405
34. McCoy MK, Cookson MR. Mitochondrial quality control and dynamics in Parkinson's disease. *Antioxidants Redox Signal.* (2011) 16:869–82. doi: 10.1089/ars.2011.4019
35. Coskun P, Wyrembak J, Schriner SE, Chen, H.-W., Marciniack C, et al. A mitochondrial etiology of Alzheimer and Parkinson disease. *Biochim Biophys Acta.* (2012) 1820:553–64. doi: 10.1016/j.bbagen.2011.08.008
36. Lönnqvist T, Paetau A, Valanne L, Pihko H. Recessive twinkle mutations cause severe epileptic encephalopathy. *Brain.* (2009) 132:1553–62. doi: 10.1093/brain/awp045
37. Mochel F, Haller RG. Energy deficit in huntington disease: why it matters. *J Clin Invest.* (2011) 121:493–9. doi: 10.1172/JCI45691
38. Bishop NA, Lu T, Yankner BA. Neural mechanisms of ageing and cognitive decline. *Nature.* (2010) 464:529. doi: 10.1038/nature08983
39. Tseng YH, Cypess AM, Kahn CR. Cellular bioenergetics as a target for obesity therapy. *Nat Rev Drug Discov.* (2010) 9:465. doi: 10.1038/nrd3138
40. Lee SR, Han J. Mitochondrial mutations in cardiac disorders. *Adv Exp Med Biol.* (2017) 982:81–111. doi: 10.1007/978-3-319-55330-6_5
41. Rebelo AP, Dillon LM, Moraes CT. Mitochondrial DNA transcription regulation and nucleoid organization. *J Inherit Metab Dis.* (2011) 34:941–51. doi: 10.1007/s10545-011-9330-8
42. O'Rourke B. Beyond the power of mitochondria. *Nat Rev Cardiol.* (2016) 13:386–8. doi: 10.1038/nrcardio.2016.95
43. Lopez-Crisosto C, Pennanen C, Vasquez-Trincado C, Morales PE, Bravo-Sagua R, Quest AFG, et al. Sarcoplasmic reticulum–mitochondria communication in cardiovascular pathophysiology. *Nat Rev Cardiol.* (2017) 14:342–60. doi: 10.1038/nrcardio.2017.23
44. Luongo TS, Lambert JP, Yuan A, Zhang X, Gross P, Song J, et al. The mitochondrial calcium uniporter matches energetic supply with cardiac workload during stress and modulates permeability transition. *Cell Rep.* (2015) 12:23–34. doi: 10.1016/j.celrep.2015.06.017
45. Bonora M, Wieckowski MR, Sinclair DA, Kroemer G, Pinton P, Galluzzi L. Targeting mitochondria for cardiovascular disorders: therapeutic potential and obstacles. *Nat Rev Cardiol.* (2019) 16:33–55. doi: 10.1038/s41569-018-0074-0
46. Davila JC, Cezar GG, Thiede M, Strom S, Miki T, Trosko J. Use and application of stem cells in toxicology. *Toxicol Sci.* (2004) 79:214–23. doi: 10.1093/toxsci/kfh100

47. Ruzzenente B, Rötig A, Metodiev MD. Mouse models for mitochondrial diseases. *Hum Mol Genet.* (2016) 25:R115–22. doi: 10.1093/hmg/ddw176
48. Li Y, Huang TT, Carlson EJ, Melov S, Ursell PC, Olson JL, et al. Dilated cardiomyopathy and neonatal lethality in mutant mice lacking manganese superoxide dismutase. *Nat Genet.* (1995) 11:376–81. doi: 10.1038/ng1295-376
49. Hu X, Charles JP, Akay T, Hutchinson JR, Blemker SS. Are mice good models for human neuromuscular disease? Comparing muscle excursions in walking between mice and humans. *Skeletal Muscle.* (2017) 7:26. doi: 10.1186/s13395-017-0143-9
50. Karakikes I, Ameen M, Termglinchan V, Wu JC. Human induced pluripotent stem cell-derived cardiomyocytes. *Circul Res.* (2015) 117:80–8. doi: 10.1161/CIRCRESAHA.117.305365
51. Mosqueira D, Smith JGW, Bhagwan JR, Denning C. Modeling hypertrophic cardiomyopathy: mechanistic insights and pharmacological intervention. *Trends Mol Med.* (2019) 25:775–90. doi: 10.1016/j.molmed.2019.06.005
52. Denning C, Borgdorff V, Crutchley J, Firth KS, George V, Kalra S, et al. Cardiomyocytes from human pluripotent stem cells: from laboratory curiosity to industrial biomedical platform. *Biochim Biophys Acta.* (2016) 1863(7 Pt B):1728–48. doi: 10.1016/j.bbamcr.2015.10.014
53. Kattman SJ, Koonce CH, Swanson BJ, Anson BD. Stem cells and their derivatives: a renaissance in cardiovascular translational research. *J Cardiovasc Transl Res.* (2011) 4:66–72. doi: 10.1007/s12265-010-9235-1
54. Burridge PW, Matsa E, Shukla P, Lin ZC, Churko JM, Ebert AD, et al. Chemically defined generation of human cardiomyocytes. *Nat Methods.* (2014) 11:855–860. doi: 10.1038/nmeth.2999
55. Burridge PW, Holmström A, Wu JC. Chemically defined culture and cardiomyocyte differentiation of human pluripotent stem cells. *Curr Protocols Human Genet.* (2015) 87:21.23.21–21.23.15. doi: 10.1002/0471142905.hg2103s87
56. Evans SM, Yelon D, Conlon FL, Kirby ML. Myocardial lineage development. *Circ Res.* (2010) 107:1428–44. doi: 10.1161/CIRCRESAHA.110.227405
57. Burridge PW, Thompson S, Millrod MA, Weinberg S, Yuan X, Peters A, et al. A universal system for highly efficient cardiac differentiation of human induced pluripotent stem cells that eliminates interline variability. *PLoS ONE.* (2011) 6:e18293. doi: 10.1371/journal.pone.0018293
58. Elliott DA, Braam SR, Koutsis K, Ng ES, Jenny R, Lagerqvist EL, et al. NKX2-5(eGFP/w) hESCs for isolation of human cardiac progenitors and cardiomyocytes. *Nat Methods.* (2011) 8:1037–40. doi: 10.1038/nmeth.1740
59. Noseda M, Peterkin T, Simoes FC, Patient R, Schneider MD. Cardiopoietic factors: extracellular signals for cardiac lineage commitment. *Circ Res.* (2011) 108:129–52. doi: 10.1161/CIRCRESAHA.110.223792
60. Lian Q, Chow Y, Esteban MA, Pei D, Tse, H.-F. Future perspective of induced pluripotent stem cells for diagnosis, drug screening and treatment of human diseases. *Thrombosis Haemostasis.* (2010) 104:39–44. doi: 10.1160/TH10-05-0269
61. Elitt MS, Barbar L, Tesar PJ. Drug screening for human genetic diseases using iPSC models. *Human Mol Genet.* (2018) 27:R89–98. doi: 10.1093/hmg/ddy186
62. Chapin RE, Stedman DB. Endless possibilities: stem cells and the vision for toxicology testing in the 21st Century. *Toxicol Sci.* (2009) 112:17–22. doi: 10.1093/toxsci/kfp202
63. Braam SR, Tertoolen L, van de Stolpe A, Meyer T, Passier R, Mummery CL. Prediction of drug-induced cardiotoxicity using human embryonic stem cell-derived cardiomyocytes. *Stem Cell Research.* (2010) 4:107–116. doi: 10.1016/j.scr.2009.11.004
64. Dick E, Rajamohan D, Ronksley J, Denning C. Evaluating the utility of cardiomyocytes from human pluripotent stem cells for drug screening. *Biochem Soc Transact.* (2010) 38:1037–1045. doi: 10.1042/BST0381037
65. Ebert ADP, Liang PMDP, Wu JCMD. P. Induced pluripotent stem cells as a disease modeling and drug screening platform. *J Cardiovascular Pharmacol.* (2012) 60:408–16. doi: 10.1097/FJC.0b013e318247f642
66. McNeish J. Embryonic stem cells in drug discovery. *Nat Rev Drug Discov.* (2004) 3:70. doi: 10.1038/nrd1281
67. Caspi O, Itzhaki I, Kehat I, Gepstein A, Arbel G, Huber I, et al. *In vitro* electrophysiological drug testing using human embryonic stem cell derived cardiomyocytes. *Stem Cells Dev.* (2009) 18:161–72. doi: 10.1089/scd.2007.0280
68. Force T, Kolaja KL. Cardiotoxicity of kinase inhibitors: the prediction and translation of preclinical models to clinical outcomes. *Nat Rev Drug Discov.* (2011) 10:111. doi: 10.1038/nrd3252
69. Eschenhagen T, Mummery C, Knollmann BC. Modelling sarcomeric cardiomyopathies in the dish: from human heart samples to iPSC cardiomyocytes. *Cardiovasc Res.* (2015) 105:424–38. doi: 10.1093/cvr/cvv017
70. Jiang Y, Park P, Hong SM, Ban K. Maturation of cardiomyocytes derived from human pluripotent stem cells: current strategies and limitations. *Mol Cells.* (2018) 41:613–21. doi: 10.14348/molcells.2018.0143
71. Schick R, Mekies LN, Shemer Y, Eisen B, Hallas T, Ben Jehuda R, et al. Functional abnormalities in induced Pluripotent Stem Cell-derived cardiomyocytes generated from titin-mutated patients with dilated cardiomyopathy. *PLoS ONE.* (2018) 13:e0205719. doi: 10.1371/journal.pone.0205719
72. Preininger MK, Jha R, Maxwell JT, Wu Q, Singh M, Wang B, et al. A human pluripotent stem cell model of catecholaminergic polymorphic ventricular tachycardia recapitulates patient-specific drug responses. *Dis Model Mech.* (2016) 9:927–939. doi: 10.1242/dmm.026823
73. Mosqueira D, Mannhardt I, Bhagwan JR, Lis-Slimak K, Katili P, Scott E, et al. CRISPR/Cas9 editing in human pluripotent stem cell-cardiomyocytes highlights arrhythmias, hypocontractility, and energy depletion as potential therapeutic targets for hypertrophic cardiomyopathy. *Eur Heart J.* (2018) 39:3879–92. doi: 10.1093/eurheartj/ehy249
74. Li X, Lu, WJ, Li Y, Wu F. MLP-deficient human pluripotent stem cell derived cardiomyocytes develop hypertrophic cardiomyopathy and heart failure phenotypes due to abnormal calcium handling. *Cell Death Dis.* (2019) 10:610. doi: 10.1038/s41419-019-1826-4
75. Bhagwan JR, Mosqueira D, Chairez-Cantu K, Mannhardt I, Bodbin SE, Bakar M, et al. Isogenic models of hypertrophic cardiomyopathy unveil differential phenotypes and mechanism-driven therapeutics. *J Mol Cell Cardiol.* (2020) 145:43–53. doi: 10.1016/j.yjmcc.2020.06.003
76. Wang G, McCain ML, Yang L, He A, Pasqualini FS, Agarwal A, et al. Modeling the mitochondrial cardiomyopathy of Barth syndrome with induced pluripotent stem cell and heart-on-chip technologies. *Nat Med.* (2014) 20:616–23. doi: 10.1038/nm.3545
77. Li S, Pan H, Tan C, Sun Y, Song Y, Zhang X, et al. Mitochondrial dysfunctions contribute to hypertrophic cardiomyopathy in patient iPSC-derived cardiomyocytes with MT-RNR2 mutation. *Stem Cell Rep.* (2018) 10:808–21. doi: 10.1016/j.stemcr.2018.01.013
78. Naue J, Hörer S, Sänger T, Strobl C, Hatzer-Grubwieser P, Parson W, et al. Evidence for frequent and tissue-specific sequence heteroplasmy in human mitochondrial DNA. *Mitochondrion.* (2015) 20:82–94. doi: 10.1016/j.mito.2014.12.002
79. Kargaran PK, Evans JM, Bodbin SE, Smith JGW, Nelson TJ, Denning C, et al. Mitochondrial DNA: hotspot for potential gene modifiers regulating hypertrophic cardiomyopathy. *J Clin Med.* (2020) 9:2349. doi: 10.3390/jcm9082349
80. Folmes CDL, Martinez-Fernandez A, Perales-Clemente E, Li X, McDonald A, Oglesbee D, et al. Disease-causing mitochondrial heteroplasmy segregated within induced pluripotent stem cell clones derived from a MELAS patient. *Stem Cells.* (2013) 32:120–125. doi: 10.1002/stem.1389
81. Perales-Clemente E, Cook AN, Evans JM, Roellinger S, Secreto F, Emmanuele V, et al. Natural underlying mtDNA heteroplasmy as a potential source of intra-person hiPSC variability. *EMBO J.* (2016) 35:1979–90. doi: 10.15252/embj.201694892
82. Mosqueira D, Lis-Slimak K, Denning C. High-throughput phenotyping toolkit for characterizing cellular models of hypertrophic cardiomyopathy *in vitro*. *Methods Protoc.* (2019) 2:83. doi: 10.3390/mps2040083
83. van Meer BJ, Krotenberg A, Sala L, Davis RP, Eschenhagen T, Denning C, et al. Simultaneous measurement of excitation-contraction coupling parameters identifies mechanisms underlying contractile responses of hiPSC-derived cardiomyocytes. *Nat Commun.* (2019) 10:4325. doi: 10.1038/s41467-019-12354-8
84. Piquereau J, Ventura-Clapier R. Maturation of cardiac energy metabolism during perinatal development. *Front Physiol.* (2018) 9:959. doi: 10.3389/fphys.2018.00959
85. Bekhite MM, González Delgado A, Menz F, Kretzschmar T, Wu JMF, Bekfani T, et al. Longitudinal metabolic profiling of cardiomyocytes derived

from human-induced pluripotent stem cells. *Basic Res Cardiol.* (2020) 115:37. doi: 10.1007/s00395-020-0796-0

86. Ramachandra CJA, Mehta A, Wong P, Ja, K. P. M. M., Fritsche-Danielson R, et al. Fatty acid metabolism driven mitochondrial bioenergetics promotes advanced developmental phenotypes in human induced pluripotent stem cell derived cardiomyocytes. *Int J Cardiol.* (2018) 272:288–97. doi: 10.1016/j.ijcard.2018.08.069
87. Horikoshi Y, Yan Y, Terashvili M, Wells C, Horikoshi H, Fujita S, et al. Fatty acid-treated induced pluripotent stem cell-derived human cardiomyocytes exhibit adult cardiomyocyte-like energy metabolism phenotypes. *Cells.* (2019) 8:1095. doi: 10.3390/cells8091095
88. Yang X, Rodriguez ML, Leonard A, Sun L, Fischer KA, Wang Y, et al. Fatty acids enhance the maturation of cardiomyocytes derived from human pluripotent stem cells. *Stem Cell Rep.* (2019) 13:657–68. doi: 10.1016/j.stemcr.2019.08.013
89. Correia C, Koshkin A, Duarte P, Hu D, Carido M, Sebastião MJ, et al. 3D aggregate culture improves metabolic maturation of human pluripotent stem cell derived cardiomyocytes. *Biotechnol Bioeng.* (2018) 115:630–44. doi: 10.1002/bit.26504
90. Eglen R, Reisine T. Photoproteins: important new tools in drug discovery. *ASSAY Drug Dev. Technol.* (2008) 6:659–72. doi: 10.1089/adt.2008.160
91. Saleem U, van Meer BJ, Katili PA, Yusof N, Mannhardt I, Garcia AK, et al. Blinded, multi-centre evaluation of drug-induced changes in contractility using human induced pluripotent stem cell-derived cardiomyocytes. *Toxicol Sci.* (2020) 76:103–23. doi: 10.1093/toxsci/kfaa058
92. Berger F, Lau C, Dahlmann M, Ziegler M. Subcellular compartmentation and differential catalytic properties of the three human nicotinamide mononucleotide adenylyltransferase isoforms. *J Biol Chem.* (2005) 280:36334–41. doi: 10.1074/jbc.M508660200
93. Ying W. $NAD^+$/NADH and $NADP^+$/NADPH in cellular functions and cell death: regulation and biological consequences. *Antioxidants Redox Signal.* (2008) 10:179–206. doi: 10.1089/ars.2007.1672
94. Di Lisa F, Menab,ò R, Canton M, Barile M, Bernardi P. Opening of the mitochondrial permeability transition pore causes depletion of mitochondrial and cytosolic $NAD^+$ and Is a causative event in the death of myocytes in postischemic reperfusion of the heart. *J Biol Chem.* (2001) 276:2571–5. doi: 10.1074/jbc.M006825200
95. Di Lisa F, Ziegler M. Pathophysiological relevance of mitochondria in $NAD^+$ metabolism. *FEBS Letters.* (2001) 492:4–8. doi: 10.1016/S0014-5793(01)02198-6
96. Eto K, Tsubamoto Y, Terauchi Y, Sugiyama T, Kishimoto T, Takahashi N, et al. Role of NADH shuttle system in glucose-induced activation of mitochondrial metabolism and insulin secretion. *Science.* (1999) 283:981–5. doi: 10.1126/science.283.5404.981
97. Zhao Y, Wang A, Zou Y, Su N, Loscalzo J, Yang Y. *In vivo* monitoring of cellular energy metabolism using SoNar, a highly responsive sensor for $NAD^+$/NADH redox state. *Nat Protocols.* (2016) 11:1345. doi: 10.1038/nprot.2016.074
98. Williamson DH, Lund P, Krebs HA. The redox state of free nicotinamide-adenine dinucleotide in the cytoplasm and mitochondria of rat liver. *Biochem J.* (1967) 103:514–27. doi: 10.1042/bj1030514
99. Zhang Q, Piston DW, Goodman RH. Regulation of corepressor function by nuclear NADH. *Science.* (2002) 295:1895–7. doi: 10.1126/science.1069300
100. Stein LR, Imai S. The dynamic regulation of NAD metabolism in mitochondria. *Trends Endocrinol Metabol.* (2012) 23:420–8. doi: 10.1016/j.tem.2012.06.005
101. Veech RL, Eggleston LV, Krebs HA. The redox state of free nicotinamide–adenine dinucleotide phosphate in the cytoplasm of rat liver. *Biochem J.* (1969) 115:609–19. doi: 10.1042/bj1150609a
102. Diguet N, Trammell SAJ, Tannous C, Deloux R, Piquereau J, Mougenot N, et al. Nicotinamide riboside preserves cardiac function in a mouse model of dilated cardiomyopathy. *Circulation.* (2018) 137:2256–73. doi: 10.1161/CIRCULATIONAHA.116.026099
103. Katsyuba E, Mottis A, Zietak M, De Franco F, van der Velpen V, Gariani K, et al. *De novo* $NAD^+$ synthesis enhances mitochondrial function and improves health. *Nature.* (2018) 563:354–9. doi: 10.1038/s41586-018-0645-6
104. Srivastava S. Emerging therapeutic roles for $NAD^+$ metabolism in mitochondrial and age-related disorders. *Clin Transl Med.* (2016) 5:25. doi: 10.1186/s40169-016-0104-7
105. Ralto KM, Rhee EP, Parikh SM. $NAD^+$ homeostasis in renal health and disease. *Nat Rev Nephrol.* (2020) 16:99–111. doi: 10.1038/s41581-019-0216-6
106. Houtkooper RH, Auwerx J. Exploring the therapeutic space around $NAD^+$. *J Cell Biol.* (2012) 199:205–9. doi: 10.1083/jcb.201207019
107. Mouchiroud L, Houtkooper, R.iekelt H., Moullan N, Katsyuba E, Ryu D, et al. The $NAD^+$/Sirtuin pathway modulates longevity through activation of mitochondrial UPR and FOXO signaling. *Cell.* (2013) 154:430–41. doi: 10.1016/j.cell.2013.06.016
108. Cerutti R, Pirinen E, Lamperti C, Marchet S, Sauve, A.nthony A., et al. $NAD^+$-dependent activation of Sirt1 corrects the phenotype in a mouse model of mitochondrial disease. *Cell Metabol.* (2014) 19:1042–9. doi: 10.1016/j.cmet.2014.04.001
109. Khan NA, Auranen M, Paetau I, Pirinen E, Euro L, Forsström S, et al. Effective treatment of mitochondrial myopathy by nicotinamide riboside, a vitamin B3. *EMBO Mol Med.* (2014) 6:721–31. doi: 10.1002/emmm.201403943
110. Braidy N, Guillemin GJ, Mansour H, Chan-Ling T, Poljak A, Grant R. Age related changes in $NAD^+$ metabolism oxidative stress and Sirt1 activity in wistar rats. *PLoS ONE.* (2011) 6:e19194. doi: 10.1371/journal.pone.0019194
111. Massudi H, Grant R, Braidy N, Guest J, Farnsworth B, Guillemin GJ. Age-associated changes in oxidative stress and $NAD^+$ metabolism in human tissue. *PLoS ONE.* (2012) 7:e42357. doi: 10.1371/journal.pone.0042357
112. Gomes, A.na P., Price, N.athan L., Ling, A.lvin J. Y., et al.avid J., Montgomery MK, Rajman L, et al. Declining $NAD^+$ induces a pseudohypoxic state disrupting nuclear-mitochondrial communication during aging. *Cell.* (2013) 155:1624–38. doi: 10.1016/j.cell.2013.11.037
113. Viscomi C, Bottani E, Civiletto G, Cerutti R, Moggio M, Fagiolari G, et al. *In vivo* correction of COX deficiency by activation of the AMPK/PGC-1α axis. *Cell Metabol.* (2011) 14:80–90. doi: 10.1016/j.cmet.2011.04.011
114. Pagliarini DJ, Calvo SE, Chang B, Sheth SA, Vafai SB, Ong, et al.-E., et al. A mitochondrial protein compendium elucidates complex I disease biology. *Cell.* (2008) 134:112–23. doi: 10.1016/j.cell.2008.06.016
115. Zhou B, Tian R. Mitochondrial dysfunction in pathophysiology of heart failure. *J Clin Invest.* (2018) 128:3716–26. doi: 10.1172/JCI120849
116. Wang Y, Kim NS, Haince, J.-F., Kang HC, David KK, et al. Poly(ADP-Ribose) (PAR) binding to apoptosis-inducing factor is critical for PAR polymerase-1–dependent cell death (Parthanatos). *Sci Signal.* (2011) 4:ra20. doi: 10.1126/scisignal.2000902
117. Niyazov DM, Kahler SG, Frye RE. Primary mitochondrial disease and secondary mitochondrial dysfunction: importance of distinction for diagnosis and treatment. *Mol Syndromol.* (2016) 7:122–37. doi: 10.1159/000446586
118. Warburg O. On the origin of cancer cells. *Science.* (1956) 123:309–14. doi: 10.1126/science.123.3191.309
119. Vander Heiden MG. Targeting cancer metabolism: a therapeutic window opens. *Nat Rev Drug Discov.* (2011) 10:671. doi: 10.1038/nrd3504
120. Zhao Y, Hu Q, Cheng F, Su N, Wang A, Zou Y, et al. SoNar, a highly responsive $NAD^+$/NADH sensor, allows high-throughput metabolic screening of anti-tumor agents. *Cell Metabol.* (2015) 21:777–89. doi: 10.1016/j.cmet.2015.04.009
121. Kasischke KA, Vishwasrao HD, Fisher PJ, Zipfel WR, Webb WW. Neural activity triggers neuronal oxidative metabolism followed by astrocytic glycolysis. *Science.* (2004) 305:99–103. doi: 10.1126/science.1096485
122. Mayevsky A, Rogatsky GG. Mitochondrial function *in vivo* evaluated by NADH fluorescence: from animal models to human studies. *Am J Physiol Cell Physiol.* (2007) 292:C615–40. doi: 10.1152/ajpcell.00249.2006
123. Blacker TS, Mann ZF, Gale JE, Ziegler M, Bain AJ, Szabadkai G, et al. Separating NADH and NADPH fluorescence in live cells and tissues using FLIM. *Nat Commun.* (2014) 5:3936. doi: 10.1038/ncomms4936

124. Cant,ó C, Auwerx J. Caloric restriction, SIRT1 and longevity. *Trends Endocrinol Metabol.* (2009) 20:325–31. doi: 10.1016/j.tem.2009.03.008
125. Yang J, Bogni A, Schuetz EG, Ratain M, Dolan ME, McLeod H, et al. Etoposide pathway. *Pharmacogenet Genom.* (2009) 19:552–3. doi: 10.1097/FPC.0b013e32832e0e7f
126. Hung YP, Albeck JG, Tantama M, Yellen G. Imaging cytosolic NADH-NAD$^+$ redox state with a genetically encoded fluorescent biosensor. *Cell Metabolism.* (2011) 14:545–54. doi: 10.1016/j.cmet.2011.08.012
127. Zhao Y, Jin J, Hu Q, Zhou, H.-M., Yi J, et al. Genetically encoded fluorescent sensors for intracellular NADH detection. *Cell Metabol.* (2011) 14:555–66. doi: 10.1016/j.cmet.2011.09.004
128. Zhao Y, Yang Y. Profiling metabolic states with genetically encoded fluorescent biosensors for NADH. *Curr Opin Biotechnol.* (2015) 31:86–92. doi: 10.1016/j.copbio.2014.08.007
129. Zhao Y, Yang Y. Frex and FrexH: Indicators of metabolic states in living cells. *Bioeng Bugs.* (2012) 3:181–8. doi: 10.4161/bbug.19769
130. Inoue M, Takeuchi A, Horigane, S.-,i., Ohkura M, Gengyo-Ando K, et al. Rational design of a high-affinity, fast, red calcium indicator R-CaMP2. *Nat Methods.* (2014) 12:64. doi: 10.1038/nmeth.3185
131. Wilms CD, Häusser M. Twitching towards the ideal calcium sensor. *Nat Methods.* (2014) 11:139. doi: 10.1038/nmeth.2814
132. Christofk HR, Vander Heiden MG, Harris MH, Ramanathan A, Gerszten RE, Wei R, et al. The M2 splice isoform of pyruvate kinase is important for cancer metabolism and tumour growth. *Nature.* (2008) 452:230. doi: 10.1038/nature06734
133. Meyers DE, Basha HI, Koenig MK. Mitochondrial cardiomyopathy: pathophysiology, diagnosis, and management. *Tex Heart Inst J.* (2013) 40:385–94.
134. Werley CA, Boccardo S, Rigamonti A, Hansson EM, Cohen AE. Multiplexed optical sensors in arrayed Islands of cells for multimodal recordings of cellular physiology. *Nat Commun.* (2020) 11:3881. doi: 10.1038/s41467-020-17607-5
135. Ashrafian H, Redwood C, Blair E, Watkins H. Hypertrophic cardiomyopathy:a paradigm for myocardial energy depletion. *Trends Genet.* (2003) 19:263–8. doi: 10.1016/S0168-9525(03)00081-7
136. Mok BY, de Moraes MH, Zeng J, Bosch DE, Kotrys AV, Raguram A, et al. (2020) A bacterial cytidine deaminase toxin enables CRISPR-free mitochondrial base editing. *Nature*. 583:631–7. doi: 10.1038/s41586-020-2477-4

**Conflict of Interest:** The authors declare that the research was conducted in the absence of any commercial or financial relationships that could be construed as a potential conflict of interest.

frontiers
in Cell and Developmental Biology

ORIGINAL RESEARCH
published: 15 February 2021
doi: 10.3389/fcell.2021.591754

# Scaffold-Mediated Developmental Effects on Human Induced Pluripotent Stem Cell-Derived Cardiomyocytes Are Preserved After External Support Removal

*Jun Li*[1]*, Jong-Kook Lee*[1,2]**, Keiko Miwa*[2,3]*, Yuki Kuramoto*[1]*, Kiyoshi Masuyama*[1]*, Hideki Yasutake*[1]*, Satoki Tomoyama*[1]*, Hiroyuki Nakanishi*[1] *and Yasushi Sakata*[1]

[1] *Department of Cardiovascular Medicine, Osaka University Graduate School of Medicine, Suita, Japan,* [2] *Department of Cardiovascular Regenerative Medicine, Osaka University Graduate School of Medicine, Suita, Japan,* [3] *Department of Medical Laboratory Science, Faculty of Health Sciences, Hokkaido University, Sapporo, Japan*

**Edited by:**
*Ning Sun,*
*Fudan University, China*

**Reviewed by:**
*Hung-Fat Tse,*
*The University of Hong Kong,*
*Hong Kong*
*Atsushi Asakura,*
*University of Minnesota, United States*

***Correspondence:**
*Jong-Kook Lee*
*jlee@cardiology.med.osaka-u.ac.jp*

**Specialty section:**
*This article was submitted to*
*Stem Cell Research,*
*a section of the journal*
*Frontiers in Cell and Developmental Biology*

**Received:** *05 August 2020*
**Accepted:** *27 January 2021*
**Published:** *15 February 2021*

**Citation:**
*Li J, Lee J-K, Miwa K, Kuramoto Y, Masuyama K, Yasutake H, Tomoyama S, Nakanishi H and Sakata Y (2021) Scaffold-Mediated Developmental Effects on Human Induced Pluripotent Stem Cell-Derived Cardiomyocytes Are Preserved After External Support Removal.*
*Front. Cell Dev. Biol. 9:591754.*
*doi: 10.3389/fcell.2021.591754*

Human induced pluripotent stem (hiPS) cells have been used as a cell source for regenerative therapy and disease modeling. The purity of hiPS-cardiomyocytes (hiPS-CMs) has markedly improved with advancements in cell culture and differentiation protocols. However, the morphological features and molecular properties of the relatively immature cells are still unclear, which has hampered their clinical application. The aim of the present study was to investigate the extent to which topographic substrates actively influence hiPS-CMs. hiPS-CMs were seeded on randomized oriented fiber substrate (random), anisotropic aligned fiber substrate (align), and flat non-scaffold substrate (flat). After culturing for one week, the hiPS-CMs on the aligned patterns showed more mature-like properties, including elongated rod shape, shorter duration of action potential, accelerated conduction velocity, and elevated cardiac gene expression. Subsequently, to determine whether this development was irreversible or was altered after withdrawal of the structural support, the hiPS-CMs were harvested from the three different patterns and reseeded on the non-scaffold (flat) pattern. After culturing for one more week, the improvements in morphological and functional properties diminished, although hiPS-CMs pre-cultured on the aligned pattern retained the molecular features of development, which were even more significant as compared to that observed during the pre-culture stage. Our results suggested that the anisotropic fiber substrate can induce the formation of geometrical mimic-oriented heart tissue in a short time.

Although the morphological and electrophysiological properties of hiPS-CMs obtained via facilitated maturation somehow rely on the existence of an exterior scaffold, the molecular developmental features were preserved even in the absence of the external support, which might persist throughout hiPS-CM development.

**Keywords: hiPS-CMs, development, tissue engineering, geometric induction, alignment, maturation**

## INTRODUCTION

Cardiovascular diseases are one of the main causes of death worldwide (Gersh et al., 2010). The treatment options for heart failure, the end stage of most cardiovascular diseases, are limited, as treatment validity among patients is mixed owing to individual differences. Recently, prominent advancements have been made toward cardiac regenerative therapy (Zhang, 2015; Ichimura and Shiba, 2017). Furthermore, pluripotent stem cell-derived cardiomyocytes (PSC-CMs) are being considered as promising candidates for understanding cardiac physiological development (Kolanowski et al., 2017; Scuderi and Butcher, 2017) and pathological progression (Yazawa et al., 2011; Sun et al., 2012; Chun et al., 2015; Sakai et al., 2018). However, the characteristics of immature CMs, from morphological features to molecular properties, are still not clear, which has hampered their clinical application (Veerman et al., 2015; Yoshida and Yamanaka, 2017). To overcome these fundamental limitations, various strategies for facilitating PSC-CM maturation, such as topographic induction (Kim et al., 2012), mechanical or electrical stimulation (Ruan et al., 2016), supplementation with biochemical factors (Engels et al., 2014; Yang et al., 2014), and genetic manipulation (Anderson et al., 2007) have been used. While these methods improved CM maturation to a certain extent, disparities with native cardiac tissue still exist (Veerman et al., 2015). For instance, the native heart tissue consists of well-aligned cardiac laminar layers (Streeter et al., 1969; LeGrice et al., 1995), which guarantee high efficiency of contractility as well as electrical conductivity (Hooks et al., 2002). Several reports have suggested that well-aligned cardiac tissue can be successfully obtained by culturing PSC-CMs on anisotropic pattern, although its effects on promotion of PSC-CM maturation are still ambiguous (Pilarczyk et al., 2016).

In this study, we confirmed the beneficial effects of aligned topography on hiPS-CM maturation. Furthermore, we investigated if the benefits remained in the mature cells even after removal of the topographic stimuli. The functional maturation of hiPS-CMs relies on extracellular exterior structural support, but the positive effects due to the support may persist throughout hiPS-CM development. Determining the hiPS-cardiac cellular “memory” for topographic effects is crucial for their application in regenerative medicine in a clinical setting.

## MATERIALS AND METHODS

### hiPSC Culture and Cardiac Differentiation

hiPS cells, 201B7 (RIKEN Bioresource Center, Tsukuba, Japan), were maintained in StemFit AK02 medium (AK02N; Ajinomoto). Cardiac differentiation was induced using the cardiomyocyte differentiation kit (A2921201; Gibco). The culture medium was replaced first with medium A and then with medium B after every 2 days, and then the cells were finally maintained in cardiomyocyte maintenance medium for 7 days. On day 14, the culture medium was replaced by non-glucose Roswell Park Memorial Institute (RPMI) medium (11879-020; Gibco) containing 5 mM lactic acid (128-00056; Wako) and 0.1% bovine serum albumin (BSA, 037-23372; Wako) (Tohyama et al., 2013) and incubated for 8 days. Then, the cultures were maintained in cardiomyocyte maintenance medium until further analysis. All cells were maintained at 37℃ in a 5% CO2-humidified incubator.

### hiPS-CMs Culture on Different Patterns

On post-differentiation day 30, hiPS-CMs were dissociated into single cells using 0.25% trypsin-ethylene diamine tetraacetic acid (25200072; Gibco) and seeded on 0.1% gelatin pre-coated flat bottom 96-well plate (PerkinElmer, 6005550)/random nanofiber substrate (NanoECM, 9601; Funakoshi)/aligned nanofiber substrate (NanoAligned, 9602; Funakoshi) either at the density of $3.125 \times 10^5$ cells/cm$^2$ for functional analysis or $3.125 \times 10^4$ cells/cm$^2$ for morphological study. The cultures were maintained in M199 (12350-039; Gibco) with 10% fetal bovine serum (FBS) for 7 days. hiPS-CMs from the same patch were seeded on 0.1% gelatin flat bottom pre-coated 24-well plate (MS-80240; Sumilon)/random nanofiber substrate (NanoECM, 2401; Funakoshi)/aligned nanofiber substrate (NanoAligned, 2402; Funakoshi) at the density of $3.125 \times 10^5$ cells/cm$^2$. After culturing for 7 days, the cells were harvested for quantitative reverse transcription-polymerase chain reaction (qRT-PCR). The plates were all xeno-free, and the nanofibers were made of polycaprolactone; the diameter of the nanofibers were approximately 700 nm.

---

**Abbreviations:** AP, action potential; APD80, AP duration at 80% repolarization; CACNA1C, L-type calcium channel; Cx-43, connexin-43; DEG, differentially expressed gene; GJA1, gap junction connexin-43; GO, gene ontology; hiPS-CMs, human induced pluripotent stem cell-derived cardiomyocytes; KCNH2, ether-a-go-go-related protein 1; KCNJ2, potassium inward rectifier; KCNQ1, potassium slow delayed rectifier channel; KRT, keratin; qRT-PCR, quantitative reverse transcription-polymerase chain reaction; MYH6, α-myosin heavy chain; MYH7, β-myosin heavy chain; MYL2, myosin light chain 2; MYL7, myosin light chain 7; PCA, principal component analysis; PGSEA, parametric gene set enrichment analysis; PTP, protein tyrosine phosphatase; PTPRH, protein tyrosine phosphatase receptor type H; SERCA2/ATP2A2, Sarco/endoplasmic reticulum calcium-ATPase; SCN5A, fast sodium ion channel.

## De-Scaffold Culture of hiPS-CMs

hiPS-CMs pre-cultured on the different patterns for 7 days were harvested and re-plated on non-scaffold (flat bottom) 96-well or 24-well plates and cultured for another 7 days. Thereafter, the cultures in the 96-well plates were used for morphological and functional studies, and those in the 24-well plates were harvested for molecular analysis.

## Immunofluorescence Staining and Imaging Analyses

Cells were fixed in 4% paraformaldehyde (PFA) for 15 min at 25°C. After permeabilization in 0.1% Triton X-100 for 10 min, the samples were blocked with 2% BSA for 1 h at RT. The primary antibodies, anti-cardiac troponin-T (1:200, catalog number MS-295-P1; Lab Vision) and anti-connexin-43 (1:200, catalog number 710700; Abcam), diluted in the blocking solution were applied to the sample and incubated overnight at 4℃. After washing thrice with phosphate-buffered saline (PBS) for 5 min each, appropriate secondary antibodies (Alexa Fluor 488 and Alexa Fluor 647; 1:500 dilution) in 2% BSA were applied and incubated in the dark for 1 h at RT. Finally, after rinsing thrice in PBS for 5 min each, the cultures were mounted with Hoechst 33342 (1:1000, Dojindo, H342). The stained images were visualized using a high content imaging system (Operetta, PerkinElmer, Waltham, MA, United States). Cell shapes were analyzed using the Harmony analysis software (PerkinElmer).

## Contractility of Spontaneously Beating hiPS-CMs

Free labeling motion analysis of hiPS-CMs was performed using the cell motion imaging system (SI8000C, Cardio Model, Sony, Tokyo, Japan), as previously reported (Iseoka et al., 2018). Briefly, spontaneously beating hiPS-CMs were monitored at 37℃ in a 5%-CO2 incubator. Images were captured using a 10 × objective at a frame rate of 150 fps for 5 s. The data were analyzed using a SI8000C analyzer software (Sony).

## Calcium Transient and Membrane Potential

For calcium transient, the cells were loaded with 5 μM Indo-1 AM (1006; Dojindo) dissolved in FluoroBrite Dulbecco's modified Eagle's medium (DMEM) (A1896701; Gibco) containing 0.1% pluronic F-127 (P3000MP; Thermo Fisher Scientific) and incubated at 37℃ for 1 h. After washing twice with PBS, the cells were incubated in FluoroBrite DMEM for 30 min at 37℃. For measuring membrane potential, the prepared cells were treated with the FluoVolt membrane potential kit (F10488; Thermo Fisher Scientific) for 30 min at 37℃. The medium was replaced with FluoroBrite DMEM containing 2% FBS and incubated for another 30 min. The calcium transient and membrane potential were measured under pacing at 1 Hz. The imaging data were acquired and analyzed using the FDSS/uCELL system (C13299; Hamamatsu Photonics, Hamamatsu, Japan).

## Optical Mapping

Cells were prepared similar to that for membrane potential measurement and treated with the membrane potential kit (F10488; Thermo Fisher Scientific). Optical mapping was performed using the MiCAM02 imaging system (BrainVision, Tokyo, Japan) combined with MyoPacer EP (IonOptix, Westwood, MA, United States), as reported previously (Nakanishi et al., 2019). Briefly, after loading the cells, the cultures were electrically stimulated using a bipolar electrode. For aligned pattern, pacing was performed parallel or perpendicular to the direction of arranged nanofibers, using the same pacing positions for random and flat patterns. The pacing rate ranged from 0.5 Hz to 2 Hz in a gradient. The whole procedure was performed at 37℃ under atmospheric conditions. Optical imaging was performed using the BV_Ana software (BrainVision, Tokyo, Japan).

## qRT-PCR

Total RNA was extracted using the RNeasy Plus mini kit (740990.250; Takara) and cDNA was synthesized using the SuperScript VILO cDNA synthesis kit (11754-250; Thermo Fisher Scientific). Next, qRT-PCR was performed using the Taqman Fast advanced master mix (4444557; Thermo Fisher Scientific) and assessed using the ViiA 7 real-time PCR system (Thermo Fisher Scientific). The expression of the target gene was normalized to that of 18S rDNA, the internal control (18s rRNA, Hs99999901_s1). The genes analyzed using the TaqMan gene expression assays were as follows: *MYH6* (Hs01101425_m1), *MYH7* (Hs01110632_m1), *MYL2* (Hs00166405_m1), *MYL7* (Hs01085598_g1), *SCN5A* (Hs00165693_m1), *GJA1* (Hs00748445_s1), *ATP2A2* (Hs00544877_m1), *CACNA1C* (Hs00167681_m1), *KCNJ2* (Hs01876357_s1), *KCNQ1* (Hs00923522_m1), and *KCNH2* (Hs04234270_g1).

## RNA-Sequencing (RNA-Seq)

Total RNA was extracted using the RNeasy Plus mini kit (740990.250; Takara), and its concentration was measured using NanoDrop (2000/2000c Spectrophotometers, Thermo Fisher Scientific). The Illumina software package, "bcl2fastq", was used for base-calling. The raw reads were mapped to the human reference genome sequence GRCh38 using TopHat (ver. 2.1.1) combined with Bowtie2 (ver. 2.3.4.1). Differential expression analysis was performed using the edgeR package, the enriched analysis was based on Gene Ontology (GO) database, and the pathway analysis by using Parametric Gene Set Enrichment Analysis (PGSEA) package (Ge et al., 2018, 2020).

## Statistical Analysis

All values are presented as the mean value of at least three independent experiments with standard deviation (SD). Two independent groups were compared using the Student's t-test, while multiple group variance was compared using one-way analysis of variance (ANOVA), followed by Tukey's test. *P*-values $< 0.05$ were considered significant for all

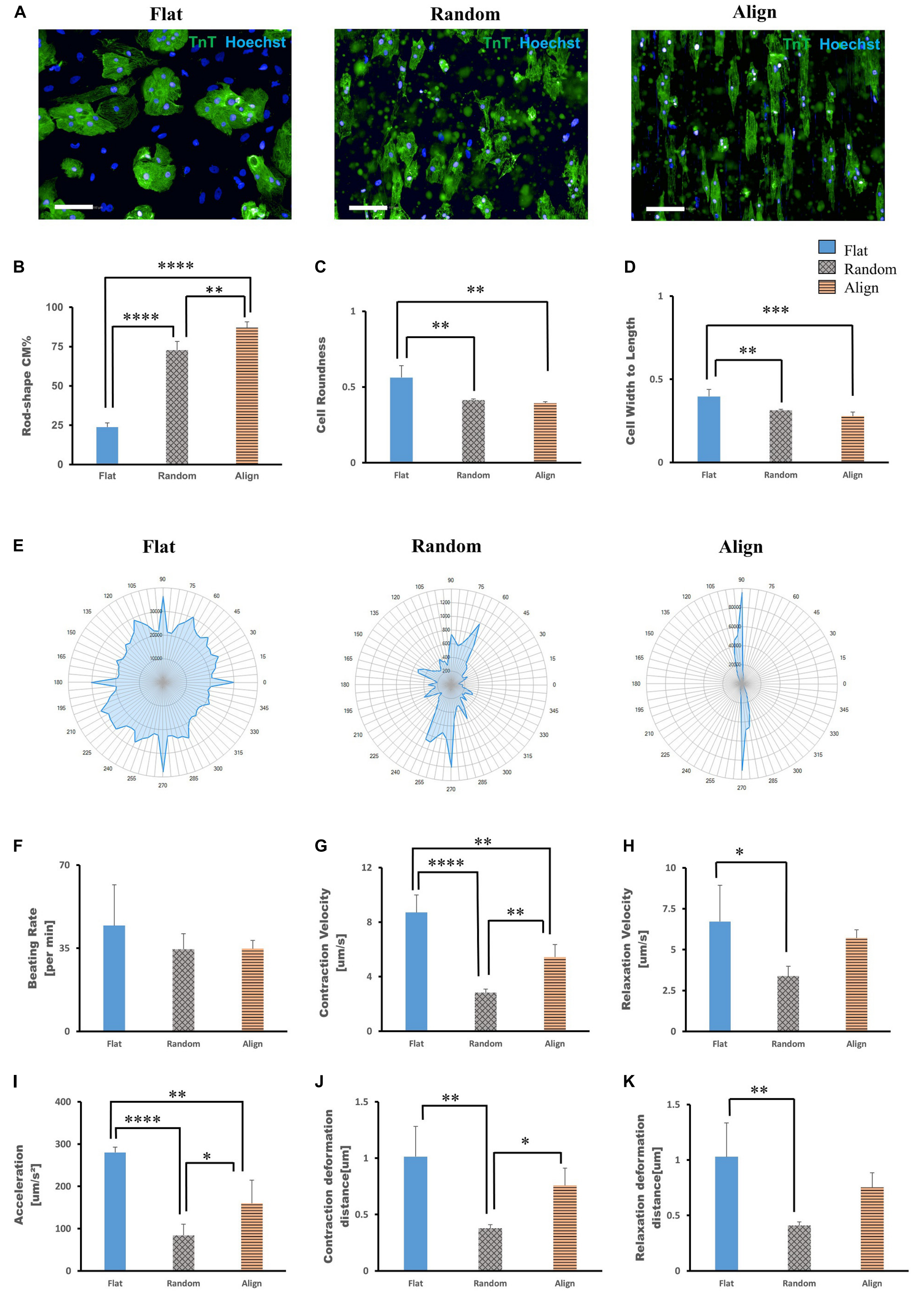

**FIGURE 1 |** Continued

**FIGURE 1 |** Morphological analysis of human induced pluripotent stem cell-derived cardiomyocytes (hiPS-CMs) on different patterns. **(A)** Immunofluorescence images of hiPS-CMs on flat, random, and aligned patterns at post-seeding day 7. hiPS-CMs were stained for cardiac troponin T (TnT, green) and the nuclei (Hoechst, blue). Scale bar, 100 μm. **(B)** Quantification of the proportion of rod-shaped hiPS-CMs on different patterns. The proportions of rod-shaped hiPS-CMs on random (72.8%) and aligned (87%) groups were both significantly higher than that in the flat group (23.7%). Error bars represent standard deviation (SD), $^{**}P < 0.01$, $^{****}P < 0.0001$; $n = 3$. **(C)** The rod-shape was evaluated via cell roundness and cell width-to-length ratio analysis. Cell roundness close to 1 meant the cell shape was circular. hiPS-CMs on the flat pattern had a value of 0.56, whereas on the random and align patterns the values were both < 0.5 (0.41 and 0.39, respectively). Error bars represent standard deviation (SD), $^{**}P < 0.01$, $^{***}P < 0.001$; $n = 3$. **(D)** Cell width-to-length ratio close to 1 suggested round shape. The cell width-to-length ratio were 0.40, 0.31, and 0.28 for the flat, random, and align patterns, respectively. Error bars represent standard deviation (SD), $^{**}P < 0.01$, $^{***}P < 0.001$; $n = 3$. **(E–K)** Motion analysis of spontaneously beating hiPS-CMs. **(E)** Representative motion vector charts of hiPS-CMs on the flat, random, and aligned patterns. The scale on the dial represents each angle of contract direction, and the blue cover area reflects the combination of the vector orientation and the ratio of vectors within the same direction. hiPS-CMs on flat pattern showed multi-directional contraction; in contrast, hiPS-CMs on aligned pattern showed bi-directional contraction along the fiber orientation. hiPS-CMs on the random pattern also showed multi-directional contraction, but they were not as widely diffused as on the flat pattern. Comparison of contractile parameters. **(F)** Beating rate, **(G)** contraction velocity, **(H)** relaxation velocity, **(I)** contractile acceleration, **(J)** contraction deformation distance, and **(K)** relaxation deformation distance of hiPS-CMs on the flat, random, and aligned patterns. Data are presented as means ± standard deviation (SD). $^{*}P < 0.05$, $^{**}P < 0.01$, $^{***}P < 0.001$, $^{****}P < 0.0001$; $n = 3$.

statistical tests. Statistical analysis was performed using JMP Pro 14.0 (SAS).

## Data Availability

RNA-Seq data were deposited in the NCBI's Gene Expression Omnibus (GEO series accession number GSE162707).

# RESULTS

## Morphological Characteristics of hiPS-CMs Cultured on Different Topographic Patterns

On post-differentiation day 28 − 30, highly purified hiPS-CMs were re-plated on three different topographic patterns: flat bottom, randomly oriented fiber matrix, and aligned fiber matrix (**Supplementary Figure 1**). After culturing for 1 week, the morphology of hiPS-CMs cultivated on different patterns showed significant differences. As shown in **Figure 1A**, the hiPS-CMs on the aligned fiber matrix were elongated and rod-shaped and were distributed along the fiber direction, whereas hiPS-CMs cultured on the other two patterns showed irregular shape and random distribution. In contrast to the hiPS-CMs on the flat bottom pattern that showed round shape and tended to aggregate, hiPS-CMs in the random group displayed multi-angular shape with smaller cell area. The cell shapes were quantified by analyzing immunofluorescence images using a high-content imaging system. Rod shape was evaluated via cell roundness and cell width-to-length ratio (**Figures 1C,D**). The cells with the morphology that met the following criteria, cell roundness ≤ 0.45 and cell width-to-length ratio of ≤ 0.5, was defined rod-shaped cell. Consequently, almost 90% and 70% hiPS-CMs were rod-shaped on the aligned and random fiber matrices, respectively; however, < 25% hiPS-CMs were rod-shaped on the flat bottom pattern (**Figure 1B**; flat(23.74 ± 2.71%) vs. random(72.76 ± 5.44%), $P < 0.0001$; flat vs. align(86.99 ± 3.77%), $P < 0.0001$; random vs. align, $P < 0.01$). To confirm our findings, we replicated the experiments using the human iPS cell line 253G1 derived cardiomyocytes. The immunofluorescence analysis showed similar results for rod-shape evaluation among the three patterns (**Supplementary Figures 2A,B**).

## Contractile Properties of hiPS-CMs

The contractile properties of hiPS-CMs were evaluated using the cell motion imaging system. In agreement with the morphology and distribution of hiPS-CMs in immunostaining images, hiPS-CMs in the aligned group showed bidirectional contraction; in contrast, hiPS-CMs in the flat and random groups performed multidirectional contraction (**Figure 1E**). hiPS-CMs cultured on these three patterns showed similar beating rates (**Figure 1F**; flat(44.65 ± 17.00/min) vs. random(34.55 ± 6.54/min) vs. align(34.8 ± 3.52/min), N.S. for among the three groups). hiPS-CMs on the flat bottom pattern showed faster contraction and relaxation velocities than those on the fiber-matrix patterns. hiPS-CMs in the random group showed the lowest contractile velocity and the smallest deformation during contraction (**Figures 1F–K**). The contractile analysis was also replicated with the 253G1 cell line of hiPS-CMs, and similar results were obtained (**Supplementary Figures 2C–H**).

## Electrophysiological Properties of hiPS-CMs

After culturing on different patterns for 1 week, the hiPS-CMs showed significant differences in contractile properties. As contraction is involved with calcium fluctuation and action potential (AP), we also analyzed calcium transient and membrane potential using the FDSS/uCELL system. The AP amplitude did not vary significantly among the three patterns (**Figures 2A,B**), although the rising and falling slopes associated with the membrane potential were highest for the hiPS-CMs on the aligned fiber matrix (**Figures 2C,D**). The AP duration at 80% repolarization (APD80) was shortened in hiPS-CMs on random and aligned fiber matrices (**Figure 2E**; flat(633.08 ± 77.44 ms) vs. random(496.20 ± 50.43 ms), $P < 0.01$; flat vs. align(497.39 ± 37.68 ms), $P < 0.01$; random vs. align, $P$ = N.S.). However, the parameters of calcium transient did not vary significantly among the hiPS-CMs cultured on these three patterns (**Figures 2F–J**), and 253G1-derived cardiomyocytes also showed similar results (**Supplementary Figures 3A–D**).

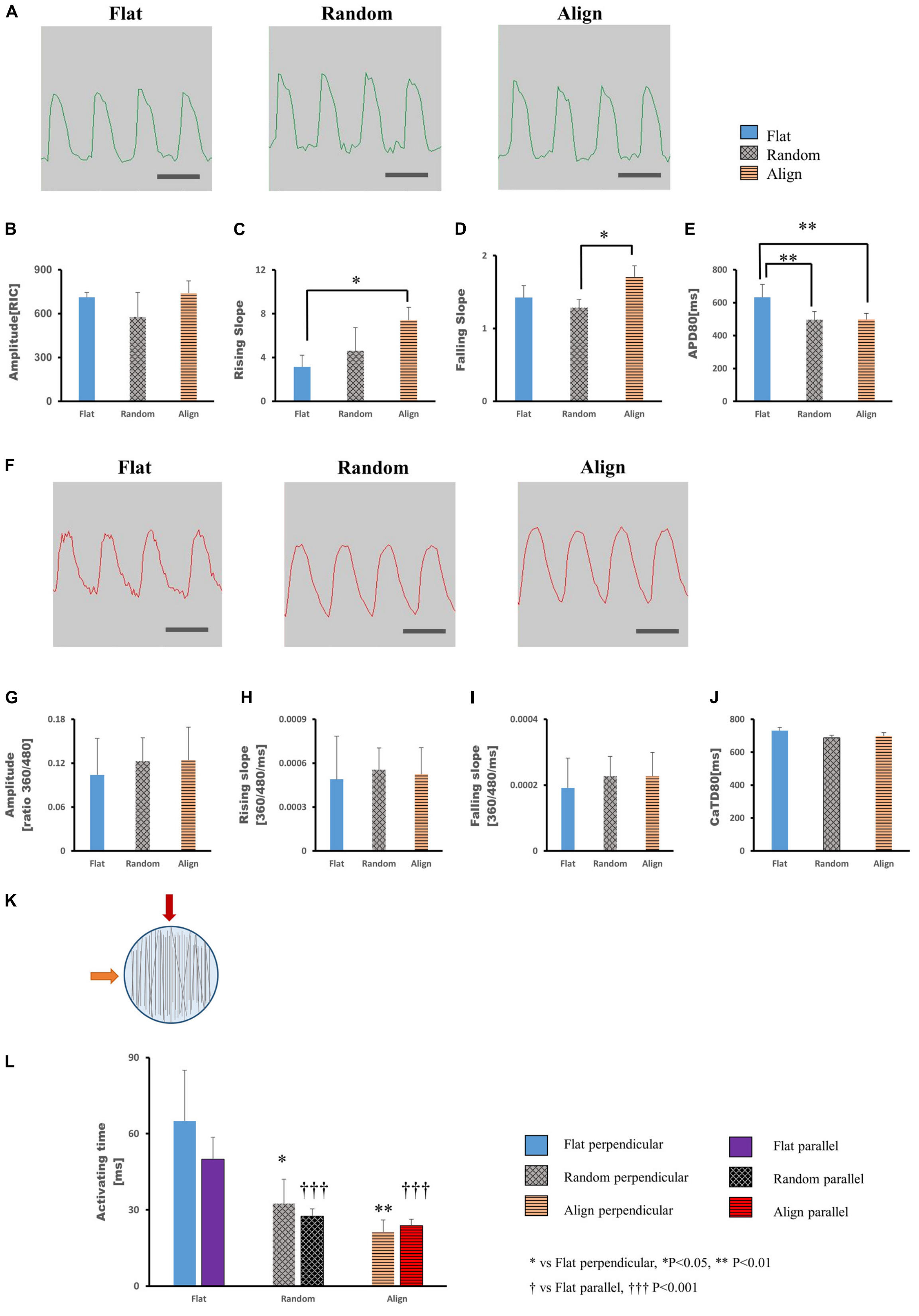

**FIGURE 2 |** Continued

**FIGURE 2 | (A–E)** Action potential of human induced pluripotent stem cell-derived cardiomyocytes (hiPS-CMs). **(A)** Representative waveforms for action potential of hiPS-CMs on flat, random, and aligned patterns. Time scale bar: 1 s. Comparison of the action potential parameters: **(B)** amplitude, **(C)** rising slope, **(D)** falling slope, and **(E)** action potential duration at 80% repolarization (APD80) of hiPS-CMs in the flat, random, and aligned groups. Data are presented as means ± standard deviation (SD). RIC, Relative Intensity Counts. $^{*}P < 0.05$, $^{**}P < 0.01$; $n = 3$. **(F–J)** Calcium transient of hiPS-CMs. **(F)** Representative waveforms for calcium transient of hiPS-CMs on flat, random, and aligned patterns. Time scale bar: 1 s. Comparison of calcium transient parameters: **(G)** amplitude, **(H)** rising slope, **(I)** falling slope, and **(J)** calcium transient duration at 80% relaxation (CaTD80) of hiPS-CMs in the flat, random, and aligned groups. The amplitude is measured by the ratio of fluorescence intensity at 360 nm and 480 nm. Data are presented as means ± standard deviation (SD). $n = 3$. The calcium transient parameters among the hiPS-CMs on different patterns did not vary significantly. **(K–L)** Evaluation of cardiac conductivity. **(K)** The schematic diagram for pacing direction. Solid red arrow indicates pacing parallel to the fiber orientation in the aligned pattern. The solid orange arrow indicates pacing perpendicular to the aligned fiber orientation. Parallel and perpendicular are relative to the fiber orientation in the aligned pattern, and accordingly, pacing at the same position in the flat and random groups. The light blue circle represents the well area; black lines represent nanofibers. **(L)** The conduction activating time of hiPS-CMs on different patterns. Irrespective of pacing parallel or perpendicular to the aligned fiber orientation, the activating time of hiPS-CMs in the random and aligned groups were both shorter than that in the flat group. In addition, on the same pattern, activating time did not vary when pacing along these two mutually vertical directions. Data are presented as means ± standard deviation (SD). $^{*}P < 0.05$, $^{**}P < 0.01$ for flat vs. random vs. aligned when pacing perpendicular to the aligned fiber orientation. $^{\dagger\dagger\dagger}P < 0.001$ for flat vs. random vs. aligned group when pacing parallel to the aligned fiber orientation. $n = 3$.

To investigate whether specific cell arrangement affected the conductivity, we assessed optical membrane potential imaging using the MiCAM02 imaging system. Considering the specific cell distribution on the aligned pattern, we performed pacing parallel (longitudinal) or perpendicular (transverse) to the orientation of the aligned fibers (**Figure 2K**) and at the same positions in the random and flat groups. As shown in **Figure 2L** (longitudinal: flat(50 ± 8.66 ms) vs. random(27.5 ± 2.89 ms), $P < 0.001$; flat vs. align(23.75 ± 2.5 ms), $P < 0.001$; random vs. align, P = N.S.; transverse: flat(65 ± 20 ms) vs. random(32.5 ± 9.57 ms), $P < 0.05$; flat vs. align(21.25 ± 4.79 ms), $P < 0.01$; random vs. align, P = N.S.), the activating time of hiPS-CMs on the fiber-matrix patterns was significantly shorter than that of hiPS-CMs on the flat bottom matrix, both along with the longitudinal and transverse directions. The longitudinal and transverse activating time in the same pattern did not vary significantly.

## Cardiac Gene Expression

Despite the lack of a standard gene expression profile for defining the mature-like hiPS-CMs, we assessed the expression of several vital cardiac genes to determine changes at the molecular level in hiPS-CMs cultured on different substrates. α-myosin heavy chain (*MYH6*) and β-myosin heavy chain (*MYH7*) are well-known mature relevant cardiac genes. As shown in **Figure 3A**, *MYH7* expression and the ratio of *MYH7* to *MYH6* expression was highest in the aligned group. Expression of *MYL2*, a ventricular cardiac gene, in the aligned group was significantly higher than that in the flat group. The expression of genes involved in calcium handling, such as sarco/endoplasmic reticulum Ca2 + -ATPase (*SERCA2A*) (*ATP2A2*), and that of L-type calcium channel (*CACNA1C*) did not show significant difference among these three groups. The expression of genes related to cardiac AP, such as fast $Na^{+}$ ion channel (*SCN5A*), $K^{+}$ inward rectifier (*KCNJ2*), ether-a-go-go-related protein 1 (*KCNH2*), and $K^{+}$ slow delayed rectifier channel (*KCNQ1*) did not differ among these three groups. The gap junction protein GJA1 was highly expressed in the fiber matrix pattern groups. Connexin-43 (Cx-43) mostly accumulated in the intercalated disks in the random or aligned group (**Figure 3B**), whereas its distribution in the flat group was not clear.

## Morphological and Functional Changes of hiPS-CMs After Reseeding on the Same Patterns

For determining whether the above morphological and functional changes in hiPS-CMs were induced by the culture substrates and disappeared after withdrawing the fiber substrates or were permanently encoded in the hiPS-CMs as inherent properties, hiPS-CMs were harvested from each pattern, replated onto the flat matrix, and incubated for another week. As shown in **Figure 4A**, after culturing on the flat bottom plates for one more week, the ratio of rod-shaped hiPS-CMs derived from fiber matrix patterns was still higher than that in the flat group, although the difference was not significant (**Figure 4B**; flat (16.09 ± 1.44%) vs. random(25.27 ± 5.23%) vs. align(24.39 ± 9.29%), P = N.S. for among the three groups).

Membrane potential and calcium transient were also similar in terms of the wave amplitude, rising/falling slopes, and wave duration (**Figures 4C–L**). Interestingly, the assessment of cardiac gene expression showed that hiPS-CMs cultivated on different patterns partially retained the genetic differences (**Figure 5**). hiPS-CMs dissociated from aligned fiber matrix showed the highest expression of structural cardiac genes, *MYH7* and *MYL2*, and high expression ratio of *MYH7* to *MYH6*. In addition, the expression of *SCN5A* and *KCNJ2* increased in hiPS-CMs pre-cultured on the aligned pattern, whereas the expression levels of *ATP2A2, CACNA1C, GJA1, KCNH2*, and *KCNQ1* did not differ among the hiPS-CMs cultivated on different patterns. Furthermore, the random and align patterns-treated samples showed a higher ratio of *MYH7*/*MYH6* than the flat group at 2 weeks post separation (**Supplementary Figure 5**, flat(1 ± 0) vs. random(3.026 ± 0.11), $P < 0.01$; flat(1 ± 0) vs. align(3.410 ± 0.92), $P < 0.01$; random vs. align, P = N.S.). We also conducted the cardiac gene expression analysis using 253G1 hiPS-CMs. Similarly, hiPS-CMs cultured on the aligned pattern for 1 week showed significantly higher levels of *MLC2*, *MYH7*, and *GJA1* than the flat and random groups did. Furthermore, *MYL7*, *ATP2A2*, and *SCN5A* also showed significantly higher expression compared to flat and random groups (**Supplementary Figure 4A**). After replating on non-scaffold (flat bottom) patterns for 1 week, consistent with 201B7 results, there is a significantly higher expression of MYL2 and

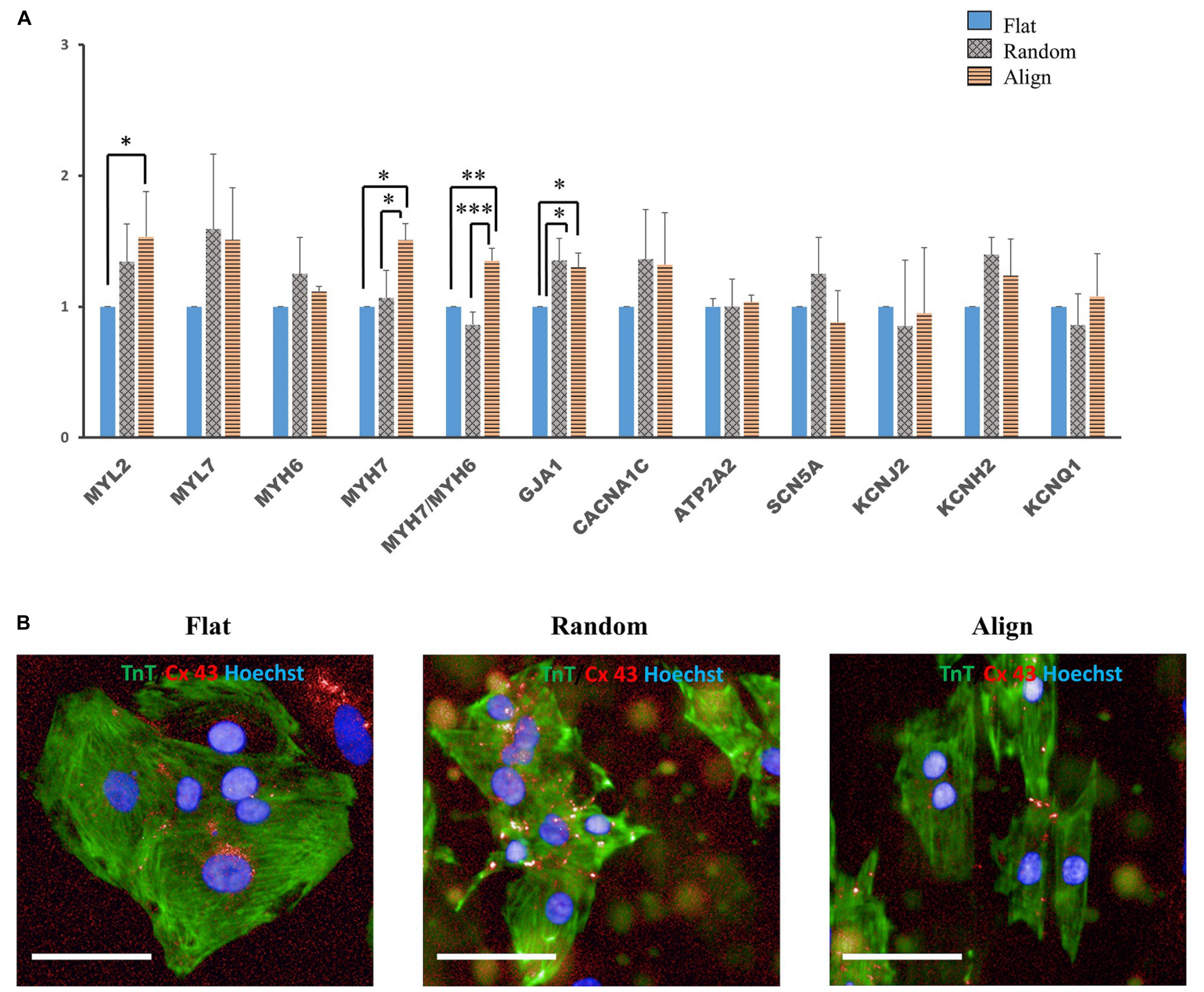

**FIGURE 3 | (A)** Cardiac gene expression. Comparison of the expression of cardiac structural genes such as myosin light chain 2 (*MYL2*), myosin light chain 7 (*MYL7*), α-myosin heavy chain (*MYH6*), β-myosin heavy chain (*MYH7*), and gap junction connexin-43 (*GJA1*), calcium handling-associated genes such as L-type calcium channel (*CACNA1C*) and Sarco/endoplasmic reticulum Ca2 + -ATPase (*SERCA2*) (*ATP2A2*), conduction-related genes such as fast sodium ($Na^+$) ion channel (*SCN5A*) and potassium ($K^+$) ion channels, including $K^+$ inward rectifier (*KCNJ2*), ether-a-go-go-related protein 1 (*KCNH2*), and $K^+$ slow delayed rectifier channel (*KCNQ1*) of human induced pluripotent stem cell-derived cardiomyocytes (hiPS-CMs) on the flat, random, and aligned patterns. The expression levels of each gene were analyzed using quantitative reverse transcription-polymerase chain reaction (qRT-PCR) and normalized to 18S rDNA expression. $^*P < 0.05$, $^{**}P < 0.01$, $^{***}P < 0.001$; $n = 3$. **(B)** Distribution of gap junction connexin-43 in hiPS-CMs. Immunofluorescence images of gap junction localization in hiPS-CMs on the flat, random, and aligned patterns. Images were obtained using a high content imaging system. hiPS-CMs were immunostained with TnT (green). The light red punctate stain represents connexin-43 (Cx-43). Cx-43 showed intercellular distribution in hiPS-CMs of the random and aligned groups, whereas, Cx-43 expression was negligible and was found at the intercellular spaces or at the cell borders in the flat group. Scale bar, 50 μm.

MYH7 in the align group than in the flat and random groups (**Supplementary Figure 4B**).

## Differential Gene Expression and Enriched Pathway Analysis

To get a comprehensive understanding of the genome-wide expression dynamics under topographic stimulation and, more importantly, to obtain insights into the underlying mechanisms of the developmental effects driven by topographic stimuli, we performed RNA-seq of hiPS-CMs after culturing on flat, random, or align patterns for 1 week. Principal component analysis (PCA) revealed that the most variance between the RNA-seq samples from flat and random patterns **(Figure 6A**). Moreover, the flat group samples occupied most of the enrichment gene expression, as shown by the Differentially expressed genes(DEGs) detected with the 'DESeq2' package and the hierarchical clustering (**Supplementary Figure 6A**). Analysis of the enriched DEGs based on GO biological processes revealed that the upregulated genes in the flat group were mainly related to the regulation of cell movement, including extracellular matrix organization, cell adhesion, and cell migration. Well-known cardiac maturation

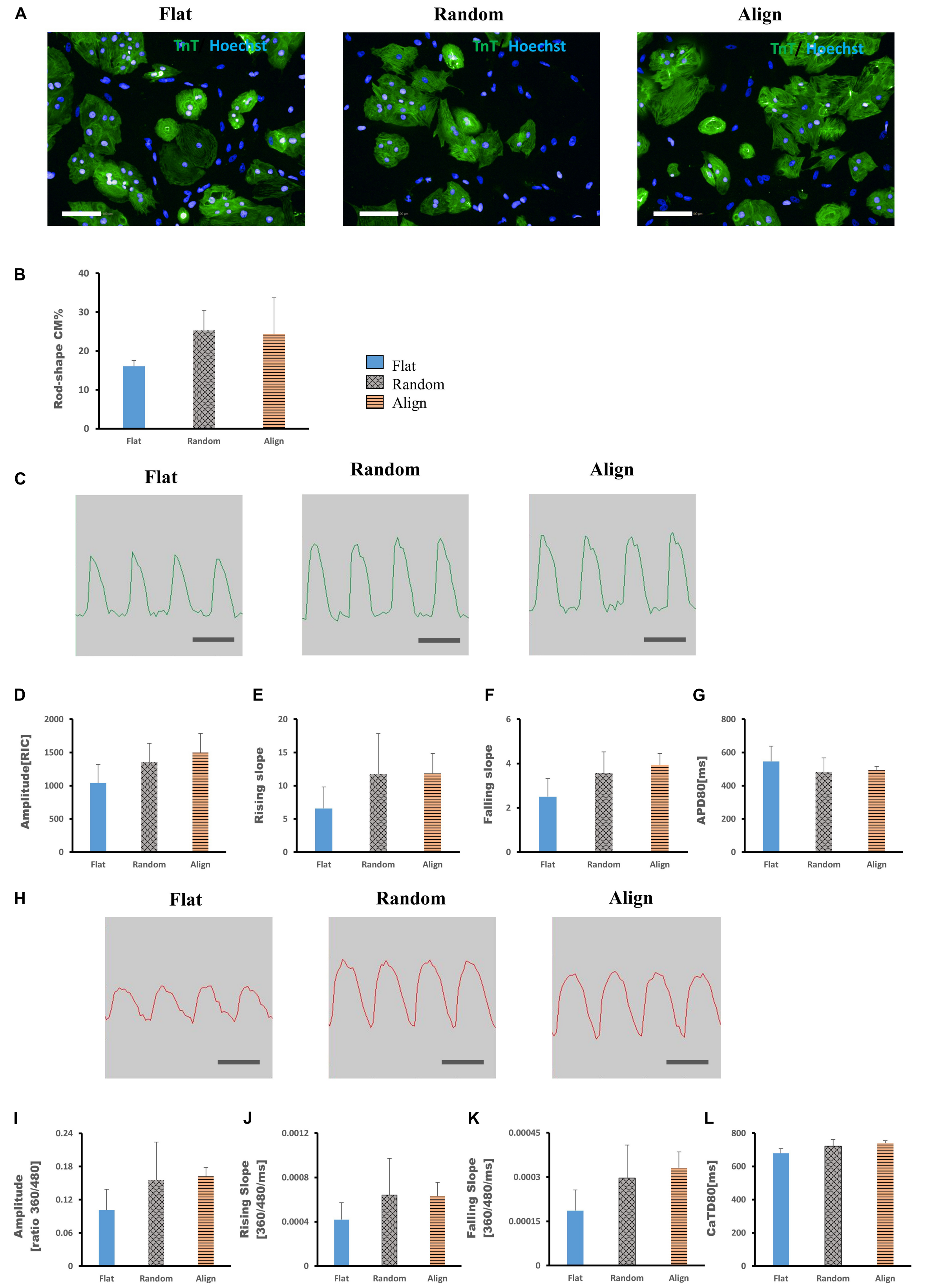

**FIGURE 4 |** Continued

**FIGURE 4 | (A,B)** Morphological changes of human induced pluripotent stem cell-derived cardiomyocytes (hiPS-CMs) after replating on non-scaffold (flat bottom) patterns. **(A)** hiPS-CMs pre-cultured on different patterns were individually replated on the flat pattern and cultured for one more week. Immunofluorescence images of hiPS-CMs pre-cultured on the flat, random, and aligned patterns. hiPS-CMs were stained for cardiac troponin T (TnT, green) and the nuclei (Hoechst, blue); scale bar, 100 μm. **(B)** Quantification of the proportion of rod-shaped hiPS-CMs. The proportion of rod-shaped hiPS-CMs did not vary significantly among these three groups. Error bars represent standard deviation (SD); data are presented as means ± SD; $n = 3$. **(C–G)** Action potential of hiPS-CMs after replating on non-scaffold (flat bottom) patterns. **(C)** Representative waveforms for action potential of hiPS-CMs pre-cultured on the flat, random, and aligned patterns. Time scale bar: 1 s. Action potential parameters: **(D)** amplitude, **(E)** rising slope, **(F)** falling slope, and **(G)** action potential duration at 80% repolarization (APD80) of hiPS-CMs did not vary significantly among these three groups. RIC, Relative Intensity Counts. Data are presented as means ± SD. $n = 3$. **(H–L)** Calcium transient of hiPS-CMs after replating on non-scaffold (flat bottom) patterns. **(H)** Representative waveforms for calcium transient of hiPS-CMs pre-cultured on the flat, random, and aligned patterns. Time scale bar: 1 s. Calcium transient parameters: **(I)** amplitude, **(J)** rising slope, **(K)** falling slope, and **(L)** calcium transient duration at 80% relaxation (CaTD80) of hiPS-CMs did not vary significantly among these three groups. The amplitude is measured by the ratio of fluorescence intensity at 360 nm and 480 nm. Data are presented as means ± standard deviation (SD). $n = 3$.

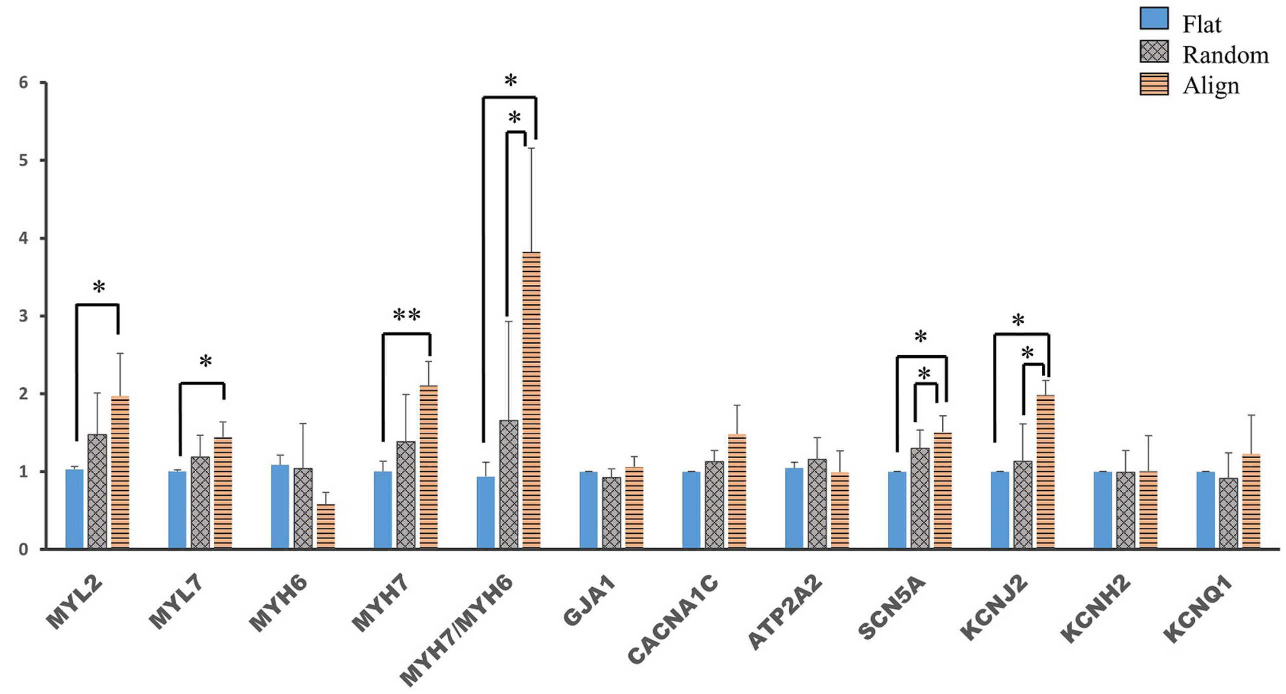

**FIGURE 5 |** Cardiac gene expression of human induced pluripotent stem cell-derived cardiomyocytes (hiPS-CMs) after replating on non-scaffold (flat bottom) patterns. Cardiac gene expression was analyzed after the hiPS-CMs were replated on non-scaffold patterns and cultured for one more week. Comparison of the expression of cardiac structural genes such as myosin light chain 2 (*MYL2*), myosin light chain 7 (*MYL7*), α-myosin heavy chain (*MYH6*), β-myosin heavy chain (*MYH7*), and gap junction connexin-43 (*GJA1*), calcium handling-related genes such as L-type calcium channel (*CACNA1C*) and sarco/endoplasmic reticulum Ca2 + -ATPase (*SERCA2*) (*ATP2A2*), conduction-related genes such as fast sodium ($Na^+$) ion channel (*SCN5A*) and potassium ($K^+$) ion channels, including $K^+$ inward rectifier (*KCNJ2*), ether-a-go-go-related protein 1 (*KCNH2*), and $K^+$ slow delayed rectifier channel (*KCNQ1*) in hiPS-CMs pre-cultured on flat, random, and aligned patterns. Each gene expression level was normalized to *18S* rDNA expression. $^*P < 0.05$, $^{**}P < 0.01$; $n = 3$.

markers (Ronaldson-Bouchard et al., 2018), such as MYH7 and TNNI3, were found to be significantly upregulated in the align group, which was consistent with the qPCR analysis results. Moreover, cardiac structural (*MLC2*, *TNNT2*, *GJA1*) and calcium handling relevant genes (*CASQ2*, *CAMK2B*, *CAV3*) also showed a higher expression in align group than that in the flat group (**Figure 6B**). The most upregulated gene sets in the align group included those related to cardiac development and heart morphogenesis pathways, negative regulation of binding, and microtubule-based processes (**Figure 6C**). In contrast, Members of the keratin(KRT) gene family, which play a role in cell movement, were found to be involved in the relatively downregulated-gene enriched pathways.

## DISCUSSION

In this study, we generated a well-organized and aligned hiPS-derived cardiac construct by culturing hiPS-CMs on anisotropic fiber matrix, which geometrically mimics the native heart tissue in only few days. Several strategies were used for constructing anisotropic cardiac tissues, ranging from the design of structures (concave-convex mode and oriented fiber like matrix) to the use of different types of substrate materials (polydimethylsiloxane, silk fibroin, and electrospun fibrous) (Stoppel et al., 2015; Han et al., 2016; Pilarczyk et al., 2016). Compared to the anisotropic microgroove modes, the nanofiber patterns used in this study maintained the intercellular space and increased intercellular

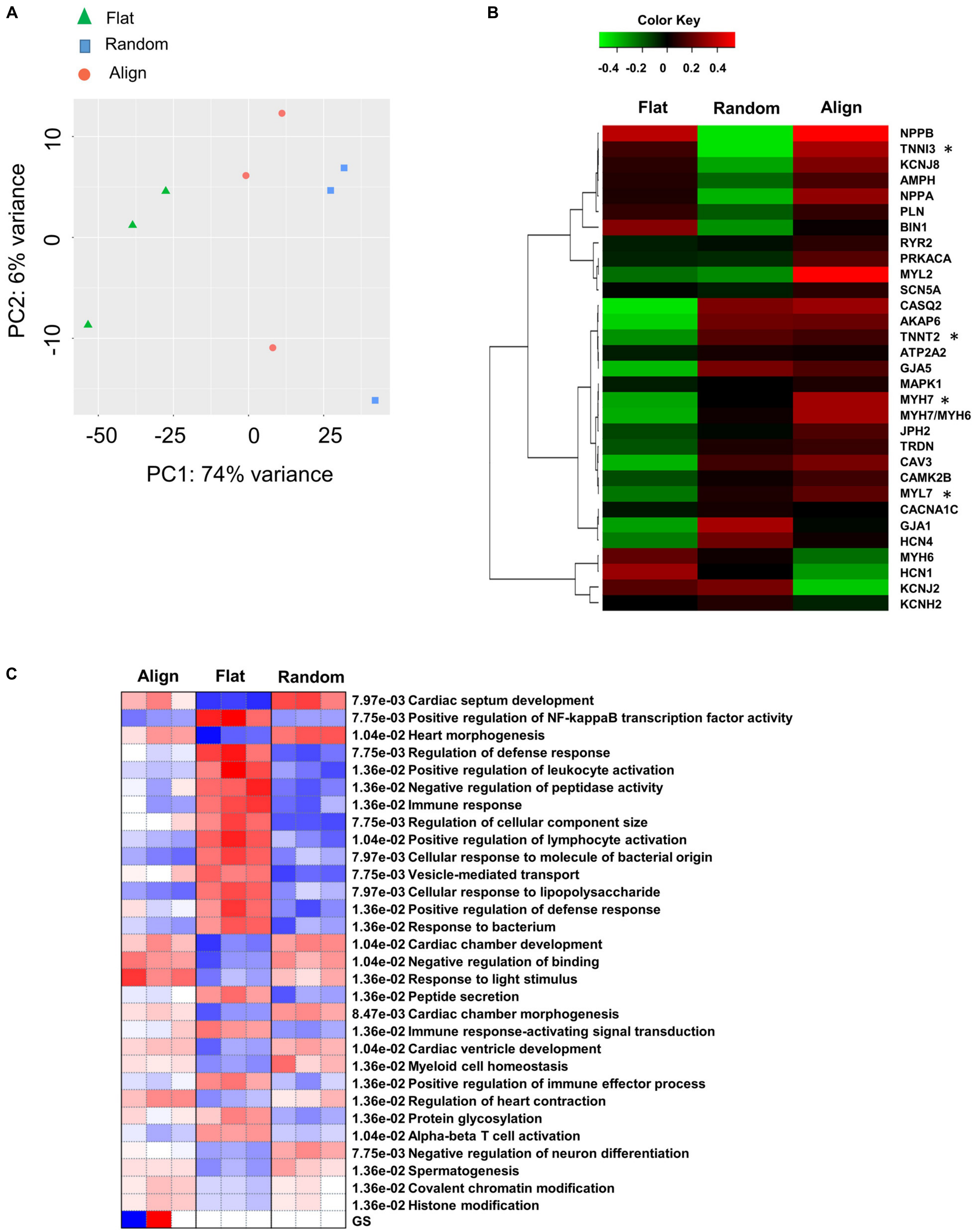

**FIGURE 6 |** Differential gene expression. **(A)** Principal component analysis (PCA) for flat, random, and align groups. Green triangles, blue squares, and pink circles represent the flat, random, and align groups, respectively. False discovery rate (FDR) < 0.05 (*n* = 3). **(B)** Heatmap for cardiac mature relevant genes on flat, random, and align groups. The data are represented by mean values for three biological replicate samples for each group. *FDR < 0.05. Cut-off Z score: -2 < z < 2 (*n* = 3). **(C)** Pathways analysis on flat, random, and align groups using the PGSEA algorithm. Pathway significance cut-off FDR < 0.05 (*n* = 3).

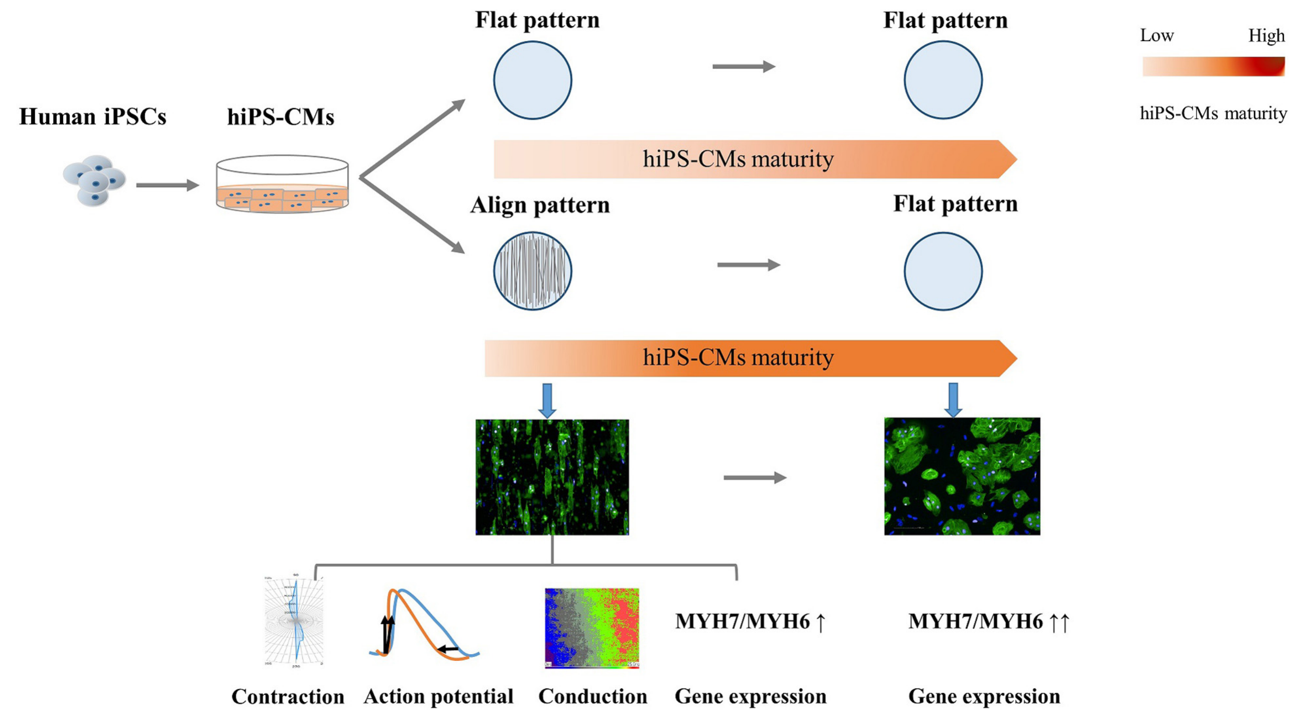

**FIGURE 7 |** Schema for the present study. Human induced pluripotent stem cell-derived cardiomyocytes (hiPS-CMs) cultivated on aligned pattern showed more mature-like properties than that on non-scaffold (flat) pattern, including elongated rod shape, bidirectional contraction, efficient action potential, faster conduction velocity, and elevated cardiac maturity-related gene expression. The morphological and electrophysiological advantages diminished once the hiPS-CMs were freed from the aligned scaffold, although the molecular developmental properties were preserved.

connection, which is similar to the microenvironment of native heart tissue. Furthermore, hiPS-CMs grown on the fiber substrates tightly integrate with the nanofibers over time, which may decrease contraction movement. However, it is noteworthy that the motion analysis of contraction kinetic parameters was the mean value of measurements from every direction and not along one of the specific orientations. Considering this, the contraction velocity along the fiber orientation may be faster in the align group than that in the flat group. Regarding energy consumption, hiPS-CMs on the aligned pattern showed bidirectional contractions, which may reduce energy loss. In contrast, the hiPS-CMs in the flat and random groups showed multidirectional contractions. Furthermore, upregulation of the mature isoforms of the sarcomeric gene *MYH7* in the aligned hiPS-CMs suggests that the bidirectional contractions of hiPS-CMs may be a mechanical stimulation that contributes to hiPS-CM maturation.

Cardiac contraction is accompanied by calcium cycling in each cardiomyocyte, and the immaturity of hiPS-CMs is manifested in low calcium release and reuptake kinetics (Denning et al., 2016). However, the hiPS-CMs on the three patterns did not differ significantly in calcium transient or the expression of calcium handling-associated genes such as *ATP2A2* and *CACNA1C*, indicating that relative to the morphological changes, the development of calcium transient in hiPS-CMs required time and was negligibly affected by matrix geography. AP is one of the most important electrophysiological properties of multiple ion currents. hiPS-CMs showed lower upstroke velocity of AP and longer action potential duration (APD) than those of adult ventricular cardiomyocytes due to the low density of functional mature ion channels (Denning et al., 2016; Kolanowski et al., 2017; Scuderi and Butcher, 2017). In our study, the upslope of AP in hiPS-CMs of the aligned group was more striking than that of the flat group; furthermore, the APD80 of the hiPS-CMs of the aligned group or random group was significantly shorter than that of the flat group. Interestingly, the expression of the cardiac AP-related genes, namely, *SCN5A*, *KCNJ2*, *KCNH2*, and *KCNQ1*, did not show the corresponding difference. Based on these results, we speculated that at least for cardiac AP, the aligned cell distribution close relative to the change of electrophysiological properties of hiPS-CMs.

Cardiac conductivity, another essential property of CMs, is also an important parameter for estimating hiPS-CM maturation. The fatal cardiac arrhythmia caused by cardiac infarction or any other induced myocardial damages is usually attributed to cardiac conduction abnormalities, which is partly due to the disorganization of cardiac cells in the injured area. With the exception of the low density of ion channels, deficiency of conductivity in immature hiPS-CMs is due to the negligible expression of gap junctions and the distribution of gap junctions at the cell circumference rather than at the intercalated disks (Denning et al., 2016). In the present study, the cardiac activating time of hiPS-CMs in the scaffold patterns was significantly shorter than that in the flat pattern, suggesting that the conductivity of hiPS-CMs on the aligned or random pattern was faster than that on the flat pattern. Immunostaining images showed that most Cx-43 was located at the intercalated disks of hiPS-CMs on the random and aligned patterns, whereas, the negligible amount of Cx-43 was observed on the flat pattern. In agreement with the result of Cx-43 immunostaining, the expression of the gap junction Cx-43-encoding gene, *GJA1*, in both the randomized and aligned groups was higher than that in the flat group. The above results indicate that the acceleration of cardiac conductivity may benefit from the accumulation of more gap junctions at the intercellular locations. Interestingly, the conduction velocities parallel and perpendicular to the fiber orientation in the aligned substrate did not differ. As the CMs in the ventricular wall are not uniformly aligned, it is possible that overlapping CMs laminate with the aligned myocytes layer by layer (Streeter et al., 1969; LeGrice et al., 1995). It is noteworthy that CM orientation affects both electrical activation and excitation propagation (Hooks et al., 2002). In addition to CMs, aligned cell arrangement also affects the induction of cardiac differentiation (Pijnappels et al., 2008). Here, the similar conduction velocities parallel and perpendicular to the CM orientation may be attributed to the immature hiPS-CMs or non-CMs and also to the heterogeneous distribution of the gap junctions.

Although a previous study suggested that the cell shape has profound effects on the function and molecular expression in cardiomyocytes (Haftbaradaran Esfahani et al., 2019), the extent to which the benefits—driven by morphological changes—on hiPS-CMs last remained unclear. Our study first investigated the memory of iPS-CMs for the aligned pattern-induced facilitation of maturity. The cells were removed from the different substrates and were then replated on the flat pattern for an additional week. Unfortunately, hiPS-CMs pre-cultured on the aligned matrix were round-shaped and randomly oriented, similar to the other two groups. Furthermore, AP and calcium transient did not differ among these three groups. However, the restoration of the morphological and functional changes indicates that cell orientation significantly affects the electrical properties of hiPS-CMs. Surprisingly, cardiac gene expression showed that hiPS-CMs pre-cultured on the aligned pattern were considerably more mature than those derived from the flat group and that the difference was even more significant than that in the pre-culture stage. Thus, the round shape and the change in AP were not because of the degeneration of hiPS-CMs; conversely, hiPS-CM maturation was still underway. In addition, the hiPS-CMs pre-cultured on the aligned pattern somehow retained the memory of the beneficial effects from topographic induced maturation, and maintained during development even without the fiber matrix.

To obtain insights into the underlying molecular pathways/signaling involved in the facilitation of hiPS-CM maturation driven by specific topographic stimuli, we performed RNA-seq on hiPS-CM samples after different patterns culturing. The RNA-seq samples of the flat group occupied most of the enrichment gene expression landscape (**Supplementary Figure 6A**), with the related pathways being mostly involved in the regulation of cell movement. This finding suggested that, without the scaffold support, the cells could induce the self-synthesis of the extracellular matrix; thus, cells on the flat pattern may induce the facilitation of cell proliferation by controlling the extracellular matrix remodeling process (Cui et al., 2018). Moreover, the hierarchical clustering results revealed that several cardiac mature markers had a higher expression in the align group (**Figure 6B**). The switch of predominant contractile isoforms between MYH6/MYH7 and TNNI2/TNNI3 is a hallmark of cardiomyocyte maturation (Taegtmeyer et al., 2010; Ames et al., 2013). RNA-seq data revealed significantly elevated expression of *MYH7* and *TNNI3* in the align group samples. In addition to providing substantial cell developmental molecular information, the differential GO pathway enrichment among hiPS-CM samples from flat, random, and align patterns also provided detailed insights on the underlying mechanisms involved in topographic stimuli-derived maturation of hiPS-CMs. The most upregulated gene sets related pathways in the align group were closely related to *FOS* and *JUN* families, which are both known to be associated with the regulation of stimuli-induced cell responses (Singal et al., 2009). Similar enriched pathways have also been seen in the random group samples; thus, it could also be related to substrate stimulation. Upon overlapping the upregulated genes in the align pattern compared to the flat or random group, six genes were found to be specifically upregulated in align vs. flat (**Supplementary Figure 6B**, including *F13A1*, *XIRP2*, *TTC29*, *PTPRH*, *TULP1*, and *LINC00702*). In particular, Protein Tyrosine Phosphatase Receptor Type H (PTPRH) was identified, which is a member of the protein tyrosine phosphatase (PTP) family that is involved in the regulation of various cellular processes including cell differentiation and mitotic cycle (O'Leary et al., 2016). Naturally, during heart development, CMs experience a transition from cell proliferation to cellular hypertrophy. Based on our findings, the aligned topographic cell arrangement may be related to the regulation of CM maturation by modulating the cell cycle. Therefore, it is relevant to investigate the underlying signaling involved in the regulation of cell growth that is driven by the aligned cell organization.

## CONCLUSION

In summary, in the present study, we constructed geometric native-like hiPS-cardiac tissue by culturing cardiomyocytes on well-oriented nanofibers. In addition to morphological improvement, which involved a change from the round irregular shape and random distribution to elongated rod shape and good organization, respectively, the CMs displayed functional improvements, including more efficient AP and faster conduction velocity (**Figure 7**). The "passive" rod-shaped hiPS-CMs were not equivalent to the adult ventricular cardiomyocytes, and these morphological changes diminished after withdrawing the exterior support. This may be analogous to a case where an "infant" wearing "adult clothes" looks mature; however, the "adult clothes," i.e., rod shape and alignment, facilitate hiPS-CM maturation. In other words, in addition to the fact that mature CMs are more functional than their immature counterparts, the functional environment also promotes CM maturation.

Importantly, these functional improvements persist during hiPS-CM development even without exterior support. This may also circumvent the concerns regarding the quality of delivered isolated cells, which may be used instead of transplanting an intact tissue, thereby providing more options for cell therapy.

## DATA AVAILABILITY STATEMENT

RNA-Seq data were deposited in the NCBI's Gene Expression Omnibus, and are accessible through GEO Series accession number GSE162707 (https://www.ncbi.nlm.nih.gov/geo/query/acc.cgi?acc=GSE162707).

## ETHICS STATEMENT

The studies involving human participants were reviewed and approved by the Institutional Review Board of Osaka University [Approval number 13254 (829-1)-3]. The patients/participants provided their written informed consent to participate in this study.

## AUTHOR CONTRIBUTIONS

JL and J-KL conceptualized the study, designed and performed the experiments, processed the data, and wrote the manuscript. KeM, YK, HN, ST, HY, KiM, and YS participated in the analysis and reviewed the manuscript. YS supervised the study. All the authors qualified for authorship and approved the final version of the manuscript, contributed to the article, and approved the submitted version.

## FUNDING

The study was partially supported by the Agency for Medical Research and Development, AMED (JP17bm0804008h0001 to J-KL), JSPS KAKENHI (Grant Number JP18H03517), and Co-Create Knowledge for Pharma Innovation with Takeda (COCKPI-T®) Funding.

## ACKNOWLEDGMENTS

We are grateful to Mayuko Matsushima for technical assistance and appreciate Teruki Yokoyama, Akira Yoshida, Taku Sakai, Aya Hino, and FY Ko for sharing valuable experimental experiences and professional suggestions. We would like to thank Editage (www.editage.com) for English language editing.

## SUPPLEMENTARY MATERIAL

The Supplementary Material for this article can be found online at: https://www.frontiersin.org/articles/10.3389/fcell.2021.591754/full#supplementary-material

## REFERENCES

Ames, E. G., Lawson, M. J., Mackey, A. J., and Holmes, J. W. (2013). Sequencing of mRNA identifies re-expression of fetal splice variants in cardiac hypertrophy. *J. Mol. Cell. Cardiol.* 62, 99–107. doi: 10.1016/j.yjmcc.2013.05.004

Anderson, D., Self, T., Mellor, I. R., Goh, G., Hill, S. J., and Denning, C. (2007). Transgenic enrichment of cardiomyocytes from human embryonic stem cells. *Mol. Ther.* 15, 2027–2036. doi: 10.1038/sj.mt.6300303

Chun, Y. W., Voyles, D. E., Rath, R., Hofmeister, L. H., Boire, T. C., Wilcox, H., et al. (2015). Differential responses of induced pluripotent stem cell-derived cardiomyocytes to anisotropic strain depends on disease status. *J. Biomech.* 48, 3890–3896. doi: 10.1016/j.jbiomech.2015.09.028

Cui, M., Wang, Z., Bassel-Duby, R., and Olson, E. N. (2018). Genetic and epigenetic regulation of cardiomyocytes in development, regeneration and disease. *Development* 145:dev171983. doi: 10.1242/dev.171983

Denning, C., Borgdorff, V., Crutchley, J., Firth, K. S. A., George, V., Kalra, S., et al. (2016). Cardiomyocytes from human pluripotent stem cells: from laboratory curiosity to industrial biomedical platform. *Biochim. Biophys. Acta* 1863, 1728–1748. doi: 10.1016/j.bbamcr.2015.10.014

Engels, M. C., Rajarajan, K., Feistritzer, R., Sharma, A., Nielsen, U. B., Schalij, M. J., et al. (2014). Insulin-like growth factor promotes cardiac lineage induction in vitro by selective expansion of early mesoderm. *Stem Cells* 32, 1493–1502. doi: 10.1002/stem.1660

Ge, S. X., Jung, D., and Yao, R. (2020). ShinyGO: a graphical gene-set enrichment tool for animals and plants. *Bioinformatics* 36, 2628–2629. doi: 10.1093/bioinformatics/btz931

Ge, S. X., Son, E. W., and Yao, R. (2018). iDEP: an integrated web application for differential expression and pathway analysis of RNA-Seq data. *BMC Bioinform.* 19:534. doi: 10.1186/s12859-018-2486-6

Gersh, B. J., Sliwa, K., Mayosi, B. M., and Yusuf, S. (2010). Novel therapeutic conceptsThe epidemic of cardiovascular disease in the developing world: global implications. *Eur. Heart J.* 31, 642–648. doi: 10.1093/eurheartj/ehq030

Haftbaradaran Esfahani, P., ElBeck, Z., Sagasser, S., Li, X., Hossain, M. B., Talukdar, H. A., et al. (2019). Cell shape determines gene expression: cardiomyocyte morphotypic transcriptomes. *Basic Res. Cardiol.* 115:7. doi: 10.1007/s00395-019-0765-7

Han, J., Wu, Q., Xia, Y., Wagner, M. B., and Xu, C. (2016). Cell alignment induced by anisotropic electrospun fibrous scaffolds alone has limited effect on cardiomyocyte maturation. *Stem Cell Res.* 16, 740–750. doi: 10.1016/j.scr.2016.04.014

Hooks, D. A., Tomlinson, K. A., Marsden, S. G., LeGrice, I. J., Smaill, B. H., Pullan, A. J., et al. (2002). Cardiac microstructure: implications for electrical propagation and defibrillation in the heart. *Circ. Res.* 91, 331–338. doi: 10.1161/01.res.0000031957.70034.89

Ichimura, H., and Shiba, Y. (2017). Recent progress using pluripotent stem cells for cardiac regenerative therapy. *Circ. J.* 81, 929–935. doi: 10.1253/circj.CJ-17-0400

Iseoka, H., Miyagawa, S., Fukushima, S., Saito, A., Masuda, S., Yajima, S., et al. (2018). Pivotal role of non-cardiomyocytes in electromechanical and therapeutic potential of induced pluripotent stem cell-derived engineered cardiac tissue. *Tissue Eng. Part A* 24, 287–300. doi: 10.1089/ten.TEA.2016.0535

Kim, D.-H., Kshitiz, Smith, R. R., Kim, P., Ahn, E. H., Kim, H.-N., et al. (2012). Nanopatterned cardiac cell patches promote stem cell niche formation and myocardial regeneration. *Integr. Biol. (Camb.)* 4, 1019–1033. doi: 10.1039/c2ib20067h

Kolanowski, T. J., Antos, C. L., and Guan, K. (2017). Making human cardiomyocytes up to date: derivation, maturation state and perspectives. *Int. J. Cardiol.* 241, 379–386. doi: 10.1016/j.ijcard.2017.03.099

LeGrice, I. J., Smaill, B. H., Chai, L. Z., Edgar, S. G., Gavin, J. B., and Hunter, P. J. (1995). Laminar structure of the heart: ventricular myocyte arrangement and connective tissue architecture in the dog. *Am. J. Physiol.* 269, H571–H582. doi: 10.1152/ajpheart.1995.269.2.H571

Nakanishi, H., Lee, J.-K., Miwa, K., Masuyama, K., Yasutake, H., Li, J., et al. (2019). Geometrical patterning and constituent cell heterogeneity facilitate electrical conduction disturbances in a human induced pluripotent stem cell-based platform: an in vitro disease model of atrial arrhythmias. *Front. Physiol.* 10:818. doi: 10.3389/fphys.2019.00818

O'Leary, N. A., Wright, M. W., Brister, J. R., Ciufo, S., Haddad, D., McVeigh, R., et al. (2016). Reference sequence (RefSeq) database at NCBI: current status, taxonomic expansion, and functional annotation. *Nucleic Acids Res.* 44, D733–D745. doi: 10.1093/nar/gkv1189

Pijnappels, D. A., Schalij, M. J., Ramkisoensing, A. A., van Tuyn, J., de Vries, A. A. F., van der Laarse, A., et al. (2008). Forced alignment of mesenchymal stem cells undergoing cardiomyogenic differentiation affects functional integration with cardiomyocyte cultures. *Circ. Res.* 103, 167–176. doi: 10.1161/CIRCRESAHA.108.176131

Pilarczyk, G., Raulf, A., Gunkel, M., Fleischmann, B. K., Lemor, R., and Hausmann, M. (2016). Tissue-mimicking geometrical constraints stimulate tissue-like constitution and activity of mouse neonatal and human-induced pluripotent stem cell-derived cardiac myocytes. *J. Funct. Biomater* 7:1. doi: 10.3390/jfb7010001

Ronaldson-Bouchard, K., Ma, S. P., Yeager, K., Chen, T., Song, L., Sirabella, D., et al. (2018). Advanced maturation of human cardiac tissue grown from pluripotent stem cells. *Nature* 556, 239–243. doi: 10.1038/s41586-018-0016-3

Ruan, J.-L., Tulloch, N. L., Razumova, M. V., Saiget, M., Muskheli, V., Pabon, L., et al. (2016). Mechanical stress conditioning and electrical stimulation promote contractility and force maturation of induced pluripotent stem cell-derived human cardiac tissue. *Circulation* 134, 1557–1567. doi: 10.1161/CIRCULATIONAHA.114.014998

Sakai, T., Naito, A. T., Kuramoto, Y., Ito, M., Okada, K., Higo, T., et al. (2018). Phenotypic screening using patient-derived induced pluripotent stem cells identified Pyr3 as a candidate compound for the treatment of infantile hypertrophic cardiomyopathy. *Int. Heart J.* 59, 1096–1105. doi: 10.1536/ihj.17-730

Scuderi, G. J., and Butcher, J. (2017). Naturally engineered maturation of cardiomyocytes. *Front. Cell Dev. Biol.* 5:50. doi: 10.3389/fcell.2017.00050

Singal, T., Dhalla, N. S., and Tappia, P. S. (2009). Regulation of c-Fos and c-Jun gene expression by phospholipase C activity in adult cardiomyocytes. *Mol. Cell. Biochem.* 327, 229–239. doi: 10.1007/s11010-009-0061-1

Stoppel, W. L., Hu, D., Domian, I. J., Kaplan, D. L., and Black, L. D. III (2015). Anisotropic silk biomaterials containing cardiac extracellular matrix for cardiac tissue engineering. *Biomed. Mater.* 10:34105. doi: 10.1088/1748-6041/10/3/034105

Streeter, D. D. J., Spotnitz, H. M., Patel, D. P., Ross, J. J., and Sonnenblick, E. H. (1969). Fiber orientation in the canine left ventricle during diastole and systole. *Circ. Res.* 24, 339–347. doi: 10.1161/01.res.24.3.339

Sun, N., Yazawa, M., Liu, J., Han, L., Sanchez-Freire, V., Abilez, O. J., et al. (2012). Patient-specific induced pluripotent stem cells as a model for familial dilated cardiomyopathy. *Sci. Transl. Med.* 4:130ra47. doi: 10.1126/scitranslmed.3003552

Taegtmeyer, H., Sen, S., and Vela, D. (2010). Return to the fetal gene program. *Ann. N. Y. Acad. Sci.* 1188, 191–198. doi: 10.1111/j.1749-6632.2009.05100.x

Tohyama, S., Hattori, F., Sano, M., Hishiki, T., Nagahata, Y., Matsuura, T., et al. (2013). Distinct metabolic flow enables large-scale purification of mouse and human pluripotent stem cell-derived cardiomyocytes. *Cell Stem Cell* 12, 127–137. doi: 10.1016/j.stem.2012.09.013

Veerman, C. C., Kosmidis, G., Mummery, C. L., Casini, S., Verkerk, A. O., and Bellin, M. (2015). Immaturity of human stem-cell-derived cardiomyocytes in culture: fatal flaw or soluble problem? *Stem Cells Dev.* 24, 1035–1052. doi: 10.1089/scd.2014.0533

Yang, X., Rodriguez, M., Pabon, L., Fischer, K. A., Reinecke, H., Regnier, M., et al. (2014). Tri-iodo-l-thyronine promotes the maturation of human cardiomyocytes-derived from induced pluripotent stem cells. *J. Mol. Cell. Cardiol.* 72, 296–304. doi: 10.1016/j.yjmcc.2014.04.005

Yazawa, M., Hsueh, B., Jia, X., Pasca, A. M., Bernstein, J. A., Hallmayer, J., et al. (2011). Using induced pluripotent stem cells to investigate cardiac phenotypes in Timothy syndrome. *Nature* 471, 230–234. doi: 10.1038/nature09855

Yoshida, Y., and Yamanaka, S. (2017). Induced pluripotent stem cells 10 years later: for cardiac applications. *Circ. Res.* 120, 1958–1968. doi: 10.1161/CIRCRESAHA.117.311080

Zhang, J. (2015). Engineered tissue patch for cardiac cell therapy. *Curr. Treat. Options Cardiovasc. Med.* 17:399. doi: 10.1007/s11936-015-0399-5

**Conflict of Interest:** The authors declare that the research was conducted in the absence of any commercial or financial relationships that could be construed as a potential conflict of interest.

frontiers
in Cell and Developmental Biology

BRIEF RESEARCH REPORT
published: 04 November 2021
doi: 10.3389/fcell.2021.737840

**Edited by:**
Jong-Kook Lee,
Osaka University, Japan

**Reviewed by:**
Hideki Uosaki,
Jichi Medical University, Japan
Masamichi Ito,
The University of Tokyo, Japan
Yoshinori Yoshida,
Kyoto University, Japan
David Lee Mack,
University of Washington,
United States

***Correspondence:**
Guillaume Gilbert
guillaume.gilbert@univ-brest.fr
Karin R. Sipido
karin.sipido@kuleuven.be

**†Present address:**
Guillaume Gilbert,
EA 4324 ORPHY, UFR Sciences et
Techniques, Université de Brest,
Brest, France
Pierre Bobin,
Institute of Cardiometabolism And
Nutrition (ICAN), Sorbonne Université,
INSERM, UMRS-1166, Paris, France

**Specialty section:**
This article was submitted to
Stem Cell Research,
a section of the journal
Frontiers in Cell and Developmental
Biology

**Received:** 07 July 2021
**Accepted:** 22 September 2021
**Published:** 04 November 2021

**Citation:**
Gilbert G, Kadur Nagaraju C,
Duelen R, Amoni M, Bobin P,
Eschenhagen T, Roderick HL,
Sampaolesi M and Sipido KR (2021)
Incomplete Assembly of the
Dystrophin-Associated Protein
Complex in 2D and 3D-Cultured
Human Induced Pluripotent Stem
Cell-Derived Cardiomyocytes.
Front. Cell Dev. Biol. 9:737840.
doi: 10.3389/fcell.2021.737840

# Incomplete Assembly of the Dystrophin-Associated Protein Complex in 2D and 3D-Cultured Human Induced Pluripotent Stem Cell-Derived Cardiomyocytes

***Guillaume Gilbert[1]*†, Chandan Kadur Nagaraju[1], Robin Duelen[2], Matthew Amoni[1], Pierre Bobin[3,4]†, Thomas Eschenhagen[3,4], H. Llewelyn Roderick[1], Maurilio Sampaolesi[2] and Karin R. Sipido[1]****

*[1] Laboratory of Experimental Cardiology, Department of Cardiovascular Sciences, KU Leuven, Leuven, Belgium, [2] Laboratory of Translational Cardiomyology, Department of Development and Regeneration, Stem Cell Institute, KU Leuven, Leuven, Belgium, [3] Institute of Experimental Pharmacology and Toxicology, University Medical Center Hamburg-Eppendorf, Hamburg, Germany, [4] German Centre for Cardiovascular Research (DZHK), Partner Site Hamburg/Kiel/Lübeck, Hamburg, Germany*

Human induced pluripotent stem cells derived cardiomyocytes (hiPSC-CM) are increasingly used to study genetic diseases on a human background. However, the lack of a fully mature adult cardiomyocyte phenotype of hiPSC-CM may be limiting the scope of these studies. Muscular dystrophies and concomitant cardiomyopathies result from mutations in genes encoding proteins of the dystrophin-associated protein complex (DAPC), which is a multi-protein membrane-spanning complex. We examined the expression of DAPC components in hiPSC-CM, which underwent maturation in 2D and 3D culture protocols. The results were compared with human adult cardiac tissue and isolated cardiomyocytes. We found that similarly to adult cardiomyocytes, hiPSC-CM express dystrophin, in line with previous studies on Duchenne's disease. β-dystroglycan was also expressed, but, contrary to findings in adult cardiomyocytes, none of the sarcoglycans nor α-dystroglycan were, despite the presence of their mRNA. In conclusion, despite the robust expression of dystrophin, the absence of several other DAPC protein components cautions for reliance on commonly used protocols for hiPSC-CM maturation for functional assessment of the complete DAPC.

**Keywords: dystrophin-associated glycoprotein complex, human induced pluripotent stem cells, hiPSC-derived cardiomyocytes, sarcoglycanopathy, hiPSC cardiomyocyte maturation, Duchenne muscular dystrophy, cardiomyopathy**

## INTRODUCTION

Muscular dystrophies are genetically inherited degenerative disorders with a progressive impairment of skeletal, respiratory, and cardiac function (Mercuri et al., 2019). The most prevalent muscular dystrophies involve proteins from the dystrophin-associated protein complex (DAPC) with dystrophin, sarcoglycans, dystroglycans, and laminin as core components (**Figure 1A**, left). The DAPC has a mechanical and signaling role in muscle cells, providing a link between the extracellular matrix and the intracellular cytoskeleton (Cohn and Campbell, 2000; Ozawa, 2010). Studies in animal models for muscular dystrophies

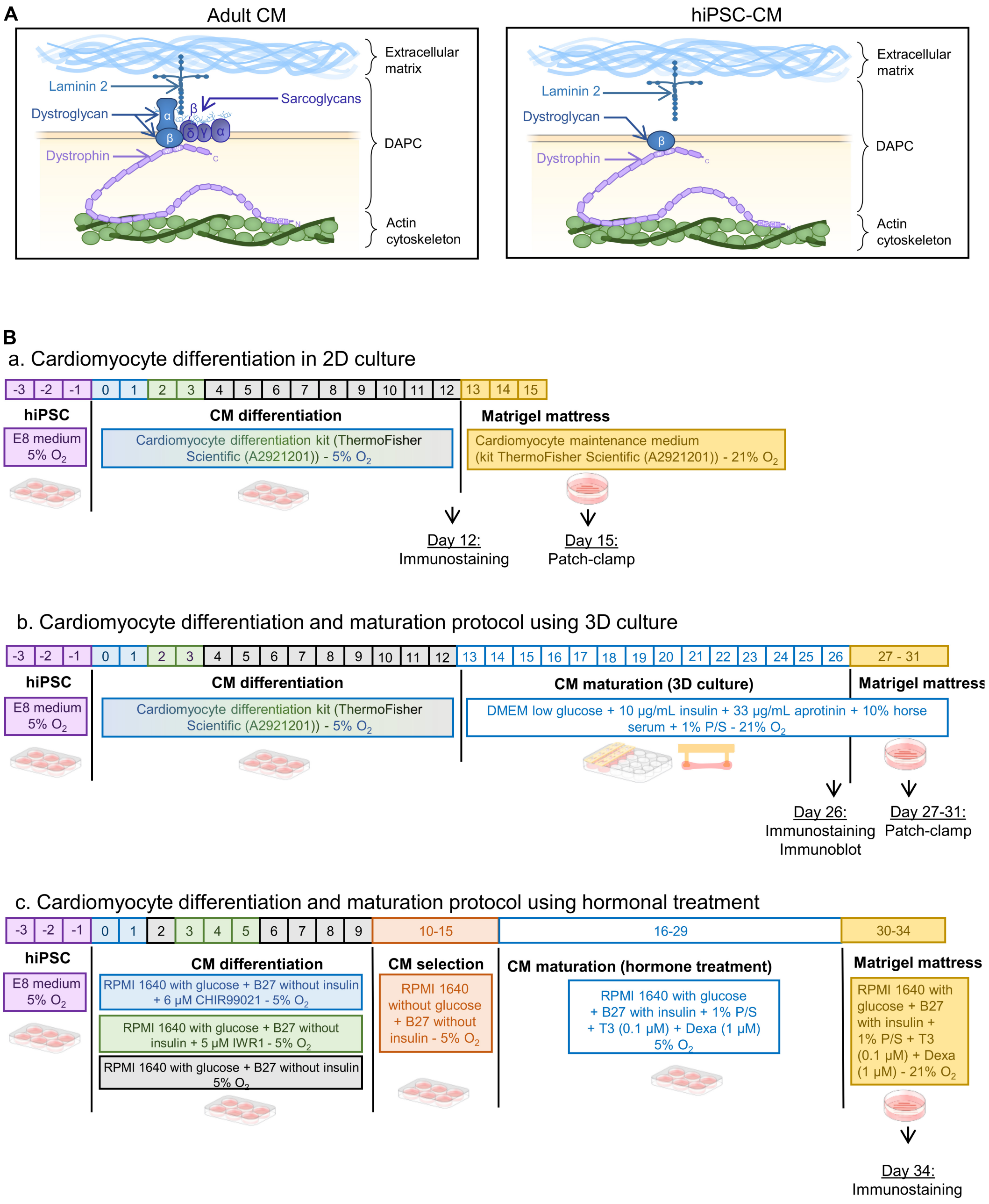

**FIGURE 1 | (A)** Schematic of the DAPC composition in adult vs. hiPSC-CM. Laminin was present in the hiPSC-CM preparations (See **Supplementary Figures 1,2**). **(B)** Differentiation protocols of hiPSC-CM: panel **(a)** in 2D monolayer culture, panel **(b)** in 3D engineered heart tissues, and panel **(c)** with thyroid hormone and glucocorticoid treatment followed by Matrigel mattresses.

provided insights into the mechanistic pathways leading to the development of cardiomyopathy (loss of membrane integrity, increase in cell permeability, cardiomyocyte cell death, and replacement fibrosis) (Ikeda et al., 2000; Heydemann et al., 2001; Lapidos et al., 2004; Fraysse et al., 2010; Law et al., 2020). However, because of the unavailability of cardiac biopsies from those patients, there remains a knowledge gap in the understanding of the cellular mechanisms underlying cardiomyopathy in humans, hampering clinical translation. To overcome this limitation, human induced pluripotent stem cell-derived cardiomyocytes (hiPSC-CM) are increasingly used as a model. A leading example is Duchenne muscular dystrophy, resulting from loss of dystrophin, which has been studied extensively with important translational insights

---

**Abbreviations:** DAPC, dystrophin-associated protein complex; CM, cardiomyocyte; DG, dystroglycan; hiPSC-CM, human induced pluripotent stem cell-derived cardiomyocytes; SG, sarcoglycan.

(Long et al., 2018; Kamdar et al., 2020; Moretti et al., 2020; Pioner et al., 2020; Mekies et al., 2021). Notwithstanding the advantages of using human cells, a general limitation of the approach is that hiPSC-CMs lack several features of adult cardiomyocytes, presumably due to incomplete maturation, resulting in a fetal or neonatal phenotype (Guo and Pu, 2020; Karbassi et al., 2020). Multiple strategies have been presented to promote hiPSC-CM maturation (reviewed in Ahmed et al., 2020). These rely on hormonal treatment, imposing load and pacing, or a 3D environment. HiPSC-CM generated *via* some of these methods have been used in the study of Duchenne muscular dystrophy (Long et al., 2018; Pioner et al., 2020), yet it has also been suggested that dystrophin is needed for hiPSC-CM maturation (Pioner et al., 2020), and presently it is unknown whether the DAPC in hiPSC-CM forms a complete functional complex.

The present study examines the presence of the DAPC in hiPSC-CM, using maturation protocols that are accessible and commonly used (**Figure 1B**). The first is the well-established technique to create a small-engineered heart tissue by culturing the cells in a 3D microenvironment. Cells are embedded in a fibrin/Matrigel hydrogel connected to silicone posts that will exert a tension force, mimicking the preload tension on a muscle fiber (Jackman et al., 2016; Breckwoldt et al., 2017; Tiburcy et al., 2017; Leonard et al., 2018; Goldfracht et al., 2020). The second maturation method is a protocol that has been shown to structurally improve iPSC-CM membrane with the presence of transverse tubules, an important hallmark of cardiomyocyte maturity, by stimulating 2D cultured hiPSC-CM with thyroid hormones and glucocorticoids (Parikh et al., 2017; Huang et al., 2020). The data are compared with the hiPSC-CM differentiated in 2D without an intensified maturation protocol, and with adult human cardiac tissue.

# METHOD

## Human Induced Pluripotent Stem Cell Lines

We used a commercial hiPSC line from ThermoFisher Scientific (A18945—lot 1793435) and three additional non-commercial hiPSC lines, one derived within the Stem Cell Institute at KU Leuven, (HC1) and two elaborated at the University Medical Center, Hamburg Lab (ERC001 and ERC018).

## Cardiomyocyte Differentiation and Maturation Protocol Using 3D Culture of Human Induced Pluripotent Stem Cell-Derived Cardiomyocytes

HiPSC were differentiated in 2D monolayers using the cardiomyocyte differentiation kit from ThermoFisher Scientific (A2921201) (**Figure 1B**, panel a). Twelve days post-differentiation, hiPSC-CM were placed in a fibrin and Matrigel based 3D environment using the system developed in the Eschenhagen group (Schaaf et al., 2014; Breckwoldt et al., 2017), modified in a mixture as described here (Jackman et al., 2016). Briefly, three wells of 2D differentiated cells were detached using collagenase A at 1 U/ml (Merk—10103586001) and pooled to prepare 3D constructs in a mixture of Matrigel (10% final volume) (Corning—354234), fibrinogen (20% final volume at 2 mg/ml) (Merk—341576), and thrombin (2% final volume at 1 U/ml) (Enzyme Research Laboratories—HT 1002a). The culture medium composition was as follows: DMEM low glucose (ThermoFisher Scientific—31885023), 10% horse serum (ThermoFisher Scientific—26050088), 1% penicillin/streptomycin, 10 μg/ml human insulin (Sigma-Aldrich—I9278-5ML), and 33 μg/ml aprotinin (Carl Roth—A162.3). The medium was replaced every 2 days for 14 days (day 26 post initial differentiation) (**Figure 1B**, panel b).

## Cardiomyocyte Differentiation and Maturation Protocol Using Chemical Treatment

The protocol used here was the same as previously described (Parikh et al., 2017). Briefly, hiPSC were differentiated in RPMI 1640 medium containing glucose (ThermoFisher Scientific—11875093) supplemented with B27 without insulin (ThermoFisher Scientific—A1895601), using 6 μM CHIR99021 (Merk—SML1046) on day 1 followed by 5 μM IWR-1 (Merk—I0161) on day 3. From days 10 to 16, glucose was removed from the medium to perform a metabolic selection and cardiomyocyte enrichment (ThermoFisher Scientific—11879020). Cells were then treated with 0.1 μM triiodo-L-thyronine hormone (Merk—T2877), 1 μM dexamethasone (Cayman—11015) in RPMI 1640 with glucose (ThermoFisher Scientific—11875093) supplemented with B27 (ThermoFisher Scientific—17504044), and 1% penicillin/streptomycin. On day 30, the 2D monolayer of hiPSC-CM was dissociated using TrypLE Express (ThermoFisher Scientific—12605010) and seeded onto Matrigel mattresses (Corning—354234) for 4 days until experiments (**Figure 1B**, panel c).

## Proteasome Inhibition Test

Three-dimensional cultured hiPSC-CM were incubated in the 37°C incubator with 10 μM of MG-132 (Merk—474787) in the culture medium for 8 h. After 8 h, the 3D hiPSC-CM were snap frozen in liquid nitrogen for further analysis by immunoblot. Proteasome inhibition efficiency was confirmed by assessing by immunoblotting for ubiquitinated proteins using a ubiquitin antibody.

## Dissociation of Human Induced Pluripotent Stem Cell From 3D Constructs

To perform electrophysiology experiments, cells grown in 3D were dissociated using 0.4 mg/ml papain (Worthington Biochemical Corporation—LS003118), 0.3 mg/ml collagenase type IV (Worthington Biochemical Corporation—LS004186), 2 mM DL-dithiothreitol (Merk—D0632), 50 μM $CaCl_2$, and 1 mg/ml bovine serum albumin (Merk—A2153) in Hank's balanced salt solution (HBSS) (ThermoFisher Scientific—14170088) for 20 min at 37°C. After centrifugation at 1200 rpm for 5 min, cells were resuspended in the 3D culture medium and seeded on Matrigel mattresses for 1–5 days until experiment, as previously described (Feaster et al., 2015). Briefly, 10 min prior to adding the dissociated cells, thin lines of 20 mm long containing 1 μl of pure Matrigel were poured using a P10 pipet on glass coverslips.

## Adult Human Cardiomyocyte Isolation

Use of tissue from non-used human donor hearts conforms with ethical guidelines, and permission for the study was obtained from the Ethical Committee of UZ Leuven (permit number S58824). Hearts were collected in an ice-cold solution containing (in mM): 130 NaCl, 27 KCl, 6 *N*-2-hydroxyethylpiperazine-*N*-2-ethanesulfonic acid (HEPES), 1.2 $MgSO_4$, 1.2 $KH_2PO_4$, and 10 glucose; pH was adjusted to 7.2 with NaOH and transported from the hospital to the laboratory. A coronary artery from a wedge of the left ventricle was cannulated. Then, the wedge was perfused for 30 min with a $Ca^{2+}$ free solution at 37°C bubbled with $O_2$ and containing (in mM): 130 NaCl, 5.4 KCl, 6 HEPES, 1.2 $MgSO_4$, 1.2 $KH_2PO_4$, and 20 glucose; pH was adjusted to 7.2 with NaOH. After this washing step, the wedge was perfused for 40 min with the same solution containing around 0.4 U/ml of Collagenase A (Merk—10103586001) and 0.1 mg/ml Protease XIV (Merk—P5147). When the tissue appeared digested, it was perfused for 20 min with a low $Ca^{2+}$ solution ($Ca^{2+}$ free solution with 0.18 mM $CaCl_2$). The mid-myocardium from the digested perfused area was cut into small pieces and triturated for 5 min in the low $Ca^{2+}$ solution. Isolated cardiomyocytes were then filtered through a 250 μm mesh and resuspended in low $Ca^{2+}$ solution until use.

## Electrophysiology

Coverslips containing the cells (isolated from 2D hiPSC-CM, 3D constructs, or adult human hearts) were mounted in a chamber perfused with normal Tyrode solution warmed at 37°C and containing (in mM): 137 NaCl, 5.4 KCl, 1.8 $CaCl_2$, 0.5 $MgCl_2$, 5.5 glucose, and 10 HEPES; pH was adjusted to 7.4 with NaOH. Patch-clamp pipettes (2–3 MΩ) (GB200-8P—Science Products) were filled with a solution containing (in mM): 120 K-Asp, 20 KCl, 10 HEPES, 5 Mg-ATP, 10 NaCl, and 0.05 Fluo-4 (ThermoFisher Scientific—F14200); pH was adjusted to 7.2 with KOH. Cells were patched in a whole-cell configuration, and action potentials were measured using an Axon 200B amplifier and Digidata 1550B (Molecular Device) in current-clamp mode. Stimulated action potentials were recorded after a 5 ms pulse of 0.1 nA at a 1 Hz frequency. To measure voltage-gated calcium currents (ICaL), the setup was set to voltage-clamp mode. A train of seven pulses of 250 ms from −70 to +10 mV was followed by a sodium channel activation pulse of 750 ms from −70 to −40 mV, and then ICaL was recorded with increasing steps of 10 mV of 250 ms from −50 to +60 mV.

## Immunostaining

Snap frozen tissue of adult human hearts embedded in optimal cutting temperature compound (OCT) were cut using a cryostat (Leica) and directly fixed with 4% paraformaldehyde for 10 min (Santacruz Biotechnology—sc-281692). HiPSC-CM in 2D monolayers were directly cultured in imaging plates (Ibidi—82406) and fixed with 4% paraformaldehyde for 15 min. HiPSC-CM in 3D constructs were directly fixed with the silicon posts with 4% paraformaldehyde for 20 min. After fixation, the samples were washed with phosphate-buffered saline (PBS) and permeabilized with 0.4% Triton X-100 (ThermoFisher Scientific—28314) diluted in PBS. Samples were washed three times with PBS and incubated with blocking buffer (4% bovine serum albumin, 0.1% Triton X-100 in PBS) for 1 h at room temperature. Primary antibodies were incubated overnight at 4°C in the blocking buffer: α-sarcoglycan (Leica A-SARC-L-CE, 1:10), β-sarcoglycan (Leica B-SARC-L-CE, 1:10), γ-sarcoglycan (Leica G-SARC-CE, 1:10), δ-sarcoglycan (Leica D-SARC-CE, 1:10), α-dystroglycan (DSHB IIH6 C4-s, 1:10), β-dystroglycan [DSHB MANDAG2(7D11)-s, 1:10], dystrophin (Leica DYS1-CE, 1:10), cTnT (Abcam ab92546, 1:200), and α-actinin (Proteintech 14221-1-AP, 1:200). The next day, after three washes in PBS, samples were incubated with secondary antibodies for 2 h at room temperature in the blocking buffer: goat anti-mouse IgG Alexa 488 (ThermoFisher Scientific—A-21121, 1:200) and goat anti-rabbit IgG Alexa 568 (ThermoFisher Scientific—A-11036, 1:200), according to the primary antibody. The sections from the human hearts were mounted using ProLong$^{TM}$ Gold Antifade Mountant with diamino-2-phenyl-indole (DAPI) (ThermoFisher Scientific—P36931). For imaging, the 3D constructs were directly placed on a coverslip. Imaging was performed using a confocal microscope (Nikon A1R configured on an Eclipse Ti2 using a ×60 1.4 NA oil immersion objective).

## Immunoblot

Adult human heart samples and 3D cultured hiPSC-CM were snap frozen in liquid nitrogen and stored at −80°C until use. Homogenization of samples was done on ice using a tissue grinder (Weathon) with the following solution: 10 mM Tris–HCl pH 7.5, 100 mM NaCl, 1 mM EDTA, 1 mM $Na_3VO_4$, 1% sodium deoxycholate, 1% Triton X-100, 1% NP-40, 0.1% sodium dodecyl sulfate (SDS), 10 mM NaF, 1 mM phenylmethylsulfonyl fluoride (PMSF), and protease inhibitor tablets (ThermoFisher Scientific—A32963). Protein concentration was estimated using the bicinchoninic acid (BCA) assay from ThermoFisher Scientific (23225), and aliquots were stored at −80°C until use. For de-glycosylation of proteins, a PNGase kit was used (New England BioLabs—NEB P0704S). Homogenized samples (30 μg) were loaded in a home-made Tris-acetate 3–15% gel, as described (Cubillos-Rojas et al., 2012). After an overnight liquid transfer (4°C at 40 V for 19 h) of the gel to a polyvinylidene difluoride (PVDF) membrane, the membrane was saturated for 45 min with 4% non-fat dry milk (Bio-Rad—1706404) diluted in PBS (pH = 7.4) with 0.05% Tween-20. The membrane was cut at around the 160 kDa marker into two pieces. The top part was used to probe for dystrophin and the lower part for sarcoglycans and dystroglycans (**Supplementary Figure 3**). Then, membranes were incubated overnight at 4°C with the primary antibodies diluted in 2% milk (same antibodies as used for immunostainings, 1:1,000 dilution). The next day, after three washes in PBS, membranes were incubated for 2 h at room temperature with secondary antibodies: goat anti-mouse IgG Alexa 680 (1:10,000, ThermoFisher Scientific—A28183). Membrane immunofluorescence was quantified with a Licor Odyssey Clx infrared imaging system.

## Polymerase Chain Reaction

Adult human heart samples and 3D-cultured hiPSC-CM were snap frozen in liquid nitrogen and stored at −80°C until use. Homogenization of samples was done using ceramide beads (MP Biomedicals—116913050-CF) in 1 ml of TRI Reagent (Merk—93289) and using the MP Biomedical Instrument FastPrep-24 grinder (MP Biomedicals) at a speed of 6 m/s for 20 s, twice. Chloroform (0.2 ml) was added per milliliter of TRI Reagent and incubated for 3 min at room temperature. After centrifugation at 12,000 *g* for 15 min at 4°C, the upper phase containing RNA was collected. To this, 0.5 ml of isopropanol per milliliter of TRI Reagent was then added and incubated for 5 min at room temperature. Samples were then centrifuged at 12,000 *g* for 10 min at 4°C and the supernatant removed. The pellet was then washed with 1 ml of ethanol 75% and centrifuged at 7,600 *g* for 5 min at 4°C and the supernatant discarded. The RNA pellet was resuspended in 20 μl of DNase/RNase-free water. cDNA was generated from the RNA extracted samples by reverse transcription using a kit (ThermoFisher Scientific—4368814). The cDNA was then polymerase chain reaction (PCR) amplified using the Platinum® Taq DNA Polymerase High Fidelity kit (ThermoFisher Scientific—11304011) with the following primers: α-SG (TGAGGTCACAGCCTACAATCG and AACTCGGCTTGGTATGGCAG), β-SG (AGCAAAGT TCCAATGGTCCTG and TCATCAATCGGAATGTATCCAGC), γ-SG (GAGCAGTACACTACAGCCACA and CGCAGTCCA TCTTTTGTTACACA), and δ-SG (GCGGAAACGATGCCT GTATTT and TGGCGTAGAGAGGTTGTAAGAA). The PCR products were resolved on a 2% agarose gel for 30 min at 50 V using SYBR® Safe DNA Gel Stain (ThermoFisher Scientific—S33102) and visualized with UV light exposure using a GelDoc Imaging System (Bio-Rad). For RT-qPCR, Platinum$^{TM}$ SYBR$^{TM}$ Green qPCR SuperMix-UDG was used (ThermoFisher Scientific—11733038) and run on a ViiA 7 Real-Time PCR System (ThermoFisher Scientific). The gene expression was normalized to housekeeping genes (GAPDH and RLP13a), and values were expressed as $2^{-\Delta\Delta CT}$ as a fold difference to adult.

## Statistics

Graphs were prepared and data analyzed using GraphPad Prism software version 9. Normality was tested with Shapiro–Wilk. Except for resting membrane potential, the data did not pass the normality test, and hence groups were compared using Kruskal–Wallis with Dunn's multiple comparison. For the analysis of the resting membrane potential, we used Welch ANOVA, with Dunnett T3 for multiple comparisons. *P*-values are indicated above each graph. Individual data points are displayed in the graphs with the mean and the standard error of the mean as error bars.

# RESULTS AND DISCUSSION

In adult cardiomyocytes, the core proteins of the DAPC [dystrophin, dystroglycans (α and β), and sarcoglycans (α, β, γ, and δ)] were present at the membrane, both in the external plasmalemma and in transverse tubules but not at the intercalated discs (**Figure 2A**, right). In contrast, hiPSC-CM generated using a common 2D monolayer protocol expressed an incomplete DAPC with only dystrophin and β-dystroglycan present (**Figure 2A**, left). We investigated whether a further maturation process could improve the expression of the proteins that comprise the DAPC, especially sarcoglycans as important mediators of dystrophy-related cardiomyopathies. To these ends, two protocols were used: the first in which we cultured hiPSC-CM in a 3D microenvironment and a second in which we combined a treatment with triiodo-L-thyronine and glucocorticoid for 14 days before seeding the cells on 2D Matrigel mattresses. However, neither maturation protocol improved DAPC expression above that seen in 2D hiPSC-CM, which only express dystrophin and β-dystroglycan but not sarcoglycans or α-dystroglycan (**Figure 2A**, middle). These findings were confirmed in immunoblots in the 3D-cultured hiPSC-CM (**Figure 2B**, panel a and b). All data presented here are from the ThermoFisher Scientific hiPSC line, and similar data were obtained in 3D cultures from three different hiPSC lines, one from the Leuven and two from the Hamburg Labs (**Supplementary Figures 1,2**). The specificity of the sarcoglycan antibodies used was further verified by deglycosylating the proteins in adult cardiac homogenates with PNGase F, and as expected, all sarcoglycans decreased in molecular weight after deglycosylation (**Figure 2B**, panel b). Inhibition of the proteasome by treatment with MG-132 (10 μM) for 8 h to reduce protein degradation had no effect and could not uncover sarcoglycan expression (**Figure 2B**, panel c). Yet, hiPSC-CM expressed sarcoglycans at the mRNA level (**Figure 2C**). Additional RT-qPCR experiments showed differences in expression of components of the DAPC between 3D culture hiPSC-CM and adult cardiac tissue (**Figure 2D**).

We examined proxies for maturation in the present experiments, focusing on aspects of excitation–contraction coupling as a key feature of cardiomyocytes. The increased sarcomeric organization in hiPSC-CM cultured in 3D and with hormonal treatment in 2D supported the assumption of advanced maturation of the myocyte phenotype under these conditions (**Figure 3A**). We also evaluated how 3D culture influences the electrophysiological properties of hiPSC-CM, compared to cells cultured in 2D monolayers and to adult human ventricular cardiomyocytes. **Figure 3B**, panel a shows representative examples of single cell action potentials. Both hiPSC-CM cultured in 2D and 3D were smaller than adult ventricular cells, in cell perimeter and electrical capacitance, though the latter was higher in 3D-cultured hiPSC-CM (**Figure 3B**, panel b). In addition, compared to 2D-cultured cells, 3D-cultured hiPSC-CM had a more negative resting membrane potential and greater action potential amplitude and duration, with values closer to that in adult ventricular cardiomyocytes (**Figure 3B**, panel c). Considering we did not correct for junction potentials, these values for resting membrane potential are comparable to those previously reported (Horvath et al., 2018). Of note, the resting membrane potential measured with microelectrodes in hiPSC-CM within the connected 3D micro-tissue are more negative than those after

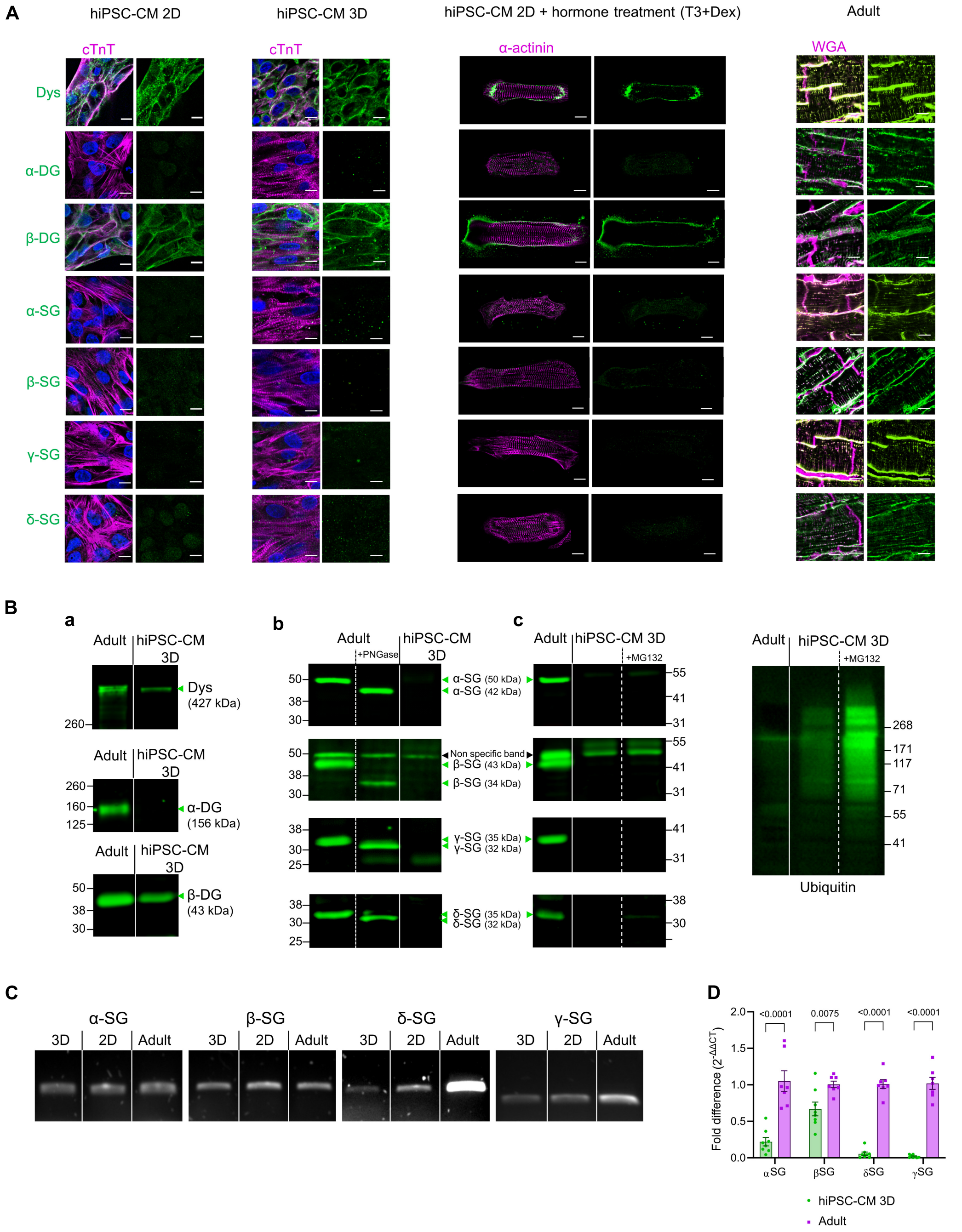

**FIGURE 2 | (A)** From left to right: confocal images of immunostained 2D monolayer cultured hiPSC-CM, 3D-cultured hiPSC-CM tissue, 2D-cultured hiPSC-CM seeded on Matrigel mattresses, and treated with T3+Dexamethasone and cryosections of adult human heart tissue. Adult heart sections were counterstained with wheat germ agglutinin (WGA) for membrane, shown in magenta. hiPSC-CM were counterstained with cardiac troponin T (cTnT) or α-actinin, shown in magenta. Nuclei were labeled with DAPI in blue. The DAPC components are in green. Results were replicated in three independent hiPSC-CM differentiations. Scale bar, 10 μm. **(B) (a)** Immunoblot of dystrophin (Dys) and dystroglycan (DG). **(b)** Immunoblot of sarcoglycans (SG) and Deglycosylation tests (+PNGase treatment) in adult cardiac homogenates and in 3D-cultured hiPSC-CM. Results were replicated in seven independent hiPSC-CM differentiations for α-SG, δ-SG, and γ-SG; 10 independent differentiations for β-SG and dystrophin and 5 independent differentiations for dystroglycan (DG). **(c)** Immunoblot for sarcoglycans from 3D-cultured hiPSC-CM treated for 8 h with MG-132 (10 μM). The proteasome inhibition efficiency was confirmed by immunoblotting of lysates with an anti-ubiquitin antibody (right). Results are from four 3D constructs prepared from one hiPSC-CM differentiation. Straight lines separate adult vs. hiPSC-CM, and dotted lines separate control vs. treatment (PNGase or MG132), from the same blot. The expected molecular weight for glycosylated and deglycosylated forms of sarcoglycans are indicated in the figure. The β-SG band at 50 kDa was considered as non-specific as its molecular weight did not decrease with deglycosylation (a similar band was also seen in β-SG-null mouse heart—**Supplementary Figure 2B**). **(C)** mRNA detection by reverse transcription PCR of expression of sarcoglycans in 2D and 3D-cultured hiPSC-CM and in adult human heart lysates. Results were replicated in three independent hiPSC-CM differentiations. **(D)** RT-qPCR of sarcoglycans in 3D-cultured hiPSC-CM and adult human heart lysates. Values are expressed as $2^{-\Delta\Delta CT}$ normalized as a fold difference to adult.

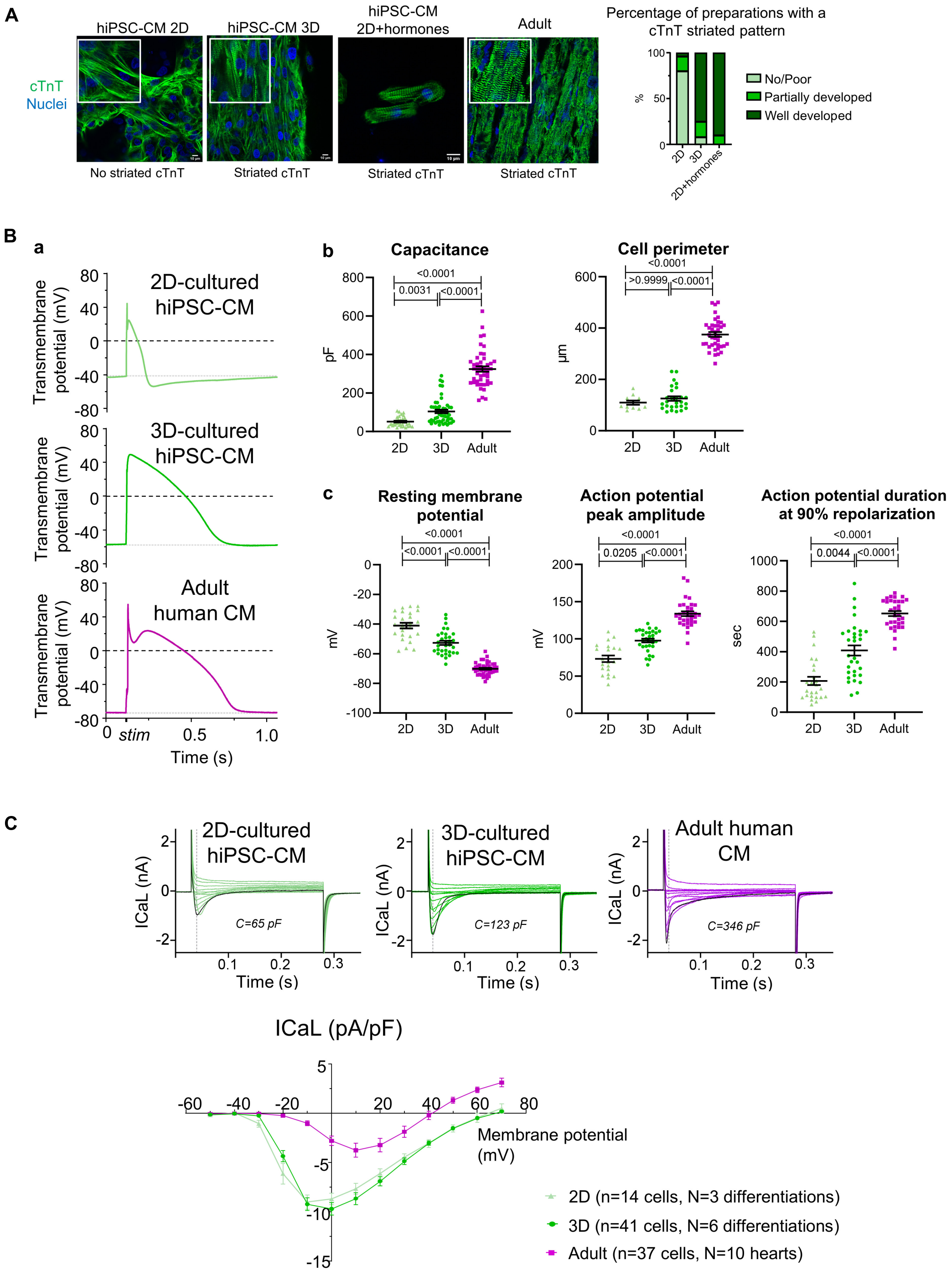

**FIGURE 3 | (A)** Cardiac troponin T (cTnT) organization in hiPSC-CM. Left: immunostaining for cTnT (green) and nuclei (blue) in hiPSC-CM cultured in 2D, 3D, or 2D+hormones seeded on Matrigel mattresses, and for comparison in adult human cardiac tissue. Right: semi-quantitative analysis of the cTnT striated pattern (2D: *n* = 25 preparation from five independent differentiations; 3D: *n* = 24 preparations from six independent differentiations; 2D+hormones: *n* = 10 preparations from two independent differentiations). **(B) (a)** Representative example of electrically stimulated action potentials. **(b)** Analysis of cell capacitance (2D-hiPSC-CM: *n* = 34 cells; 3D-hiPSC-CM: *n* = 52 cells; adult cardiomyocytes: *n* = 46 cells) and cell perimeter (2D-hiPSC-CM: *n* = 11 cells; 3D-hiPSC-CM: *n* = 27 cells; adult cardiomyocytes: *n* = 39 cells). **(c)** Analysis of resting membrane potential (2D-hiPSC-CM: *n* = 25 cells; 3D-hiPSC-CM: *n* = 33 cells; adult cardiomyocytes: *n* = 43 cells), action potential amplitude (2D-hiPSC-CM: *n* = 21 cells; 3D-hiPSC-CM: *n* = 31 cells; adult cardiomyocytes: *n* = 32 cells), and duration at 90% repolarization (2D-hiPSC-CM: *n* = 21 cells, *N* = 3 differentiations; 3D-hiPSC-CM: *n* = 31 cells, *N* = 6 differentiations; adult cardiomyocytes: *n* = 32 cells, *N* = 10 hearts). **(C)** Top: representative example of ICaL over membrane potentials spanning from –40 to +70 mV. The black curve represents the voltage step at 0 mV. Bottom: current-voltage curve of the ICaL measured at the peak current (*n* numbers are indicated in the graph). *P*-values are indicated above each graph; Kruskal–Wallis with a Dunn's multiple comparison test was used for all, except for resting membrane potential where a Welch ANOVA test, followed by Dunnett T3 for multiple comparisons, was used.

isolation (Horvath et al., 2018). These features seen in 3D culture (lower resting membrane potential and longer action potential duration) are considered a characteristic of a more adult and ventricular-like cardiomyocyte phenotype. Compared to adult cardiomyocytes, both 2D and 3D-cultured hiPSC-CM had a higher density of L-type voltage-gated calcium channel current (ICaL) (**Figure 3C**), probably related to the absence of T-tubules and consequent smaller membrane surface area. Adult cardiomyocytes typically have a fast inactivation phase of ICaL caused by $Ca^{2+}$ release from the internal store, followed by a slow phase. ICaL in 2D-cultured hiPSC-CM typically has a single inactivation phase, while ICaL in 3D-cultured hiPSC-CM can have either type of inactivation time course. These data highlight that the link between calcium influx and sarcoplasmic reticulum release of calcium may improve in 3D but remains poorly developed.

Taken together, our findings show that despite evidence for a more advanced maturation, 3D-cultured-hiPSC-CM lack the complete DAPC seen in adult cardiomyocytes: dystrophin and β-dystroglycan are present, but sarcoglycans and α-dystroglycan are not (**Figure 1B**). The lack of a full DAPC in hiPSC-CM, even after additional culture in 3D or with hormonal treatment, may reflect the incomplete maturity of the cells. Interestingly, during the early stages of human fetal development, the heart expresses sarcoglycans at the mRNA but not at the protein level, only expressing dystrophin and β-dystroglycan (Mora et al., 1996; Fougerousse et al., 1998), and this is in line with the immaturity or "fetal-like" phenotype of hiPSC-CM. The expression of dystrophin in hiPSC-CM, even already present in 2D monolayer differentiated cells, confirms the use of hiPSC-CM to study Duchenne muscular dystrophy. However, the lack of sarcoglycans undermines the use of hiPSC-CM as a model for sarcoglycanopathies and suggests caution in the interpretation of the dystrophin studies. The absence of α-dystroglycan, as recently observed (Kamdar et al., 2020), would prevent the linking of the complex to laminin and the extracellular matrix, thereby potentially affecting mechanosensing signaling, which is important for cell adaptation and maturation. However, we cannot rule out that we did not detect α-dystroglycan in our samples due to its release into the culture medium, as this extracellular protein could be poorly retained in an immature DAPC. It is conceivable that the incomplete DAPC is one of the hurdles to progression to an adult phenotype of hiPSC-CM. Recent protocols using co-cultures with fibroblasts and endothelial cells may further improve maturation but, because of their complexity, are not yet widely adopted (Giacomelli et al., 2020).

## CONCLUSION

In conclusion, because of the unique insight into patient-specific genetic and functional background they provide, hiPSC-CM are a highly relevant model to study genetic cardiac diseases. However, our findings indicate that it is important to recognize the limitations of the hiPSC-CM model for the study of dystrophy-related cardiomyopathies. Further understanding of the mechanisms that govern the stabilization of sarcoglycans and α-dystroglycan within the DAPC can improve the use of hiPSC-CM as a model system and as a bridge to medical applications such as regenerative medicine and drug screening.

## DATA AVAILABILITY STATEMENT

The original contributions presented in the study are included in the article/**Supplementary Material**, further inquiries can be directed to the corresponding authors.

## ETHICS STATEMENT

The studies involving human participants were reviewed and approved by the Ethical Committee of UZ Leuven (permit number S58824). Written informed consent for participation was not required for this study in accordance with the national legislation and the institutional requirements.

## AUTHOR CONTRIBUTIONS

GG, MS, and KS: conceptualization. GG and KS: formal analysis, visualization, and writing—original draft. GG, KS, HLR, MS, and RD: funding acquisition. GG, CK, RD, and MA: investigation. GG, RD, CK, PB, and TE: methodology. KS and MS: project administration. KS, MS, HLR, and TE: resources. GG: software. KS, MS, and HR: supervision. KS: validation. All authors contributed to the writing—review and editing.

## FUNDING

This work was supported by the Fund for Scientific Research-Flanders (FWO): project grant G0C7319N for KS, project grant G08861N and Odysseus Project 90663 for HLR, project grant G0D4517N for MS and FWO postdoctoral fellowship for GG. MS was also supported by project CARIPLO#2015_0634 and C1-KUL 3DMUSYC #C14/17/111. RD was supported by the "Rondoufonds voor Duchenneonderzoek," project #EQQ-FODUCH-O2010.

## ACKNOWLEDGMENTS

The authors thank the heart failure and transplant team of UZ Leuven for their contributions to obtaining adult human heart tissue.

## SUPPLEMENTARY MATERIAL

The Supplementary Material for this article can be found online at: https://www.frontiersin.org/articles/10.3389/fcell.2021.737840/full#supplementary-material

# REFERENCES

Ahmed, R. E., Anzai, T., Chanthra, N., and Uosaki, H. (2020). A brief review of current maturation methods for human induced pluripotent stem cells-derived cardiomyocytes. *Front. Cell Dev. Biol.* 8:178. doi: 10.3389/fcell.2020.00178

Breckwoldt, K., Letuffe-Breniere, D., Mannhardt, I., Schulze, T., Ulmer, B., Werner, T., et al. (2017). Differentiation of cardiomyocytes and generation of human engineered heart tissue. *Nat. Protoc.* 12, 1177–1197. doi: 10.1038/nprot.2017.033

Cohn, R. D., and Campbell, K. P. (2000). Molecular basis of muscular dystrophies. *Muscle Nerve* 23, 1456–1471.

Cubillos-Rojas, M., Amair-Pinedo, F., Tato, I., Bartrons, R., Ventura, F., and Rosa, J. L. (2012). Tris-acetate polyacrylamide gradient gels for the simultaneous electrophoretic analysis of proteins of very high and low molecular mass. *Methods Mol. Biol.* 869, 205–213. doi: 10.1007/978-1-61779-821-4_17

Feaster, T. K., Cadar, A. G., Wang, L., Williams, C. H., Chun, Y. W., Hempel, J. E., et al. (2015). Matrigel mattress: a method for the generation of single contracting human-induced pluripotent stem cell-derived cardiomyocytes. *Circ. Res.* 117, 995–1000. doi: 10.1161/CIRCRESAHA.115.307580

Fougerousse, F., Durand, M., Suel, L., Pourquie, O., Delezoide, A. L., Romero, N. B., et al. (1998). Expression of genes (CAPN3, SGCA, SGCB, and TTN) involved in progressive muscular dystrophies during early human development. *Genomics* 48, 145–156. doi: 10.1006/geno.1997.5160

Fraysse, B., Nagi, S. M., Boher, B., Ragot, H., Laine, J., Salmon, A., et al. (2010). Ca2+ overload and mitochondrial permeability transition pore activation in living delta-sarcoglycan-deficient cardiomyocytes. *Am. J. Physiol. Cell Physiol.* 299, C706–C713. doi: 10.1152/ajpcell.00545.2009

Giacomelli, E., Meraviglia, V., Campostrini, G., Cochrane, A., Cao, X., van Helden, R. W. J., et al. (2020). Human-iPSC-derived cardiac stromal cells enhance maturation in 3D cardiac microtissues and reveal non-cardiomyocyte contributions to heart disease. *Cell Stem Cell* 26, 862.e11–879.e11. doi: 10.1016/j.stem.2020.05.004

Goldfracht, I., Protze, S., Shiti, A., Setter, N., Gruber, A., Shaheen, N., et al. (2020). Generating ring-shaped engineered heart tissues from ventricular and atrial human pluripotent stem cell-derived cardiomyocytes. *Nat. Commun.* 11:75. doi: 10.1038/s41467-019-13868-x

Guo, Y., and Pu, W. T. (2020). Cardiomyocyte maturation: new phase in development. *Circ. Res.* 126, 1086–1106. doi: 10.1161/CIRCRESAHA.119.315862

Heydemann, A., Wheeler, M. T., and McNally, E. M. (2001). Cardiomyopathy in animal models of muscular dystrophy. *Curr. Opin. Cardiol.* 16, 211–217. doi: 10.1097/00001573-200105000-00009

Horvath, A., Lemoine, M. D., Loser, A., Mannhardt, I., Flenner, F., Uzun, A. U., et al. (2018). Low resting membrane potential and low inward rectifier potassium currents are not inherent features of hiPSC-derived cardiomyocytes. *Stem Cell Rep.* 10, 822–833. doi: 10.1016/j.stemcr.2018.01.012

Huang, C. Y., Peres Moreno Maia-Joca, R., Ong, C. S., Wilson, I., DiSilvestre, D., Tomaselli, G. F., et al. (2020). Enhancement of human iPSC-derived cardiomyocyte maturation by chemical conditioning in a 3D environment. *J. Mol. Cell Cardiol.* 138, 1–11. doi: 10.1016/j.yjmcc.2019.10.001

Ikeda, Y., Martone, M., Gu, Y., Hoshijima, M., Thor, A., Oh, S. S., et al. (2000). Altered membrane proteins and permeability correlate with cardiac dysfunction in cardiomyopathic hamsters. *Am. J. Physiol. Heart Circ. Physiol.* 278, H1362–H1370. doi: 10.1152/ajpheart.2000.278.4.H1362

Jackman, C. P., Carlson, A. L., and Bursac, N. (2016). Dynamic culture yields engineered myocardium with near-adult functional output. *Biomaterials* 111, 66–79. doi: 10.1016/j.biomaterials.2016.09.024

Kamdar, F., Das, S., Gong, W., Klaassen Kamdar, A., Meyers, T. A., Shah, P., et al. (2020). Stem cell-derived cardiomyocytes and beta-adrenergic receptor blockade in duchenne muscular dystrophy cardiomyopathy. *J. Am. Coll. Cardiol.* 75, 1159–1174. doi: 10.1016/j.jacc.2019.12.066

Karbassi, E., Fenix, A., Marchiano, S., Muraoka, N., Nakamura, K., Yang, X., et al. (2020). Cardiomyocyte maturation: advances in knowledge and implications for regenerative medicine. *Nat. Rev. Cardiol.* 17, 341–359. doi: 10.1038/s41569-019-0331-x

Lapidos, K. A., Kakkar, R., and McNally, E. M. (2004). The dystrophin glycoprotein complex: signaling strength and integrity for the sarcolemma. *Circ. Res.* 94, 1023–1031. doi: 10.1161/01.RES.0000126574.61061.25

Law, M. L., Cohen, H., Martin, A. A., Angulski, A. B. B., and Metzger, J. M. (2020). Dysregulation of calcium handling in duchenne muscular dystrophy-associated dilated cardiomyopathy: mechanisms and experimental therapeutic strategies. *J. Clin. Med.* 9:520.

Leonard, A., Bertero, A., Powers, J. D., Beussman, K. M., Bhandari, S., Regnier, M., et al. (2018). Afterload promotes maturation of human induced pluripotent stem cell derived cardiomyocytes in engineered heart tissues. *J. Mol. Cell Cardiol.* 118, 147–158. doi: 10.1016/j.yjmcc.2018.03.016

Long, C., Li, H., Tiburcy, M., Rodriguez-Caycedo, C., Kyrychenko, V., Zhou, H., et al. (2018). Correction of diverse muscular dystrophy mutations in human engineered heart muscle by single-site genome editing. *Sci. Adv.* 4:eaa9004. doi: 10.1126/sciadv.aap9004

Mekies, L. N., Regev, D., Eisen, B., Fernandez-Gracia, J., Baskin, P., Ben Jehuda, R., et al. (2021). Depressed beta-adrenergic inotropic responsiveness and intracellular calcium handling abnormalities in Duchenne Muscular Dystrophy patients' induced pluripotent stem cell-derived cardiomyocytes. *J. Cell Mol. Med.* 25, 3922–3934. doi: 10.1111/jcmm.16341

Mercuri, E., Bonnemann, C. G., and Muntoni, F. (2019). Muscular dystrophies. *Lancet* 394, 2025–2038. doi: 10.1016/S0140-6736(19)32910-1

Mora, M., Di Blasi, C., Barresi, R., Morandi, L., Brambati, B., Jarre, L., et al. (1996). Developmental expression of dystrophin, dystrophin-associated glycoproteins and other membrane cytoskeletal proteins in human skeletal and heart muscle. *Brain Res. Dev. Brain Res.* 91, 70–82. doi: 10.1016/0165-3806(95)00169-7

Moretti, A., Fonteyne, L., Giesert, F., Hoppmann, P., Meier, A. B., Bozoglu, T., et al. (2020). Somatic gene editing ameliorates skeletal and cardiac muscle failure in pig and human models of Duchenne muscular dystrophy. *Nat. Med.* 26, 207–214. doi: 10.1038/s41591-019-0738-2

Ozawa, E. (2010). Our trails and trials in the subsarcolemmal cytoskeleton network and muscular dystrophy researches in the dystrophin era. *Proc. Jpn. Acad. Ser. B Phys. Biol. Sci.* 86, 798–821. doi: 10.2183/pjab.86.798

Parikh, S. S., Blackwell, D. J., Gomez-Hurtado, N., Frisk, M., Wang, L., Kim, K., et al. (2017). Thyroid and glucocorticoid hormones promote functional T-tubule development in human-induced pluripotent stem cell-derived cardiomyocytes. *Circ. Res.* 121, 1323–1330. doi: 10.1161/CIRCRESAHA.117.311920

Pioner, J. M., Guan, X., Klaiman, J. M., Racca, A. W., Pabon, L., Muskheli, V., et al. (2020). Absence of full-length dystrophin impairs normal maturation and contraction of cardiomyocytes derived from human-induced pluripotent stem cells. *Cardiovasc. Res.* 116, 368–382. doi: 10.1093/cvr/cvz109

Schaaf, S., Eder, A., Vollert, I., Stohr, A., Hansen, A., and Eschenhagen, T. (2014). Generation of strip-format fibrin-based engineered heart tissue (EHT). *Methods Mol. Biol.* 1181, 121–129. doi: 10.1007/978-1-4939-1047-2_11

Tiburcy, M., Hudson, J. E., Balfanz, P., Schlick, S., Meyer, T., Chang Liao, M. L., et al. (2017). Defined engineered human myocardium with advanced maturation for applications in heart failure modeling and repair. *Circulation* 135, 1832–1847. doi: 10.1161/CIRCULATIONAHA.116.024145

**Conflict of Interest:** TE is co-founder of EHT Technologies GmbH, Hamburg.

The remaining authors declare that the research was conducted in the absence of any commercial or financial relationships that could be construed as a potential conflict of interest.

# Advantages of publishing in Frontiers

**OPEN ACCESS**
Articles are free to read
for greatest visibility
and readership

**FAST PUBLICATION**
Around 90 days
from submission
to decision

**HIGH QUALITY PEER-REVIEW**
Rigorous, collaborative,
and constructive
peer-review

**TRANSPARENT PEER-REVIEW**
Editors and reviewers
acknowledged by name
on published articles

**Frontiers**
Avenue du Tribunal-Fédéral 34
1005 Lausanne | Switzerland

**Visit us:** www.frontiersin.org
**Contact us:** frontiersin.org/about/contact

**REPRODUCIBILITY OF RESEARCH**
Support open data
and methods to enhance
research reproducibility

**DIGITAL PUBLISHING**
Articles designed
for optimal readership
across devices

**FOLLOW US**
@frontiersin

**IMPACT METRICS**
Advanced article metrics
track visibility across
digital media

**EXTENSIVE PROMOTION**
Marketing
and promotion
of impactful research

**LOOP RESEARCH NETWORK**
Our network
increases your
article's readership